Title

Pavement Recycling: Shrinkage Crack Mitigation in Cement-Treated Pavement Layers — Phase 2a Literature Review and FDR-C Test Road Construction and Monitoring

Permalink

https://escholarship.org/uc/item/31n5j963

Authors

Louw, Stephanus
Jones, David
Hammack, Joseph
et al.

Pavement Recycling:
Shrinkage Crack Mitigation in Cement-Treated Pavement Layers — Phase 2a Literature Review and FDR-C Test Road Construction and Monitoring

Authors:

Stephanus Louw, David Jones, Joseph Hammack, and John Harvey

PREPARED FOR:

California Department of Transportation
Division of Research, Innovation and System Information
Office of Materials and Infrastructure Roadway Research

PREPARED BY:

University of California
Pavement Research Center
UC Davis and UC Berkeley

TECHNICAL REPORT DOCUMENTATION PAGE

1. REPORT NUMBER UCPRC-RR-2019-05	2. GOVERNMENT ASSOCIATION NUMBER	3. RECIPIENT'S CATALOG NUMBER
4. TITLE AND SUBTITLE Pavement Recycling: Shrinkage Crack Mitigation in Cement-Treated Pavement Layers — Phase 2a Literature Review and FDR-C Test Road Construction and Monitoring	5. REPORT PUBLICATION DATE	
	6. PERFORMING ORGANIZATION CODE	
7. AUTHOR(S) Stephanus Louw (ORCID 0000-0002-1021-7110) David Jones (ORCID 0000-0002-2938-076X) Joseph Hammack John Harvey (ORCID: 0000-0002-8924-6212)	8. PERFORMING ORGANIZATION REPORT NO. UCPRC-RR-2019-05 UCD-ITS-RR-22-36	
9. PERFORMING ORGANIZATION NAME AND ADDRESS University of California Pavement Research Center Department of Civil and Environmental Engineering, UC Davis 1 Shields Avenue Davis, CA 95616	10. WORK UNIT NUMBER	
	11. CONTRACT OR GRANT NUMBER 65A0628	
12. SPONSORING AGENCY AND ADDRESS California Department of Transportation Division of Research, Innovation, and System Information P.O. Box 942873 Sacramento, CA 94273-0001	13. TYPE OF REPORT AND PERIOD COVERED Research Report	
	14. SPONSORING AGENCY CODE	

16. ABSTRACT

The California Department of Transportation has been using full-depth recycling (FDR) as a rehabilitation strategy since 2001. Early projects were recycled with foamed asphalt and cement, but cement-only treatments were permitted from 2015 to improve the properties of more marginal materials. However, shrinkage cracking associated with the hydration and curing of the cement-treated layers remains a concern, especially with regard to crack reflection through asphalt concrete surfacings and the related problems caused by water ingress.

Considerable research has been undertaken on crack mitigation, and a range of measures related to improved mix designs and construction practices have been implemented by road agencies. One of the most promising measures, used in conjunction with appropriate mix designs, is that of microcracking the cement-treated layer between 24 and 72 hours after construction. In theory, this action creates a fine network of cracks in the layer that limit or prevent the wider and more severe block cracks typical of cement-treated layers. Limited research to assess microcracking as a crack mitigation measure had been completed on a number of projects in the United States. Recommendations from these studies were first implemented by the Texas Department of Transportation and then later by other state departments of transportation. However, longer-term monitoring of a range of projects revealed that microcracking has not always been successful in preventing cracking, with some projects showing reflected transverse and block cracks in a relatively short time period, attributable to a number of factors including but not limited to cement content, cement spreading, the method of curing, and the interval between base construction and placement of surfacing.

The research discussed in this report builds on earlier work with a focus on gaining a better understanding of microcracking mechanisms and identifying key factors influencing performance, including, but not limited to aggregate properties, cement content, the time period before microcracking starts, layer moisture contents, roller weights and vibration settings, the number of roller passes, the field test methods and criteria used to assess the degree of microcracking, and the effects of early opening to traffic. In this phase of the study, a 36-cell test road was designed, constructed, and monitored to evaluate shrinkage crack mitigation procedures. The main findings from the study included revised mix design procedures based on the initial consumption of stabilizer and target unconfined compressive strengths of 450 psi (3.1 MPa) with a maximum permissible limit of 600 psi (4.1 MPa), the importance of appropriate curing, and a revised microcracking window of between 48 and 56 hours after compacting the layer. It is further recommended that a stiffness reduction target of 40% of the stiffness prior to microcracking, measured with the soil stiffness gauge, be considered instead of the current method specification.

17. KEY WORDS Full-depth recycling with cement, FDR-C, cement treatment, cement stabilization, shrinkage cracking, crack mitigation, microcracking	18. DISTRIBUTION STATEMENT No restrictions. This document is available to the public through the National Technical Information Service, Springfield, VA 22161

19. SECURITY CLASSIFICATION (of this report) Unclassified	20. NUMBER OF PAGES 323	21. PRICE None

UCPRC ADDITIONAL INFORMATION

1.	DRAFT STAGE Final	2.	VERSION NUMBER 1
3.	PARTNERED PAVEMENT RESEARCH CENTER STRATEGIC PLAN ELEMENT NUMBER 4.65	4.	DRISI TASK NUMBER 3194
5.	CALTRANS TECHNICAL LEAD AND REVIEWER(S) Alan King and Deepak Maskey	6.	FHWA NUMBER CA223194A

7. PROPOSALS FOR IMPLEMENTATION
    i) Base decision on which full-depth recycling strategy on field investigation findings.
    ii) Follow the mix design procedure recommendations in the In-Place Recycling Guide, which includes doing an initial consumption of stabilizer test.
    iii) Consider reducing the target allowable strength for FDR-C mix design strengths to 250 to 450 psi (≈1.7 MPa to 3.1 MPa), with a maximum of 600 psi (4.1 MPa).
    iv) Revise nSSP/Section 30 specification language for microcracking as follows:

        "During the period from 48 to 56 hours after compaction, microcrack the surface by applying 2 to 3 single passes, equivalent to 2.8 to 4.3 kN/cm of energy, using a 12-ton vibratory steel drum roller at maximum vibration amplitude travelling from 2 to 3 mph."

    v) Consider a performance microcracking specification that requires a 40% stiffness reduction after microcracking, measured with a soil stiffness gauge.

8. RELATED DOCUMENTS
    UCPRC-TM-2015-02; UCPRC-RR-2015-02; UCPRC-RR-2016-07; UCPRC-GL-2020-01; UCPRC-RR-2020-04

9. LABORATORY ACCREDITATION
    The UCPRC laboratory is accredited by AASHTO re:source for the laboratory testing discussed in this report

10. SIGNATURES

D. Jones **FIRST AUTHOR**	J.T. Harvey **TECHNICAL REVIEW**	C. Fink **EDITOR**	J.T. Harvey **PRINCIPAL INVESTIGATOR**	A. King **CALTRANS TECH. LEAD**	T.J. Holland **CALTRANS CONTRACT MANAGER**

Reproduction of completed page authorized

DISCLAIMER STATEMENT

This document is disseminated in the interest of information exchange. The contents of this report reflect the views of the authors who are responsible for the facts and accuracy of the data presented herein. The contents do not necessarily reflect the official views or policies of the State of California or the Federal Highway Administration. This publication does not constitute a standard, specification or regulation. This report does not constitute an endorsement by the Department of any product described herein.

For individuals with sensory disabilities, this document is available in alternate formats. For information, call (916) 654-8899, TTY 711, or write to California Department of Transportation, Division of Research, Innovation and System Information, MS-83, P.O. Box 942873, Sacramento, CA 94273-0001.

PROJECT OBJECTIVES

This study is a continuation of PPRC Project 4.52b addressing the project titled "Microcracking of Cement-Treated Layers." The objective of this project is to develop guidelines for mitigation measures to limit/prevent shrinkage cracking in cement-treated layers. This will be achieved in three phases through the following tasks (revised after completion of Phase 1):

- Phase 1: Literature review, preliminary laboratory testing, field testing, and modeling (completed)
  + Task 1: Conduct a literature review on research related to crack mitigation in cement-treated materials.
  + Task 2: Conduct preliminary laboratory testing to understand crack mitigation mechanisms and identify criteria for modeling the effects of crack mitigation on long-term pavement performance.
  + Task 3: Monitor the construction and early performance of FDR-C projects where crack mitigation measures have been used.
  + Task 3: Model the effects of crack mitigation on long-term pavement performance.
  + Task 4: Prepare a summary report with recommendations for Phase 2 testing, if appropriate.

- Phase 2: FDR-C Test Road and pilot study construction and monitoring, and laboratory testing
  + Task 1: Update the literature review.
  + Task 2: Continue monitoring the construction and performance of FDR-C field projects where crack mitigation measures have been used.
  + Task 3: Design, construct, and monitor a test road to better understand the effects of different crack mitigation strategies without the influence of traffic.
  + Task 4: Conduct laboratory testing of specimens sampled from the test road and other field projects to compare laboratory test results with measurements on constructed roads and to identify suitable criteria for refining mechanistic-empirical design procedures and performance models for pavements with cement-treated layers.
  + Task 5: Prepare research reports and guidelines for crack mitigation in FDR-C layers.

This report covers Phase 2a (Tasks 1, 2, 3, and 5) and should be read in conjunction with the report prepared for Phase 2b (Tasks 4 and 5, report number UCPRC-RR-2020-04).

EXECUTIVE SUMMARY

Introduction

Cement-treated layers are prone to cracking. This is, and has been, a concern for using cement to improve the strength and stiffness properties of recycled materials that have limited fine materials and/or plasticity. The research discussed in this report, which aims to identify appropriate shrinkage crack mitigation procedures for recycled pavement layers treated with cement, builds on previous work on microcracking as a shrinkage crack mitigation measure by the Texas Transportation Institute and others. The process involves a combination of optimum curing times before microcracking and number of roller passes (or stiffness reduction) to minimize drying shrinkage crack width, which will maximize long-term stiffness and fatigue life.

Studies by the Texas Transportation Institute and other organizations agreed that microcracking is a potentially effective shrinkage crack mitigation study. However, gaps in the knowledge were identified, specifically a full understanding of microcracking mechanisms, the influence of cement content/design strength, the optimal timing of microcracking, and roller type. This study addressed these gaps primarily through continued long-term monitoring of pilot studies, the construction and monitoring of a 37-cell test road, and a comprehensive laboratory testing study.

Summary of Research

<u>Literature Review</u>

An extensive literature review was performed to develop an understanding of how cement-treated layers fail, how the fatigue life of cement-treated layers is modeled, why shrinkage cracks are a concern, and how they can be mitigated.

<u>Test Road Design</u>

The construction of a test road to evaluate different microcracking variables was recommended after the conclusion of preliminary field studies. This allowed for the inclusion of control sections where no shrinkage crack mitigation measures were taken as well as a significantly wider factorial than could be achieved on any full-depth recycling projects with cement (FDR-C), which typically do not include control sections. The FDR-C Test Road design considered the various issues

identified during the pilot studies, literature review, and on the foundational work done in Texas. The following factors were considered in the experiment design:

- Mix design strength (2.5% and 4% cement)
- The number of curing hours between completion of construction and start of microcracking (48, 72, and 48 and 72 hours [i.e., microcracking on the same section at two different times])
- Roller weight (12-ton single drum steel roller and 10-ton double drum steel roller)
- Roller vibration amplitude (low and high settings)
- Number of roller passes (method and performance-based specifications)
- Stiffness reduction during microcracking (measured with a soil stiffness gauge and a light weight deflectometer)
- Stiffness recovery/gain after microcracking (measured with a falling weight deflectometer)
- Crack propagation and crack properties (measured during visual assessments)

<u>Test Road Construction</u>

The FDR-C Test Road was constructed over a two-day period (4% cement-content sections on day 1 and 2.5% cement-content sections on day 2). Construction and quality control procedures adhered to Caltrans guidance and specifications. Microcracking followed construction over a three-day period depending on the experiment factorial. A microsurfacing was applied after completion of the microcracking. All stages of construction were closely monitored, and observations and results indicated that the FDR-C Test Road was suitable for longer-term monitoring for the microcracking study.

<u>Test Road Monitoring</u>

Monitoring on the FDR-C Test Road included regular visual assessments focusing primarily on crack monitoring, preliminary coring to check for any indication of crushing or carbonation, and falling weight deflectometer deflection measurements, from which stiffness changes over time were backcalculated. Observations and findings include the following:

- Reflected cracks were observed in a limited number of cells on the 2.5% cement-content section. Cracks directly associated with instrumentation were not considered as cracks associated with microcracking and were therefore excluded from the analysis.
- Cracks reflected through the microsurfacing earlier on the 4% cement-content section compared to the 2.5% cement-content section.
- Crack density increased more rapidly on the 4% cement-content section compared to the 2.5% cement-content section.

- Microcracking reduced crack density compared to the results recorded on the control cells.
- Crack density generally reduced with an increase in the number of microcracking passes applied.
- The 2.5% cement-content cells had a lower crack density after 128 days than the 4% cement-content cells.
- The 2.5% cement-content cells did not show any observable trends in crack density with microcracking passes.
- Only the 4% cement-content cells microcracked after 72 hours showed a reduction in crack density with increased energy input (microcracking passes) using the single drum steel roller at high amplitude (1.42 kN/cm per pass).
- Microcracking the 4% cement-content cells after 48 hours resulted in a greater crack density reduction compared to microcracking after 72 hours. One pass after 48 hours was sufficient to reduce the crack spacing significantly. The crack density continued to reduce with increasing number of passes at 72 hours.
- The crack density results from the 10-ton double drum steel roller were inconsistent with the results from the 12-ton single steel drum roller at high amplitude. The results from the 10-ton roller showed that microcracking after 72 hours resulted in reduced cracking on both the 2.5% and 4% cement-content sections.
- Crack width was a function of microcracking effort and curing time before microcracking.
- The microcracked cells had a narrower crack-width distribution than the control cells.
- Microcracking after 48 hours resulted in narrower cracks compared to microcracking after 72 hours.
- An increase in microcracking effort (i.e., number of passes/increased energy) contributed to a further reduction in crack widths.
- The 4% cement-content control cells (i.e., no microcracking) had higher stiffnesses compared to the 2.5% cement-content control cells, as expected.
- The 2.5% cement-content cells microcracked after 48 hours had higher stiffnesses than the control cells and those cells microcracked after 72 hours.
- Increasing energy input through multiple microcracking passes reduced the long-term stiffness proportionately.

Monitoring Result Analysis

Statistical analyses of the FDR-C Test Road material testing, microcracking, crack monitoring, and stiffness results were undertaken to better understand and explain the observations on the road. Findings include the following:

- Crack density and spacing
  + Crack density increased with increasing design strength.

+ Increased energy input (i.e., number of roller passes) was most effective at reducing the crack density of the material with the higher design strength, while the lower design strength material did not show a sensitivity to energy input in terms of crack density reduction. The 2.5% cement-content material had on average one full-width reflective crack in the 49-m long cell, regardless of the microcracking input, whereas the number of reflective cracks on the 4% cement-content cells reduced from approximately seven cracks down to three cracks with increased energy input during microcracking.

+ Increased energy input was the primary factor in reducing crack width.

+ The 2.5% cement-content material had significantly less shrinkage potential (remaining shrinkage to be incurred) after microcracking than the 4% cement-content material after a given curing time. Shrinkage that continued after microcracking after 48 or 72 hours did not induce a sufficient number of cracks to minimize widths of the reflected cracks. The cracks that developed before microcracking thus controlled the reflective cracking. Microcracking earlier after final compaction (e.g., within 24 hours) could potentially yield more fine shrinkage cracks in the FDR-C layer and further minimize crack widths to mitigate reflective cracking.

+ The 4% cement-content material had significantly more shrinkage potential remaining after microcracking than the 2.5% cement-content material. The additional increase in the number of drying shrinkage cracks that developed with increased energy input during microcracking (resulting in lower strength) reduced the total width of cracks that developed before microcracking. Microcracking was performed sufficiently early on the 4% cement-content material to change the drying shrinkage cracking from a few wide reflective cracks to numerous thinner cracks with only a small number of them wide enough to reflect through the surface layer.

+ Microcracking should ideally be performed as early as possible to benefit from the shrinkage potential after microcracking while the material strength is still low.

● Stiffness

+ The long-term stiffness of the 4% cement-content material dropped significantly in the cells where the FDR-C layer was microcracked after 72 hours compared to stiffnesses recorded in the cells with microcracking after 48 hours.

+ The 2.5% cement-content material did not show a significant difference in long-term stiffness when microcracked after 48 or 72 hours.

+ Increasing the energy input (i.e., the number of roller passes) reduced the stiffness.

+ Low energy input during microcracking resulted in long-term stiffnesses exceeding those of the control cells for the 2.5% cement content section.

+ The original stiffness prior to microcracking is mostly recovered, and often exceeded, after microcracking on FDR-C layers with strengths at the lower end of the specified

range (i.e., 2.1 MPa [≈300 psi]). Stiffness is significantly reduced on higher strength layers (i.e., >3.5 MPa [≈500 psi]) after microcracking, and it may not recover to the same stiffness measured before microcracking.

+ Higher-strength layers are more sensitive to the timing of the microcracking. The greatest reduction in long-term stiffness is associated with microcracking after 72 hours, with significantly lower stiffnesses measured compared to those measured when the layer was microcracked after 48 hours. The lower strength layers were not sensitive to the time of microcracking in the 48 to 72-hour time window.

+ The mechanistic parameters measured during microcracking (percent stiffness reduction and stiffness after microcracking) did not provide any clear explanation for the trend in the FWD-backcalculated stiffness results. This was attributed in part to stiffness measurements being taken at the same fixed locations in each cell regardless of any surface distresses that may have influenced the results.

Conclusions

The following conclusions were drawn on completion of this phase of the research:

• Microcracking does not prevent shrinkage cracking, but it is an effective shrinkage crack mitigation procedure. Microcracking induces a network of fine cracks, which generally do not reflect through asphalt concrete surfacings as wide shrinkage cracks tend to do.

• Microcracking has limitations and will not mitigate all shrinkage cracks on all FDR-C projects. Design strength, construction procedures, curing time before microcracking, number of microcracking passes, and stiffness reduction achieved during microcracking will all influence the level of mitigation achieved.

• The original stiffness prior to microcracking is mostly recovered, and often exceeded, after microcracking on FDR-C layers with strengths at the lower end of the specified range (i.e., 2.1 MPa [≈300 psi]). Stiffness is significantly reduced on higher strength layers (i.e., >3.5 MPa [≈500 psi]) after microcracking, and it may not recover to the same stiffness measured before microcracking.

• Higher-strength layers are more sensitive to the timing of microcracking. The greatest reduction in the long-term stiffness is associated with microcracking after 72 hours, with significantly lower stiffnesses measured than those measured when the layer is microcracked after 48 hours.

• Microcracking will be most effective if the seven-day unconfined compressive strength falls in the range of 250 to 450 psi (1.7 to 3.1 MPa) and preferably no higher than 600 psi (4.1 MPa). Layers with design strengths greater than 600 psi will likely have shrinkage cracks forming before the road can be microcracked.

- The current Caltrans method specification for microcracking could lead to significantly different stiffness reduction results as it is currently phrased, given that 12-ton rollers from different manufacturers apply different levels of energy.

Recommendations

The following recommendations are made based on the work completed in this phase of the study:

- The mix design procedure for FDR-C layers should include an initial consumption of stabilizer tests to ensure that an optimum cement content that will result in a durable layer is selected. Starting cement content in the mix design tests should be ICS + 1%. If this results in a seven-day unconfined compressive strength higher than 600 psi (4.1 MPa), the pavement design and or choice of stabilizer/recycling agent should be reviewed.
- Microcracking will be most effective if the seven-day unconfined compressive strength falls in the range of 250 to 450 psi (1.7 to 3.1 MPa) and preferably no higher than 600 psi (4.1 MPa).
- Microcracking should be done as close as possible to 48 hours after final compaction, especially if design strengths exceed 450 psi (3.1 MPa).
- The Caltrans method specification language for microcracking should be changed to the following (the energy requirement will encourage contractors to check the ratings of their rollers):
  + During the period from 48 to 56 hours after compaction, microcrack the surface by applying 2 to 3 single passes, equivalent to 2.8 to 4.3 kN/cm of energy, using a 12-ton vibratory steel drum roller at maximum vibration amplitude travelling from 2 to 3 mph.
- If a performance specification is considered, then a maximum stiffness reduction of 40%, measured with a soil stiffness gauge is suggested (i.e., initial measurement before the first roller pass and then measurements after each roller pass until a 40% reduction is achieved).
- The research cited in the literature review and testing in this phase of the study assessed microcracking on cement-treated layers between 10 and 12 in. (250 and 300 mm) thick. Research on layers thicker than 12 in. should continue to assess whether uniform compaction and effective microcracking can be achieved over the full depth of the layer, especially on weak subgrades, and the implications on shrinkage and fatigue cracking if it cannot.
- Although the soil stiffness gauge is considered to be an appropriate instrument for measuring stiffness reduction during microcracking, testing procedures will need to be refined and precision and bias statements prepared to ensure that reasonable quality control procedures are followed.

TABLE OF CONTENTS

LIST OF TABLES

LIST OF FIGURES

LIST OF ABBREVIATIONS

AASHTO	American Association of State Highway and Transportation Officials
AC	Asphalt concrete
ACI	American Concrete Institute
AMPT	Asphalt mix performance tester
APT	Accelerated pavement testing
ASTM	American Society for Testing and Materials
Caltrans	California Department of Transportation
CL	Low plasticity gravel (USCS classification)
CSB	Cement stabilized base
CTB	Cement-treated base
DCP	Dynamic cone penetrometer
DSR	Double drum steel roller
DV	Dielectric constant value
ESAL	Equivalent single axle loads
FDR	Full-depth recycling
FDR-EA	Full-depth recycling with emulsified asphalt emulsion
FDR-FA	Full-depth recycling with foamed asphalt
FDR-N	Full-depth recycling with no stabilizer
FDR-C	Full-depth recycling with portland cement
FEM	Finite element method
FHWA	Federal Highway Administration
FWD	Falling weight deflectometer
GC	Clayey gravel (USCS classification)
GP	Poorly graded gravel (USCS classification)
HCl	Hydrochloric acid
HMA	Hot mix asphalt
HVS	Heavy vehicle simulator
ICL	Initial consumption of lime
ICS	Initial consumption of stabilizer
IDT	Indirect tensile
ITS	Indirect tensile strength
LL	Liquid limit
LTE	Load transfer efficiency
LWD	Light weight deflectometer
MC	Microcracking
MDD	Maximum dry density

OMC	Optimum moisture content
OPC	Ordinary portland cement
NCHRP	National Cooperative Highway Research Program
PCA	Portland Cement Association
PI	Plasticity index
PL	Plastic limit
RAP	Reclaimed asphalt pavement
RVE	Representative volume element
RHMA-G	Gap-graded rubberized hot mix asphalt
SC	Clayey sand (USCS classification)
SEM	Scanning electron microscope
SSG	Soil stiffness gauge
SSR	Single drum steel roller
TST	Tube suction test
TxDOT	Texas Department of Transportation
UAV	Unmanned aerial vehilce
UCPRC	University of California Pavement Research Center
UCS	Unconfined compressive strength
USCS	Unified soil classification system (ASTM)
W/C	Water to cement ratio
W/C_C	Water to cement for cementation ratio

TEST METHODS CITED IN THE TEXT

AASHTO

T 11   Standard Method of Test for Materials Finer Than 75-µm (No. 200) Sieve in Mineral Aggregates by Washing

T 27   Standard Method of Test for Sieve Analysis of Fine and Coarse Aggregates

T 89   Standard Method of Test for Determining the Liquid Limit of Soils

T 90   Standard Method of Test for Determining the Plastic Limit and Plasticity Index of Soils

T 307   Standard Method of Test for Determining the Resilient Modulus of Soils and Aggregate Materials

T 310   Standard Specification for In-Place Density and Moisture Content of Soil and Soil-Aggregate by Nuclear Methods (Shallow Depth)

ASTM

C150   Standard Specification for Portland Cement

D1557   Standard Test Methods for Laboratory Compaction Characteristics of Soil Using Modified Effort (56,000 ft-lbf/ft^3 (2,700 kN-m/m^3))

D1633   Standard Test Methods for Compressive Strength of Molded Soil-Cement Cylinders

D2049   Test Method for Relative Density of Cohesionless Soils

D2487   Standard Practice for Classification of Soils for Engineering Purposes (Unified Soil Classification System)

D6276   Standard Test Method for Using pH to Estimate the Soil-Lime Proportion Requirement for Soil Stabilization

D6931   Standard Test Method for Indirect Tensile (IDT) Strength of Asphalt Mixtures

D7830   Standard Test Method for In-Place Density (Unit Weight) and Water Content of Soil Using an Electromagnetic Soil Density Gauge

AUSTRALIAN STANDARD (AS)

AS 1289.6.8.1   Methods of Testing Soils for Engineering Purposes - Soil Strength and Consolidation Tests - Determination of the Resilient Modulus and Permanent Deformation of Granular Unbound Pavement Materials

Caltrans Test

CT 216   Method of Test for Relative Compaction of Untreated and Treated Soils and Aggregates

EUROPEAN STANDARD (EN)

EN 13286-7   Unbound and Hydraulically Bound Mixtures - Part 7: Cyclic Load Triaxial Test for Unbound Mixtures

Texas Test

Tex-144-E   Tube Suction Test

CONVERSION FACTORS

SI* (MODERN METRIC) CONVERSION FACTORS				
APPROXIMATE CONVERSIONS TO SI UNITS				
Symbol	When You Know	Multiply By	To Find	Symbol
Length				
in.	inches	25.4	millimeters	mm
ft.	feet	0.305	meters	m
yd.	yards	0.914	meters	m
mi.	miles	1.61	kilometers	km
Area				
in^2	square inches	645.2	square millimeters	mm^2
ft^2	square feet	0.093	square meters	m^2
yd^2	square yards	0.836	square meters	m^2
ac.	acres	0.405	hectares	ha
mi^2	square miles	2.59	square kilometers	km^2
Volume				
fl. oz.	fluid ounces	29.57	milliliters	mL
gal.	gallons	3.785	liters	L
ft^3	cubic feet	0.028	cubic meters	m^3
yd^3	cubic yards	0.765	cubic meters	m^3
Mass				
oz.	ounces	28.35	grams	g
lb.	pounds	0.454	kilograms	kg
T	short tons (2,000 pounds)	0.907	metric ton	t
Temperature (exact degrees)				
°F	Fahrenheit	(F-32)/1.8	Celsius	°C
Forces and Pressure or Stress				
lbf	poundforce	4.45	newtons	N
lbf/in^2	poundforce per square inch	6.89	kilopascals	kPa
APPROXIMATE CONVERSIONS FROM SI UNITS				
Symbol	When You Know	Multiply By	To Find	Symbol
Length				
mm	millimeters	0.039	inches	in.
m	meters	3.28	feet	ft.
m	meters	1.09	yards	yd.
km	kilometers	0.621	miles	mi.
Area				
mm^2	square millimeters	0.0016	square inches	in^2
m^2	square meters	10.764	square feet	ft^2
m^2	square meters	1.195	square yards	yd^2
ha	hectares	2.47	acres	ac.
km^2	square kilometers	0.386	square miles	mi^2
Volume				
mL	milliliters	0.034	fluid ounces	fl. oz.
L	liters	0.264	gallons	gal.
m^3	cubic meters	35.314	cubic feet	ft^3
m^3	cubic meters	1.307	cubic yards	yd^3
Mass				
g	grams	0.035	ounces	oz.
kg	kilograms	2.202	pounds	lb.
t	metric ton	1.103	short tons (2,000 pounds)	T
Temperature (exact degrees)				
°C	Celsius	1.8C+32	Fahrenheit	°F
Force and Pressure or Stress				
N	newtons	0.225	poundforce	lbf
kPa	kilopascals	0.145	poundforce per square inch	lbf/in^2

*SI is the abbreviation for the International System of Units. Appropriate rounding should be made to comply with Section 4 of ASTM E380.
(Revised March 2021)

Blank page

1   INTRODUCTION

1.1   Background

The California Department of Transportation (Caltrans) has been using full-depth recycling (FDR) as a rehabilitation strategy since 2001. Most projects to date have used a combination of foamed asphalt (FDR-FA) and portland cement as the stabilizing agent. However, emulsified or foamed asphalt are not always appropriate recycling strategies for all projects and therefore alternative FDR strategies need to be considered. This study investigates the use of portland cement alone (FDR-C) as a stabilizer, specifically for projects where more marginal materials are present in the recycled layer.

Cement-treated (or stabilized) materials in FDR projects are mixtures of soil, aggregate, and/or reclaimed asphalt pavement materials, together with measured amounts of portland cement and water, that are shaped and compacted to form new subbase or base layers in pavement structures. In situ subgrade soils can also be treated to improve the properties of the pavement foundation. Cement-treated layers have been widely used as pavement bases for highways, roads, streets, parking areas, airports, and materials-handling and storage areas. Because they typically have better bearing capacity and durability than bases constructed with untreated materials, they allow for thinner and usually more cost-effective pavement structures. They have been widely used in the past in California, nationally, and internationally, and considerable research has been undertaken and experience gained on their design, construction, and long-term performance. This report does not document this past research on cement-treated bases.

A well-documented concern about cement-treated layers, and therefore FDR-C layers, is the potential for shrinkage cracking associated with the hydration and curing of the treated layers. Observations of this cracking date back to ancient Roman times, when horsehair was added to concrete roadways and the structural members in buildings in an attempt to reduce the risk of cracking while the concrete set *(1)*. As hydration and curing progress, the drying shrinkage of cement-treated materials is known to contribute the most to shrinkage cracking *(2-4)*. In pavements, shrinkage cracks from underlying cement-treated layers, including FDR-C layers, can reflect through the asphalt concrete surfacing, allowing water to infiltrate into the treated layer.

Frequent cracks coupled with water infiltration leads to a loss in stiffness in the treated layer, resulting in a faster rate of overall deterioration compared to pavements that are not cracked.

Although no costs for shrinkage crack repair are readily available for California highways, the Texas Department of Transportation estimated savings of between $3.3 million and $8.6 million in annual net present value maintenance costs if shrinkage cracking could be prevented on projects where cement-treated layers are placed *(5)*.

A variety of crack mitigation approaches have been investigated in recent years, including but not necessarily limited to the following:

- Optimizing pavement designs with a specific focus on cement content and design strengths.
  + The current Caltrans non-standard special provision for FDR-C specifies a design strength range of 300 to 600 psi (≈2.0 to 4.1 MPa), considerably lower than the standard specification design-strength envelope for Class A cement-treated base layers (minimum unconfined compressive strength [UCS] of 750 psi [≈ >5.1 MPa] after a seven-day cure).
  + The Portland Cement Association recommends an FDR-C mix design strength range of 250 to 400 psi (≈1.7 to 2.8 MPa) *(6)* to limit shrinkage cracking.
- Improved construction procedures with a specific focus on curing and microcracking of the treated layers with a vibrating steel drum roller to alter shrinkage crack development patterns.

Limited unpublished research has also been undertaken to assess the influence of using small quantities of emulsified or foamed asphalt in combination with the cement to alter the hydration process and potential shrinkage.

Microcracking is currently the most commonly used shrinkage crack mitigation approach because of its relative simplicity, low cost, and measurable effect. The technique was originally developed in Austria to limit the amount of shrinkage cracking in cement-treated layers. The process entails driving a vibrating steel drum roller over the layer between 48 and 72 hours after its construction. In theory, this action creates a fine network of cracks in the layer that limits or prevents the wider and more severe block cracks typical of cement-treated layers. At the time this study started, limited testing had been completed on a number of projects in Texas, Utah, and New Hampshire. Recommendations from these studies have been implemented by Caltrans and other state departments of transportation. However, longer-term monitoring on a range of projects in

California, Texas, and other states revealed that microcracking has not always been successful in preventing cracking, with some projects showing reflected transverse and block cracks in a relatively short time period (Figure 1.1). Discussions with the Texas researchers indicated that additional research was necessary to better understand the microcracking mechanism and to identify the key factors that influence performance. These factors include, but are not limited to, aggregate properties, cement content and design strength, the time period before microcracking is initiated, layer moisture contents, curing procedures, roller weights and vibration settings, the number of roller passes applied, the time period before placing the surfacing, the time period before opening the road to traffic, and the field test methods and criteria used to assess the degree of microcracking achieved.

Figure 1.1: Reflected shrinkage cracks on an FDR-C pavement seven years after construction.

1.2 Related Studies

During the period covered by the 2011–2014 Caltrans-UCPRC Partnered Pavement Research Contract, a test track was constructed to assess four different FDR strategies (with no stabilization [FDR-N], using foamed asphalt with portland cement [FDR-FA], using emulsified asphalt [FDR-EA], and using only portland cement [FDR-C]) *(7)*. An additional microcracking experiment was included in the test track design, but problems with the control of the cement application on the day of construction prevented any testing on this lane and limited any further research at the time. A 0.2 ft. (60 mm) asphalt concrete surfacing was placed on all the reclaimed layers. Accelerated wheel-load tests with a Heavy Vehicle Simulator (HVS) were carried out on sections on the four lanes under dry and then wet conditions. Limited laboratory testing on cores sampled from the test track was also undertaken. The FDR-C sections designated for HVS testing were not

microcracked and some shrinkage cracking was observed on the tested base approximately 15 days after construction and through the asphalt concrete surfacing approximately six months after construction. Findings from the accelerated wheel load testing include the following:

- On the dry test, no cracking was observed in the asphalt concrete on the test section after more than one million wheel-load repetitions (≈43.3 million equivalent single axle loads [ESALs]) under dry conditions. However, deflection tests indicated considerable loss of stiffness in the structure during the testing period (i.e., from ±2,900 ksi [20 GPa] to ±1,885 ksi [13 GPa]), which was attributed in part to shrinkage and potentially fatigue cracking in the base and to breakdown of the cemented bonds during trafficking. Continued HVS testing on this section may therefore have led to the cracks reflecting through the asphalt concrete surface. The rut depth after testing was 1 mm.
- The wet test, started approximately 12 months after the end of the dry test, was conducted on an untrafficked section that included an original reflected shrinkage crack. New reflected shrinkage cracks were observed after approximately 100,000 load repetitions (100,000 ESALs). Water ingress through these cracks eventually led to debonding between the asphalt concrete and FDR-C layers, which in turn led to fatigue cracking in the asphalt concrete layer, starting at the shrinkage cracks, and ultimately covering most of the section during the remainder of HVS testing. Terminal cracking (0.75 ft/ft^2 [2.5 m/m^2]) was reached after 530,000 load repetitions (≈1.69 million ESALs). Localized loss of stiffness was observed in the vicinity of the reflected shrinkage cracks.

1.3   Problem Statement

Microcracking is a promising technique for limiting or preventing shrinkage cracking in FDR-C and other cement-treated layers that could reflect through asphalt concrete and other types of asphalt surfacings. However, insufficient research has been conducted to fully understand its mechanism, to develop procedures for microcracking (i.e., time interval between construction and microcracking, vibration settings, the number of microcracking cycles, etc.), and to identify suitable criteria for mechanistic-empirical design procedures and performance models of pavement structures that incorporate a microcracked FDR-C or cement-treated layer (which could theoretically have a different mechanistic behavioral life cycle than structures with FDR-C or cement-treated layers that have not been microcracked). The current Caltrans specifications currently require microcracking only on FDR-C layers, but the instructions state only that:

During the period from 48 to 72 hours after compaction, microcrack the surface by applying 3 passes of the vibratory steel drum rollers used during final compaction at high amplitude, regardless of whether asphaltic emulsion has been applied.

No additional information is provided, and no tests are required by the specification to determine whether microcracking was effective in reducing initial stiffness. The results of using this method specification had not been evaluated in California prior to the start of this UCPRC study.

At the start of this study, the following problem statements requiring additional research or refinement/calibration of existing information for California conditions were identified:

- No comprehensive guidelines exist to guide design engineers, contractors, and project specification writers on how to decide on the optimal microcracking procedure for a specific layer design and how to determine whether the desired result has been achieved.
- The research completed in Texas was limited to a small number of projects with a limited range of materials and cement contents. Subsequent observations have found that cement content, curing, and layer durability can have a significant influence on the effectiveness of microcracking. Additional research is required to determine the key factors that influence the effectiveness of microcracking. These may include but are not limited to the following:
  + Adjusting the time interval between the completion of construction and the start of microcracking
  + Selecting a specific weight of roller
  + Selecting specific vibration settings
  + Selecting one or multiple microcracking actions
  + Setting required specific changes in measured stiffness after microcracking
- There is no established procedure for accurately measuring the effectiveness of microcracking actions. Currently, a percentage change in stiffness measured with a falling weight deflectometer (FWD), light weight deflectometer (LWD), or soil stiffness gauge (SSG) is recommended. Implementable guidelines based on actual field performance need to be prepared for this activity. Consideration needs to be given to whether the load applied during FWD testing causes additional microcracking in the drop zone, thereby influencing conclusions regarding the level of stiffness change that was achieved by the roller.
- There is no procedure for simulating microcracking in the laboratory as part of a mix design/ pavement design process. Such a procedure needs to be developed.
- There is no documented research linking microcracking with layer curing, with opening to traffic, and to the period between construction and paving.
- There is no documented research investigating the use of alternative strategies to microcracking to reduce shrinkage cracking, such as adding small quantities of emulsified

or foamed asphalt or synthetic polymer emulsion to enhance crack mitigation when using microcracking or using fibers or retarders to slow the rate of hydration.

- There is limited research quantifying the benefits of microcracking in terms of extended pavement life.

1.4 Project Objective/Goal

This study is a continuation of PPRC Project 4.36 ("Guidelines for Full-Depth Reclamation of Pavements") and addresses the project titled "Microcracking of Cement-Treated Layers." The objective of this project is to develop guidelines for mitigation measures to limit/prevent shrinkage cracking in cement-treated layers. It is planned that this will be achieved in two phases through the following tasks (revised workplan after completion of Phase 1 *[8]*). Accelerated wheel-load testing was originally included in the workplan as a potential third phase but was removed with the agreement of Caltrans based on findings from the early phases of the FDR research study *(7)* and from Phase 1 of the FDR-C crack mitigation research (completed in 2016 *[2,9]*):

- Phase 1: Literature Review, Preliminary Laboratory Testing, Field Testing, and Modeling
  - Task 1: Conduct a literature review on research related to crack mitigation in cement-treated materials.
  - Task 2: Conduct preliminary laboratory testing to understand crack mitigation mechanisms and identify criteria for modeling the effects of crack mitigation on long-term pavement performance.
  - Task 3: Monitor the construction and early performance of FDR-C projects where crack mitigation measures have been used.
  - Task 4: Prepare a summary report with recommendations for Phase 2 testing if appropriate.

- Phase 2: FDR-C Test Road and Pilot Study Construction and Monitoring
  - Task 1 Update the literature review.
  - Task 2 Continue monitoring the construction and performance of FDR-C field projects where crack mitigation measures have been used.
  - Task 3 Design, construct and monitor an experimental FDR-C Test Road to better understand the effects of different crack mitigation strategies without the influence of heavy traffic.
  - Task 4 Conduct laboratory testing of specimens sampled from the FDR-C Test Road and other field projects to compare laboratory test results with measurements on

constructed roads and to identify suitable criteria for refining mechanistic-empirical design procedures and performance models for pavements with FDR-C layers.

Task 5   Prepare research reports and guidelines for crack mitigation in FDR-C layers.

This report covers Phase 2a (Tasks 1, 2, 3, and 5) and should be read in conjunction with the report prepared for Phase 2b (Tasks 4 and 5, report number UCPRC-RR-2020-04 *[10]*) and guidelines for partial- and full-depth recycling in California *(11)*.

1.5   Study Hypotheses

The hypotheses for this research are the following:

- Microcracking can mitigate the effects of drying shrinkage cracking by inducing a network of hairline cracks to relieve the restraint stress and minimize drying shrinkage crack widths.
- Improved mix design and laboratory characterization methods can increase the effective fatigue life of an FDR-C layer by accepting the presence of drying shrinkage cracks in the layer and focusing the mix design to minimize the effects of these cracks.

These hypotheses are based on the current understanding of the theoretical fatigue mechanism of cement-treated layers under traffic originally proposed by De Beer and illustrated in Figure 1.2 *(12)*. Cement-treated layers develop drying shrinkage cracks due to the restraint stresses that develop between the treated layer and the layer below it caused by volumetric reduction of the treated layer. Researchers have shown that these cracks are the starting point for other distresses due to the increased stresses and strains caused by traffic traveling over the crack *(3,13-15)*. Refining the mix design and microcracking the treated layer can improve fatigue life and reduce shrinkage crack reflection by minimizing drying shrinkage crack widths, which increases aggregate interlock and improves load transfer efficiency (LTE) across the crack. Increasing the LTE can reduce the stresses and strains adjacent to the cracks. A revised theoretical fatigue mechanism of cement-treated layers under traffic after implementing these improvements is proposed in Figure 1.3 *(16)*.

1.6   Report Layout

This research report presents an overview of the work carried out in meeting the objectives of Phase 2, Task 2 of the study, and is organized as follows:

- Chapter 2 summarizes the findings from Phase 1 and discusses an additional, more detailed forensic investigation on the test track FDR-C sections tested with a Heavy Vehicle Simulator.
- Chapter 3 summarizes the updated literature review relevant to microcracking.
- Chapter 4 details the study experimental design and the mix design for the FDR-C Test Road.
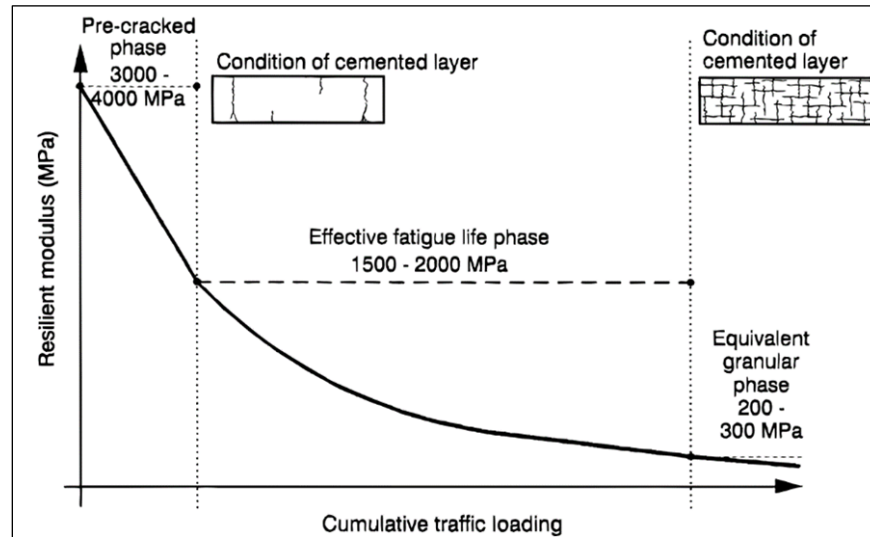
Figure 1.2: Theoretical structural life cycle of cement-treated pavement layers *(12)*.
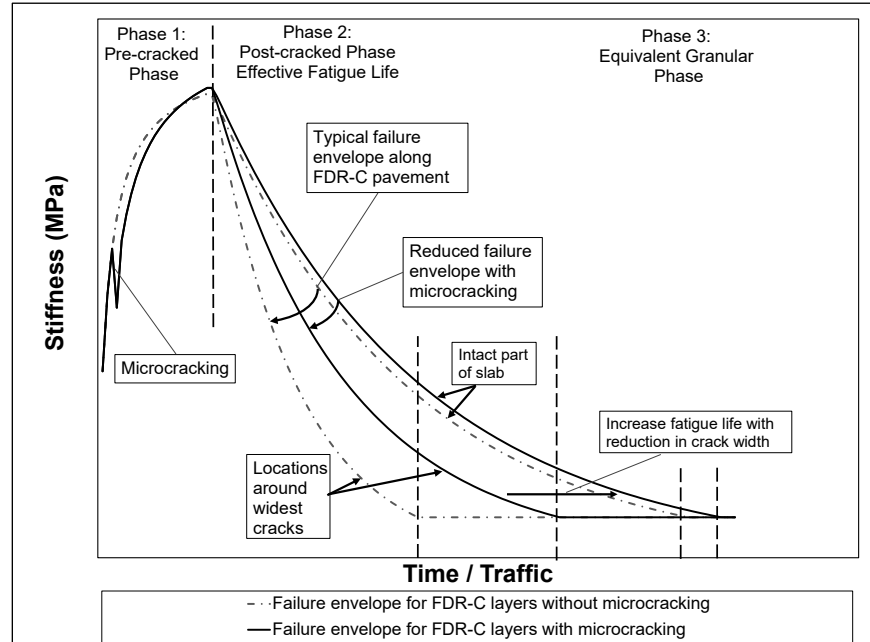
Figure 1.3: Revised theoretical structural life cycle of cement-treated pavement layers *(16)*.

- Chapter 5 details construction of the FDR-C Test Road and the microcracking program.
- Chapter 6 discusses the visual assessments and FWD testing on the FDR-C Test Road in the first 12 months after construction.

- Chapter 7 summarizes the statistical analyses of the data collected during construction, microcracking, and monitoring of the FDR-C Test Road.
- Chapter 8 provides a project summary, conclusions, and preliminary recommendations.
- Appendix A summarizes the microcracking research completed by the Texas Transportation Institute, on which the research covered in this Phase was based.
- Appendix B provides plots of the monitoring results for each cell on the test road.
- Appendix C contains soil stiffness gauge results that were used in the analyses in Chapter 7.

1.7 Measurement Units

Although Caltrans has returned to the use of US standard measurement units, metric units have always been used by the UCPRC in the design and layout of test tracks, and for laboratory, accelerated wheel load testing, field measurements, and data storage. In this report, both English and metric units (provided in parentheses after the English units) are provided in general discussion. In keeping with convention, metric units are used in the FDR-C Test Road and laboratory testing data analyses and reporting. A conversion table is provided on page xxii at the beginning of this report.

Blank page

2 SUMMARY OF FINDINGS FROM PHASE 1

The following sections summarize and supplement the findings from the Phase 1 study *(9)* and cover the longer-term monitoring of the four field test sections conducted since preparation of the Phase 1 report. No significant new relevant literature specifically on the topic of microcracking of full-depth recycled pavements with cement treatment (FDR-C) was located since completion of the literature review discussed below. A more detailed literature review on factors influencing shrinkage cracking in cement treatment layers in general is discussed in Chapter 3.

2.1 Initial Literature Review

An initial review of the literature on shrinkage crack mitigation revealed that microcracking in combination with appropriate cement-content determination is likely the most appropriate approach to be implemented in California at this time given the research already conducted. However, other approaches, especially the investigation of hybrid stabilizers (e.g., cement with emulsified asphalt) deserve further investigation for possible future application. The literature review also identified a range of devices that could be used for measuring the effect of microcracking on the stiffness of cement-treated layers. Each device has limitations that have not been fully quantified in terms of either their suitability for verifying whether microcracking has resulted in satisfactory stiffness reduction and/or their applicability as a microcracking quality control procedure on construction projects. These issues are being considered in this Phase 2 study.

2.2 Phase 1 Field Testing

Performance models developed for pavements rehabilitated with FDR-C all assume that construction followed specifications with uniform cement distribution, appropriate curing, and effective bonding between the FDR-C and asphalt concrete surfacing. Four FDR-C projects were monitored to evaluate construction procedures and deviations from specifications on shrinkage cracking and other distresses. Project details are provided in Table 2.1. Unfortunately, none of the projects included control sections with no microcracking and therefore evaluations could not be based on a comparison of sections with and without microcracking. Construction,

microcracking, and initial stiffness measurements are discussed in the Phase 1 report *(9)* and are not repeated in this report. Long-term performance evaluations and FWD tests results, along with observations considered relevant to further analysis of the FDR-C Test Road and the Phase 2b laboratory testing are discussed in Sections 2.2.1 and 2.2.2.

Table 2.1: Summary of FDR-C Projects Evaluated

Project	Agency	Location	FDR-C Thickness (mm [ft.])	7-Day UCS Strength (MPa [psi])	Cement Content (%)
CR32B	County	Yolo	350 [1.15]	3.4 [500]	4.0[a]
CR27	County	Yolo	350 [1.15]	2.8 [400]	3.0
CR99	County	Yolo	300 [1.00]	2.4 [350]	4.0
PLU-147	Caltrans	Plumas	260 [0.87]	2.4 [350]	2.5 and 4.0[b]

[a] An additional 2.0% cement was added to the first 833 ft. due to construction issues.
[b] Two mix designs were prepared for this project to accommodate changes in material properties. The cement content changed from 2.5% to 4.0% at station 8250.

2.2.1 Long-Term Performance

Road CR32B

Construction generally followed standard specification procedures. Project specifications required that microcracking reduce the initial stiffness by 40%, as measured with an SSG before microcracking at each test location. Stiffness was measured after every two microcracking passes. Between two and four roller passes were required to achieve this target. Microcracking was done with either a 12-ton single drum steel roller or a 10-ton dual drum steel roller between 48 and 72 hours after completion of final compaction.

Over the initial 36-month monitoring period, and subsequent monitoring since then, extensive longitudinal and some transverse cracking were observed in both directions (Figure 2.1 and Figure 2.2). Cracks were mostly attributed to shrinkage associated with cement accumulations in overlap areas and those caused by dragging hoses during construction (discussed in Section 2.2.2).

Backcalculated falling weight deflectometer (FWD) test results (backcalculated using *CalBack* software) are plotted in Figure 2.3. The results show that stiffness continued to increase in the 15 months after construction and then plateaued thereafter (the last measurement was in June 2020). However, there was a significant range in stiffnesses along the road (note the difference

between minimum and maximum stiffness in Figure 2.3), attributed to material variability, early distresses, and other factors discussed in Section 2.2.2. The lowest stiffnesses were those recorded around shrinkage and other cracks.

Figure 2.1: CR32B: Example longitudinal cracks.

Figure 2.2: CR32B: Example transverse cracks.
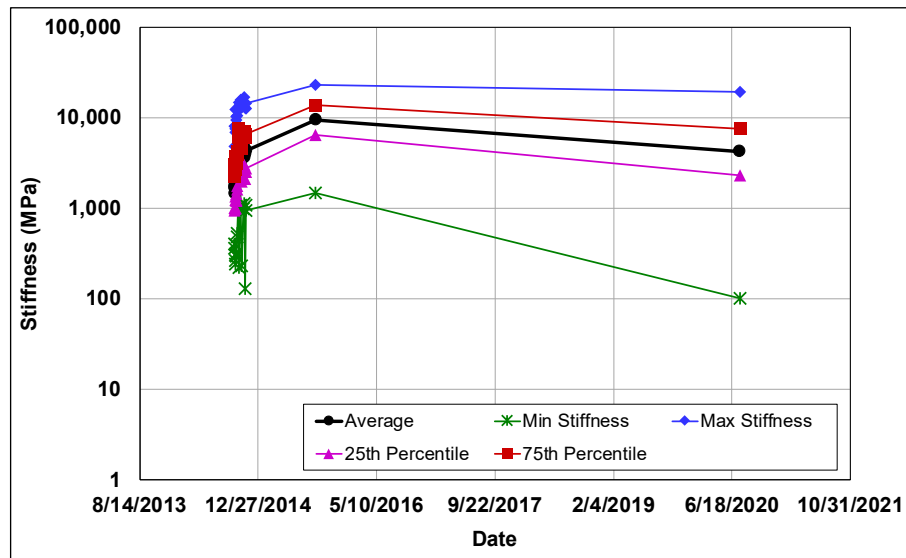
Figure 2.3: CR32B: Backcalculated FWD stiffnesses over time.

Road CR27

Construction generally followed Caltrans specifications. Deviations from standard practice included the timing of compaction after stabilization, which required that final compaction be completed within two hours after the start of mixing the materials. One section was compacted 16 hours after recycling, and another 5 hours after recycling. The material at either end of the project also had a finer gradation compared to the material in the center of the project, but this was not accounted for in the mix design. Microcracking followed the 2015 Caltrans specifications

with three passes applied between 48 and 72 hours after completion of final compaction using a 12-ton single steel drum roller.

No distresses were noted during the 36-month monitoring period and no additional FWD testing beyond that reported in the Phase 1 study was conducted.

Road CR99

Construction on this project generally followed Caltrans specifications. Deviations from standard practice included overworking (filling of low spots after padfoot roller compaction) of the material with the grader. This led to areas with material segregation, disintegration of the layer on the crown, and delaminations that were fixed by mixing the loose, segregated material with cement and water and then recompacting it. Microcracking followed the 2015 Caltrans specifications, with three passes applied between 48 and 72 hours after completion of final compaction using a 12-ton single steel drum roller.

No distresses were noted during the 36-month monitoring period and no additional FWD testing beyond that reported in the Phase 1 study was conducted.

Road PLU-147

Construction on this project generally followed standard specification procedures. Deviations from standard practice included not using a push bar between the water tanker and the reclaimer, which resulted in the water hose dragging cement along the road and accumulating it at the end of the section, and only applying one microcracking pass with a single steel drum roller between 24 and 48 hours after completion of final compaction.

Over the 36-month monitoring period, five transverse cracks were observed in areas of known cement accumulations (Figure 2.4 and Figure 2.5). Cracks were mostly attributed to shrinkage associated with these cement accumulations in overlap areas and those caused by dragging hoses (discussed in Section 2.2.2).

Figure 2.4: PLU-147: Example transverse crack.

Figure 2.5: PLU-147: Example transverse crack.

Backcalculated FWD test results are plotted in Figure 2.6. The results show that the stiffness increased after construction, then decreased during early trafficking, and then plateaued for the remainder of the monitoring period (the last measurement was in August 2020). Similar to CR32B, there was a notable range in stiffnesses along the road, attributed to material variability, early distresses, and other factors discussed in Section 2.2.2. The lowest stiffnesses were those recorded around the shrinkage cracks. There was limited difference in stiffness between the 2.5% and 4% cement-content sections, indicating that using two mix designs for the different materials on the projects was appropriate.
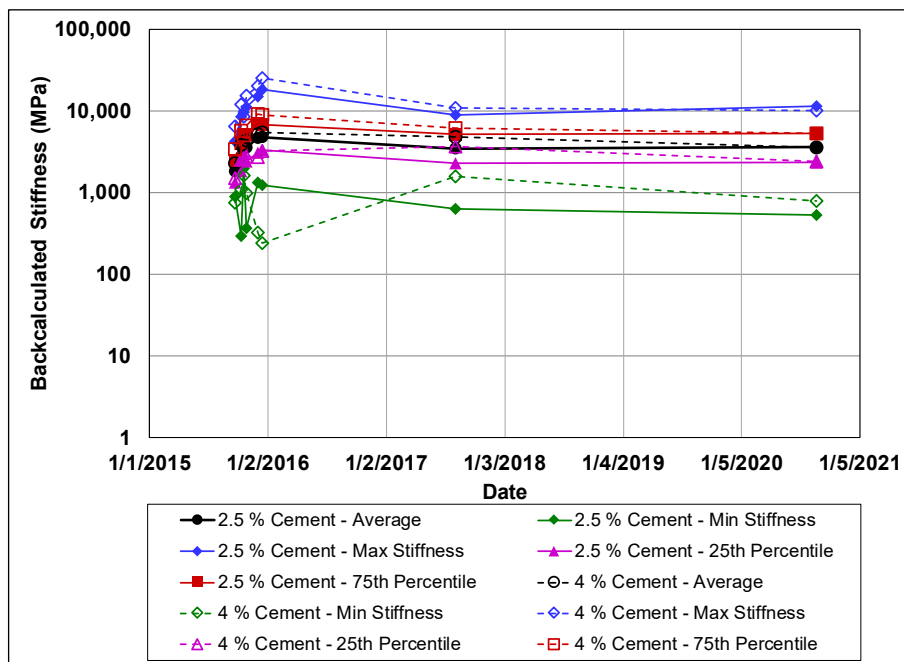
Figure 2.6: PLU-147: Backcalculated FWD stiffnesses over time.

2.2.2 Observations Taken into Considerations for the FDR-C Microcracking Study

Visual assessments and SSG measurements, followed by FWD measurements after the roads were pave,d were all undertaken as part of the investigation. The following observations were made over the evaluation period (up to June 2020):

- There was a wide variation in pavement materials and in pavement construction quality across the four projects. On the county road projects, where minimal sampling and testing appears to have been carried out in the project assessment phase, the mix designs did not necessarily accommodate the variation in materials and pavement conditions.

- In addition to being useful for assessing unbound layer thicknesses and the subgrade conditions of the existing road prior to full-depth recycling, dynamic cone penetrometer (DCP) tests can also provide a quick indication of weak areas on the project after final compaction.

- The SSG can provide repeatable and reproducible results provided that the testing method is strictly adhered to and that operators are suitably trained and experienced. The device is useful for measuring/checking stiffness gain over time in the period between final compaction and microcracking, for determining the number of roller passes required to achieve a satisfactory level of stiffness reduction by microcracking, and for checking that a satisfactory decrease in stiffness was achieved after microcracking. It can also be used to check areas suspected of having too little or too much cement, especially those areas at the beginning and end of construction sections, and in lane-overlap areas. However, the rate at which SSG testing can be conducted is slower than the pace of construction activities and more than one SSG may be required on site on the day of microcracking to keep up with the equipment.

- FWD testing provided useful insights into the stiffness change in FDR-C layers over time and how this change is affected by material variability, the distribution of cement during construction, the effectiveness of the microcracking process, and the appearance of cracks.

- FWD and SSG results both indicate that microcracking does result in an immediate and notable drop in stiffness in the FDR-C layer after the procedure has been completed. However, much of the stiffness was recovered by recementation in the days after microcracking, after which stiffness appeared to plateau. Stiffness change over time appears to be influenced by temperature; however, insufficient data have been collected to draw any firm conclusions about longer-term performance.

- Specifications are not always being followed to the fullest extent by contractors and they are not being fully enforced by agency engineers. This was attributed to limited agency resources and a lack of understanding of the specifications and the associated consequences of not following them closely. Resident engineers and inspectors should be

encouraged to decline requests for deviations from the specification if they are inexperienced with FDR and therefore unable to fully understand the potential impacts to pavement performance. Examples include the following:

+ Dragging of the water hose connecting the reclaimer and the water tanker was evident on all four projects (Figure 2.7). This led to accumulations of cement along one of the edges of a construction section and at the ends of each section, resulting in areas with cement contents both above and below the design content. The Caltrans FDR-C specifications require that the water pipe be fastened to a push-bar connecting the recycler and water tanker. However, this requirement was not adhered to by the contractors or enforced by the resident engineers. When asked, contractor site personnel noted that push bars can slow the progress and cause damage to water tankers (equipment manufacturers disagree that damage will be caused to equipment when using a correctly installed push-bar).

+ In some instances, hoses between the reclaimer and the water tanker did not have effective non-return valves, which led to water spills during water tanker changes. At several locations on projects, accidental disconnects also resulted in soft, wet areas (Figure 2.8 and Figure 2.9). The increased water content in these areas resulted in localized poor compaction and increased the risk of cracks associated with the potential for increased autogenous and drying shrinkage.

Figure 2.7: Hose dragging cement.

Figure 2.8: Water spill during tanker change.

Figure 2.9: Wet spot from spill still visible after final compaction.

+ Accumulation and redistribution of cement in front of the reclaimer mixing chamber as it proceeded along a section was observed on all four projects (Figure 2.10). This excess cement was deposited at the end of the construction section (Figure 2.11), resulting in localized areas where the cement content was significantly higher than the design cement content and the cement content of the surrounding areas. This results in isolated areas of high cement content, which will perform differently to areas with the target cement content. Additional drying shrinkage can be expected from these areas because of the extra cement. Reflected shrinkage cracks in the known vicinity of cement accumulations were noted on two of the four projects assessed (Figure 2.12). The problem can be controlled by adjusting pressure settings on the mixing chamber doors.

+ Overlaps in cement spreading where cement had already been spread or mixed were also noted (Figure 2.13). This effectively results in a doubling of the design cement content in localized areas, which can lead to shrinkage cracking in those areas as noted previously.

Figure 2.10: Cement redistribution in front of mixing chamber.

Figure 2.11: Accumulation of cement at end of recycling section.

Figure 2.12: Early shrinkage crack in the vicinity of known cement accumulation.

Figure 2.13: Cement spreading overlaps.

+ Depth control issues associated with prepulverization were observed on all projects in that the prepulverization depth was equal to the design depth instead of the generally

recommended 2 in. (50 mm) less than the design depth. Following the recommended guidance ensures that the reclaimer operator positions the drum correctly in subsequent passes and that no untreated pulverized material is left beneath the recycled layer. On one of the projects, the road was prepulverized to the design recycling depth of 1.15 ft. (350 mm), after which the 0.4 ft. (125 mm) was removed to accommodate the 0.4 ft. of asphalt concrete surfacing so that final levels matched the existing road. After cement spreading, the reclaimer recycled to the 1.15 ft. design depth. This all resulted in a decrease of 11% and 14% RAP and aggregate base, respectively, and an increase of 25% of the subbase/subgrade in the FDR-C layer compared to the combined material proportions that were used in the mix design. Consequently, the materials in the FDR-C layer on the road were notably different to those used in the mix design. Site balancing requirements must be taken into consideration when sampling for mix design testing to ensure that representative materials are tested and that strengths on the road are consistent with those achieved in the mix design.

+ After opening to traffic, vehicle speeds on the compacted FDR-C layer prior to microcracking and placing the asphalt concrete surfacing were often equal to or higher than the normal speed limit for the road, and considerably higher than the posted limit in the construction zone. This led to rapid raveling of the surface and increased surface roughness on projects where water curing was used. Speed limits should be strictly enforced in construction zones, both for safety reasons and to preserve the newly constructed surface.

+ Microcracking often identified areas of poor construction including isolated block cracking in areas of known accumulation of cement resulting from dragging hoses or overlaps (Figure 2.14), sliver fills (i.e., when thin lifts of material are bladed onto the FDR-C layer surface to meet grade requirements [Figure 2.15]), and inadequate water curing (i.e., not maintaining a constant moisture content on the FDR-C layer, leading to multiple wetting and drying cycles that in turn leads to carbonation on the top of the surface). In many instances the distressed material could be removed by light brushing (Figure 2.16), and spraying phenolphthalein after brushing indicated that carbonation had often occurred (i.e., no color reaction in the sprayed area when compared to intact areas [Figure 2.17]).

+ FDR-C layers were not broomed on any of the projects prior to spraying the tack coat in preparation for the asphalt concrete surfacing. Brooming is required in the Caltrans FDR-C specifications. Without bonding between layers, the effective pavement thickness is reduced, and can result in premature fatigue failure of the surface layer.

Figure 2.14: Block cracking after microcracking in known area of cement accumulation.

Figure 2.15: Sliver fill damaged by microcracking.

Figure 2.16: Distressed area after microcracking attributed to inappropriate curing.

Figure 2.17: Carbonated area (no color in sprayed area) attributed to inappropriate curing.

2.3   Phase 1a: Laboratory Microcracking Methods

Preliminary laboratory testing was undertaken to identify methods that can be used to simulate microcracking of laboratory-prepared specimens. Three laboratory-scale microcracking methods were considered. Based on observations of the specimens before and after microcracking, the method that uses a dual steel drum vibrating roller to microcrack specimens in a specially constructed pit appeared to provide the best results of the three approaches.

2.4   Phase 1b: Preliminary Laboratory Testing

The stiffness results from laboratory testing on specimens prepared using the techniques described previously were, however, considered to be inconclusive and generally too low compared to backcalculated FWD stiffnesses on projects where samples were taken. Factors contributing to this include the following:

- The sensitivity to confining stress of the resilient modulus of FDR-C materials determined using the conventional AASHTO T 307 setup suggested that the material behaves more like an unbound material, which is unlikely given its cemented nature.

- Testing with the conventional AASHTO T 307 setup could not effectively differentiate between the different cement contents of different curing intervals.

- The resilient modulus test results did not accurately reflect the expected effects of microcracking (i.e., they were not similar to those measured on field projects with a stiffness gauge), cement content, and curing time of the laboratory-compacted specimens. The primary reason for this was attributed to the laboratory microcracking procedures developed in Phase 1a not being representative of actual microcracking procedures on FDR-C projects. The approach did not appear to reduce the stiffness of the samples in a repeatable and consistent manner, and in many instances it resulted in cracking and disintegration of the specimens.

- The large variability in the resilient modulus results from tests on both the control and microcracked specimens points to the compaction method that was followed. Based on previous findings from earlier UCPRC research on FDR with foamed asphalt, the sample preparation (quartering and batching) and mixing method were considered to be consistent and unlikely to have contributed much to the variability. However, the compaction method used, although consistent with the AASHTO T 307 method, was considered to be too operator dependent and probably a significant contributor to the variability.

- The brittleness of the laboratory-compacted FDR-C samples caused the edges of the specimens to chip during handling and testing, which in turn led to tears in the latex membrane used for confining the specimen during testing. These tears led to a loss of confinement, which might also have contributed to the wide variation in the test results.

2.5 Observations from the FDR-C Accelerated Wheel Loading Test Section

A more detailed forensic investigation of the two FDR-C sections, tested as part of the FDR accelerated wheel loading study on the UCPRC test track *(7)*, was carried out to better understand the origins and causes of cracks on both the trafficked and untrafficked areas. This work complements the initial forensic investigations conducted on the track *(7)*. These additional investigations covered crack patterns, crack widths, and the effect of different crack types on the FDR-C layer stiffness.

2.5.1   Summary of the FDR-C Test Track Lane History

A summary of the events that occurred on the FDR-C test track lane is provided in Table 2.2. The events include construction, FWD testing, HVS testing, and forensic investigations. Figure 2.18 provides a plan view of the FDR-C lane that had two cells built with 5% and 6% cement, the two HVS test sections in the cell with 5% cement, and the forensic test pit. A short overview of each event is discussed below to provide context for the discussion on the crack investigation.

Table 2.2: History of Events on the FDR-C Test Track Lane

Days after Compaction	Event	Location
0	FDR-C test track lane construction	Entire lane
57	Asphalt concrete layer placement[1]	Entire lane
67, 68	FWD testing along entire lane at 1.2 m intervals	Entire lane
287, 288	FWD testing before HVS testing under dry conditions	Dry HVS test section
308	Start of HVS testing under dry conditions[2]	Dry HVS test section
405	End of HVS testing under dry conditions	Dry HVS test section
588, 592	FWD testing after testing under dry conditions	Dry HVS test section
788, 789	FWD testing before HVS testing under wet conditions	Wet HVS test section
868	Start of HVS testing under wet conditions[2]	Wet HVS test section
957	End of HVS testing under wet conditions	Wet HVS test section
1,047	FWD testing after HVS testing under wet conditions	Wet HVS test section
1,182	FWD testing after long term curing after HVS testing	Wet HVS test section
1,712	Forensic investigation	Through both sections

[1] The gap between recycling and placing of asphalt concrete is not typical and was due to contractual issues.
[2] Period between completion of construction and start of HVS testing was due to testing on other FDR sections being completed prior to start of testing on the FDR-C sections.
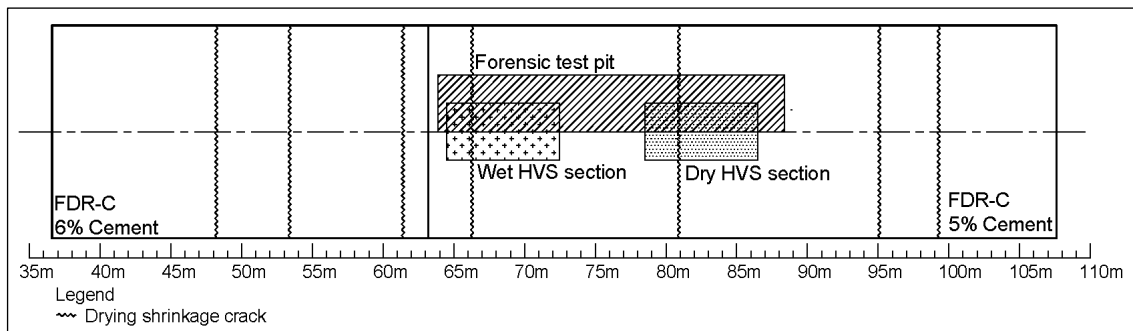
Figure 2.18: Layout of test sections and shrinkage cracks on the FDR-C test track lane.

The pavement design was 0.2 ft. (60 mm) of hot mix asphalt over 0.85 ft. (250 mm) FDR-C, over 1.0 ft. of Class 2 aggregate base over silty clay subgrade. The FDR-C layer consisted of the materials recycled from the previous HVS testing study (gap-graded rubberized hot mix asphalt [RHMA-G] with and without warm-mix additives), including 25% RHMA-G, 25% hot mix asphalt

(HMA), and 50% aggregate base. Standard FDR-C construction procedures were followed. The FDR-C layer was not microcracked as part of the study.

<u>FWD Testing</u>

The first set of FWD tests was done after the asphalt concrete layer was placed. This testing was performed along the centerline of the lane at 1.2 m (≈4 ft.) intervals (Figure 2.19). Additional FWD tests were done before and after each HVS test.
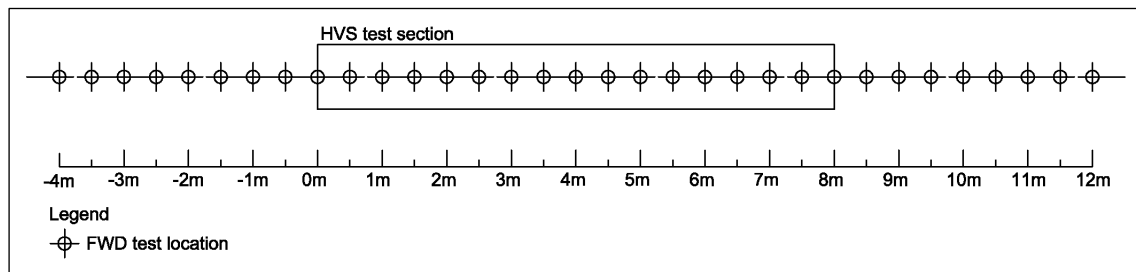
Figure 2.19: FWD testing layout on the HVS test sections.

<u>HVS Testing</u>

The HVS loading programs for testing under dry and wet conditions are summarized in Table 2.3. The main observations relevant to this Phase 2 study from testing under dry conditions were the following:

- There were no visible reflected drying shrinkage cracks on the section at the start of the test.
- Minor rutting attributed to densification in the asphalt concrete was measured over the course of the test. Although no surface cracks were observed at the end of the test, significant reductions in stiffness implied that the FDR-C layer was damaged and that cracks would have appeared if trafficking had been continued.

The main observations from testing under wet conditions were the following:

- One shrinkage crack at Station 66.0 m had reflected through the asphalt concrete layer prior to the start of the test.
- The section was considered failed after 530,000 load repetitions (≈1.7 million equivalent single axle loads [ESALs]) based on the crack density criteria, which exceeded 2.5 m/m² (0.76 ft./ft²). Apart from the one reflected shrinkage crack, fatigue cracks were predominantly in the asphalt concrete layer and were caused by debonding between the asphalt concrete and FDR-C layers, which resulted in high tensile stresses at the bottom of

the asphalt concrete layer. Trafficking was continued beyond the point of failure to observe behavior as the cracking intensified.

Table 2.3: Summary of HVS Loading on FDR-C Test Sections

Load	Dry Test		Wet Test	
(kN)	Repetitions	ESALs	Repetitions	ESALs
40	315,000	315,000	315,000	315,000
60	200,000	1,098,028	200,000	1,098,028
80	235,000	4,319,106	235,000	4,319,106
100	810,565	38,030,837	250,000	11,729,731
Total	1,560,565	43,762,970	1,000,000	17,461,864

Reflected Drying Shrinkage Cracks

Surface cracking outside of the HVS test sections on the FDR-C lane was not closely monitored over the duration of the project. Reflected drying shrinkage cracks were observed between one and five years after construction. The test track was closed to all traffic and none of the cracking was therefore attributed to traffic loading. The reflective drying shrinkage crack at Station 81.0 m (Figure 2.18) only appeared one year after completion of HVS testing and extended across the width of the lane. Since no other cracks reflected through the asphalt concrete after HVS testing, this crack was also considered to be a reflected drying shrinkage crack. The reflected drying shrinkage cracks observed on the track on completion of all testing (i.e., prior to the test track being reconstructed) are plotted in Figure 2.20 relative to the HVS sections and the different cement contents.
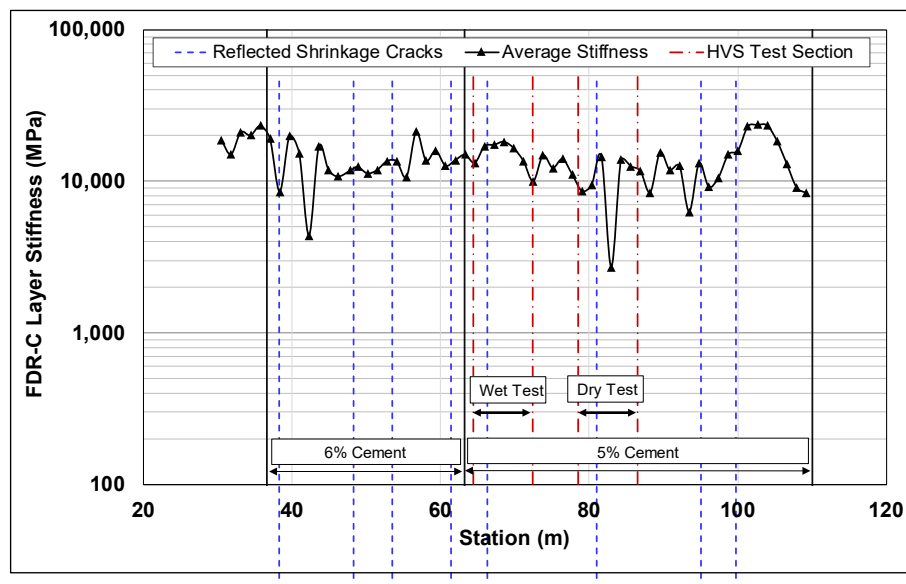
Figure 2.20: Shrinkage crack location and stiffnesses (67 days after construction).

The backcalculated FDR-C layer stiffnesses, collected 67 days after construction, are also shown in the figure. There appears to be no significant difference in stiffness between the different cement content sections. The sharp reductions in stiffness at some stations along the length of the project coincided with the location of the reflected shrinkage cracks. The large drop in stiffness at Station 83 m (272.3 ft.) was attributed to a pressure cell that was installed in the FDR-C layer at that location.

FDR-C Layer Stiffness Change

FWD testing before and after HVS testing was focused on assessing the effect of temperature at each given test interval since the FDR-C layer was expected to have some temperature sensitivity due to the layer consisting of 50% recycled asphalt and 50% aggregate base. Two sets of FWD tests were completed to check this sensitivity. Each set included tests performed when the surface temperature was below and above 25°C (77°F). Backcalculated stiffnesses were normalized to 40 kN (9,000 lb.) to remove any stress sensitivity and to 25°C to account for any temperature sensitivity. Note that a longer-term set of FWD tests on the wet HVS test section, collected four months after HVS testing could not be normalized to 25°C since both datasets were collected in the winter months when the pavement temperature did not exceed 20°C (68°F). This dataset was therefore normalized to 15°C (59°F). The apparent increase in stiffness of the longer-term data was attributed to the lower normalized temperature of this dataset. The very low stiffness adjacent to the crack in this dataset was attributed to thermal contraction at the lower temperatures, which would have led to an increased crack width and reduced load transfer efficiency across the crack.

Backcalculated FDR-C layer stiffnesses determined before and after each HVS test are provided in Figure 2.21 and Figure 2.22, for the dry and wet sections, respectively. The results show that the stiffness reduction, or damage, was most pronounced around the drying shrinkage cracks, with the lowest stiffnesses of 1,500 MPa and 4,500 MPa for the dry and wet tests, respectively. The lower stiffnesses/higher damage recorded on the dry section were attributed to the higher number of ESALs applied to this section.

Figure 2.23 summarizes the change in layer stiffnesses over time.
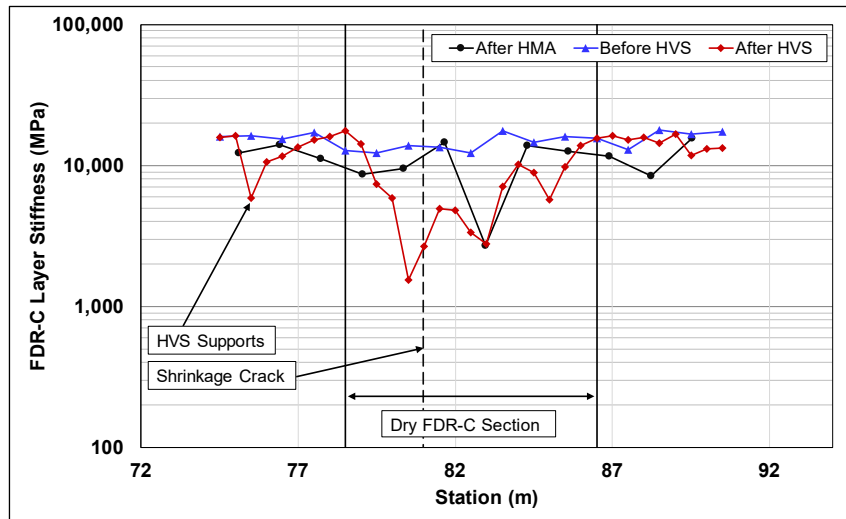
Figure 2.21: Backcalculated FWD stiffnesses on the dry HVS test section.
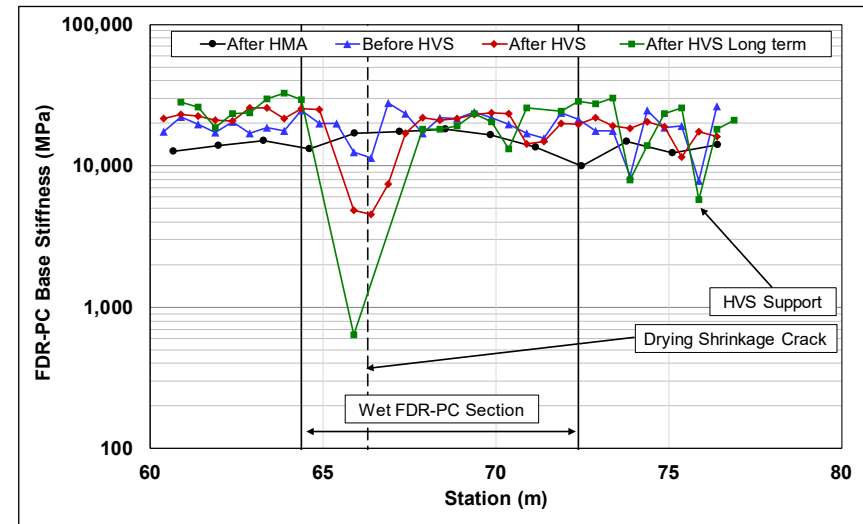
Figure 2.22: Backcalculated FWD stiffnesses on the wet HVS test section.
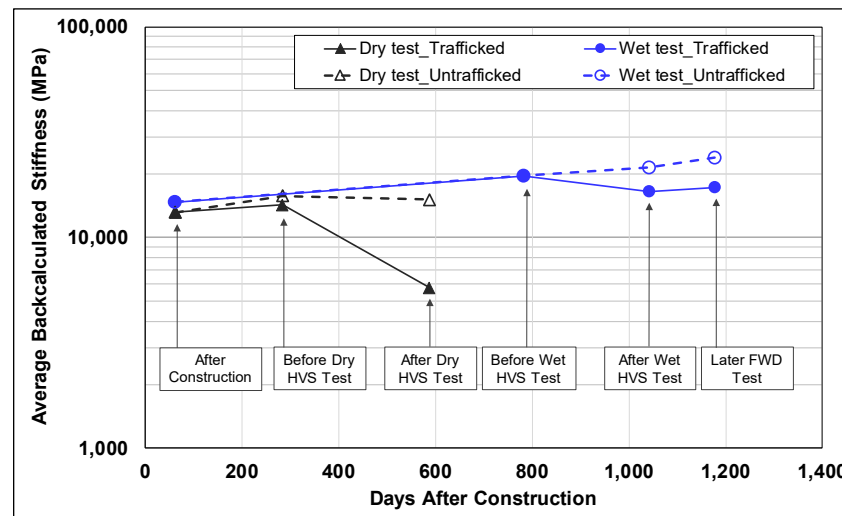
Figure 2.23: Change in FDR-C layer stiffness over time.

The effect of HVS trafficking on the dry and wet sections is clearly shown by comparing the reduction in stiffnesses in the trafficked areas compared with that in the untrafficked areas. The mean FDR-C layer stiffness for the dry section across the trafficked area reduced from 14.3 to 5.8 GPa (≈2,074 to 841 ksi), and for the wet section, it reduced from 19.8 to 18.2 GPa (≈2,872 to 2,640 ksi). The average stiffness change over time of the untrafficked areas indicates that the stiffness of the FDR-C layer continued to increase after the asphalt concrete surfacing was placed, attributed to continued hydration/curing of the layer.

These FWD test results were consistent with those discussed in other similar studies *(17)*, which noted that damage in cement-treated layers was more pronounced around drying shrinkage cracks. Excluding these results from analyses can have a significant impact on fatigue model prediction results, which could lead to overestimating the life of FDR-C layers.

2.5.2   Forensic Investigation

A longitudinal forensic test pit (Figure 2.18) was excavated through both test sections and the space between them to relate the structural condition of the FDR-C layer to the backcalculated stiffness results. The test pit was 24 m (≈78 ft.) long, 1.0 m (≈3 ft.) wide, and 310 mm (≈1 ft.) deep (i.e., excavated to the bottom of the FDR-C layer). One side of the pit was cut through the centerline of the sections to provide a clean, visible profile of the FDR-C layer to locate and identify cracks. The plan for the test pit was to identify and locate the following:

- Drying shrinkage cracks
- Fatigue cracking
- Horizontal cracking in the FDR-C layer
- Crushed material
- Debonding between the asphalt concrete surfacing and the FDR-C layer

Crack widths were measured to the nearest 0.1 mm (0.004 in.) using either a crack-width gauge (Figure 2.24) or a crack measuring microscope (Figure 2.25). Cracks and debonding were measured in relation to the location of the HVS, the test area, and other shrinkage cracks.
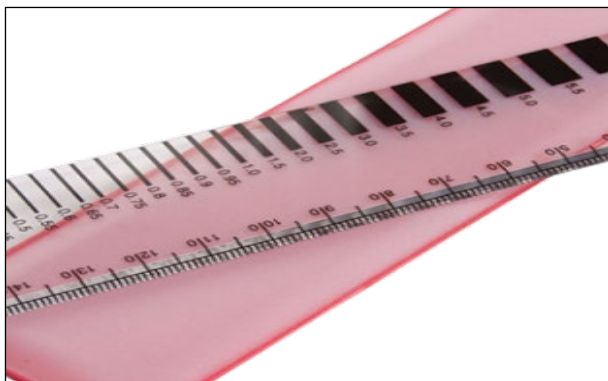
Figure 2.24: Crack width gauge.

Figure 2.25: Crack measuring microscope.

<u>Crack Type and Crack Location</u>

The distinction between drying shrinkage cracks and fatigue cracks in the FDR-C layer was made primarily based on the location of the crack relative to the test sections, the crack spacing, and the distance to adjacent reflective cracks. The following process of elimination was used to determine the likely cause of each crack:

- Identify any visible drying shrinkage cracks (reflected cracks outside the trafficked areas). These could be present anywhere along the entire lane and were classified based on one or more of the following criteria:
  + Any cracks in the FDR-C layer that were identified from the FWD test results prior to any HVS trafficking.
  + Any cracks in the FDR-C layer that reflected through the asphalt concrete surfacing due to thermal expansion and contraction of the FDR-C layer before HVS trafficking.
  + Any cracks in the FDR-C layer that were located approximately midway between two existing drying shrinkage cracks. These cracks could be located anywhere within the FDR-C layer and have either a top-down or bottom-up initiation pattern. The authors hypothesized that top-down cracks occurred due to evaporation of moisture from the top of the FDR-C layer during the curing phase after construction. This could have resulted in a moisture gradient in the FDR-C layer, resulting in tensile stresses at the surface of the layer due to the volumetric reduction. Bottom-up cracks would have been caused by the frictional forces between the FDR-C layer and the subbase as the FDR-C layer contracted due to hydration.
- Look for cracks caused by obvious flaws (e.g., instrumentation cables).
- Identify cracks or other distresses (e.g., crushing) not caused by drying shrinkage or trafficking (e.g., those caused by the HVS supports).

- Determine the cause of cracking in areas outside the trafficked areas, which would most likely be drying shrinkage cracks. Spacing between already identified drying shrinkage cracks were key.
- Confirm that fatigue cracks should only be present in the trafficked areas. These would have a bottom-up initiation pattern caused by tensile strains at the bottom of the FDR-C layer due to wheel loading, or at the bottom of the asphalt concrete layer if this layer had debonded from the FDR-C layer. The spacing of these cracks could be random.
- Look for horizontal cracks or layering in the FDR-C layer. These would be attributed to poor compaction, material segregation, excessive blading during construction, and/or carbonation during curing.

Photographs of the cracks in the test pit are provided in Figure 2.26 through Figure 2.28. The location and length of the cracks are illustrated in Figure 2.29 relative to the HVS test sections. Cracking observations are summarized in Table 2.4.

Figure 2.26: Dry FDR-C test section.

Figure 2.27: Area between dry and wet test sections.

Figure 2.28: Wet FDR-C test section.
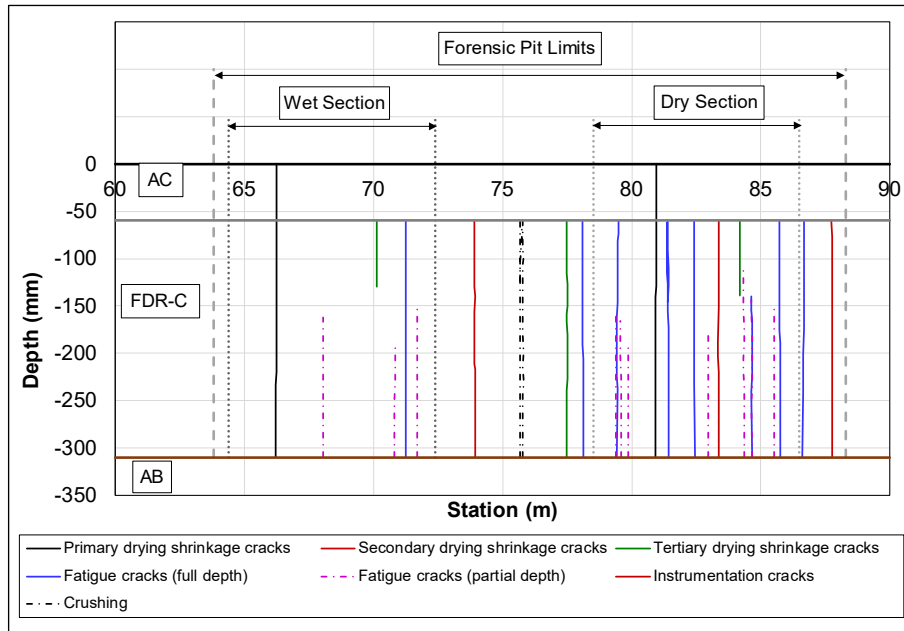
Figure 2.29: Locations of cracks in the test pit.

Table 2.4: Summary of Cracks Observed in the Test Pit.

Crack Type	Number of Cracks	Percent of Total
Drying shrinkage cracks	7	25.0
FDR-C layer cracks (full-depth, fatigue)	8	28.6
FDR-C layer cracks (partial-depth, bottom up fatigue)	10	35.7
FDR-C layer cracks (full-depth, instrumentation)	1	3.6
Crushing	2	7.1
Horizontal or layering cracks	0	0.0
Total number of cracks	28	100

The overall observation from the forensic test pit was that the crack patterns seen on the surface did not match the cracking in the FDR-C layer. A total of 28 vertical cracks were observed along the profile of the pit, but only two of these, identified as drying shrinkage cracks, had reflected through the asphalt concrete surfacing layer at the time of the investigation. Two of the cracks in the center of the pit lined up with the location of the HVS supports, with signs of crushing observed in the area around these cracks. The partial depth cracks with bottom-up initiation patterns were located within the limits of the HVS test sections and were attributed to fatigue resulting from HVS testing. Two partial-depth top-down cracks were also identified within the trafficked areas. These were designated as tertiary drying shrinkage cracks likely caused by continued moisture loss during curing.

The remaining full-depth cracks in the FDR-C layer (i.e., cracks that extended from the bottom to the top of the FDR-C layer) were either caused by trafficking or were a result of continued drying shrinkage. The difference between the drying shrinkage and fatigue cracks can only be hypothesized given that the exact time the cracks developed could not be determined.

The primary reflected drying shrinkage cracks were most likely the first and widest cracks that developed soon after construction. The secondary drying shrinkage cracks (i.e., those that developed after the primary shrinkage cracks had developed) were midway between the primary shrinkage cracks and likely resulted from the accumulation of restraint stress in the FDR-C layer caused by friction between the underlying aggregate base and the FDR-C layer. These cracks were outside the HVS test sections and were therefore not traffic related. The three tertiary drying shrinkage cracks developed midway between the primary and secondary cracks. Two of these cracks were in the HVS test sections and were partial-depth with a top-down origin. The third was full length and outside of the trafficked areas.

A full-depth crack was identified below the cable of a pressure cell. This represented a flaw in the form of a stress concentration as well as a reduction in the cross-section thickness in the FDR-C layer, and the crack could have propagated due to trafficking, drying shrinkage, or both.

Crack Spacing

Spacing between the drying shrinkage cracks in the forensic pit is summarized in Table 2.5. The ratios of the slab lengths between cracks after the development of secondary and tertiary cracks to the previous crack types (i.e., the ratio of the slab length between two secondary cracks and the slab length from a tertiary crack to a secondary crack) are also provided. These spacings show that the secondary and tertiary drying shrinkage cracks developed approximately midway between the earlier primary cracks. This agrees with the theory discussed by George (3) that cracks occur in the center of the slabs.

Table 2.5: Summary of Crack Spacing in Test Pit

Shrinkage Crack Type	Average Spacing (m [ft.])	Ratio
Primary	14.7 (48.2)	N/A
Secondary	7.1 (23.3)	0.5
Tertiary	3.6 (11.8)	0.5

Crack Width

Each crack was measured at four different vertical points to determine an average width, defined as the distance between the opposing faces on the profile. Several cracks were too thin to accurately measure, and these were assigned a width of 0.1 mm. Crack widths are plotted in Figure 2.30. The widths of the secondary drying shrinkage cracks were thinner than the primary ones, and the tertiary cracks were in turn thinner than the secondary ones. This was attributed to the length of the slab between cracks, with reduced spacing between secondary and tertiary cracks corresponding to a reduction in the potential to shrink.
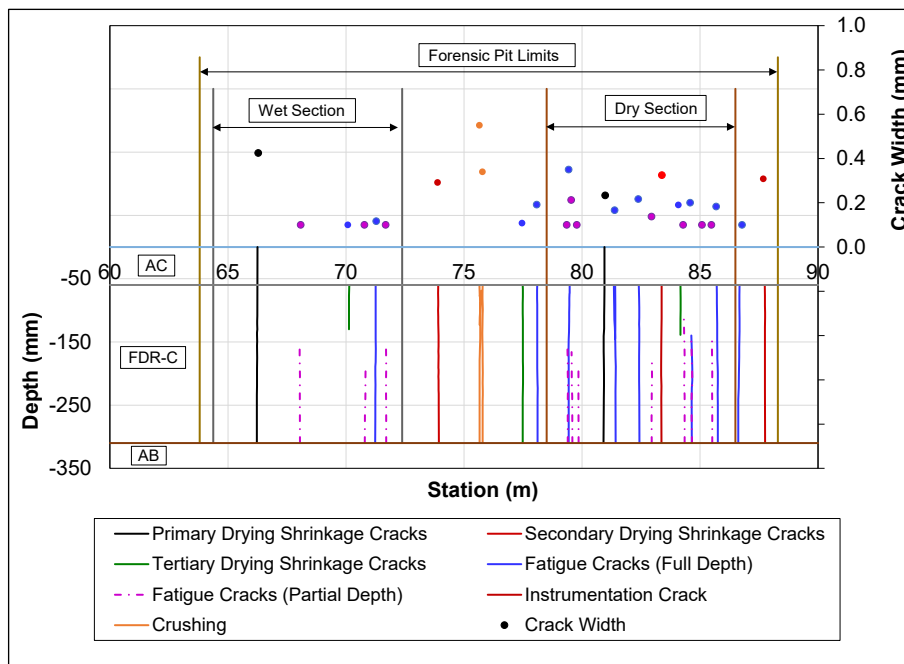
Figure 2.30: Crack type and width.

The full-depth cracks in the trafficked section were on average wider than the partial depth, tertiary drying shrinkage cracks. The increased width of these full-depth cracks is an indication of the loss of aggregate interlock as the faces of the cracks were abraded during trafficking caused by the differential movement of the two faces. Partial-depth, bottom-up fatigue cracks were consistently thin with sufficient aggregate interlock at the time of the investigation to not have shown signs of crack face deterioration.

The widest cracks were those caused by the weight of the HVS supports that resulted in localized crushing of the FDR-C layer. Even though these cracks were wider than the primary shrinkage

cracks, they had not reflected through the asphalt concrete surface at the time of the investigation. This was primarily attributed to timing of the HVS tests (starting approximately two years after construction) relative to the occurrence of the drying shrinkage cracks, which initiated immediately after construction.

2.5.3 Effect of Crack Width and Type on Stiffness

The crack widths measured in the forensic pit, sorted by the different crack types, together with the backcalculated FDR-C layer stiffnesses, are plotted in Figure 2.31 and Figure 2.32, for the dry and wet tests, respectively. There is a weak correlation between increased crack width and stiffness reduction, which indicates that increased crack width reduced the load transfer efficiency in the vicinity of the crack.

The stiffness reduction on the dry section was most evident in regions where the crack widths exceeded 0.2 mm (0.008 in.), especially around the reflected primary shrinkage crack, and the crack caused by the instrumentation cable. Similarly, the stiffness reduction on the wet section was most evident around the primary drying shrinkage crack. The bottom-up fatigue cracks appear to have had an insignificant effect on the FWD backcalculated stiffnesses.
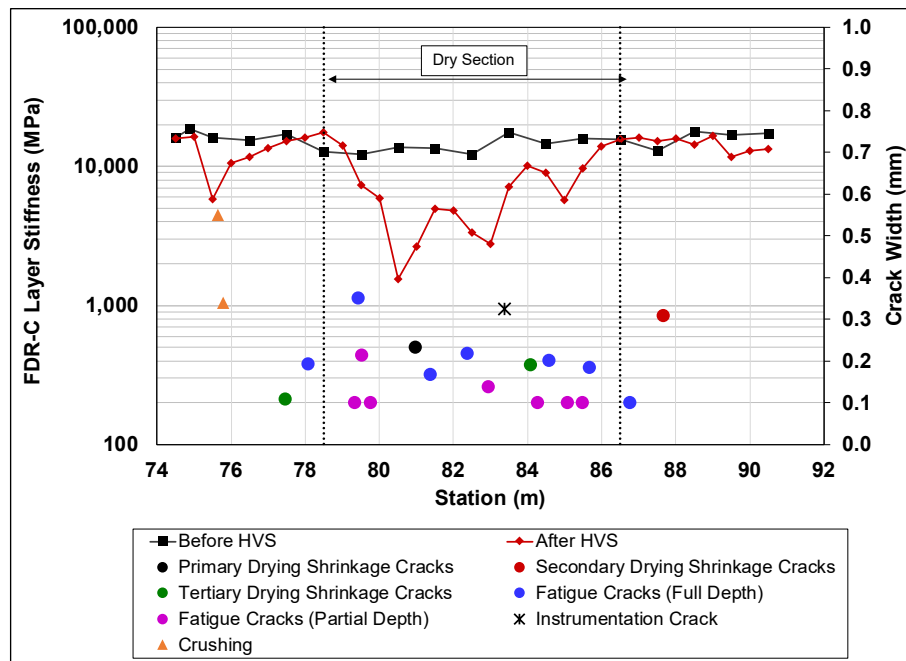
Figure 2.31: Dry section: Crack width vs. stiffness.
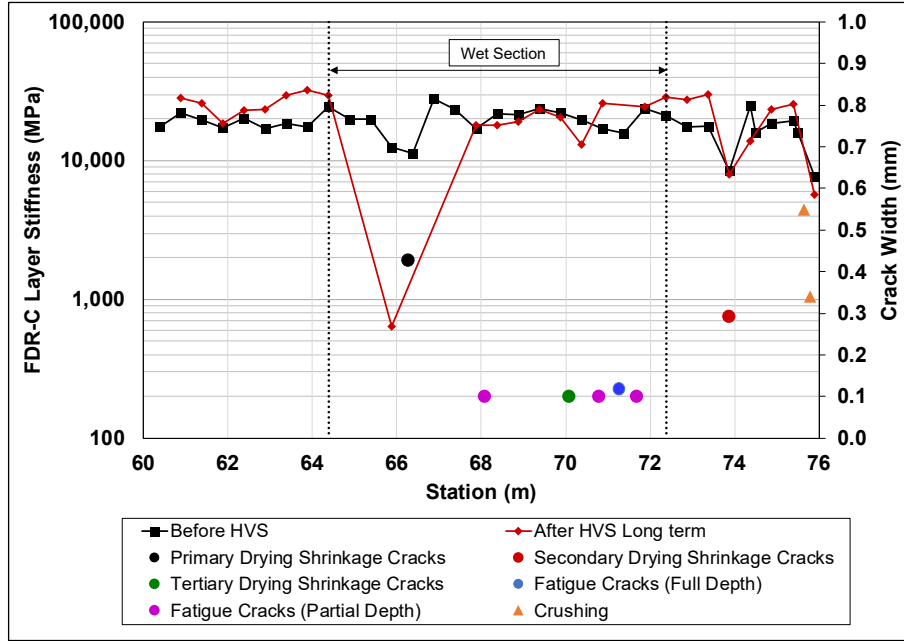
Figure 2.32: Wet section: Crack width vs. stiffness.

2.5.4 Effect of Crack Spacing on Reflective Cracks

Reflective shrinkage cracks in pavements with cement-treated layers are typically initiated by the tensile strain at the tip of the crack at the top of the treated layer where it is bonded to the bottom of the asphalt concrete. The asphalt concrete layer is often placed soon after construction, often before shrinkage cracks have formed in the FDR-C layer. Consequently, the asphalt concrete layer, where it spans a crack in the FDR-C layer, is subjected to the shrinkage and thermal strains that develop with daily temperature variation over the length of the slab between the cracks. The crack width is a function of the slab length, as shown in Equation 2.1, and will increase as the crack spacing increases. The highest potential for reflective cracks is therefore after the development of primary shrinkage cracks. The potential for subsequent shrinkage cracks to reflect from non-traffic factors reduces as additional shrinkage cracks develop and slab lengths decrease.

$$\Delta d = L \times \varepsilon_s \qquad \text{(2.1)}$$

Where: Δd = Change in slab length (mm)

L = Slab length (mm)

ε_s = Thermal strain due to temperature change, calculated with Equation 2.2

$$\varepsilon_s = CoTE \times \Delta T \qquad \text{(2.2)}$$

Where: = Coefficient of thermal expansion

ΔT = Temperature change (°C)

2.5.5 Tensile Stress and Strain in the FDR-C Layer

FWD testing indicated that the largest stiffness reduction related to HVS testing was in the vicinity of the reflected drying shrinkage cracks. This was also the location where the wet test section failure started, with failure attributed to water ingress through the crack leading to debonding of the asphalt concrete layer from the FDR-C layer, followed by fatigue failure of the asphalt concrete layer as a result of the debonding.

The typical approach to designing pavements with cement-treated layers involves the use of layer elastic theory to determine the expected tensile stresses or strains in the layers for the expected traffic loads and to calculate the fatigue life accordingly. Layer elastic theory assumes that the layer is uniform, homogeneous, and without cracks. The calculated stress or strain represents the stress or strain expected in the interior of the treated layer slab where no cracks are present. The observations on the test track, as well as by various researchers *(3,4,14,17-21)* over time, have all shown that the area of concern is not the intact part of the slab but rather the wide reflected shrinkage cracks where failure is initially observed. The interior of the slab does not show the level of damage compared to the area in the vicinity of the cracks. Therefore, using the stress or strain calculated using layer elastic theory and not considering cracks will overestimate the fatigue life. Kota *(14)* proposed increasing the calculated stress in the interior of the slab by a factor of two to represent critical stresses adjacent to cracks for use in fatigue life determination.

Blank page

3   LITERATURE REVIEW

3.1   Introduction to Cement Treatment of Pavement Layers

Cement treatment of pavement materials involves the mixing of virgin aggregate, reclaimed asphalt pavement (RAP), recycled concrete aggregate, and/or soil with cement and water. Cement treatment increases the stiffness and shear strength of an aggregate material, while reducing the permeability and mitigating the plasticity effects of clay particles. It can be a cost-effective method to improve the properties of marginal materials and to increase the bearing capacity of soils with a plasticity index (PI) less than 20 *(22)*. However, treatment can lead to shrinkage cracking in the layer due to moisture loss through evaporation and self-desiccation *(23)*. Reflection of shrinkage cracks through the overlying asphalt surface layer(s) allows water to infiltrate the pavement, leading to a loss of stiffness in the underlying layers and potential pumping of fines, resulting in faster deterioration compared to a pavement which is not cracked.

3.2   Flexible Pavement Distresses Associated with Cement-Treated Layers

Failures in cement-treated layers typically lead to one distress or a combination of distresses on the surface of flexible pavements, including transverse cracking, longitudinal cracking, block cracking, fatigue cracking, and/or rutting. The causes of these distresses can be load related, non-load related (e.g., environmental effects such as temperature, moisture, and/or freeze-thaw), or a combination of the two. This study only focuses on cracks related to distresses in the cement-treated layer.

Cement-treated layers are typically located below the surface layer, which can consist of asphalt concrete, a thin surface treatment (e.g., chip seal, cape seal, microsurfacing), or portland cement concrete. The cement-treated layer can also be constructed as a subbase, as in the case of inverted pavements, with an unbound granular or recycled material base layer and thin asphalt concrete surfacing above it. Inverted pavements were developed in South Africa *(24)*, mainly to reduce the cost of major roads, by building a stiff, cement-treated subbase onto which a granular base layer can be compacted to serve as the main load bearing layer. A benefit of this pavement

type is that drying shrinkage cracks are isolated from the surface layer and are generally unable to reflect through the unbound granular layer *(25-27)*.

3.2.1 Shrinkage Cracks

Transverse cracks in asphalt concrete layers over a cement-treated layer (Figure 3.1) may be reflected shrinkage cracks from the treated layer. The primary mechanisms of shrinkage cracking include:

- Autogenous shrinkage due to the hydration of cement
- Drying shrinkage due to moisture loss
- Thermal contraction due to low temperature

Figure 3.1: Reflected shrinkage cracks on a pavement with an FDR-C base.

Several researchers *(3,13-15)* have shown that wide drying shrinkage cracks are the dominant factor leading to premature failure of cement-treated layers. Widespread traffic-induced fatigue is seldom a problem before localized failures occur in the vicinity of wide drying shrinkage cracks. These cracks lead to water ingress, layer delamination, and a rough riding surface. Research over the past 30 years *(7,13,15,28,29)* has shown that the typical failure mode around drying shrinkage cracks involved layer debonding between the asphalt concrete surface and the treated layer, caused by water ingress.

Autogenous Shrinkage

Autogenous shrinkage occurs during hydration of the cement where the products produced between cement and water have a lower volume than that of the individual constituents. This phenomenon is also known as Le Chatelier Contraction.

Drying Shrinkage

Drying shrinkage occurs with moisture loss after construction resulting from desiccation through evaporation from exposed surfaces *(30)*. The rate of desiccation depends on the exposed surface area, moisture migration pathways, and the drying environment *(31)*. Loss of moisture results in a moisture gradient with depth that causes a high matric suction to develop in the pore water in the voids. Osmotic suction caused by dissolved salts in the pore water may also contribute significantly to the suction. This total suction, combined with the friction between the layers, is the main force causing drying shrinkage to develop *(32).*

Thermal Shrinkage

Thermal shrinkage has been well quantified for concrete materials and is attributed to the high heat of hydration associated with the mass of cement in concrete, which, as a general rule, is about 5°C to 8°C of adiabatic temperature rise per 45 kg of cement *(33)*. During the hydration process, concrete is subject to elastic and nonelastic expansion. The elastic portion of the expansion recovers when the concrete cools, while the non-elastic portion results in permanent thermal shrinkage *(34)*. This risk of thermal shrinkage increases as the cement content increases due to the associated increased heat of hydration *(35)*. Cement-treated layers are particularly susceptible to shrinkage cracking during the initial stages of curing due to their relatively low strength. Thermal shrinkage can also lead to shrinkage cracks later in the life of cement-treated layers if the stress from thermal shrinkage due to changes in temperature exceeds the strength of the material under restraint conditions *(36)*. George *(23)* showed that the stresses induced by thermal expansion and contraction is negligible compared to stresses induced by drying shrinkage of the material.

Effect of Cement Content

Earlier studies *(23)* on shrinkage control on cement-treated layers have shown that an optimal cement content can minimize shrinkage cracks. The effect of higher cement contents can increase shrinkage cracking problems as follows *(4)*:

- Higher cement contents require higher water contents for hydration, which can lead to increased autogenous shrinkage.

- Higher cement contents lead to higher tensile strengths, which increases crack spacing and crack width.

3.2.2 Transverse Cracking

A survey conducted by Wen et al. as part of a National Cooperative Highway Research Program (NCHRP) study *(21)* revealed that transverse and block cracking were considered to be the most severe distresses associated with cement-treated layers. Transverse cracks are often caused by shrinkage, which initiates soon after completion of compaction as hydration reactions begin and the layer dries from evaporation and desiccation. The restraints from friction between the treated and underlying layers and between the treated layer and the asphalt concrete cause tensile stresses to exceed the tensile strength of the treated layer, resulting in transverse cracks *(3)*.

Cracks in cement-treated layers can reflect through asphalt concrete due to the bond between the two layers. Reflective cracking often starts at a crack front (i.e., where a crack started due to shrinkage, fatigue, thermal cycling, surface distresses, or existing discontinuities) as in the case of an asphalt concrete layer bonded to a cement-treated base with shrinkage cracks. The crack front often progresses under repeated traffic or environmental loading. The rate of reflection of these cracks is typically dependent on the thickness of the surface layers and the cement content of the treated layer (higher cement contents typically result in wider cracks with higher associated stress fields and therefore faster reflection).

Transverse cracks in cement-treated layers depend on aggregate interlock to transfer shear loads across the cracks. Load transfer across the cracks decreases with increasing crack width. When widths exceed 6 mm (≈0.25 in.), the once monolithic structure is considered to change to a jointed structure with higher deflections across the joint *(36)*. Accompanied by the ingress of water, subbase support erodes through pumping of fines, and the structure deteriorates around the crack *(3,4,14,17-19)*.

3.2.3 Longitudinal Cracking

Longitudinal cracking in flexible pavements with a cement-treated layer (Figure 3.2) has also been recorded *(37-41)*. Longitudinal cracking, originating in the treated layer, is commonly caused by overlapping cement applications and other inappropriate construction practices *(40)*. Pretorius

and Monismith *(39)* showed how longitudinal cracks can develop perpendicular to transverse cracks where the critical tensile stresses at the bottom of the layer are parallel to the transverse crack direction (Figure 3.3).

Figure 3.2: Longitudinal cracking on an FDR-C pavement.

Figure 3.3: Longitudinal and transverse cracking on an FDR-C pavement.

3.2.4   Block Cracking

Block cracking (Figure 3.4) in asphalt concrete surfaces can be attributed to extensive reflected drying shrinkage and longitudinal cracks that have intercepted in cement-treated layers. These form blocks as a result of trafficking and thermal expansion and contraction *(37)*.

3.2.5   Fatigue Failure

Fatigue failure in cement-treated layers is caused by repeated traffic loading resulting in tensile strains at the bottom of the layer. The rate of fatigue failure typically increases as the strain increases *(12)*. These cracks develop transverse to the direction of traffic. Pretorius and Monismith *(39)* described the development of longitudinal cracks originating at shrinkage cracks as a form of fatigue cracking due to the mechanism of how they can develop under traffic loading.

Fatigue cracking in asphalt concrete surface layers over cement-treated layers can result from high strains at the bottom of the asphalt concrete layer due to debonding. These strain levels increase as the surface of the treated layer weakens. Debonding can also result from the formation of weak areas at the top of the treated layer during construction caused by carbonation (Figure 3.5), laminations, or overcompaction, all of which can create conditions of reduced friction between the different layers *(42)*.
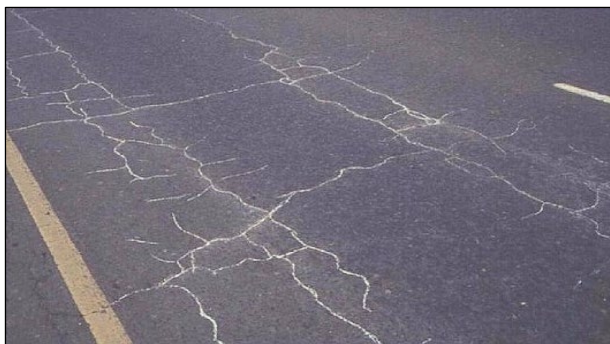
Figure 3.4: Block cracking on an FDR-C pavement (note pumping of fines through cracks).

Figure 3.5: Surface carbonation on an FDR-C layer.

3.2.6 Crushing Failure

Crushing-related failures and associated surface distresses are usually only observed on pavements with cement-treated layers under thin asphalt concrete or surface treatments (<50 mm [0.15 ft.]). High vertical compressive stresses at the top of the treated layer can lead to crushing, which, for the purpose of this study, is defined as the breakdown of the material matrix due to compressive stresses exceeding the compressive strength of the material. The two critical parameters are the maximum tensile stress or strain (σ, ε) at the bottom of the treated layer for fatigue and the vertical compressive stress (σ_v) at the top of the treated layer for crushing. Surface distresses can be cracking, rutting, or potholes.

3.2.7 Rutting

Rutting in pavements with well-constructed cement-treated layers is rare given the relatively high strengths and stiffnesses of the treated material. However, on pavements with severe cracking that allows water to infiltrate into the treated layer, rutting often occurs as a result of deformation of the water-softened materials under traffic loading (Figure 3.6).

Figure 3.6: Rutting and fatigue cracking on a pavement with a cement-treated layer.

3.3 Accelerated Pavement Testing on Cement-Treated Layers

Accelerated pavement testing (APT) has been performed on pavements with cement-treated layers in several countries *(7,12,17)*. Analysis of the results have mostly followed the philosophy proposed by Otte *(19)*, which considers the fatigue life of only "intact" treated layers where no drying shrinkage cracks are present *(43)* (i.e., the strongest part of the pavement), rather than also considering the failure around shrinkage cracks (i.e., the weakest part of the pavement), which can have a significant effect on fatigue life. The authors *(7)* and Yeo *(17)* both note that the areas around shrinkage cracks fail faster than "intact" lengths of treated layers between cracks.

3.3.1 South Africa

A good understanding of the long-term behavior of cement-treated layers was developed through years of laboratory and accelerated pavement testing in South Africa. This research (Figure 1.2) was summarized by Theyse et al. *(44)* and proposed three phases in the service life of a cement-treated layer. In phase one, the "pre-cracked phase," two stages occur, namely the intact stage and the shrinkage cracked stage. The duration of these two stages on overall performance is negligible (typically less than 15 days) in relation to the other phases *(12)*, and it is thus not considered in current models to predict the layer life for cemented material. Traffic-induced cracking occurs in phase two, the "effective fatigue life phase," in which the pavement serves the majority of its life. In phase three, or the "equivalent granular phase," all the cementitious bonds are assumed to be broken, and the layer has a stiffness equivalent to that of a compacted untreated granular layer.

Transfer functions, or performance equations used to relate calculated pavement response (stress, strain) to performance (fatigue cracking, crushing), were developed *(12)* for cement-treated materials to determine their effective fatigue and crushing lives. These functions were derived primarily from data collected on relatively thin pavement structures with thin surface treatments, which are not typically representative of pavements in the United States. The effective fatigue life was defined in this work as the number of 8.2 kN equivalent single-axle loads (ESALs) that a pavement can carry before the stiffness reduces to the equivalent granular layer stiffness. Two crushing conditions were defined, namely crush initiation, with 2 mm (0.08 in.) of

deformation on top of the layer, and advanced crushing with 10 mm (0.4 in.) of deformation and extensive breakdown of the material.

Equation 3.1 and Equation 3.2 provide the effective fatigue and crushing functions developed from the research, respectively *(44)*. The effective fatigue transfer function, primarily developed by Otte *(19,45)* using laboratory beam fatigue tests and validation with APT, is a relationship between the tensile strain at the bottom of the layer and the tensile strain at break. The crushing transfer function, developed by De Beer *(12)* using APT data, is a relationship between the vertical compressive stress at the top of the layer and the measured or estimated unconfined compressive strength (UCS) of the layer. The equations were developed for different classes of roads in South Africa based on the reliability of the design. The fitting parameters *k1* and *k2*, are provided in Table 3.1.

$$\text{NEFF} = 10^{k_1\left(1 - \frac{\varepsilon}{k_2 \varepsilon_b}\right)} \tag{3.1}$$

Where: NEFF = Effective fatigue life for a cemented material, after which it is assumed to be in the equivalent granular phase

k_1, k_2 = Fitting parameters

ε = Maximum principal strain at the bottom the cement-treated layer

ε_b = Tensile strain at break of the material

$$N_{C_i \atop a} = 10^{k_1\left(1 - \frac{\sigma_v}{k_2 UCS}\right)} \tag{3.2}$$

– Crush initiation, with approximately 2 mm deformation on top of the layer

N_{C_a} = Advanced crushing, with approximately 10 mm deformation on top of the layer

k_1, k_2 = Fitting parameters

σ_v = Vertical compressive stress at the top of the cement-treated layer (kPa)

UCS = Unconfined compressive strength of the cement-treated material (kPa)

Table 3.1: Fitting Parameters for Effective Fatigue and Crushing Functions *(44)*

Road Category	Effective Fatigue N_{EFF}		Crush Initiation N_{Ci}		Advanced Crushing N_{Ca}	
	k_1	k_2	k_1	k_2	k_1	k_2
A	6.72	7.49	7.386	1.09	8.064	1.19
B	6.84	7.63	7.506	1.10	8.184	1.20
C	6.87	7.66	7.706	1.13	8.384	1.23
D	7.06	7.86	8.516	1.21	8.894	1.31

The tensile strain at break at the bottom of the treated layer (ε_b) and UCS value for a South African Class 3 cemented layer are 125 μstrain and 2.25 MPa (326 psi), respectively *(44)*. These are similar to the current design strength of cement stabilized bases (CSBs) in California (as defined in Section 27 of the 2018 Caltrans Standard Specifications). A shift factor is provided for effective fatigue since the transfer function does not allow for different layer thicknesses. The shift factor for typical layer thicknesses used in CSBs (between 100 and 225 mm thick [4.0 and 9.0 in.]) is provided in Equation 3.3.

$$SF = 10^{(0.00285d-0.293)} \tag{3.3}$$

Where: SF = Shift factor
d = Layer thickness (mm)

3.3.2 Australia

A more recent APT study on cement-treated materials in Australia *(46)* tested pavement structures that closely resemble typical pavement structures in the United States. The treated layers were constructed with two different materials: siltstone with 4% cement, and hornfels with 3% cement. The pavement structure was 30 mm (0.1 ft.) of asphalt concrete over 150 mm (0.5 ft.) of CSB over subgrade. A schematic of the test sections along with the locations of cracks is shown in Figure 3.7.

The main criteria of failure for mechanistic empirical modelling used for this study were:

- Surface deformations exceeding 20 mm (0.8 in.), which is commonly used for Australian pavements
- A 50% or greater reduction in backcalculated stiffness compared to the initial backcalculated stiffness

There was no criterion for crack density as a measure of failure in this study.

The particular section of interest was Section 3310, which had reflective drying shrinkage cracks around the 25 m and 32 m stations prior to the start of testing with an 80 kN wheel load. Post-test forensic analyses *(17)* showed that, after 323,000 wheel passes, the area around the drying shrinkage cracks deteriorated to an equivalent granular state (Figure 3.8). The rest of the section, between the shrinkage cracks, showed extensive transverse fatigue cracks but was still cemented

(Figure 3.9). No reflected fatigue cracks were visible on the surface. This forensic investigation visually showed the magnitude of the effect a drying shrinkage crack has on the performance of a cement-treated layer when compared to an area that is initially intact.
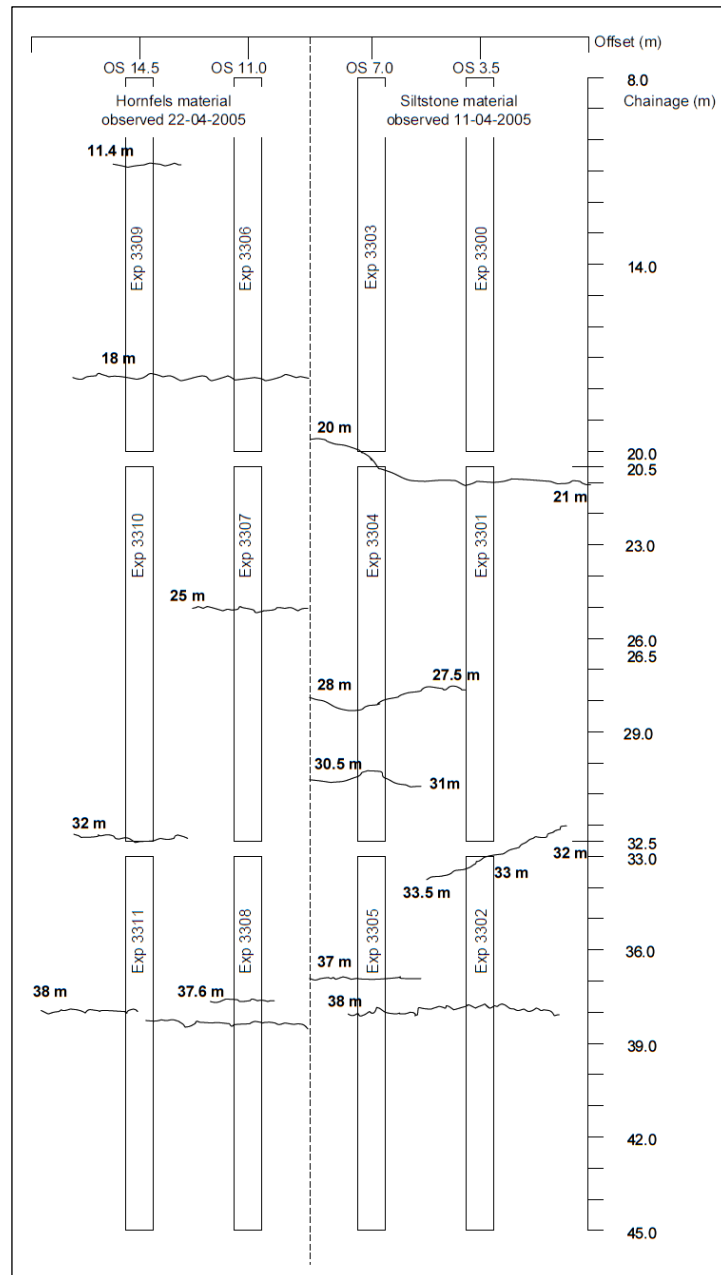

Figure 3.7: Australian test section layout showing reflective drying shrinkage cracks *(17)*.

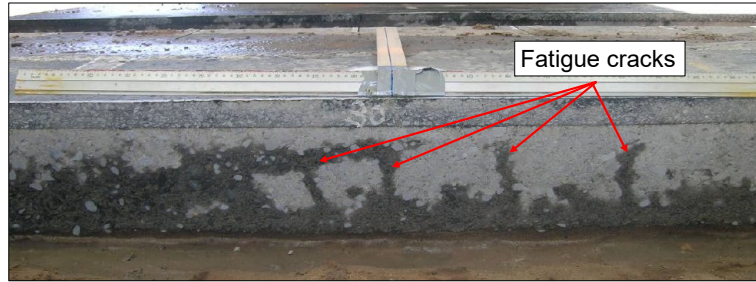**Figure 3.8: Disintegrated equivalent granular state of the cemented layer *(17)*.**

Figure 3.9: Fatigue cracks in the intact cemented layer *(17)*.

Test section and laboratory data were used to develop a fatigue model, provided in Equation 3.4. The fatigue life in this model is defined as the number of load cycles to reduce the stiffness of the CSB layer to 50% of the initial stiffness. No cracking criteria were included in the definition of fatigue life. The fitting parameters are provided in Table 3.2.

$$\log(N) = -k_1 \log(strain) + k_2 \qquad\qquad \text{(3.4)}$$

Where: N = Number of load cycles to 50% of the initial stiffness

$Strain$ = Horizontal strain at the bottom of the treated layer

k_1, k_2 = Fitting parameters

Table 3.2: Fitting Parameters for Australian Fatigue Model *(17)*

Material Type	k_1	k_2
Hornfels	4.7	13.7
Siltstone	6.1	17.0

This transfer function was developed for "intact" areas and does not capture the performance of the material around the drying shrinkage cracks, which have a lower fatigue life compared to the intact areas. The risk with this methodology that strives to increase fatigue life of the CSB is that layer strengths can simply be increased to improve the tensile properties of the material, thereby prolonging the fatigue life. However, higher cement contents can lead to wider drying shrinkage cracks, which could have led to the failures observed.

3.3.3 California

Accelerated pavement testing on the UCPRC FDR test track is discussed in Section 2.5. The findings from this study and the studies done in South Africa and Australia clearly show that there is a spectrum of performance along the length of cement-treated layers and that the performance is poorest around shrinkage cracks.

3.4 Models for Cement-Treated Material Strength

The primary strength tests performed on cement-treated materials for mix design and performance evaluations are UCS and indirect tensile strength (ITS) tests. The UCS test is typically performed following ASTM D1633 and the ITS test following ASTM D6931. The strength of cement-treated materials increases with increasing cement content *(47)*.

Strength and stiffness values are dependent on the material used *(48)*. Suman et al. *(49)* developed a material-specific model (Equation 3.5) to predict the UCS of cement-treated material using artificial neural networks. The model assumes specimens are compacted to MDD. The model does not account for curing time and different cement types, both of which can affect strength gain rates *(50)*. The inputs for the model include the coarse, sand, and fine portion of the grading envelope, liquid limit (LL), plasticity index (PI), moisture content, and cement content.

$$UCS = -17.1 - 0.0155 \times LL - 0.0305 \times PI + 0.203 \times C + 0.228 \times S + 0.248 \times G - 0.0223 \times MC - 0.268 \times CC \tag{3.5}$$

Where: *UCS*   =   UCS (N/m^2)
         LL   =   Liquid limit (%)
         PI   =   Plasticity index (%)
         C   =   Clay content (%)
         S   =   Sand content (%)
         G   =   Gravel content (%)
         MC   =   Moisture content (%)
         CC   =   Cement content (%)

Generalized models to predict UCS with time have also been developed. The US Air Force *(51)* uses Equation 3.6 to predict the increase in UCS of soil-cement. Lim and Zollinger *(52)* adapted the American Concrete Institute (ACI) model in Equation 3.7, which was developed for concrete

strength gain, for cement-treated material. The model was calibrated using aggregate base material with 4% and 8% Type I cement. The coefficients for the model are provided in Table 3.3.

$$UCS(t) = UCS(t_0) + K \times \log\left(\frac{t}{t_0}\right)$$ (3.6)

Where: $UCS(t)$ = UCS at time t (days)
UCS_{t_0} = UCS after t_0 days
K = 70 × C for cement
t = Curing time (days)
C = Cement content (%)

$$f_c(t) = f_c(28) \times \frac{t}{a+b\times t}$$ (3.7)

Where: $f_c(t)$ = Compressive strength at time t (MPa)
$f_c(t)$ = Compressive strength after 28 days (MPa)
a,b = Experiment coefficients
C = Cement content (%)

Table 3.3: Coefficients for American Concrete Institute Strength Gain Model

Coefficient	Concrete	Cement-Treated Base
a	4.0	2.5
b	0.85	0.9

The relationship between UCS and ITS of cement-treated material is generally linear (Equation 3.8). The coefficients are provided in Table 3.4.

$$S_{IDT} = a \times UCS - b$$ (3.8)

Where: S_{IDT} = Indirect tensile strength (psi)
UCS = Unconfined compressive strength (psi)
a,b = Experiment coefficients

Table 3.4: Coefficients for Different UCS and ITS Relationships

Year	Researcher	a	b
1973	Kennedy and Hudson *(53)*	0.166	11.38
2009	Gnanendran and Piratheepan *(54)*	0.114	0
2012	Scullion et al. *(55)*	0.177	9.31
2014	Wen et al. *(21)*	0.120	0
2018	Rashidi et al. *(56)*	0.120	0

Laboratory UCS and ITS tests often produce highly variable results, attributed in part to the specimens being smaller than the representative volume element (RVE), defined as the smallest

material volume large enough for the global characteristics of the material to remain constant, regardless of the location of the RVE *(57)*. Harvey et al. *(58)* noted that, when the specimen is smaller than the RVE, random results occur (i.e., the variability in the results increase). Both the UCS and ITS tests use predominantly 100 mm (≈4 in.) diameter specimens with a nominal aggregate size of 19 mm (≈0.75 in.). An additional explanation for the variability is the methodology followed during the compaction process where the material for each specimen is scooped from a large volume of material, which can introduce bias in the grading of each specimen.

Rashidi et al. *(56)* developed a stiffness model as a function of the UCS (Equation 3.9). This model is specific to the material and mix design used by Rashidi.

$M_r = 7.4 \times UCS - 1940$ **(3.9)**

Where: M_r = Stiffness (ksi)

UCS = Unconfined compressive strength (psi)

3.5 Models for Shrinkage Cracking in Cement-Treated Layers

Shrinkage cracks are caused by tensile stresses exceeding the tensile strength of the material *(59,60)*. Various factors contribute to autogenous shrinking of the cemented layer, but moisture loss through self-desiccation and evaporation is a primary reason *(23,61,62)*. As previously noted, factors that contribute to shrinkage and cracking of cement-treated bases include subbase restraints due to friction *(63)*, tensile strength of the cement-treated layer *(23,61,62)*, shrinkage of the layer with decreasing temperatures, and traffic loading *(63)*.

George *(63)* noted the following three independent factors that influence the spacing of shrinkage cracks:

- Shrinkage and thermal stresses in the pavement
- Variation of material strength throughout the pavement, termed "flaw distribution"
- Width of the zone of stress relief surrounding individual cracks

Initial drying shrinkage cracks develop where increasing surficial tension in the slab exceeds the strength of the flaws (the term "slab," as used by George in his research, refers to either the cement-treated layer after compaction or the length of the cement-treated layer between

shrinkage cracks). Further cracking will continue to be randomly distributed as the tensile stress exceeds the strength of the flaws. Uniform crack spacings can be expected where the tensile stress exceeds zones of isotropic strength. Theoretically, due to the restraint between the treated layer and the subgrade, drying shrinkage cracks should develop in the center of the slab as the tensile stress increases *(3)*.

3.5.1 Crack Width and Crack Density Models

George *(23)* derived formulas to determine crack spacing and crack width in cement-treated layers, as shown in Equation 3.10 and Equation 3.11.

$$L_{max} = \frac{2\sigma_u}{\mu\gamma} \tag{3.10}$$

$$\delta_T = \varepsilon_c L - \frac{\mu\gamma L^2}{4E_t} \tag{3.11}$$

Where: L_{max} = Slab length at which tensile stress becomes critical (m)

σ_u = Ultimate tensile strength of the cement-treated layer (kPa)

μ = Coefficient of sliding friction between the cement-treated layer and the underlying layer

γ = Unit weight of the material (kg/m³)

δ_T = Total crack width (m)

ε_c = Total shrinkage strain (m/m)

E_t = Modulus of elasticity of the material (kPa)

These models were based on the assumption of elasticity. George showed that the predictions from these models correlated poorly with field-measured crack width results. To improve the models, he incorporated the viscoelastic properties of soil-cement in Equation 3.12 and Equation 3.13, based on Burger's model, and assuming that the subgrade resistance to horizontal slab movement *(64)* is linearly time dependent and that the space variation of stress is linear. Slab length and crack width can be determined with these models as a function of shrinkage rate, tensile strength, time, and the deformational properties of the material. George *(65)* concluded that the agreement between field-measured and predicted crack width and slab length significantly improved by incorporating the viscoelastic properties of the material.

$$L_{max} = \frac{2\sigma_u}{\mu\gamma} \tag{3.12}$$

Where: L_{max} = Slab length at which tensile stress becomes critical (m)

$$\sigma_u = \left(\frac{\varepsilon_1}{t_1}\right) E_m \left[\frac{\eta_m}{E_m} + \frac{1-\frac{1}{\alpha\tau}}{\beta-\alpha}\exp(-\alpha t) + \frac{1-\frac{1}{\beta\tau}}{\alpha-\beta}\exp(-\beta t)\right]$$

$$\frac{\alpha}{\beta} = \frac{1}{2}\left(\frac{E_k+E_m}{\eta_k} + \frac{E_m}{\eta_m}\right) \pm \frac{1}{2}\sqrt{\left(\frac{E_k+E_m}{\eta_k} + \frac{E_m}{\eta_m}\right)^2 - 4\frac{E_k E_m}{\eta_k \eta_m}}$$

$$\tau = \frac{\eta_k}{E_k}$$

$\dfrac{\varepsilon_1}{t_1}$ = Shrinkage rate

E_k, E_m, η_k, η_m = Burger's model parameters

$$\delta_T = \varepsilon_c L - \frac{\mu\gamma L^2}{4E_t} = \delta_1 - \delta_2 \tag{3.13}$$

Where: δ_1 = Slab contraction caused by shrinkage, not affected by the viscous properties of the material

$$\sigma_2 = \frac{\mu\gamma L^2}{4E_t}\left\{\frac{t}{t_1}\left(\frac{1}{E_m} + \frac{1}{E_k} + \frac{t}{2\eta_m}\right) + \frac{1}{E_k}\frac{\tau}{t_1}\left[\exp\left(-\frac{t}{\tau}\right) - 1\right]\right\} \text{ for } t < t_1$$

$$\sigma_2 = \frac{\mu\gamma L^2}{4E_t}\left\{\frac{1}{E_m} + \frac{1}{E_k} + \frac{1}{\eta_m}\left(t - \frac{t_1}{2}\right) + \frac{1}{E_k}\frac{\tau}{t_1}\left[\exp\left(-\frac{t}{\tau}\right) - \exp\left(-\frac{t-t_1}{\tau}\right)\right]\right\} \text{ for } t > t_1$$

Zhang and Li *(66)* developed analytical models to predict shrinkage induced stress and displacements in concrete pavements resulting from subgrade restraints. A bilinear relation was used to describe the frictional stress-slippage behavior of the slab/base interface in the models. Frictional stress-slippage relations of six different subbase materials calibrated for the model are provided in Table 3.5.

Table 3.5: Friction Restrained Coefficients for Different Base Materials

Base Type	τ_0 (MPa)	δ_0 (mm)
Cement-treated base	0.106	0.025
Granular	0.023	0.500
Asphalt concrete	0.021	0.060
Asphalt treated base	0.015	1.000
Lime treated clay	0.012	0.300
Natural clay	0.008	1.300

The bilinear relation is illustrated in Figure 3.10. Test results for a concrete slab sliding on different supporting materials have shown that shear stress increases linearly up to a certain value, termed the steady state value, at τ_0 and δ_0. The shear stress stays constant at the steady state value with continued slippage.

Shrinkage due to drying can be modeled in two stages:

Stage 1: Displacement due to shrinkage, $|u| \leq \delta_0$
Stage 2: Displacement due to shrinkage, $|u| > \delta_0$
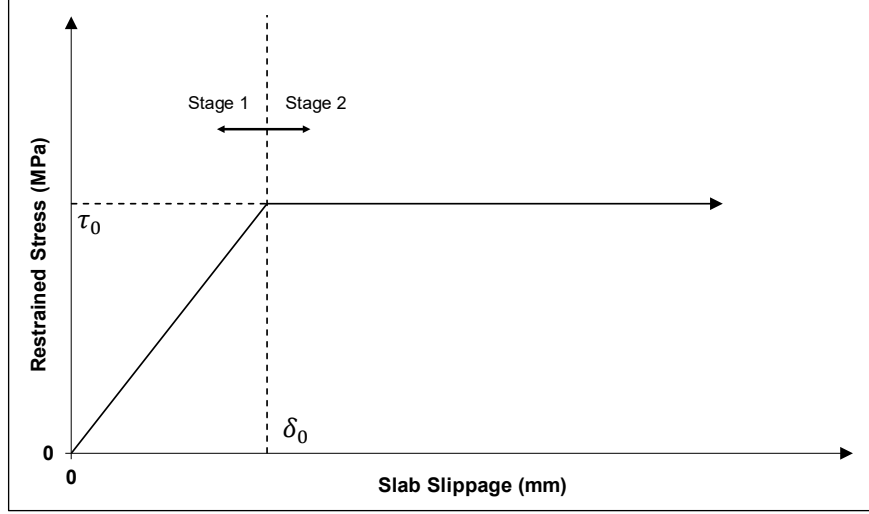
Figure 3.10: Bilinear friction stress-slab slippage relationship *(66)*.

The closed-form solutions of the displacement and shrinkage stresses for Stage 1 are provided in Equation 3.14 and Equation 3.15, and the closed-form solutions of the maximum displacement and shrinkage stresses for Stage 2 are provided in Equation 3.16 and Equation 3.17.

$$u_m = -\frac{1}{\beta}\left(\frac{\sigma_{c0}}{E_c} + \varepsilon_c\right)\tanh\beta\frac{L}{2} \tag{3.14}$$

$$\sigma_{cm} = -E_c\varepsilon_c\left(1 - \frac{1}{\cosh\beta\frac{L}{2}}\right) + \sigma_{c0}\left(1 - \frac{1}{\cosh\beta\frac{L}{2}}\right) \tag{3.15}$$

$$u_m = \delta_0\left(1 - \frac{1}{2}\beta^2 x_0^2\right) - \left(\frac{\sigma_{c0}}{E_c} + \varepsilon_c\right)x_0 \tag{3.16}$$

$$\sigma_{cm} = -E_c\varepsilon_c\left(1 - \frac{1}{\cosh\beta\left(\frac{L}{2}-x_0\right)}\right) + (E_c\beta^2\delta_0 x_0 + \sigma_{c0})\frac{1}{\left(\cosh\beta\left(\frac{L}{2}-x_0\right)\right)} \tag{3.17}$$

Where:

u_m = Maximum shrinkage displacement (mm)

σ_{cm} = Maximum shrinkage stress at the middle of the slab (MPa)

β = $\sqrt{\tau_0/(E_c H \delta_0)}$

τ_0 = Steady state frictional stress (MPa)

H = Slab thickness (mm)

δ_0 = Slippage up to steady state (mm)

σ_{c0} = Average axial stress at the edge of the slab (MPa)

E_c = Young's modulus (MPa)

ε_c = Drying shrinkage strain (%)

L = Length of the slab (mm)

x_0 = Length of slab over which shrinkage stress are fully developed (mm)

Wang *(67)* developed models to predict drying shrinkage, shrinkage crack spacing, and shrinkage crack widths in cement-treated layers based on a variety of inputs obtained from different observation measurements and tests, including:

- Crack width
- Layer thickness
- Coefficient of friction between the base and subgrade layer
- Dry density
- Age in days when cracks were observed
- Water content
- Average daily temperature variation
- Coefficient of thermal expansion
- 28-day UCS strength
- Ultimate drying shrinkage
- Shrinkage at the surface of the layer

The coefficient of determination for shrinkage crack spacing was 0.99 for fine-graded material and 0.31 for coarse-graded material. The coefficient of determination for shrinkage crack width was 0.60 for fine-graded material and 0.19 for coarse-graded material. The proposed shrinkage model in Equation 3.18 and the drying shrinkage model with time at different depths in the layer in Equation 3.19 do not consider different cement contents, which is considered to be a critical determinant of the ultimate drying shrinkage of any material.

$$\varepsilon_{su} = C_1(w^{m_1} + m_2) \tag{3.18}$$

Where: ε_{su} = Ultimate drying shrinkage strain (μstrain)
w = Optimum water content (kg/m^3)
C_1 = Binder type factor (0.993 for cement)
m_1, m_2 = Regression coefficients (m_1 = 3.17, m_2 = 313.76)

$$\varepsilon_g(t) = \varepsilon_{su}\left[1 - \left(\frac{RH_c}{100}\right)^{a_6}\right] \tag{3.19}$$

Where: $\varepsilon_g(t)$ = Drying shrinkage strain with moisture gradient at t days after construction (μstrain)
RH_c = Calculated relative humidity (%)

Where: RH_c = $RH + (100 - RH)f(t)^{a_5}$
RH = Atmospheric relative humidity (%)

$$f(t) = 1/\left(1 + \frac{t}{b}\right)$$

Where: t = Time since construction (days)

$$b = a_1(d + a_2)^{a_3} \left(\frac{w}{c}\right)^{a_4}$$

d = Depth from evaporation surface (ft.)

$\frac{w}{c}$ = Water/calcium ratio in mass

a_i = Regression coefficients (Table 3.6)

Table 3.6: Regression Coefficients for Drying Shrinkage Strain Model in Equation 3.19

a_1	a_2	a_3	a_4	a_5	a_6
1,289,202	0.085	0.94	1.24	10,209	4.51

Other drying shrinkage crack models to predict crack spacing and crack width were developed by Penev and Kawamura *(68)*, each of which assumed the following:

- The cement-treated layer is constructed without a change in the construction practices along a project.
- Cement distribution is uniform.
- The material is isotropic.
- Mixing water content is consistent.
- The curing method is applied appropriately and consistently.
- Compaction is uniform.

3.5.2 Effect of Layer Thickness on Crack Width and Crack Spacing

Based on the experimental data from George *(63)*, increasing the layer thickness reduces the number of cracks (i.e., increases the crack spacing). This was attributed to the reduction in the critical depth (defined as the zone at which the shrinkage stress exceeds the strength) with increasing layer thickness.

3.5.3 Effect of Strength on Crack Width and Crack Spacing

The drying shrinkage models developed by George *(65)* and Zhang and Li *(66)* show that crack width and spacing in cement-treated layers both increase as the strength of the material increases. George *(63,65)* calculated crack width and spacing for the different treated soils tested in his study and showed that "at low cement contents, although shrinkage is at a minimum, the base, on account of its low tensile strength, tends to exhibit closely spaced cracks. Conversely, when cement content is increased, tensile strength is also increased, and cracks occur at wider spacings." The model by Zhang and Li indicated the same trends in crack width and spacing observed by George *(63)*.

Studies have shown that increasing the design strength of the base results in increased reflective drying shrinkage cracks, which often leads to failures in asphalt surfacings due to crack disintegration and moisture intrusion *(3,4,14)*. Considering these observations in terms of the modeled results above, it is clear that reduced crack spacing and widths associated with lower strength designs are preferred to increased crack spacing and increased crack width common in higher strength layers. Increased crack widths associated with higher design strengths can lead to a greater likelihood of these cracks reflecting through asphalt concrete layers under traffic as a result of reduced load transfer efficiency.

Other studies on factors affecting shrinkage cracks have determined the following:

- Increasing the cement content requires more hydration water, leading to increased shrinkage cracking *(4)*.
- The amount and type of clay (smectite clays contribute more to shrinkage than other clays) increases shrinkage cracking *(23)*. Some agencies impose restrictions on percentage passing the 0.075 mm (#200) sieve to control the clay fraction *(69)*.
- There are conflicting results regarding the effect of compaction density on shrinkage cracking *(70)*, but there is consensus on keeping compaction moisture content to a minimum, or dry of the optimum moisture content *(4,23,62)*. No literature was found to determine what effect reducing the water content would have on the cementation reactions and on minimizing the risk of shrinkage cracking.

3.6   Design and Construction Considerations to Mitigate Shrinkage Cracks

3.6.1   Design Strength and Cracking Development

George *(3)* provided an insightful discussion on the design philosophy of cement-treated layers. Instead of designing for a specific strength, the concept of designing for a specific drying shrinkage was proposed to minimize the crack susceptibility of a mixture. The goal of this design philosophy was not to eliminate cracks but to mitigate the cracks by distributing them so that their effect on the pavement is minimized. Two scenarios were proposed to contrast the effect with focus on material stiffness (which is positively correlated with strength):

- Scenario-1: a rigid, high strength layer with wide cracks spaced far apart. This scenario is undesirable for the following reasons:
  + High cement content/high strength layers develop wide cracks with poor LTE *(14)*.

- + Wide cracks are more likely to reflect through asphalt concrete layers because of the high stress concentrations at crack tips in contact with the asphalt concrete layer.
  - + Wide cracks result in a rough riding surface and promote localized failures.
- Scenario-2: a less rigid, lower strength layer with closely spaced, finer cracks. This scenario is more desirable for the following reasons:
  - + Improved LTE and reduced shear movement of the crack edges though improved aggregate interlock reduces degradation along the crack *(14,71)*.
  - + Improved LTE reduces the development of secondary cracks of which longitudinal wheelpath cracks are the most detrimental.

George *(3,63)* provided recommendations on design strength and drying shrinkage criteria to minimize crack widths. The proposed criteria for coarse-grained materials, typical of many FDR-C projects in California, based on George's models and an extensive literature review, are:

- A maximum seven-day UCS of 2.1 MPa to 2.4 MPa (300 psi to 350 psi)
- A maximum drying shrinkage of 310 μstrain to limit crack widths to below 2.5 mm

These recommendations accept that drying shrinkage cracks are inherent in cement-treated layers, but by lowering the design strength, crack width and spacing can both be reduced, which mitigates their effect on pavement performance.

The Portland Cement Association (PCA) has advocated for the use of seven-day UCS values that are lower than those traditionally proposed in the past in California *(72)*. A range of strengths between a minimum of 2.1 MPa (≈300 psi) and a maximum of 2.8 MPa (≈400 psi) are now recommended by the PCA *(73)* in combination with durability limits. These strengths are considerably lower than the PCA's previously recommended strength range of 3.5 MPa to 5.2 MPa (≈500 psi to 750 psi) *(74)*.

The PCA *(75)* also recommends that thicker layers up to 300 mm (≈12 in.) be constructed at these lower strengths to create a quality FDR-C layer with a balanced design that can support design loads and be sufficiently durable and impermeable to resist volume changes, the effects of freeze-thaw cycles, and the effects of moisture changes. Thinner layers, between 150 to 200 mm (≈6 to 8 in.), tend to be more brittle and susceptible to more severe shrinkage cracking due to the reduced thickness over which to distribute frictional stresses between the subgrade and treated layer. Compaction can be achieved on these thicker layers using heavy vibrating padfoot or

segmented wheel rollers. The PCA further recommended increasing the recycling depth to greater than 300 mm in areas where the subgrade material is too soft to support the FDR-C layer, especially during compaction. The PCA acknowledges that compaction will likely not be achieved at the bottom of the layer.

The Texas Department of Transportation (TxDOT) has reduced required strengths even further in some districts, from previously specified minimum seven-day strengths of 3.4 MPa (≈500 psi) to between 1.4 and 2.1 MPa (≈200 and 300 psi) in an attempt to better mitigate shrinkage cracking problems experienced in the state *(37)*. This reduction was based on UCS tests on cores sampled from roads with cement-treated layers, which showed that seven-day laboratory-determined strengths of 3.4 MPa typically translated to higher strengths on the road. The high cement contents required to achieve these strengths resulted in a layer susceptible to high shrinkage and to cracking associated with the brittle nature of the compacted material.

The Federal Highway Administration (FHWA) *(76)* recommends a seven-day UCS strength of 2.1 to 3.5 MPa (≈300 to 500 psi) for FDR-C.

At the time of preparing this report, the specified Caltrans design strength range for cement-treated base layers *(77)* was 6.9 and 8.6 MPa (≈1,000 psi to 1,250 psi). The specified seven-day UCS for FDR-C was 2.1 to 4.1 MPa (≈300 to 600 psi). Caltrans does not require durability testing for cement-treated layers.

Other construction considerations to limit the severity of shrinkage cracking include the following:
- Using the lowest possible moisture content needed to compact the layer that will still achieve the target strength and density *(4)*.
- Applying appropriate techniques to slow the rate of curing of the layer. These include maintaining constant moisture content in the layer with regular water spraying (avoiding wetting and drying cycles), using a curing membrane (i.e., emulsified asphalt seal), and/or applying the surfacing layer as soon as the target moisture content reduction has been achieved *(3)*.
- Using stress relief layers to decrease the potential for shrinkage cracks to reflect through the surface layer. Interlayers include a bituminous surface treatment, geofabrics, or geogrids *(4)*.

- Designing inverted pavements with a granular or recycled material layer between the asphalt concrete surface and the cement-treated subbase *(24)*.

3.6.2 Mechanistic Design Considerations

Cement-treated layers are designed based on the fatigue concept that relates to crack initiation at the bottom of the treated layer, and the number of load repetitions required for the crack to propagate to the surface of the layer *(14)*. Layer-elastic theory algorithms are often used to predict the pavement response for mechanistic design procedures by assuming a semi-infinite half space and axisymmetric loading. These assumptions are equivalent to determining the pavement response for an interior loading case where no cracks are present. The critical stress for pavement thickness design when considering fatigue life is the maximum tensile stress at the bottom of the treated layer, which is valid as long as the treated layer is not cracked.

Several researchers have shown that pavements with cement-treated layers typically fail around wide shrinkage cracks *(13,14,15)*. Pretorius and Monismith *(39)* described how the critical stress condition for the cement-treated layer transitions from the interior of the slab (intact area) toward the edge of the slab in the post-cracked phase after shrinkage cracks have developed. The tensile stresses in the post-cracked phase depend on crack width and LTE across the crack, with the critical case equivalent to edge loading for wide cracks. Maximum tensile stress occurs when the load is adjacent to the crack. This stress acts parallel to the crack *(20)* and results in the development of longitudinal cracks *(39)*. Different researchers have proposed the following concepts to determine fatigue life using mechanistic modeling:

- Thompson et al. *(78)* suggested increasing the tensile stress calculated for the interior loading case by 50% to account for edge-loading conditions.
- Thompson *(79)* proposed limiting the stress ratio (tensile stress to tensile strength ratio) from 0.60 to 0.65 by increasing the layer thickness, or strength, to increase fatigue life.
- Kota et al. *(14)* recommended a correction factor of two for the tensile stress calculated for the interior case to adjust the critical tensile stresses adjacent to cracks.

These design concepts provide a conservative approach to account for drying shrinkage cracks present in the layer in the post-cracking phase.

3.7 Shrinkage Crack Mitigation Using Microcracking

Shrinkage cracks in FDR-C and other cement-treated layers can be mitigated through a number of different approaches. Most research has focused on design, in terms of optimizing cement content and layer thicknesses, and on construction, in terms of better mixing, curing, and quality control. At the time this study started, limited research had been undertaken on microcracking the layer soon after construction to alter its cracking behavior and thereby reduce the severity of shrinkage cracks, or on other mitigation measures such as changing the cement chemistry, adding fibers to the cement, or adding emulsified asphalt or synthetic polymer emulsions to the mixing water to alter hydration reactions in the cement.

3.7.1 Early Research on Microcracking

The concept of microcracking was first introduced by George *(23)*, who proposed that the mechanism of microcracking with a static roller is due to bearing capacity failure of the cement-treated layer. Slip planes caused by the bearing capacity failure develop underneath the roller, transverse to the direction of rolling and perpendicular to the surface in the treated layer. These slip planes represent weak planes in the slab which would eventually "heal" during curing but would also serve as zones of weakness or "flaws" from where cracks can initiate.

Litzka and Haslehner *(80)* summarized the findings of their microcracking research in Austria as loading the cement-treated layer with up to five passes of a vibratory roller 24 to 72 hours after final compaction to create a microcracked structure in the treated layer. They concluded that microcracking prevents the development of larger stress cracks, which in turn prevents reflective cracking through the asphalt overlay. Further work in Austria by Brandl *(81)* concluded that the use of microcracking was effective after 24 hours but that additional microcracking is required if the compressive strength exceeds 5.7 MPa (≈725 psi) after two days of curing.

Apart from the early work in Austria, TxDOT appears to have undertaken the most comprehensive work on the topic, but the researchers acknowledge that the interim recommendations published to date were based on a limited experimental design and limited testing and that the findings were not necessarily conclusive based on these limitations *(82)*. Research in Texas was conducted between 2000 and 2005, during which five projects, with a total of 36 test sections, were

evaluated *(5,37,55,70,83)*. The study showed a significant reduction in surface cracking, as well as stiffness recovery after microcracking. Based on the findings, Sebesta *(5)* proposed a method specification that requires that microcracking be performed with three or four single passes of a steel drum roller, with maximum vibration frequency and amplitude settings, between 48 and 72 hours after compaction. After further testing, Scullion *(37)* suggested including a stiffness reduction performance parameter of 40% of the stiffness measured before microcracking, measured with a soil stiffness gauge. No research comparing the effect of roller weight or vibration frequency and amplitude settings appears to have been published. The microcracking research conducted by the Texas Transportation Institute is discussed in greater detail in Appendix A *(2)*.

Smaller studies on the effectiveness of microcracking were undertaken in both Mississippi *(84)* and New Zealand *(85)* as part of larger base stabilization studies. The details of the microcracking process were not documented in the reports prepared from the studies. However, George *(84)* noted that shrinkage cracks could be controlled by "precracking at an early age (24 to 72 hours after construction) by three to four passes of a vibratory roller with 100% coverage." The research focused on stabilizing soil with 5.5% cement by weight of dry material and comparing the effects of precutting joints to induce cracks at controlled distances and precracking (microcracking) to a control section without any crack mitigation measures. There were no significant differences in the FWD-backcalculated stiffness for these three treatments after three years, indicating that the microcracked section regained stiffness, or 'healed,' after microcracking. The microcracked section had 4.8% lineal shrinkage cracks per area of the section compared to approximately 17% and 14% lineal shrinkage cracks per area for the control and precut sections, respectively.

The research in New Zealand *(85)* focused on stabilizing aggregate base materials with different quantities of cement and lime. One section was treated with 4% cement and microcracked to 40% of the initial stiffness (no information was provided on the roller, number of passes, or curing age before microcracking). The microcracked section did not regain stiffness after microcracking, with results comparable to that of a section treated with 1% cement.

3.7.2 Effect of Early Trafficking

Early opening to traffic (i.e., opening to traffic after completion of construction each day) will also result in some degree of microcracking and has been observed to reduce the severity of shrinkage cracking in Texas *(81)*, Mississippi *(86)*, New England states *(87)*, and Japan *(88)*. In Mississippi, an experimental section, where traffic was allowed on a section immediately after construction, performed better than the control section where traffic was diverted for seven days. Conversely, in the New England experiments, data suggested that early trafficking adversely affected the initial strength gain and base layer stiffness in the cement-treated sections. After two days of curing, trafficked cement-treated sections had FWD-backcalculated stiffness values that were 50% lower than those measured on the corresponding untrafficked sections. However, stiffnesses on the trafficked cement-treated sections were still significantly greater than on untreated sections on the same project.

One concern of early opening to traffic is the potential for raveling of the surface. This can be addressed by regular watering of the compacted layer, by applying dilute asphalt emulsion to the surface during or immediately after compaction of the treated layer, or by applying a bituminous surface treatment such as a microsurfacing or chip seal after construction. The latter approach has been used in Texas with reported success *(89,90)*. Work zone traffic speeds need to be enforced on the newly opened sections for the remainder of the construction period and pilot cars should be used when possible.

3.7.3 Other Mitigation Measures

In limited studies, Steyn and Jones *(91)*, and Jones et al. *(92)* observed what appeared to be differences in shrinkage behavior of treated materials when cement and emulsified asphalt or cement and foamed asphalt were combined. In these studies, it was hypothesized that drops of asphalt encapsulated the cement particles, thereby retarding or altering the hydration process and consequently limiting shrinkage. Further research on using this approach to mitigate shrinkage cracking on cement-treated layers is considered to be appropriate but was beyond the scope of this study.

3.8   Field Stiffness Measurements for Assessing Microcracking Effectiveness

Current specifications generally do not require any measurements of stiffness change during microcracking. However, if it is determined that the amount of microcracking is controlling the shrinkage cracking and/or that a treated layer can be "over" microcracked to the point that it has similar strength/stiffness to an untreated layer, an effective method for measuring the reduction in stiffness would be required. Various methods are available for measuring field stiffness of pavement layers, including FWD, lightweight deflectometer (LWD), and SSG. Clegg Hammers have also been used to monitor field stiffness *(87,93)*, but results indicated that they were insensitive to the effects of microcracking *(94)*.

3.8.1   Falling Weight Deflectometer

The FWD is the most commonly used instrument for measuring surface deflection on pavements (Figure 3.11). The surface deflection bowl can be used to backcalculate layer stiffnesses using various software packages based on linear elastic theory of multiple layers.

Figure 3.11: Falling weight deflectometer.

Sebesta and Scullion *(70)* used an FWD to monitor stiffness reduction during microcracking and recommended a target reduction of 60%. There are, however, concerns that the heavier load from the FWD can cause additional microcracking in the influence zone where the weight contacts the layer surface in the early life of the pavement. It is therefore recommended that SSG and LWD measurements are taken before FWD testing *(95)* when comparing different instruments on newly constructed layers. Additional damage caused by the FWD could increase stiffness reduction, leading to conditions underneath the plate that may not be representative of the surrounding pavement. This could lead to halting the microcracking process prematurely. The

surface of FDR-C layers can also be rough and uneven, which can lead to uneven embedment of the plate and poor seating of the geophones, resulting in nonrepresentative deflection results.

In pavement design using mechanistic-empirical inputs, the resultant pavement response (deflection or strain) under applied loads, rather than the stiffness, is the primary focus. Backcalculation of FWD data provides an average stiffness value to characterize the overall deformation resistance of the material under different stress states similar to that under traffic loading.

3.8.2 Light Weight Deflectometer

Light weight deflectometers (Figure 3.12) are portable devices that were developed for measuring the deflection of subgrades and newly constructed unbound aggregate bases. They consist of a load plate, a vertical sliding plate, and several sensors (up to three). Like the FWD, they can be used to measure surface deflection from which layer stiffnesses can be backcalculated. They include a hand-held storage device for acquiring the data. LWDs are customizable with different load plate sizes, load masses, and drop heights. The maximum measurable layer thickness and measurable layer stiffness are typically in the region of 200 to 300 mm (≈8 to 12 in.) and 15 to 70 MPa (≈2.18 to 10.15 ksi), respectively, using a 10 kg (22 lb.) weight. These devices can only be used to calculate the surface modulus of the half space below the instrument. The depth of influence can exceed the thickness of FDR-C layers and will depend on the properties of the underlying materials. On treated layers, this stiffness range is exceeded within days after construction, limiting the use of LWDs to only early-age stiffness measurements.

Figure 3.12: Light weight deflectometer.

Stiffness can be calculated using Boussinesq's equation (Equation 3.20) assuming layer elastic theory. Stress distribution factors determining the shape factor for the distribution of the contact stress between the plate and the soil, and the Poisson's ratio of the soil provided in Table 3.7, were defined by Terzaghi et al. *(96)* as a function of plate rigidity and soil type. For LWDs with single sensors (i.e., one accelerometer in the middle of the plate), the stress distribution and the Poisson's ratio are fixed, with $A = \pi$, $v = 0.5$.

$$E_{vd} = \frac{2 \times F_{peak} \times (1 - v^2)}{A \times \omega_{peak} \times r_0}$$ (3.20)

Where: E_{vd} = Surface Modulus (MN/m^2)

F_{peak} = Maximum Force (MN)

v = Poisson's ratio

ω_{peak} = Settlement amplitude (mm)

r_0 = Plate radius (mm)

A = Stress distribution factor (Table 3.7)

Table 3.7: Stress Distribution Factors for Different Soil Types

Soil Type	Factor (A)
Uniform (mixed soil)	π
Granular material (parabolic)	$3\pi/4$
Cohesive (inverse parabolic)	4

3.8.3   Soil Stiffness Gauge

Soil stiffness gauges are offered by a number of different manufacturers and were also originally developed as an alternative to density measurements on compacted unbound layers. They are portable (Figure 3.13) and typically weigh around 10 kg (22 lbs.). They can take measurements with little preparation of the surface. On hard and rough surfaces typically encountered on projects, a patch of damp sand is used to provide an even footing for the instrument, with the device placed on the sand and twisted to seat the foot.

Soil stiffness is measured by imparting small deflections to the ground at up to 25 different frequencies, ranging between 100 and 196 Hz. Measurable stiffnesses range between 26.2 and 610 MPa (≈3.8 and 89 ksi), with a depth of measurement between 225 and 300 mm (≈9 to 12 in.). Similar to the LWD, this measurement depth can exceed the thickness of an FDR-C layer and results can be influenced by the underlying layer. Stiffness measurements are also a surface modulus of the half space below the instrument. The devices display the average stiffness, the

associated signal-to-noise ratio, which is an indication of the ambient vibrations in the ground, and the standard deviation between the measurements. The measurable stiffness range is lower than those for LWDs and is often exceeded when testing FDR-C layers prior to microcracking.

Figure 3.13: Soil stiffness gauge.

A Young's modulus can be derived from the user specified Poisson's ratio and the measured stiffness using Equation 3.21 *(95)*.

$$S = \frac{P}{\delta}$$

(3.21)

Where: S = Stiffness (MN/m)
P = Force (MN)
δ = Surface displacement (m)

3.8.4 Comparison of Stiffness Measurement Devices

Light Weight Deflectometer and Soil Stiffness Gauge

An LWD and an SSG were used on projects in Utah and Wyoming to monitor microcracking of a cement-treated layer with 4% cement *(94)*. A regression analysis was conducted on the results, and a coefficient of determination of 56.4 was obtained from a dataset containing more than 300 measurements with each instrument. The relationship between the SSG and LWD, developed from this dataset, is shown in Equation 3.21. Reasons for the poor fit were not provided by the authors, but it could be attributed to the increase in variability of the measurements as the stiffness reached the maximum limits of the individual instruments.

$$E_{SSG} = 0.065 \times E_{LWD}$$

(3.21)

Where: E_{SSG} = Stiffness measured with a soil stiffness gauge
E_{LWD} = Stiffness measured with an LWD

Falling Weight Deflectometer and Soil Stiffness Gauge

The data collected by Scullion *(97)* on FDR-C layers were used to compare measurements taken with an SSG to the backcalculated stiffnesses from the FWD data using TxDOT's *Modulus 6.0* software. The relationship is provided in Equation 3.23.

$$E_{FWD} = 27.953 \times E_{SSG} - 6550.5 \text{ (n=9, R}^2 = 0.838)$$ **(3.23)**

Where: E_{FWD} = Stiffness measured with an FWD

              E_{SSG} = Stiffness measured with an SSG

A similar relationship (Equation 3.24) was determined by Chen *(98)*, who compared an SSG and an FWD to characterize subgrade soils and granular bases in Minnesota.

$$E_{FWD} = 37.654 \times E_{SSG} - 261.96 \text{ (n=8, R}^2 = 0.82)$$ **(3.24)**

Where: E_{FWD} = Stiffness measured with an FWD

              E_{SSG} = Stiffness measured with an SSG

The large differences in stiffness measured between the FWD and SSG by different researchers were attributed to the higher loading capacity of the FWD and its ability to measure deflection of the entire pavement structure using multiple sensors compared to the lighter loading capacity of the SSG, which generally only measures stiffness to a depth of between 200 and 300 mm with one sensor. A comparison of studies *(94)* revealed that FWDs generally measured a two-fold reduction in stiffness compared to stiffness gauges (Figure 3.14).
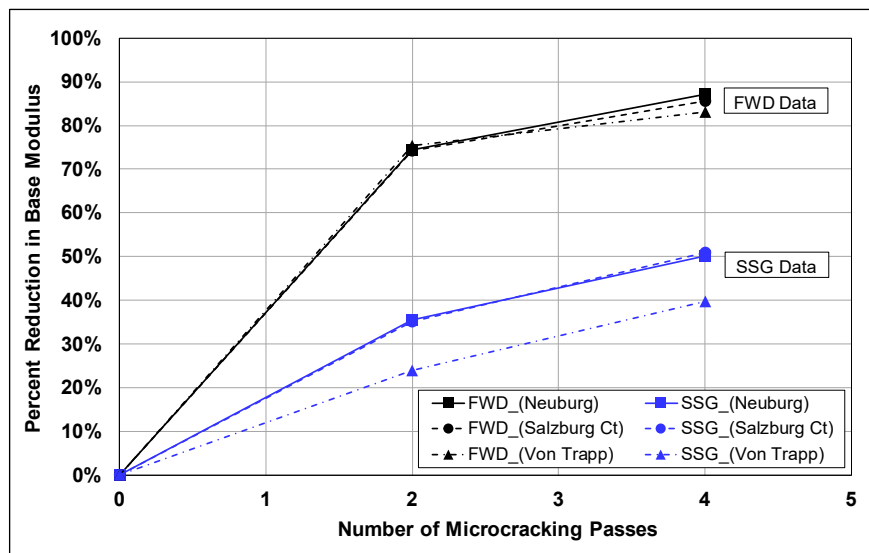
Figure 3.14: Measured stiffness reduction with FWD and SSG during microcracking *(94)*.

3.9 Laboratory Resilient Modulus Triaxial Testing

3.9.1 Different Test Setups for Triaxial Testing

The resilient modulus triaxial test is often used to measure the stiffness of untreated and treated specimens. This is a nondestructive elastic modulus stiffness test which determines the resilient modulus of a specimen under different deviatoric and confinement stress conditions, as described in AASHTO T 307. This method was developed for testing soils and aggregate base materials and can be used to simulate the estimated stress state of unbound material layers in the pavement under traffic. Although not originally developed for testing treated materials, it has been used by numerous researchers for this purpose, including Fu *(99)* who tested FDR-FA materials and Louw et al. *(Error! Reference source not found.)*, Puppala et al. *(100)*, and Potturi *(101)*, who tested FDR-C materials. Alabaster et al. *(85)*, Arnold *(102)*, Gonzalez *(103)*, and Arnold et al. *(104)* tested aggregate treated with foamed asphalt following European Standard EN 13286-7, which has a similar setup to AASHTO T 307. Gnanendran and Woodburn *(105)* and Arulrajah et al. *(106)* tested cement-treated crushed building demolition material with Australian Standard AS 1289.6.8.1, which also has a similar test setup to AASHTO T 307.

Each of the three test methods (i.e., AASHTO T 307, EN 13286-7, and AS 1289.6.8.1) prescribes the use of external transducers, mounted on the actuator, to measure deflection (i.e., the LVDTs measure deflection on the top loading platen of the triaxial cell and not on the specimen, as shown in Figure 3.15).

The applied load is small compared to the strength of unbound materials and is applied repeatedly, resulting in close to completely recoverable deformation proportional to the load. Resilient modulus is defined as the recoverable strain at the peak deviatoric stress, with the deviatoric stress being the difference between the axially applied stress and the confining stress. Since the applied load is small compared to the bearing strength of the material, the same sample can be used repeatedly for multiple tests under different loading and environmental conditions.
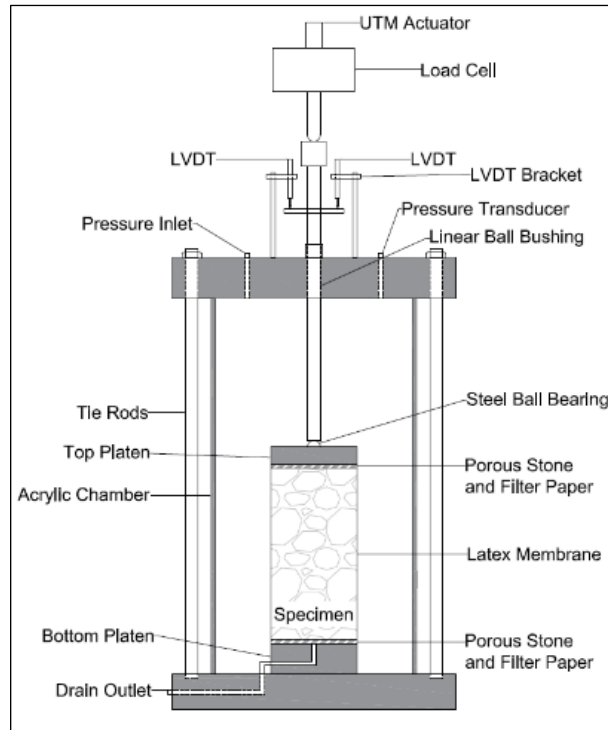
Figure 3.15: Transducer locations for AASHTO T 307 test setup.

Various aspects of triaxial setups for testing pavement materials have been documented since the 1960s *(107)*. One of the key issues identified was non-uniform strain and stress distributions in the specimen. Taylor *(108)* found that the use of porous stone plates in the setup created frictional ends, which led to surface traction and prevented radial deformation at the ends of the specimen when subjected to axial loading. This results in "dead zones" at the specimen ends, leading to the classical hour-glass shape seen after failure in monotonic tests (Figure 3.16 showing FDR-C and FDR-FA specimens), caused by stress states in those zones that are different to those in the middle of the specimen. The magnitude and impact of the "dead zones" depend on material type, degree of stabilization, material stress history, test procedure, and the purpose of the test *(107-109)*.

Several methods have been developed to counter the effect of this non-uniform stress distribution, including the use of lubricated ends *(107)*, frictionless ends *(110)*, or increased height-to-diameter ratio specimens, which provide a larger area of uniform stress distribution across the specimen center *(111,112)*.

Figure 3.16: Typical hour glass shear failure of FDR specimens after UCS testing.

Chiu et al. *(112)* showed that the secant modulus and peak deviatoric stress are reasonably constant with specimen size ratios between 2:1 and 2.5:1. Specimens with height-to-diameter ratios above 2.5:1 tend to buckle under loading and are not recommended *(107)*. Peng *(110)* showed that vertical strains decrease from the specimen ends to a more uniform strain distribution over the middle third of granite and steel specimens with the use of frictional ends. This effect is known as the Saint-Venant's principle. Peng also developed a test setup for more uniform testing that uses Teflon-lined steel inserts between the specimen and the end platens.

Burland and Symes *(113)* found that small strain measurements can be accurately collected using on-specimen transducers. The Transportation Research Board *(114)* discussed various options for measuring on-specimen strain levels using contact methods such as transducers mounted between clamps on the specimen, noncontact methods including proximity gauges, and optical measurements using cameras. For contact measurements, it proposed a method for mounting on-specimen transducers at quarter-points to limit transducer noise.

Hilbrich and Scullion *(115)* mounted LVDTs at quarter-points on 300×150 mm (≈12×6 in.) specimens to measure resilient modulus over the center of the specimen during testing on cement-treated materials and reported satisfactory results. Two LVDTs were mounted at 180° offsets at each quarter-point in these studies. However, they reported considerable sensitivity in

terms of specimen preparation on measured results and reported high variability in excess of 25%. Araya et al. *(116)* tested unbound granular materials for resilient deformation using European Standard EN 13286-7, but with on-specimen LVDTs at third-points.

Louw *(117)* experimented with mounting gauge-points on laboratory compacted FDR-C specimens to measure dynamic modulus at different temperatures in an Asphalt Mix Performance Tester (AMPT) on 150×100 mm (≈6×4 in.) specimens (1.5:1 height-to-diameter ratio compared to typical triaxial test specimens, which have a 2:1 ratio) and obtained reasonable results comparable to backcalculated FWD field measurements at the locations where samples to prepare the dynamic modulus test specimens were taken.

Rashidi et al. *(56)* tested cement-treated specimens and used two sets of noncontact proximity gauges mounted at 180° offsets and also reported satisfactory results.

Groeger et al. *(118)* provided a detailed discussion on AASHTO T 307 and listed several aspects for consideration for an updated version of the specification. Issues included load cell location, deformation measurement, and the number and positioning of LVDTs. The following was recommended:

- The load cell should be located inside the triaxial cell, provided that the LVDTs are mounted on the specimen. The load cell strain measurements should be external to the LVDT strain measurements.
- The LVDTs should be mounted on the specimen to negate any drift in the system if the deflection is measured outside the cell and to alleviate any stress concentrations at the ends of the specimen.
- Two or more LVDTs should be mounted at equal spacing around the specimen.

At the time this report was prepared, no changes had been made to the AASHTO T 307 method for testing treated materials.

3.9.2 Typical AASHTO T 307 Resilient Moduli for Cement-Treated Material

The resilient modulus of cement-treated aggregate determined using AASHTO T 307 typically varies between 200 and 1,000 MPa. Potturi *(101)* compared untreated aggregates with aggregates treated with 2% and 4% cement. The untreated materials had resilient moduli

between 200 and 310 MPa. Cement treatment improved the resilient modulus on average by 52 MPa for 2% cement and 74 MPa for 4% cement compared to the unbound material, equating to improvements of 19% and 28% for the two cement contents, respectively. Puppala et al. *(100)* compared the resilient moduli of untreated RAP materials and those treated with cement contents between 2% and 4%. The RAP treated with 2% cement had resilient moduli between 220 and 450 MPa and the 4% cement between 250 and 500 MPa, equating to increases in resilient moduli of 32% and 50%, respectively, compared to the untreated RAP.

Alabaster et al. *(85)* tested cement-treated materials for rutting using EN 13286-7. Cement contents ranged from 1.5% to 6%. The untreated material had a resilient modulus similar to the results from Potturi *(101)*, ranging from 170 to 300 MPa. The effect of cement treatment was more significant, resulting in stiffness increases between three and six times that of the untreated control specimens, with the largest increase in stiffness determined for the 2% cement treatment, which had a resilient modulus between 900 and 1,150 MPa. The test setup appeared to be insensitive to changes in cement content, with specimens with lower cement contents showing higher stiffnesses than the specimens with higher cement contents. The stiffness of the specimens with 1.5% cement was the same as the stiffness for the specimens with 3% cement, which as not representative of field-determined stiffnesses with an FWD.

These results illustrate the lack of sensitivity of the test setups to changes in material properties associated with using external LVDTs to measure deflection on stiff, cement-treated specimens. The authors noted similar trends in attempts to measure the resilient modulus of FDR-C materials with different cement contents *(9)* using AASHTO T 307 and initiated an investigation to improve the test setup for resilient modulus tests on treated materials in the laboratory. This work is discussed in the Phase 2b research report *(10)*.

3.9.3   Stress Dependency of Unbound and Bound Materials

Unbound materials typically exhibit a nonlinear effect with changes in confining stress. Resilient moduli typically increase with increases in confining and deviatoric stresses, which in turn leads to stress-hardening effects *(108)*, even at relatively low stress levels. This nonlinear behavior can be theoretically explained by two phenomena *(119)*:

- The specimen density increases as particles slide under increasing stresses, resulting in more contact points between the particles.
- An increase in the interparticle forces results in a stronger bond between particles.

For these phenomena to apply to cemented material, it would be necessary for the shear forces between contact points to exceed the friction between the grains and the strength of the cementitious bonds. It can thus be expected that there would be little to no effect of confinement until the cementitious bonds have been broken, whereafter the specimen will behave as an unbound material. This has been proven for concrete *(120)*, frozen silts *(121)*, and lightly cemented soil *(122)* for confining pressures between 90 and 500 kPa.

The sensitivity of cemented materials to shear stress is discussed by Lovelady and Picornell *(119)* and Capdevila and Rinaldi *(122)*. These authors show that the stiffness of cement-treated soils is predominantly controlled by cementation at small strains. Modulus was not sensitive to increased vertical stress at small strains. As the cementitious bonds broke down, resulting in increased strains, the modulus was increasingly controlled by the water menisci. This observation supported the findings by Cho and Santamarina *(123)* and Fernandez and Santamarina *(124)*, who tested cemented sands. A threshold strain was thus observed where the material became stress sensitive due to the breakdown of cementitious bonds, and the material response to stress became more similar to unbound material.

The test results described above from Alabaster et al. *(85)*, Puppala et al. *(100)*, and Potturi *(101)* all suggest that cement-treated materials behave similar to unbound materials (i.e., stress hardening) under different confinement stresses and not according to the phenomena described by Lovelady and Picornell *(119)*, given that the resilient moduli increase with increasing confining pressure and shear stress. This behavior is unlikely to be caused by high stresses exceeding the strength of the cementitious bonds since the resilient modulus test is highly repeatable, and the levels of the axial and confining stresses are low enough to not cause permanent damage in unbound materials. None of these authors discussed this discrepancy and reported that the cement-treated materials were stress sensitive.

3.10 Simulating Microcracking in the Laboratory

The literature regarding laboratory methods for simulating microcracking in cement-treated materials was limited to a few experimental procedures. These procedures had varying degrees of success in inducing microcracking, and control over the percentage stiffness reduction was limited. Reduction in stiffness of up to 60% should be achievable based on the recommendations by Scullion et al. *(97).*

3.10.1 Experimental Methods

George et al. *(3,84)* used a vibratory table, complying with ASTM D2049, to induce microcracks in beam specimens by subjecting them to a 10 Hz vibration for 7 to 10 minutes after 24 hours and again after 48 hours of curing. The beams were confined in steel molds during vibration. The effect of this microcracking was evaluated using modal analysis by measuring changes in the natural vibration frequency of the beams at different times, including before and after microcracking and over time after microcracking, to measure stiffness gain. The vibrating table microcracking method managed to induce damage, or microcracking, and reduced the stiffness in three specimens by 9%, 12%, and 18%. The specimens with 9% and 12% stiffness reductions regained stiffness over time, but the specimen with 18% reduction did not. This method was experimental and is considered to be a viable option in the development of a method to microcrack specimens in the laboratory.

Another potential method for simulating microcracking is the submaximal modulus test, where a stress, corresponding to a certain stress/strength ratio, is cycled for a certain number of cycles to induce damage and determine the effect of the cyclic stress on the resilient modulus of the specimen. Rashidi et al. *(56)* used the submaximal modulus test to measure resilient moduli of cement-treated materials with cement contents between 2% and 5%, after seven days of curing. The specimens were 150 mm (≈6 in.) in diameter and 300 mm (≈12 in.) tall. The cyclic stresses were stress/strength ratios of 20%, 40%, and 60% of the UCS strength of the material. A total of 5,000 cycles were applied axially. The results showed that the modulus generally reduced as the stress/strength ratio increased. This method does not control the reduction in the stiffness. At the high stresses used in this method, damage is induced, cementitious bonds are broken, and

the material behaves in a stress-sensitive manner. This test has also been used by Paul and Gnanendran *(125)*, using a sequence of stress/strength ratios between 20% and 70%, with 200 cycles per sequence.

3.10.2 Specimen Types for Simulating Microcracking

Resilient modulus testing on cement-treated materials is typically done using cylindrical specimens and less frequently using beam specimens. Cylindrical specimens of cement-treated material have been tested by several researchers *(85,100-102,115,119,122)*. They are easier to handle than beam specimens and can be tested at different stress states to control damage, and axial, radial, and volumetric strains can be easily measured.

Beam specimens tested by Yeo *(17)* and Paul and Gnanendran *(125)* were 450×150×150 mm (≈18×6×6 in.) in size and were cured for at least 28 days in a curing chamber before being tested in a four-point beam jig. The beams tested by George et al. *(3)* were 287×76×76 mm (≈11.2×3×3 in.) in size and were tested 24 hours after compaction, but the beams did not have to support the loading point of the four-point bending jig. Jones et al. *(92)* tested FDR-FA beams that were 450×150×800 mm (≈18×6×3.6 in.) in size and noted that the beams were difficult to handle, control of the stress and strain levels were challenging, and the beams often failed under their own weight. This was also observed by Long and Ventura *(126)*.

3.11 Cement Chemistry

ASTM C150 defines eight types of portland cement used in North America. The differences between these are the percentages of different compounds in each cement formulation. Each cement type has different characteristics, including sulfate resistance, high ultimate strength, rate of strength gain, or control of heat of hydration. The cement type primarily used in pavement layers (subgrade and layer stabilization and FDR-C) is Type II, which is moderately sulfate resistant. The tricalcium silicate (C_3A) in Type II cement is limited to 8% to control the heat of hydration. For the purposes of this research study, the literature review focuses only on aspects of cement chemistry associated with understanding early-age strength gain in cement-treated pavement materials.

3.11.1 Cement Notation

Ordinary portland cement (OPC) consists of various compounds of calcium. These compounds are typically reported in terms of oxides of the element present and are abbreviated as shown in Table 3.8. The composition of the main compounds in Type II cement is typically about 30% C_3S, 46% C_2S, 5% C_3A, and 13% C_4AF.

Table 3.8: Cement Chemistry Notation *(127)*

Cement mineral	Compound	Abbreviation	Oxide	Abbreviation
Tricalcium silicate	$3CaO \cdot SiO_2$	C_3S	CaO	C
Dicalcium silicate	$2CaO \cdot SiO_2$	C_2S	SiO_2	S
Tricalcium aluminate	$3CaO \cdot Al_2O_3$	C_3A	Al_2O_3	A
Tetracalcium aluminoferrite	$4CaO \cdot Al_2O_3 \cdot Fe_2O_3$	C_4AF	Fe_2O_3	F
Tetracalcium sulphoaluminate	$4CaO \cdot 3Al_2O_3 \cdot SO_3$	$C_4A_3\bar{S}$	MgO	M
Tricalcium silicate hydrate	$3CaO \cdot 2SiO_2 \cdot 3H_2O$	$C_3S_2H_3$	SO_3	$\bar{S}$
Calcium sulfate dihydrate	$CaSO_4 \cdot 2H_2O$	$C\bar{S}H_2$	H_2O	H

3.11.2 Cement Hydration

The hydration process of cement is dependent on two primary mechanisms. The first is termed through-solution hydration, which is the dissolution of anhydrous compounds into their ionic constituents. This results in the formation of hydrates in the solution, or cement-water paste, which eventually precipitate from the super-saturated solution. The second mechanism is termed the topochemical reaction, during which reactions only take place on the surface of the anhydrous cement without going into solution. Scanning electron microscope (SEM) studies have shown that the through-solution mechanism is dominant in the early stages of hydration, while the topochemical reaction occurs in later stages when ionic mobility becomes restricted.

Cement starts to hydrate as soon as the anhydrous compounds are mixed with water. The compounds do not hydrate at the same rate, with the silicates (C_2S, C_3S) hydrating at a much slower rate than the aluminates (C_3A, C_4AF). Cement paste stiffening (loss of consistency) and setting (solidification) is primarily determined by the hydration reactions of the aluminates. The hardening process (rate of strength development) is dominated by the hydration reaction of the silicates, which constitutes about 75% of the anhydrous cement.

The reaction rate of C_3A is retarded to enable the cement paste to be workable for an extended time period. Gypsum, or calcium sulfate dihydrate ($CaSO_4.2H_2O$), reacts with C_3A and acts as a retarder to the hydration of C_3A by lowering its solubility in the presence of hydroxyl, alkali, and sulfate ions in solution. Two crystalline products precipitate, depending on the ratio of aluminates to sulfate ions. These products are calcium aluminate trisulfate hydrate (ettringite) or calcium aluminate monosulfate hydrate (monosulfate). Ettringite is usually the first hydrate to precipitate in the high ratio of sulfate to aluminate ions in the solution. Ettringite crystallizes as short prismatic needles and contributes to stiffening of the mixture, setting, and early strength gain. During the later stages of hydration, when the sulfate concentration is low and the aluminate ion concentration increases due to the renewed hydration of C_3A and C_4AF, ettringite becomes unstable and converts to monosulfate, the final product of hydration of portland cement. The latter pertains to anhydrous cement containing more than 5% C_3A. If there is a small excess of sulfate, both ettringite and monosulfate will be produced in the final material. With increasing sulfate concentration, more ettringite and less monosulfate will be precipitated, which can be deleterious to structures because of the high rate of expansion of ettringite *(22,127)*.

Hydration of the silicate produces calcium silicate hydrates (CSH gel). The precipitate is poorly crystalline, forming a porous solid with properties similar to a rigid gel. The hydration reaction also forms calcium hydroxide ($Ca(OH)_2$), which raises the pH to 12.4 and is required for the long-term durability of the cementitious products *(22)*. C_3S hydrates at a faster rate than C_2S due to differences in crystal structures *(127)* and contributes to the final set and the majority of the early age strength after setting about one hour in the hardened cement paste. C_2S contributes predominately to the hardened paste strength after seven days of curing.

3.11.3 Soil Modification and Cementation

Strength development in cement-treated aggregate and the rate at which it develops depend on the following *(22)*:

- Soil type properties
- Quantity of stabilizer added
- Type and fineness of stabilizer
- Mixing uniformity

- Temperature during compaction
- Compaction density
- Curing period and condition

Soil modification occurs rapidly during the initial stages of treatment and involves neutralizing reactions of ion exchange and flocculation of the clay mineral fraction of the soil *(128)*. Soil modification partially or completely alters the clay minerals in order to reduce soil plasticity. Ion exchange is the process whereby the calcium ion (Ca^{2+}) displaces the sodium (Na^+) and hydrogen (H^+) ions on the surface of the negatively charged clay particles to change the soil from a hydrophilic condition to a hydrophobic condition. This process releases bound water held by the Na^+ ion and allows the water to evaporate, thereby drying the material. Flocculation occurs together with ion exchange. Crowding of the Ca^{2+} ions on the surface of the negatively charged particles raises the positive electrical charge of the clay particles. The divalent Ca^{2+} ions that replace the univalent Na^+ and H^+ ions increases the attraction force between clay particles, resulting in flocculation and decreased plasticity.

Cementation, or stabilization, usually takes longer than modification and will continue as long as there is sufficient moisture and the pH is in excess of about 12.4 *(22)*. The end product is a material with decreased plasticity and significantly increased shear and tensile strength properties.

3.11.4 Initial Consumption of Stabilizer

The amount of cement required for cementation is greater than that required for modification, which only requires enough stabilizer to satisfy the Ca^{2+} demand to modify the soil and to maintain a constant pH. This quantity of stabilizer is referred to as the initial consumption of stabilizer (ICS). Failure to satisfy the ICS can result in reversion of the plasticity of the material *(22,114,129)* and or carbonation (discussed in Section 3.11.5) of the top of the layer. Additional stabilizer will only contribute to cementation if the ICS demand is met. Paige-Green and Jones *(22)* recommended the addition of a minimum 1% additional stabilizer to the ICS to ensure sufficient residual stabilizer remains to maintain a sustained high pH to prevent carbonation and to ensure durability of the treated material. Additional cement can be added if required to meet UCS requirements.

The initial consumption of lime (ICL) test method (ASTM D6276) can be followed to determine the ICS, with the following key differences *(11,22)*:

- Cement is used instead of lime.
- The test is done on the aggregate passing a 19 mm (3/4 in.) sieve.
- The ICS is the percent cement required to achieve constant pH rather than a pH of 12.4.

3.11.5 Carbonation of Cement Treatment Pavement Layers

The adverse effect carbonation has on cementation in cement-treated layers has been documented since the 1960s. Carbonation occurs when lime and cementation products, including those that develop during hydration reactions of cement treatment, react with carbon dioxide (CO_2) in the atmosphere or soil air *(130)*. Carbonation can occur in the treated layer due to ineffective curing techniques or through exposure to the atmosphere for extended periods. It can occur from the top, from the bottom, and from the sides of the road as well as through cracks. The product of these reactions is calcium carbonate ($CaCO_3$), resulting in a reduction of the pH of the treated material to that of calcite (about 8.3) and causing instability of the remaining cementitious products *(22)*.

Common causes of carbonation of treated layers include cement contents that do not satisfy initial consumption (discussed in the previous section) and/or inappropriate curing methods used during construction. Wet curing of the layer requires maintaining a near constant moisture content throughout the curing period. In reality, this often entails multiple wetting and drying cycles, which results in weakening or loosening of the top 6 to 25 mm ($\approx$0.25 to 1 in.) of the treated layer. This thin, loose layer rapidly carbonates, resulting in a weakly cemented layer with an increasing presence of $CaCO_3$ and a reduction in pH *(22)*. If carbonation of the surface of the treated layer is not addressed, either by removing the loose layer or applying an asphaltic curing membrane, it can lead to debonding between the treated layer and the asphalt concrete overlay *(131)*.

Carbonation causes disintegration of the treated layer through:

- Volume increase (approximately 10%) as $Ca(OH)_2$ reacts with CO_2 to produce $CaCO_3$
- Volume decrease (approximately 2%) as the cementation products revert to silica and $CaCO_3$

The stresses generated by these volume changes can induce microcracking. If these microcracks coalesce, the material can lose strength and be prone to raveling and densification (rutting) under traffic *(132)*. Microcracking due to carbonation should not be confused with microcracking for shrinkage crack mitigation, which is discussed in Section 3.7.

Identifying Carbonation

Carbonation can be identified using indicator tests such as phenolphthalein and hydrochloric acid *(22)*. Phenolphthalein, when applied to the surface of the treated layer, turns crimson in the presence of high pH (>10). A lighter pink color indicates a pH between 8.4 and 10. If no reaction with the phenolphthalein is observed, hydrochloric acid (HCl) can be used to determine if any carbonates are present. Carbonated stabilizer will effervesce in the presence of HCl. Care should be taken where carbonate aggregates and soil are present (limestones, dolomites, caliche, etc.), as the HCl will react with these, masking any reaction with the stabilizer.

Preventing Carbonation

Carbonation can be prevented by choosing a cement content that satisfies initial consumption and provides adequate strength, and by following appropriate construction and curing methods *(22)*. Construction procedures to minimize carbonation include the following:

- Compacting the layer to as high a density as possible and as soon as possible after mixing with the stabilizer
- Ensuring that final grading and shaping procedures only cut the surface and do not attempt to address low spots or unevenness by spreading thin layers of treated material in problem areas
- Sealing treated layers with an appropriate curing membrane as soon as possible after compaction

The effectiveness of a variety of curing techniques is discussed in Paige-Green et al. *(130)*. The most effective curing technique to minimize carbonation was a prime coat applied immediately after final compaction. The treated layer should be kept continuously wet between construction and priming and must be relatively damp at the time of priming.

3.12 Microcracking in Concrete

It is theorized that a basic understanding of microcracking in cement-treated pavement layers can be gained from understanding microcracking in concrete. The fundamentals of microcracking in concrete are the following *(133)*:

- Compressive failure of concrete is always preceded by microcracking *(134-136)*.
- The plane of the microcracks is parallel to the direction of the maximum compressive stress.
- Microcracking causes the nonlinearity observed in the ascending stress strain behavior under uniaxial and triaxial compression *(137)*.
- No plasticity exists in the nonlinear stage of loading.
- The accumulation of microcracking causes the concrete to degenerate internally and is therefore called atrophy, not damage, which is caused by external actions.
- Failure of concrete under compressive loading occurs when the limiting atrophy is reached, which occurs the moment when the absorbed loading energy equals the loss of energy due to degeneration *(138)*.

In concrete, interfacial cracks form at the boundary between the mortar and the coarse aggregate due to volume changes in the cement paste *(139)*. Under compressive loads of less than 30% of the compressive strength, no additional cracks form *(137)*. When the compressive load exceeds 70% of the compressive strength, microcracks start to propagate throughout the mortar, forming continuous cracks parallel to the compressive load direction, until failure is achieved *(140)*.

Cyclic loading has been shown to cause measurable damage at low loads *(141)*, which has been linked to the formation of hairline cracks under compressive loading *(142)*. Attiogbe and Darwin *(143)* established a relationship between nonlinear deformation and cracking of cement paste.

To relate microcracking in concrete to microcracking in cement-treated layers, it is theorized that since cement-treated material gains its improved properties from cementitious bonds, similar to how concrete achieves its high strength, microcracks will form in cement-treated layers in the same way that they form in concrete. The authors acknowledge that there are differences between concrete and cement-treated materials but consider that the fundamental method of microcracking is not affected. These differences include the following:

- Concrete is consolidated, but not compacted, to release entrapped air, whereas cement treated layers are compacted to improve aggregate interlock, prevent permanent deformation, and reduce air voids.
- Concrete typically contains more than 11% cement by weight of dry aggregate, whereas cement-treated materials, with design strengths of less than 4.1 MPa (≈600 psi), typically contain less than 6% cement
- The ideal water to cement ratio for concrete is between 0.38 and 0.44 *(144)*, compared to the water to cement ratio of cement-treated material, which is usually between 1.0 and 1.3.

3.12.1 Autogenous Healing

Autogenous healing in concrete occurs when microcracks heal. Autogenous healing has been attributed to the following four factors occurring between the cracks *(145)*:

- Formation of calcium carbonate or calcium hydroxide
- Sedimentation of particles
- Continued hydration
- Swelling of the cement matrix

The type of precipitate is dependent on the crack width. Yang et al. *(146)* reported CSH precipitates in cracks less than 20 μm wide and calcium carbonate ($CaCO_3$) in cracks greater than 50 μm, regardless of concrete age. Neville *(147)* determined that the healing mechanism is dependent on the age of the concrete with continued hydration, with CSH precipitating in young concrete, and $CaCO_3$ precipitating in older concrete. While differing opinions exist regarding the healing mechanisms, there is consensus that water must be present through continued hydration for healing to occur *(148)*. Autogenous healing of cracks with widths of up to 300 μm have been reported *(149)*.

Autogenous healing in cement-treated layers has been observed by a number of researchers *(3,38,70,84,94)* in subsequent days after microcracking, during which the pavement recovered nearly all of its original stiffness. George et al. *(3)* developed a theory for the healing observed in damaged (i.e., microcracked) specimens whereby the CSH gel formation continues to be active in cracked specimens, along with the growth and nucleation of $Ca(OH)_2$ crystals in the continuum pore space. George further stated that fresh $Ca(OH)_2$ could permeate into existing microcracks to bridge crack openings, resulting in cracked specimens regaining stiffness to the same level of

uncracked specimens. Both cracked and uncracked specimens thus benefit from CSH gel formation and cementation, while precracked materials benefit more from Ca(OH)$_2$ in crack openings.

3.12.2 Effect on Permeability

Concrete permeability is influenced by two primary factors: (1) porosity and interconnectivity of pores in the cement paste and (2) microcracks *(127)*. The porosity and interconnectivity of the pores are predominantly affected by the water-to-cement ratio, degree of compaction, and degree of hydration. Microcracks are caused by drying shrinkage, thermal shrinkage, and externally applied loads.

Several researchers have investigated the effects of microcracking on the permeability of concrete:

- Kermani *(150)* tested the permeability of 200×100 mm (≈8×4 in.) mature concrete specimens under different uniaxially applied stress levels. Permeability increased significantly when stress levels exceed 40% of the compressive strength of the material.
- Hearn *(151)* induced microcracks in 200×100 mm (8×4 in.) mature concrete specimens by loading the specimens uniaxially up to 80% of the average compressive strength. He determined that load-induced microcracks had no measurable effect on the permeability of mature concrete that was unloaded when tested for permeability. This was attributed to the elastic recovery of the concrete that caused the cracks to close after unloading.
- Banthia et. al. *(152)* tested 200x100 mm concrete specimens for permeability after one and three curing days under both loaded and unloaded conditions. The results showed that the permeability in the loaded case increased significantly over the unloaded case when the specimens were loaded to 40% of the compressive strength of the specimens.

3.13 Literature Review Summary

The following conclusions with regard to understanding microcracking as a shrinkage crack mitigation method for cement-treated materials were drawn based on the literature review:

- Microcracking can reduce the number of shrinkage cracks in cement-treated layers compared to no microcracking by inducing a network of fine cracks early in the life of the layer.
- Lowering the cement content, or reducing the strength of a material, will result in more frequent, but thinner, shrinkage cracks.

- There is no comprehensive literature available on the mechanism of microcracking in cement-treated layers in pavements.
- There are no established laboratory test methods to reliably induce microcracking in the laboratory or for testing the effects of microcracking.
- Mechanistic-empirical models have not been developed to account for the effect of microcracking on the fatigue and crushing properties of cement-treated layers.
- The literature on field microcracking methods is limited. The current method for microcracking is three passes with a 12-ton roller, between 48 and 72 hours after final compaction. No published information was located that details the effect of microcracking on layers with different strengths and thicknesses. Research to develop these preliminary recommendations did not consider all the variables that might influence the effectiveness of microcracking.
- A range of devices are available for measuring the effect of microcracking on the stiffness of cement-treated layers. Each device has limitations that have not been fully quantified in terms of its suitability for use as a microcracking quality control procedure on construction projects. There is no consensus on which instrument to use to effectively measure the effect of microcracking on the stiffness of FDR-C layers.

This literature review discussed the problems associated with cement-treated layers and the adverse effects of shrinkage cracks and provided a review of existing work that highlighted the potential benefits of microcracking. The following statement was developed to formulate the specifications of microcracking as a construction procedure used to extend the service life of cement-treated layers and the pavements that are constructed/rehabilitated with them:

Microcracking is a method consisting of a combination of the optimum number of passes (or stiffness reduction) and curing times before starting the process that maximizes the long-term stiffness to maximize fatigue life and minimize crack width to minimize failures associated with drying shrinkage cracks.

4 TEST ROAD EXPERIMENT DESIGN

4.1 Introduction

The construction of a test road to evaluate different microcracking variables was recommended after the conclusion of the preliminary field studies *(9)*. This approach allowed for the inclusion of control sections where no shrinkage crack mitigation measures were taken as well as a significantly wider factorial than could be achieved on any FDR-C field projects, which typically do not include control sections. The FDR-C Test Road design considered the various issues identified during the pilot studies and on the foundational work done in Texas *(37)*, and the knowledge gaps identified in the literature review. The following factors were considered when designing the experiment:

- Mix design strength (i.e., cement content)
- The number of curing hours between completion of construction and start of microcracking
- Roller weight
- Roller vibration amplitude
- Number of roller passes
- Stiffness reduction during microcracking
- Stiffness recovery/gain after microcracking
- Crack propagation and crack properties

Outcomes from the experiment would be used to achieve the following:

- Determine the effect of mix design on stiffness and drying shrinkage cracking behavior of FDR-C layers.
- Evaluate the effect of microcracking on drying shrinkage cracking behavior and stiffness gain, considering roller weight, vibration amplitude, and curing time before microcracking.
- Determine whether microcracking causes new cracks or results in crushing of the surface of FDR-C layers.
- Recommend revisions to Caltrans FDR-C mix design requirements and specifications, if justified.

4.2 FDR-C Test Road Location

The FDR-C Test Road was located on the University of California, Davis campus, on a road that is used by a combination of light-vehicle traffic and some heavier agricultural equipment.

Occasional heavy vehicle traffic meant that the distresses would be limited primarily to those associated with environmental- and material-related factors, rather than load-related factors. The proximity of the test road to the UCPRC (Figure 4.1) allowed for frequent visual assessments, stiffness testing, and crack monitoring.
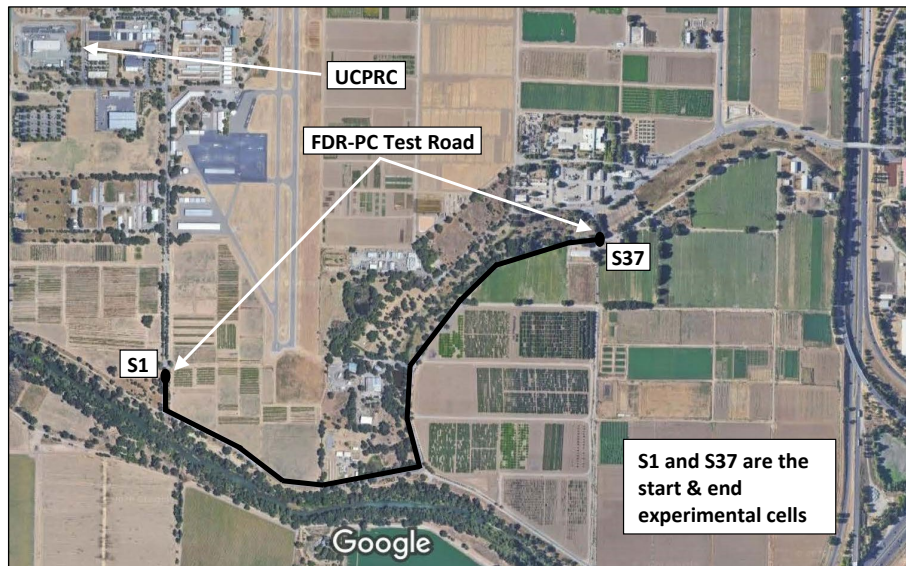
Figure 4.1: Test road location (Google Earth).

4.3 FDR-C Test Road Pavement Design

The FDR-C Test Road design was based on typical Caltrans FDR projects on rural roads, which generally consist of multiple asphalt concrete layers on an unbound base layer. Although of interest to the study, experimentation with higher plasticity materials, where cement stabilization would have specific benefits, was not considered. Although Caltrans FDR projects are typically designed with a minimum 0.2 ft. (≈60 mm) thick asphalt concrete layer, the FDR-C Test Road was designed with a 0.25 in. (≈6 mm) thick microsurfacing so that cracking behavior could be readily observed. The pavement design is shown in Figure 4.2.

The existing road consisted of 0.15 ft. (≈50 mm) of distressed asphalt concrete over a thin, marginal aggregate base of varying thickness, over silty-clay subgrade. To meet the proposed design, 0.6 ft. (≈175 mm) of asphalt concrete millings were imported and spread on top of the existing pavement prior to recycling. Recycle depth was set at 0.85 ft. (≈255 mm), thereby incorporating the imported millings, the existing asphalt concrete layer, and approximately 1 in. (≈25 mm) of the underlying material.
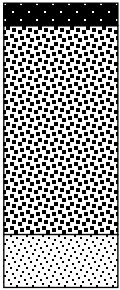
Figure 4.2: FDR-C Test Road pavement design (not to scale).

4.4 FDR-C Test Road Experiment Design

The experiment design for the FDR-C road is summarized in Table 4.1. A total of 37 cells (S1 through S37) were included in the factorial. Common attributes among the cells were the contractor, cement type, recycling depth, parent material, and subgrade. Factors investigated included design strength (i.e., cement content), curing time before microcracking, roller type, applied energy, vibration amplitude, and microcracking effort (i.e., number of roller passes).

Although the different microcracking actions were applied across the full width of the road, only the eastbound lane was evaluated (Figure 4.3). The westbound lane was used to maneuver the roller so that the behavior on one test section would not be affected by microcracking activities on an adjacent section. To further minimize actions on one section influencing another section, only the middle 39 m (≈128 ft.) of each test section was evaluated, with the 5 m (≈16 ft.) on either end of each section being considered as a transition zone between sections.

4.4.1 Design Strengths

The two mix design strengths considered for this study were the lower and upper ranges of seven-day UCS that were specified by Caltrans for FDR-C in California at the time of construction (2015 Standard Specifications), namely between 300 and 600 psi (≈2.1 and 4.1 MPa). The lower strength mix design would target the lower strength of the specification (i.e., 300 psi) or the strength determined using the minimum cement contents determined by the initial consumption of stabilizer (ICS) and tube suction tests (TST).

Table 4.1: FDR-C Test Road Microcracking Factorial

	Higher Design Strength (Target 600 psi [4.1 MPa] UCS)						Lower Design Strength (Target 300 psi [2.1 MPa] UCS)				
Cell	Curing Time (hrs)	Roller Type[a]	Vibration Amplitude	Roller Passes	Instruments[b]	Cell	Curing Time (hrs)	Roller Type[a]	Vibration Amplitude	Roller Passes	Instruments[b]
S1*	Control. SSG/LWD/FWD Calibration Cell				-	S17	48	DSR	High	3	-
S2	48	SSR	Low	3	Yes	S18	72	DSR	High	3	-
S3	48	SSR	High	1	Yes	S19	48	SSR	High	3	-
S4	48	SSR	High	3	-	S20	48 & 72	SSR	High	3	-
S5	48 & 72	SSR	High	3	-	S21	48	SSR	High	2	-
S6*	Control				-	S22	48	SSR	High	1	Yes
S7	72	SSR	Low	3	-	S23	72	SSR	High	3	Yes
S8	72	SSR	High	1	-	S24	48	SSR	Low	3	Yes
S9	72	SSR	High	2	-	S25*	Control				Yes
S10	72	SSR	High	2	-	S26	72	SSR	High	1	-
S11	72	SSR	High	3	Yes	S27	72	SSR	High	2	-
S12	48	SSR	High	3	Yes	S28*	Control. SSG/LWD/FWD Calibration Cell				-
S13*	Control				-	S29	72	SSR	Low	3	-
S14	48	DSR	High	3	-	S30	48 & 72	SSR	High	3	-
S15	72	DSR	High	3	-	S31	48	SSR	High	3	-
S16	72	SSR	High	3	-	S32	72	SSR	High	3	-
S37	48	SSR	High	2	Yes	S33*	Control				-
						S34	48	SSR	High	2	Yes
						S35	48	SSR	Low	1	Yes
						S36*	Control				Yes

[a] Roller Type SSR = 12-ton single steel smooth drum vibratory roller
   DSR = 10-ton double steel smooth drum vibratory roller
[b] Instruments included moisture gauges and vibrating-wire strain gauges
* Control cells with no microcracking

Figure 4.3: Test section planning.

4.4.2 Curing Time Before Microcracking

The 2015 Caltrans Standard Specifications (current at the time of construction) required that microcracking is completed during a 24-hour period from 48 to 72 hours after compaction. This is also the period during which cement hydration is occurring rapidly. Curing periods of 48 and 72 hours were therefore considered in the factorial along with one cell in each design-strength section to assess microcracking after 48 hours and again after 72 hours. The 48- and 72-hour single microcracking event options were considered relevant given that the roller used for microcracking is typically one of the rollers that is being used for layer compaction, and it may not be readily available for microcracking at the same time each day.

The 48- and 72-hour double-microcracking events (i.e., microcracking after 48 hours and again after 72 hours) were considered to evaluate whether this approach might be beneficial for higher cement content sections and what effect this extensive action would have on cement hydration—whether the FDR-C layer would continue to hydrate and gain strength or whether the extensive breakdown of bonds and the visible microcracks on the surface would be detrimental to the life of the pavement.

4.4.3 Roller Type

The 2015 Caltrans Standard Specifications specifies that "a 12-ton vibratory steel drum roller …" should be used for microcracking, which is based on the work done by Scullion *(37)*. A 12-ton single steel drum vibratory roller (SSR) is commonly used for final compaction of FDR-C layers. A 10-ton dual steel drum vibratory roller (DSR), which is often used for breakdown compaction of asphalt concrete layers and available on FDR-C construction projects closer to the time that the asphalt concrete surface layer will be placed, was included in the factorial. Use of this roller for microcracking was noted on one of the field projects monitored during Phase 1 of the study. The rollers used on microcracking projects discussed in the literature had weights of 12 tons and

greater. Given that there is limited data on using lighter-weight rollers for microcracking, they were added as a consideration in the factorial, which included a 12-ton SSR (Figure 4.4) and a 10-ton DSR (Figure 4.5). The roller properties are provided in Table 4.2.

Figure 4.4: 12-ton SSR used for microcracking on FDR-C Test Road.

Figure 4.5: 10-ton DSR roller used for microcracking on FDR-C Test Road.

Table 4.2: Vibratory Roller Information.

Roller Parameter	12-Ton Roller	10-Ton Roller
Operating weight (tons)	12	10
Drum width (mm)	2,134	1,675
Drum diameter (mm)	1,534	1,220
Static load (kg/cm)	33.4	29.5
Weight on drum (kg)	7,128	4,948
Static force (kN/cm)	0.3	0.3
Centrifugal linear force (kN/cm) – Low	0.6	0.4
Centrifugal linear force (kN/cm) – High	1.1	1.0

4.4.4 Applied Energy

The magnitude of the force applied by the roller provides a measure of the energy input during microcracking. Each roller was equipped with an eccentric mass in the drum, which generates a force vector of constant magnitude. The orientation of the vector is varied by rotating the eccentric mass assembly. The vertical component of the centrifugal force, $F(t)$, can be calculated using Equation 4.1.

$$F(t) = F_{ev} \cos(\Omega t) \qquad \qquad \textbf{(4.1)}$$

Where: F_{ev} = Amplitude of $F(t)$
Ω = Circular excitation frequency
t = Time (s)

The total force (F_s) transmitted to the layer is illustrated in Figure 4.6 and can be determined using Equation 4.2. The total force applied during microcracking for the two rollers used in the study is

provided in Table 4.3. Equation 4.2 does not consider the effect of the drum leaving the surface of the pavement (i.e., if and when it bounces).
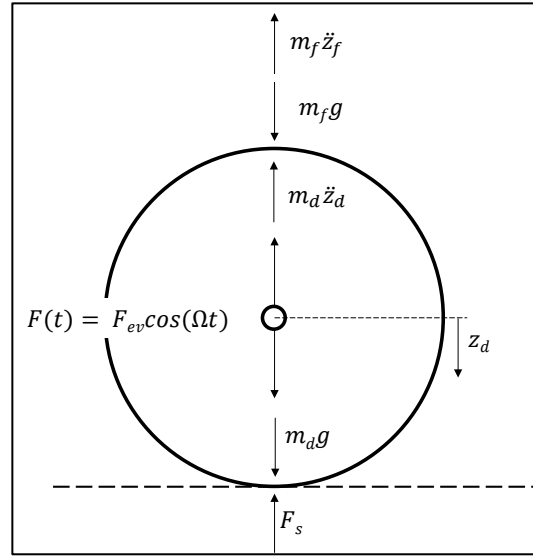
Figure 4.6: Roller drum force diagram.

$$F_s = F_{ev} \cos(\Omega t) + (m_f + m_a)g - m_a \ddot{z}_d - m_f \ddot{z}_f \tag{4.2}$$

Where: F_s = Force transmitted to layer (N)

m_d, m_f = Mass of drum and frame respectively (kg)

g = Acceleration of gravity (kg/m^2)

$\ddot{z}_d, \ddot{z}_f$ = Drum and frame accelerations respectively (kg/m^2)

Table 4.3: Total Force Applied During Microcracking

Roller Operating Weight (tons)	Vibration Amplitude	Total Force (kN)	Linear Total Force (kN/cm)
10	High	220	1.31
12	Low	203	0.95
12	High	304	1.42

The inertia of the frame ($m_f \ddot{z}_f$) has been shown to be negligible *(153)* and is often not calculated. The two rollers used on the FDR-C Test Road were not equipped to measure the vertical displacement of the drum, and therefore the drum inertia factor was not considered. Vibration amplitude values are therefore reported as an indication of the excitation force amplitude. The vertical compressive forces calculated using Equation 4.2 for the 12-ton roller at no, low, and high vibration amplitude are provided in Figure 4.7.
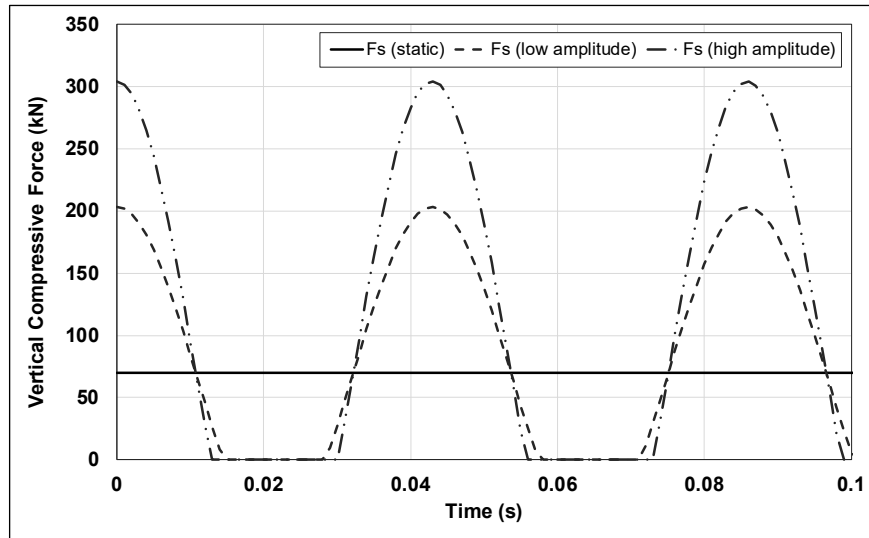
Figure 4.7: 12-ton vibration loading at different amplitudes at 30.5 Hz.

4.4.5 Vibration Amplitude

The 2015 Caltrans Standard Specifications specify that a "… 12-ton vibratory steel drum roller at maximum amplitude …" should be used for microcracking. The specifications do not specify the vibration amplitude magnitude, only the setting, and it is conceivable that this will vary by roller manufacturer and the condition of individual rollers. To evaluate this effect, the low and high vibration amplitude settings on the 12-ton vibratory roller were used as variables in the microcracking factorial. The nominal amplitude of the low and high amplitude setting were 0.9 mm (0.035 in.) and 1.8 mm (0.07 in.), respectively (sourced from Caterpiller specification sheets). The standard vibration frequency of the 12-ton roller used on the project was fixed at 31.9 Hz and could not be adjusted. The effect of vibration amplitude was not evaluated for the 10-ton roller. On this roller, the vibration amplitude was set to the maximum (0.64 mm [0.025 in.]) for both drums during microcracking.

4.4.6 Microcracking Effort/Number of Roller Passes

The 2015 Caltrans Standard Specifications specify to "… microcrack the surface by applying three single passes with a 12-ton…". This is a method specification, and it does not require measurement of the effectiveness of the applied treatment. The recommendation by Scullion *(37)* was closer to a performance specification, requiring that a certain percentage reduction in stiffness be met, as measured with a soil stiffness gauge. Cells were therefore included in the

FDR-C Test Road factorial to quantify the implications of only following a method specification. The microcracking efforts ranged between one and three vibratory roller passes. Microcracking effect was measured after each roller pass had been applied to determine the percent stiffness reduction. Soil stiffness gauges (SSG, Figure 4.8) and two light weight deflectometers (LWD, Figure 4.9), from different manufacturers, were used for these measurements.

Figure 4.8: Testing with soil stiffness gauges.
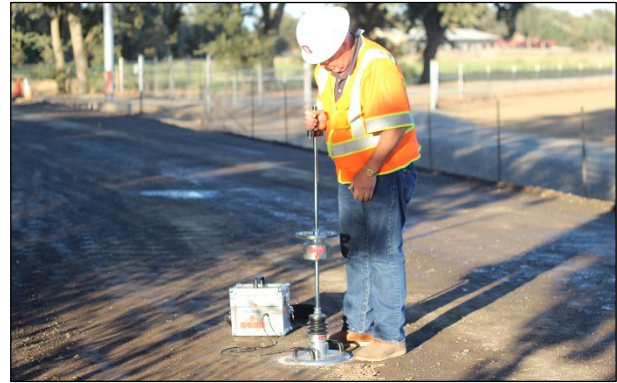
Figure 4.9: Testing with light weight deflectometer.

4.5   FDR-C Layer Mix Design

The mix design for the FDR-C layer needed to be conducted on materials representative of typical FDR projects in California. These are typically multiple asphalt overlays over a base layer, often constructed with marginal aggregates, over subgrade. Some lower volume traffic pavements may simply be asphalt concrete layers placed directly on prepared subgrade. RAP millings were used in the mix design to represent the asphalt concrete layers, while base and subgrade material were sourced from the project site. Two mixing ratios were used to evaluate the effects of including a greater portion of subgrade and to determine the depth to which the existing pavement should be recycled. The mixing portions were 80:20 (typical Caltrans FDR project) and 50:50 (same as the UCPRC FDR Test Track) RAP to subgrade material. The cement type used for the mix design was Type II/V, the same type of cement that is specified for all FDR-C projects in California.

Different tests were performed to determine the target cement contents for the study, including the following:

- Material characterization tests, which included a grading analysis, Atterberg limits, optimum moisture content (OMC), and maximum dry density (MDD)

- Initial consumption of stabilizer (ICS) tests to determine the minimum amount of stabilizer required to maintain a constant pH
- Tube suction testing (TST) to provide a measure of the moisture sensitivity of the mix
- Unconfined compressive strength (UCS) testing

The 2015 Caltrans Specifications required a seven-day UCS to be between 300 and 600 psi (≈2.1 and 4.1 MPa). No other tests are currently required to test for sufficient cement for cementation or for durability. The mix design procedure in this study followed the specified method but added ICS and TST tests to identify the starting lowest cement content required to achieve a durable mix.

4.5.1 Material Classification

Grading analyses were performed according to AASHTO T 11 and AASHTO T 27 for wet and dry sieving, respectively, of the RAP and unbound in situ materials. The RAP and unbound materials were combined in the ratios of 80:20 and 50:50. The results are plotted in Figure 4.10.

Atterberg limits of the RAP, in situ unbound, and combined materials were determined according to AASHTO T 89 (liquid limit [LL]) and AASHTO T 90 (plastic limit [PL]). The RAP was classified as non-plastic and the in situ unbound material had a plasticity index (PI) of 18. The Unified Soil Classification System (USCS, ASTM D2487) classifications of the RAP, in situ unbound, and combined materials are provided in Table 4.4.
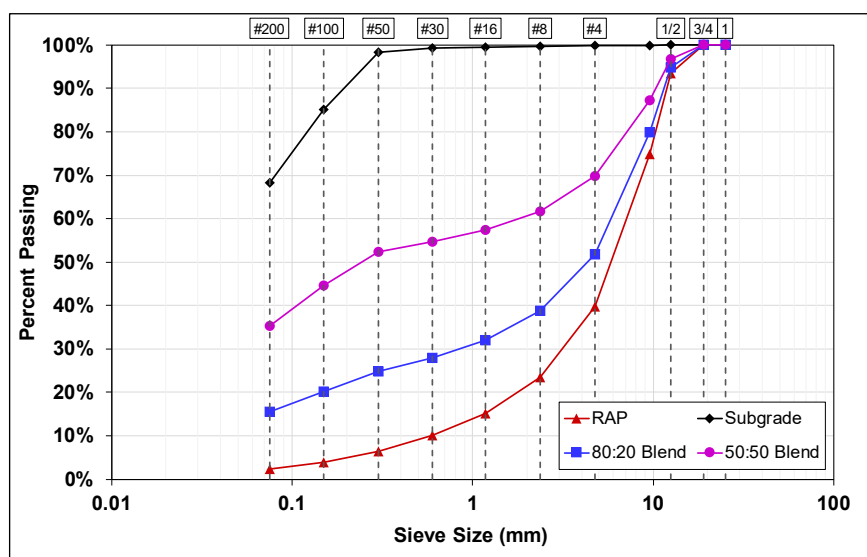
Figure 4.10: Sieve analyses of FDR-C Test Road materials.

Table 4.4: Material Classification

Material	USCS	LL	PI	P0.075mm[c]
RAP	Poorly-graded gravel (GP)	NM[a]	NP[b]	2
In situ unbound	Low plasticity clay (CL)	38	18	68
80% RAP:20% subgrade	Clayey gravel (GC)	32	13	15
50% RAP:50% subgrade	Clayey sand (SC)	35	14	35

[a] NM = not measurable (soil sample slipped)
[b] NP = non-plastic
[c] P0.075 = percent passing the 0.075 mm (#200) sieve

4.5.2 Optimum Moisture Content and Maximum Dry Density

The OMC and MDD were determined according to the ASTM D1557 modified Proctor standard (Method B). The results are provided in Table 4.5. The results show that the density reduced as the percent RAP reduced and the OMC increased with increasing unbound in situ material content.

Table 4.5: Optimum Moisture Content and Maximum Dry Density Results

Material Blend (RAP to Subgrade)	OMC	MDD	
	%	kg/m³	lb/ft³
80:20	4.9	2,217	138.4
50:50	6.2	2,143	133.8

4.5.3 Initial Consumption of Stabilizer

The purpose of the ICS test is to determine the minimum stabilizer content that provides a stable pH value after 60 minutes. This minimum stabilizer content is required to satisfy the neutralizing reactions of the clay particles (soil modification), which is indicated by a stable/constant pH. Any additional stabilizer above the ICS ensures permanent cementation, durability (i.e., limit carbonation and prevents the reversion of plasticity), and higher strengths. ASTM D6276, originally developed for determining the initial consumption of lime in lime-treated soils, was followed with modifications to increase the maximum aggregate size to 0.75 in. (≈19 mm) and to change the target pH from a requirement of 12.4 to a requirement of constant pH only. This modification made the test more representative of FDR-C materials. Cement contents are percent cement by weight of dry aggregate.

The ICS test results are plotted in Figure 4.11 for the individual materials and the two blends, along with the pH of the deionized water and the pH of the cement mixed with the deionized water. The pH values plateaued at approximately 2% cement for the 80:20 blend and at 4%

cement for the 50:50 blend. According to ASTM D6276, the minimum cement content should be adjusted upward by 1% to ensure durable cementation, since the minimum ICS cement content may only provide modification (i.e., reversible). On this basis, minimum cement contents of 3% and 5% cement would therefore be required for the 80:20 and 50:50 blends respectively to achieve durable cementation.
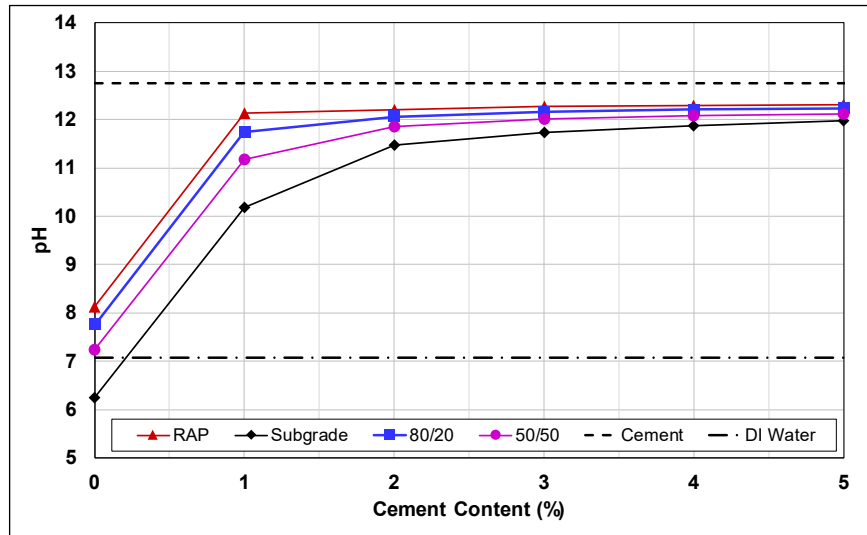
Figure 4.11: Initial consumption of stabilizer test results.

4.5.4 Tube Suction Test

The TST (Tx 144-14) is used to determine the susceptibility of pavement materials to water intrusion. The test was developed by the Texas Department of Transportation (TxDOT) to investigate the use of ground penetrating radar signals as a nondestructive method for assessing in-service roads. The tube suction test measures the electrical capacitance of the material by means of dielectric permittivity. The dielectric constant value (DV) can be used to characterize a material in terms of its relationship to moisture content *(154)*. Guthrie et al. *(155)* showed that materials with a DV less than 10 are less susceptible to moisture intrusion.

The TST is not a standard test in California but provides useful information on the moisture susceptibility of the treated material. Cement contents used in the testing were set at 0%, 2.5%, and 5%, slightly lower and slightly higher than the ICS+1% cement values determined in the ICS test. The two blends (80:20 and 50:50) of material were mixed with the cement at OMC and compacted to MDD according to ASTM D1557. Two replicate specimens of each blend at each cement content were prepared and allowed to cure for seven days in a humidity chamber set to

25°C (77°F). After curing, the specimens were sealed with latex membranes and placed in a shallow water tray for the test.

The results of the TSTs on the 80:20 and 50:50 blends are plotted in Figure 4.12 and Figure 4.13, respectively. The dielectric permittivity increased with increasing moisture in the specimen, as expected. The results also show the sensitivity of the material to the particle size with respect to gradation and cement content. The 80:20 blend was overall less sensitive to moisture penetration compared to the 50:50 blend. The moisture sensitivity also reduced as the cement content increased. The 80:20 blend specimens with 5% cement showed no change in dielectric permittivity, indicating that moisture could not move to the top of the specimen through capillary suction at this cement content.

The TST criteria for selecting a mix design is the cement content that reduces the dielectric permittivity below 10 DV at the end of the 10-day test period *(155)*. The cement content required to achieve that permittivity level for the 80:20 blend was between 2.5% and 5.0%, consistent with the cement contents identified from the ICS test results. The 50:50 blend exceeded 10 DV even with 5% cement, indicating that the 50:50 blend would be more susceptible to moisture intrusion, likely due to the higher clay content and finer gradation.
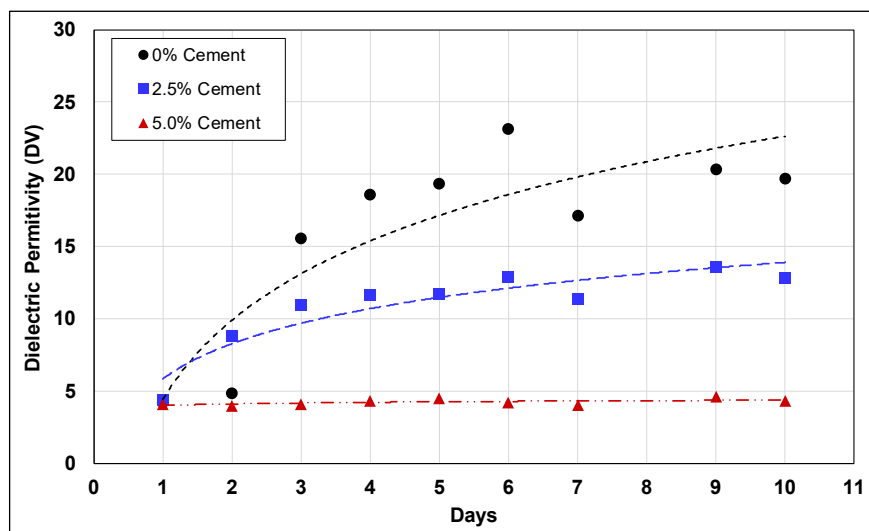
Figure 4.12: TST results for the 80:20 blend.
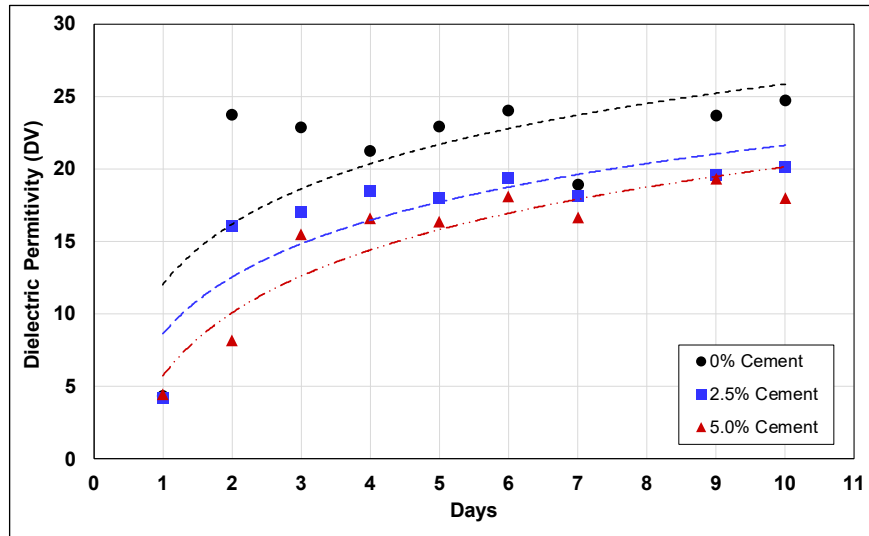
Figure 4.13: TST results for the 50:50 blend.

4.5.5 Unconfined Compressive Strength Testing

The aim of the mix design was to determine the cement contents required to achieve UCS results as close to 2.1 MPa (≈300 psi) and 4.1 MPa (≈600 psi) as possible for the two material blends. Mix designs were evaluated in terms of the seven-day UCS according to the modified ASTM D1633 method, which requires specimens be wrapped and sealed in 76 µm-thick (≈3 mil) plastic wrap and then cured in an oven at 38°C (≈100 F) for seven days. This approach is intended to simulate the expected curing conditions in a thick FDR-C layer.

Based on the results for the ICS and TST testing, a full-range of cement contents (0% to 6% at 1% intervals) was used for UCS tests on the 80:20 blend, and a smaller range (0%, 2%, 4%, and 6%) on the 50:50 blend. Materials were mixed with the different cement contents at the predetermined OMC. Untreated control mixes were also prepared. The specimens were capped with gypsum prior to UCS testing to provide plane, parallel, and smooth contact surfaces.

The results of the UCS tests are summarized in Table 4.6 and plotted in Figure 4.14 and Figure 4.15 for the 80:20 and the 50:50 blends, respectively. A logarithmic curve is fitted through the UCS results along with the confidence and prediction intervals at 95% confidence levels.

Additional statistical analyses of the UCS results are discussed in Section 7.2.

Table 4.6: Unconfined Compressive Strength Test Results

Cement Content (%)[a]	UCS for 80:20 Blend (MPa)	(psi)	UCS for 50:50 Blend (MPa)	(psi)
0	1.2	174	0.9	131
1	2.4	348	Not tested	
2	3.3	479	2.6	377
3	3.9	566	Not tested	
4	4.4	638	3.8	551
5	5.6	812	Not tested	
6	5.8	841	4.9	638

[a] percent of dry weight of aggregate
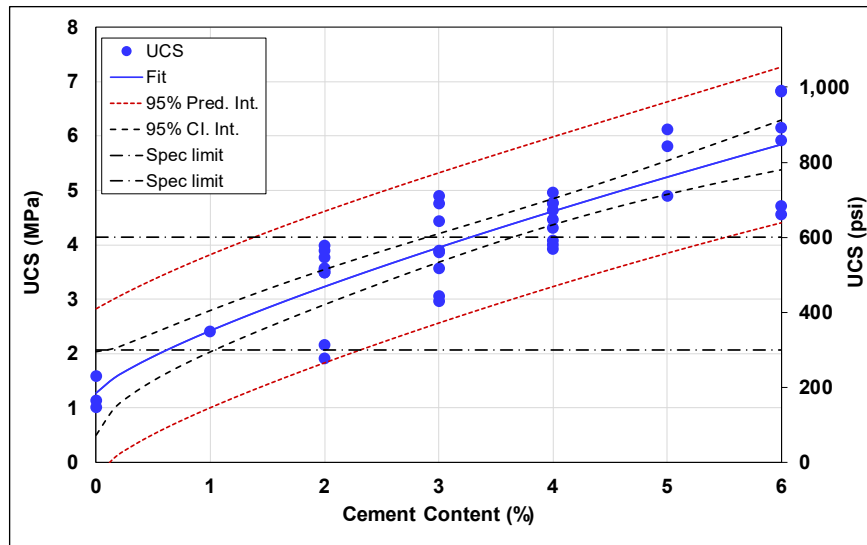
Figure 4.14: Unconfined compressive strength test results for the 80:20 blend.
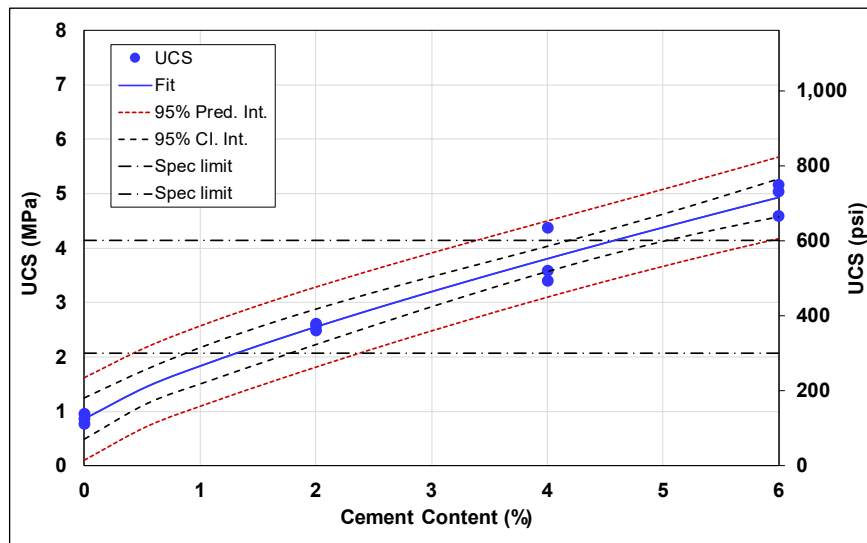
Figure 4.15: Unconfined compressive strength test results for the 50:50 blend.

4.5.6 Water-to-Cement Ratio

The water-to-cement ratio (w/c) is often used in concrete to optimize material strengths and handling characteristics, but it is typically not considered when designing cement-treated layers. Using the ICS values, the water-to-cement-for-cementation ratio (w/c_c) can be calculated, where cement for cementation is the difference between the selected cement content to achieve the desired seven-day UCS and the ICS value. This w/c_c can be used as an indicator of the relative amount of water available for cementation. The w/c_c values were 9.80 and 2.45 for the 2.5% and 4% cement content sections, respectively. These are very high compared to the range of 0.42 to 0.45 that is typically used for concrete mixes. Since concrete does not include any fines or clayey material and it is not compacted, most of the cement is consumed during initial cementation. In the case of cement-treated layers, the water content is optimized to maximize the density that can be achieved in the layer during compaction. The portion of cement approximated by the ICS is required for modification, with the remainder used for stabilization and meeting target strengths.

The difference of 7.35 in the w/c_c ratios of the 2.5% and 4% cement contents indicates that there was considerably more water available for cement hydration in the 2.5% cement material than in the 4% cement material. It was therefore hypothesized that the stiffness would recover more readily after microcracking if the w/c_c was sufficiently high to satisfy rehydration demands for recementation.

4.5.7 Selected Mix Designs

The following conclusions were drawn based on the test results presented in Section 4.5.1 through Section 4.5.6:

- The test results indicated that the 80:20 blend best suited the requirements of the experimental design in terms of being representative of typical Caltrans FDR projects.
- The minimum cement content determined from the ICS test (i.e., ICS+1%) resulted in a UCS strength of 4 MPa (580 psi), close to the higher-strength target, indicating that the material would be more suited to treatment with an asphalt recycling agent (emulsified or foamed asphalt [11]). Given that there was only a marginal difference in pH between the 2% and 3% cement contents, a cement content of 2.5% of the dry weight of the aggregate was selected

for the lower-strength test sections. A cement content of 4% of the dry weight of the aggregate was selected for the higher-strength test sections.

- The 2.5% cement content just met the minimum TST requirement of 10 DV. Given that the focus of the study was on shrinkage crack mitigation, that the location of the project was not subject to standing water, and that the water table was well below the pavement, this value was considered to be acceptable for the project.

The 2.5% and 4% cement contents resulted in mix design strengths of approximately 3.5 and 4.5 MPa (≈500 and 650 psi), respectively. Although higher than the experimental design targets, they were still considered appropriate for evaluating the effectiveness of microcracking to mitigate shrinkage cracking in FDR-C layers. An OMC of 5% was selected as the target moisture content, and 2,220 kg/m^3 (≈138.6 lb/ft^3) was selected as the target maximum dry density.

Blank page

5 TEST ROAD CONSTRUCTION

5.1 Introduction

The FDR-C Test Road was constructed during August and September of 2016. It took two days to complete the recycling (4% cement sections on day 1 and 2.5% cement sections on day 2) and three days to complete the microcracking. Maximum temperature and minimum humidity levels on the two recycling days were 37°C (≈98.6°F) and 14% and 33°C (≈91.4°F) and 15%.

5.2 Site Preparation

Based on the pavement design discussed in Section 4.3, additional RAP needed to be imported to increase the total thickness of the asphalt concrete layer from the existing ±50 mm (≈2 in.) to 200 mm (≈8 in.) to achieve the design FDR-C layer thickness of 250 mm (≈10 in.) with a ratio of 80% RAP to 20% unbound materials. RAP millings were trucked in from a local milling project and belly- or end-dumped onto the road (Figure 5.1). A grader was used to distribute and shape the RAP to the required thickness and levels (Figure 5.2 and Figure 5.3).

Figure 5.1: Dumping imported RAP.

Figure 5.2: Spreading imported RAP.

Figure 5.3: Shaped road prior to recycling.

5.3   Full-Depth Recycling with Cement

The construction of the FDR-C layer followed standard procedures and the 2015 Caltrans Standard Specifications. The contractor opted to stabilize the layer in a single pass (i.e., no prepulverization) since the imported RAP millings were already pulverized and had not been compacted. Cement spread rates were checked at the start of each day with a tray placed in the middle of the lane in front of the cement spreader (Figure 5.4). The required spread rates were achieved for the two different cement content sections. Overlapping cement spreading was also minimized with strict supervision of start and stop locations and application of adjacent passes (Figure 5.5).

Figure 5.4: Checking cement spread rate.

Figure 5.5: Checking cement spread overlaps.

After spreading the cement, the reclaimer, with the push bar-attached water tanker, started reclaiming the layer (Figure 5.6). The mixed material appeared consistent throughout the recycling process (Figure 5.7). Primary compaction with a segmented padfoot roller followed the reclaimer (Figure 5.8). Once primary compaction had been achieved, the road was leveled with a grader (Figure 5.9) followed by final compaction with a smooth drum roller (Figure 5.10).

Figure 5.6: Water tanker and reclaimer.

Figure 5.7: Recycled material behind the reclaimer.

Figure 5.8: Primary compaction with a segmented padfoot roller.

Figure 5.9: Leveling with a grader.

Figure 5.10: Final compaction with a smooth drum roller.

The compacted FDR-C layer was sprayed with water at regular intervals to retard the rate of drying for four days after compaction before spraying the asphalt curing membrane. Timing of water sprays was strictly controlled to ensure that moisture content was kept constant.

Visual observations during construction included moisture content, gradation, recycling depth, recycled material consistency, and roller coverage and passes.

5.4　FDR-C Layer Quality Control

Quality control testing on the FDR-C layer included the following in each cell:

- Sampling to measure the gravimetric moisture content (ASTM D7830)
- Measuring in-place density with a nuclear gauge (AASHTO T 310)
- Sampling for compaction of specimens to determine the density at field moisture content (ASTM D1557) and the seven-day UCS (modified ASTM D1633)

5.4.1　Moisture Content

Two gravimetric moisture contents were determined in each cell using material collected behind the reclaimer. Laboratory-determined moisture content and density results for the materials

sampled in each cell are summarized in Figure 5.11. The average moisture content results for the 4% and 2.5% cement content sections were 5.3% and 5.5%, respectively, both higher than the laboratory-determined mix design OMC of 4.9%. An assessment of the range of measurements indicated that 54% of the 4% cement content sections were within ±0.5% of the mix design OMC, while 44% of the 2.5% cement content sections were within this range.

The results show that there was considerable variation between the different cells, attributed to the time of day that the sample was taken, elapsed time between taking the sample and starting the test (typically between 15 and 60 minutes), location of the cell (i.e., in the shade or in direct sunlight), and variability in the material and in situ moisture content.
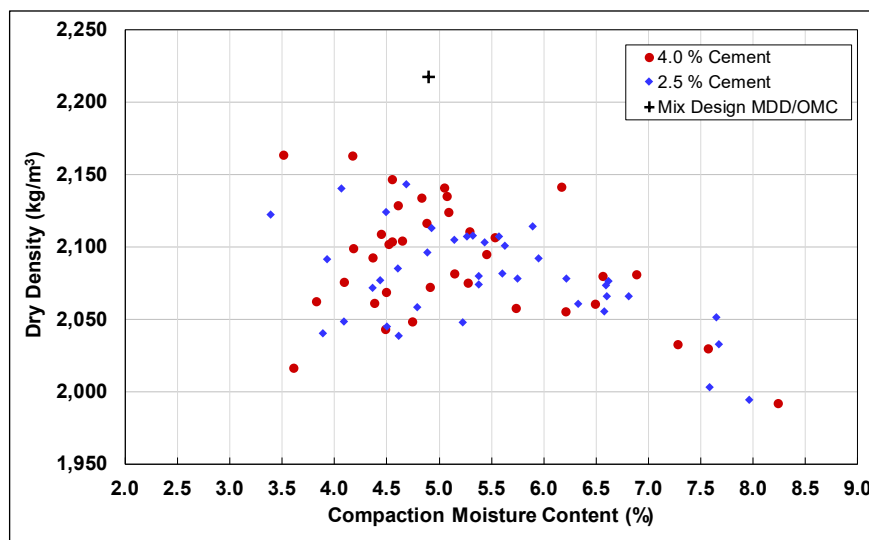
Figure 5.11: Laboratory-determined moisture content and maximum dry density.

5.4.2   Density

In-place field densities were determined after final compaction at one location in each cell. The specified relative compaction density for the project was 97% of the modified Proctor density determined in the laboratory. Although the 2015 Caltrans specifications called for 97% of the Caltrans CT 216 density, modified Proctor (ASTM D1557) was used instead to facilitate analysis in relation to the mix design density and to the UCS test results, both of which are based on modified Proctor compaction. Wet densities were measured at four different depths (50, 100, 200, and 250 mm [2, 4, 8, and 10 in.]), with the 250 mm measurement providing an indication of the density at the top of the subgrade. The nuclear gauge measures the wet density and the moisture

content and can calculate the dry density with these results. However, moisture content readings can be influenced by hydrogen atoms present in the asphalt *(156)*, which can skew the calculated result. The gauge-determined dry density was therefore documented for record purposes only, but the gravimetric moisture content determined for each cell was used for dry density calculations in that cell.

The nuclear gauge wet density results and compaction relative to the laboratory-determined moisture and modified Proctor density results are summarized in Table 5.1 and plotted in Figure 5.12 through Figure 5.21 for the 4% and 2.5% cement sections. Estimates of the compaction relative to CT 216 are provided in the table and in Figure 5.18 and Figure 5.19 based on limited unpublished comparative data collected as part of ongoing UCPRC research on in-place pavement recycling. This research has shown that CT 216 density will typically be between 93% and 97% of the modified Proctor density for recycled materials containing between 50% and 100% RAP.

Table 5.1: Average Density and Relative Compaction Results

Property	Test Location	4% Cement		2.5% Cement	
		Average	Std. Dev.	Average	Std. Dev.
Wet Density (kg/m^3)	FDR-C	2,161	49.0	2,129	40.1
	Subgrade	2,159	67.7	2,136	51.3
Dry Density (kg/m^3)	FDR-C[a]	2,048	51.3	2,013	38.4
	Lab. Mod. Proctor[b]	2,089	40.9	2,078	33.6
Relative Compaction (%)	FDR-C[c]	98	N/A	97	N/A
	Estimated CT-216[d]	103	N/A	102	N/A

[a] Dry density calculated using nuclear gauge wet density and laboratory-determined gravimetric moisture content
[b] Laboratory-determined modified Proctor compaction at field moisture content
[c] Calculated as percentage of calculated field dry density[a] divided by laboratory-determined dry density[b]
[d] Estimated from limited unpublished UCPRC laboratory test results comparing ASTM D1557 and CT 216

The modified Proctor relative compaction target of 97% was met or exceeded in 22 of the 37 cells. The estimated CT 216 relative compaction target was exceeded in all cells. The results for all cells show some variability in the field density, and that density increased with depth in the FDR-C layer with both cement contents. The variability in results was attributed to a number of possible reasons, including but not limited to the following, in addition to those cited in Section 5.4.1 for variation in moisture content:
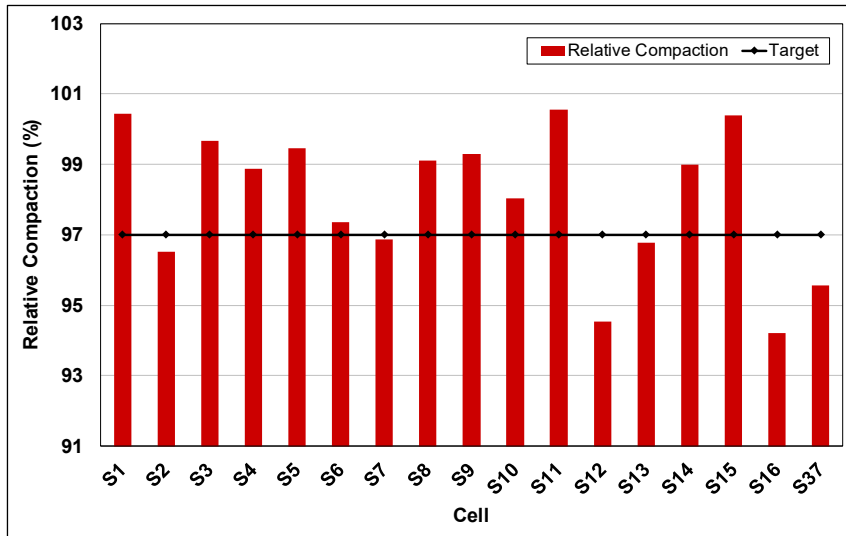
Figure 5.12: 4% Cement: Relative compaction in each cell (modified Proctor).
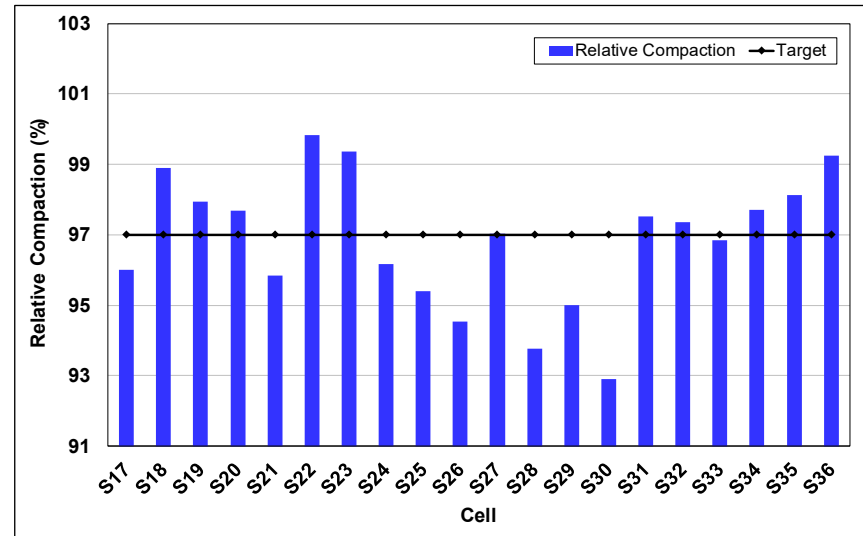
Figure 5.13: 2.5% Cement: Relative compaction in each cell (modified Proctor).
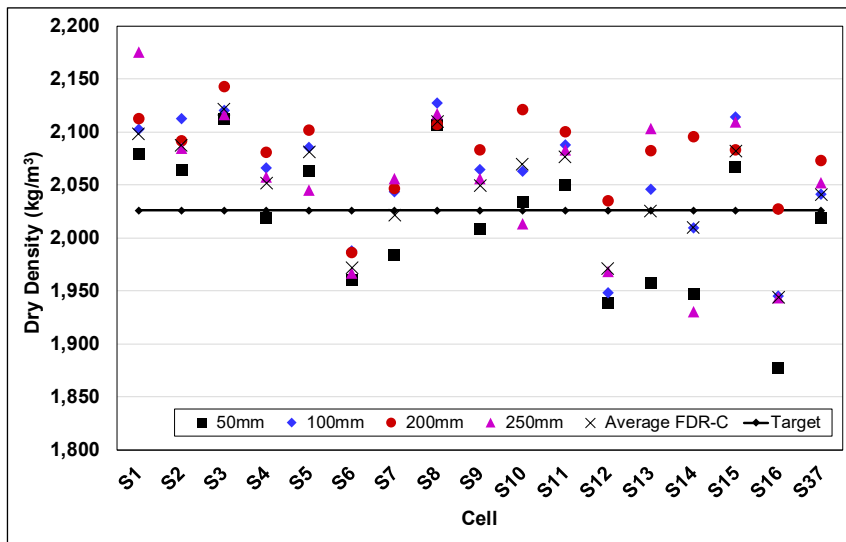
Figure 5.14: 4% Cement: In-place density at different depths.
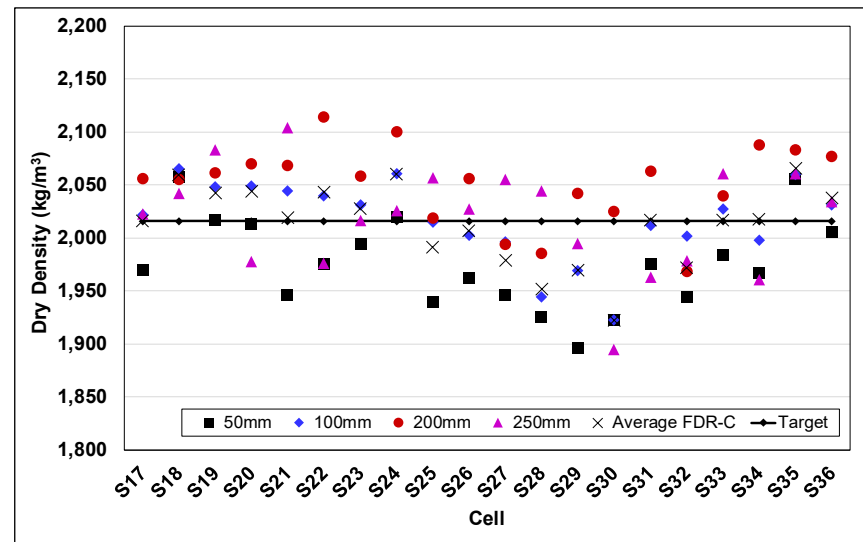
Figure 5.15: 2.5% Cement: In-place density at different depths.
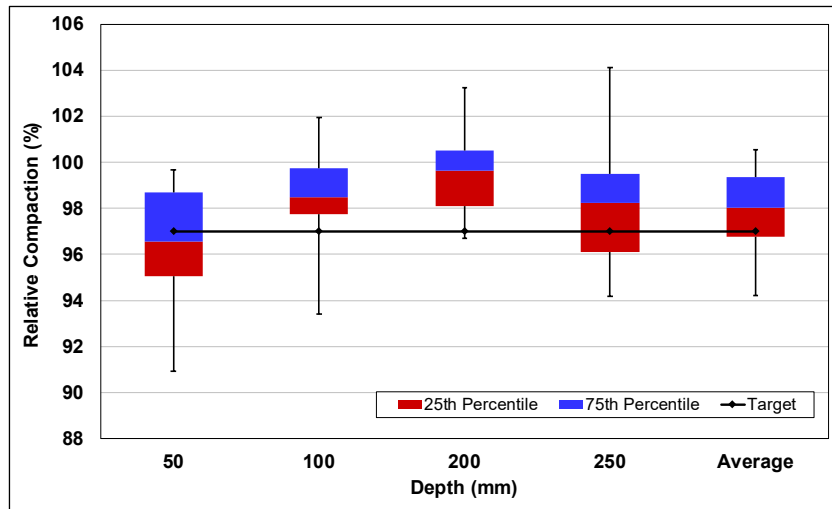
Figure 5.16: 4% Cement: Box plot of average in-place density at different depths.
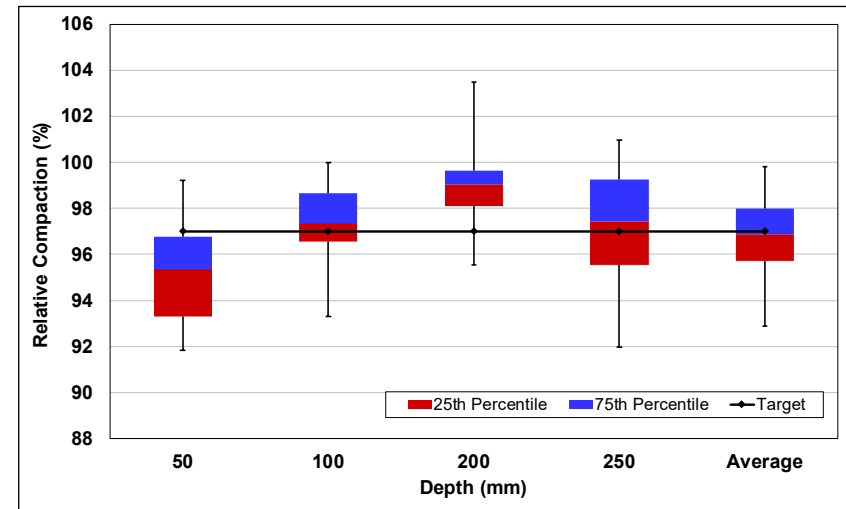
Figure 5.17: 2.5% Cement: Box plot of average in-place density at different depths.
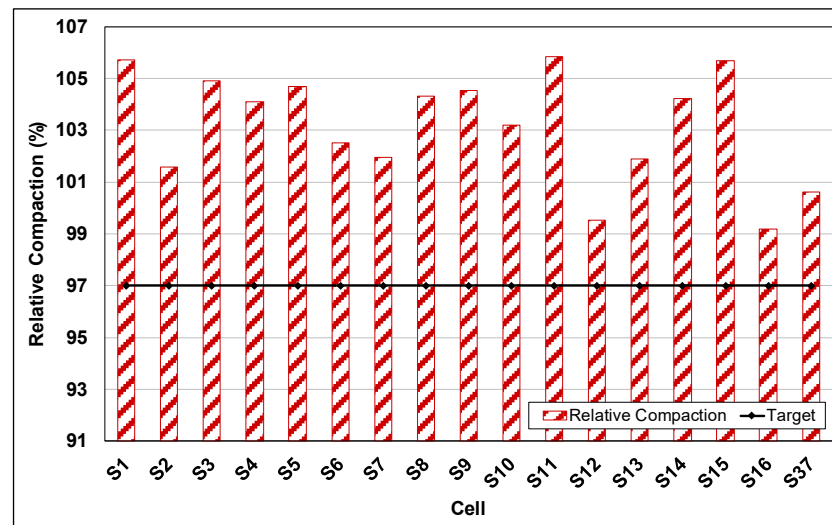
Figure 5.18: 4% Cement: Relative compaction in each cell (estimated CT 216).
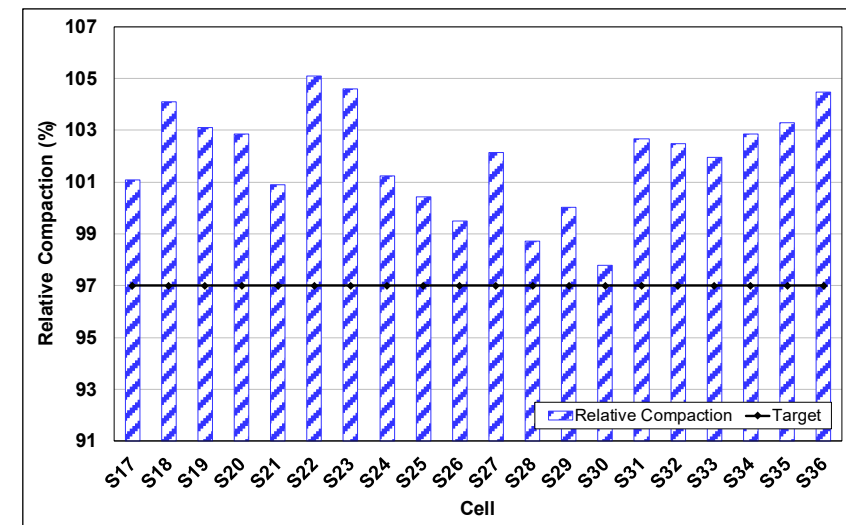
Figure 5.19: 2.5% Cement: Relative compaction in each cell (estimated CT 216).

- Potential small differences in the percentage of RAP in the pavement compared to the blend used for the mix design, resulting from variation during spreading of the imported RAP and from recycling depth.
- Choice of roller (i.e., static segmented wheel roller instead of vibrating padfoot roller), and/or insufficient roller passes.
- Difficulty in determining appropriate reference densities for each cell. Determining a reference density for each cell was beyond the scope of the study. Using the maximum dry density determined during the mix design, which did not include the cement, would not necessarily be representative of the recycled layer. Using the density at field moisture content, the method followed in this study, could have been influenced by the potential moisture content variations discussed in Section 5.4.1.
- Inherent variability in the materials along the project, slight differences in roller pass coverage at the different testing locations, and potentially some drying out of the surface material during initial compaction due to the hot, dry conditions.

5.4.3 Unconfined Compressive Strength

UCS specimens were compacted to modified Proctor density at field moisture content within two hours after sampling. After compaction, the specimens were wrapped in plastic and oven-cured at 40°C (≈104°F) for seven days before testing. Test results are plotted in Figure 5.20.
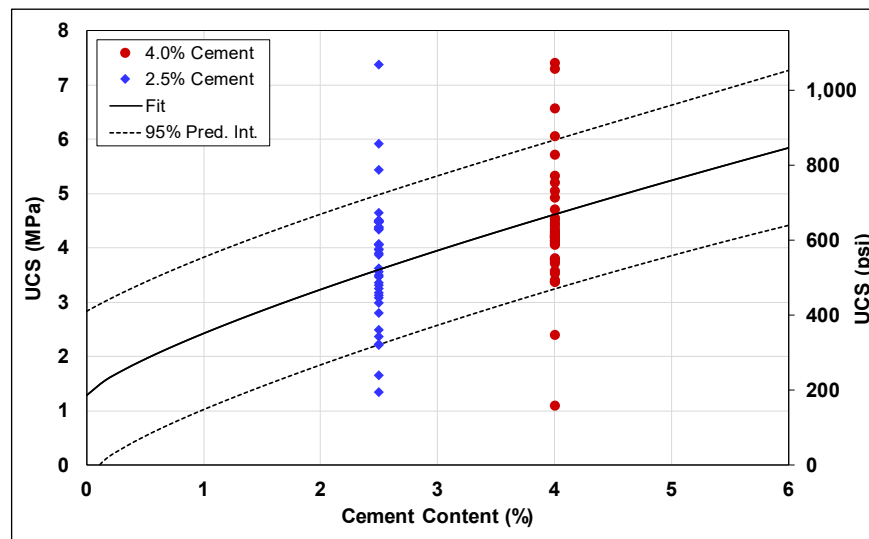
Figure 5.20: FDR-C Test Road unconfined compressive strengths.

The average UCS values for the 4% and 2.5% cement contents were 4.4 MPa and 3.7 MPa, respectively. The variability in UCS values between the different cells at each cement content was significant. Although the average UCS results were consistent with the design strengths

determined in the mix design, the variability in moisture content and density discussed in the previous two sections resulted in a wide range of UCS results. This variability and its potential for different cracking behavior and stiffness gain rates in the different cells was factored into visual assessments and test result analysis.

5.5 Preparation for Microcracking

The equipment used to measure stiffness reduction during microcracking included an SSG and LWD. Falling weight deflectometer (FWD) testing was not considered during this part of the testing because of concerns that the intensity of the drop would induce additional damage to the layer. FWD testing was therefore only started after the microsurfacing had been placed. The equipment used to measure deflection/stiffness on the FDR-C Test Road over the course of the study is shown in Figure 5.21.

Figure 5.21: Stiffness measuring equipment used on the FDR-C Test Road.
(FWD, SSG, and LWD).

5.5.1 Stiffness Testing Equipment Comparison and Validation

Neither the SSG or LWD were originally designed for testing cement-treated materials and both have recommended maximum limits that can be measured. The SSG can effectively measure stiffness between 26 and 610 MPa. The LWD, with a 10 kg (≈22 lb.) weight and a 300 mm (≈12 in.) diameter plate, can reliably measure a surface modulus between 15 and 70 MN/m^2. Despite these limitations, Scullion *(37)* and Hope *(94)* both reported successful use of SSGs to measure stiffness reduction during microcracking of cement-treated bases with seven-day design strengths of less than 3.5 MPa (≈500 psi).

Both instruments will return a reading, even if the layer stiffness exceeds the limits of the gauge. This can provide the user with incorrect or misleading information. To better understand the limits of the two instruments used in the microcracking evaluation, two test cells (S1 and S28) were dedicated to comparing them against an FWD. Tests were performed on the day of construction, and two days after construction. The sequence of testing was ordered by applied stresses—namely SSG, LWD, then FWD—to minimize the potential for induced damage from testing with one of the other instruments. Different testing locations were used on the different days (Figure 5.22).
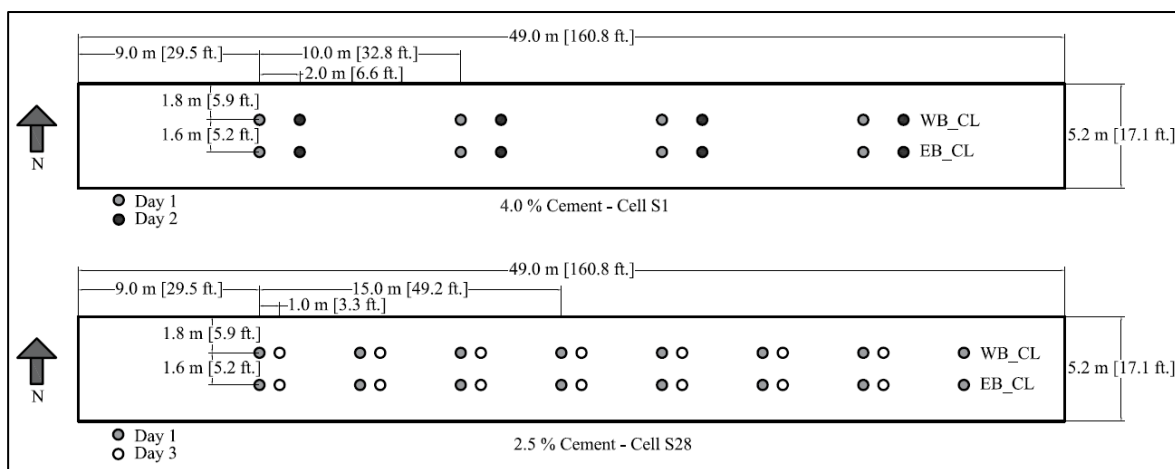
Figure 5.22: Testing layout for stiffness instrument comparison.

The SSG and LWD results are plotted against the FWD backcalculated stiffnesses of the FDR-C layer in Figure 5.23 and Figure 5.24, respectively. The SSG stiffnesses collected on the 2.5% cement content cell on both days were within the calibrated range of the gauge and were linearly correlated with the FWD backcalculated stiffnesses. The SSG stiffnesses collected on the 4% cement content cell were higher than those on the 2.5% cement content cell results but were poorly correlated with the FWD stiffnesses. This indicates that the SSG could return inaccurate and potentially misleading results on layers that had backcalculated FWD stiffnesses exceeding 2,500 MPa.

The LWD surface moduli measured during the equipment comparisons exceeded the calibrated range of the instrument on both cement content sections. The correlations between the LWD and the FWD were similar to those observed between the SSG and the FWD. These results suggest that additional work is required to validate the use of the LWD on FDR-C layers that have

stiffnesses exceeding the LWD's calibrated range. This work was not carried out as part of this study.

Additional statistical analyses comparing SSG- and FWD-determined stiffnesses are discussed in Section 7.3.
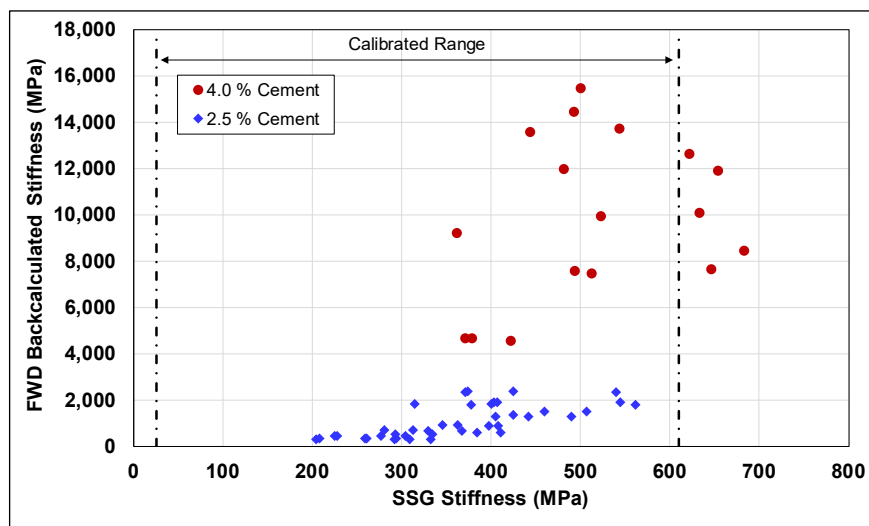
Figure 5.23: Relationship between SSG and FWD stiffnesses.
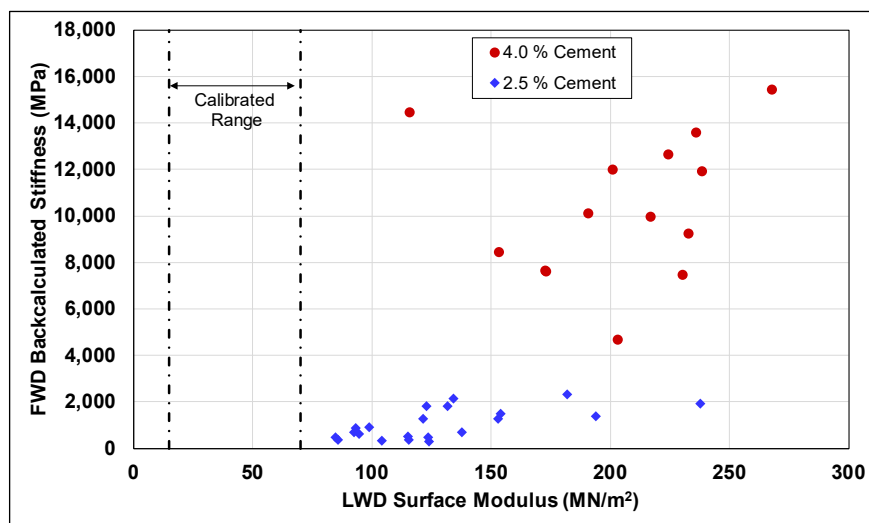
Figure 5.24: Relationship between LWD and FWD stiffnesses.

5.5.2 Experiment to Determine Expected Number of Microcracking Roller Passes

Cell S4 was used as a trial cell to determine the average stiffness reduction per microcracking pass. A microcracking pass was defined as one movement of the 12-ton single steel drum roller in one direction from one end of the cell to the other. Four SSG devices were used during

microcracking together with one LWD. Each instrument was operated by a different operator to limit the variability to one instrument/operator combination. Testing locations in the cell are shown in Figure 5.25.
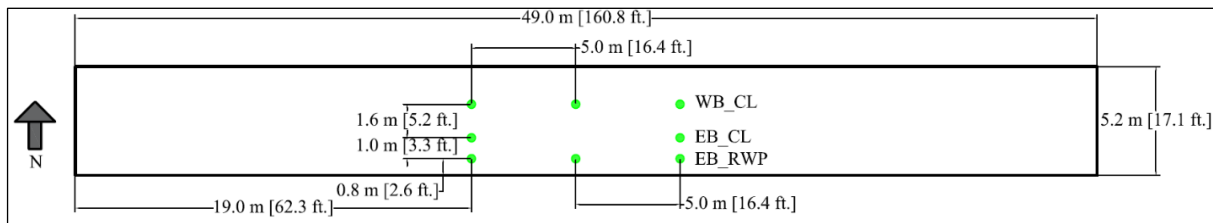
Figure 5.25: Cell S4: Trial SSG and LWD testing locations.

SSG Results

The SSG stiffness results are plotted in Figure 5.26. Average stiffness was reduced from approximately 500 MPa to 250 MPa after three microcracking passes. Gauge C505 measured an increase in stiffness after pass 1, which the authors believe was due to minor inconsistencies in the operator's procedure in conducting the test. Similar anomalies were periodically observed in both the SSG and LWD results, with no clear explanation as to why this happened. The stiffness results before microcracking (i.e., pass 0, 48 hours after completion of compaction) were already close to the documented upper limit of the measurable range of the SSGs.

The stiffness reduction results for each SSG, normalized to the stiffness result prior to microcracking (pass 0), are provided in Figure 5.27. The results from Gauge C533 (experienced UCPRC SSG operator) followed the expected trend, with the stiffness reducing with each consecutive microcracking pass. Gauge C451 (technical representative from the equipment manufacturer) measured a similar trend, except that the stiffness result before microcracking was not measured. Gauges C505 (trained UCPRC operator with one year of SSG testing experience) and C550 (trained UCPRC operator with no prior SSG testing experience) had more variability in the readings.

Since there were no clear trends specific to operator experience and expected gauge result, all results were grouped in the analysis. Figure 5.28 shows the SSG stiffness reduction results, normalized to the mean stiffness at pass 0 of all four SSGs for each test location. The results show that each measuring location responded differently to microcracking. Location S4-19-EB-CL had

the highest rate of stiffness reduction per pass, with a measured reduction of 60% after two passes. Location S4-29-EB-CL had the lowest stiffness reduction, with only 30% reduction after three passes, despite these locations being on the same line and receiving the same coverage.

Based on the observations and taking the observed operator/gauge variability into account, it was concluded that uniform stiffness reduction was potentially not achieved in Cell S4 likely due to some variability in the materials and/or layer compaction.

The average rate of stiffness reduction was 150 MPa per pass with the 12-ton roller at high vibration amplitude. Additional passes were not applied to achieve a minimum average stiffness reduction of 60% as this could have resulted in irreversible damage in the weaker areas. Observations from the trial cell include the following:

- Three passes were considered the maximum that should be applied for the pavement structure and material.
- One pass reduced the average stiffness by about 15%.
- Two passes reduced the average stiffness by about 30%.
- Three passes reduced the average stiffness by about 45%.

LWD Results

The LWD was operated by a representative from the equipment manufacturer for the duration of the project. Results for Cell S4 are plotted in Figure 5.29. Stiffness reduction results for each testing location, normalized to the stiffness before microcracking (pass 0) for that location, are plotted in Figure 5.30.

The LWD results showed less variation than the SSG results. The stiffness reduced, on average, by 32% with the first microcracking pass, after which it plateaued, with an average stiffness reduction of 38% after three passes. The stiffness of the material, however, exceeded the documented measurable range of the LWD (70 MN/m^2). Although the LWD did record a stiffness reduction, it is acknowledged that the equipment was not originally designed to measure the stiffness of cement-treated materials. Since the stiffness results exceeded the range of the LWD by a considerable margin, only the SSG results were used as a measure of the percentage stiffness reduction after microcracking in this report.
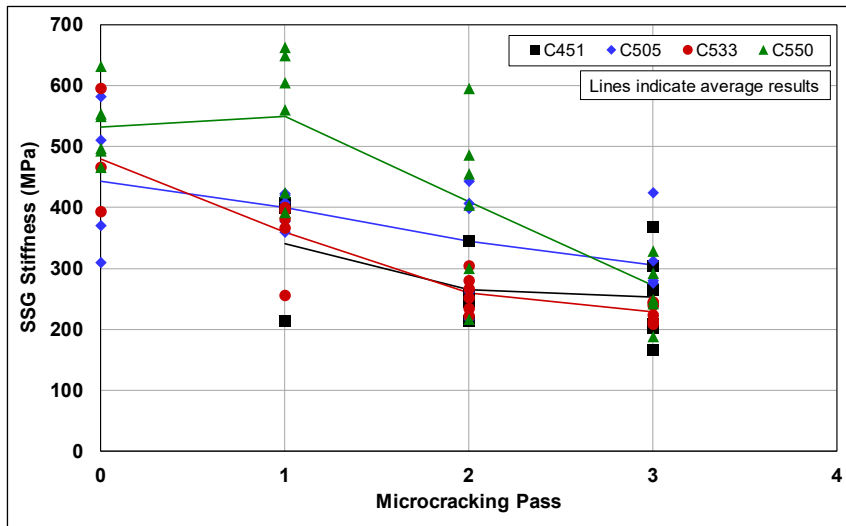
Figure 5.26: Cell S4: SSG stiffness results per gauge during microcracking.
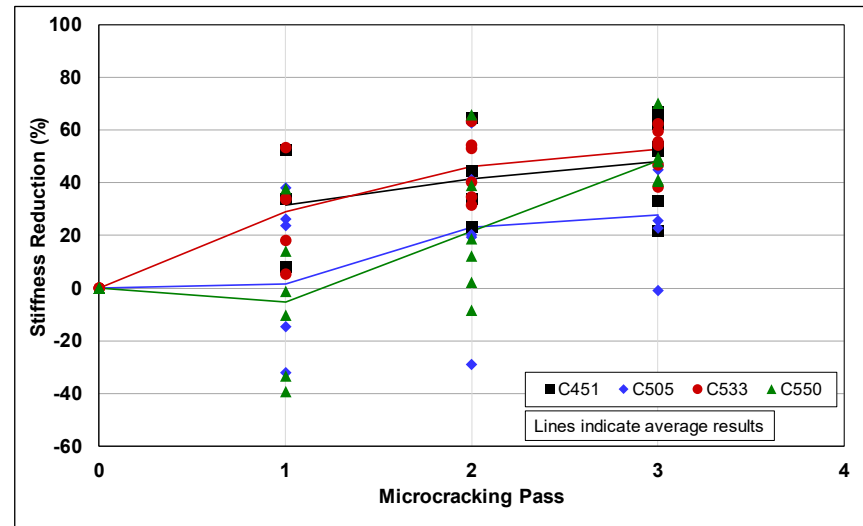
Figure 5.27: Cell S4: SSG stiffness reduction per gauge during microcracking.
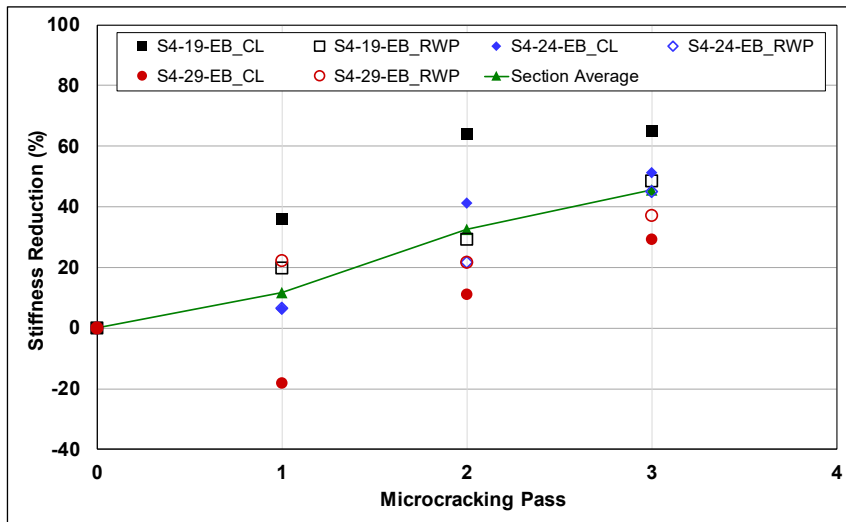
Figure 5.28: Cell S4: SSG stiffness reduction results per station during microcracking.
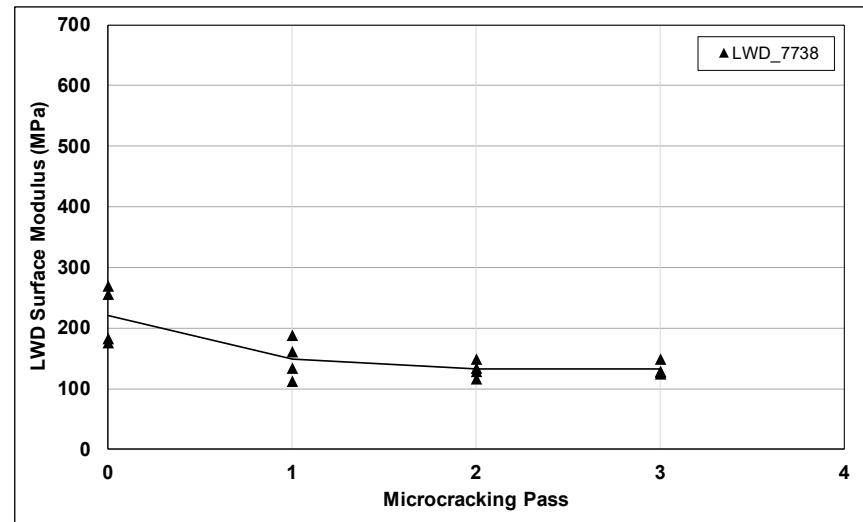
Figure 5.29: Cell S4: LWD stiffness results during microcracking.
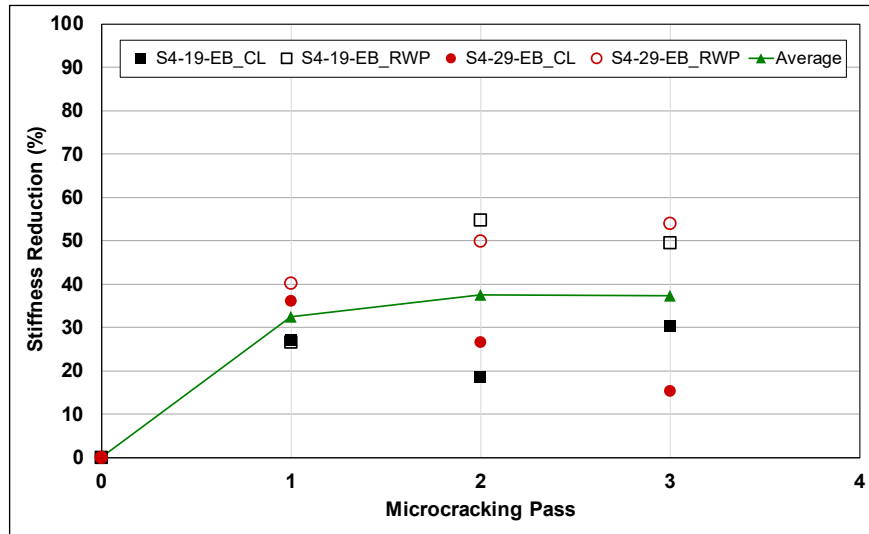
Figure 5.30: Cell S4: LWD stiffness reduction during microcracking.

5.6 FDR-C Test Road Microcracking

Microcracking of the FDR-C layer followed the factorial in Table 4.1. Actual curing time between completion of final compaction and start of microcracking was within one hour of the curing time listed in the table. Visual observations and SSG and LWD stiffnesses before and after microcracking were recorded.

5.6.1 Visual Observations

Visual observations recorded during microcracking included observations by the authors, who closely monitored the microcracking efforts in each of the different cells, and those of the roller operator, who provided opinions on how the roller responded during each microcracking pass. Observations were centered on the test factorial and focused on curing hours between completion of final compaction, number of roller passes, roller weight, vibration amplitude, and surface deformation and distresses.

On hard surfaces, vibrations were transmitted from the drum into the frame of the roller as the drum bounced on the surface. On softer surfaces, drum vibration was less apparent to the operator. If the drum response transmitted increasingly less vibrations into the roller frame with increasing microcracking passes, this was taken as an indication that the FDR-C layer was being damaged (i.e., the stiffness was reducing) with each pass. The operator, with several years of experience microcracking FDR-C layers, noted how the frame vibration reduced with consecutive

microcracking passes, and provided some insights on when he thought that another pass might risk permanent damage to the FDR-C layer. The observations are summarized in Table 5.2 and discussed as follows:

- The response of the roller during microcracking was difficult to quantify without accelerometer data from the roller. Although requested by the UCPRC, the contractor did not have intelligent compaction rollers available at the time of construction.
- The most significant difference in roller response was observed during the first microcracking pass on the 4% cement-content cells after 48 and 72 hours. The differences in roller response on the 2.5% cement-content cells were not as noticeable.
- The 12-ton single drum roller response at high vibration amplitude was remarkably similar for the same number of passes on the 4% and 2.5% cement-content cells. The perceived frame vibration decreased with each microcracking pass, indicating that a larger percentage of the force was being transmitted into the FDR-C layer with each pass.
- Roller weight had a significant impact on the reduction in perceived frame response. The 10-ton roller frame vibration, with both drums set to high vibration amplitude, did not change significantly between the three passes that were applied. The response of the 12-ton roller was, however, more significant at high vibration amplitude.
- The 12-ton roller frame response at high vibration amplitude appeared to change more perceptibly compared to that felt at low vibration amplitude. The roller operator indicated that there was no perceived difference in the frame vibration over three passes with the vibration amplitude set to low.
- Surface deformation and/or distresses were generally not observed on the cells microcracked with one, two, or three passes. Figure 5.31 and Figure 5.32 show the surface condition of one of the 4% cement-content cells (Cell S4) after microcracking with the 12-ton SSR at high amplitude. No crushing or raveling of the surface was observed.
- The roller operator was of the opinion that three roller passes was the maximum number that should be applied before risking unrecoverable damage/stiffness to the FDR-C layer. The effect of a fourth pass was observed on Cell S5 (4% cement with microcracking after 48 hours and again after 72 hours), where the surface disintegrated on the first pass after 72 hours of curing, 24 hours after the initial three microcracking passes had been applied. The 2.5% cement-content cells with microcracking efforts after 48 hours and again after 72 hours also showed effects of over-microcracking (Figure 5.33 and Figure 5.34), with the surface disintegrating after two passes after 72 hours. These cells, however, showed less damage after the second 72-hour microcracking pass than was observed after the first 72-hour pass on the 4% cement-content cells.

Table 5.2: Visual Observations During Microcracking of the FDR-C Layer

4% Cement				2.5% Cement			
Cell	Roller	Passes	Observation (MC = Microcracking)	Cell	Roller	Passes	Observation (MC = Microcracking)
S1*	N/A	N/A	No cracks	S17	DSR	3@48	No change in frame vibration
S2	SSR	3@48	No change in frame vibration	S18	DSR	3@72	No change in frame vibration
S3	SSR	1@48	No change in frame vibration	S19	SSR	3@48	Frame vibration reduced with each pass. No surface damage
S4	SSR	3@48	Frame vibration lower with each pass. No surface damage	S20	SSR	3@48 2@72	Surface disintegration after 2nd 72-hr pass. Operator advised to stop MC
S5	SSR	3@48 1@72	Surface disintegration after 1st 72-hr pass. Operator advised to stop MC	S21	SSR	2@48	2 passes after 48 hours. Surface disintegrated
S6*	N/A	N/A	No cracks	S22	SSR	1@48	No surface damage
S7	SSR	3@72	Shrinkage crack before MC, no change in frame vibration	S23	SSR	3@72	Frame vibration reduced with each pass. No surface damage
S8	SSR	1@72	Shrinkage crack before MC, no surface damage	S24	SSR	3@48	Frame vibration reduced with each pass. No surface damage
S9	SSR	2@72	Shrinkage crack before MC, no surface damage	S25*	N/A	N/A	No cracks
S10	SSR	2@72	Shrinkage crack before MC, no surface damage	S26	SSR	1@72	No surface damage
S11	SSR	3@72	Frame vibration reduced with each pass. No surface damage	S27	SSR	2@72	No surface damage
S12	SSR	3@48	Shrinkage crack before MC. Frame vibration reduced with each pass.	S28*	N/A	N/A	No cracks
S13*	N/A	N/A	No cracks	S29	SSR	3@72	Frame vibration reduced with each pass. No surface damage
S14	DSR	3@48	No change in frame vibration	S30	SSR	3@48 2@72	Minor cracks and delamination after 2nd 72-hr pass. Operator advised to stop MC
S15	DSR	3@72	No change in frame vibration	S31	SSR	3@48	Frame vibration reduced with each pass. No surface damage
S16	SSR	3@72	Frame vibration reduced with each pass. No surface damage	S32	SSR	3@72	Frame vibration reduced with each pass. No surface damage
S37	SSR	2@48	Frame vibration reduced with each pass. No surface damage	S33*	N/A	N/A	No cracks
* Control cells with no microcracking				S34	SSR	2@48	Frame vibration reduced with each pass. No surface damage
				S35	SSR	1@48	No surface damage
				S36*	N/A	N/A	No cracks

Figure 5.31: Surface condition after three passes with SSR at high vibration amplitude.

Figure 5.32: Close-up of microcracked surface.

Figure 5.33: Surface damage after second microcracking effort at 72 hours.

Figure 5.34: Close-up of surface damage after second microcracking effort at 72 hours.

5.6.2 Stiffness Reduction During Microcracking

Stiffness testing was done during microcracking to measure the reduction in stiffness of the FDR-C layer and to determine if the energy input from the roller could be characterized as stiffness loss. The total stiffness was expected to reduce for each consecutive pass as a result of energy input through the applied stress and resultant strains in the FDR-C layer. Stiffness tests were done mid-cell in the east bound lane (Figure 5.35). The west bound lane was used to access different cells, and therefore no measurements were taken in this lane because the results would have been influenced by the roller movements. Testing was limited to four points to optimize testing across all sections over the three microcracking days.
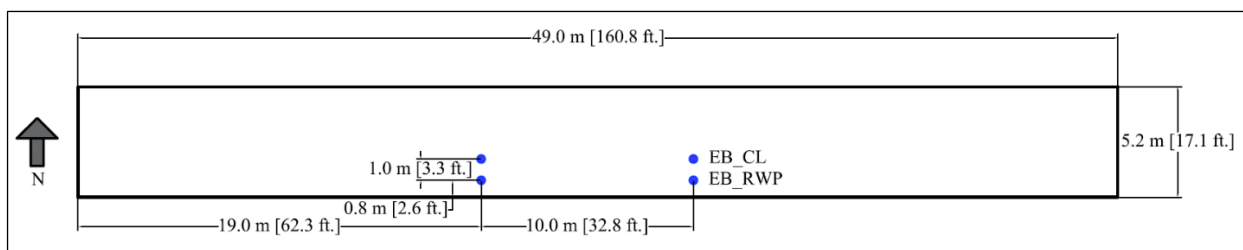
Figure 5.35: SSG and LWD testing locations in each cell.

Detailed results of the effects of microcracking on stiffness measured with the SSGs and the LWD for each cell are provided in Appendix B. Results include stiffness measured before, during (when applicable), and after microcracking. Average stiffness reduction results, normalized to the stiffness before microcracking, for all the cells with similar factorials in terms of curing time before microcracking, roller weight, vibration amplitude, cement content, and microcracking effort are provided in Appendix C.

The average stiffness reduction results for each cell measured with the SSGs are provided in Table 5.3. Given that applying a microcracking roller pass was much faster than the time taken to do a series of SSG measurements, it was not feasible to take some measurements after each roller pass in every cell (indicated as NT [not tested] in the table). Grey-shaded cells indicate that second, third, fourth, or fifth roller passes were not included in the experiment factorial for that cell.

Statistical analyses of the relationships between microcracking activities and stiffness measurements are discussed in Section 7.4.

5.7   Surfacing

5.7.1   Prime Coat Application

A prime coat was applied to the FDR-C Test Road four days after construction of the FDR-C layer started. The layer was not broomed prior to the application of the prime coat. An SS-1H asphalt emulsion was applied to the surface at a rate of 0.1 gal./yd^2 (0.45 L/m^2) (Figure 5.36). Application appeared to be consistent but was easily damaged/raveled by light vehicle traffic in areas with loose material and fallen leaves that were not cleaned prior to spraying.

Table 5.3: SSG Stiffness Results

4% Cement

Cell	Measured Stiffness After Each Microcracking Pass (MPa)						Stiffness Reduction (%)	Target Reduction (%)
	0	1	2	3	4	5		
S1*	Cell used to compare FWD, SSG, and LWD							
S2	427	415	351	350	NM	NM	NM	NM
S3	467	350	NT	NT	NM	NM	NM	NM
S4	491	425	324	263	NM	NM	46	60
S5	479	376	346	347	291	NM	23	N/A
S6*	Control							
S7	426	NT	NT	316	NM	NM	29	N/A
S8	420	276		NM	NM	NM	34	20
S9	447	329	342	NM	NM	NM	27	40
S10	401	310	262	NM	NM	NM	36	40
S11	382	NT	NT	253	NM	NM	34	60
S12	361	411	309	321	NM	NM	10	N/A
S13*	Control							
S14	418	277	235	210	NM	NM	50	N/A
S15	432	NT	NT	318	NM	NM	28	N/A
S16	445	NT	NT	250	NM	NM	42	N/A
S37	377	NT	382	NM	NM	NM	1	40

* Control cells with no microcracking
NM – Microcracking pass not specified in experimental plan
NT – Not tested due to equipment availability

2.5% Cement

Cell	Measured Stiffness After Each Microcracking Pass (MPa)						Stiffness Reduction (%)	Target Reduction (%)
	0	1	2	3	4	5		
S17	490	340	338	294	NM	NM	40	N/A
S18	351	NT	NT	244			31	N/A
S19	415	273	207	221			48	N/A
S20	367	NT	302	344	NT	229	33	N/A
S21	307	201	194	NM	NM	NM	36	60
S22	366	293	NM	NM	NM	NM	26	20
S23	534	NT	NT	243	NM	NM	54	60
S24	448	NT	NT	315	NM	NM	31	N/A
S25*	Control							
S26	384	174	NM	NM	NM	NM	56	20
S27	439	NT	269	NM	NM	NM	39	40
S28	Cell used to compare FWD, SSG, and LWD							
S29	295	NT	NT	213	NM	NM	27	60
S30	350	NT	NT	225	NT	157	47	N/A
S31	358	NT	240	256	NM	NM	30	N/A
S32	285	NT	NT	174	NM	NM	39	N/A
S33*	Control							
S34	377	374	237	NM	NM	NM	38	40
S35	461	404	NM	NM	NM	NM	13	20
S36*	Control							

Figure 5.36: Prime coat application.

5.7.2 Microsurfacing

The microsurfacing was applied in two passes on September 26, 2016. A half-width pass of 7.0 ft. (≈2.1 m) was applied starting in Cell 1 on the west side of the project (Figure 5.37) and ending in Cell 37. This was followed by a full-width pass of 14 ft. (≈4.2 m) starting in Cell 37 and ending in Cell 1 (Figure 5.38). An average overlap of 1.0 ft. (≈300 mm) was maintained.

Figure 5.37: First microsurfacing pass.

Figure 5.38: Second microsurfacing pass.

5.8 Decision to Proceed with Microcracking Study

Construction monitoring and quality control testing results indicated that the FDR-C Test Road was suitable for longer term monitoring for the microcracking study.

Blank page

6   TEST ROAD MONITORING

6.1   Introduction

Test road monitoring included regular visual assessments focusing primarily on crack monitoring, preliminary coring to check for any indication of crushing or carbonation, and falling weight deflectometer (FWD) deflection measurements, from which stiffness changes over time were backcalculated.

6.2   Crack Monitoring

6.2.1   Methodology

The FDR-C Test Road (Figure 6.1) was visually monitored every second day for the first 90 days after microcracking, once every seven days for the following 90 days, and then every 30 days for the next 18 months. The location, orientation, length, and width of the cracks were logged to compare the effectiveness of the different microcracking treatments. At the time of this research, to the best of the authors' knowledge, no digital method was available to accurately locate cracks with widths less than 2.0 mm (Figure 6.2).

Figure 6.1: FDR-C Test Road.

Figure 6.2: Narrow crack width of drying shrinkage crack at first appearance.

Crack monitoring focused primarily on the middle 39 m (≈128 ft.) of each cell (Figure 6.3). Although the 5 m (≈16 ft.) sections at each end of each cell were also monitored, the observations and measurements were not included in the analysis. This area was where the rollers slowed down, stopped, and returned during microcracking activities in each cell, and thus the area may have received inconsistent energy inputs that could have influenced the results.
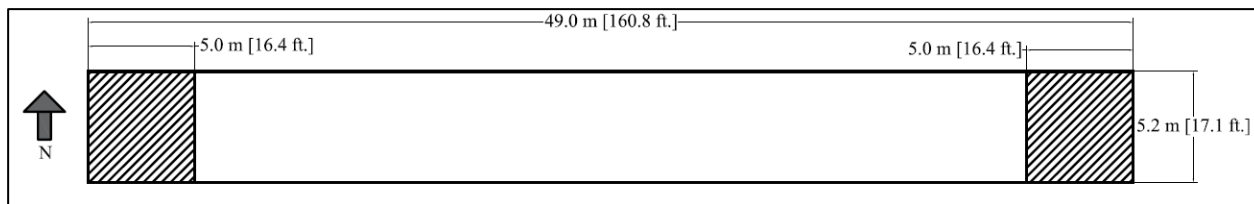
Figure 6.3: Focus area for crack monitoring.

Based on the authors' previous experience with searching for cracks on asphalt concrete surfaces, ideal conditions for locating cracks were considered to be:

- The earliest parts of the day when the surface was coldest and when the sun was at a low angle
- During overcast periods
- The period after wetting the road surface by rain or water spraying, while the water evaporates from the surface (Figure 6.4 and Figure 6.5)

Crack monitoring during the warmer parts of the day, or when the sun had heated the pavement surface, proved to be challenging. Under these conditions, crack widths reduced and were often imperceptible to the naked eye.

Figure 6.4: Crack identification by differential drying after water spraying.

Figure 6.5: Crack identification by discoloration after water spraying.

The parameters of interest regarding cracking performance were crack width, crack density, and crack spacing, which are defined as follows:

- Crack width is the width of the crack opening at the road surface. Reflected cracks are often wider on the top of the surface layer than at the bottom. Severity is considered in three categories by Caltrans *(157)*: low (≤0.25 in. [≈≤6 mm]), moderate (>0.25 in. to ≤0.5 in [≈>6 mm to ≤12 mm]), and high (>0.5 in. [≈>12 mm]). In this study, all cracks were measured and only actual measurements were used in the analyses. No attempt was made to categorize severity or to use severity in the analyses.

- Crack density is the ratio of the sum of the lengths of all the cracks in an area to the size of that area. The failure criteria for crack density on asphalt concrete surfaces used by Caltrans is 2.5 m/m^2 (≈0.76 ft./ft^2). For reference, a single, full-width transverse crack on a 5-m wide by 49-m long cell, in the test road, would contribute 0.02 m/m^2 (0.006 ft./ft^2) to the crack density.
- Crack spacing is the distance between two adjacent transverse cracks. There are no performance failure criteria associated with this parameter, but for analysis purposes, it provides a measure of frequency at which cracks occur.

The process followed to mark, measure, and log cracks included the following:

- Locate the crack on the pavement.
- Mark the crack along its length with spray paint (Figure 6.6).
- Measure the location of the crack from the start of the FDR-C Test Road (i.e., Cell S1).
- Measure the crack length and width.
- Categorize the type of crack.
- Capture an aerial photograph of the crack with a scale for reference (using an unmanned aerial vehicle [UAV]) (Figure 6.7).
- Digitize the crack by tracing a scaled line along its length using the *MATLAB®* software package.

This process provided x and y coordinates of the cracks, which were used to calculate crack density and crack spacing and to develop plan views for the crack maps provided in Appendix B.

Figure 6.6: Marked crack with location.
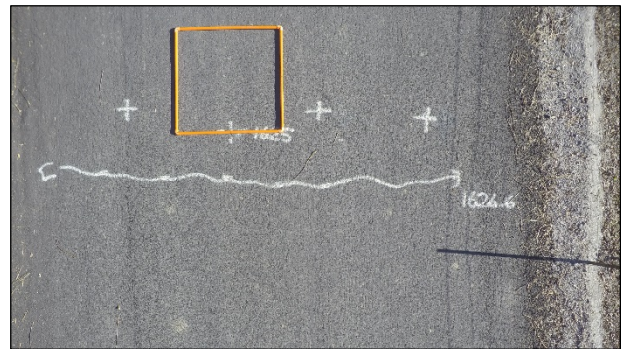
Figure 6.7: Aerial photograph of crack with 1 m×1 m scale.

Crack lengths were measured with a standard tape measure. Crack widths were measured using the same crack-width gauge (Figure 2.24) discussed in Section 2.5. A crack microscope was not used because of the longer time required to take measurements and potential safety implications

in terms of the investigator being distracted in a partial traffic closure. Crack widths varied along the road and even along the length of individual cracks. This was attributed to:

- The location on the crack where the measurement was taken (center vs. ends)
- Condition of the edges of the crack at the surface (spalled vs. intact)
- Temperature of the pavement

Given this variability, crack widths were reported as the average of five equally spaced points along crack.

6.2.2 Cracks Prior to Microcracking

Drying shrinkage cracks were observed prior to microcracking in five cells (S7 [one transverse], S8 [three transverse], S9 [three transverse], S10 [two transverse], and S12 [one transverse]), all on the 4% cement-content sections. The first shrinkage cracks were observed approximately 48 hours after construction (Figure 6.8 and Figure 6.9). The measuring tape shown in Figure 6.9 provides a reference for the crack width. No visible cracks were observed on any of the 2.5% cement-content cells before microcracking. However, it is possible that some cracks were not observed because the surface had not been broomed and there was some loose material and fines on the surface, which may have concealed any fine cracks.

Figure 6.8: 4% Cement: Shrinkage crack on Cell S9 after 48 hours.

Figure 6.9: 4% Cement: Shrinkage crack width on Cell S9 after 48 hours.

The location and spacing between cracks, prior to any microcracking, is provided in Figure 6.10, and the distribution of the initial crack spacing in Figure 6.11. The plots show that the majority of the drying shrinkage cracks were spaced between 8 and 13 m (≈26 and 43 ft.) apart. The crack spacing of the reflected drying shrinkage cracks on the test track, considered as primary shrinkage cracks, was 14 m (Section 2.5). Given that the FDR-C layer on the test track was thicker and that

it had a lower design strength, it was expected to have cracks with shorter crack spacings. This 8 to 13 m crack spacing, was thus anecdotally considered to be the primary crack spacing for the FDR-C Test Road cells with 4% cement.
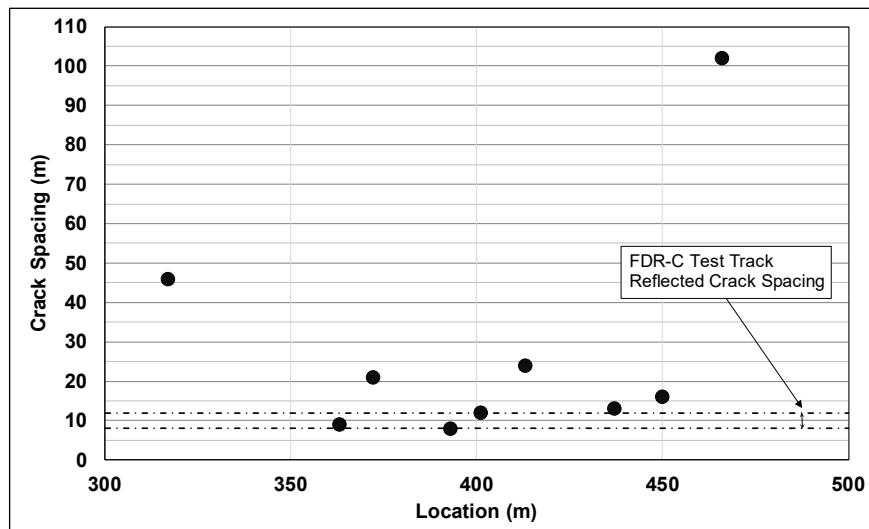
Figure 6.10: Crack location and spacing 48 hours after construction, prior to microcracking.
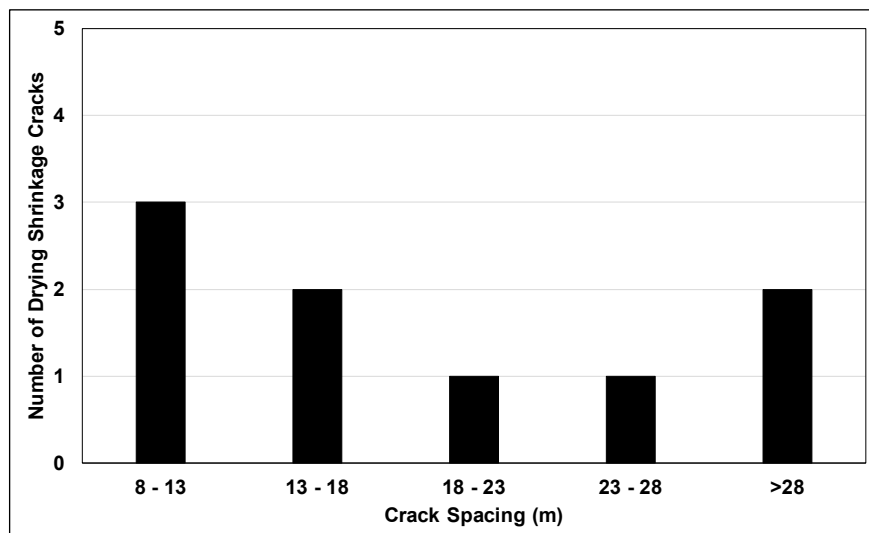
Figure 6.11: Initial crack spacing distribution after 48 hours curing, prior to microcracking.

6.2.3 Crack Density 128 Days after Construction

Reflected cracking observations in the microsurfacing in the first 128 days after construction are summarized in Table 6.1. Crack density, which is the cumulative length of reflected cracks relative to the size of the cell, was used as a measure of the extent of the cracking. Crack patterns for all cells are provided in Appendix B.

Table 6.1: Drying Shrinkage Crack Summary After 128 Days (shaded cells are controls)

4% Cement								2.5% Cement							
	No. of Cracks		Crack Details						No. of Cracks		Crack Details				
Cell	Transverse	Longitudinal	Width (mm)	Density (m/m²)	Spacing (m)	Day First Observed	Instrument Influence?	Cell	Transverse	Longitudinal	Width (mm)	Density (m/m²)	Spacing (m)	Day First Observed	Instrument Influence?
S1*	4	0	1.07	0.125	8.3	15		S17	6	0	0.60	0.106	8.5	37	
S2	8	0	0.72	0.143	10.3	28	Yes	S18	2	0	0.89	0.021	9.9	91	
S3	1	0	0.88	0.031	0.0	72	Yes	S19	0	0	0.00	0.000	0.0	0	
S4	3	0	0.61	0.010	13.2	43		S20	0	0	0.00	0.000	0.0	0	
S5	4	0	0.52	0.020	6.7	91		S21	0	0	0.00	0.000	0.0	0	
S6*	10	1	1.08	0.300	4.8	21		S22	0	0	0.62	0.000	0.0	64	Yes
S7	8	0	0.69	0.148	7.6	18		S23	2	0	0.25	0.016	7.8	79	
S8	4	0	1.33	0.126	10.3	18		S24	3	0	<0.2	0.036	6.4	38	Yes
S9	4	0	0.71	0.098	12.3	18		S25*	1	0	<0.2	0.041	0.0	30	Yes
S10	8	0	0.81	0.084	7.1	28		S26	0	0	0	0.000	0.0	0	
S11	6	0	0.53	0.061	14.4	28	Yes	S27	0	0	0	0.000	0.0	0	
S12	4	0	0.31	0.059	15.2	22	Yes	S28*	4	0	<0.2	0.042	7.1	30	
S13*	5	0	1.58	0.103	10.2	23		S29	0	0	0	0.000	0.0	0	
S14	6	0	0.95	0.128	8.0	37		S30	2	0	<0.2	0.021	3.0	30	
S15	3	0	1.94	0.040	12.0	72		S31	0	0	0	0.000	0.0	0	
S16	4	0	0.47	0.055	15.3	37		S32	0	0	0	0.000	0.0	0	
S37	0	0	0	0	0	0		S33*	5	0	<0.2	0.072	4.9	38	
* Control cells with no microcracking								S34	1	0	<0.2	0.011	0.0	38	Yes
								S35	0	0	<0.2	0.000	0.0	52	Yes
								S36*	3	0	<0.2	0.017	0.0	30	Yes

The first cracks that reflected through the microsurfacing were those observed on the control cells (no microcracking) on both cement-content sections. Cracks in these cells appeared after 15 days on the 4% cement-content cells, and after 30 days on the 2.5% cement-content cells.

Reflected cracks were observed in the locations where instrumentation was installed in select cells on the test road (Table 6.1). This was attributed to stress concentrations that formed around instrument cables causing weak points from which cracks initiated with drying shrinkage. Cracks caused by instrumentation were excluded from further analyses.

The crack density increase for the cells on the 4% and 2.5% cement-content sections are plotted in Figure 6.12 and Figure 6.13, respectively. The results show the following:

- Cracks reflected through the microsurfacing earlier on the 4% cement-content section compared to the 2.5% cement-content section.
- Crack density increased more rapidly on the 4% cement-content section compared to the 2.5% cement-content section.
- Reflected cracks were not observed in all the cells on the 2.5% cement-content section. Cracks directly associated with instrumentation were not considered as cracks associated with microcracking and were therefore excluded from the analysis.

The crack density data for the different rollers and amplitude combinations are plotted in Figure 6.14 through Figure 6.16. Note that 3/1 microcracking passes with curing times before microcracking after 48/72 hours indicates that three microcracking passes after 48 hours and one microcracking pass after 72 hours were applied.

The following observations were made regarding the crack density reduction results and how they relate to microcracking passes:

- Microcracking reduced crack density compared to the results recorded on the control cells.
- Crack density generally reduced with an increase in the number of microcracking passes applied.
- The 2.5% cement-content cells had a lower crack density after 128 days compared to the 4% cement-content cells.
- The 2.5% cement-content cells did not show any observable trends in crack density with microcracking passes.
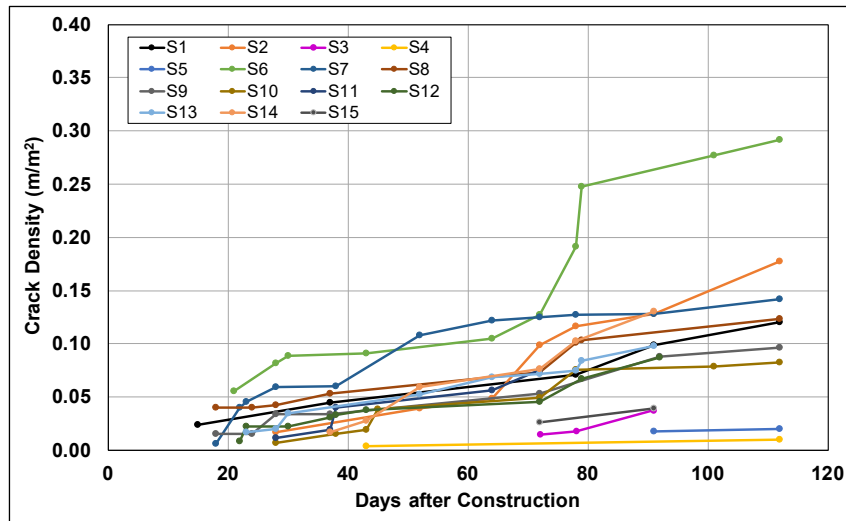
Figure 6.12: 4% Cement: Average crack density increase over time.
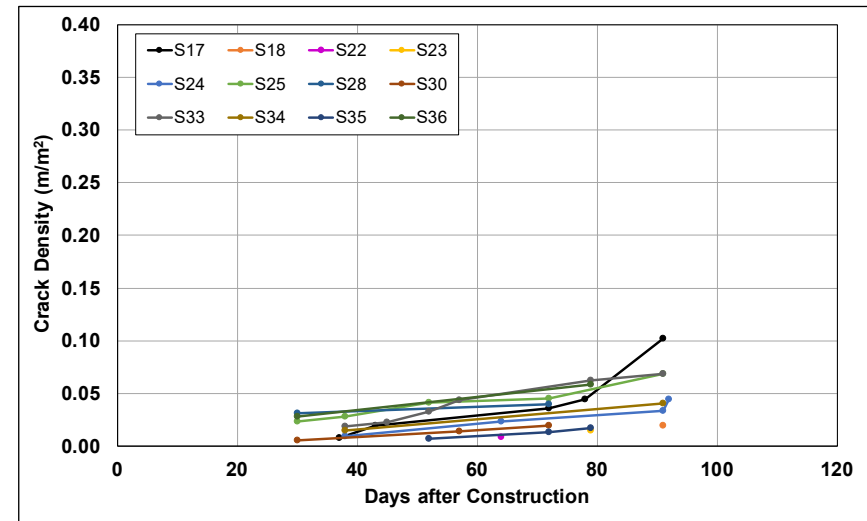
Figure 6.13: 2.5% Cement: Average crack density increase over time.
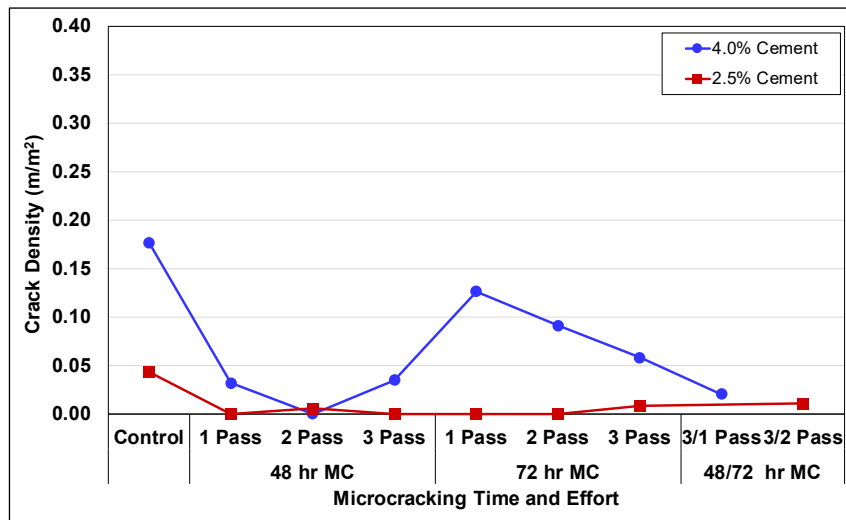
Figure 6.14: SSR/high amplitude (1.42 kN/cm): Average crack density summary.
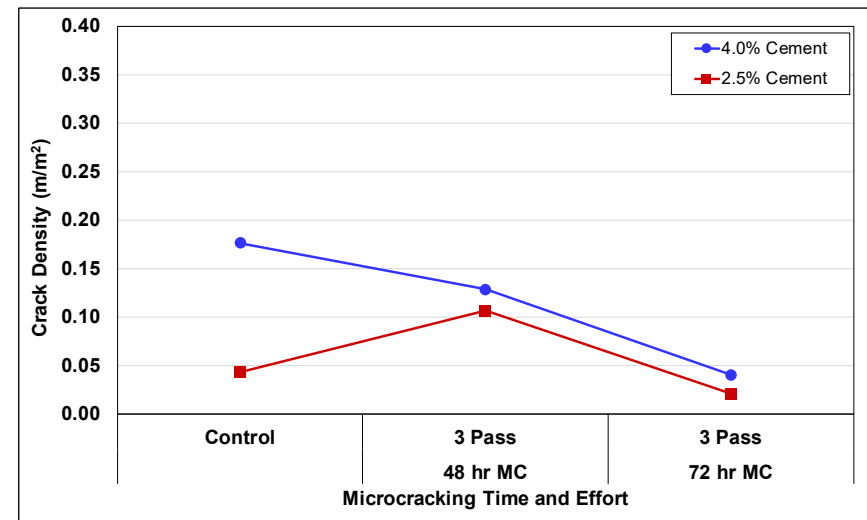
Figure 6.15: DSR/high amplitude (1.31 kN/cm): Average crack density summary.

132
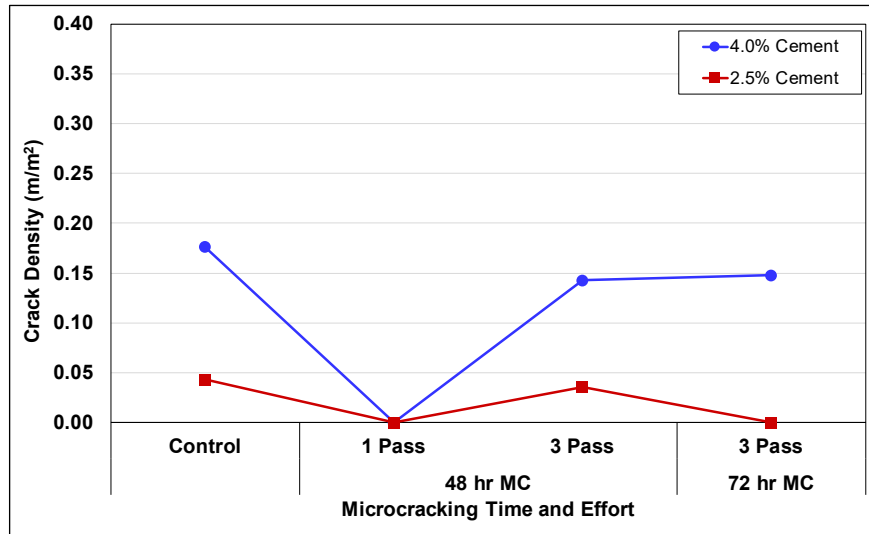
Figure 6.16: SSR/low amplitude (0.95 kN/cm): Average crack density summary.

- Only the 4% cement-content cells microcracked after 72 hours showed a reduction in crack density with increased energy input (microcracking passes) using the SSR roller at high amplitude (1.42 kN/cm per pass).
- Microcracking the 4% cement-content cells after 48 hours resulted in a greater crack density reduction compared to microcracking after 72 hours. At least one pass after 48 hours was sufficient to reduce the crack density significantly. The crack density continued to reduce with an increasing number of passes at 72 hours.
- The crack density results from the 10-ton roller were inconsistent with the results from the 12-ton roller at high amplitude. The results from the 10-ton roller showed that microcracking after 72 hours resulted in reduced cracking on both the 2.5% and 4% cement-content sections.

Statistical analyses of the factors influencing crack density are discussed in Section 7.5.1.

6.2.4   Crack Width 128 Days After Construction

The crack width results for the 4% cement-content cells are provided in Figure 6.17 through Figure 6.19. The crack widths on the 2.5% cement content cells could not be accurately measured because they were too narrow and were thus assigned a width of 0.2 mm (Table 6.1).

The average crack width results in Figure 6.17 for the 4% cement content cells, microcracked with the 12-ton roller with a high vibration amplitude, show the following:

- Crack width was a function of microcracking effort and curing time before microcracking.
- The microcracked cells had a narrower crack-width distribution than the control cells.
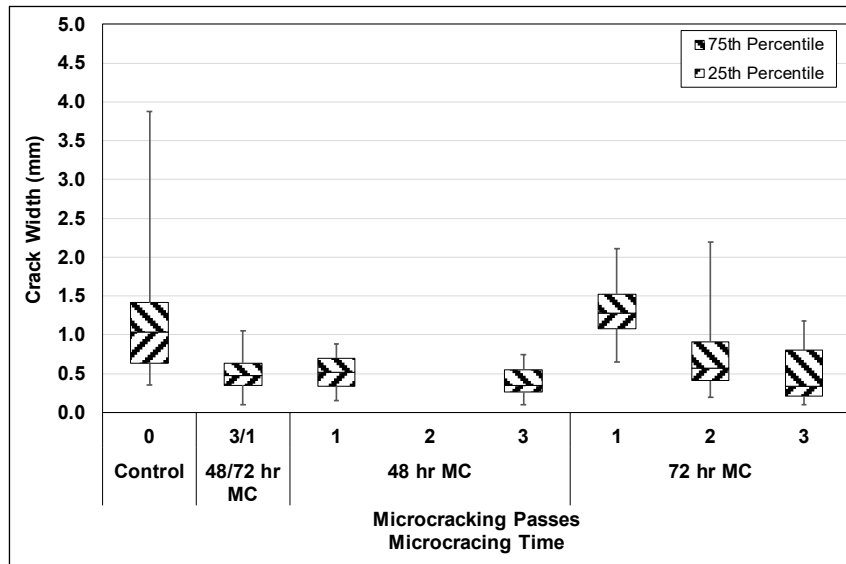
Figure 6.17: 4% Cement: Crack width results after 128 days: SSR with high amplitude.
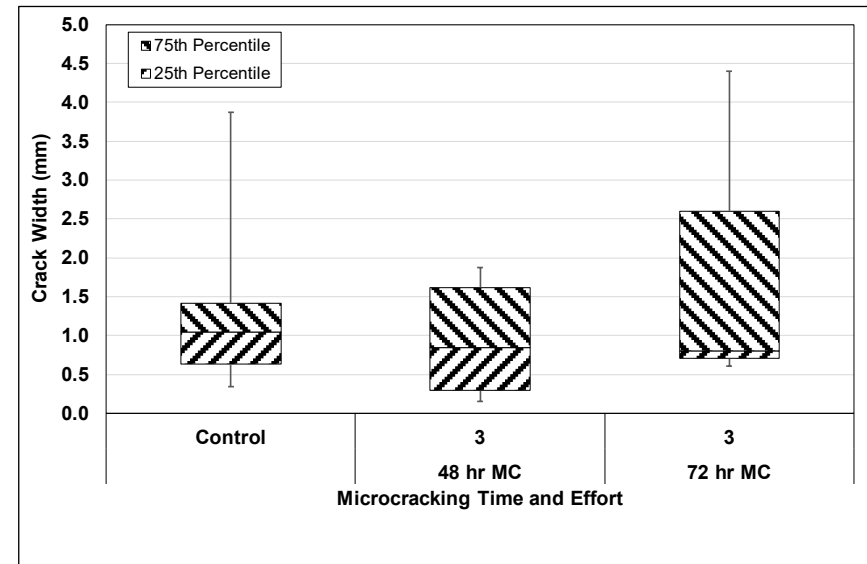
Figure 6.18: 4% Cement: Crack width results after 128 days: DSR with high amplitude.
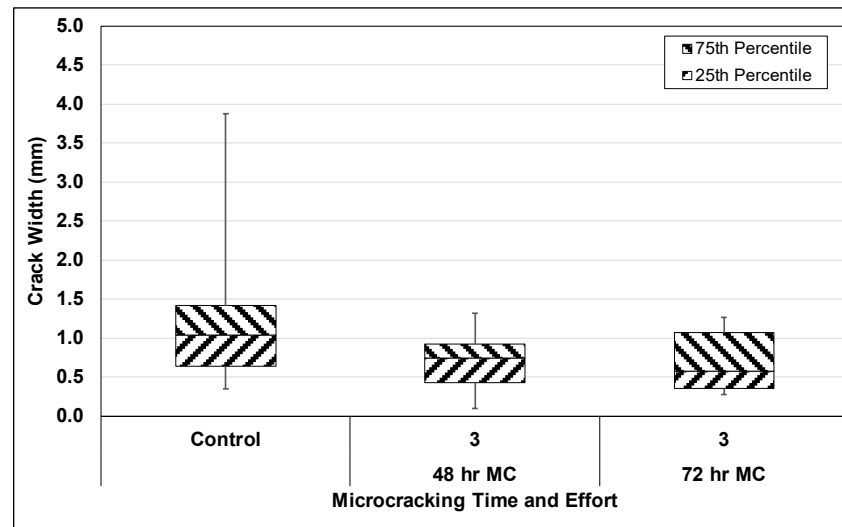
Figure 6.19: 4% Cement: Crack width results after 128 days: SSR with low amplitude.

- Microcracking after 48 hours resulted in narrower cracks compared to microcracking after 72 hours.
- An increase in microcracking effort (i.e., number of passes/increased energy) contributed to a further reduction in crack widths.

Statistical analyses of the factors influencing crack width are discussed in Section 7.5.2.

6.3 Preliminary Coring

Cores were sampled from Cell S20 (2.5% cement, microcracked after 48 hours and again after 72 hours with the SSR at high vibration amplitude) 18 months after construction to check for any surface carbonation, crushing, formation of interlayers, and effective layer thickness reduction due to microcracking. This cell was selected based on observations during microcracking that showed crushing and raveling on the surface. The microcracking on this layer was considered to be excessive, and the contractor agreed that it is not normal practice to microcrack a layer to this extent. Cores were not taken from additional cells to limit any new distresses from forming that were associated with coring operations.

Two cores were extracted. One was sampled from an area with no visible distresses, and the second from an area with a drying shrinkage crack (Figure 6.20). The condition of the two cores is shown in Figure 6.21 and Figure 6.22. Observations from the cores included the following:

- Core thicknesses matched the design thickness of the FDR-C layer.
- The surface of the cores appeared weak and deteriorated, indicating that crushing may have occurred as a result of the multiple microcracking passes on this cell.
- Drying shrinkage cracks initiated from the top of the layer.
- The cores did not appear to have any permanent damage that had originated from the bottom of the FDR-C layer as a result of microcracking. It was initially suspected that high tensile stresses at the bottom of the FDR-C layer, induced by the roller during microcracking, could lead to fatigue cracking. It appears, however, that if any fatigue cracks did develop at the time of microcracking, they had recemented over time.
- Indicator tests using phenolphthalein were performed on the cores and on the surface of the FDR-C layer directly below the microsurfacing to investigate whether the layer had carbonated prior to surfacing, which may have contributed to the weak surface condition. The results show that the layer had carbonated down to a depth of approximately 35 mm (≈1.4 in.) (Figure 6.23 and Figure 6.24). Carbonation of the surface was attributed in part to

the cement content being lower than the recommended initial consumption plus 1% (discussed in Section 4.5) and to some wetting and drying cycles during the four-day water curing period between microcracking and placing the microsurfacing (effective curing requires constant moisture content).

Figure 6.20: Core location through shrinkage crack.

Figure 6.21: Core taken from area with no surface distress.

Figure 6.22: Core taken across shrinkage crack.

Figure 6.23: Carbonation with depth in core hole.

Figure 6.24: Carbonation extent beneath microsurfacing.

UCPRC-RR-2019-05

Carbonation results in loss of cementation, which in turn results in reduced compressive strength in the affected area (Figure 6.25 and Figure 6.26). This carbonated layer represents a poorly cemented interlayer between the top of the treated layer and the surfacing, which can lead to crushing and/or debonding of the surface from the treated layer. The structural capacity of the pavement will reduce as a result *(22)*.

Figure 6.25: Disintegration of FDR-layer surface attributed to carbonation (vertical view).

Figure 6.26: Disintegration of FDR-layer surface attributed to carbonation (side view).

6.4   Stiffness Testing after Placement of the Microsurfacing

An FWD was used to measure stiffness changes over time in the FDR-C layer after the surfacing was placed. Testing was performed on fixed points at weekly intervals for 128 days, starting 10 days after construction of the FDR-C layer. Testing locations in each cell are shown in Figure 6.27. These changes can be used to determine the long-term effect that the microcracking treatments had on the fatigue life of the layer, which can be modeled as a function of the tensile strain at the bottom of the layer *(12)*. Increasing the stiffness of the treated layer can decrease the stress and strain at the bottom of the layer.
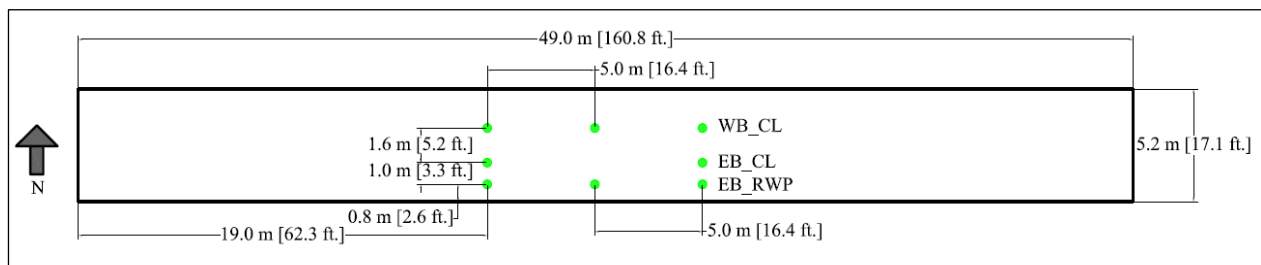
Figure 6.27: FWD testing locations in each cell to monitor stiffness change over time

The FWD stress and deflection results were used to backcalculate FDR-C layer stiffness in each cell using the *CalBack* software package. A two-layer (FDR-C and subgrade) pavement structure was used in the backcalculation. The microsurfacing was not considered in the analysis because it was too thin to contribute any structural capacity.

Detailed results for each testing location in each cell are provided in Appendix B. Table 6.2 summarizes the average and standard deviation of the initial stiffness after 10 and 128 days, as well as the stiffness change measured over the 128-day monitoring period.

The average stiffness results after 128 days, for both the 4% and 2.5% cement-content sections, are plotted in Figure 6.28 through Figure 6.30. The results show that:

- The FWD results were highly variable.
- The 4% cement-content control cells (i.e., no microcracking) had higher stiffnesses compared to the 2.5% cement-content control cells, as expected.
- The 2.5% cement-content cells microcracked after 48 hours had higher stiffnesses than the control cell.
- The cells microcracked after 48 hours had higher stiffnesses than those microcracked after 72 hours.
- Increasing energy input through multiple microcracking passes reduced the long-term stiffness proportionately.

Statistical analyses of the backcalculated stiffness data are discussed in Section 7.6.

Table 6.2: Stiffness Change Summary After 128 Days (shaded cells are controls)

	4% Cement						2.5% Cement				
Cell	Stiffness After 10 Days (MPa)	Std. Dev. After 10 Days (MPa)	Stiffness After 128 Days (MPa)	Std. Dev. After 128 Days (MPa)	Stiffness Increase (%)	Cell	Stiffness After 10 Days (MPa)	Std. Dev. After 10 Days (MPa)	Stiffness After 128 Days (MPa)	Std. Dev. After 128 Days (MPa)	Stiffness Increase (%)
S1*	14,397	3,025	15,874	6,838	10	S17	2,952	1,504	4,935	2,175	67
S2	4,644	1,826	6,627	3,207	43	S18	2,640	1,266	3,874	2,803	47
S3	2,959	1,279	5,752	4,427	94	S19	5,877	4,385	8,524	4,976	45
S4	2,628	814	3,860	522	47	S20	1,907	1,002	4,488	2,406	135
S5	1,930	1,127	3,437	1,237	78	S21	2,406	1,846	4,262	2,005	77
S6*	3,227	1,270	6,648	3,815	106	S22	2,017	1,051	3,520	1,773	74
S7	2,444	639	4,090	1,779	67	S23	1,299	798	2,857	1,585	120
S8	3,314	2,625	5,244	3,391	58	S24	2,044	927	2,385	1,193	17
S9	2,264	2,308	2,892	2,105	28	S25*	3,850	1,776	5,881	4,320	53
S10	2,286	1,529	2,949	1,877	29	S26	2,283	1,004	4,614	1,916	102
S11	1,829	1,391	1,945	883	6	S27	2,204	557	3,360	875	52
S12	5,341	2,042	5,417	2,142	1	S28*	1,347	604	2,100	730	56
S13*	7,820	2,992	10,815	6,292	38	S29	657	127	1,762	270	168
S14	3,779	1,302	5,078	2,014	34	S30	1,048	206	1,454	453	39
S15	7,900	3,256	10,720	5,186	36	S31	1,012	308	2,212	936	119
S16	3,734	1,616	5,256	1,269	41	S32	1,241	367	3,001	766	142
S37	4,168	1,871	6,052	3,684	45	S33*	2,138	500	3,448	427	61
* Control cells with no microcracking						S34	2,300	815	3,973	1,469	73
						S35	2,331	699	4,790	2,008	106
						S36*	1,599	735	2,991	2,171	87
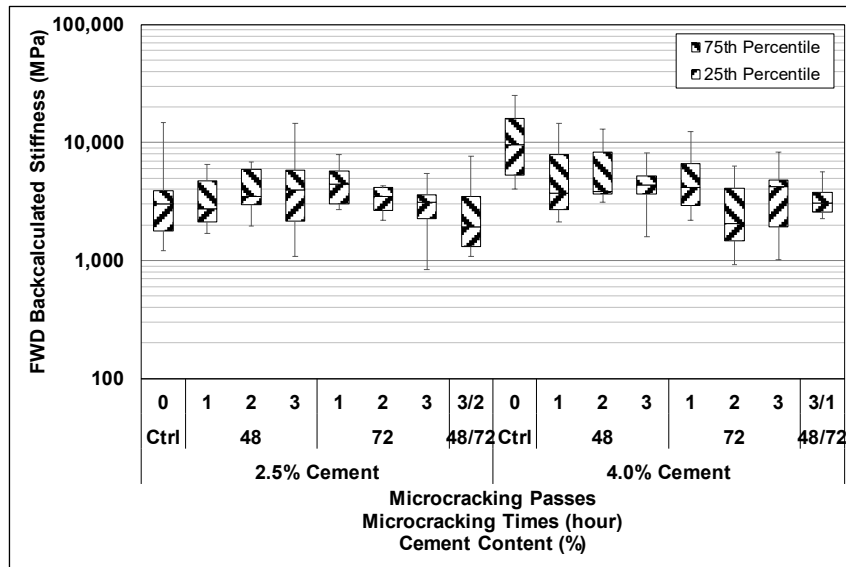
Figure 6.28: Stiffness after 128 days: SSR with high amplitude.
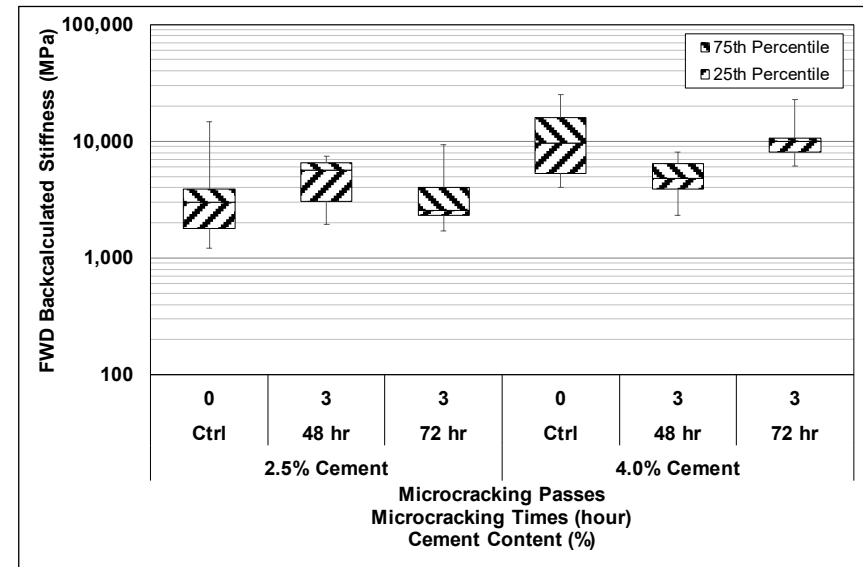
Figure 6.29: Stiffness after 128 days: DSR with high amplitude.
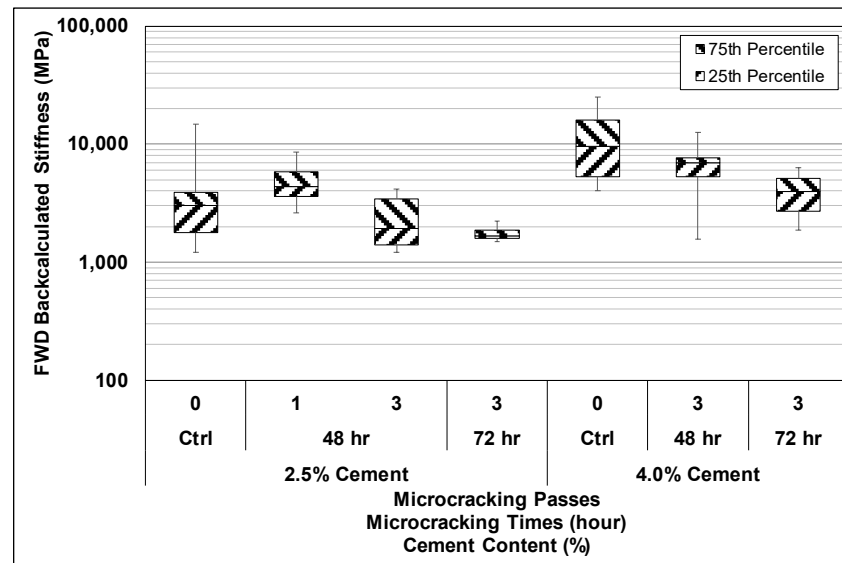
Figure 6.30: Stiffness after 128 days: SSR with low amplitude.

7 TEST ROAD RESULTS ANALYSIS

7.1 Introduction

This chapter discusses statistical analyses of the FDR-C Test Road material testing, microcracking, crack monitoring, and stiffness results to supplement the information presented in Chapters 4, 5, and 6.

7.2 Unconfined Compressive Strength

The mix design unconfined compressive strength (UCS) results were further analyzed to predict whether crushing failure was likely to occur during microcracking. Various published models that predict UCS increase over time were considered. The US Air Force model *(51)*, shown in Equation 7.1, was selected as the most appropriate for modeling UCS increase with time, as it had only one model coefficient, *K*, which minimized the risk of overfitting considering the limited available data from the mix design tests.

$$UCS(t) = UCS(t_0) + K \times \log(\frac{t}{t_0}) \tag{7.1}$$

Where: $UCS(t)$ = UCS at time t (days)
            $UCS(t_0)$ = UCS of a material after t_0 days
            K = 70×*C* for cement
            t = Curing time (days)
            C = Stabilizer content (%)

The UCS results listed in Section 4.5.5 together with the predicted UCS results using Equation 7.1 are plotted in Figure 7.1. The rate of strength increase is a function of the cement content and a value which accelerates the strength gain. With *K*=70×cement content, the rate of strength increase was overestimated compared to the laboratory-measured results.

A regression analysis was performed using Equation 7.2 to determine if there was a difference in *K* for the 2.5% and 4% cement-content specimens. The results for the regression coefficients are summarized in Table 7.1. The R^2 for the fit was 0.99, indicating a strong correlation between the variables assessed.
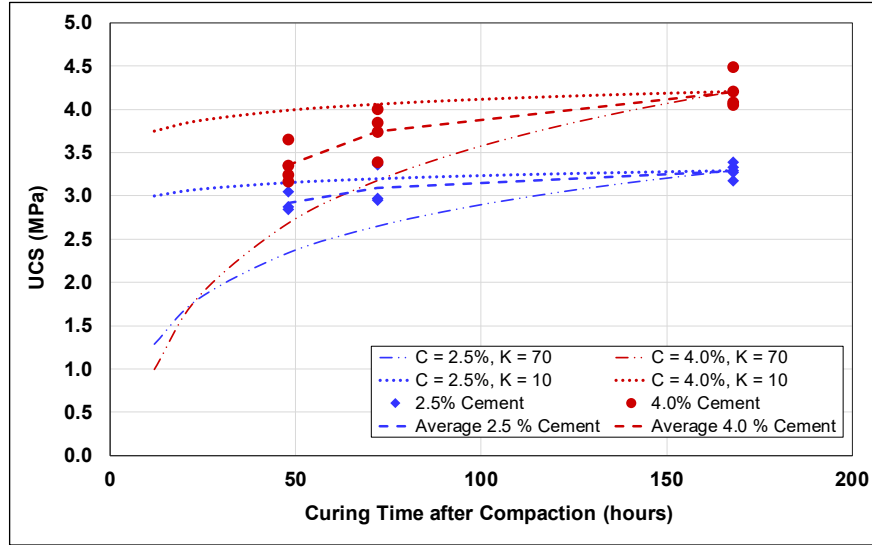
Figure 7.1: Measured and predicted UCS strength gain over time.

$$UCS(t) = \beta_0 \times UCS(t_0) + \beta_1 \times C \times \log\left(\frac{t}{t_0}\right) + \beta_2 X_1 \times C \times \log\left(\frac{t}{t_0}\right) \tag{7.2}$$

Where: β_1, β_2 = Strength gain rate coefficient $[K = \beta_i \times C]$

X_1 = Indicator variable; 0 = 2.5% cement, 1 = 4% cement

Table 7.1: Regression Coefficients for Equation 7.2

Coefficient	Estimate	Std. Error	t-value	P(>|t|)
β_0	1.00	0.02	54.58	<2E-16
β_1	26.35	8.57	3.07	0.01
β_2	11.19	8.18	1.37	0.19

A t-test was performed to determine if there was a difference between the strength gain rates for the two cement contents. The t-test had a confidence interval of 95%, with the null hypothesis that β_2 = 0, and the alternative hypothesis that $\beta_2 \neq 0$. The t-value of 1.37 was less than the t-distribution value at t(0.975,17) = 2.11. The null hypothesis was therefore concluded, indicating that there was no significant difference between the strength gain coefficients for the two cement contents, and that, within the cement-content range of 2.5% to 4%, the strength gain coefficient was not dependent on the cement content. Equation 7.2 was therefore considered to be appropriate for modeling the strength gain of the different cement contents used in this analysis.

The regression analysis was repeated using Equation 7.3 to determine the strength gain coefficient for the FDR-C material considering the data sets for both cement contents. The regression coefficients are summarized in Table 7.2. The coefficient of determination was 0.99,

indicating that this model can be used for calculating the strength of FDR-C layers at different curing times, with only one UCS result at one specific time. The fitted results are plotted in Figure 7.2.

$$UCS(t) = UCS(t_0) + K \times \log\left(\frac{t}{t_0}\right)$$

(7.3)

Where: K = 35.1×C for FDR-C layers treated with Type II/V cement

Table 7.2: Regression Coefficients used in Equation 7.3

Coefficient	Estimate	Std. Error	t-value	P(>|t|)
β_0	1.0	0.02	53.91	<2E-16
β_1	35.1	5.81	6.05	1.01E-05
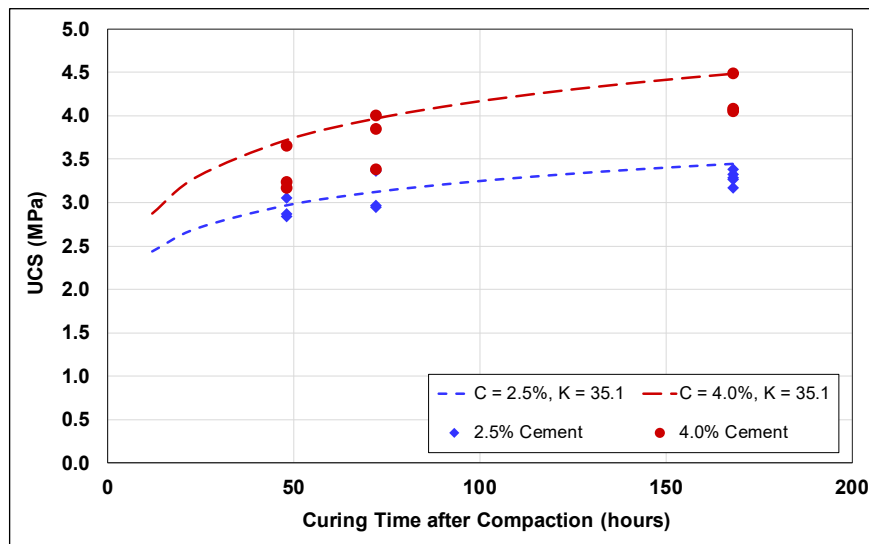
Figure 7.2: Calculated UCS over time using Equation 7.3.

7.3   Relationship between SSG and FWD

A relationship between SSG stiffness and FWD backcalculated stiffness measured on the FDR-C Test Road was required to determine representative stiffnesses for simulating microcracking using finite element method (FEM) analysis (discussed in the Phase 2b report *[10]*). The SSG and FWD results collected on the same location in cell S28 (2.5% cement) are provided in Figure 7.3. Several relationships have already been developed to relate SSG results to FWD stiffness, using the model in Equation 7.4 and the coefficients in Table 7.3 *(97,98)*.
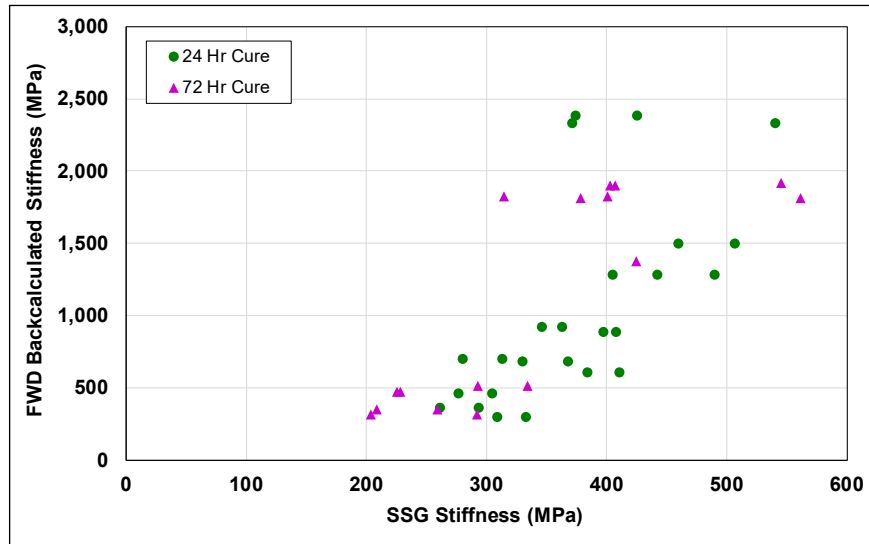
Figure 7.3: Relationship between SSG and FWD stiffnesses.

$$E_{FWD} = \beta_0 + \beta_1 \times E_{SSG} \hspace{4cm} \textbf{(7.4)}$$

Where: E_{FWD} = Backcalculated FWD stiffness (MPa)

E_{SSG} = SSG stiffness (MPa)

β_0, β_1 = Regression coefficients

Table 7.3: Coefficients for Existing Relationships between SSG and FWD

Researcher	β_0	β_1
Scullion et al. *(97)*	-6550.5	27.953
Chen *(98)*	-261.96	37.654

Linear regression was used to fit the results in Figure 7.3 to Equation 7.4 to determine which model coefficients would best represent the Test Road FDR-C layer. These model coefficients are provided in Table 7.4. The R^2 of the fit was 0.47, indicating a poor correlation between the two devices.

Table 7.4: Regression Coefficients for Equation 7.4

Term	Coefficients	Estimate	Std. Error	t-value	Pr(>|t|)
(Intercept)	β_0	-863.03	327.29	-2.64	0.012
E_{SSG}	β_1	5.32	0.88	6.08	4.06E-07

The relationship between the SSG and FWD, calculated for the FDR-C layer in the Test Road, is less sensitive than those calculated by Scullion et al. *(97)* and Chen *(98)*, likely due to differences in the pavement structures that could have influenced the shallow measurements of the SSG. The poor correlatoin between SSG and FWD stiffnesses is also indicative of the variability of replicate

SSG measurements and using fixed locations to take measurements in each cell (i.e., measurements may have been taken in the vicinity of distress in some cells but not in others).

7.4 Factors Affecting Stiffness Reduction Measured with a Soil Stiffness Gauge

Factors identified as having a potential effect on stiffness reduction after microcracking of the Test Road FDR-C layer included curing time before microcracking, number of microcracking passes, unconfined compressive strength, energy per pass, total energy input from the roller, and stiffness reduction during microcracking. These factors were assessed in a correlation analysis to identify any strong relationships. Data were sourced as follows:

- Curing time (MC_{Time}) and number of microcracking passes (MC_{Pass}) were actual values from the different cells on the FDR-C Test Road.
- The compressive strength of the FDR-C layer (UCS_{MPa}) was represented by the UCS at the time of microcracking, calculated with Equation 7.3.
- Energy per pass from the roller (EPP) was calculated using the linear applied force using (Equation 4.2 in Section 0) for the different vibration amplitudes of the rollers listed in Table 7.5. Total energy input during microcracking (Energy) was calculated with Equation 7.5.
- Stiffness reduction during microcracking (MC_{Red}) were the actual values measured with a soil stiffness gauge in each cell.

Table 7.5: Rollers Used for Microcracking on FDR-C Projects

Project	Operating Weight (ton)	Drum Width (mm)	Vibration Amplitude	Total Force (kN)	Linear Total Force (kN/cm)
Test Road	12	2,135	High	304	1.42
Test Road	12	2,135	Low	203	0.95
Test Road	10	1,675	High	220	1.31
CR27	10	2,135	High	291	1.36
CR32B	10	2,135	High	291	1.36
CR32B	10	1,675	High	220	1.31
CR99	12	2,135	High	351	1.64
PLU-147	10	2,135	High	289	1.35

$$Energy_T = LinearForce \times MCPass \qquad \qquad (7.5)$$

Where: $Energy_T$ = Total energy applied during microcracking (kN/cm)
  $LinearForce$ = Total applied force by the vibratory roller per unit width (kN/cm), calculated using Equation 4.2
  $MCPass$ = Microcracking pass

A correlation plot of the individual factors against the SSG results in shown in Figure 7.4. Strong relationships were noted between stiffness reduction, the number of microcracking passes, and the energy input of the roller.
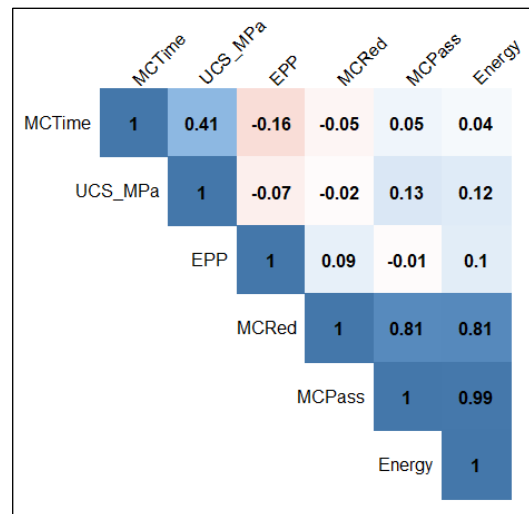
Figure 7.4: Correlation plot for stiffness reduction measured with an SSG.

The effects of selected individual factors on stiffness reduction of the FDR-C Test Road cells and other projects monitored were analyzed using linear regression by fitting results to Equation 7.6. The regression coefficients are provided in Table 7.6.

$$E_{Red} = \beta_0 + \beta_1 \times Energy_T + \beta_2 \times UCS + \beta_3 \times MCTime \tag{7.6}$$

Where: E_{Red} =   Stiffness reduction during microcracking, normalized to stiffness at Pass 0 (%)
         UCS =   7-day unconfined compressive strength (MPa)
         $MCTime$ =   Curing time before microcracking (hours)
         $\beta_0, \beta_1, \beta_2, \beta_3$ =   Regression coefficients

Table 7.6: Regression Coefficients for Equation 7.6

Term	Coefficients	Estimate	Std. Error	t-value	Pr(>|t|)
(Intercept)	β_0	0.212	0.029	7.397	4.50E-13
$Energy_T$	β_1	0.096	0.003	28.862	< 2e-16
UCS	β_2	-0.032	0.008	-4.063	5.46E-05
$MCTime$	β_3	-8.74E-04	4.48E-04	-1.951	5.15E-02

The R^2 for the fit was 0.573, indicating a marginal relationship between the selected factors. To determine whether any of the variables were significant, a t-test was performed with a null hypothesis that β_0 = …= β_3 = 0, and an alternative hypothesis that β_0 = …= β_3 ≠ 0. The t-value at a

95% confidence interval was t(0.975, 627) = 1.964. The t-value for all the independent variables exceeded this t-value, indicating that the alternative hypothesis can be accepted for these variables while taking limitations of observed variability between tests cells and using fixed points for stiffness measurements, regardless of localized distresses, into consideration. The results show the following:

- Increased energy input reduces the stiffness, as expected.
- FDR-C layers with higher seven-day design strengths (e.g. >4.1 MPa [≈600 psi]) will have a lower rate of stiffness reduction compared to layers with a lower seven-day design strength.
- The rate of stiffness reduction reduces as the time between final compaction and microcracking increases (i.e., microcracking sooner after construction [e.g., 48 hours] could increase the rate of stiffness reduction per pass).

7.4.1 Discussion

The critical parameter dictating the rate of stiffness reduction was the total energy applied during microcracking. The applied energy was modeled as the increase in force per unit width of the roller, with increased microcracking passes. The force per unit width of a specific roller depends on the centrifugal force, drum mass, drum diameter, drum width, and frame mass, and this can differ based on the manufacturer for rollers with the same operating weight. A summary of the different rollers used on projects monitored during this study is provided in Table 7.5. Note that the operating weight of the roller, which is commonly used to specify rollers, does not control the rate of stiffness reduction, which is dependent on the force per unit width the roller can apply. Vibratory rollers that apply a greater force per unit width will cause a greater stiffness reduction per pass compared to a roller with a lower force per unit width. Currently available rollers with the same operating weight can apply different forces per unit width by changing the vibration amplitude settings.

Based on this discussion, the current Caltrans method specification for microcracking (quoted in Section 1.3) could lead to significantly different stiffness reduction results as it is currently phrased. Options for limiting this outcome include specifying:

- A percent stiffness reduction as measured by a soil stiffness gauge if a performance specification is desired

- Using vibratory rollers with a specified peak force per unit width if a method specification is desired

7.5 Factors Affecting Crack Density and Crack Width

7.5.1 Crack Density

Crack density provided a measure of the distress of the FDR-C layer and the ability of microcracking to mitigate drying shrinkage cracks. Analyses in the previous section established that stiffness reduction during microcracking is a function of the strength of the FDR-C layer, curing time before microcracking, and energy input. In this section, factors potentially affecting crack density were investigated in terms of the force per unit width that the roller applies and the following relationships:

- Crack density, design strength, and curing time before microcracking
- Crack density and the total energy applied during microcracking
- Stiffness after microcracking, or the stiffness reduction during microcracking, measured with an SSG, and whether this is a good predictor of crack density

Linear regression was used to determine the relationship and significance of different variables to crack density. The curing time before microcracking could not be considered as a continuous variable to compare the crack density of the control cells to the crack density of the microcracked cells because the control cells were not microcracked. Categorical variables were therefore introduced in the analysis to indicate if microcracking was applied after 48 hours (MC_{48}) or after 72 hours (MC_{72}). The correlation plot of the crack density data is shown in Figure 7.5.

Good correlations between microcracking after 48 hours and after 72 hours and between the percent stiffness reduction during microcracking (E_{Red}) and the stiffness after microcracking (E_{MC}) were noted. Consequently, only MC_{48} and E_{Red} were considered for the regression model in Equation 7.7. The coefficient results are provided in Table 7.7. The R^2 for the fit was 0.506. To determine whether any of the variables were significant, a t-test was performed with a null hypothesis that $\beta_0 = \ldots = \beta_5 = 0$, and an alternative hypothesis that $\beta_0 \ldots \beta_5 \neq 0$. The t-value at a 95% confidence interval was t(0.975, 9) = 2.04.
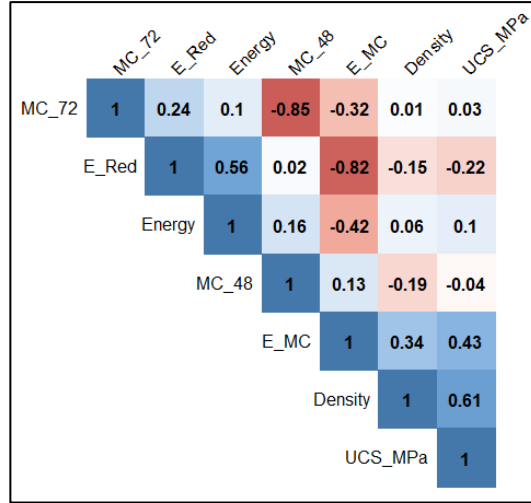
Figure 7.5: Correlation plot for crack density data.

$$DSC_\gamma = \beta_0 + \beta_1 \times UCS + \beta_2 \times Energy_T + \beta_3 \times MC_{48} + \beta_4 \times E_{RED} + \beta_5 \times UCS \times Energy_T \quad \textbf{(7.7)}$$

Where: DSC_γ = Drying shrinkage crack density (m/m^2)

UCS = 7-day unconfined compressive strength (MPa)

MC_{48} = 1 if microcracking was applied after 48 hours, else 0

E_{RED} = Stiffness reduction during microcracking, normalized to stiffness at Pass 0 (%)

$Energy_T$ = Total energy applied during microcracking (kN/cm)

$\beta_0, \beta_1, \beta_2, \beta_3\ \beta_4, \beta_5$ = Regression coefficients

Table 7.7: Regression Coefficients for Equation 7.7

Term	Coefficient	Estimate	Std. Error	t-value	Pr(>|t|)
(Intercept)	β_0	-0.378	0.113	-3.351	0.002
UCS	β_1	0.119	0.029	4.152	2.39E-04
$Energy_T$	β_2	0.064	0.032	1.999	0.054
MC_{48}	β_3	-0.016	0.017	-0.935	0.357
E_{RED}	β_4	-0.026	0.067	-0.396	0.695
$UCS \times Energy_T$	β_5	-0.019	0.008	-2.232	0.033

The t-tests showed that the t-values for β_3 and β_4 were less than 2.04, and thus the alternative hypothesis can be rejected for these variables. The remainder of the variables all had a significant effect on the crack density. The model was reduced to only the significant variables, and the data were fitted to Equation 7.8 using linear regression. The R^2 for the final model was 0.49. The coefficient results are provided in Table 7.8.

$$DSC_\gamma = \beta_0 + \beta_1 \times UCS + \beta_2 \times Energy_T + \beta_3 \times UCS \times Energy_T \qquad \textbf{(7.8)}$$

Table 7.8: Regression Coefficients for Equation 7.8

Term	Coefficient	Estimate	Std. Error	t-value	Pr(>|t|)
(Intercept)	β_0	-0.395	0.108	-3.649	0.001
UCS	β_1	0.123	0.028	4.388	1.11E-04
$Energy_T$	β_2	0.061	0.031	1.949	0.060
$UCS \times Energy_T$	β_3	-0.019	0.008	-2.278	0.029

The model shows the following:

- The crack density increased with increased design strength.
- Neither the percent stiffness reduction nor microcracking after 48 hours provided significant explanation for the crack density reduction. Given the high correlation of the latter variables with the stiffness after microcracking and microcracking after 72 hours, it can be concluded that these variables do not provide significant explanation for the reduction in crack density. Using fixed locations for stiffness measurements regardless of the proximity of any distresses may be a reason for the weaker relationships.
- The effect of the total applied energy and the interaction between design strength and energy input are illustrated in Figure 7.6. This shows that increased energy input was most effective at reducing the crack density of the material with the higher design strength, while the lower design strength material did not show a sensitivity to energy input in terms of crack density reduction. The 2.5% cement-content material had on average one full-width reflective crack in the 49-m long cell, regardless of the microcracking input, whereas the number of reflective cracks on the 4% cement-content cells reduced from approximately seven cracks down to three cracks with increased energy input during microcracking.
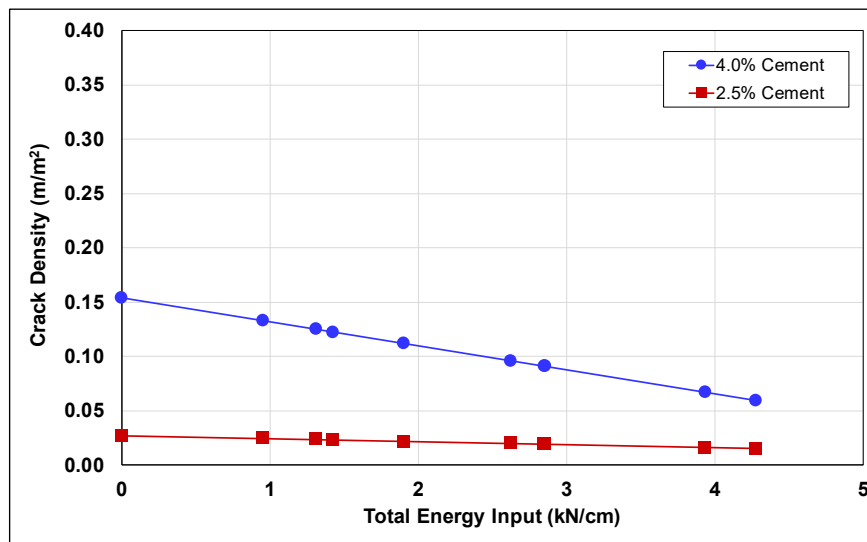
Figure 7.6: Fitted crack density results using Equation 7.8.

7.5.2 Crack Width

The crack width results on the 4% cement-content cells were analyzed following the same framework used for the crack density results. The effects of the following variables on crack width were considered in the analyses:

- Curing time before microcracking
- Total energy input during microcracking
- Percent stiffness reduction during microcracking
- Stiffness after microcracking measured with an SSG

The correlation plot of the crack width data is provided in Figure 7.7. Good correlations were noted between microcracking after 48 hours (MC_{48}) and microcracking after 72 hours (MC_{72}), as well as between the percent stiffness reduction during microcracking (E_{Red}) and the stiffness after microcracking (E_{MC}). Consequently, microcracking after 48 hours, stiffness reduction, and energy input were all considered in the model. Linear regression was used to fit the results to Equation 7.9, with the coefficients provided in Table 7.9.
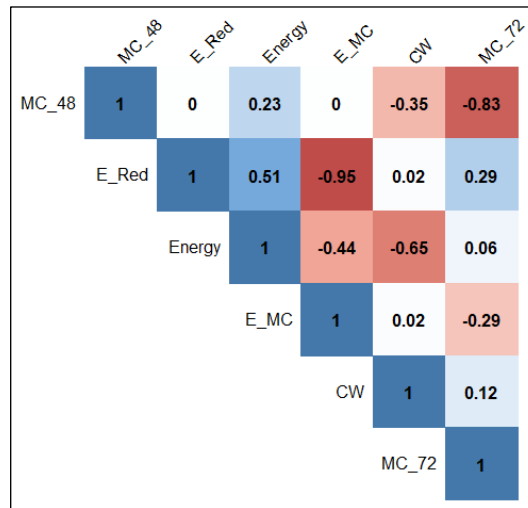
Figure 7.7: Correlation plot for crack width data.

$$CW = \beta_0 + \beta_1 \times Energy_T + \beta_2 \times E_{RED} + \beta_3 \times MC_{48} \tag{7.9}$$

Where:
CW = Crack width (mm)
$Energy_T$ = Total energy applied during microcracking (kN/cm)
E_{RED} = Stiffness reduction during microcracking, normalized to stiffness at Pass 0 (%)
MC_{48} = 1 if microcracking was applied after 48 hours, else 0
$\beta_0, \beta_1, \beta_2, \beta_3$ = Regression coefficients

Table 7.9: Regression Coefficients for Equation 7.9

Term	Coefficient	Estimate	Std. Error	t-value	Pr(>|t|)
(Intercept)	β_0	1.220	0.118	10.371	<2e-16
$Energy_T$	β_1	-0.205	0.059	-3.462	8.11E-04
E_{RED}	β_2	0.722	0.596	1.212	0.228
MC_{48}	β_3	-0.006	0.144	-0.045	0.964

The R^2 for the fit was 0.197. To determine whether any of the variables were significant, a t-test was performed with the hypothesis that $\beta_0 = ... = \beta_4 = 0$, and an alternative hypothesis that $\beta_0 ... \beta_4 \neq 0$. The t-value at a 95% confidence interval was t(0.975, 6) = 2.44. Based on the t-test results, only the alternative hypothesis for β_0 and β_1 can be accepted and the remaining coefficients rejected at a 95% confidence interval. This crack width regression model shows the following:

- Increased energy input was the primary factor in reducing crack width.
- The percent stiffness reduction and microcracking after 48 hours, and, by extension, the stiffness after microcracking after 48 hours and again after 72 hours did not provide a significant explanation for the crack width reduction. Using fixed locations for stiffness measurements regardless of the proximity of any distresses may be a reason for the weak relationships.

7.5.3 Discussion

Kota et al. *(14)* and George *(23)* have shown how reducing the design strength of a cement-treated layer reduces the number of reflective drying shrinkage cracks that reflect through the asphalt concrete. This was attributed to the reduced crack width and increased load transfer efficiency of the drying shrinkage cracks. Reducing the design strength increases the number of cracks in the cement-treated layer, thereby reducing the slab lengths between cracks. However, the narrower crack widths result in fewer cracks reflecting through the surface layer. This was the design philosophy proposed by George *(3)* to improve the mix design process for cement-treated layers and mitigate reflective drying shrinkage cracks. The crack width and crack spacing behavior with increased design strength are also supported by the models developed by George *(23)* and Zhang and Li *(66)*.

All the crack measurements on the FDR-C Test Road used in this analysis were collected after the microsurfacing was placed. These cracks can therefore all be considered as reflected drying shrinkage cracks. Considering the observations from the crack measurements on the FDR-C Test

Road in terms of the literature observations, the reduced crack density on the 2.5% cement-content cells, compared to the crack density on the 4% cement-content cells, is indicative of reduced crack widths, and, by extension, reduced crack spacing in the FDR-C layer.

The difference in the effect of microcracking on the crack development between the two mix designs can be attributed to the strength of the material, the shrinkage development, and the time of microcracking. Figure 7.8 provides the calculated shrinkage strain from models developed from laboratory shrinkage tests on the material used in the test road (discussed in the Phase 2b report *[10]*).
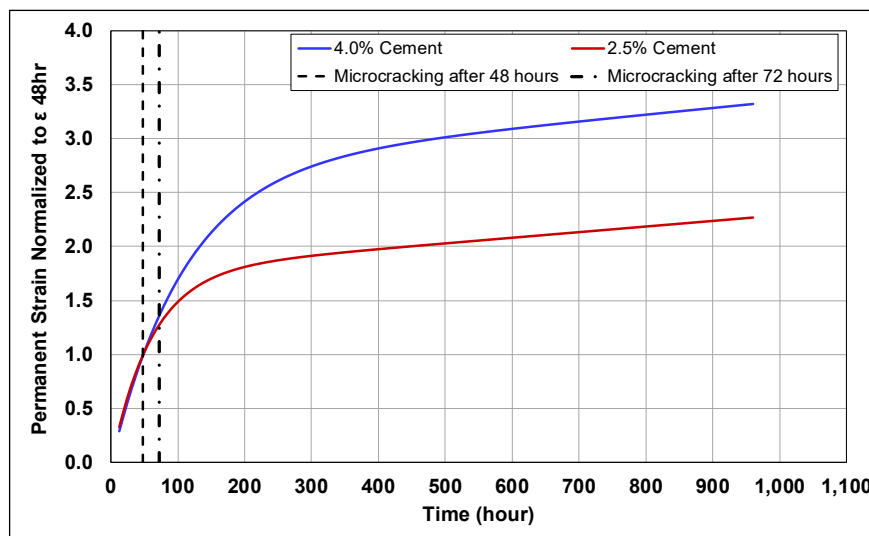
Figure 7.8: Calculated shrinkage strain normalized to the strain after 48 hours.

The microcracking simulation discussed in the Phase 2b report *(10)* showed that most of the crack events, where the stress from shrinkage exceeded the tensile strength of the layer, occur within the first 24 hours after compaction. In the case of microcracking, the material strength reduction is the primary reason for the material being more susceptible to shrinkage cracking. However, the additional shrinkage cracks reduce the crack widths, which in turn reduces the susceptibility to reflective cracking. Since the pavement already contains cracks due to shrinkage before microcracking, the stress induced from continued shrinkage in the slab is significantly less than the stress immediately after construction as a result of the reduced slab lengths. The different behavior in the continuing shrinkage after microcracking is what controls the effect of microcracking on crack development for different cement contents:

- The 2.5% cement-content material had significantly less shrinkage potential (remaining shrinkage to be incurred) after microcracking than the 4% cement-content material (Figure 7.8) after a given curing time. Shrinkage that continued after microcracking after 48 or 72 hours did not induce a sufficient number of cracks to minimize widths of the reflected cracks. The cracks that developed before microcracking thus controlled the reflective cracking (Figure 7.6). Microcracking earlier after final compaction (e.g., within 24 hours) could potentially yield more shrinkage cracks in the FDR-C layer and further minimize crack widths to mitigate reflective cracking.

- The 4% cement-content material had significantly more shrinkage potential remaining after microcracking than the 2.5% cement-content material. The additional increase in the number of drying shrinkage cracks that developed with increased energy input during microcracking (resulting in lower strength) reduced the total width of cracks that developed before microcracking. Microcracking was performed sufficiently early on the 4% cement-content section to change the drying shrinkage cracking from a few wide reflective cracks to numerous thinner cracks with only a small number of them wide enough to reflect through the surface layer.

These results show that microcracking should ideally be performed as early as possible to benefit from the shrinkage potential after microcracking while the material strength is still low. The shrinkage potential for the 4% cement-content material was sufficient to further reduce the crack widths by inducing more cracks after microcracking. The 2.5% cement-content material would probably show a significant reduction in reflective cracks if microcracking was applied after 24 hours. This is considered in the microcracking simulations discussed in the Phase 2b report.

7.6   Stiffness Result Analysis

The FWD backcalculated stiffness results after 128 days were analyzed with linear regression to evaluate the relationship between the measured variables and to determine the significance of each. The effects of the following variables were considered in the analyses:

- The effect of energy input during microcracking on the long-term stiffness of the layer
- The influence of microcracking on the stiffness of FDR-C layers with different design strengths
- Whether the percent stiffness reduction or stiffness soon after microcracking provides any indication of the long-term stiffness
- The effect of microcracking on long-term stiffness compared to the stiffnesses recorded on the control cells

The curing time between final compaction and microcracking was considered as an indicator variable, similar to the linear regression analyses for the crack density and crack width results. The correlation plot of the FWD backcalculated stiffness data with the stiffness after microcracking is provided in Figure 7.9. The plot shows that microcracking after 48 hours and microcracking after 72 hours, as well as the stiffness after microcracking and the percent stiffness reduction are highly correlated. Note that this is a partial data set, as stiffness in some of the control cells was not measured with an SSG when microcracking had been completed in the other cells.
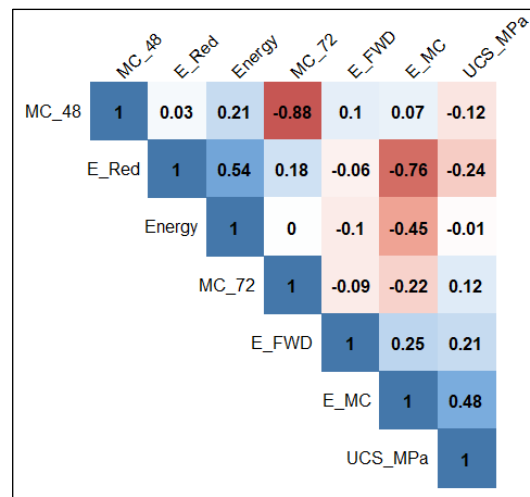
Figure 7.9: Correlation plot for FWD-backcalculated stiffnesses.

The correlation plot with all the data, including the sections without available data for stiffness after microcracking, is provided in Figure 7.10. This dataset has a lower correlation between microcracking after 48 and 72 hours, and both can be included in Equation 7.10 to fit the results using linear regression without the risk of overfitting. The R^2 of the fit was 0.23. The coefficient results are provided in Table 7.10. To determine whether any of the variables were significant, a t-test was performed with a hypothesis that $\beta_0 = ...= \beta_7 = 0$, and an alternative hypothesis that $\beta_0 ... \beta_7 \neq 0$. The t-value at a 95% confidence interval was t(0.975, 140) = 1.977. Based on the t-test results, the alternative hypothesis for β_5 can be rejected, and the remaining coefficients accepted at a 95% confidence interval. The low R^2, together with the highly significant variables, is indicative of high variances in the data, as shown by the high standard deviation results in

Table 6.2. Using fixed locations for FWD measurements regardless of the proximity of any distresses may be a reason for the weak relationships and high standard deviations.
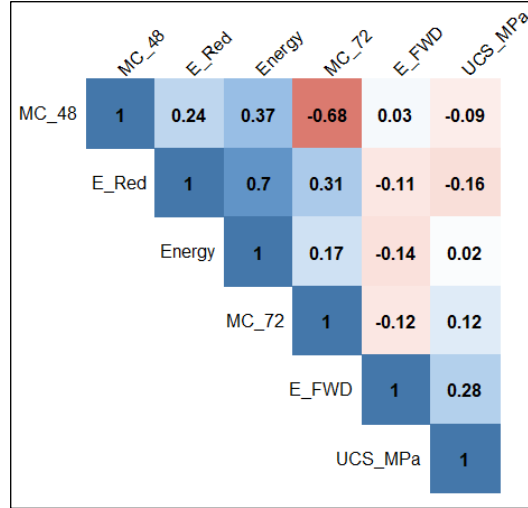
Figure 7.10: Correlation plot for FWD-backcalculated stiffnesses in all cells.

$$E_{FWD} = \beta_0 + \beta_1 \times Energy_T + \beta_2 \times UCS + \beta_3 \times MC_{48} + \beta_4 \times MC_{72} + \beta_5 \times E_{RED} + \beta_6 \times UCS \times MC_{48} + \beta_7 \times UCS \times MC_{72} \qquad \textbf{(7.10)}$$

Where: E_{FWD} = FWD-backcalculated stiffness (MPa)

UCS = 7-day unconfined compressive strength (MPa)

MC_{48} = 1 if microcracking was applied after 48 hours, else 0

MC_{72} = 1 if microcracking was applied after 72 hours, else 0

E_{RED} = Stiffness reduction during microcracking, normalized to stiffness at Pass 0 (%)

$Energy_T$ = Total energy applied during microcracking (kN/cm)

$\beta_0, \beta_1, \beta_2, \beta_3\ \beta_4, \beta_5, \beta_6, \beta_7$ = Regression coefficients

Table 7.10: Regression Coefficients for Equation 7.10

Term	Coefficient	Estimate	Std. Error	t-value	Pr(>|t|)
(Intercept)	β_0	4.382	0.828	5.293	4.54E-07
$Energy_T$	β_1	-0.105	0.040	-2.593	0.011
UCS	β_2	1.017	0.211	4.819	3.70E-06
MC_{48}	β_3	2.794	1.024	2.727	7.21E-03
MC_{72}	β_4	3.910	1.074	3.640	3.83E-04
E_{RED}	β_5	0.232	0.485	0.477	0.634
$UCS \times MC_{48}$	β_6	-0.684	0.254	-2.690	8.01E-03
$UCS \times MC_{72}$	β_7	-1.020	0.263	-3.871	1.65E-04

The results were fitted again to the revised model in Equation 7.11. The R^2 of the fit was 0.23. The coefficient results are provided in Table 7.11. The regression model results are plotted in

Figure 7.11 to illustrate the interaction effects between design strength and the time of microcracking.

$$\log(E_{FWD}) = \beta_0 + \beta_1 \times Energy_T + \beta_2 \times UCS + \beta_3 \times MC_{48} + \beta_4 \times MC_{72} + \beta_5 \times UCS \times MC_{48} + \beta_6 \times UCS \times MC_{72}$$ **(7.11)**

Table 7.11: Regression Coefficients for Equation 7.11

Term	Coefficient	Estimate	Std. Error	t-value	Pr(>|t|)
(Intercept)	β_0	4.382	0.826	5.308	4.21E-07
$Energy_T$	β_1	-0.096	0.036	-2.673	8.39E-03
UCS	β_2	1.017	1.45E-03	4.833	3.48E-06
MC_{48}	β_3	2.909	0.993	2.929	3.97E-03
MC_{72}	β_4	4.035	1.039	3.883	1.58E-04
$UCS \times MC_{48}$	β_5	-0.703	1.73E-03	-2.806	5.73E-03
$UCS \times MC_{72}$	β_6	-1.037	1.80E-03	-3.984	1.08E-04
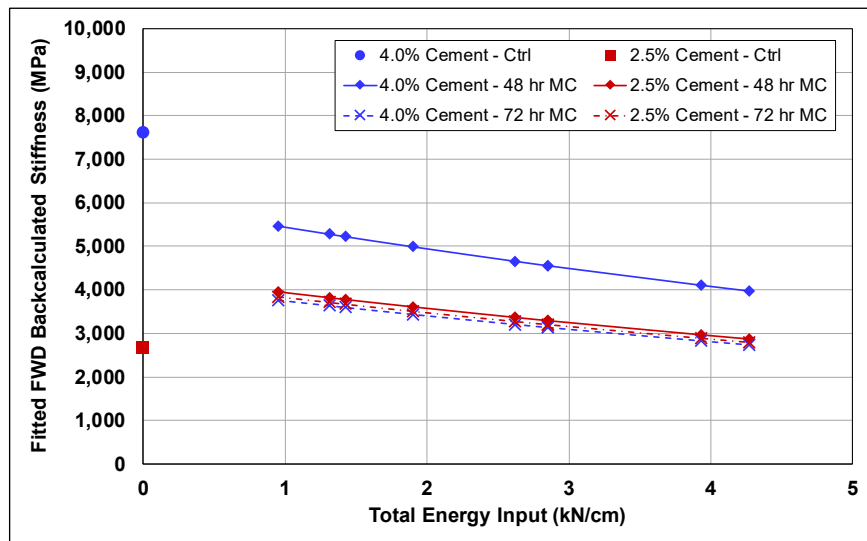
Figure 7.11: Fitted FWD-backcalculated stiffness results using Equation 7.11.

The results confirm the visual observations of the microcracking results discussed in Chapter 6 and further show the following:

- The long-term stiffness of the 4% cement-content material dropped significantly in the cells where the FDR-C layer was microcracked after 72 hours compared to stiffnesses recorded in the cells with microcracking after 48 hours.
- The 2.5% cement-content material did not show a significant difference in long-term stiffness when microcracked after 48 or 72 hours.
- Increasing the energy input reduced the stiffness.
- Low energy input during microcracking resulted in long-term stiffnesses exceeding those of the control cells for the 2.5% cement content section.

7.6.1 Discussion

The linear regression analyses of the FWD-backcalculated stiffness results indicated the following:

- Stiffness reduces with increasing energy input.
- The original stiffness prior to microcracking is mostly recovered, and often exceeded, after microcracking on FDR-C layers with strengths at the lower end of the specified range (i.e., 2.1 MPa [≈300 psi]). Stiffness is significantly reduced on higher strength layers (i.e., >3.5 MPa [≈500 psi]) after microcracking, and it may not recover to the same stiffness measured before microcracking.
- Higher-strength layers are more sensitive to the timing of microcracking. The greatest reduction in the long-term stiffness is associated with microcracking after 72 hours, with significantly lower stiffnesses measured compared to those measured when the layer is microcracked after 48 hours. The lower strength layers were not sensitive to the time of microcracking in the 48- to 72-hour time window.
- The mechanistic parameters measured during microcracking (percent stiffness reduction and stiffness after microcracking) did not provide any clear explanation for the trend in the FWD-backcalculated stiffness results. This was attributed in part to stiffness measurements being taken at the same fixed locations in each cell regardless of any surface distresses that may have influenced the results.

The results in the second and third discussion points support the conclusions that George *(3)* made regarding autogenous healing observed in the lower strength layers that were microcracked. George concluded that "… in precracked material, additionally fresh calcium hydroxide (Ca(OH)$_2$) could permeate into existing microcracks, healing the cracks by bridging crack openings. It is this additional bonding that brought about the rejuvenation of the cracked beam, resulting in stiffness attaining a level comparable to that of the control beam." The FDR-C materials studied on the FDR-C Test Road reflected this observation by George but with additional findings.

A noteworthy difference between the two mix designs studied on the FDR-C Test Road was not only the cement content, but the water to cement for cementation ratio (w/c$_c$). The w/c$_c$ for the 2.5% cement-content material was 735% greater than that of the 4% cement-content material. The additional free water in the 2.5% cement-content material provided the water necessary to mobilize the Ca(OH)$_2$ into the cracks formed during microcracking, resulting in the autogenous

healing observed in the long-term stiffness data. Increased energy input caused the microcrack width to increase, which reduced the ability of the $Ca(OH)_2$ precipitate to bridge the cracks.

The stiffness increase after microcracking in the lower-strength layer is an indication that microcracking can be beneficial in terms of the fatigue life of the material. The higher strength material, which experienced an overall reduction in stiffness after microcracking, would have a reduced fatigue life.

Blank page

8 CONCLUSIONS AND RECOMMENDATIONS

Cement-treated layers are prone to cracking. This is, and has been, a concern for using cement to improve the strength and stiffness properties of recycled materials that have limited fine materials and/or plasticity. The research discussed in this report, which aims to identify appropriate shrinkage crack mitigation procedures for recycled pavement layers treated with cement, builds on previous work on microcracking as a shrinkage crack mitigation measure by the Texas Transportation Institute and others. The process involves a combination of optimum curing times before microcracking and number of roller passes (or stiffness reduction) to minimize drying shrinkage crack width, which will maximize long-term stiffness and fatigue life.

Studies by the Texas Transportation Institute and other organizations agreed that microcracking is a potentially effective shrinkage crack mitigation study. However, gaps in the knowledge were identified, specifically a full understanding of microcracking mechanisms, influence of cement content/design strength, optimal timing of microcracking, and roller type. This study addressed these gaps primarily through continued long-term monitoring of pilot studies, the construction and monitoring of a 37-cell test road, and a comprehensive laboratory testing study.

8.1 Summary of Research

8.1.1 Literature Review

An extensive literature review was performed to develop an understanding of how cement-treated layers fail, how the fatigue life of cement-treated layers is modeled, why shrinkage cracks are a concern, and how they can be mitigated.

The following findings with regard to understanding microcracking as a shrinkage crack mitigation method for FDR-C and other cement-treated layers were made:

- The adverse effects of shrinkage cracks on the fatigue life of cement-treated layers were observed in two accelerated pavement testing studies.
- Microcracking can reduce the number of shrinkage cracks in cement-treated layers compared to no microcracking by inducing a network of fine cracks early in the life of the layer that are less likely to reflect through the asphalt concrete surfacing.

- Selecting a cement content to achieve a target seven-day unconfined compressive strength of 450 psi (≈3.1 MPa), with minimum and maximum strengths of 250 and 600 psi (≈1.7 and 4.1 MPa), will result in more frequent, but thinner, shrinkage cracks.

- No comprehensive literature available on the mechanism of microcracking in cement-treated layers in pavements was located.

- There are no established laboratory test methods to reliably induce microcracking in the laboratory or for testing the effects of microcracking.

- Mechanistic-empirical models have not been developed to account for shrinkage cracking in cement-treated layers or for the effect of microcracking on fatigue and crushing properties.

- The literature on field microcracking methods is limited. The current generally followed method for microcracking is three passes with a 12-ton roller between 48 and 72 hours after final compaction. No published information was located that details the effect of microcracking on layers with different strengths and thicknesses.

- A range of devices are available for measuring the effect of microcracking on the stiffness of FDR-C layers. Each device has limitations that have not been fully quantified in terms of its suitability for use as a microcracking quality control procedure on construction projects. There is no consensus on which instrument to use to effectively measure the effect of microcracking on the stiffness of FDR-C layers.

8.1.2   Pilot Study Testing

Long-term monitoring of select pilot studies continued throughout the project.

8.1.3   FDR-C Test Road Design

The construction of a test road to evaluate different microcracking variables was recommended after the conclusion of preliminary field studies. This allowed for the inclusion of control sections where no shrinkage crack mitigation measures were taken as well as a significantly wider factorial than could be achieved on any FDR-C field projects, which typically do not include control sections. The FDR-C Test Road design considered the various issues identified during the pilot studies, literature review, and on the foundational work done in Texas. The following factors were considered in the experiment design:

- Mix design strength (2.5% and 4% cement)
- The number of curing hours between completion of construction and start of microcracking (48, 72, and 48 and 72 hours [i.e., microcracking on the same section at two different times])
- Roller weight (12-ton single drum steel roller and 10-ton double drum steel roller)

- Roller vibration amplitude (low and high settings)
- Number of roller passes (method and performance-based specifications)
- Stiffness reduction during microcracking (measured with a soil stiffness gauge and a light weight deflectometer)
- Stiffness recovery/gain after microcracking (measured with a falling weight deflectometer)
- Crack propagation and crack properties (measured during visual assessments)

8.1.4   FDR-C Test Road Construction

The FDR-C Test Road was constructed over a two-day period (4% cement-content sections on day 1 and 2.5% cement-content sections on day 2). Construction and quality control procedures adhered to Caltrans guidance and specifications. Microcracking followed construction over a three-day period depending on the experiment factorial. A microsurfacing was applied after completion of the microcracking. All stages of construction were closely monitored, and observations and results indicated that the FDR-C Test Road was suitable for longer-term monitoring for the microcracking study.

8.1.5   FDR-C Test Road Monitoring

Monitoring of the FDR-C Test Road included regular visual assessments focusing primarily on crack monitoring, preliminary coring to check for any indication of crushing or carbonation, and falling weight deflectometer (FWD) deflection measurements, from which stiffness changes over time were backcalculated. Observations and findings include the following:

- Reflected cracks were observed in a limited number of cells on the 2.5% cement-content section. Cracks directly associated with instrumentation were not considered as cracks associated with microcracking and were therefore excluded from the analysis.
- Cracks reflected through the microsurfacing earlier on the 4% cement-content section compared to the 2.5% cement-content section.
- Crack density increased more rapidly on the 4% cement-content section compared to the 2.5% cement-content section.
- Microcracking reduced crack density compared to the results recorded on the control cells.
- Crack density generally reduced with an increase in the number of microcracking passes applied.
- The 2.5% cement-content cells had a lower crack density after 128 days than the 4% cement-content cells.

- The 2.5% cement-content cells did not show any observable trends in crack density with microcracking passes.
- Only the 4% cement-content cells microcracked after 72 hours showed a reduction in crack density with increased energy input (microcracking passes) using the single drum steel roller at high amplitude (1.42 kN/cm per pass).
- Microcracking the 4% cement-content cells after 48 hours resulted in a greater crack density reduction compared to microcracking after 72 hours. One pass after 48 hours was sufficient to reduce the crack spacing significantly. The crack density continued to reduce with increasing number of passes at 72 hours.
- The crack density results from the 10-ton double drum steel roller were inconsistent with the results from the 12-ton single steel drum roller at high amplitude. The results from the 10-ton roller showed that microcracking after 72 hours resulted in reduced cracking on both the 2.5% and 4% cement-content sections.
- Crack width was a function of microcracking effort and curing time before microcracking.
- The microcracked cells had a narrower crack-width distribution than the control cells.
- Microcracking after 48 hours resulted in narrower cracks compared to microcracking after 72 hours.
- An increase in microcracking effort (i.e., number of passes/increased energy) contributed to a further reduction in crack widths.
- The 4% cement-content control cells (i.e., no microcracking) had higher stiffnesses compared to the 2.5% cement-content control cells, as expected.
- The 2.5% cement-content cells microcracked after 48 hours had higher stiffnesses than the control cells and those cells microcracked after 72 hours.
- Increasing energy input through multiple microcracking passes reduced the long-term stiffness proportionately.

8.1.6 Monitoring Result Analysis

Statistical analyses of the FDR-C Test Road material testing, microcracking, crack monitoring, and stiffness results were undertaken to better understand and explain the observations on the road. Findings include the following:

- Crack density and spacing
  + Crack density increased with increasing design strength.
  + Increased energy input (i.e., number of roller passes) was most effective at reducing the crack density of the material with the higher design strength, while the lower design strength material did not show a sensitivity to energy input in terms of crack density reduction. The 2.5% cement-content material had on average one full-width reflective

crack in the 49-m long cell, regardless of the microcracking input, whereas the number of reflective cracks on the 4% cement-content cells reduced from approximately seven cracks down to three cracks with increased energy input during microcracking.

+ Increased energy input was the primary factor in reducing crack width.

+ The 2.5% cement-content material had significantly less shrinkage potential (remaining shrinkage to be incurred) after microcracking than the 4% cement-content material after a given curing time. Shrinkage that continued after microcracking after 48 or 72 hours did not induce a sufficient quantity of cracks to minimize widths of the reflected cracks. The cracks that developed before microcracking thus controlled the reflective cracking. Microcracking earlier after final compaction (e.g., within 24 hours) could potentially yield more fine shrinkage cracks in the FDR-C layer and further minimize crack widths to mitigate reflective cracking.

+ The 4% cement-content material had significantly more shrinkage potential remaining after microcracking than the 2.5% cement-content material. The additional increase in the number of drying shrinkage cracks that developed with increased energy input during microcracking (resulting in lower strength) reduced the total width of cracks that developed before microcracking. Microcracking was performed sufficiently early on the 4% cement-content material to change the drying shrinkage cracking from a few wide reflective cracks to numerous thinner cracks with only a small number of them wide enough to reflect through the surface layer.

+ Microcracking should ideally be performed as early as possible to benefit from the shrinkage potential after microcracking while the material strength is still low.

• Stiffness

+ The long-term stiffness of the 4% cement-content material dropped significantly in the cells where the FDR-C layer was microcracked after 72 hours compared to stiffnesses recorded in the cells with microcracking after 48 hours.

+ The 2.5% cement-content material did not show a significant difference in long-term stiffness when microcracked after 48 or 72 hours.

+ Increasing the energy input (i.e., the number of roller passes reduced the stiffness.

+ Low energy input during microcracking resulted in long-term stiffnesses exceeding those of the control cells for the 2.5% cement content section.

+ The original stiffness prior to microcracking is mostly recovered, and often exceeded, after microcracking on FDR-C layers with strengths at the lower end of the specified range (i.e., 2.1 MPa [≈300 psi]). Stiffness was significantly reduced on higher strength layers (i.e., >3.5 MPa [≈500 psi]) after microcracking, and it may not recover to the same stiffness measured before microcracking.

+ Higher-strength layers were more sensitive to the timing of the microcracking. The greatest reduction in long-term stiffness was associated with microcracking after 72 hours, with significantly lower stiffnesses measured compared to those measured when the layer was microcracked after 48 hours. The lower strength layers were not sensitive to the time of microcracking in the 48 to 72-hour time window.

+ The mechanistic parameters measured during microcracking (percent stiffness reduction and stiffness after microcracking) did not provide any clear explanation for the trend in the FWD-backcalculated stiffness results. This was attributed in part to stiffness measurements being taken at the same fixed locations in each cell regardless of any surface distresses that may have influenced the results.

8.2 Conclusions

The following conclusions were drawn on completion of this phase of the research:

- Microcracking does not prevent shrinkage cracking, but it is an effective shrinkage crack mitigation procedure. Microcracking induces a network of fine cracks, which generally do not reflect through asphalt concrete surfacings as wide shrinkage cracks tend to do.

- Microcracking has limitations and will not mitigate all shrinkage cracks on all FDR-C projects. Design strength, construction procedures, curing time before microcracking, number of microcracking passes, and stiffness reduction achieved during microcracking will all influence the level of mitigation achieved.

- The original stiffness prior to microcracking is mostly recovered, and often exceeded, after microcracking on FDR-C layers with strengths at the lower end of the specified range (i.e., 2.1 MPa [≈300 psi]). Stiffness is significantly reduced on higher strength layers (i.e., >3.5 MPa [≈500 psi]) after microcracking, and it may not recover to the same stiffness measured before microcracking.

- Higher-strength layers are more sensitive to the timing of microcracking. The greatest reduction in the long-term stiffness is associated with microcracking after 72 hours, with significantly lower stiffnesses measured than those measured when the layer is microcracked after 48 hours.

- Microcracking will be most effective if the seven-day unconfined compressive strength falls in the range of 250 to 450 psi (1.7 to 3.1 MPa) and preferably no higher than 600 psi (4.1 MPa). Layers with design strengths greater than 600 psi will likely have shrinkage cracks forming before the road can be microcracked.

- The current Caltrans method specification for microcracking could lead to significantly different stiffness reduction results as it is currently phrased, given that 12-ton rollers from different manufacturers apply different levels of energy.

- The hypothesis proposed early in the study that microcracking would increase the fatigue life of pavements with cement-treated layers, illustrated in Figure 8.1, was confirmed.
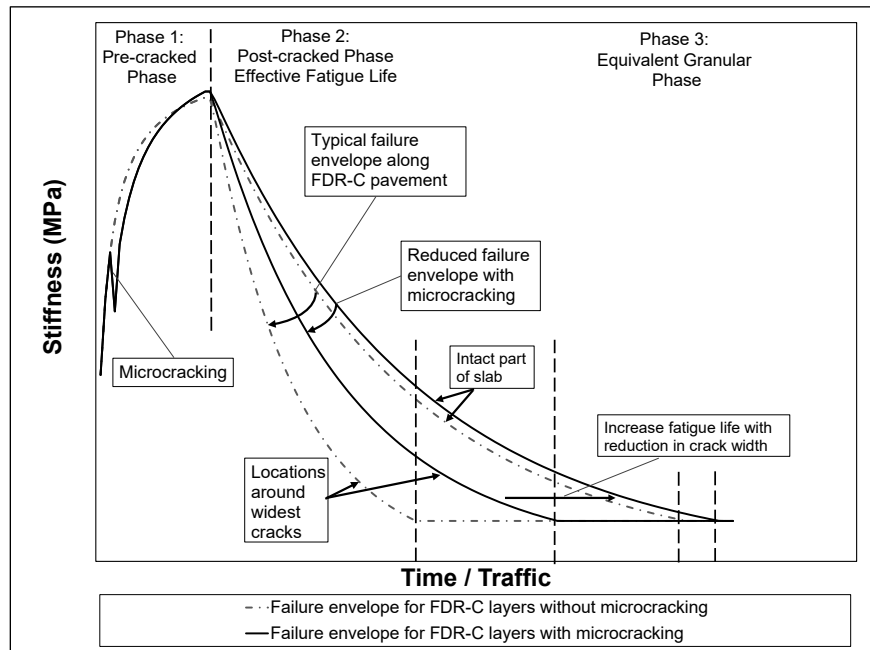
Figure 8.1: Revised theoretical structural life cycle of cement-treated pavement layers.

8.3   Recommendations

The following recommendations are made based on the work completed in this phase of the study:

- The mix design procedure for FDR-C layers should include an initial consumption of stabilizer tests to ensure an optimum cement content that will result in a durable layer is selected. Starting cement content in the mix design tests should be ICS + 1%. If this results in a seven-day unconfined compressive strength higher than 600 psi (4.1 MPa), the pavement design and or choice of stabilizer/recycling agent should be reviewed.
- Microcracking will be most effective if the seven-day unconfined compressive strength falls in the range of 250 to 450 psi (1.7 to 3.1 MPa) and preferably no higher than 600 psi (4.1 MPa).
- Microcracking should be done as close as possible to 48 hours after final compaction, especially if design strengths exceed 450 psi (3.1 MPa).
- The Caltrans method specification language for microcracking should be changed to the following (the energy requirement will encourage contractors to check the ratings of their rollers):

+ During the period from 48 to 56 hours after compaction, microcrack the surface by applying 2 to 3 single passes, equivalent to 2.8 to 4.3 kN/cm of energy, using a 12-ton vibratory steel drum roller at maximum vibration amplitude travelling from 2 to 3 mph.

- If a performance specification is considered, then a maximum stiffness reduction of 40%, measured with a soil stiffness gauge is suggested (i.e., initial measurement before the first roller pass and then measurements after each roller pass until a 40% reduction is achieved).

- The research cited in the literature review and testing in this phase of the study assessed microcracking on cement-treated layers between 10 and 12 in. (250 and 300 mm) thick. Research on layers thicker than 12 in. should continue to assess whether uniform compaction and effective microcracking can be achieved over the full depth of the layer, especially on weak subgrades, and the implications on shrinkage and fatigue cracking if it cannot.

- Although the soil stiffness gauge is considered an appropriate instrument for measuring stiffness reduction during microcracking, testing procedures will need to be refined and precision and bias statements prepared to ensure that reasonable quality control procedures are followed.

REFERENCES

1. Leoci, R. 2014. *Animal By-Products (ABPs): Origins, Uses, and European Regulations.* Mantova, Italy: Universitas Studiorum.

2. Louw, S. and Jones, D. 2015. *Pavement Recycling: Literature Review on Shrinkage Crack Mitigation in Cement-Stabilized Pavement Layers*, Technical Memorandum UCPRC-TM-2015-02, Davis and Berkeley, CA: University of California Pavement Research Center.

3. George, K.P. 2002. *Minimizing Cracking in Cement treated Materials for Improved Performance.* Skokie, IL: Portland Cement Association.

4. Adaska, W.S. and Luhr, D.R. 2004. Control of Reflective Cracking in Cement Stabilized Pavements. *Cracking in Pavements: Mitigation, Risk Assessment and Prevention.* Proceedings of the 5th International RILEM Conference. Bagneux, France: RILEM Publications.

5. Sebesta, S. 2005. *Continued Evaluation of Microcracking in Texas.* College Station, TX: Texas Transportation (Report 0-4502-2).

6. Reeder, G.D., Harrington, D.S., Ayers, M.E. and Adaska, W. 2019. *Guide to Full-Depth Reclamation (FDR) with Cement*, SR1006P, Skokie, IL: Portland Cement Association.

7. Jones, D., Louw, S. and Wu, R. 2016. *Full-Depth Recycling Study: Test Track Construction and First-Level Analysis of Phase 1 and Phase 2 HVS Testing, Forensic Investigation, and Phase 1 Laboratory Testing*, Research Report UCPRC-RR-2015-02, Davis and Berkeley, CA: University of California Pavement Research Center.

8. Jones, D., Louw, S., Buscheck, J. and Harvey, J. 2018. *Pavement Recycling: Workplan for Continued Development of Guidelines for Shrinkage Crack Mitigation in Cement treated Layers*, UCPRC-WP-2017-10.3, Davis and Berkeley, CA: University of California Pavement Research Center.

9. Louw, S., Jones, D. and Hammack, J. 2016. *Pavement Recycling: Shrinkage Crack Mitigation in Cement treated Pavement Layers — Phase 1 Laboratory Testing.* Davis and Berkeley, CA: University of California Pavement Research Center. (UCPRC-RR-2016-07).

10. Louw, S., Jones, D. Hammack, J., and Harvey, J. 2020. *Pavement Recycling: Shrinkage Crack Mitigation in Cement treated Pavement Layers — Phase 2b Laboratory Testing and*

Performance Modeling, Research Report: UCPRC-RR-2020-04, Davis and Berkeley, CA: University of California Pavement Research Center.

11. Jones, D., Louw, S. and Harvey, J. 2020. *Guide for Partial- and Full-Depth Pavement Recycling in California*, Guidleine: UCPRC-GL-2020-01, Davis and Berkeley, CA: University of California Pavement Research Center.

12. De Beer, M. 1990. *Aspects of the Design and Behaviour of Road Structures Incorporating Lightly Cementitious Layers.* Doctor of Philosophy Thesis, Pretoria, South Africa: University of Pretoria.

13. Kadar, P., Baran, E. and Gordon, R.G. 1989. *The Performance of CTB Pavements under Accelerated Loading: The Beerburrum (Queensland) ALF Trial, 1986/87*. Victoria, Australia: ARRB Group LTD.

14. Kota, P.B., Scullion, T. and Little, D.N. 1995. Investigation of Performance of Heavily Stabilized Bases in Houston, Texas, District. *Transportation Research Record: Journal of the Transportation Research Board, No. 1486*. Washington, D.C.: Transportation Research Board.

15. Little, D.N., Scullion, T., Kota, P.B.V.S. and Bhuiyan, J. 1995. *Guidelines for Mixture Design of Stabilized Bases and Subgrades. Report No. FHWA/TX-45/1287-3 F*. Texas Transportation Institute, Texas A&M University System.

16. Louw, S. 2020. *Models and Validation of Mechanisms and Mitigation of Early Age Shrinkage Cracking in Cement Stabilized Bases*. Doctor of Philosophy Dissertation. Davis, CA: University of California, Davis.

17. Yeo, R. 2012. *The Performance of Cemented Pavement Materials under Heavy Axle Loading*. Doctor of Philosophy, Monash University.

18. Fossberg, P., Mitchell, J. and Monismith, C. 1972. Load-Deformation Characteristics of a Pavement with Cement-Stabilized Base and Asphalt Concrete Surfacing. *Proceedings Third International Conference on the Structural Design of Asphalt Pavements*, London, England, (pp. 11-15).

19. Otte, E. 1977. *A Structural Design Procedure for Cement treated Layers in Pavements*. Doctor of Engineering, University of Pretoria, Pretoria, South Africa.

20. Otte, E. 1978. Analysis of a Cracked Pavement Base Layer. *Transportation Research Record: Journal of the Transportation Research Board, No. 725.* Washington, D.C.: Transportation Research Board.

21. Wen, H., Muhuntham, B., Wang, J., Li, X., Edil, T. and Tinjum, J.M. 2014. *Characterization of Cementitiously Stabilized Layers for Use in Pavement Design and Analysis.* Washington, DC: Transportation Research Board, (NCHRP Report 789).

22. Paige-Green, P. and Jones, D. 2003. *Gautrans Stabilization Manual (2nd Revision).* Pretoria, South Africa: Gauteng Department of Public Roads and Works.

23. George, K.P. 1968. Cracking in Pavements Influenced by Visoelastic Properties of Soil-Cement, *Highway Research Record,* Issue 263, (pp 49-59).

24. Freeme, C.R., Otte, E., and Mitchell, M.F. 1980. *The Economics of Pavement Type and Selection for Major Roads.* Pretoria, South Africa: Pavement Type Selection Committee, National Transport Commission.

25. Barksdale, R.D. and Todres, H.A. 1983. *A Study of Factors Affecting Crushed Stone Base Performance.* Atlanta, Georgia: Georgia Institute of Technology (Georgia Department of Transportation Project 7603).

26. Li, Y., Metcalf, J.B., and Romanoschi, S.A. 1999. "Performance and Failure Modes of Louisiana Asphalt Pavements with Soil-Cement Bases Under Full-Scale Accelerated Loading." *Transportation Research Record: Journal of the Transportation Research Board, No.1673.* Washington, D.C.: Transportation Research Board.

27. Titi, H., Rasoulian, M., Martinez, M., Becnel, B., and Keel, G. 2003. "Long-Term Performance of Stone Interlayer Pavement." *Journal of Transportation Engineering, Vol. 129, Issue 2,* (pp. 118-126).

28. Metcalf, J.B., Romanoschie, S.A. and Li, Y. 1988. *The Louisiana Accelerated Loading Facility. Report 2, Experiment 1, Phase 3.* Baton Rouge, LA: Louisiana Transportation Research Center, Louisiana Department of Transportation and Development.

29. Caltabiano, M.A. and Rawlings, R.E. 1992. Treatment of Reflection Cracks in Queensland. *In 7th International Conference on Asphalt Pavements, Vol. 4,* Nottingham, United Kingdom. (pp 1-21).

30. Lerch, W. 1957. "Plastic Shrinkage." *Journal of the American Concrete Institute,* 53 (8)*, pp 797–802.

31. Chakrabarti, S. and Kodikara, J. 2006. "Modeling Drying Shrinkage of Cement Stabilised Crushed Rock." *Construction Materials,* 159 (2), pp 67-75.

32. Dao, V.N.T., Morris, P.H. and Dux, F. 2008. "On Equations for the Total Suction and Its Matric and Osmotic Components." *Cement and Concrete Research, 38 (1)*, pp 1302-1305.

33. Liu, J., Tian, Q. and Miao, C. 2012. Investigation on the Plastic Shrinkage of Cementitious Materials Under Drying Conditions: Mechanism and Theoretical Model, *Magazine of Concrete Research, 64 (6)*, pp 551-561.

34. Holt, E.E. 2001. *Early Age Autogenous Shrinkage of Concrete*. Espoo, Finland: Technical Research Centre of Finland (VTT), Publication 446.

35. White, G.W. 2006. *Laboratory Characterization of Cementitiously Stabilized Pavement Materials*. Master's Thesis, University of New South Wales.

36. Williams, R.I.T. 1986. *Cement treated Pavement: Materials, Design and Construction.* London, England: Elsevier Applied Science Publishers.

37. Scullion, T. 2002. Field Investigation: Pre-Cracking of Soil-Cement Bases to Reduce Reflection Cracking. *Transportation Research Record: Journal of the Transportation Research Board, No. 1787.* Washington, DC: Transportation Research Board.

38. Halsted, G.E. 2010. "Minimizing Reflective Cracking in Cement-Stabilized Pavement Bases." *In Proceedings Annual Conference of the Transportation Association of Canada*, Halifax Nova Scotia.

39. Pretorius, P.C., and Monismith, C.L. 1972. "Fatigue Crack Formation and Propagation in Pavements Containing Soil-Cement Bases." *Transportation Research Record: Journal of the Transportation Research Board,* 407*.* Washington, D.C.: Transportation Research Board.

40. Atkinson, D.J. 1990. "Evaluation of Rehabilitation Measures for Cracked Cement treated Pavements". *In Proceedings 6th Road Engineering Association of Asia and Australasia (REAAA) Conference*. Kuala Lumpur, Malaysia.

41. Khazanovich, L. 2004. *Guide for Mechanistic-Empirical Design of New and Rehabilitated Pavement Structures,* NCHRP 1-37, Washington D.C.: Transportation Research Board.

42. Netterberg, F. and Paige-Green, P. 1984. *Carbonation of Lime and Cement Stabilized Layers in Road Construction*. Pretoria, South Africa: National Institute for Transport and Road Research.

43. Thompson, M.R. 1994. "High-Strength Stabilized Base Thickness Design Procedure." *Transportation Research Record: Journal of the Transportation Research Board, No. 1440*. Washington, D.C.: Transportation Research Board.

44. Theyse, H.L., De Beer, M. and Rust, F.C. 1996. Overview of the South African Mechanistic Pavement Design Analysis Method. *In Proceedings 75th Annual Transportation Research Board Meeting*, January 7 - 11, 1996, Washington, D.C.

45. Otte, E. 1972. The Stress-Strain Properties of Cement Stabilized Materials. Master of Science, University of Pretoria, Pretoria, South Africa.

46. Yeo, R. 2008. Fatigue Performance of Cemented Materials under Accelerated Loading: Influence of Vertical Loading on the Performance of Unbound and Cemented Materials. Sydney, Australia: Austroads.

47. Davidson, D.T., Pitre, G.L., Mateos, M. and George, K.P. 1962. "Moisture-Density, Moisture-Strength and Compaction Characteristics of Cement treated Soil Mixtures." *In Proceedings 41st Annual Meeting of the Highway Research Board.* Washington D.C.

48. Gonzalez, A., Howard, A. and De Carteret, R. 2010. *Cost Effective Structural Treatments for Rural Highways: Cemented Materials*. Sydney, Australia: Austroads.

49. Suman, S., Mahamaya, M. and Das, S.K. 2016. "Prediction of Maximum Dry Density and Unconfined Compressive Strength of Cement Stabilised Soil Using Artificial Intelligence Techniques." *International Journal of Geosynthetics and Ground Engineering*, 2 *(1)*, pp. 1-11.

50. Paige-Green, P. and Netterberg, F. 2004. *Cement Stabilization of Road Pavement Materials: Laboratory Testing Program Phase 1*. Contract Report: CR-2003/42, Pretoria, South Africa: Division of Roads and Transport Technology, CSIR.

51. Air Force Manual 88-6. 1982. *Soil Stabilization for Roadways and Airfields*. Department of the Air Force.

52. Lim, S. and Zollinger, D.G. 2003. "Estimation of the Compressive Strength and Modulus of Elasticity of Cement treated Aggregate Base Materials." *Transportation Research Record: Journal of the Transportation Research Board*, 1837. Washington, D.C.: Transportation Research Board.

53. Kennedy, T.W. and Hudson, W.R. 1973. *Tensile Properties of Subbases for Use in Rigid Pavement Design*. Report No. CFHR 3-8-66-98-14F. Austin, Texas: Center for Highway Research, University of Texas.

54. Gnanendran, C.T. and Piratheepan, L.J. 2009. "Determination of Fatigue Life of a Granular Base Material Lightly Stabilized with Slag Lime from Indirect Diametral Tensile Testing." *Journal of Transportation Engineering*, 136 (8), pp. 736-745.

55. Scullion, T., Sebesta, S., Estakhri, C.K., Harris, P., Shon, C.S., Harvey, O. and Rose-Harvey, K. 2012. *Full-Depth Reclamation: New Test Procedures and Recommended Updates to Specifications*. College Station, TX: Texas Transportation Institute, Texas A&M University.

56. Rashidi, M., Ashtiani, R.S., Si, J.S., Richard, P.I. and McDaniel, M. 2018. "A Practical Approach for the Estimation of Strength and Resilient Properties of Cementitious Materials." *Transportation Research Record: Journal of the Transportation Research Board,* 2672 (52), Washington, D.C.: Transportation Research Board. pp. 152-163.

57. Weissman, S.L. and Sackman, J.L. 1997. *The Mechanics of Permanent Deformation in Asphalt-Aggregate Mixtures: A Guide to Laboratory Test Selection*. Berkeley, CA: University of California, Berkeley.

58. Harvey, J., Guada, I. and Long, F. 2000. Effect of Material Properties, Specimen Geometry and Specimen Preparation Variables on Asphalt Concrete Tests for Rutting. *Asphalt Paving Technology*, 69, pp. 236-280.

59. Haas, R.C. and Topper, T. 1969. *Thermal Fracture Phenomena in Bituminous Surfaces*. Denver, CO: National Research Council: Colorado Department of Highways.

60. Hajek, J.J. and Haas, R.C. 1972. Predicting Low-Temperature Cracking Frequency of Asphalt Concrete Pavements. *In Proceedings 51st Annual Meeting of the Highway Research Board*. Washington, DC: Highway Research Board.

61. Ingles, O.G. and Metcalf, J.B. 1972. *Soil Stabilization Principals and Practice*. London, England: Butterworth and Company Publishers Ltd.

62. Bofinger, H., Hassan, H. and Williams, R.I.T. 1978. The Shrinkage of Fine-Grained Soil-Cement. *In Proceedings 1978 Australian Road Research Board Symposium*.

63. George, K.P. 1973. Mechanism of Shrinkage Cracking of Soil-Cement Bases. *In Proceedings 52nd Annual Meeting of the Highway Research Board,* 442, Washington, DC: Highway Research Board, pp 1-10.

64. Teller, L.W. and Sutherland, E.C. 1935. The Structural Design of Concrete Pavements. *Public Roads*, 16.

65. George, K.P. 1968. Cracking in Pavements Influenced by Visoelastic Properties of Soil-Cement, *Highway Research Record*, 263, pp. 49-59.

66. Zhang, J. and Li, V.C. 2001. Influence of Supporting Base Characteristics on Shrinkage-Induced Stresses in Concrete Pavements. *Journal of Transportation Engineering, Vol. 127*, Issue 6, (pp. 455-462).

67. Wang, J. 2013. *Characterization and Modeling of Shrinkage Cracking of Cementitiously Stabilized Layers in Pavement*. PhD Dissertation, Washington State University.

68. Penev, D. and Kawamura, M. 1993. Estimation of the Spacing and the Width of Cracks Caused by Shrinkage in the Cement treated Slab under Restraint. *Cement and Concrete Research*, 23, pp. 925-932.

69. Kuhlman, R.H. 1994. Cracking in Soil Cement: Cause, Effect, Control. *Journal of the American Concrete Institute*, 16 (8), pp. 56-59.

70. Sebesta, S. and Scullion, T. 2004. *Effectiveness of Minimizing Reflective Cracking in Cement treated Bases by Microcracking*, Report No. FHWA/TX-05/0-4502-1. College Station, TX: Texas Transportation Institute, Texas A&M University.

71. Shahid, M.A., and Thom, N.H. 1996. Performance of Cement–Bound Bases with Controlled Cracking. *In Proceedings 3rd International RILEM Conference on Reflective Cracking in Pavement*, Maastricht, Netherlands.

72. California Department of Transportation. 2013. *Maintenance Technical Advisory Guide Volume 1 - Flexible Pavement Preservation*, 2nd Edition. Sacramento, CA: California Department of Transportation. www.dot.ca.gov/hq/maint/Pavement/Offices/Pavement_Engineering/PDF/FDR_C_Design_Guide_April_2013.pdf.

73. Luhr, D.R., Adaska, W.S. and Halsted, G.E. 2008. *Guide to Full-Depth Reclamation (FDR) with Cement*. Skokie, IL: Portland Cement Association.

74. Hall, J.W. 2005. *Stabilized and Drainable Base for Rigid Pavement: A Design and Construction Guide*, Report No. IPRF-01-G-002-021(G). Champagne, IL: Applied Research Associates.

75. Reeder, G.D., Harrington, D., Ayers, M.E. and Adaska, W.S. 2017. *Guide to Full-Depth Reclamation (FDR) with Cement*. Ames, IA: National Concrete Pavement Technology Center, Iowa State University.

76. Bang, S., Lein, W., Comes, B., Nehl, L., Anderson, J., Kraft, P., deStigter, M., Leibrock, C., Roberts, L., Sebaaly, P. and Johnston, D. 2011. *Quality Base Material Produced Using Full Depth Reclamation on Existing Asphalt Pavement Structure–Task 4: Development of FDR Mix Design Guide*, FHWA-HIF-12-015, Washington, DC: Federal Highway Administration.

77. California Department of Transportation. 2019. *Construction Manual*. Sacramento, CA: California Department of Transportation.
www.dot.ca.gov/-/media/dot-media/programs/construction/documents/policies-procedures-publications/construction-manual/sec4-27.pdf.

78. Thompson, M.R. and Dempsey, B.J. 1984. *Development of a Preliminary ALRS Stabilization Material Pavement Analysis System (SPAS)*, ESL-TR-83-84, Tyndall AFB, Florida: US Air Force Engineering and Services Center.

79. Thompson, M.R. 1988. *A Proposed Thickness Design Procedure for High Strength Stabilized Base (HSSB) Pavements*, Transportation Engineering Series 48, Illinois Cooperative and Highway Research Program, Urbana-Champaign, IL: University of Illinois.

80. Litzka, J. and Haslehner, W. 1995. Cold In-Place Recycling on Low-Volume Roads in Austria. *In Proceedings 6th Transportation Research Board International Conference on Low Volume Roads*. Minneapolis, MN.

81. Brandl, H., Barends, F.B.J., Lindenberg, J., Luger, H.J., de Quelerij, L. and Verruit, V. 1999. Mixed in Place Stabilization of Pavement Structures with Cement and Additives. *In Proceedings 12th European Conference on Soil Mechanics and Geotechnical Engineering*. Amsterdam, Netherlands: Balkema.

82. Scullion, T. 2014. *Personal Communication*. College Station, TX: Texas Transportation Institute, Texas A&M University.

83. Sebesta, S. 2005a. *Continued Evaluation of Microcracking in Texas*. Report 0-4502-2. College Station, TX: Texas Transportation.

84. George, K.P. 2006. *Soil Stabilization Field Trial*, Jackson, MS: University of Mississippi.

85. Alabaster, D., Patrick, J., Arampamoorthya, H. and Gonzalez, A. 2013. *The Design of Stabilised Pavements in New Zealand*, Research Report No. 498, Auckland, New Zealand: New Zealand Transport Agency.

86. Teng, T.C.P. and Fulton, J.P. 1974. Field Evaluation Program of Cement treated Bases. *In Proceedings 53rd Annual Meeting of the Highway Research Board*, Washington, DC: Highway Research Board.

87. Miller, H.J., Guthrie, W.S., Crane, R.A. and Smith, B. 2012. *Evaluation of Cement-Stabilized Full-Depth Recycled Base Materials for Frost and Early Traffic Conditions*, Dartmouth, MA: University of Massachusetts Dartmouth.

88. Yamanouchi, T. and Ihido, M. 1963. Laboratory and In-Situ Experiments on the Problem of Immediate Opening of Soil-Cement Base to General Traffic. *In Proceedings of 4th Australia-New Zealand Conference*.

89. Syed, I.M. and Scullion, T. 1998. *In-Place Engineering Properties of Recycled and Stabilized Pavement Layers*, Report No. TX-00/3903-S. College Station, TX: Texas Transportation Institute, Texas A&M University.

90. Syed, I.M. 2007. *Full-Depth Reclamation with Portland Cement: A Study of Long-Term Performance*. Skokie, IL: Portland Cement Association.

91. Steyn, W. and Jones, D. 2006. *Heavy Vehicle Simulator Testing of N12-19 East, Section 2*, Contract Report CSIR/BE/IE/ER/2007/0001/B, Pretoria, South Africa: Council for Scientific and Industrial Research.

92. Jones, D., Fu, P., Harvey, J. and Halles, F. 2008. *Full-Depth Pavement Reclamation with Foamed Asphalt: Final Report*, Research Report UCPRC-RR-2008, Davis and Berkeley, CA: University of California Pavement Research Center.

93. Guthrie, W.S., Young, T.B., Blankenagel, B.J. and Cooley, D.A. 2005. Early-age Strength Assessment of Cement treated Base Material. *Transportation Research Record: Journal of the Transportation Research Board*, 1936. Washington, D.C.: Transportation Research Board.

94. Hope, C.A. 2011. *Evaluation of Portable Devices for Monitoring Microcracking of Cement treated Base Layers.* Masters in Science, Brigham Young University.

95. Humboldt Manufacturing Company. 2002. *User Guide: Model H-4140 Soil Stiffness and Modulus Gauge*. Norridge, Il: Humboldt Manufacturing Company.

96. Terzaghi, K., Peck, R.B. and Mesri, G. 1995, *Soil Mechanics in Engineering Practice*. 3rd Edition, John Wiley & Sons.

97. Scullion, T., Guthrie, S. and Sebesta, S. 2003. *Field Performance and Design Recommendations for Full-depth Recycling in Texas*, Report No. FHWA/TX-03/4182-1, College Station, TX: Texas Transportation Institute, Texas A&M University.

98. Chen, D.H. 2007. Field and Lab Investigations of Prematurely Cracking Pavements. *Journal of Performance of Constructed Facilities*, 21 (4), pp. 293-301.

99. Fu, P. 2009. *Micromechanics for Foamed Asphalt Stabilized Materials*, Doctor of Philosophy Dissertation, University of California, Davis.

100. Puppala, A.J., Hoyos, L.R. and Potturi, A.K. 2011. Resilient Moduli Response of Moderately Cement treated Reclaimed Asphalt Pavement Aggregates, *Journal of Materials in Civil Engineering*, 23 (7), pp. 990-998.

101. Potturi, A.K. 2006. *Evaluation of Resilient Modulus of Cement and Cement-Fiber Treated Reclaimed Asphalt Pavement (RAP) Aggregates using Repeated Load Triaxial Test*. Master of Science in Civil Engineering, University of Texas at Arlington.

102. Arnold, G. 2009. Reducing the Risk of Pavement Failure and Utilisation of Local Materials in New Zealand through Repeated Load Triaxial and Beam Fatigue Tests. *In Proceedings 13th International Flexible Pavements Conference*, Vol. 12. Surfers Paradise, Australia.

103. Gonzalez, A.A. 2009. *An Experimental Study of the Deformational and Performance Characteristics of Foamed Bitumen Stabilised Pavements*. Doctor of Philosophy Thesis, University of Canterbury.

104. Arnold, G., Werkmeister, S. and Morkel, C. 2010. *Development of a Basecourse/Sub-Base Design Criterion*. Research Report No. 498. Auckland, New Zealand: New Zealand Transport Agency.

105. Gnanendran, C.T. and Woodburn, L.J. 2003. Recycled Aggregate for Pavement Construction and the Influence of Stabilisation. *In Proceedings of the 21st ARRB and 11th REAAA Conference*. Victoria, Australia: Australian Road Research Board.

106. Arulrajah, A., Disfani, M.M., Haghighi, H., Mohammadinia, A. and Horpibulsuk, S. 2015. *Modulus of Rupture Evaluation of Cement Stabilized Recycled Glass/Recycled Concrete Aggregate Blends. Construction and Building Materials*, 84, pp.146-155.

107. Olson, R.E. and Jiunnren, L. 2004. *Apparatus Details for Triaxial Testing*. Taichung City, Taiwan: Chaoyang University of Technology.

108. Taylor, D.W. 1940. *Soil Mechanics Research Program on Cylindrical Compression Testing in Cooperation with US Engineering Department*. Cambridge, MA: Massachusetts Institute of Technology.

109. Shockley, W.G. and Ahlvin, R.G. 1960. *Nonuniform Conditions in Triaxial Test Specimens. In Proceedings ASCE Research Conference on Shear Strength of Cohesive Soils*, pp. 341-357.

110. Peng, S.D. 1971. Stresses Within Elastic Circular Cylinders Loaded Uniaxially and Triaxially. *International Journal of Rock Mechanics and Mining Sciences and Geomechanics Abstracts*, 8 (5), pp. 399-432.

111. Brown, E.T. 1981. *Rock Characterization, Testing and Monitoring: ISRM Suggested Methods*. Oxford, United Kingdom: Pergamon Press.

112. Chiu, H.K., Johnston, I.W. and Donald, I.B. 1983. Appropriate Techniques for Triaxial Testing of Saturated Soft Rock. *International Journal of Rock Mechanics and Mining Sciences and Geomechanics Abstracts*, 20 (3), pp. 107-120.

113. Burland, J.B., and Symes, M.J.P.R. 1982. A Simple Axial Displacement Gauge for use in the Triaxial Apparatus. *Geotechnique*, 32 (1).

114. Transportation Research Board. 1976. *State of the Art: Lime Stabilization, Reactions, Properties, Design, Construction*. Transportation Research Circular, 180, Washington, D.C.: Transportation Research Board.

115. Hillbrich, S.L. and Scullion, T. 2007. Rapid Alternative for Laboratory Determination of Resilient Modulus Input Values on Stabilized Materials for AASHTO Mechanistic-Empirical Design Guide. *Transportation Research Record: Journal of the Transportation Research Board*, 2026, Washington, D.C.: Transportation Research Board, pp 63-69.

116. Araya, A.A., Molenaar, A. and Houben, L. 2010. Characterization of Unbound Granular Materials Using Repeated Load CBR and Triaxial Testing. *In Proceedings GeoShanghai International Conference*. Shanghai, China.

117. Louw, S.J.H. 2014. *Characterizing Cement Stabilized Base Material Containing Reclaimed Asphalt Pavement*. Masters in Science, University of California, Davis.

118. Groeger, J.L., Rada, G.R., and Lopez, A. 2003. *AASHTO T 307 — Background and Discussion. Resilient Modulus Testing for Pavement Components*, STP1437-EB, Durham, G., DeGroff, W., and Marr, W., Ed., West Conshohocken, PA: ASTM International pp. 16-29.

119. Lovelady, P.L. and Picornell, M. 1990. Sample Coupling in Resonant Column Testing of Cemented Soils. *Dynamic Elastic Modulus Measurements in Materials*. West Conshohocken, PA: ASTM International.

120. Richart, F.E., Brandtzaeg, A. and Brown, R.L. 1928. *A Study of the Failure of Concrete under Combined Compressive Stresses*. Urbana-Champaign: Il: University of Illinois.

121. Vinson, T., Wilson, C. and Bolander, P. 1983. Dynamic Properties of Naturally Frozen Silt. *In Proceedings of 4th International Conference on Permafrost*. Washington D.C.: National Academy Press, pp.469-481.

122. Capdevila, J.A. and Rinaldi, V.A. 2015. Stress-Strain Behavior of a Heterogeneous and Lightly Cemented Soil under Triaxial Compression Test. *Journal of Geotechnical Engineering*, 20 (591), pp. 6745-6760.

123. Cho, G.C. and Santamarina, J.C. 2001. Unsaturated Particulate Materials—Particle-Level Studies. *Journal of Geotechnical and Geoenvironmental Engineering*, 127 (1), pp. 84-96.

124. Fernandez, A.L. and Santamarina, J.C. 2001. Effect of Cementation on the Small-Strain Parameters of Sands. *Canadian Geotechnical Journal*, 28 (38), pp. 191-199.

125. Paul, D.K. and Gnanendran, C.T. 2015. Characterization of Lightly Stabilized Granular Base Materials Using Monotonic and Cyclic Load Flexural Testing. *Journal of Materials in Civil Engineering*, 28 (1).

126. Long, F.M. and Ventura, D.F.C. 2003. Laboratory Testing for the Heavy Vehicle Simulator Sections on the N7 (TR11/1). Contract Report CR-2003/56, Pretoria, South Africa: Council for Scientific and Industrial Research.

127. Mehta, P.K. 1986. *Concrete. Structure, Properties and Materials*. Englewood Cliffs, NJ: Prentice-Hall, Inc.

128. Ballantine, R.W. and Rossouw, A.J. 1989. *Stabilization of Soils*. Johannesburg, South Africa: PPC Lime.

129. Pinard, M.I. and Jackalas, P. 1987. Durability Aspects of Chemically Stabilized Weathered Basaltic Materials for Low Volume Road Base Construction. *Transportation Research Record: Journal of the Transportation Research Board*, 1106, Washington, D.C.: Transportation Research Board, pp 89-102.

130. Paige-Green, P., Netterberg, F. and Sampson, L.R. 1990. *The Carbonation of Chemically Stabilised Road Construction Materials: Guide to its Identification and Treatment*. Pretoria, South Africa: Transportek, Council for Scientific and Industrial Research.

131. Netterberg, F. and De Beer, M. 2012. Weak Interlayers in Flexible and Semi-Flexible Road Pavements: Part 1. *Journal of the South African Institution of Civil Engineers*, 54 (1), pp. 31-42.

132. Paige-Green, P. 1991. The Long-Term Durability of Lime-Treated Soils. *Geotechnics in the African Environment*. Rotterdam, Netherlands:Baikema, pp 193-196.

133. Blechman, I. 1995. Microcracking in Concrete under Compression: Its Gradient Mechanisms and Reflection in Macro. *In Proceedings 2nd Fracture Mechanics of Concrete Structures*, pp. 445-460.

134. Berg, O.Y. 1950. The Problem of the Strength and Plasticity of Concrete. *Doklady Akad. Nauk, SSSR*, 70, pp. 617-620.

135. Berg, O.F. 1961. The Physical Principals of the Theory of Strength of Concrete and Reinforced Concrete. *Gosstroiizdat*, Moscow, Russia.

136. Floyd, O.S., Nilson, A.H. and Martinez, S. 1986. Mechanical Properties of High-Strength Lightweight Concrete. *Journal of the American Concrete Institute*, 83 (4), pp. 606-613.

137. Hsu, T.T., Slate, F.O., Sturman, G.M. and Winter, G. 1963. Microcracking of Plain Concrete and the Shape of the Stress-Strain Curve. *Journal of the American Concrete Institute*, 60 (2), pp. 209-224.

138. Blechman, I. 1992. Differential Equation of Concrete Behaviour under Uniaxial Short-Term Compression in Terms of Atrophy (Degeneration) and its Solution. *Magazine of Concrete Research*, 44 (159), pp. 107-115.

139. Thomas, T.C. 1963. Mathematical Analysis of Shrinkage Stresses in a Model of Hardened Concrete. *Journal of the American Concrete Institute*, 60 (3), pp. 371-390.

140. Abou-Zeid, M., Fowler, D.W., Nawy, E.G., Allen, J.H., Halvorsen, G.T., Poston, R.W., Barlow, J.P., Hansen, W., Rhoads, R.J. and Brander, M.E. 2001. *Control of Cracking in Concrete Structures*. Report No. 224, Farmington Hills, MI: American Concrete Institute Committee, pp. 12-16.

141. Spooner, D.C., Pomeroy, C.D. and Dougill, J.W. 1976. Damage and Energy Dissipation in Cement Pastes in Compression. *Magazine of Concrete Research*, 28 (94), pp. 21-29.

142. Yoshimoto, A., Kawasaki, K. and Kawakami, M. 1976. Microscopic Cracks in Cement Matrix and Deformation Behaviour of Concrete. *In Proceedings of 19th Japan Congress on Materials Research*, Kyotop, Japan, pp. 126-131.

143. Attiogbe, E.K. and Darwin, D. 1988. Strain Due to Submicrocracking in Cement Paste and Mortar. *Materials Journal*, 85, pp. 3-11.

144. Suits, L.D. and Sprinkle, M.M. 2006. Control of Cracking in Concrete: State of the Art. *Transportation Research Circular, No. E-C107*. Washington, D.C.: Transportation Research Board.

145. Ter Heide, N. 2005. *Crack Healing in Hydrating Concrete*. Masters of Science, Delft University of Technology, Delft, Netherlands.

146. Yang, Y., Yang, E.H. and Li, V.C. 2011. Autogenous Healing of Engineered Cementitious Composites at Early Age. *Cement and Concrete Research*, 41 (2), pp.176-183.

147. Neville, A. 2002. Autogenous Healing—A Concrete Miracle? *Concrete International*, 24, pp. 76-82.

148. Van Tittelboom, K. and De Belie, N. 2013. Self-Healing in Cementitious Materials—A Review. *Materials*, 6, pp. 2182-2217.

149. Clear, C.A. 1985. The Effects of Autogenous Healing Upon the Leakage of Water through Cracks in Concrete. *Cement and Concrete Association*, Wexham Spring, England.

150. Kermani, A. 1991. Permeability of Stressed Concrete: Steady-State Method of Measuring Permeability of Hardened Concrete Studies in Relation to the Change in Structure of Concrete under Various Short-Term Stress Levels. *Building Research and Information*, 19 (6), pp.360-366.

151. Hearn, N. 1999. Effect of Shrinkage and Load-Induced Cracking on Water Permeability of Concrete. *Materials Journal*, 96 (2), pp.234-241.

152. Banthia, N., Biparva, A. and Mindess, S. 2005. Permeability of Concrete under Stress. *Cement and Concrete Research*, 35 (9), pp.1651-1655.

153. Rinehart, R. and Mooney, M. 2009. Measurement Depth of Vibratory Roller-Measured Soil Stiffness. *Géotechnique, Vol. 59*, (pp. 609-619).

154. Guthrie, W.S. and Scullion, T. 2003. *Interlaboratory Study of the Tube Suction Test.* College Station, TX: Texas Transportation Institute, Texas A & M University System, (Report No. FHWA/TX-03/0-4114-2).

155. Guthrie, W.S., Sebesta, S. and Scullion, T. 2002. *Selecting Optimum Cement Contents for Stabilizing Aggregate Base Materials*. College Station, TX: Texas Transportation Institute, Texas A & M University System, (Report No. FHWA/TX-05/7-4920-2).

156. Troxler Electronic Laboratories. 2001. *A Report Addressing the Use of the Moisture Correction when Using any Nuclear Moisture Gauge, Focusing on the 3411B, and the Importance of the Application of Necessary Moisture Correction Factors to Field Compaction Tests made with Nuclear Moisture Gauges*. Research Triangle Park, NC: Troxler Electronic Laboratories.

157. Feldman, D., Pyle, T. and Lee, J. 2019. *Automated Pavement Condition Survey Manual*. Sacramento, CA: California Department of Transportation.

Blank page

APPENDIX°A: TEXAS TRANSPORTATION INSTITUTE MICROCRACKING RESEARCH

A.1 City of College Station (Edelweiss)

The Edelweiss project consisted of four test sections (one control and three microcracked) constructed in the summer of 2000 *(1)*. The pavement structures were comprised of 6 in. (≈150 mm) of lime-treated subgrade, 6 in. (≈150 mm) of cement-treated base (CTB), and a 2 in. (≈50 mm) hot mix asphalt (HMA) surfacing. The base design was based on a seven-day unconfined compressive strength (UCS) of 500 psi (≈3.5 MPa), which required a cement content of 7% by mass of the dry aggregate.

Microcracking was performed after 24 hours on two of the sections and after 48 hours on the third using a 12-ton steel drum roller set at maximum vibration amplitude and moving at 2 mph (≈3.2 km/h, i.e., walking pace). A web of surface cracks was observed in some areas of the layer after microcracking. The effect of the microcracking on base stiffness was measured with a soil stiffness gauge (SSG) and a falling weight deflectometer (FWD) before starting microcracking, after two roller passes, and after four roller passes. A second round of FWD measurements was taken approximately six months after construction. The results are summarized in Table A.1.

Table A.1: College Station Project: Stiffness Measurements

Time	Number of Roller Passes	FWD		Stiffness Gauge	
		Stiffness (GPa)	Stiffness Change (% of original)	Stiffness (MN/m)[1]	Stiffness Change (% of original)
Construction	0	8.1	0	55.4	0
	2	2.1	75% reduction	38.0	31% reduction
	4	1.2	85% reduction	29.5	47% reduction
+ 48 hours[2]	N/A	Not measured		41.2	26% reduction
+ 6 months[3]	N/A	12	48% increase	Not measured	
[1] MN/m = meganewtons per meter		[2] 48 hours after microcracking		[3] Approximately 6 months after microcracking	

The FWD measurements show that the first two roller passes caused a significant (75%) reduction in stiffness, while the third and fourth roller passes resulted in only a small (additional 10%) reduction. The stiffness gauge results differed from those of the FWD and did not follow the same trend in stiffness reduction after two and four roller passes. It is not clear whether the impact of the falling weight caused an additional reduction in stiffness in the drop zone. Both the FWD and the stiffness gauge results show that the drop in stiffness after microcracking was temporary and

that stiffness had recovered to that of the control section, which was not microcracked, during the six-month interval between evaluations. Transverse cracks were noted on all sections after six months. Crack lengths were between 2.4 and 5.6 ft. per 100 ft. (≈0.5 and 1.2 m per 100 m) of pavement on the three microcracked sections, and 27.3 ft. per 100 ft. (≈5.8 m per 100 m) of pavement on the control section. The TxDOT researchers concluded that microcracking did not adversely affect the load bearing capacity of the bases and appeared to significantly reduce shrinkage cracking in the first six months after construction. Further monitoring was recommended to assess longer-term performance over a number of seasonal wetting and drying cycles.

A.2   Bryan District (Road SH47)

Road SH47 was rehabilitated in 2002 using a full-depth reclamation process *(2)*. The road was pulverized to a depth of 14 in. (≈350 mm) after which 3% cement was mixed in and then compacted. The laboratory mix design indicated a seven-day UCS of 384 psi (2.6 MPa). The road was divided into 12 sections, based on the day of construction. The CTB was microcracked with a 25-ton roller 24 hours (eight sections of the project), 48 hours (three sections), and 72 hours (one section) after compaction. Three full passes were applied. A 4 in. HMA overlay was placed on the CTB as a surfacing 72 hours after microcracking of the last section. The effect of microcracking on stiffness was monitored with an FWD on five of the sections (three of the 24-hour sections and two of the 48-hour sections). Average stiffness reduction after microcracking was 60% of the stiffness measured before microcracking, with no significant differences noted for the different microcracking intervals. FWD measurements were repeated after 12 months and stiffnesses were approximately double the stiffness measured prior to microcracking. No cracking was observed at this time. A statistical analysis indicated that the time interval between compaction and microcracking (i.e., between 24 and 48 hours) did not influence the stiffnesses measured after 12 months.

A visual evaluation in 2004 (i.e., 24 months after construction) revealed two transverse cracks on one of the sections. No cracks were observed on the remainder of the project. A follow up evaluation in 2005 found that additional cracking had occurred on the original section with cracks

and that new cracks had formed on four additional sections, all of which had been microcracked after 24 hours. Crack lengths on each section varied between 16 and 1,404 ft. (≈5 m and 428 m). Some of the cracks were attributed to construction problems (e.g., longitudinal joints) and not to shrinkage in the cement-treated layer. The change in stiffness before and after microcracking was not measured on the section with the most cracks, and consequently it was not possible to determine whether the additional cracking on this section could have been attributed to inadequate microcracking. The researchers concluded that measurements of stiffness reduction with an FWD, light weight deflectometer, or stiffness gauge should be a specified project requirement to ensure that adequate and consistent stiffness reduction is achieved during microcracking.

A.3 San Antonio District (Road SH16)

Road SH16 was rehabilitated in 2003 using a full-depth reclamation process *(2)*. The existing road was pulverized to a depth of 8 in. (≈200 mm), treated with 3% cement, and compacted to form a subbase. A new 5 in.-thick base was imported and treated with 2% cement. The road was divided into four sections, based on the day of construction. Section 1 was not microcracked and served as a control, Section 2 was microcracked with a 12-ton roller 24 hours after compaction, and Section 3 and Section 4 were microcracked with three and two passes, respectively, with the same roller 48 hours after compaction. Maximum vibration amplitude was used on all sections. The effect of microcracking on stiffness was monitored with an FWD. Stiffness reductions of 42%, 73%, and 46% were recorded on Sections 2, 3 and 4, respectively (Table A.2).

Table A.2: San Antonio District Project: Stiffness Measurements

Section	MC[1] Process (hours/passes)	Stiffness (ksi [GPa])			% Change of Original	
		Initial	After MC[1]	+ 3 months	After MC	+ 3 months
1	0/0	100 (0.7)	N/A	340 (2.3)	N/A	240% increase
2	24/3	120 (0.8)	70 (0.5)	410 (2.8)	42% reduction	242% increase
3	48/3	390 (2.7)	105 (0.7)	435 (3.0)	73% reduction	12% increase
4	48/2	250 (1.7)	135 (0.9)	255 (1.8)	46% reduction	2% increase
[1] MC = Microcracking						

A surface treatment (chip seal) was applied as an initial wearing course, followed by 2 in. of HMA. The sections were retested with an FWD after three months (Table A.3 and Figure A.1). The reason for the limited stiffness increase on Section 4 could not be explained. No cracks were

observed. A second visual assessment of the project was conducted after 13 months. All of the sections had cracks, with crack length on Section 2 slightly less than that on the other sections (77 ft. [≈23.5 m] compared to 90, 94, and 95 ft. [≈27.4, 28.7, and 30.0 m] on Sections 1, 3 and 4, respectively).
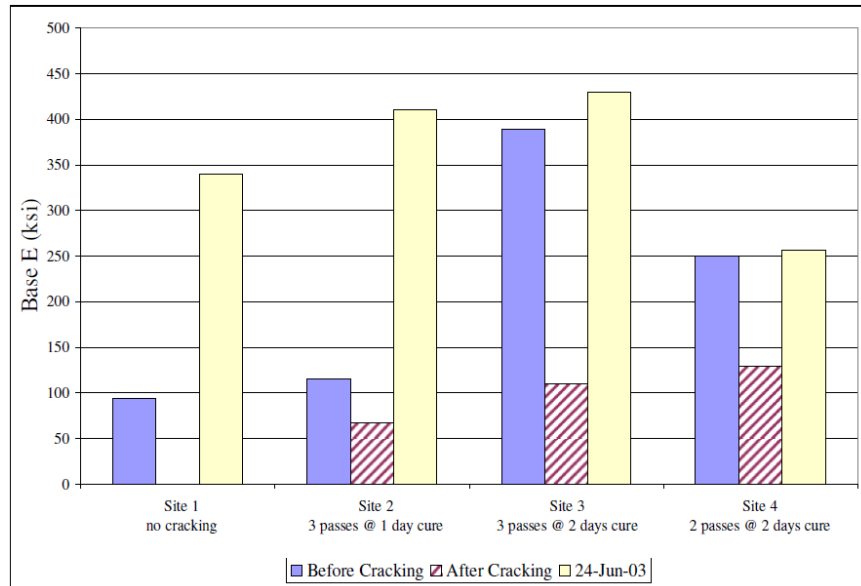
Figure A.1: San Antonio District Project: Average modulus results *(2)*.

A.4 Texas A&M Riverside Campus

This project was constructed at the Texas A&M Riverside campus in September 2003 to facilitate monitoring of microcracked pavements under controlled conditions *(2)*. Two roads (Avenue C and Avenue D) were selected for the project. The existing material was pulverized and compacted to form a 6 in. (≈150 mm) subbase. New aggregate base was placed on the subbase, treated with cement, and then compacted. Avenue C was constructed with a cement content of 8% and Avenue D with 4%. The roads were not surfaced for the duration of the study to allow researchers to monitor the cracking behavior. Each road was divided into six sections with a different crack mitigation treatment, as follows:

- No moist curing, no microcracking (control)
- Moist cure on Day 0, no microcracking, prime coat curing membrane on Day 1
- Moist cure on Days 0 through 3, microcrack on Day 1
- Moist cure on Days 0 through 3, microcrack on Day 2
- Moist cure on Days 0 through 3, microcrack on Day 3

- Moist cure on Days 0 through 3, no microcracking

Stiffness on the sections was measured with an FWD after microcracking and again after 10 and 21 months. Crack lengths were measured after 21 months. The results are summarized in Table A.3 and Table A.4 and in Figure A.2 and Figure A.3.

Table A.3: Texas A&M Riverside Project: Stiffness Measurements

Cement Content (%)	Treatment	Stiffness Before Microcracking (ksi) (GPa)		Stiffness After Microcracking (ksi) (GPa)		Stiffness After 10 Months (ksi) (GPa)		Stiffness After 21 Months (ksi) (GPa)	
4	Dry cure, no MC[1]	911	(6.3)	N/A		1,030	(7.2)	681	(4.8)
	Prime Coat Day 1	1,006	(6.9)	N/A		1,200	(8.4)	1,035	(7.2)
	MC Day 1	525	(3.6)	253	(1.7)	1,960	(13.7)	1,175	(8.2)
	MC Day 2	900	(6.2)	262	(1.8)	2,170	(15.2)	1,161	(8.1)
	MC Day 3	860	(5.9)	348	(2.4)	2,495	(17.5)	1,089	(7.6)
	Moist cure, no MC	924	(6.4)	N/A		2,000	(14.0)	1,582	(11.1)
8	Dry cure, no MC	802	(5.5)	N/A		2,300	(16.1)	1,746	(12.2)
	Prime Coat Day 1	1,692	(11.7)	N/A		1,200	(8.4)	1,178	(8.3)
	MC Day 1	1,650	(11.4)	507	(3.5)	4,050	(28.4)	2,401	(16.8)
	MC Day 2	1,450	(5.9)	485	(3.3)	2,500	(17.5)	2,093	(14.7)
	MC Day 3	2,120	(14.7)	890	(6.1)	2,800	(19.6)	1,651	(11.6)
	Moist cure, no MC	2,824	(19.5)	N/A		1,400	(9.8)	1,597	(11.2)

[1] MC = Microcracking

Table A.4: Texas A&M Riverside Project: Crack Measurements

Treatment	4% Cement		8% Cement	
	Crack Length			
	(ft.)	(m)	(ft.)	(m.)
Dry cure, no MC[1]	89	27	277	84
Prime Coat Day 1	78	24	328	100
MC Day 1	76	23	92	28
MC Day 2	34	10	105	32
MC Day 3	81	25	88	27
Moist cure, no MC	50	15	70	21

[1] MC = Microcracking

A.5   IH 45 Frontage Road

This project was constructed in Huntsville, Texas, on the IH 45 frontage road *(2)*. Construction took place in December 2004 and May 2005. The design consisted of 10 in. (≈250 mm) of lime-treated subgrade, 12 in. (≈300 mm) of pug mill-mixed CTB, and 5 in. (≈125 mm) of HMA. Seven-day UCS strengths and tube suction dielectric values were assessed for a range of cement contents between 2% and 8%. A cement content of 4% was selected, giving a UCS of 1,137 psi (≈7.8 MPa) and dielectric value of 7.3. Although the strength was significantly higher than the

300 psi (≈2.1 MPa) typically targeted by TxDOT, the decision to go with the higher cement content was based on the dielectric value *(2)*.
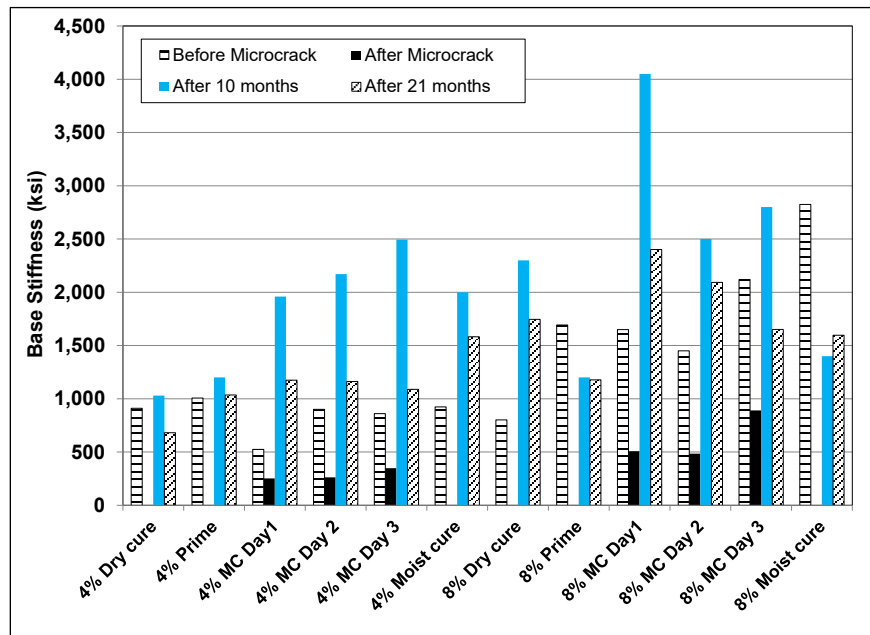
Figure A.2: Texas A&M Riverside Project: Stiffness measurements.
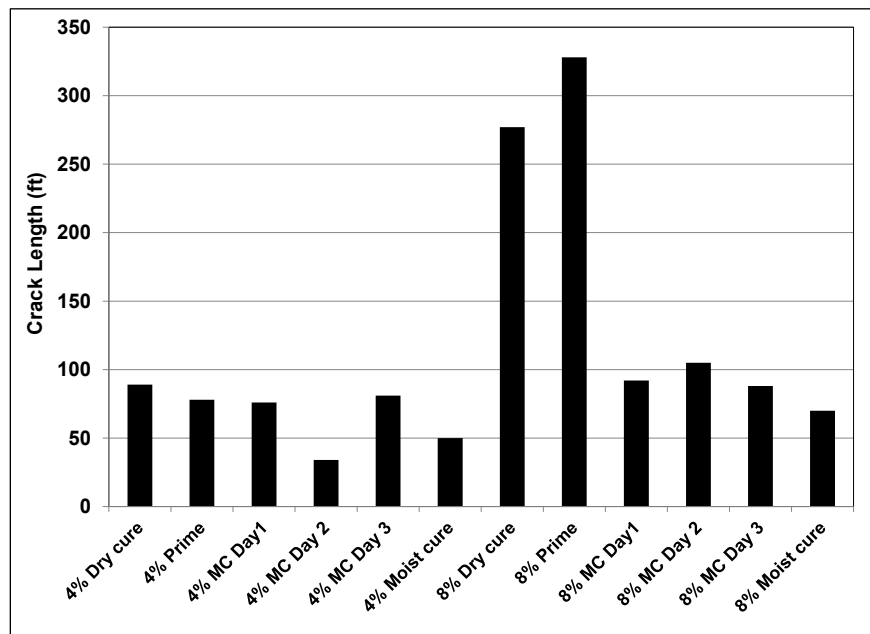
Figure A.3: Texas A&M Riverside Project: Crack length.

All cement-treated sections were microcracked with the exception of a 200 ft. (≈60 m) control section. The sections constructed in December 2004 were microcracked after four days due to the slow strength gain attributed to the cold weather. The sections constructed in May 2005 were

microcracked after two days. A light weight deflectometer (LWD) was used to measure any change in stiffness. On the December 2004 construction sections, average stiffnesses before microcracking ranged between 173 and 358 ksi (≈1.2 and 2.5 GPa). After microcracking, average stiffnesses ranged between 130 and 245 ksi (≈0.9 and 1.7 GPa), corresponding to stiffness reductions of 24% to 38%. On the May 2005 construction sections, the average stiffnesses before and after microcracking were 476 ksi (≈3.3 GPa) and 204 ksi (≈1.4 GPa), respectively, corresponding to a 57% stiffness reduction. A visual evaluation along with FWD measurements was conducted in August 2005. No cracks were observed and there was no difference in the stiffnesses between the microcracked and control sections.

A.6   Conclusions and Recommendations

Conclusions drawn from the Texas research include the following *(2)*:

- Microcracking, when properly applied, did not result in pavement damage and the base modulus recovered to the same as that measured on the control sections that were not microcracked.
- Problematic cracking occurred on pavements with very high base course cement contents if microcracking was not applied. Problematic cracking implies increased crack width, increased total crack length, or both.
- Microcracking reduced the severity of shrinkage cracks in the base, regardless of cement content, and in some cases also significantly reduced total crack length.
- Appropriate laboratory design combined with microcracking by three passes of a vibratory roller at high amplitude after two to three days of curing provided a marked reduction in shrinkage cracking problems.
- In cooler temperatures when cement curing is slower, microcracking had to be delayed. The study recommended that a minimum modulus value of 200 ksi (≈1.4 GPa) be attained before the layer is microcracked.
- A target reduction in average base modulus of 60% if an FWD is used and 40% to 50% if a light weight deflectometer or soil stiffness gauge is used was recommended.
- Asphalt curing membranes were minimally effective at reducing cracking problems.
- When compared to moist curing with microcracking, moist curing without microcracking resulted in more severe (wider) cracks that quickly reflected through the surfacing.
- The use of higher cement contents in general did not provide a significantly increased base modulus, but did result in more severe cracking problems. Historically, seven-day UCS targets were based upon achieving a high degree of confidence that the material would

meet durability criteria and that it would not be necessary to perform the labor- and time-intensive durability tests. With the recent development of simpler, less time-consuming durability tests (e.g., tube suction), strength requirements should be eased and checked against the new durability requirements. Cement content design should be based on a combination of adequate strength, durability, and moisture resistance.

Based on the research, TxDOT provided the following recommendations for the design and construction of cement-treated bases:

- Design
  + Seven-day UCS: ≥300 psi (2.1 MPa) (according to ASTM D1633, i.e., moist cure)
  + Dielectric value after tube suction test: ≤10
- Construction
  + After placement and compaction of the CTB to project specifications, moist cure for two days.
  + Microcrack the section using the same (or equivalent) vibratory steel drum roller that was used for compaction. If microcracking after two days is not feasible, waiting until the base age reaches three days is preferable to microcracking after only one day of curing. Layers should not be microcracked until a minimum modulus of 200 ksi (1.4 GPa) has been attained.
  + Continue moist curing to an age of at least 72 hours from the day of placement of the CTB.

A.7   References

1.   Scullion, T. 2002. Field Investigation: Pre-Cracking of Soil-Cement Bases to Reduce Reflection Cracking. *Transportation Research Record: Journal of the Transportation Research Board*, 1787, Washington, DC: Transportation Research Board.

2.   Sebesta, S. 2005. *Continued Evaluation of Microcracking in Texas*, Report 0-4502-2, College Station, TX: Texas Transportation.

APPENDIX B: MONITORING RESULTS FOR EACH CELL

This appendix presents soil stiffness gauge (SSG), light weight deflectometer (LWD), and FWD-backcalculated stiffness, and crack monitoring results for each cell on the test road. Plots include the following:

- SSG stiffness distributions after construction and during microcracking
- SSG-measured stiffness during microcracking per gauge
- SSG-measured stiffness reduction during microcracking per testing location
- LWD measured surface modulus during microcracking (select cells only)
- LWD measured surface modulus during microcracking per testing location (select cells only)
- FWD-backcalculated stiffness per testing location over 128 days
- Change in crack spacing over time (only for cells with visible cracks)
- Increase in crack density over time (only for cells with visible cracks)
- Plan view of cracking observed over 128 days (only for cells with visible cracks)
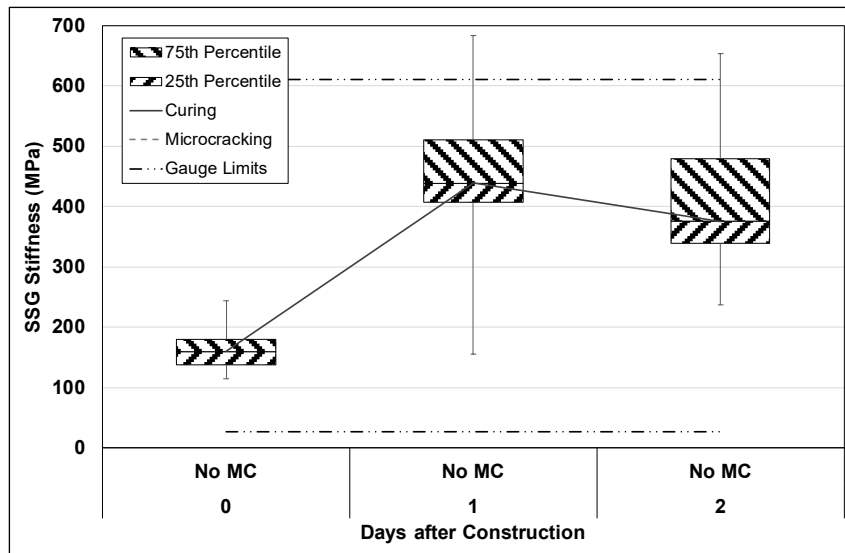
Figure B.1: Cell S1: SSG measured stiffness.
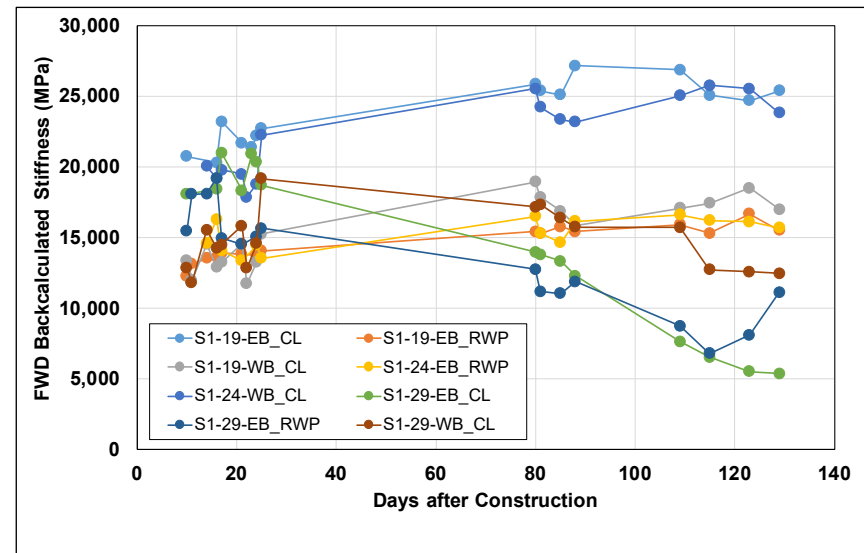
Figure B.2: Cell S1: Change in FWD-backcalculated stiffness.
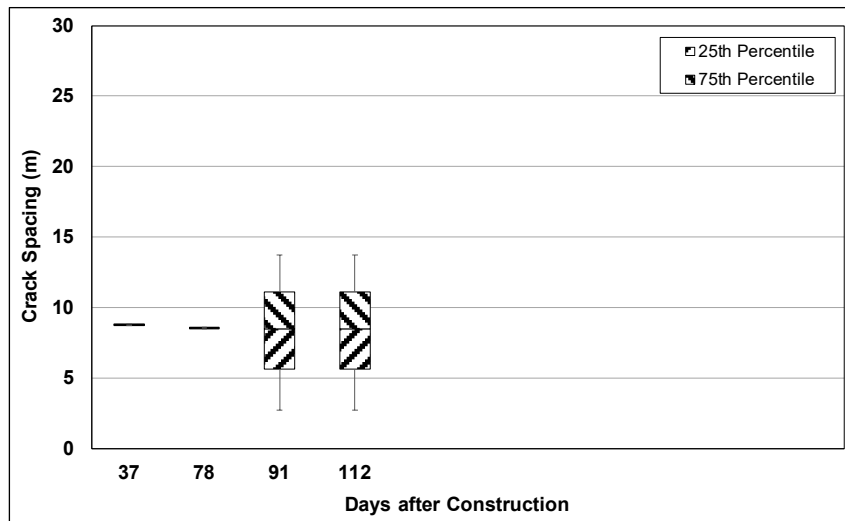
Figure B.3: Cell S1: Change in crack spacing.
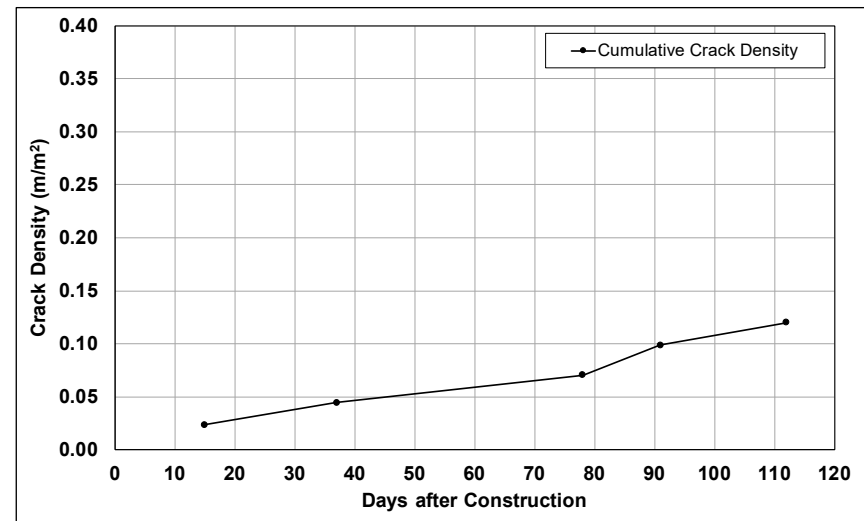
Figure B.4: Cell S1: Change in crack density.
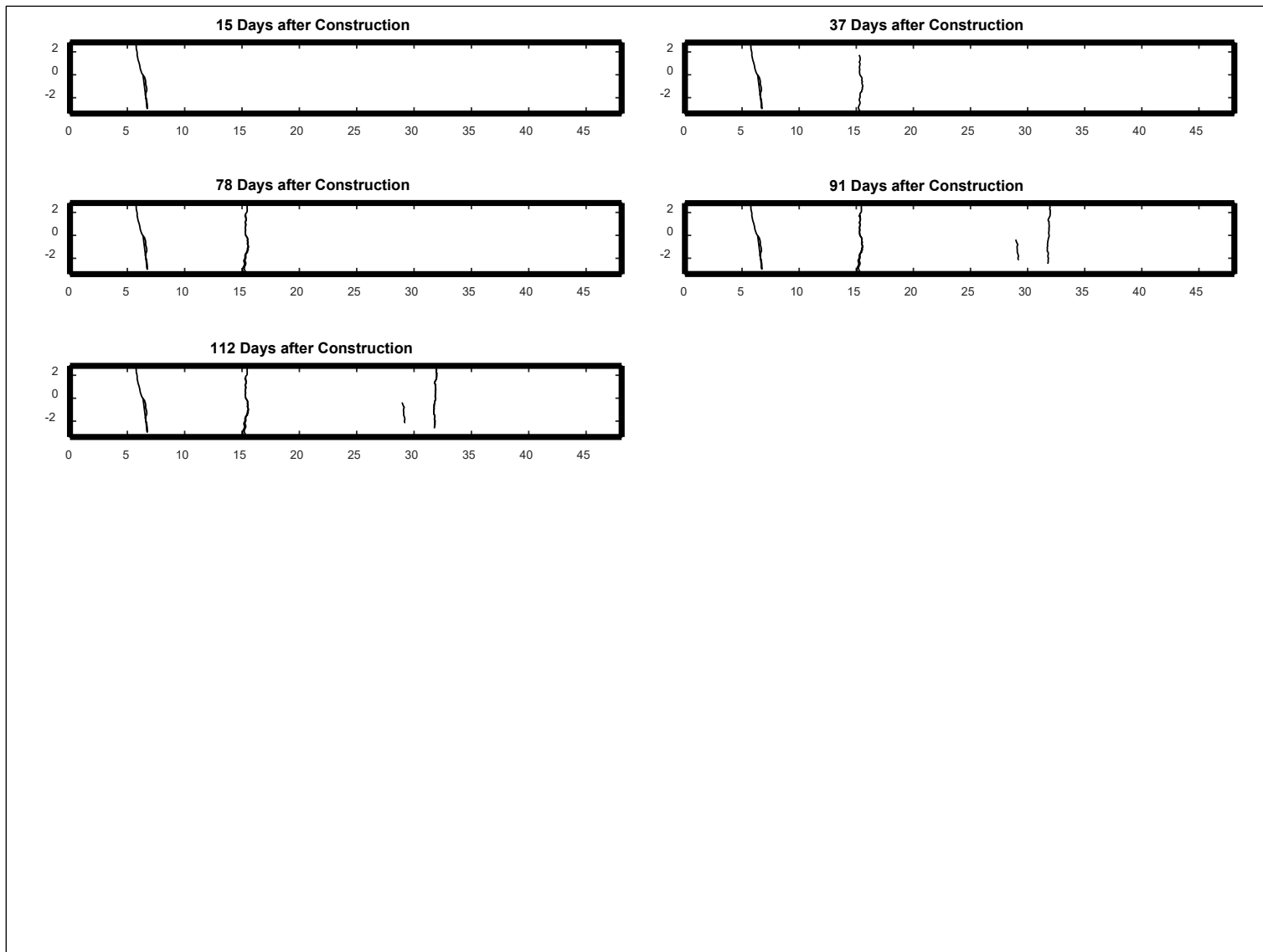
Figure B.5: Cell S1: Crack development.
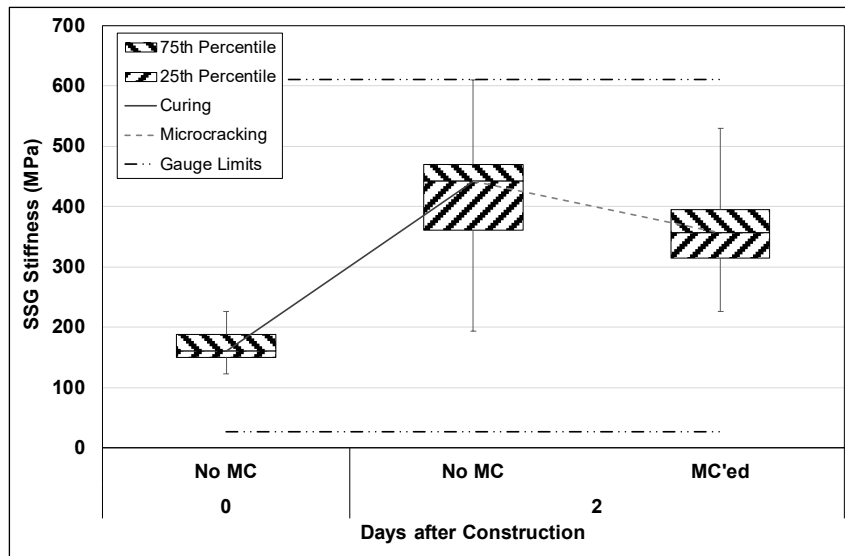
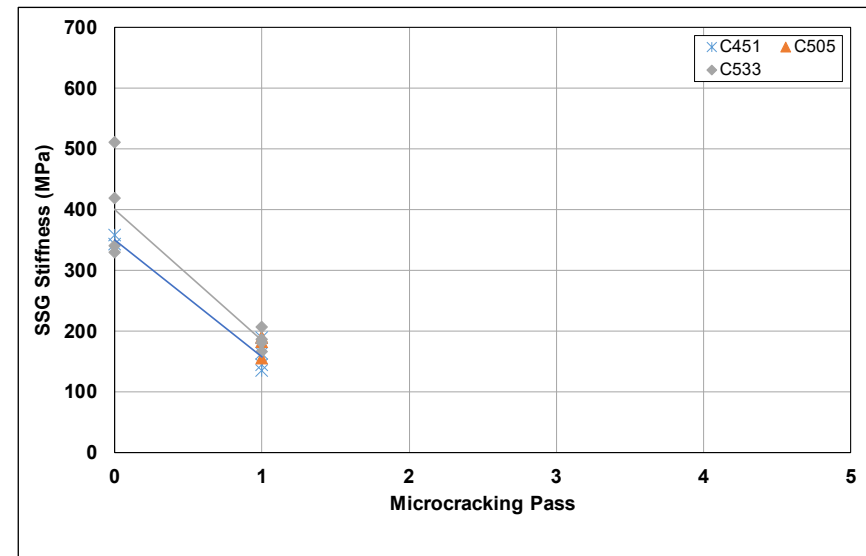**Figure B.6: Cell S2: SSG measured stiffness.**
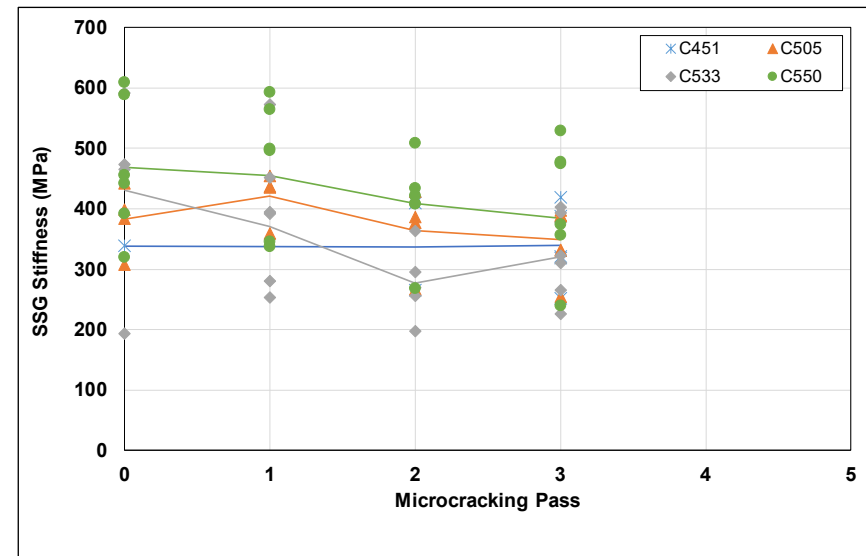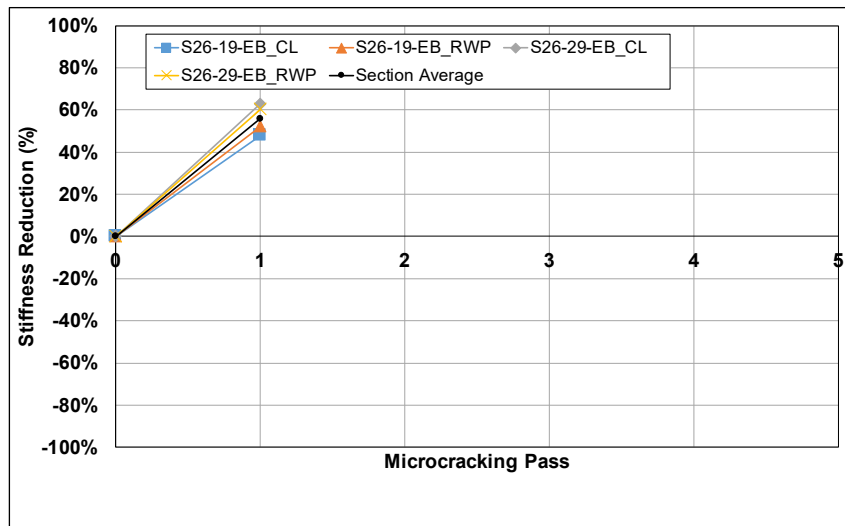

Figure B.7: Cell S2: SSG stiffness results per gauge.
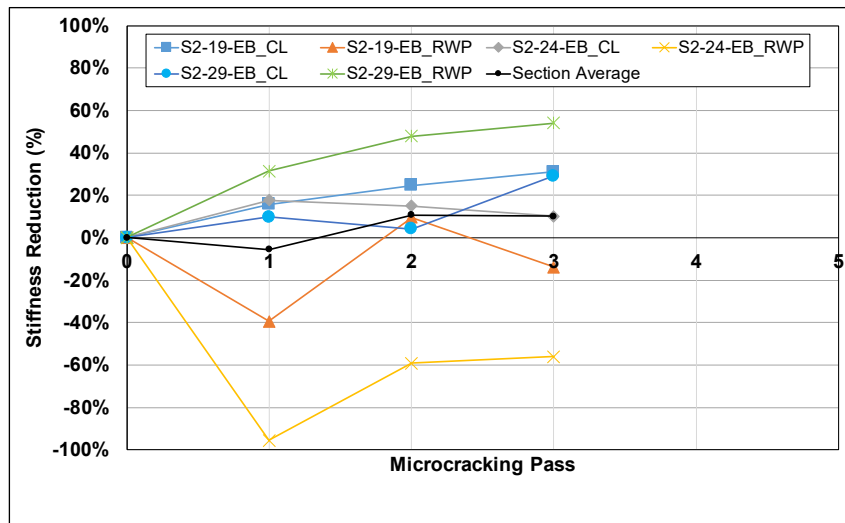
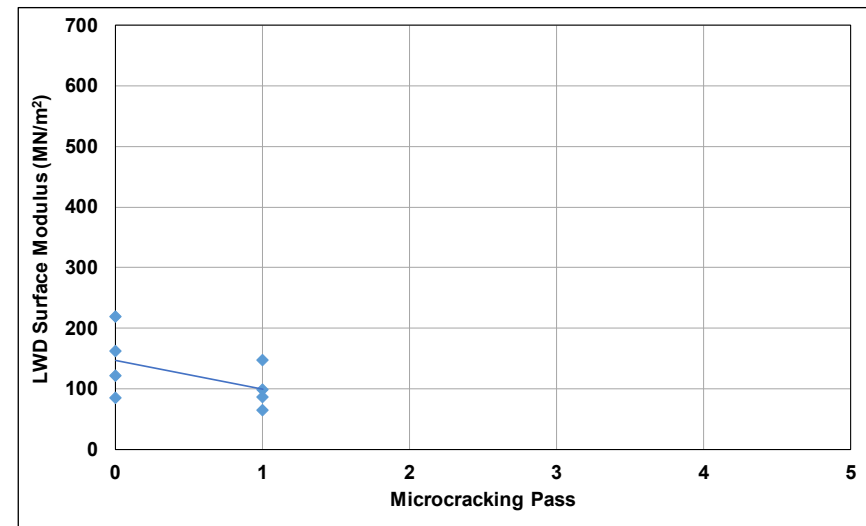**Figure B.8: Cell S2: SSG stiffness reduction per station.**
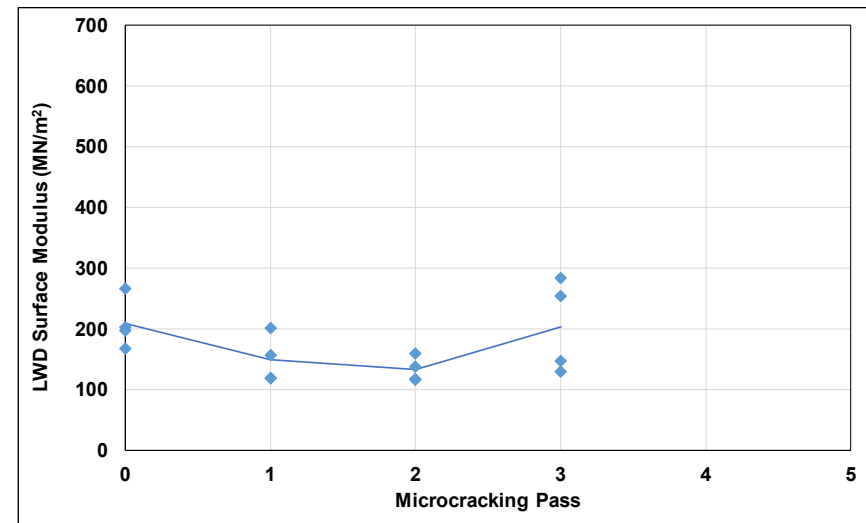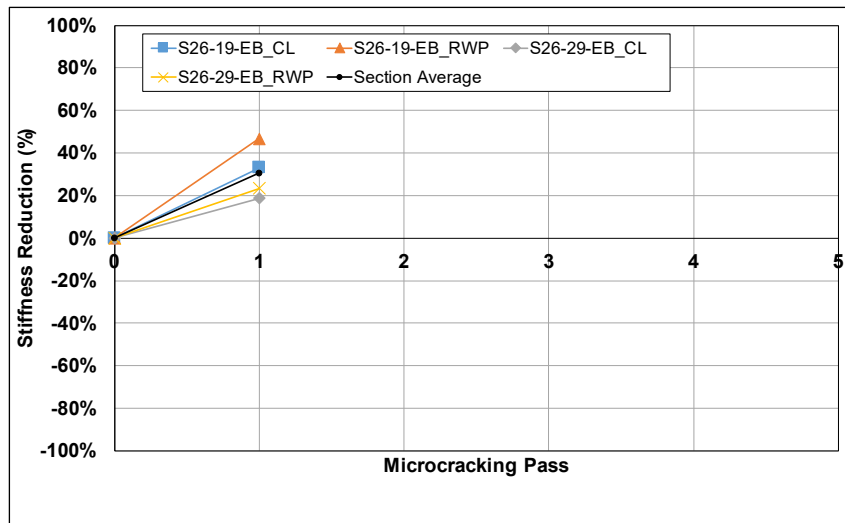

Figure B.9: Cell S2: LWD measured surface modulus.
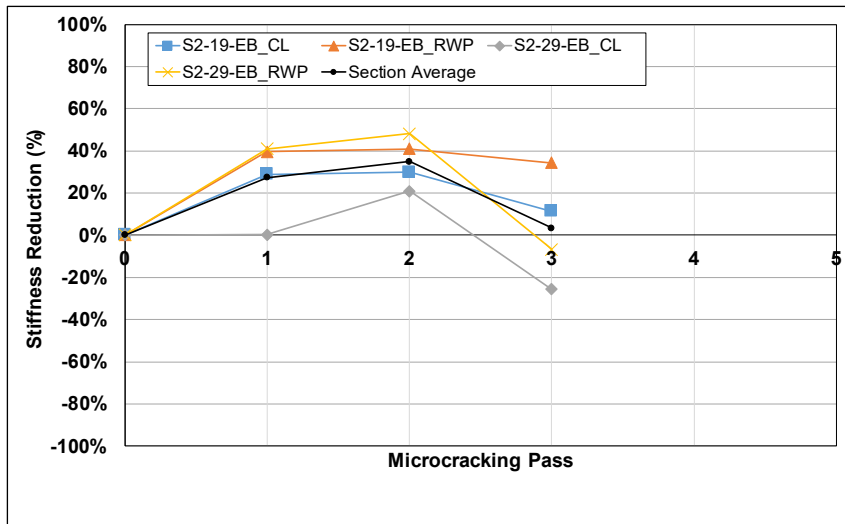
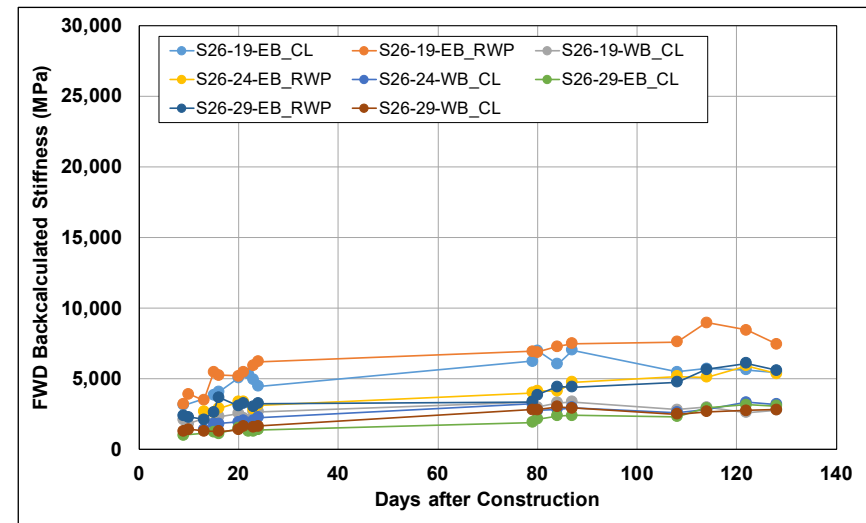**Figure B.10: Cell S2: LWD modulus reduction per station.**
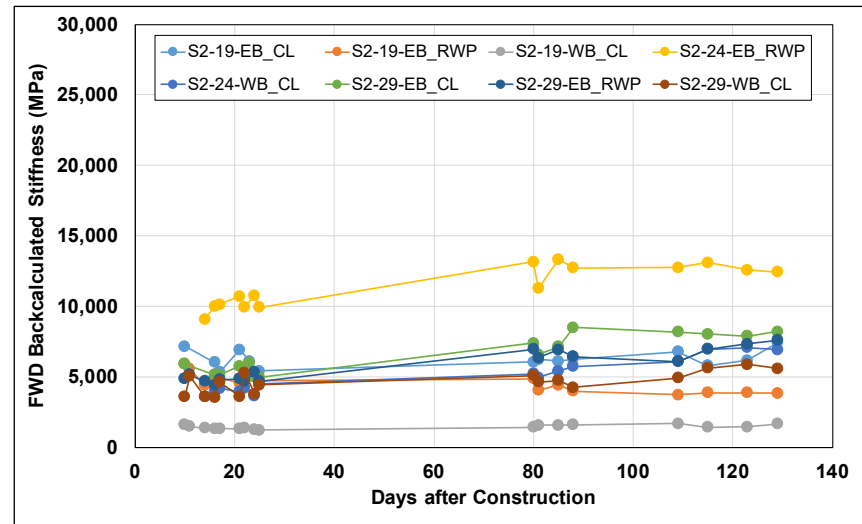
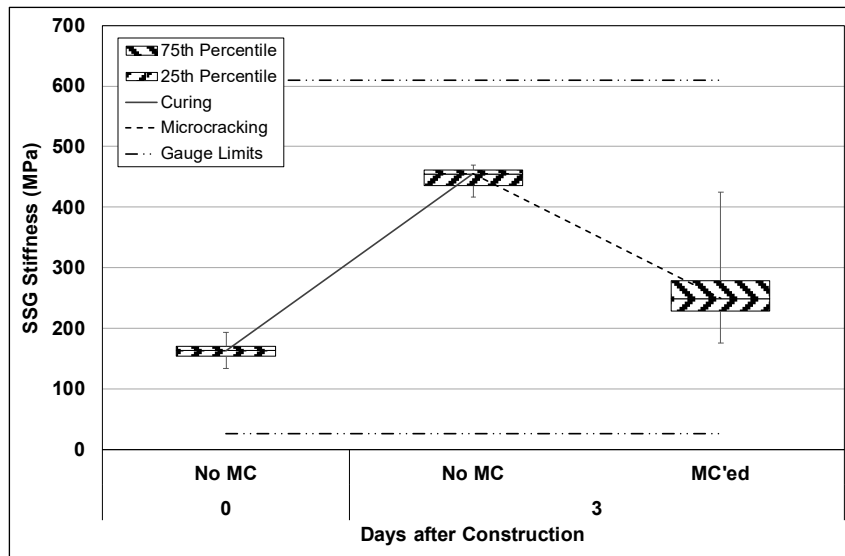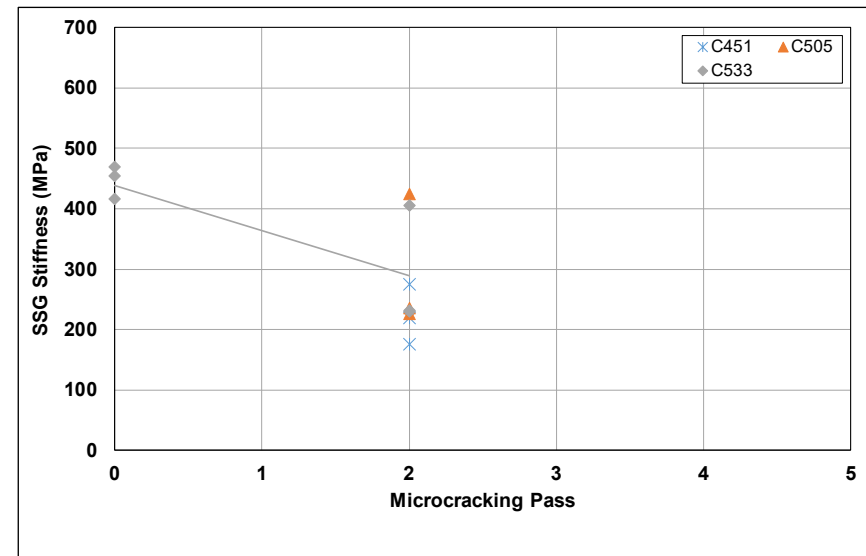**Figure B.11: Cell S2: Change in FWD-backcalculated stiffness.**
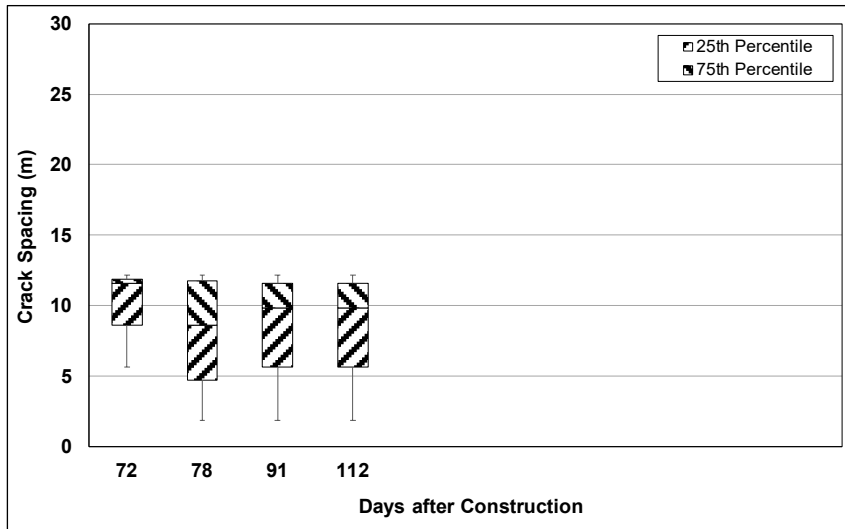
Figure B.12: Cell S2: Change in crack spacing.
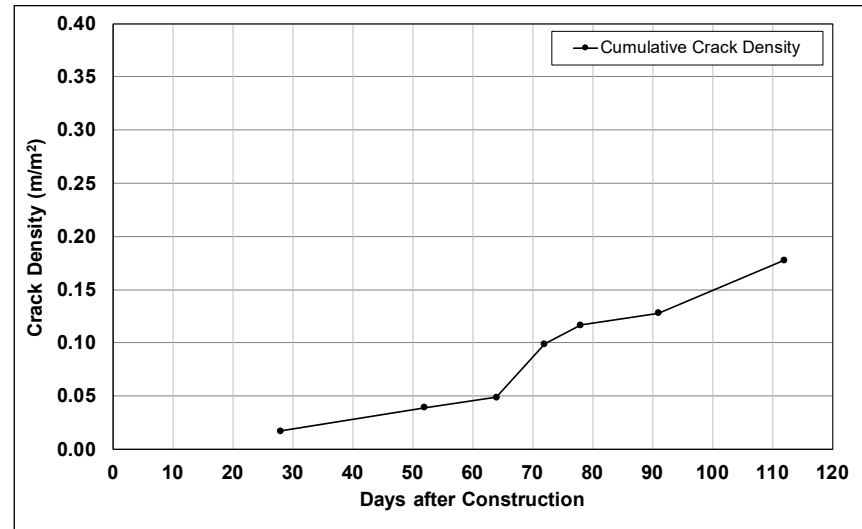
Figure B.13: Cell S2: Change in crack density.
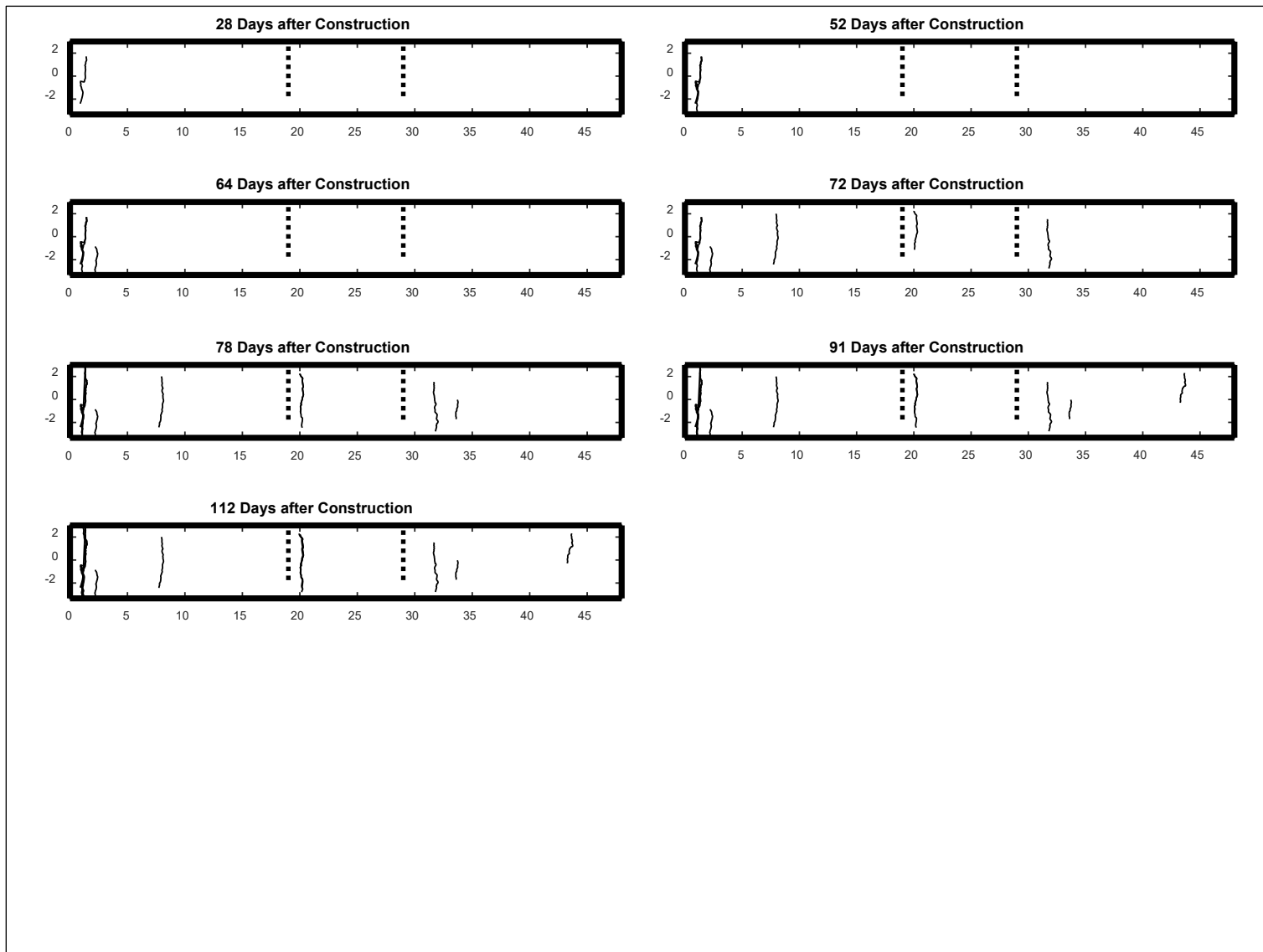
Figure B.14: Cell S2: Crack development.
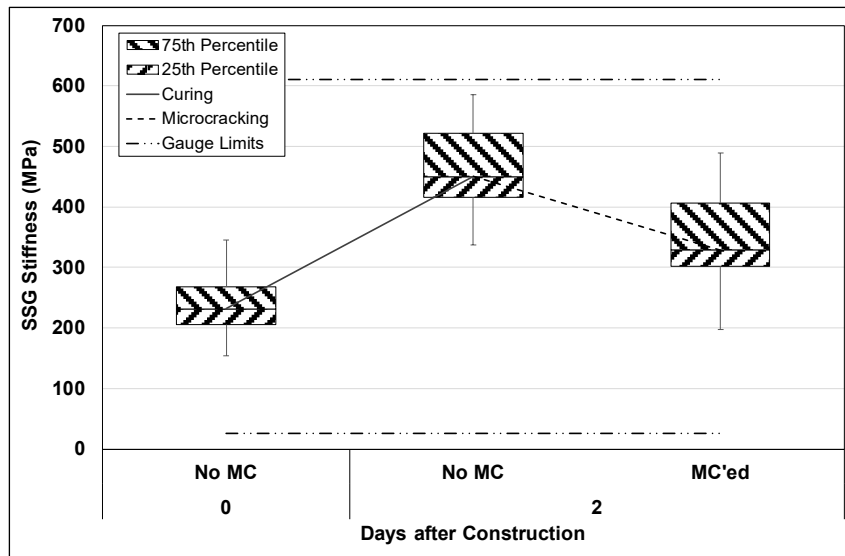
Figure B.15: Cell S3: SSG measured stiffness.
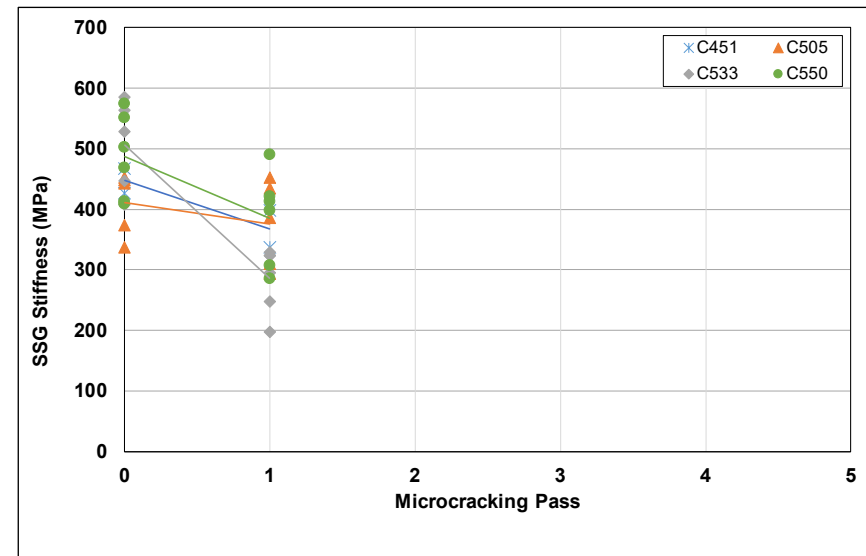
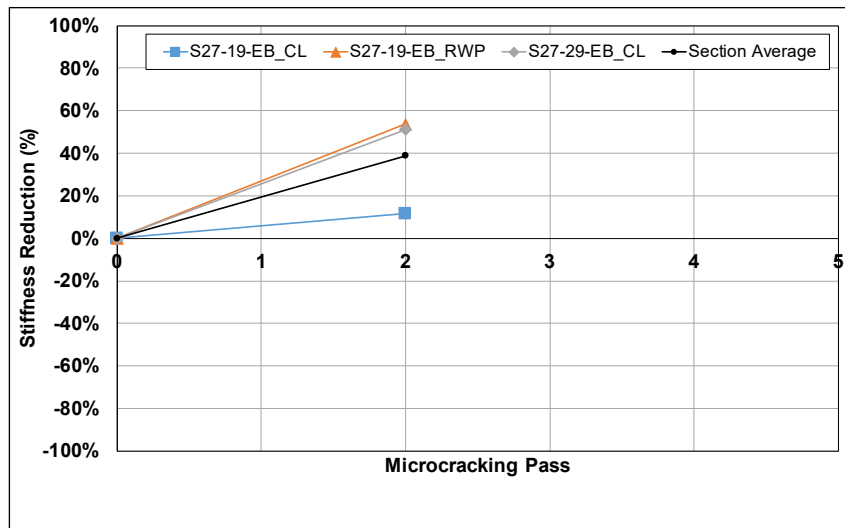**Figure B.16: Cell S3: SSG stiffness results per gauge.**
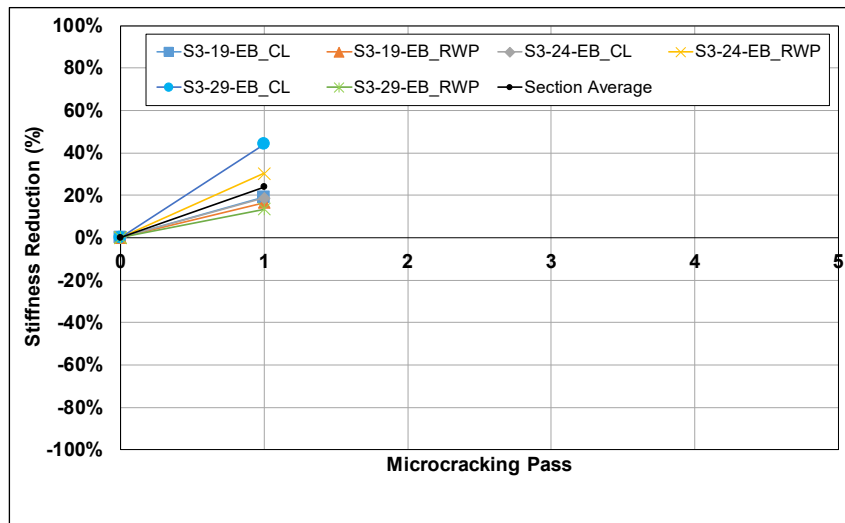
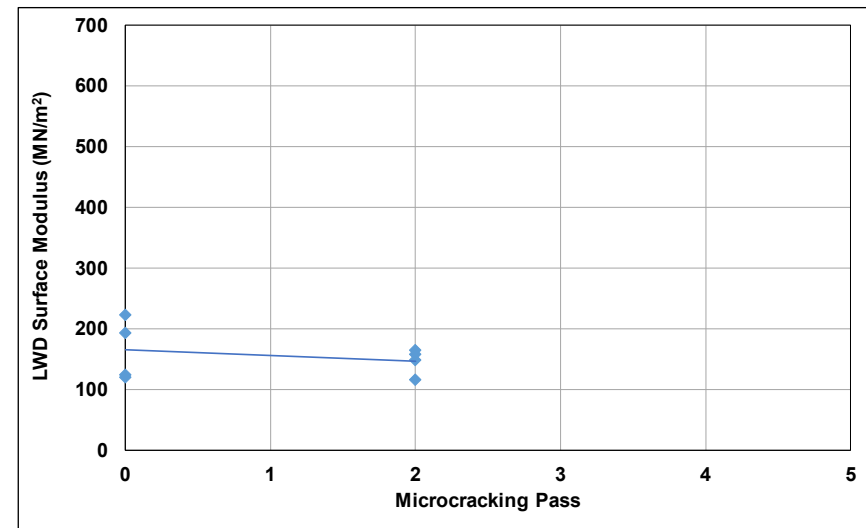**Figure B.17: Cell S3: SSG stiffness reduction per station.**
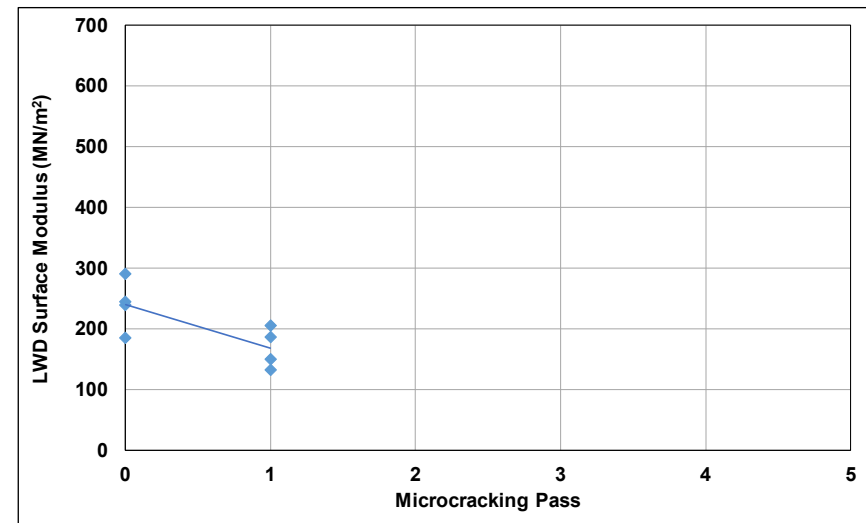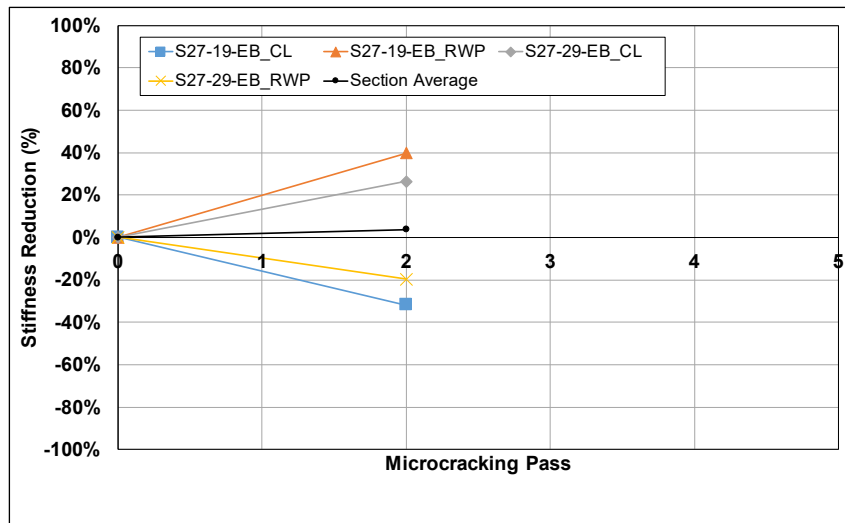

Figure B.18: Cell S3: LWD measured surface modulus.
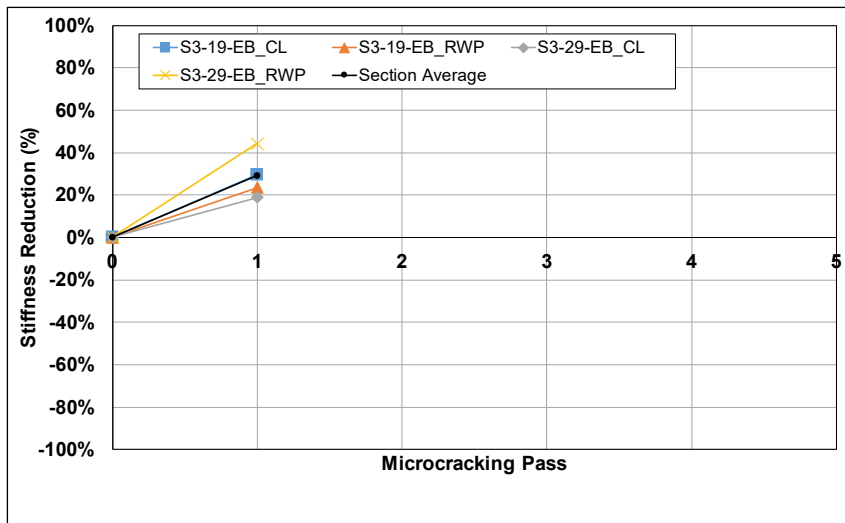
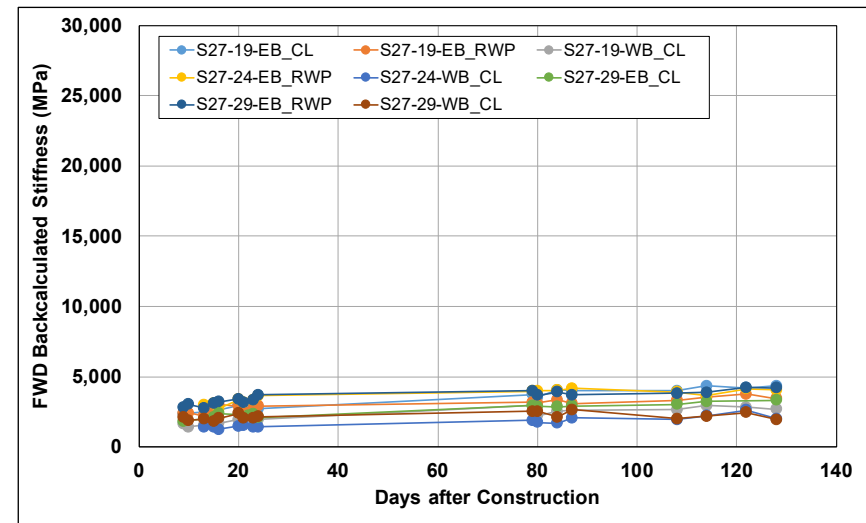Figure B.19: Cell S3: LWD modulus reduction per station.
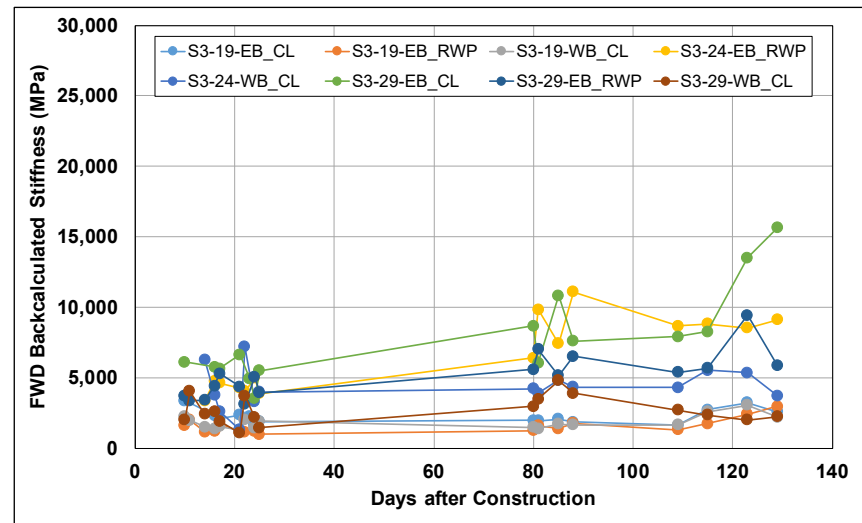
Figure B.20: Cell S3: Change in FWD-backcalculated stiffness.
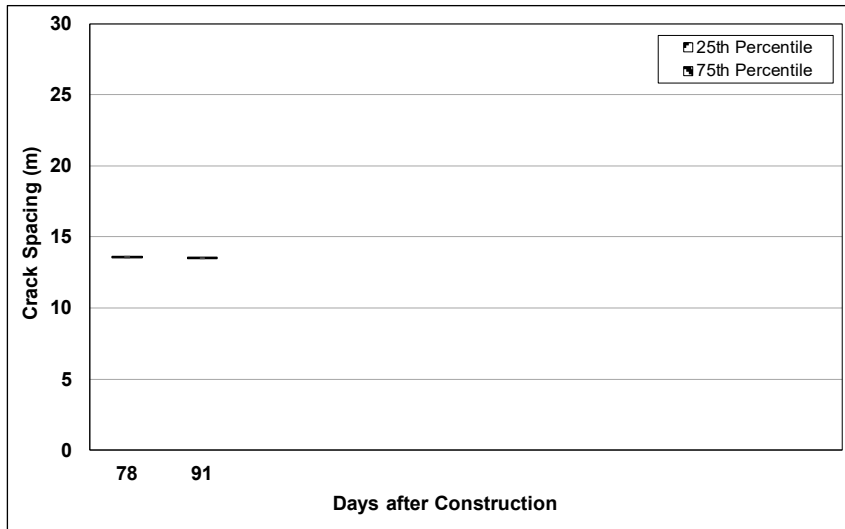
Figure B.21: Cell S3: Change in crack spacing.
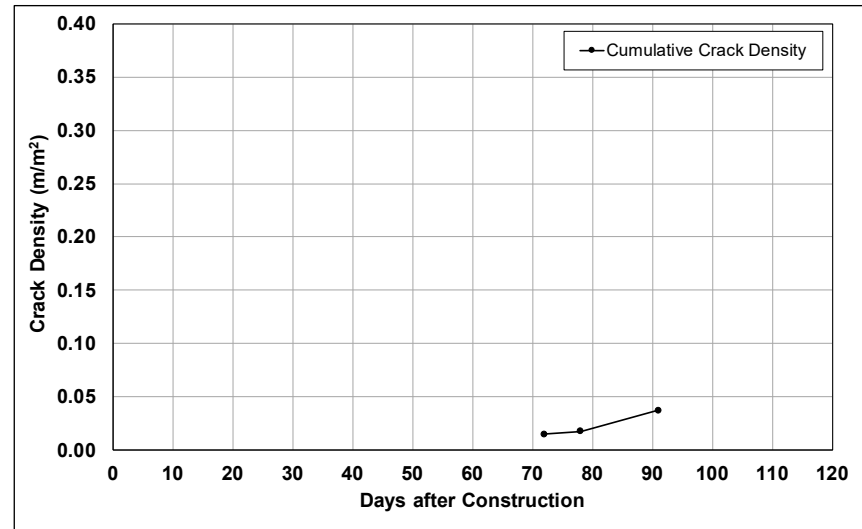
Figure B.22: Cell S3: Change in crack density.

72 Days after Construction

78 Days after Construction

91 Days after Construction
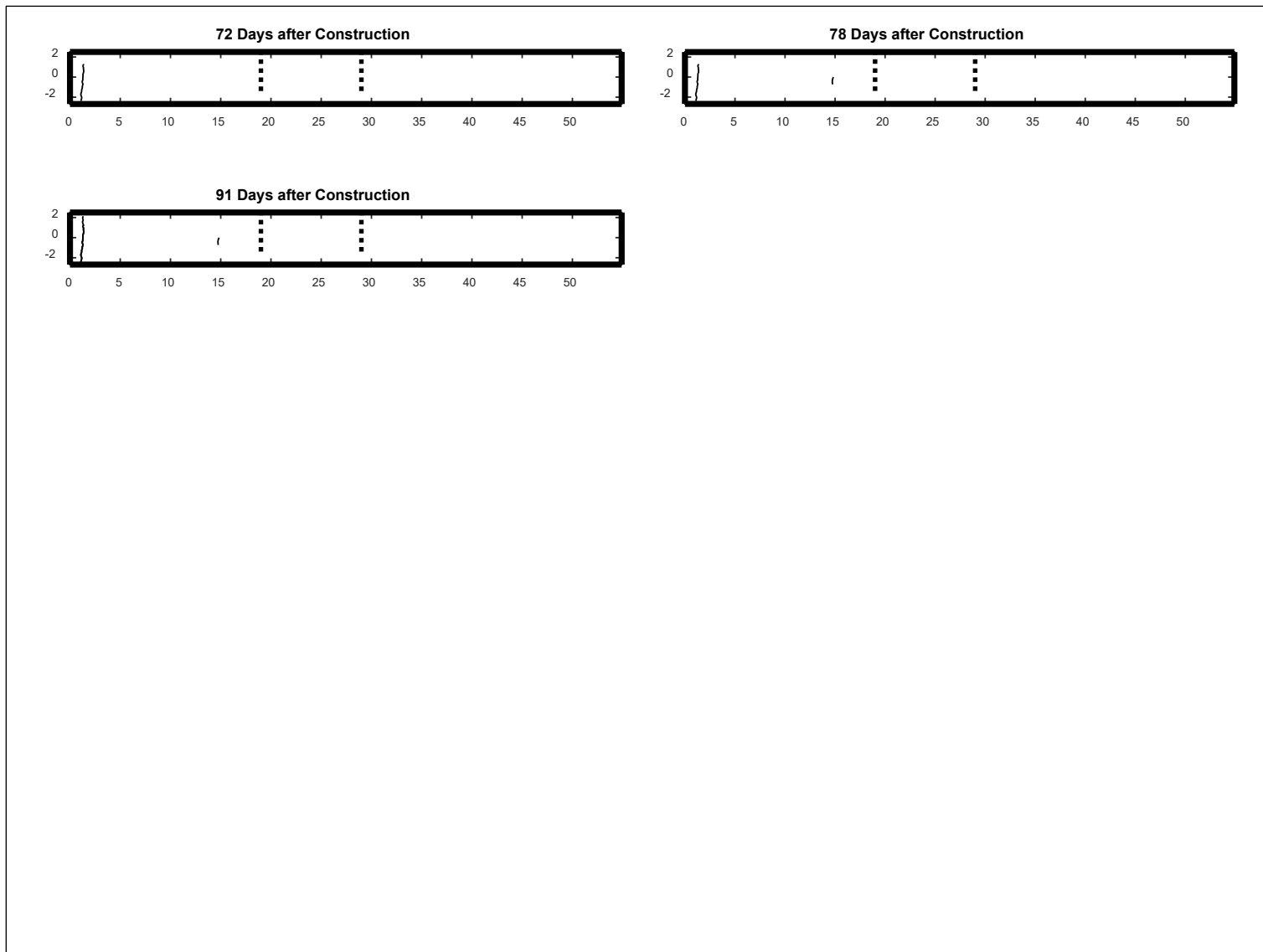
Figure B.23: Cell S3: Crack development.
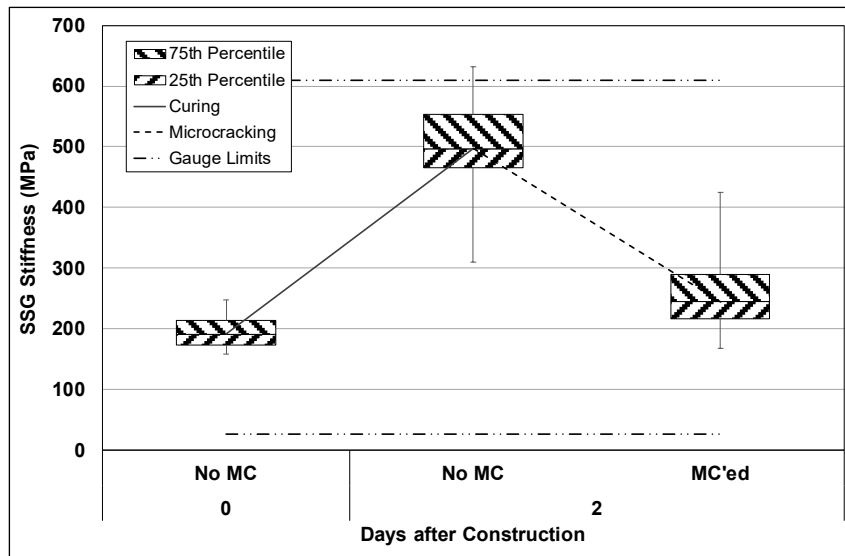
Figure B.24: Cell S4: SSG measured stiffness.
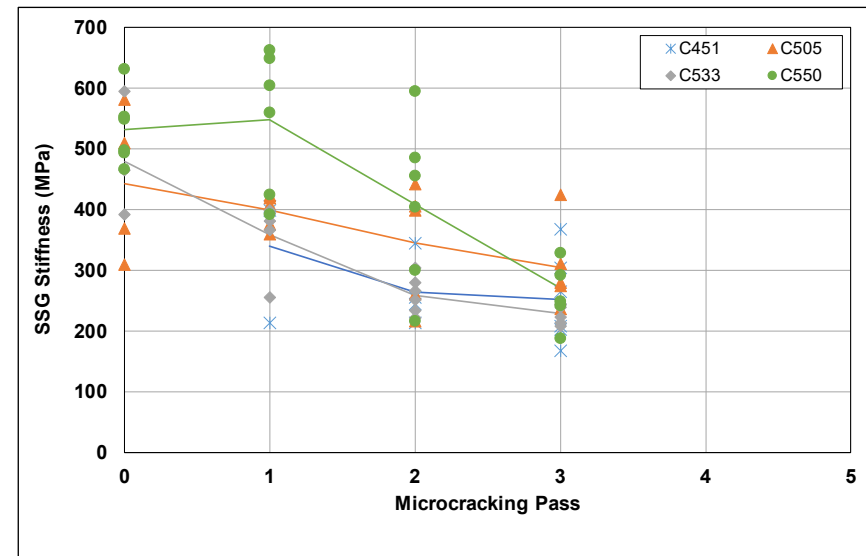
Figure B.25: Cell S4: SSG stiffness results per gauge.
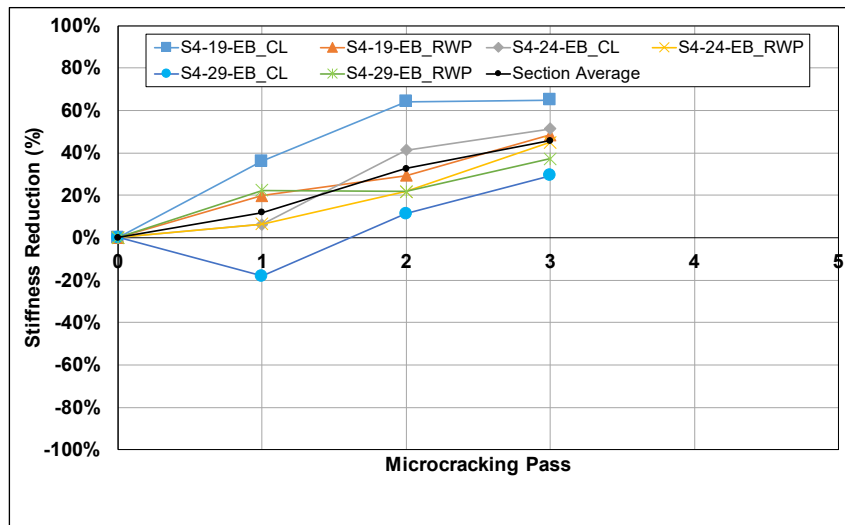
Figure B.26: Cell S4: SSG stiffness reduction per station.
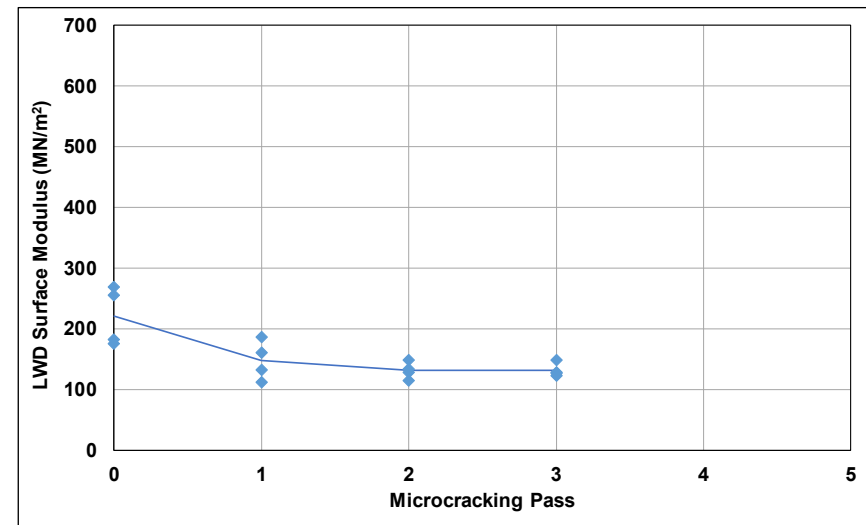
Figure B.27: Cell S4: LWD measured surface modulus.
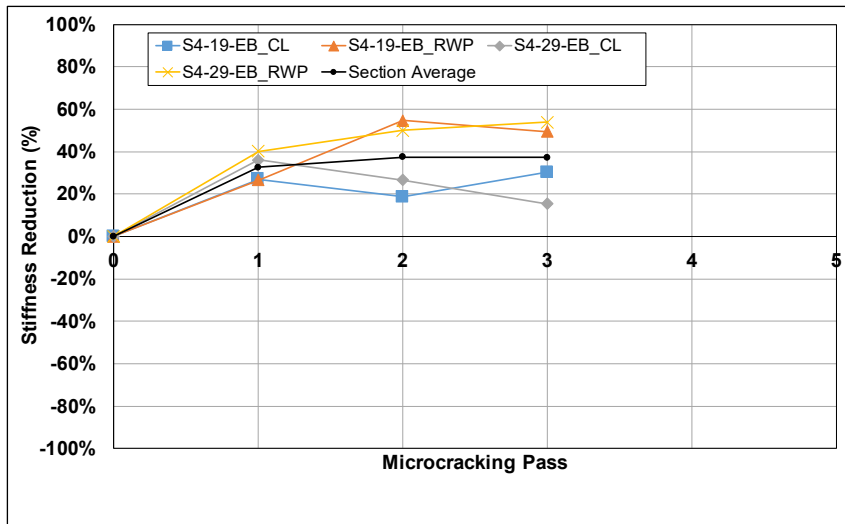
Figure B.28: Cell S4: LWD modulus reduction per station.
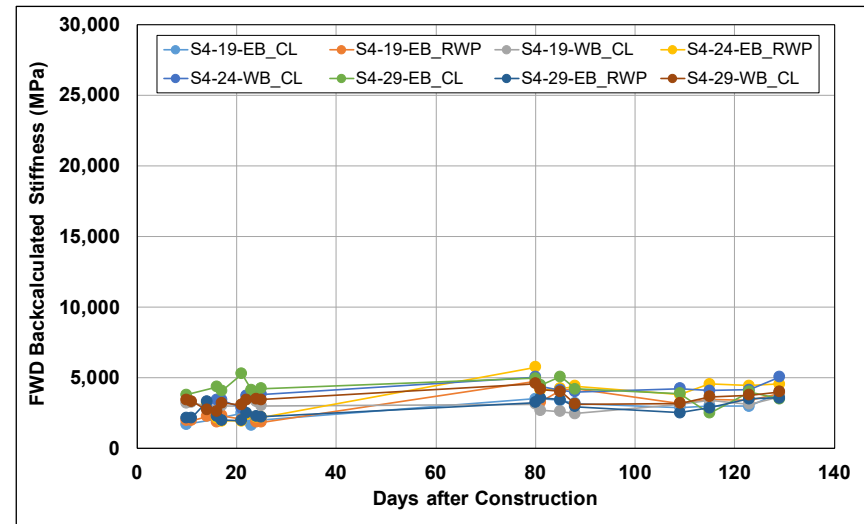
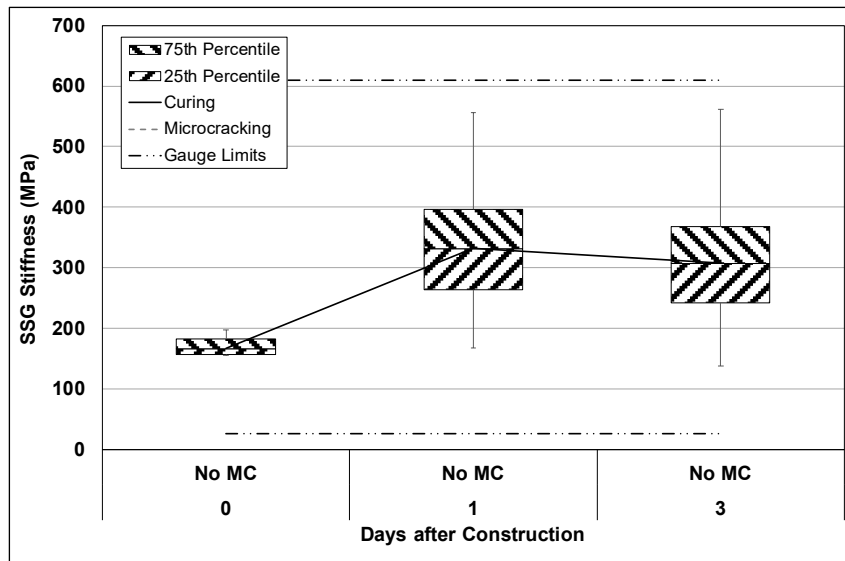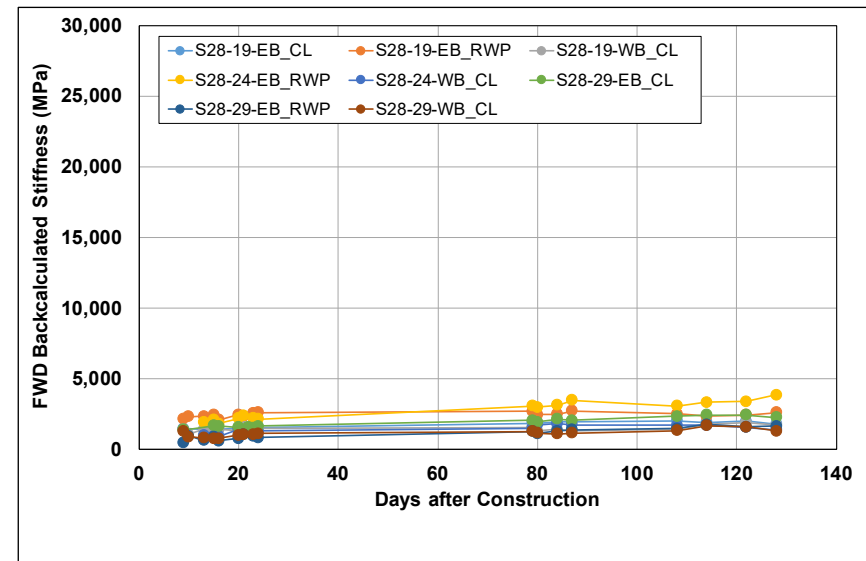**Figure B.29: Cell S4: Change in FWD-backcalculated stiffness.**
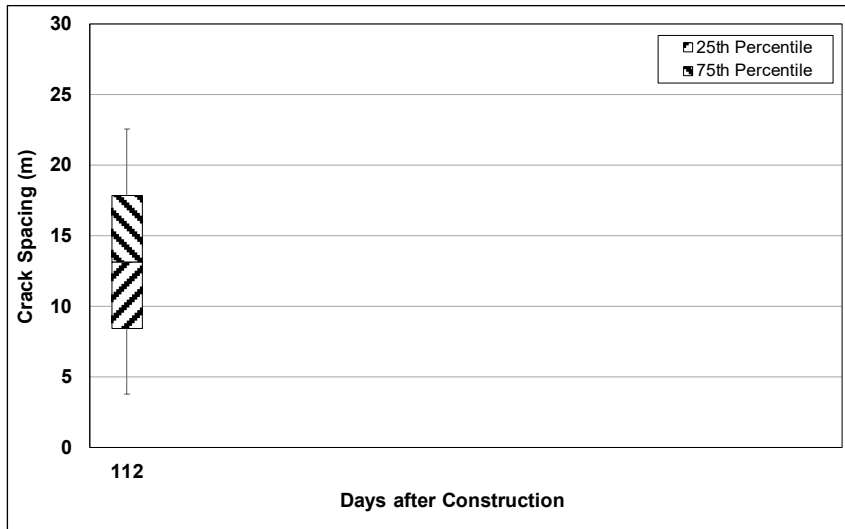
Figure B.30: Cell S4: Change in crack spacing.
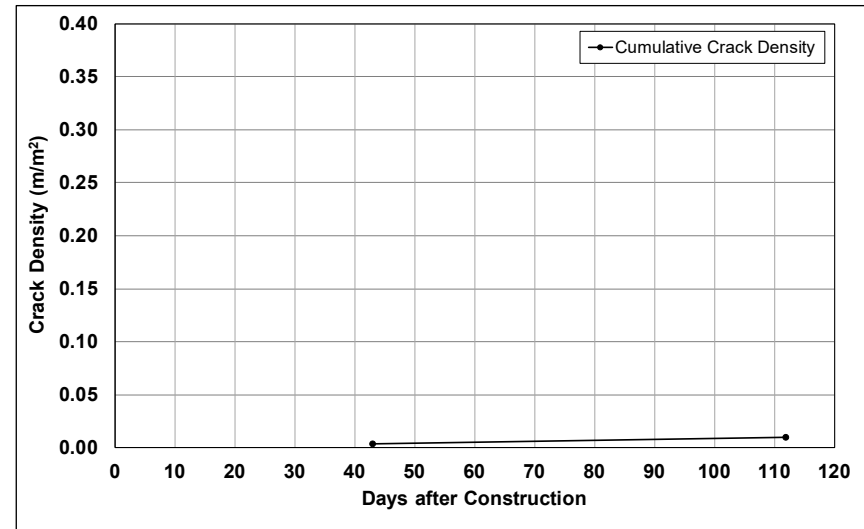
Figure B.31: Cell S4: Change in crack density.

43 Days after Construction

112 Days after Construction
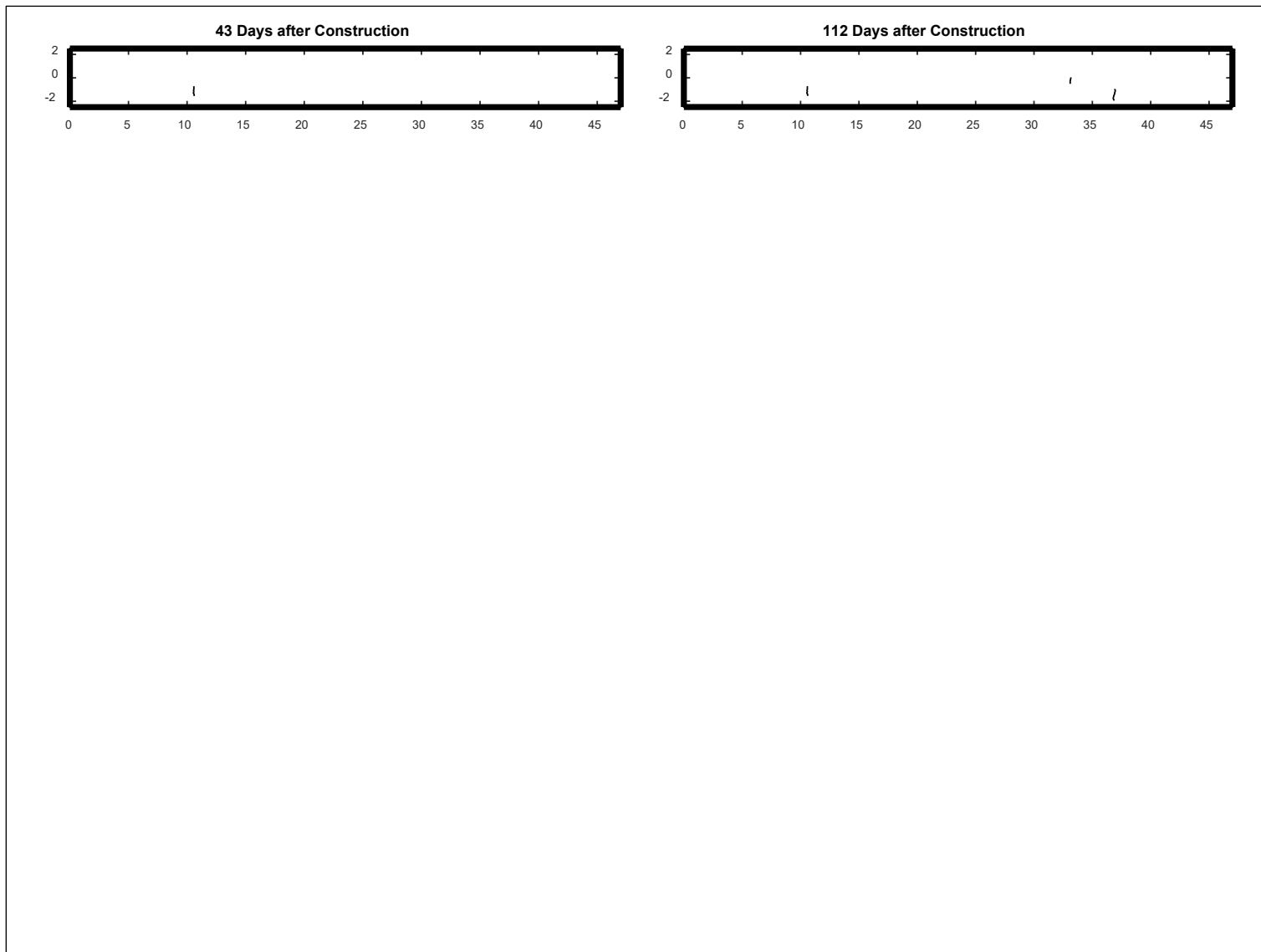
Figure B.32: Cell S4: Crack development.
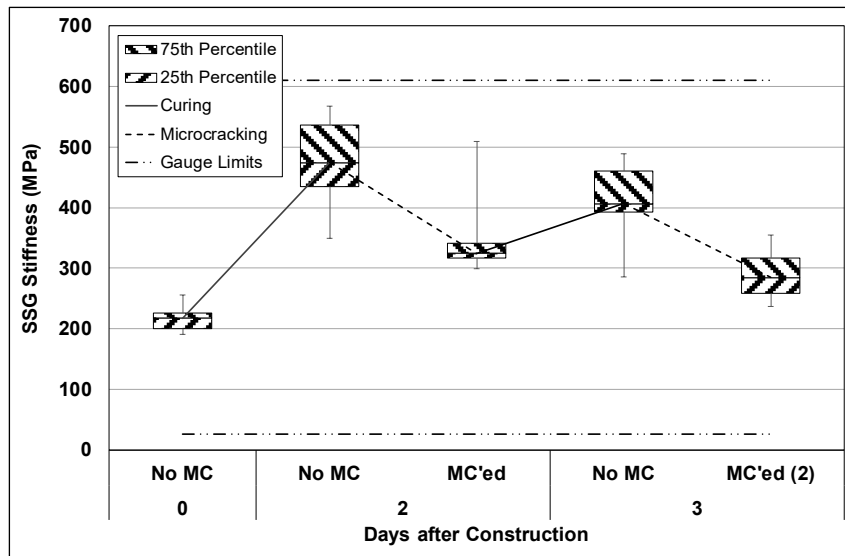
Figure B.33: Cell S5: SSG measured stiffness.
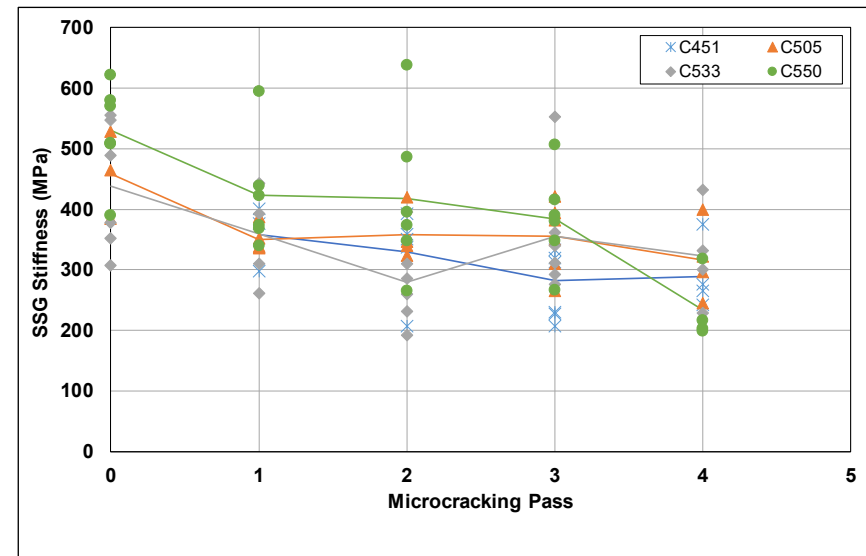
Figure B.34: Cell S5: SSG stiffness results per gauge.
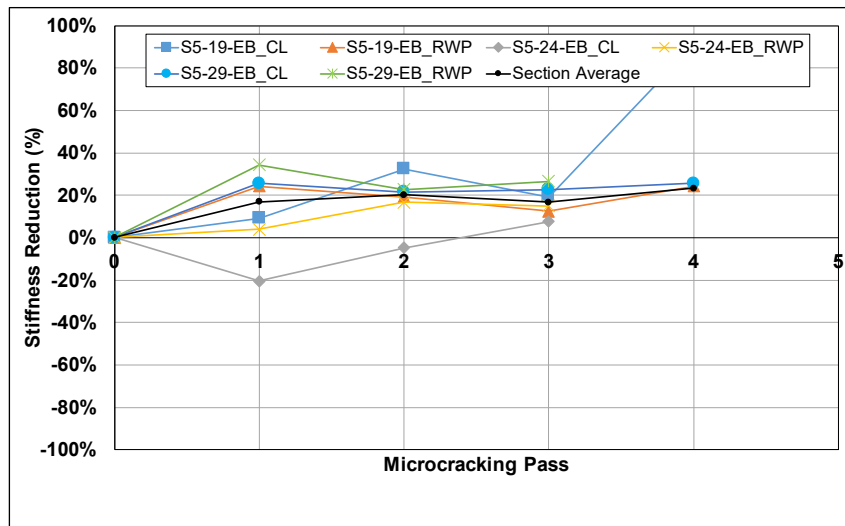
Figure B.35: Cell S5: SSG stiffness reduction per station.
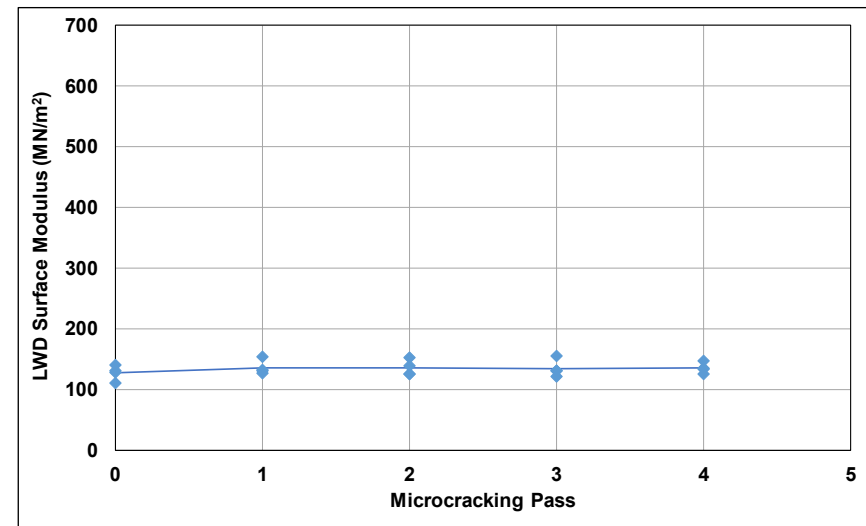
Figure B.36: Cell S5: LWD measured surface modulus.
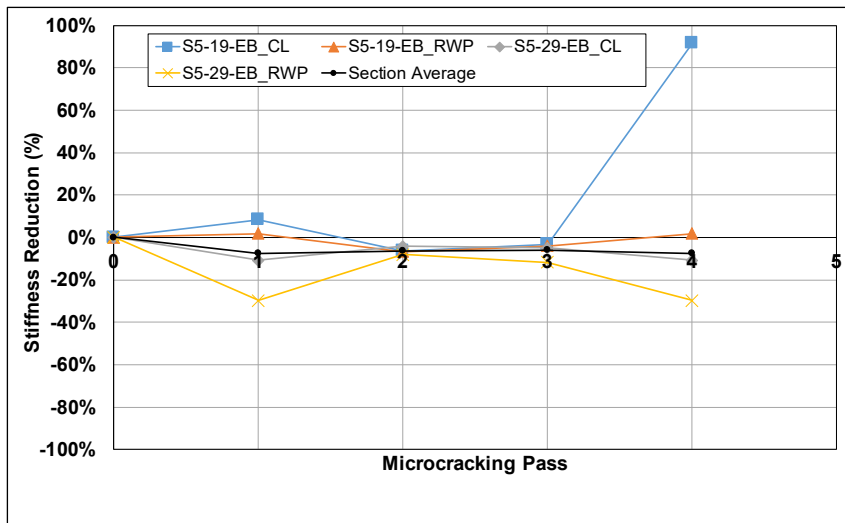
Figure B.37: Cell S5: LWD modulus reduction per station.
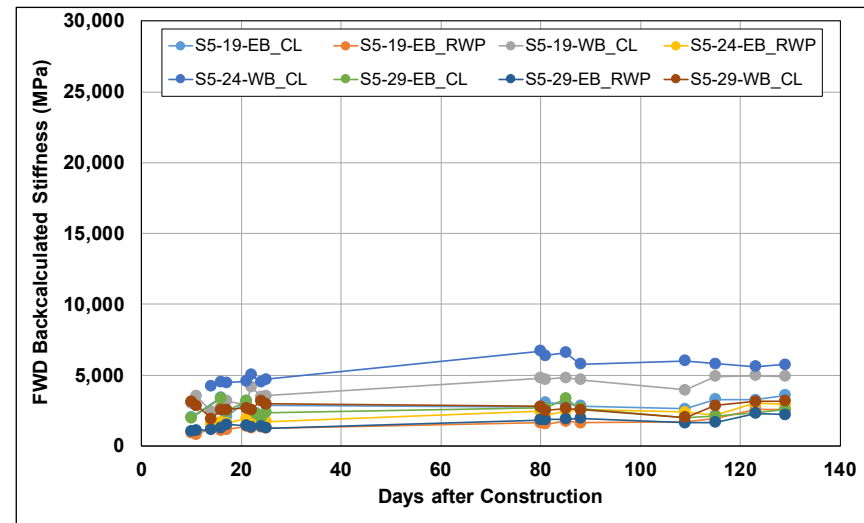
Figure B.38: Cell S5: Change in FWD-backcalculated stiffness.
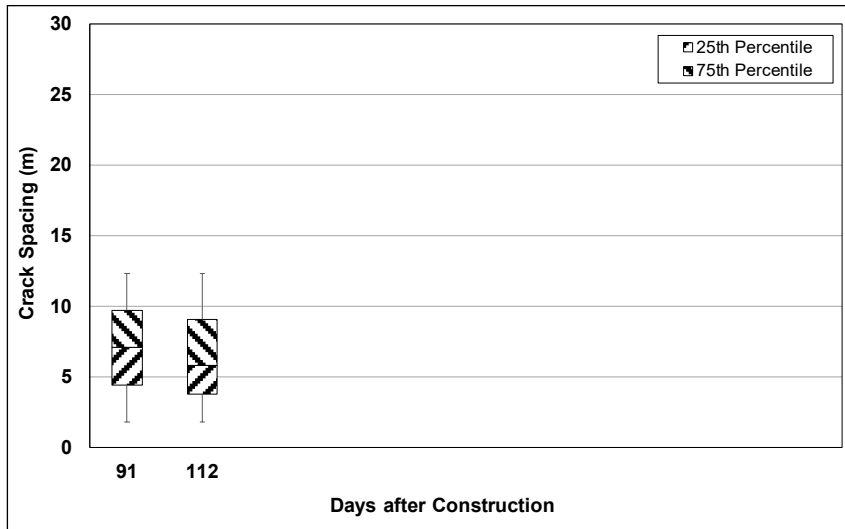
Figure B.39: Cell S5: Change in crack spacing.
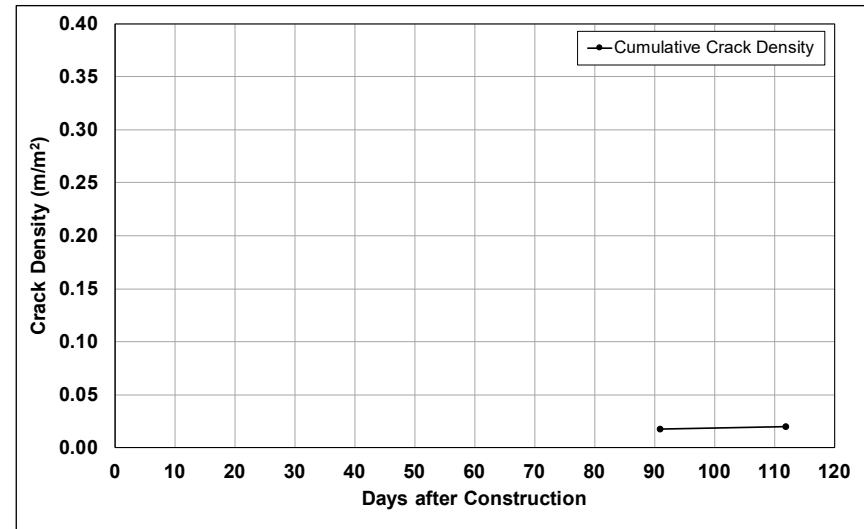
**Figure B.40: Cell S5: Change in crack density.**
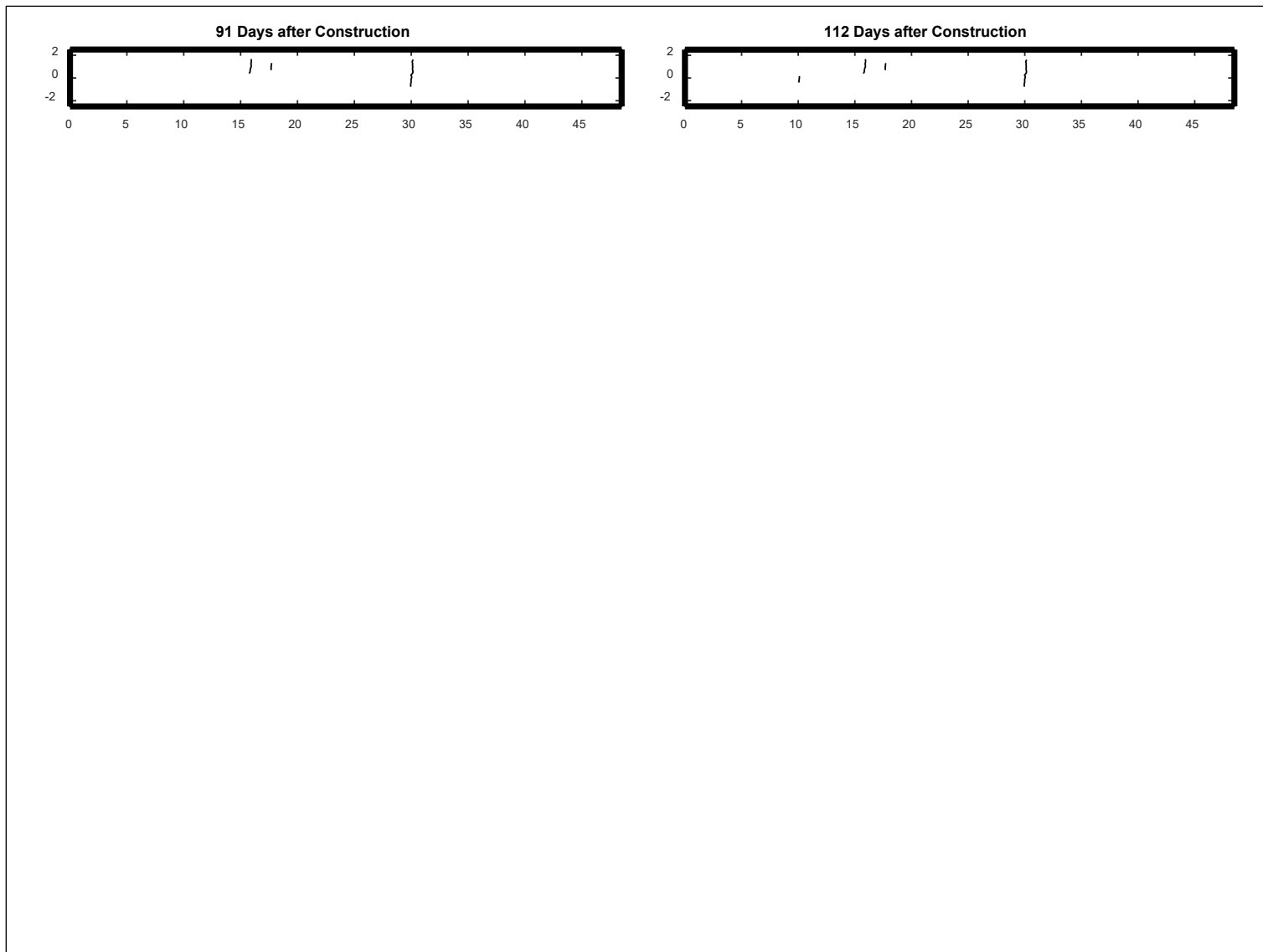
Figure B.41: Cell S5: Crack development.
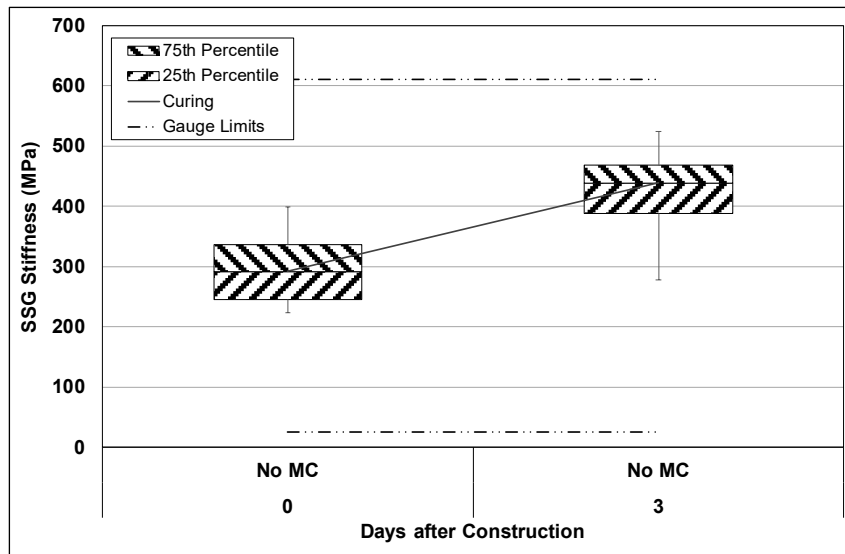
Figure B.42: Cell S6: SSG measured stiffness.
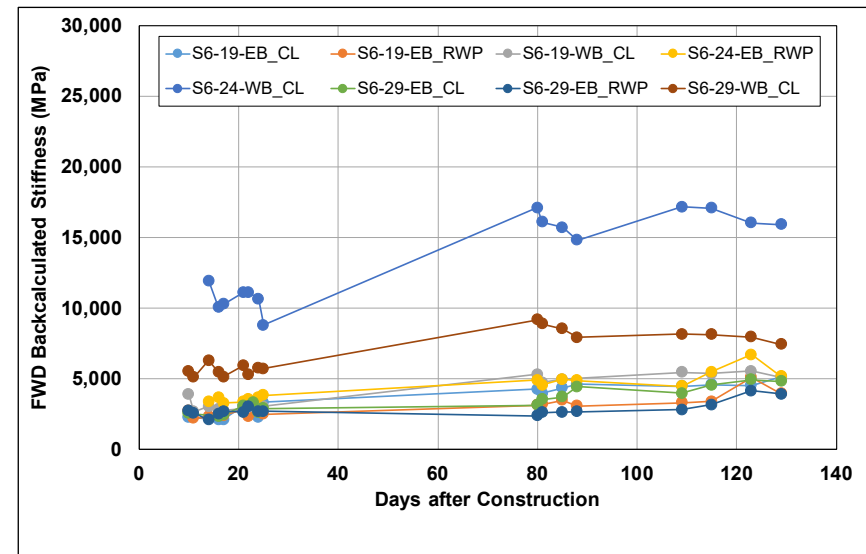
Figure B.43: Cell S6: Change in FWD-backcalculated stiffness.
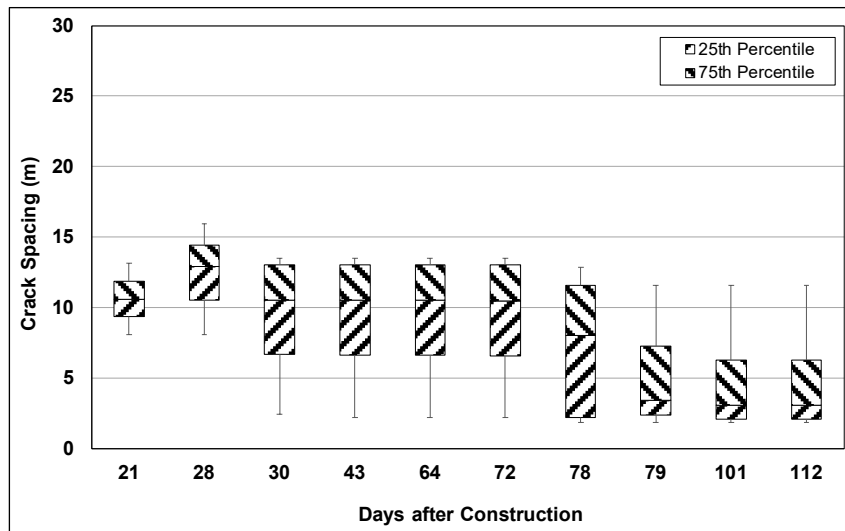
Figure B.44: Cell S6: Change in crack spacing.
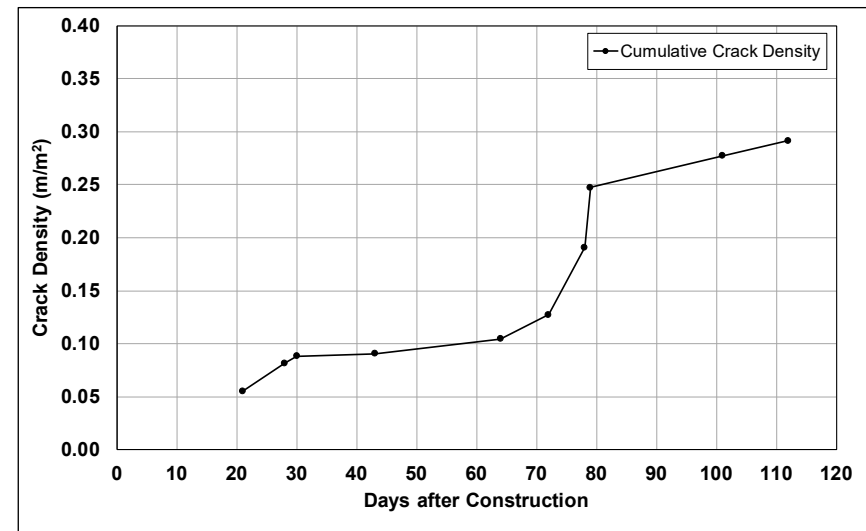
Figure B.45: Cell S6: Change in crack density.
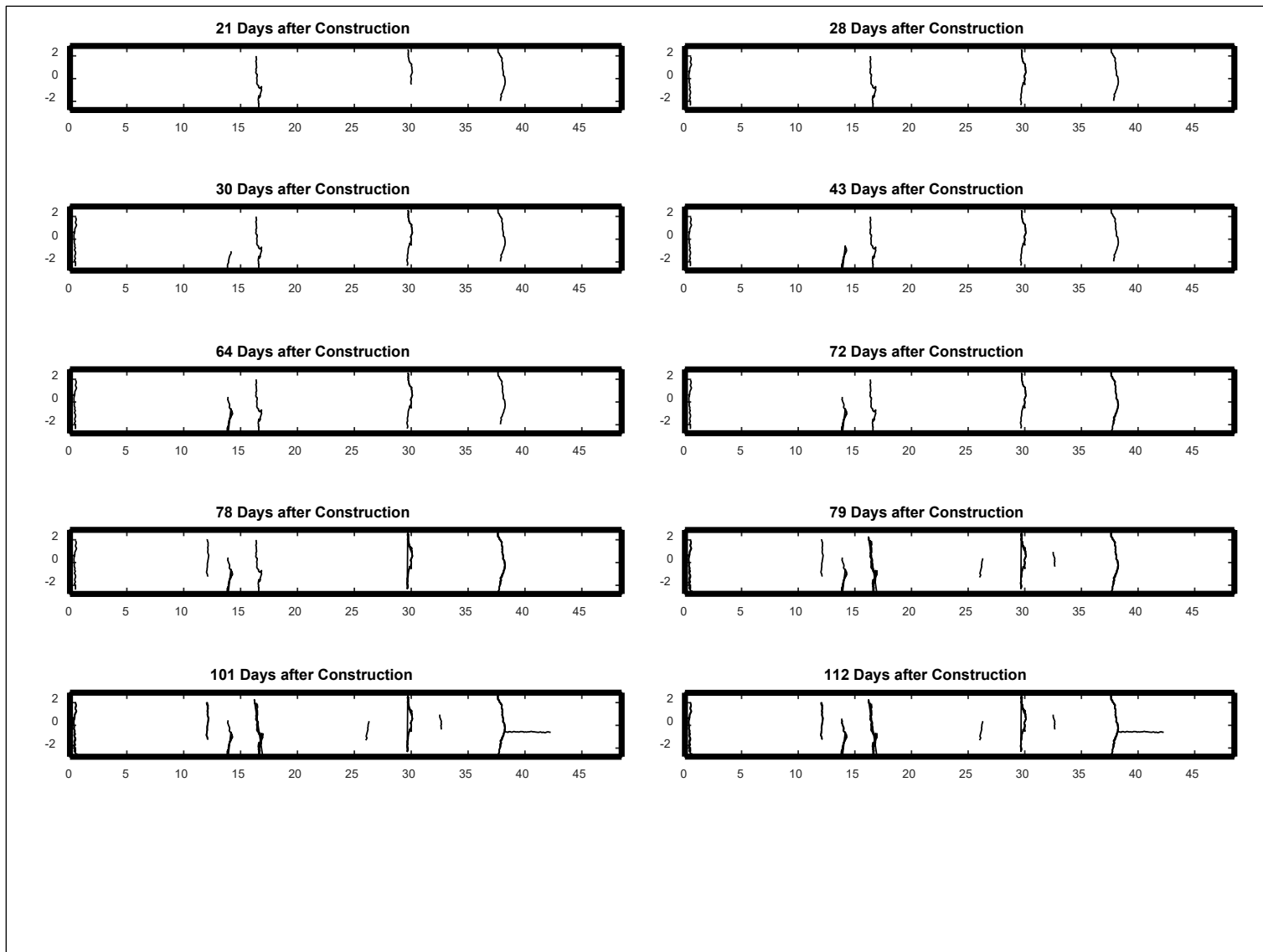
Figure B.46: Cell S6: Crack development.
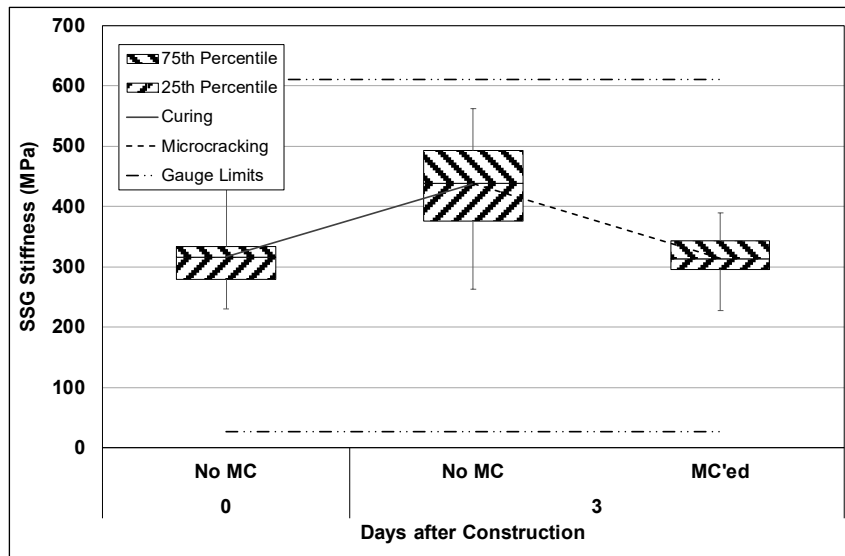
Figure B.47: Cell S7: SSG measured stiffness.
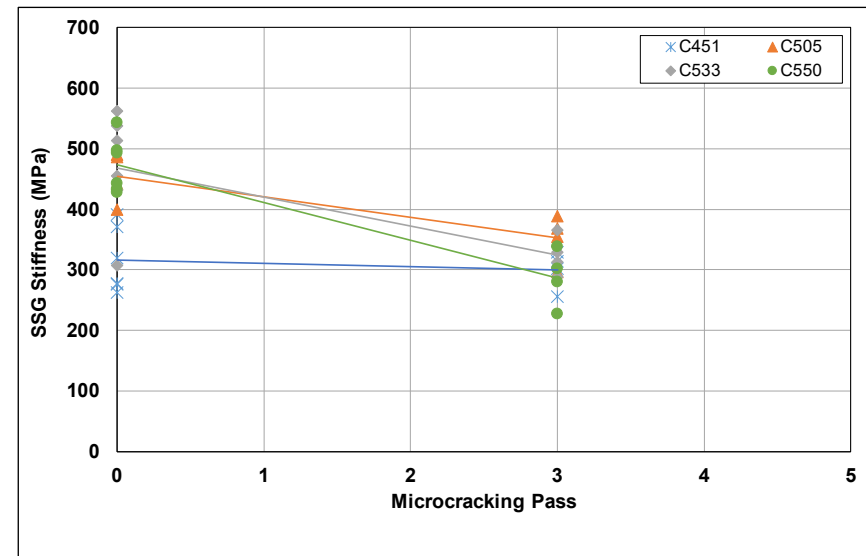
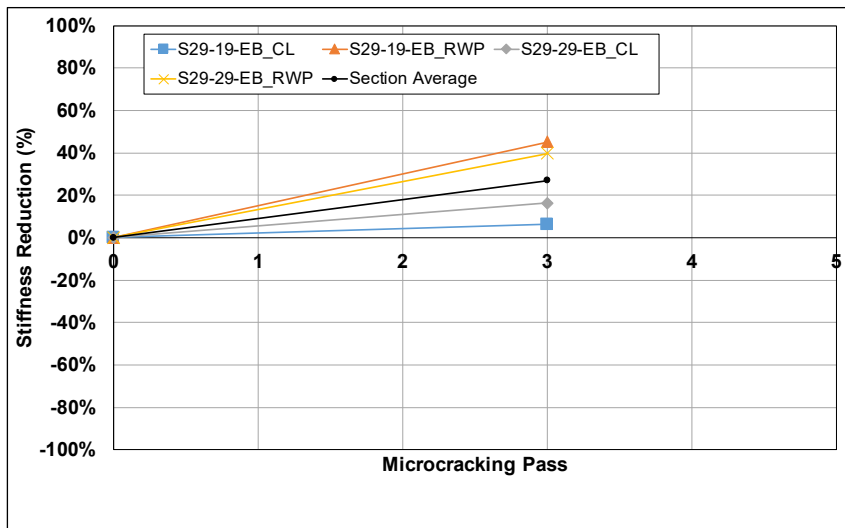**Figure B.48: Cell S7: SSG stiffness results per gauge.**
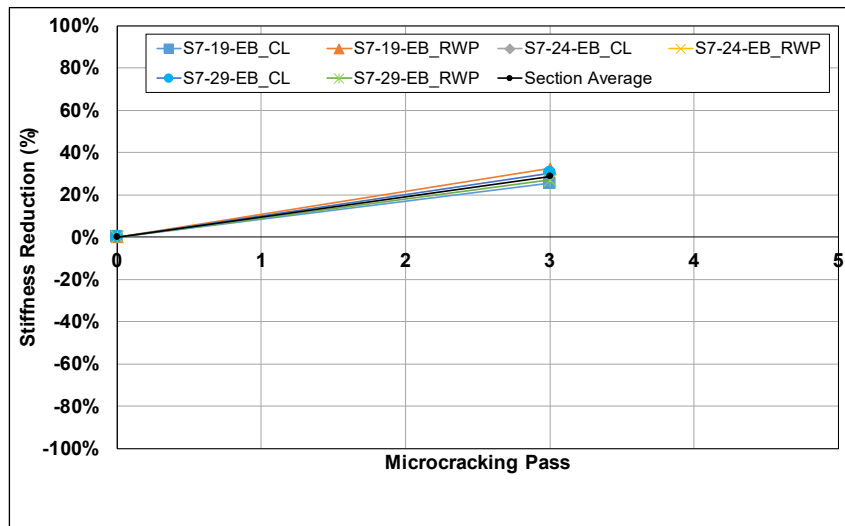
Figure B.49: Cell S7: SSG stiffness reduction per station.
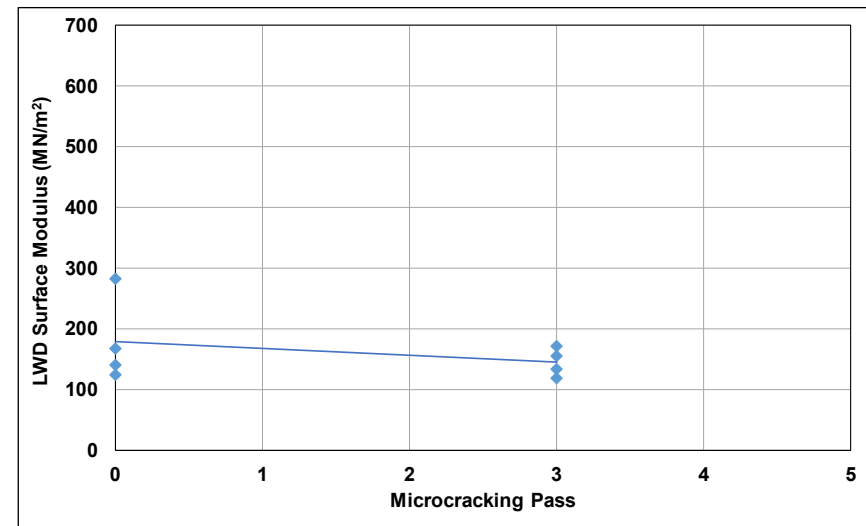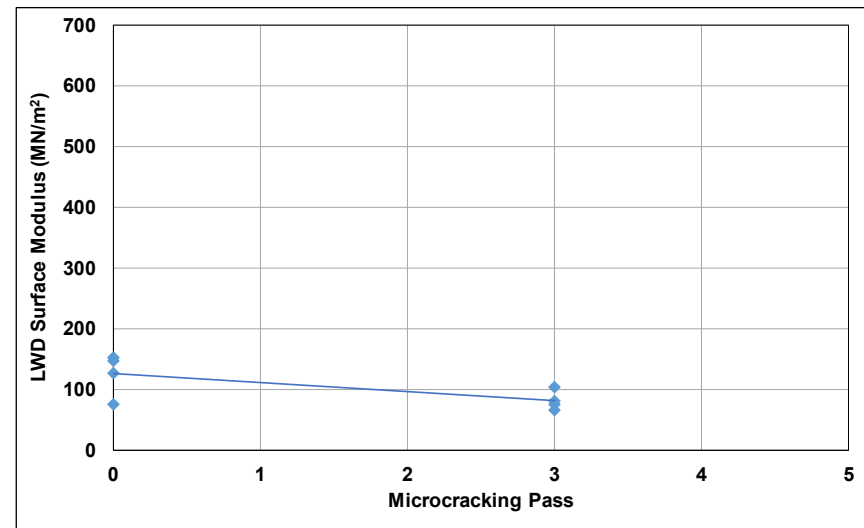

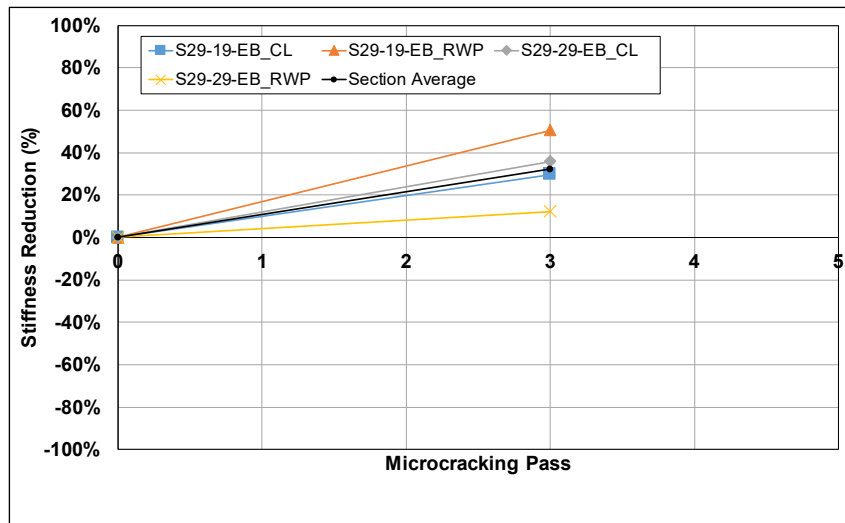**Figure B.50: Cell S7: LWD measured surface modulus.**
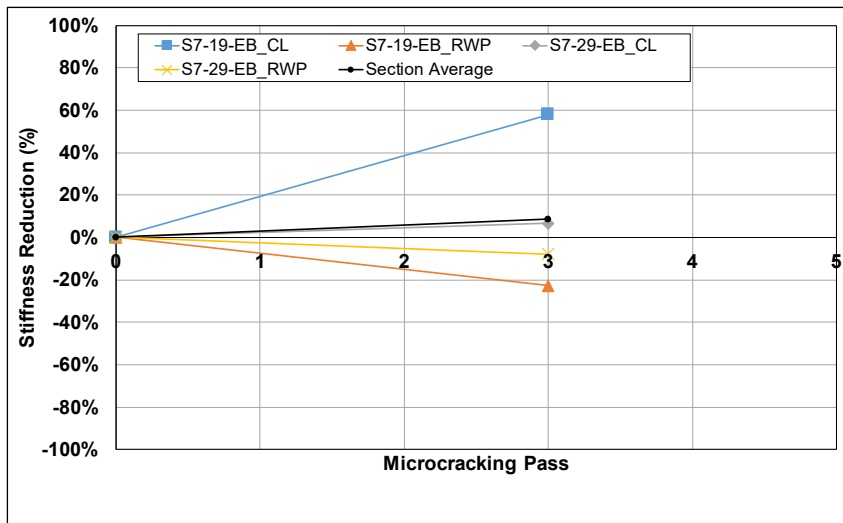
Figure B.51: Cell S7: LWD modulus reduction per station.
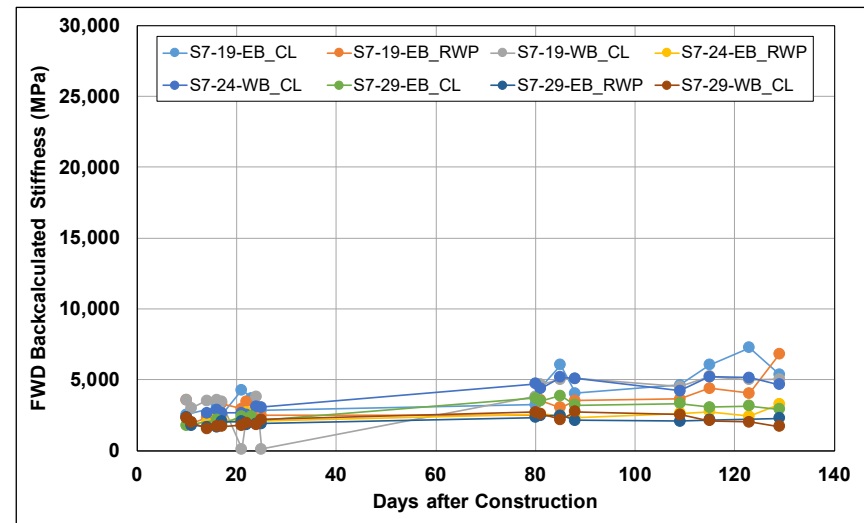
Figure B.52: Cell S7: Change in FWD-backcalculated stiffness.
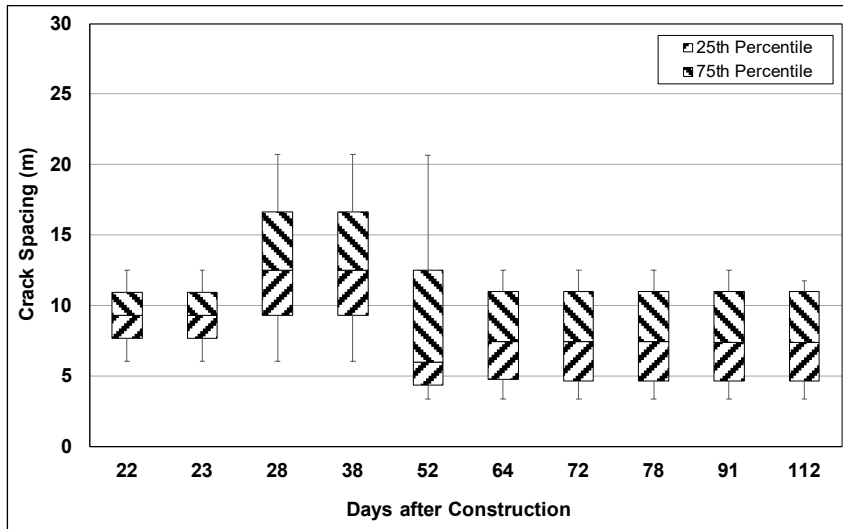
Figure B.53: Cell S7: Change in crack spacing.
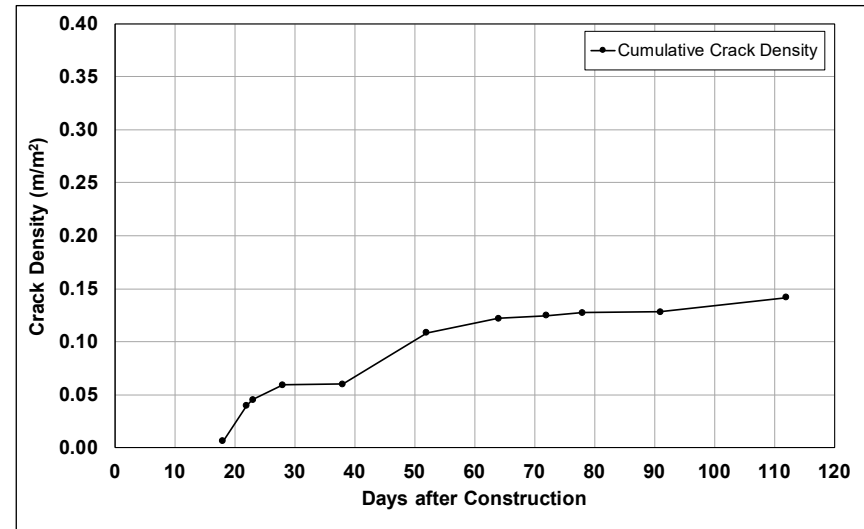
Figure B.54: Cell S7: Change in crack density.
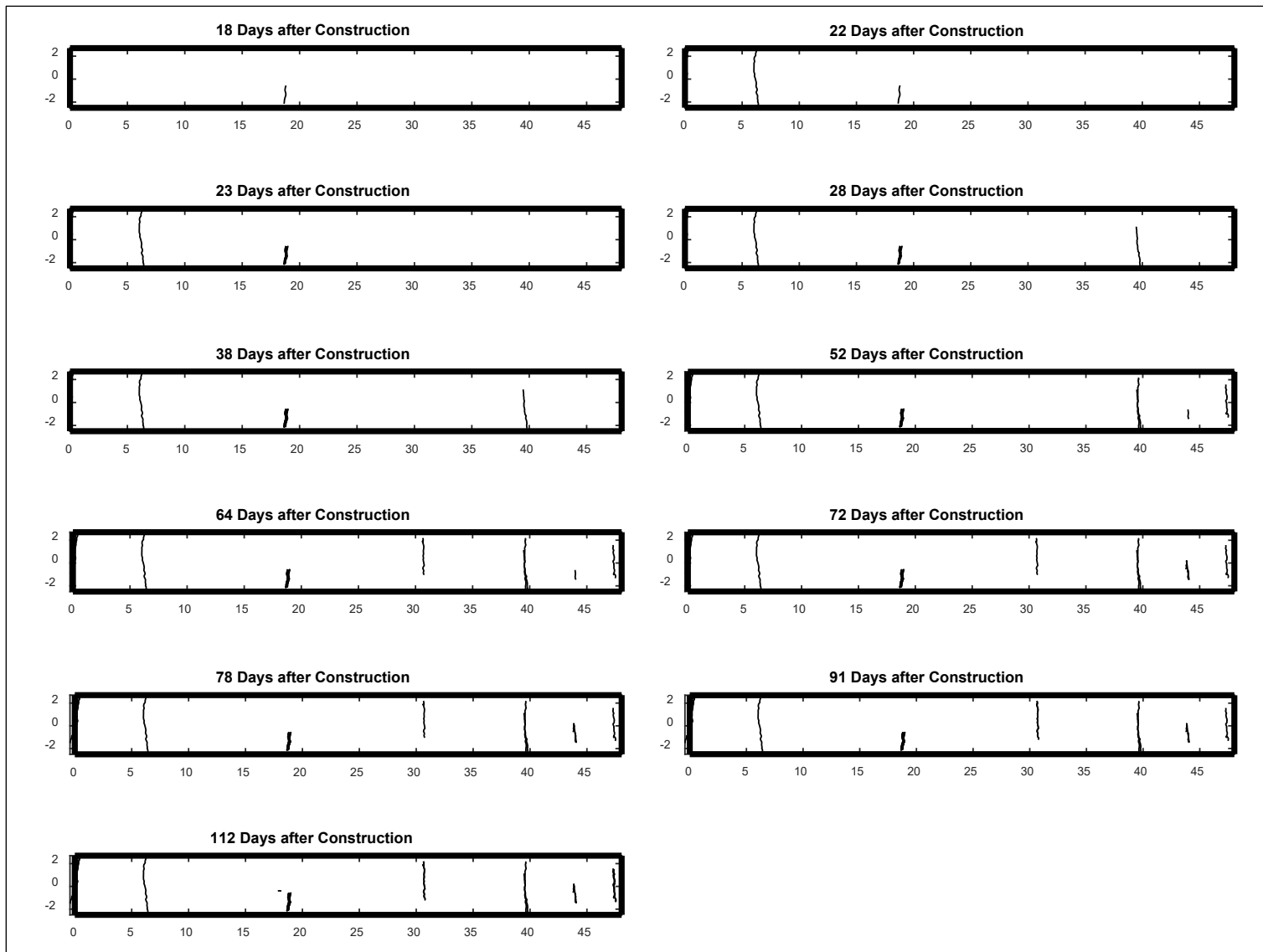
Figure B.55: Cell S7: Crack development.
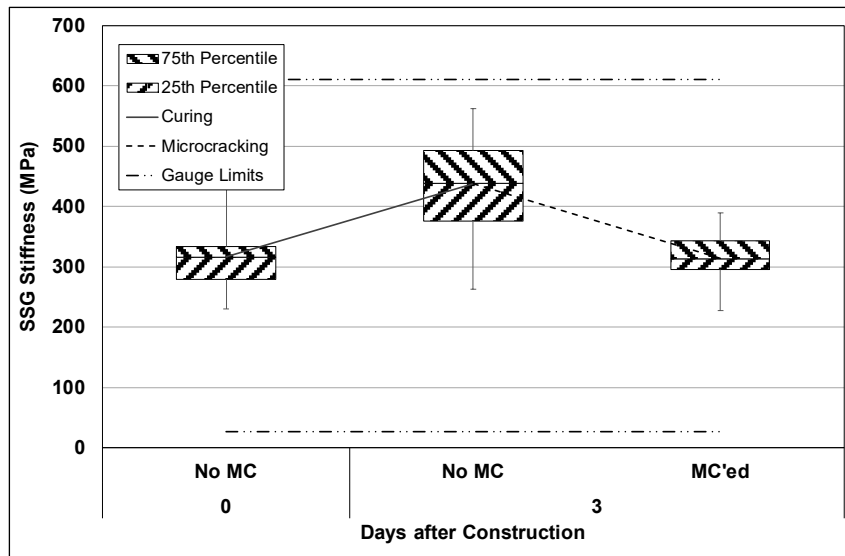
Figure B.56: Cell S8: SSG measured stiffness.
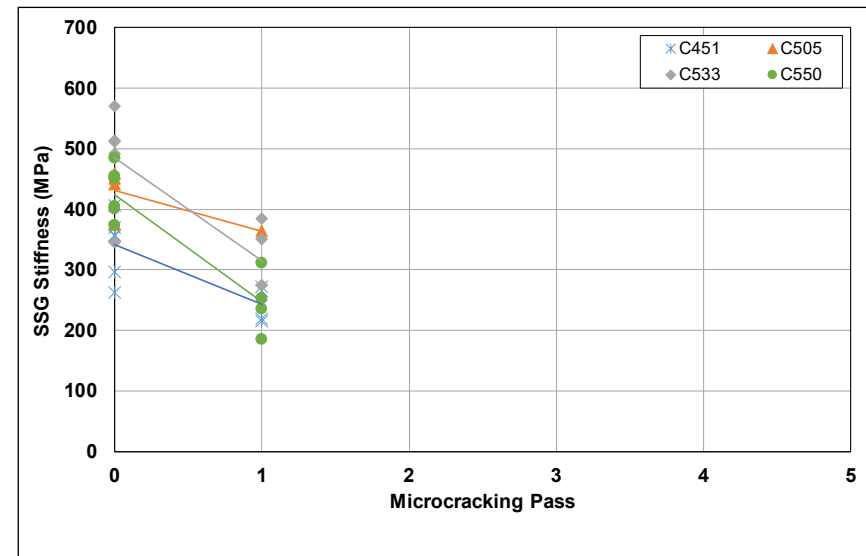
Figure B.57: Cell S8: SSG stiffness results per gauge.
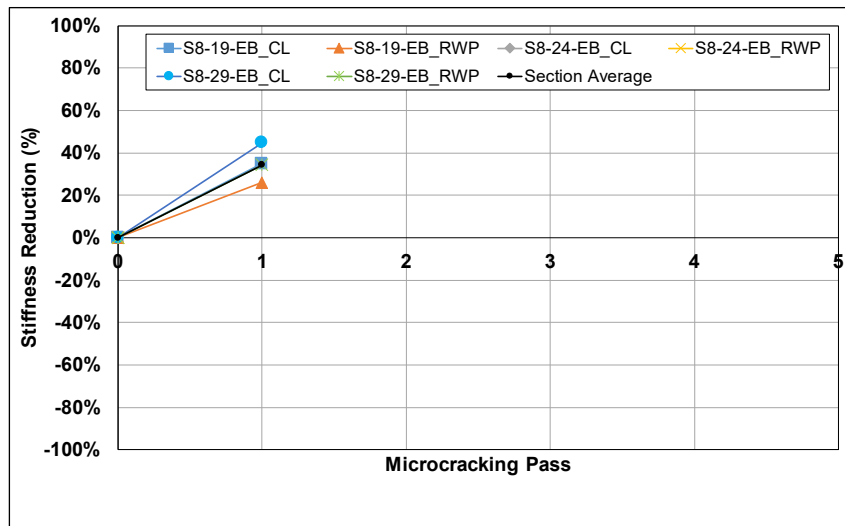
Figure B.58: Cell S8: SSG stiffness reduction per station.
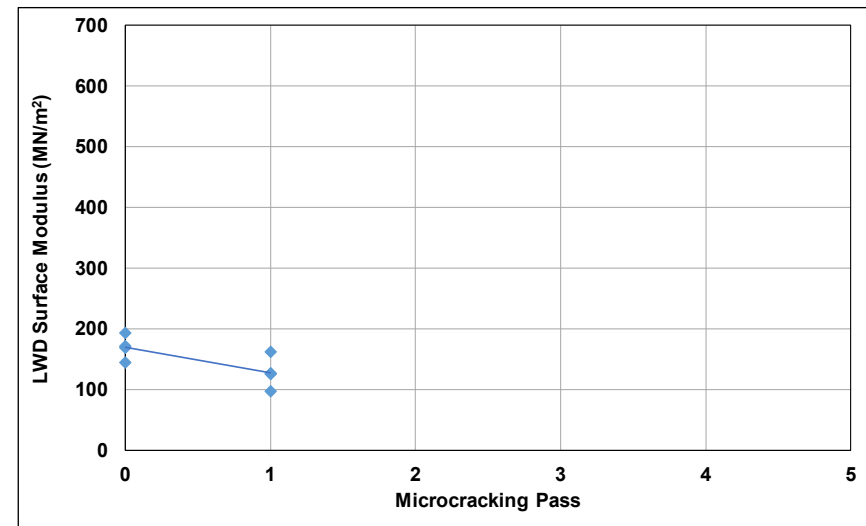
Figure B.59: Cell S8: LWD measured surface modulus.
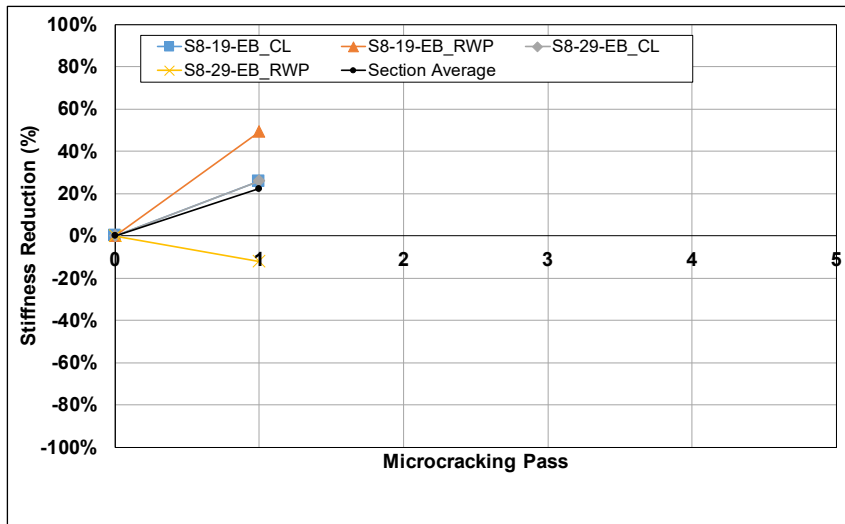
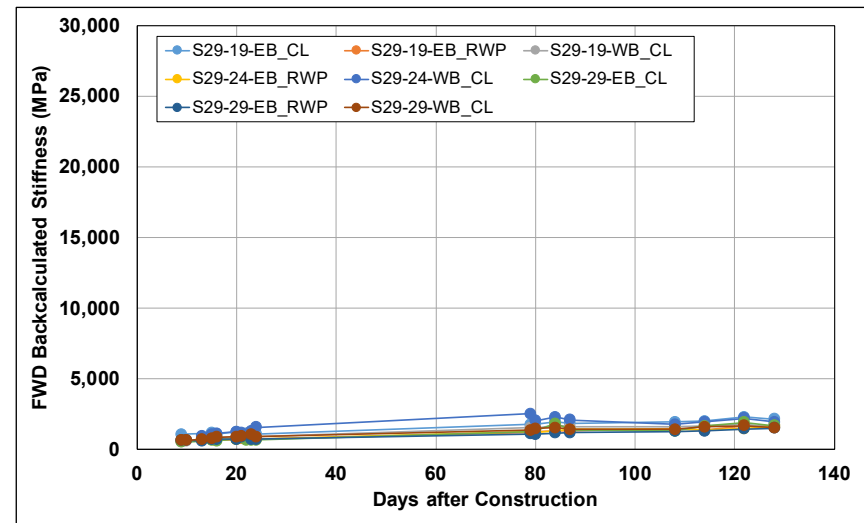**Figure B.60: Cell S8: LWD modulus reduction per station.**
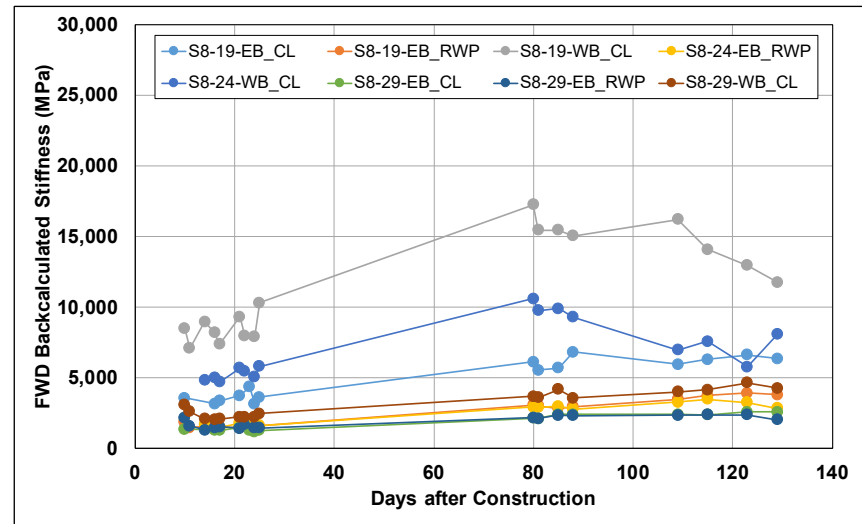
**Figure B.61: Cell S8: Change in FWD-backcalculated stiffness.**
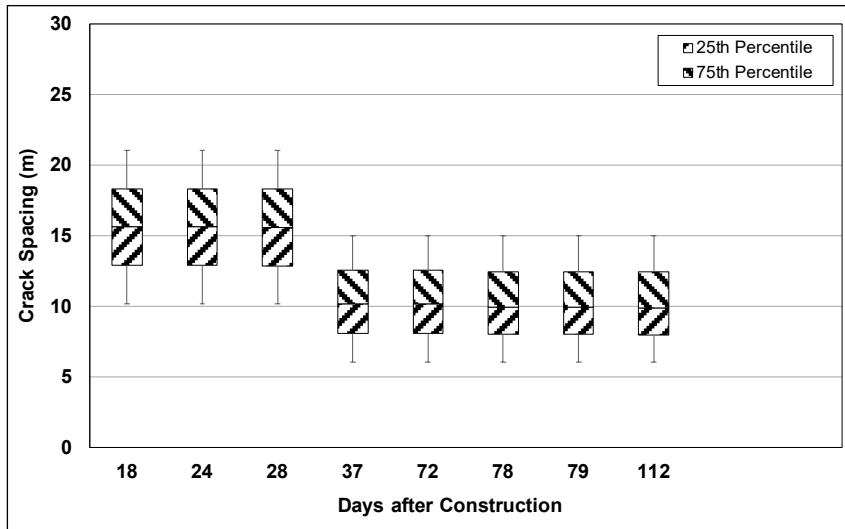
Figure B.62: Cell S8: Change in crack spacing.
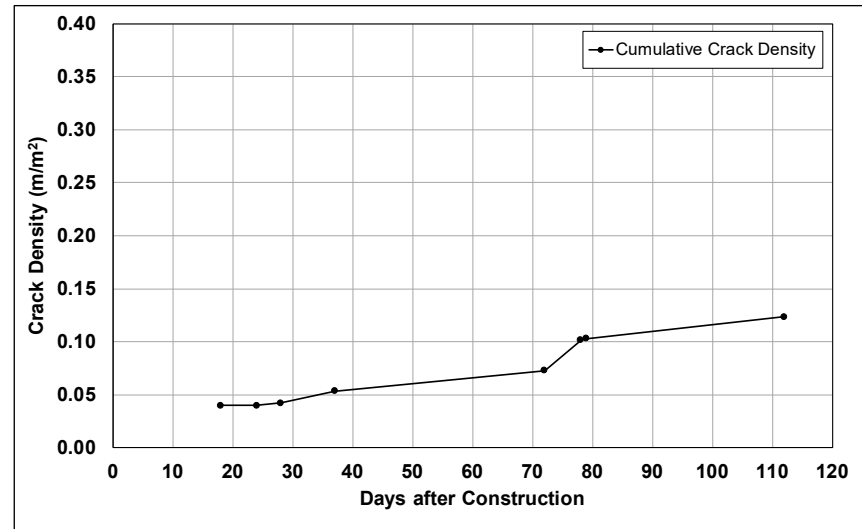
Figure B.63: Cell S8: Change in crack density.

214
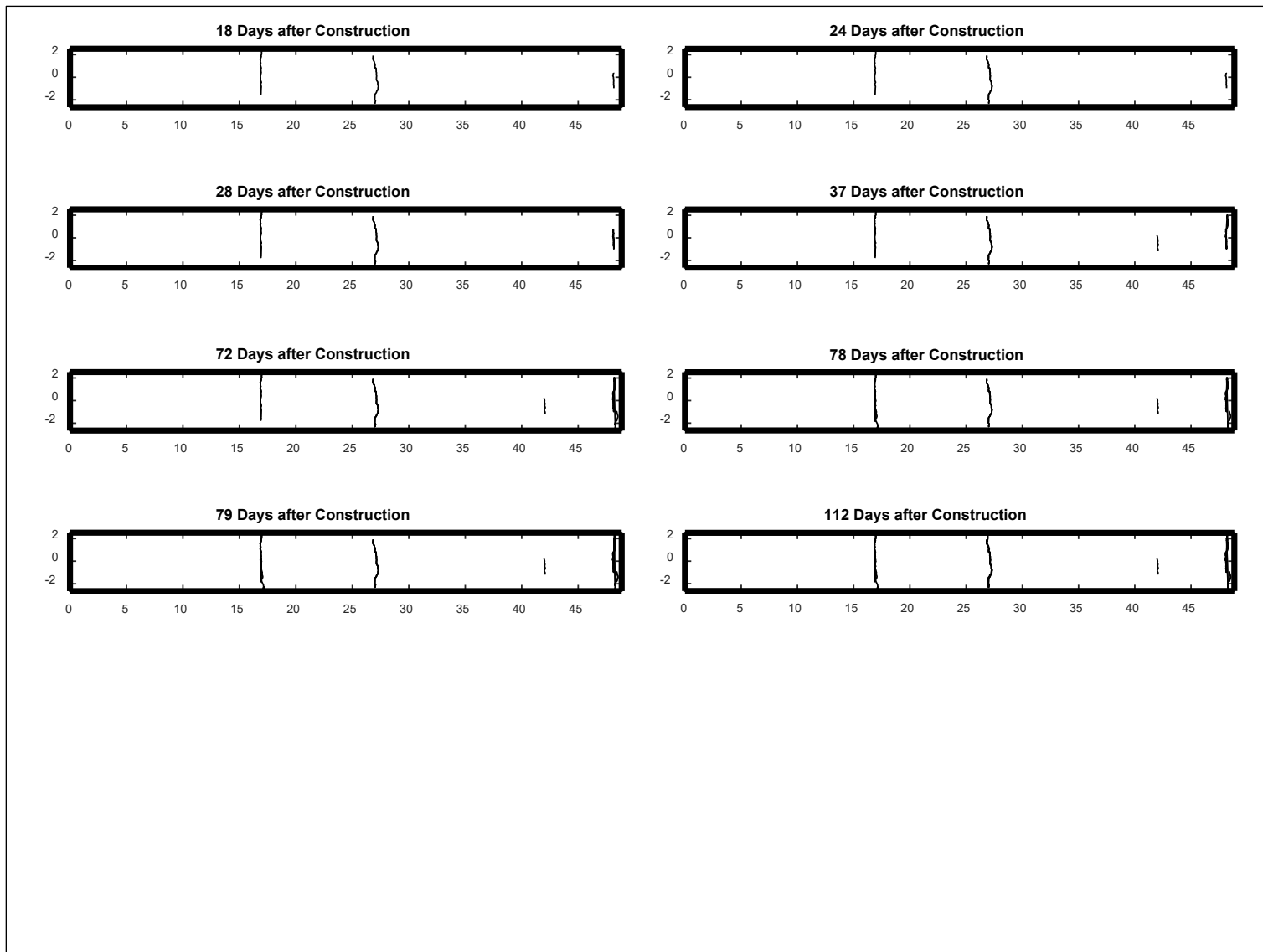
Figure B.64: Cell S8: Crack development.
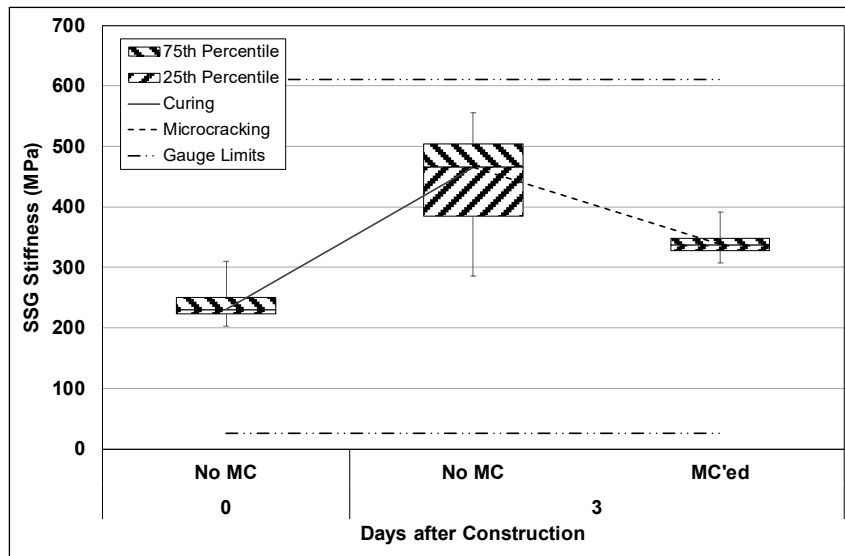
Figure B.65: Cell S9: SSG measured stiffness.
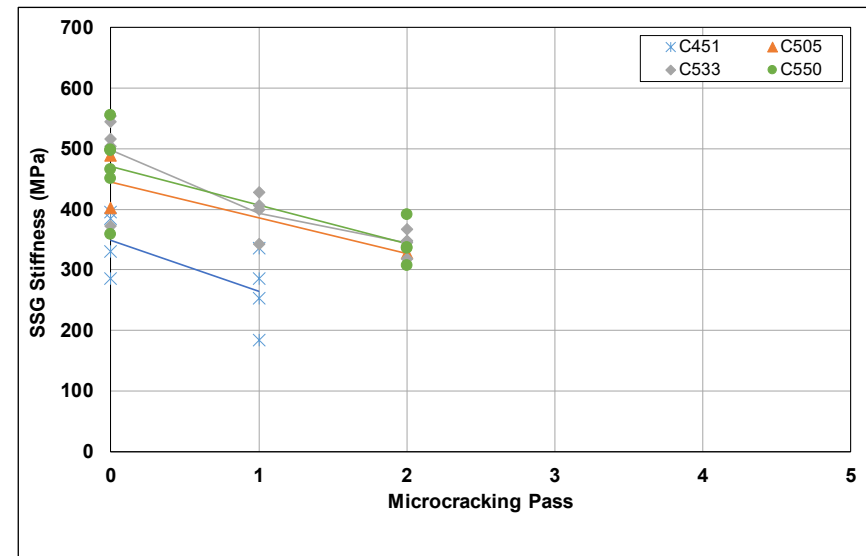
Figure B.66: Cell S9: SSG stiffness results per gauge.
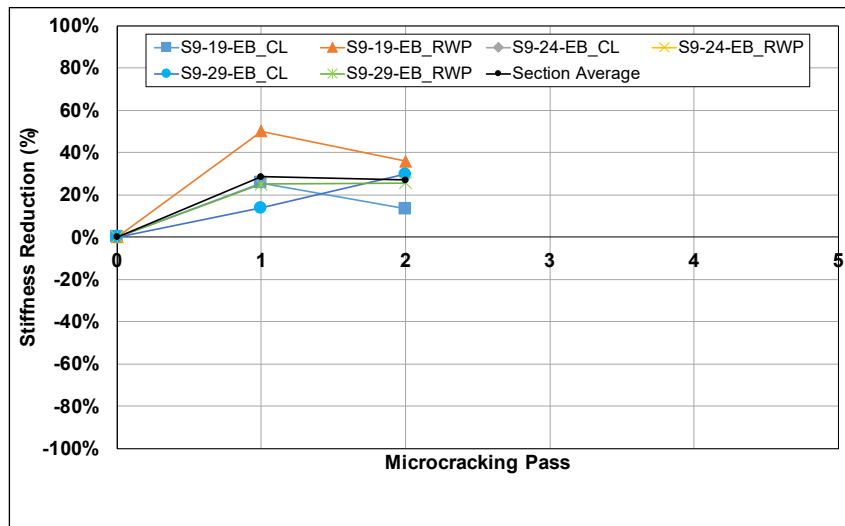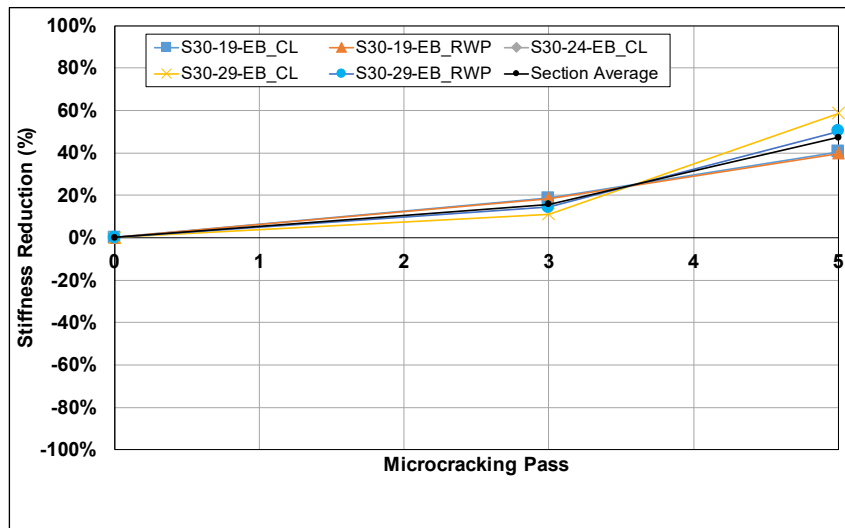

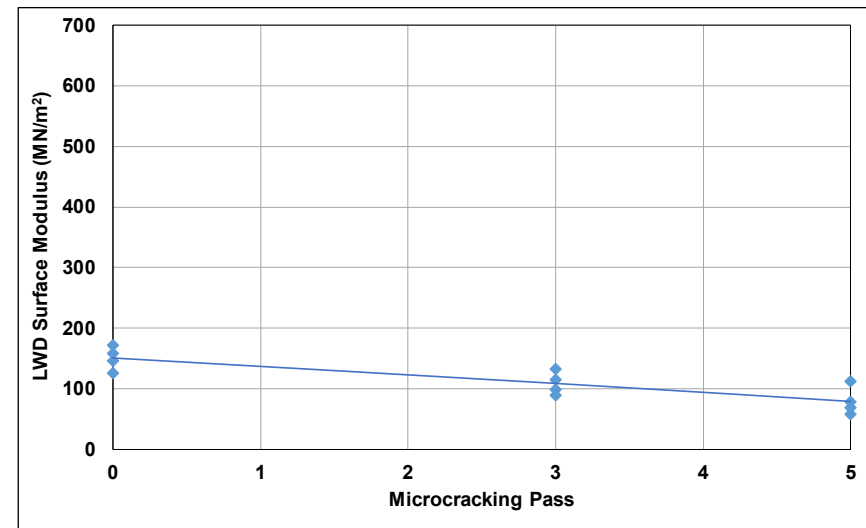**Figure B.67: Cell S9: SSG stiffness reduction per station.**
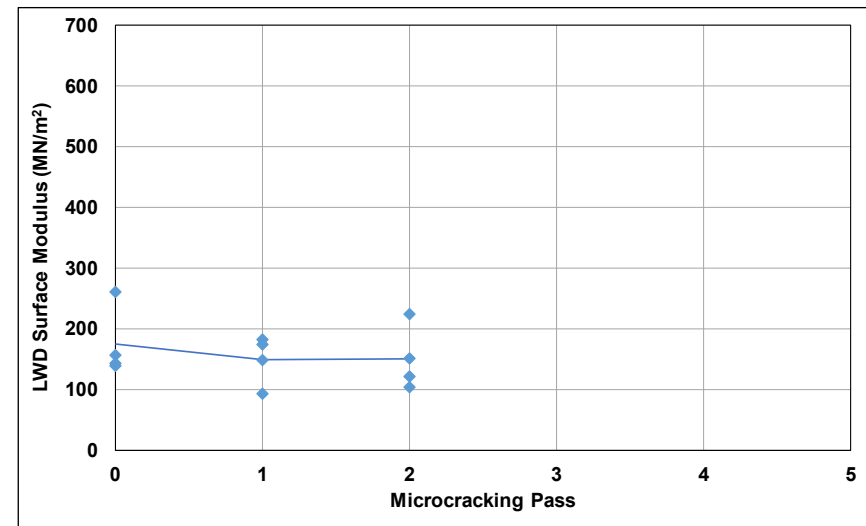
Figure B.68: Cell S9: LWD measured surface modulus.
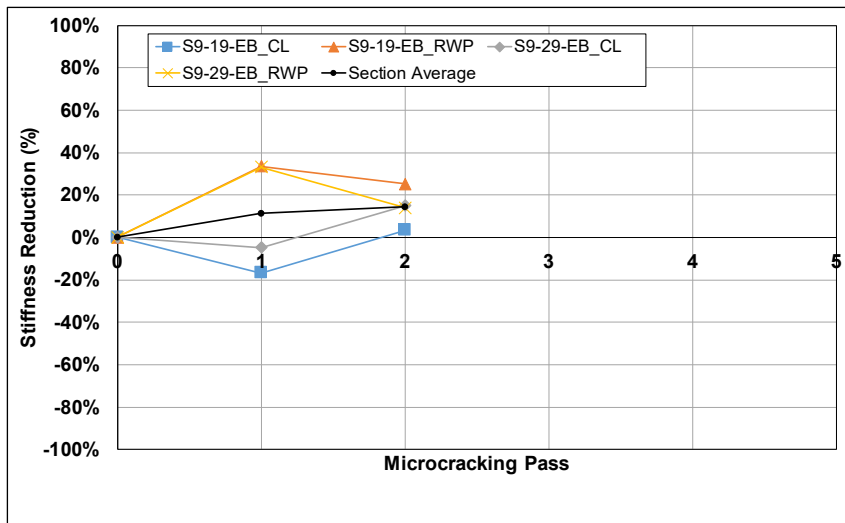
Figure B.69: Cell S9: LWD modulus reduction per station.
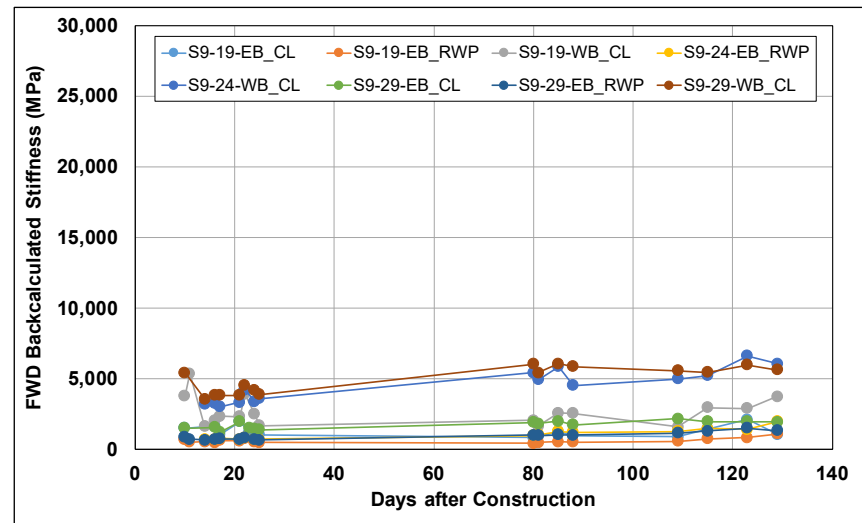
Figure B.70: Cell S9: Change in FWD-backcalculated stiffness.
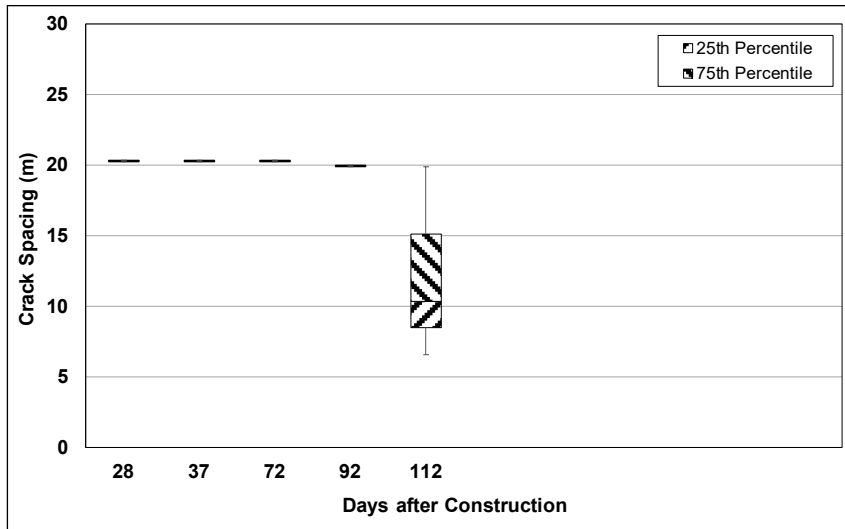
Figure B.71: Cell S9: Change in crack spacing.
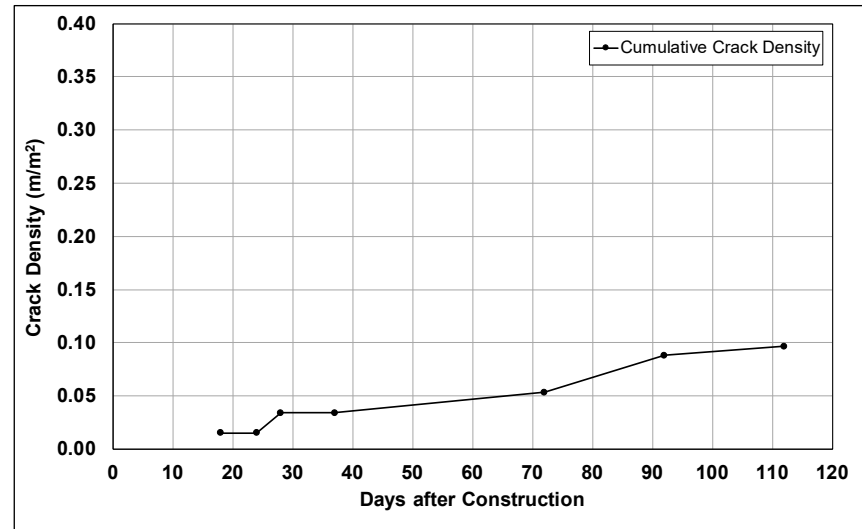
Figure B.72: Cell S9: Change in crack density.
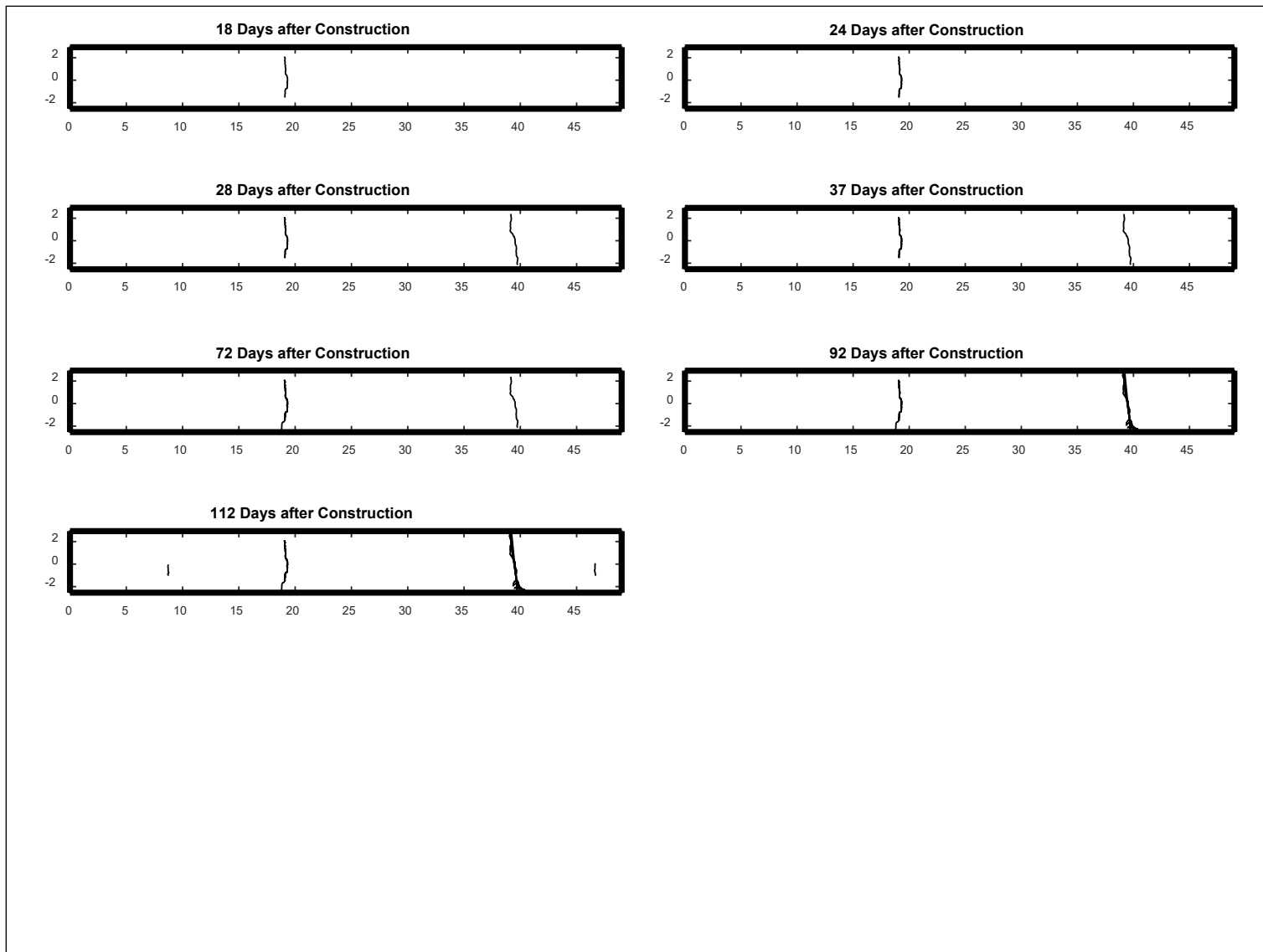
Figure B.73: Cell S9: Crack development.
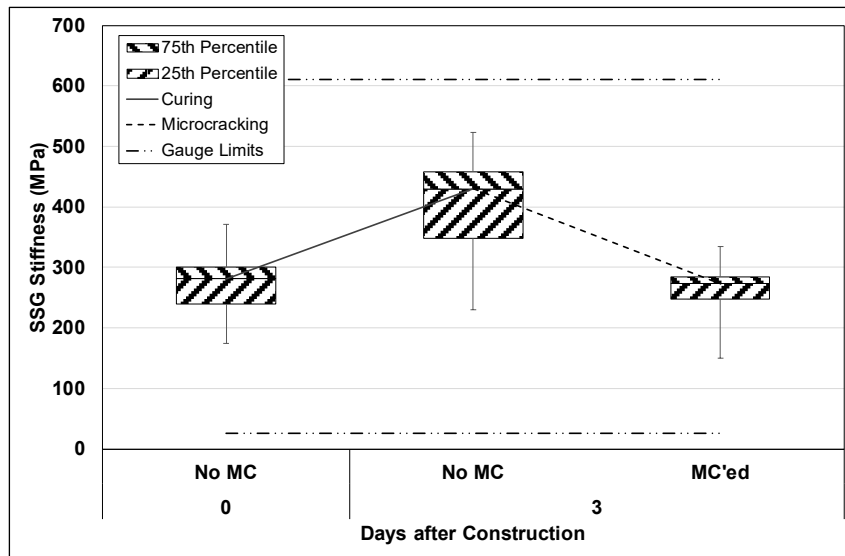
Figure B.74: Cell S10: SSG measured stiffness.
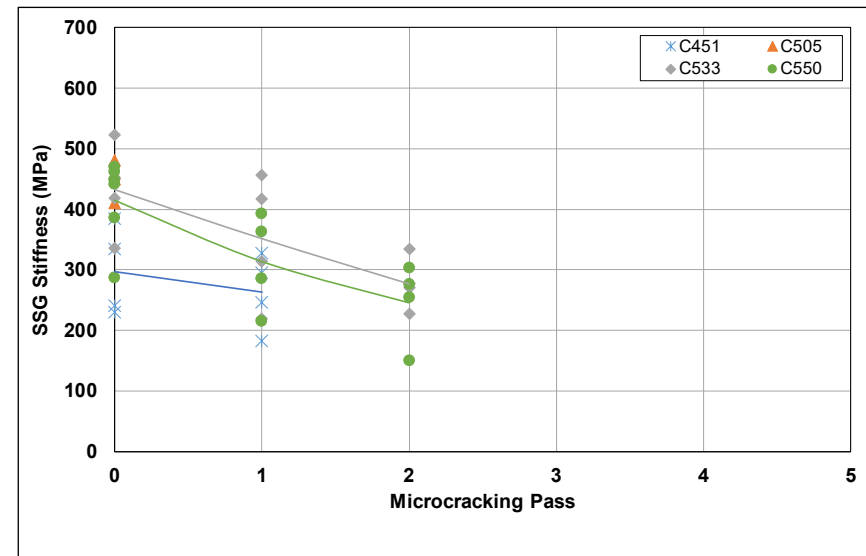
Figure B.75: Cell S10: SSG stiffness results per gauge.
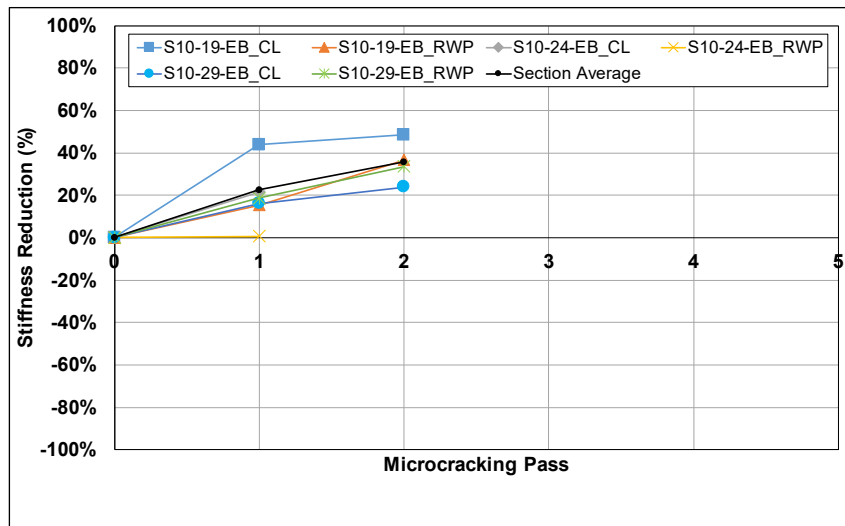
Figure B.76: Cell S10: SSG stiffness reduction per station.
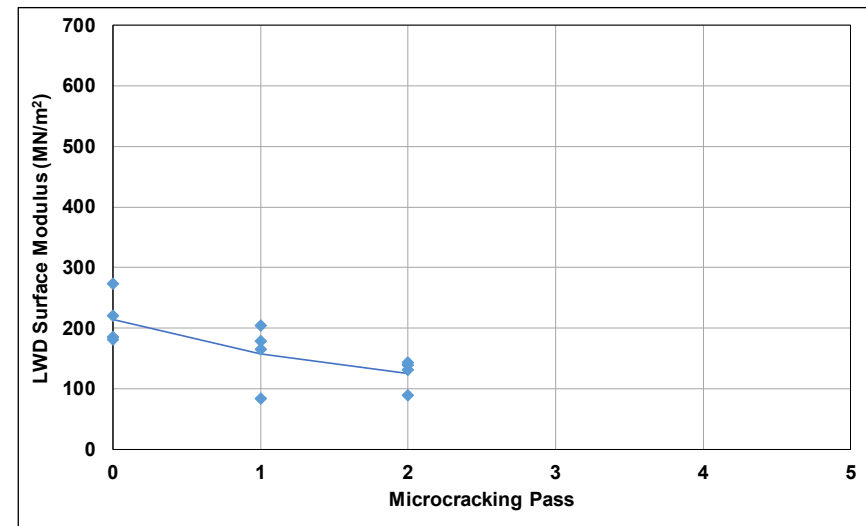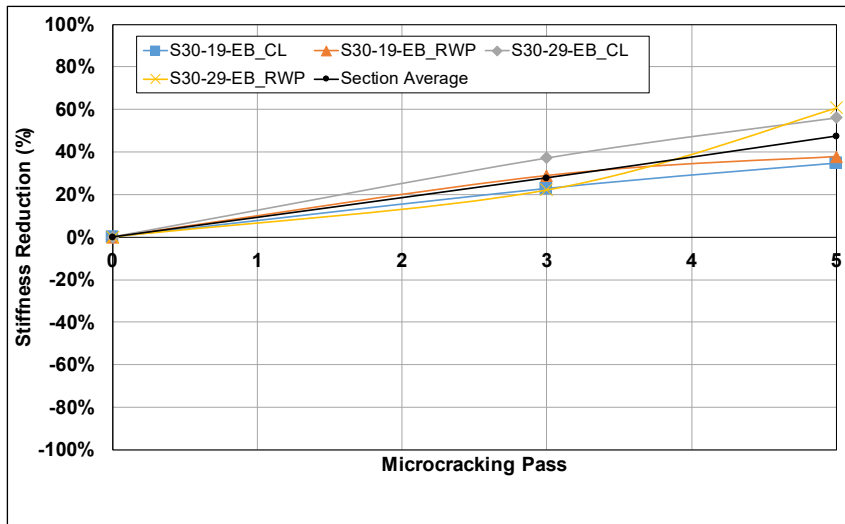

Figure B.77: Cell S10: LWD measured surface modulus.
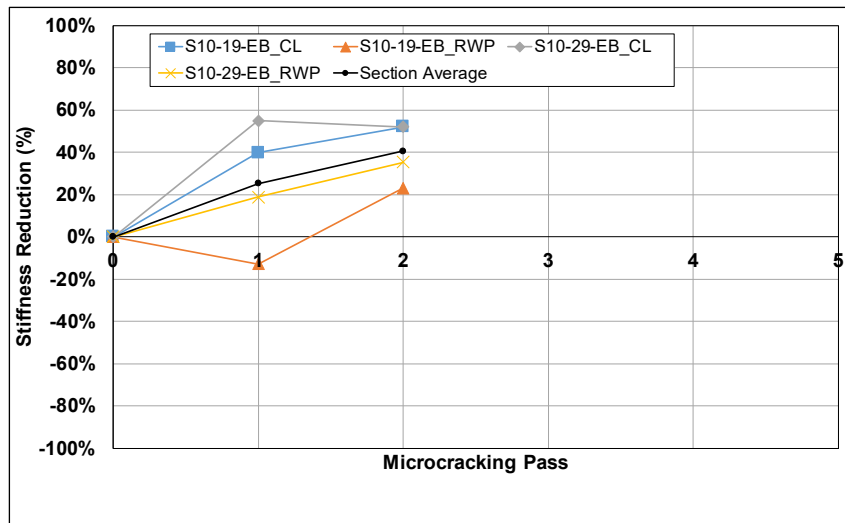
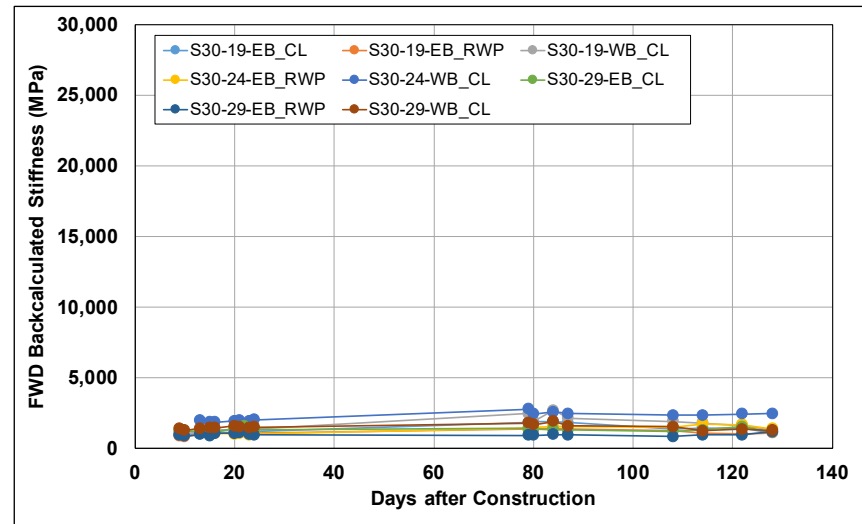**Figure B.78: Cell S10: LWD modulus reduction per station.**
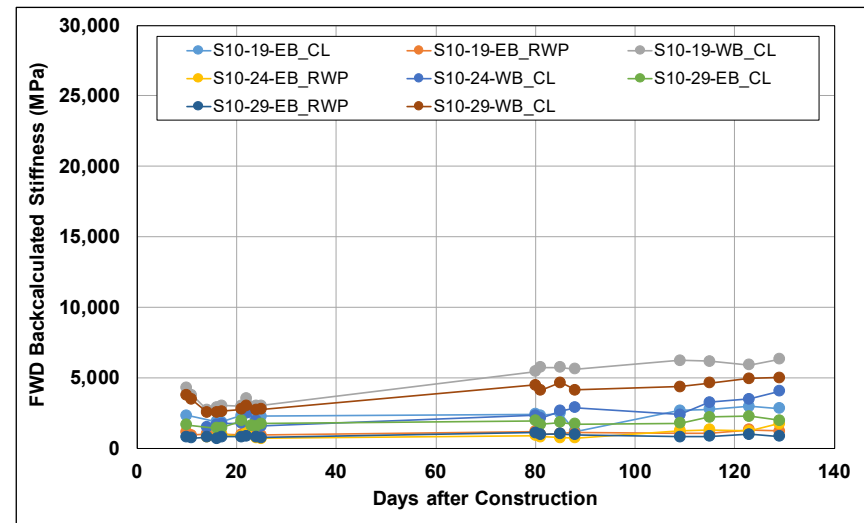
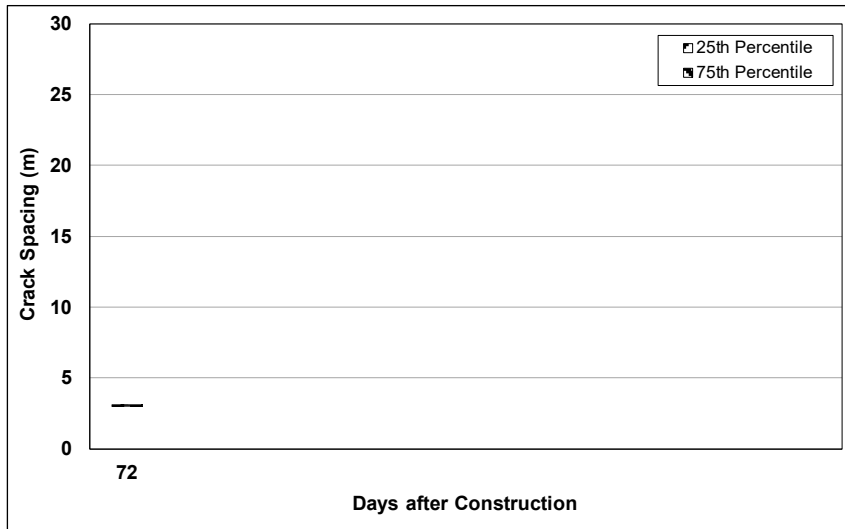**Figure B.79: Cell S10: Change in FWD-backcalculated stiffness.**
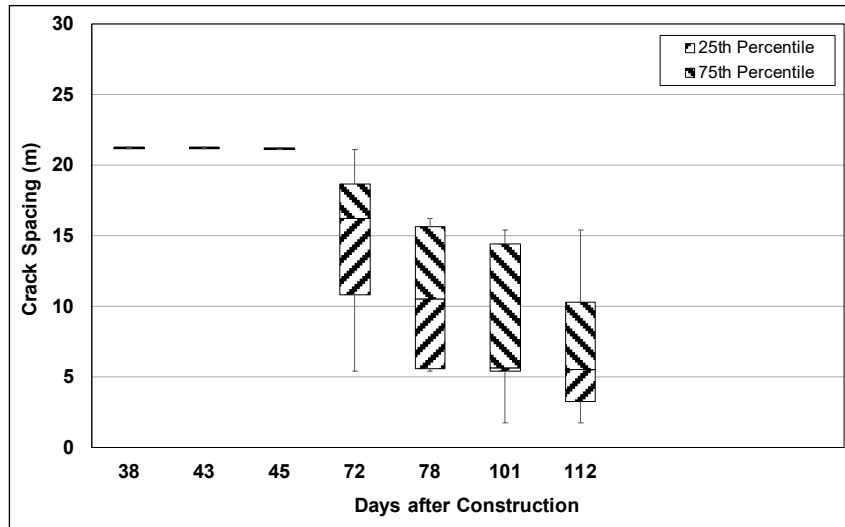
**Figure B.80: Cell S10: Change in crack spacing.**
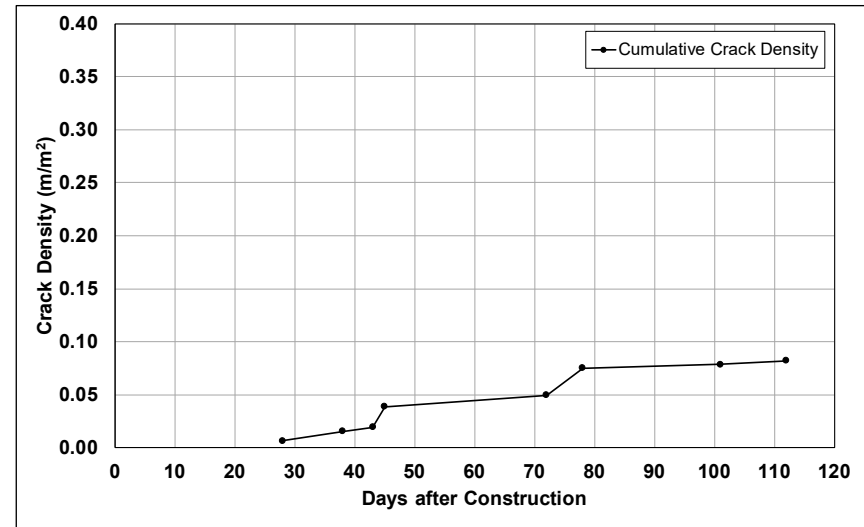
**Figure B.81: Cell S10: Change in crack density.**
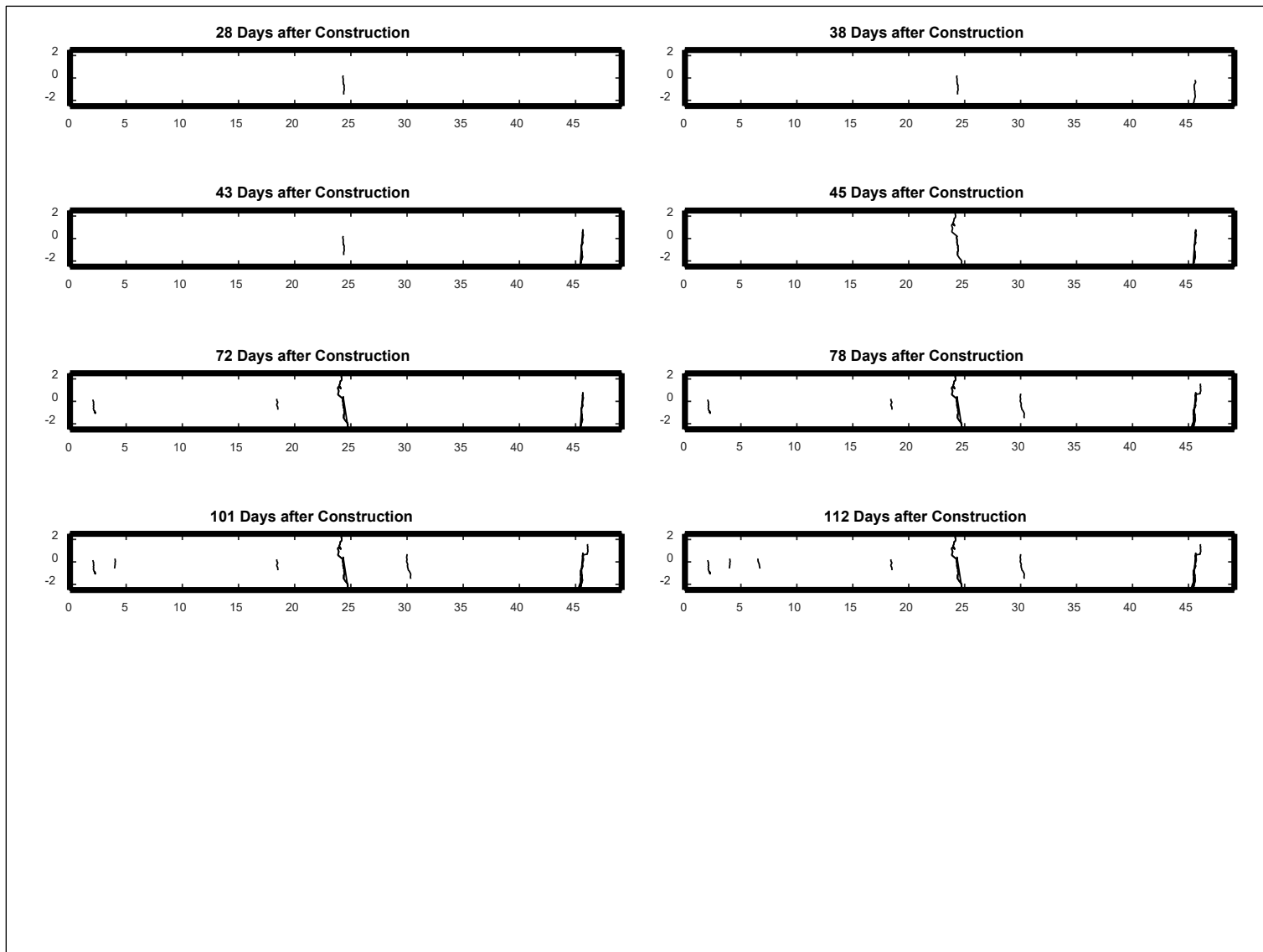
**Figure B.82: Cell S10: Crack development.**
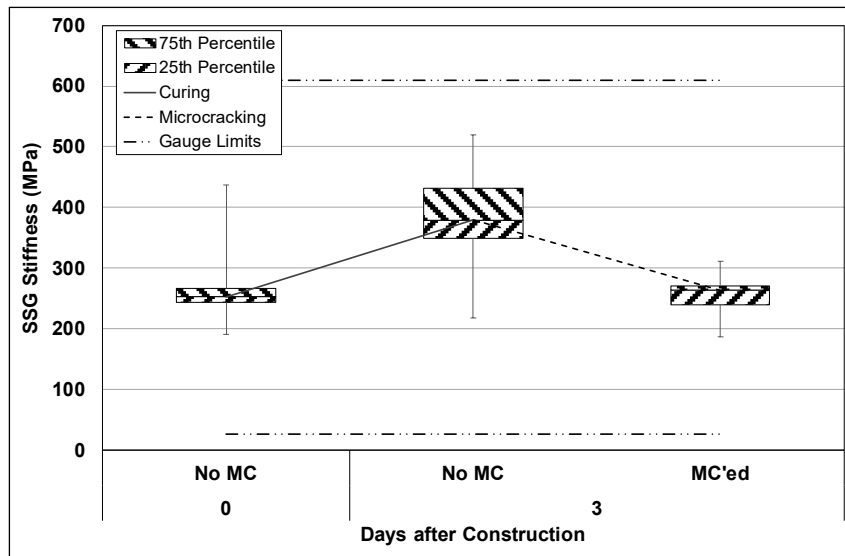
Figure B.83: Cell S11: SSG measured stiffness.
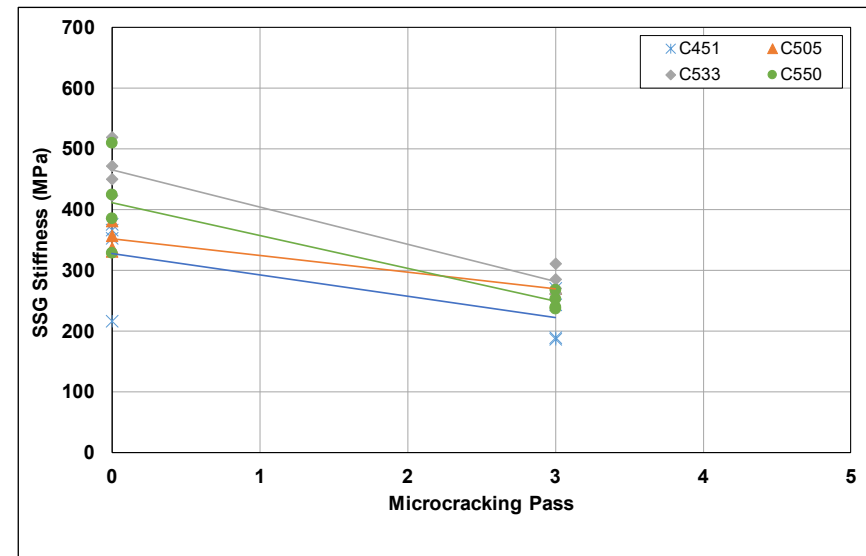
Figure B.84: Cell S11: SSG stiffness results per gauge.
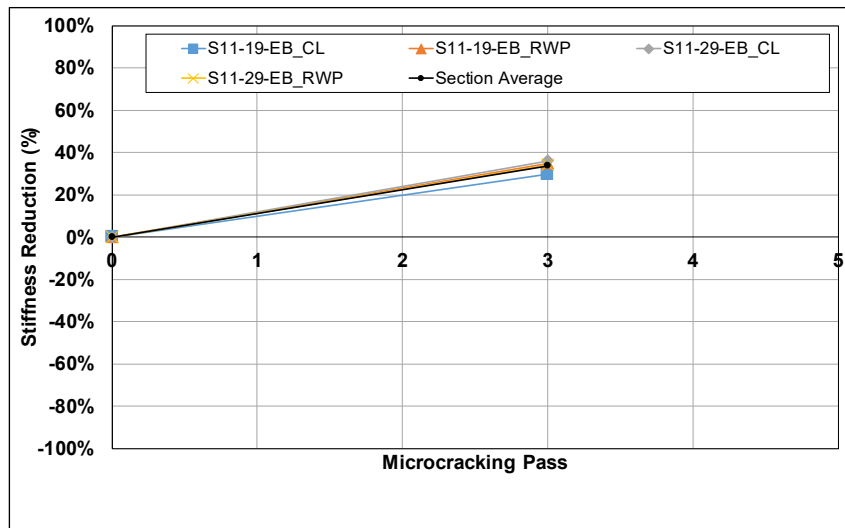
Figure B.85: Cell S11: SSG stiffness reduction per station.
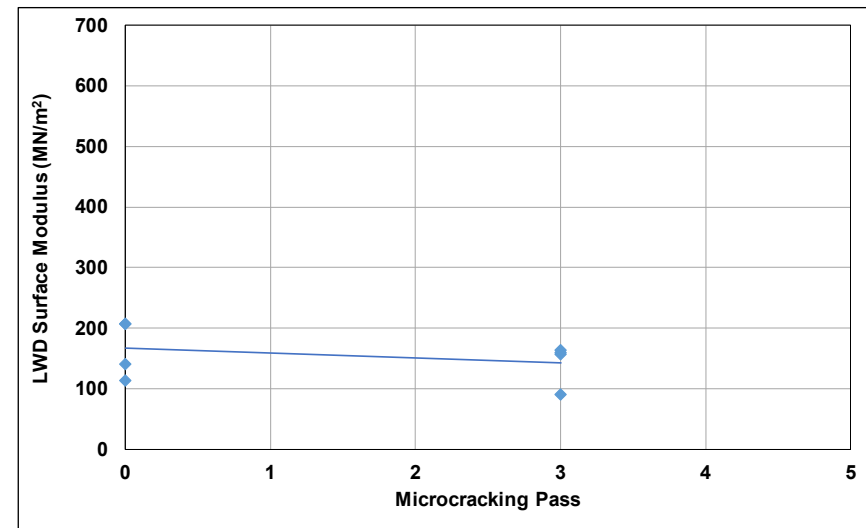
Figure B.86: Cell S11: LWD measured surface modulus.
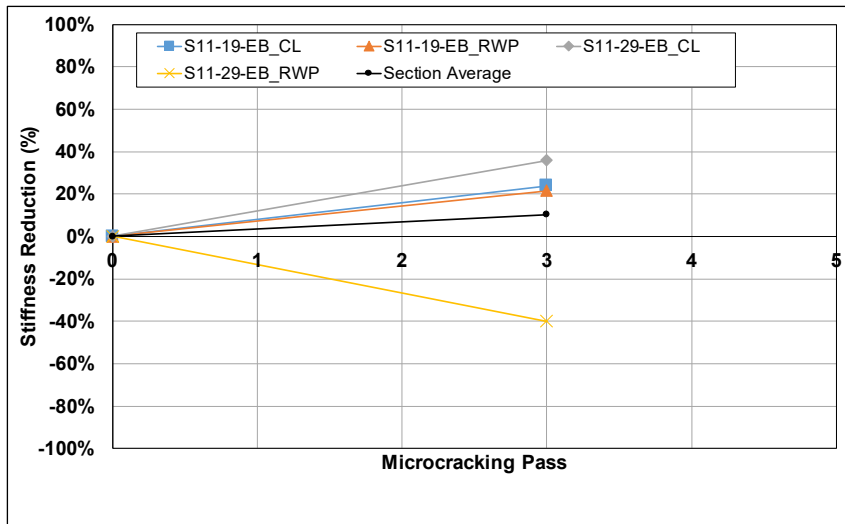
Figure B.87: Cell S11: LWD modulus reduction per station.
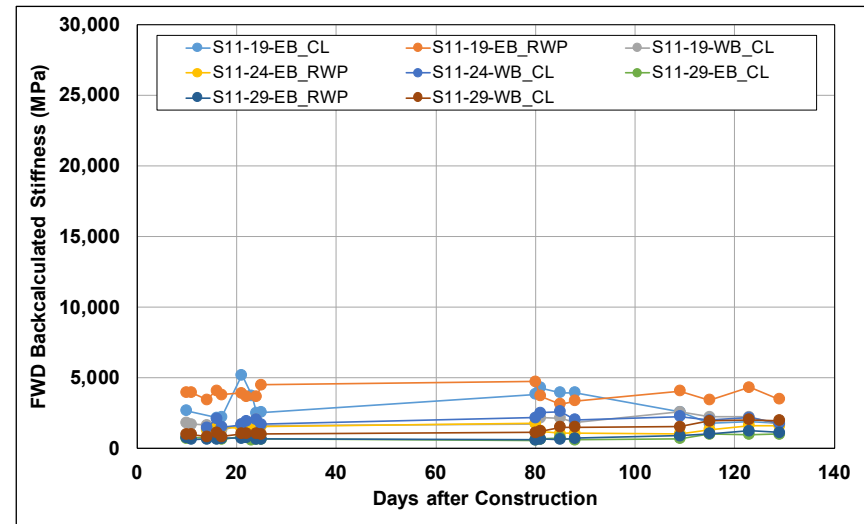
Figure B.88: Cell S11: Change in FWD-backcalculated stiffness.
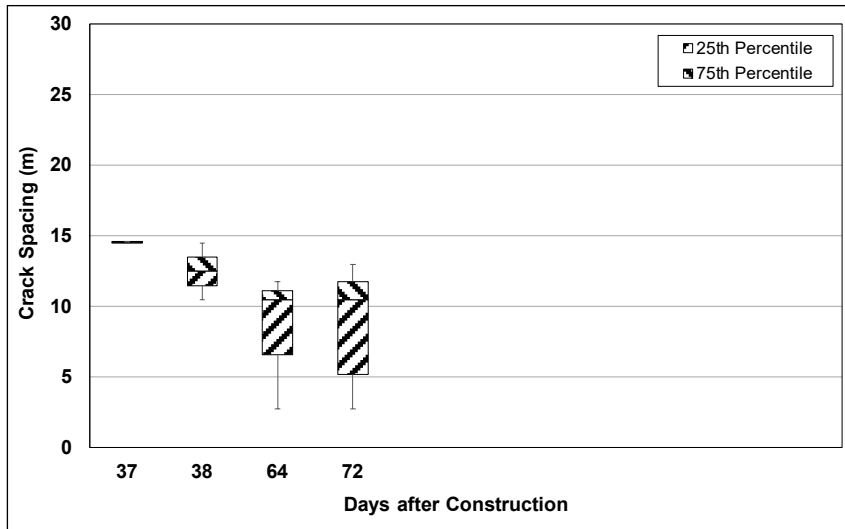
Figure B.89: Cell S11: Change in crack spacing.
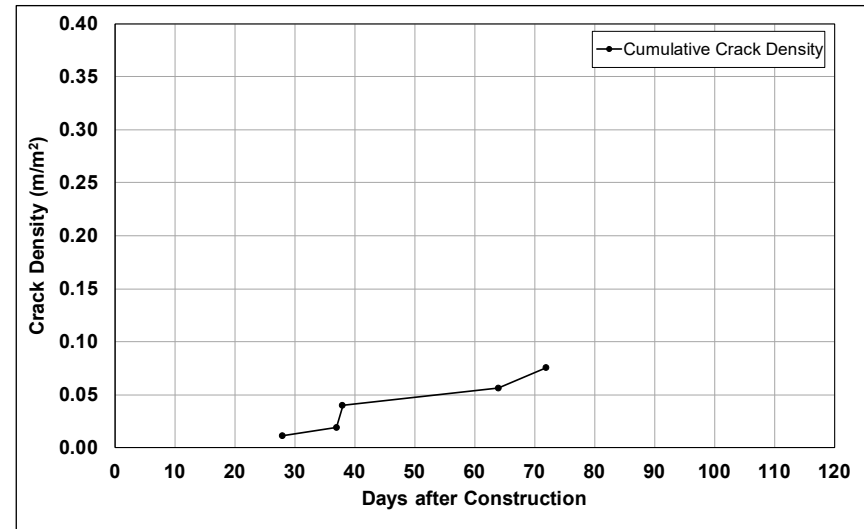
Figure B.90: Cell S11: Change in crack density.
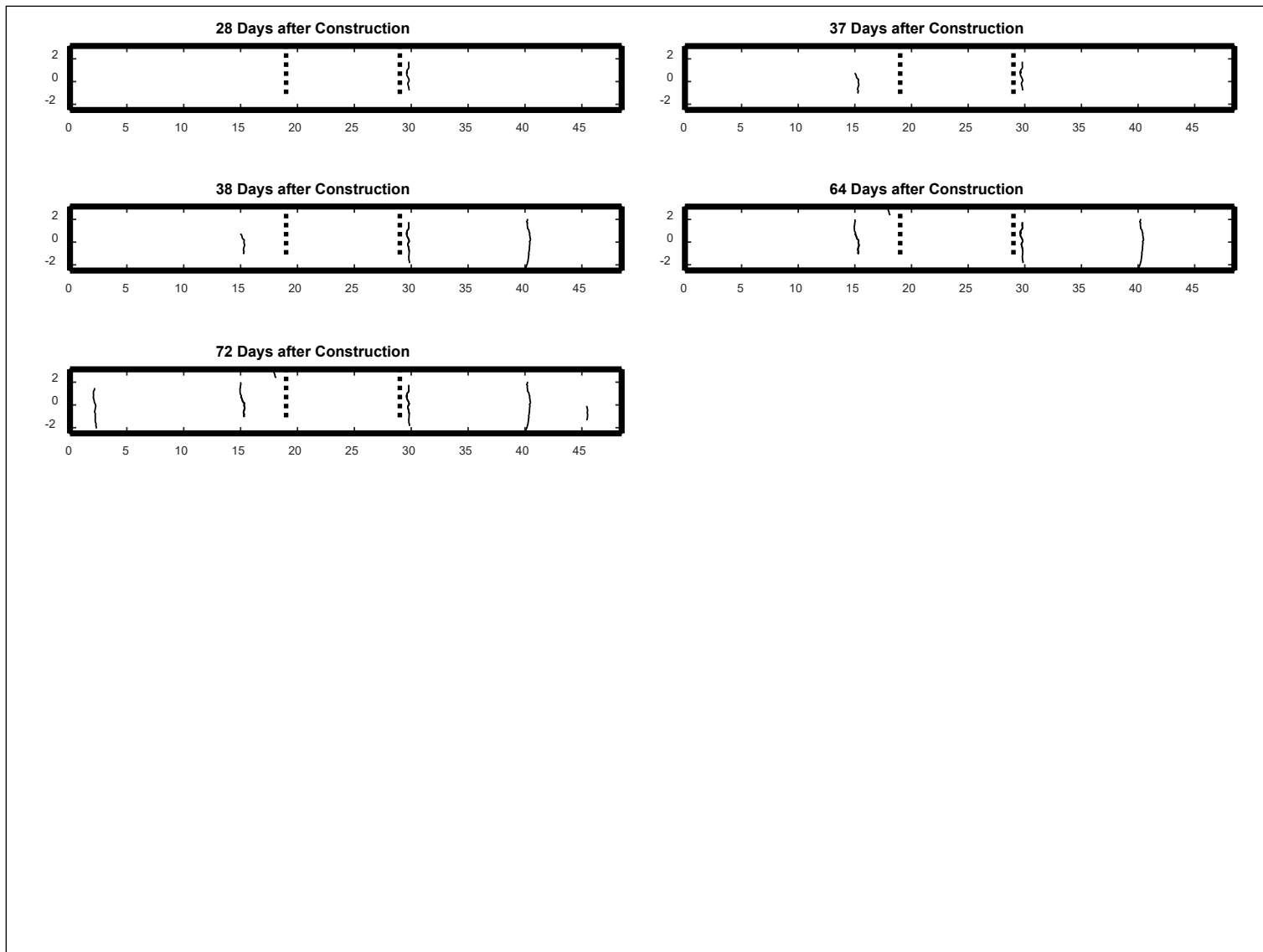
Figure B.91: Cell S11: Crack development.
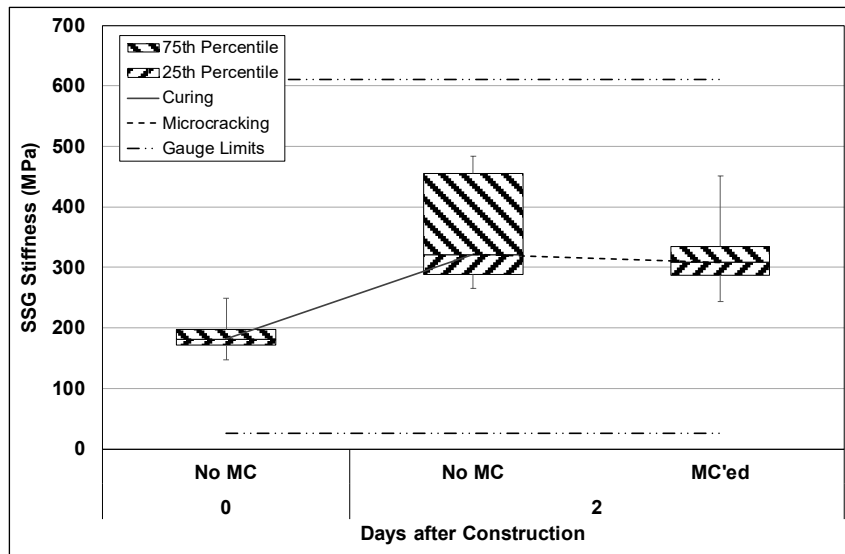
Figure B.92: Cell S12: SSG measured stiffness.
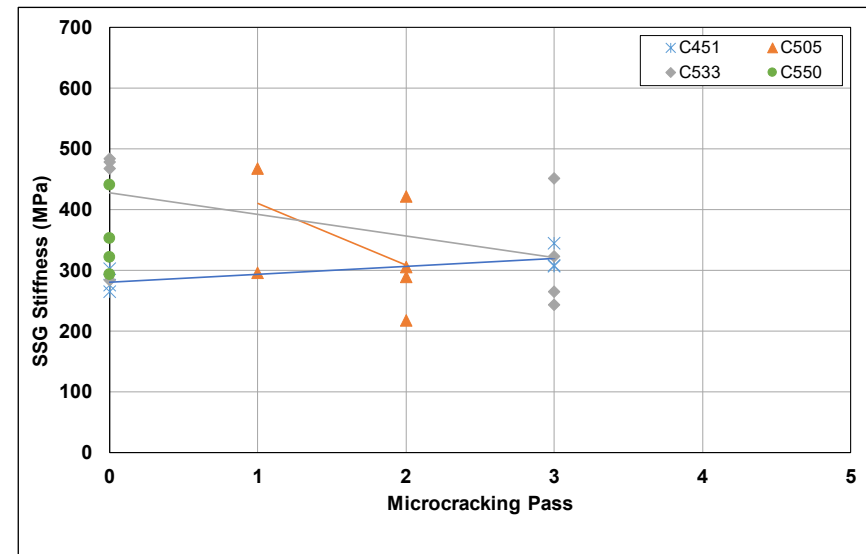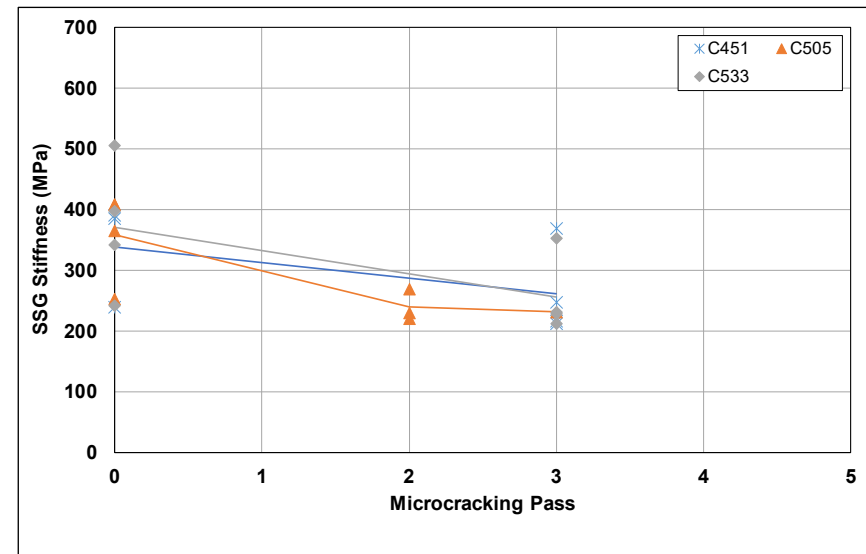

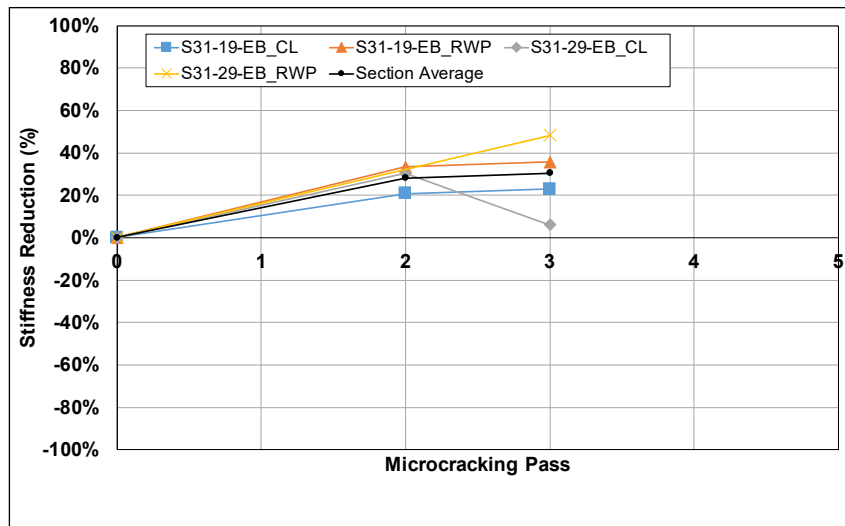**Figure B.93: Cell S12: SSG stiffness results per gauge.**
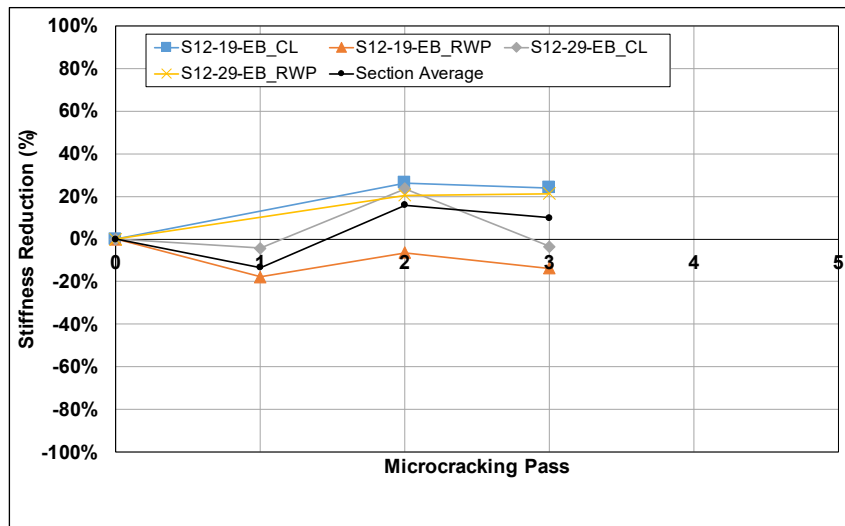
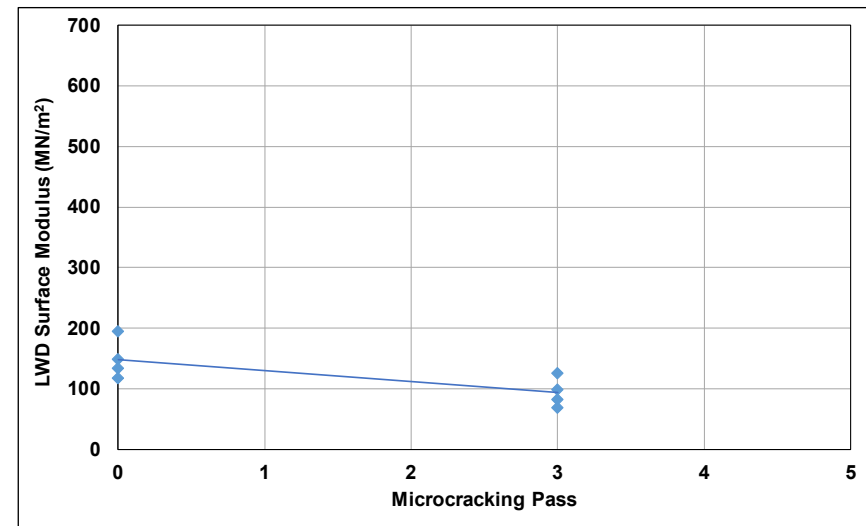**Figure B.94: Cell S12: SSG stiffness reduction per station.**
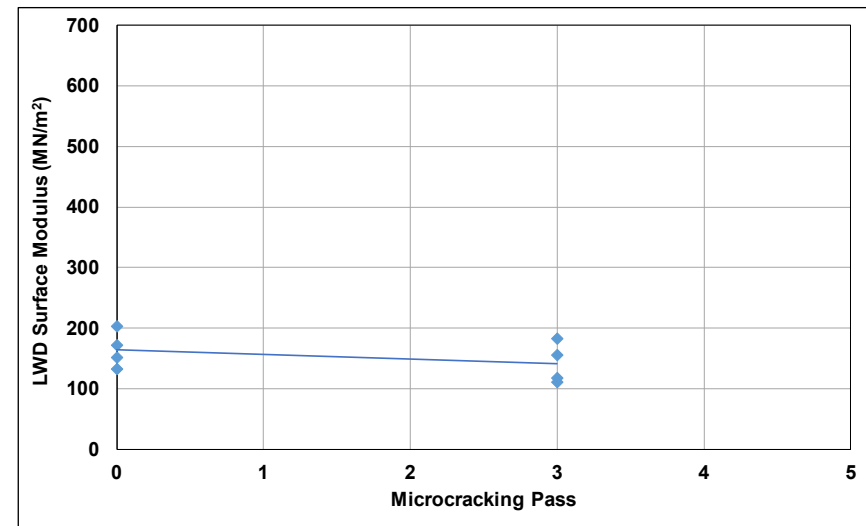
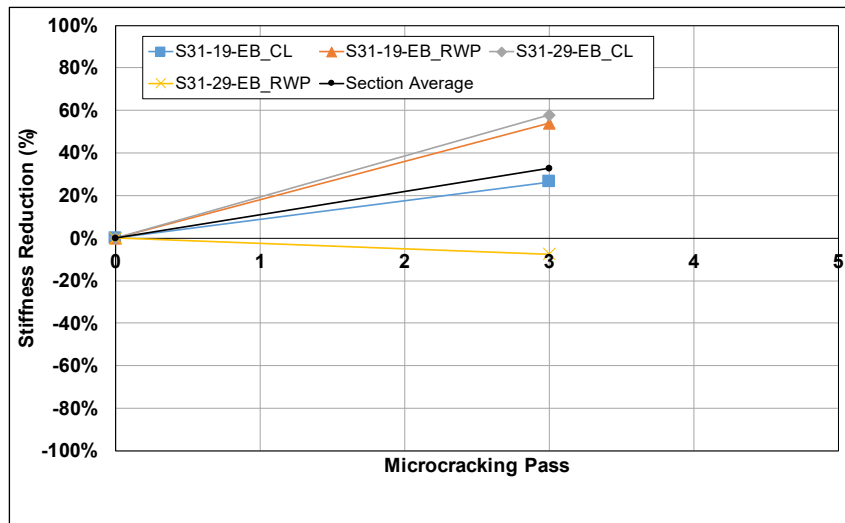**Figure B.95: Cell S12: LWD measured surface modulus.**
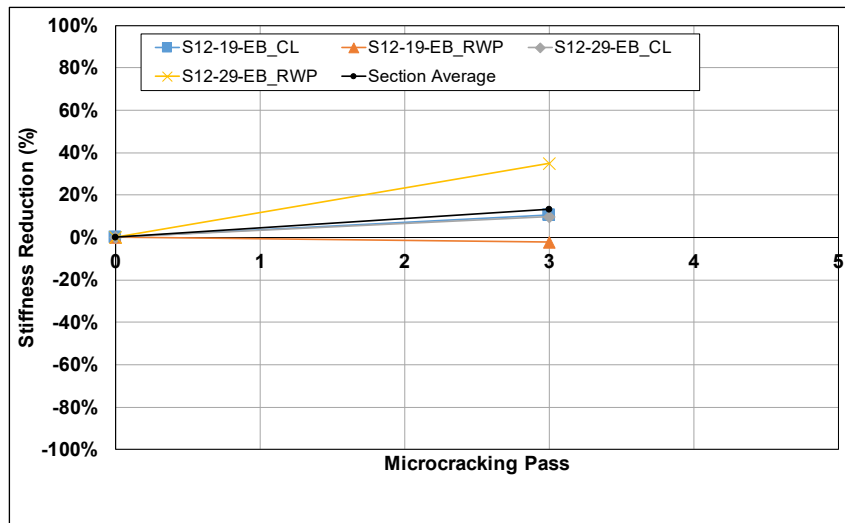
Figure B.96: Cell S12: LWD modulus reduction per station.
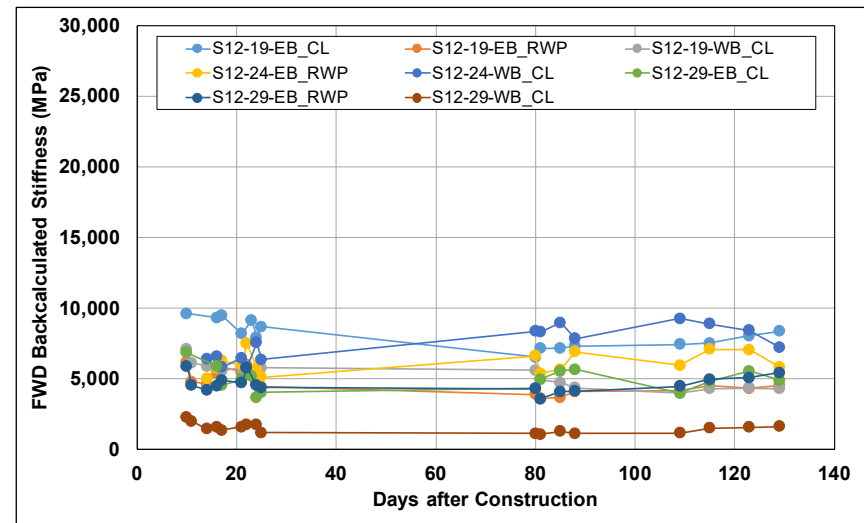
Figure B.97: Cell S12: Change in FWD-backcalculated stiffness.
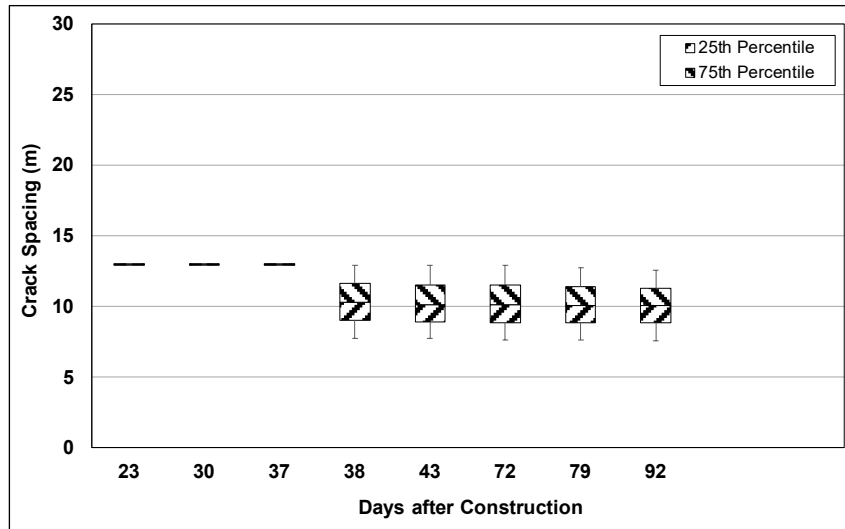
Figure B.98: Cell S12: Change in crack spacing.
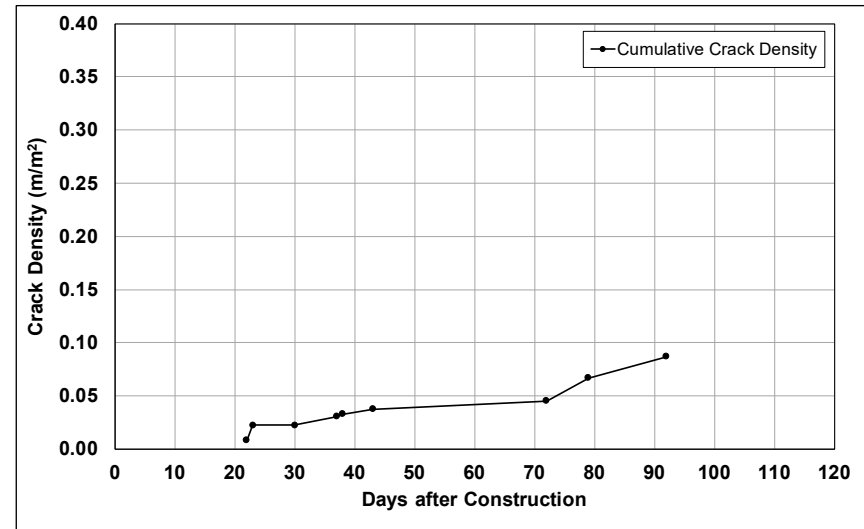
Figure B.99: Cell S12: Change in crack density.
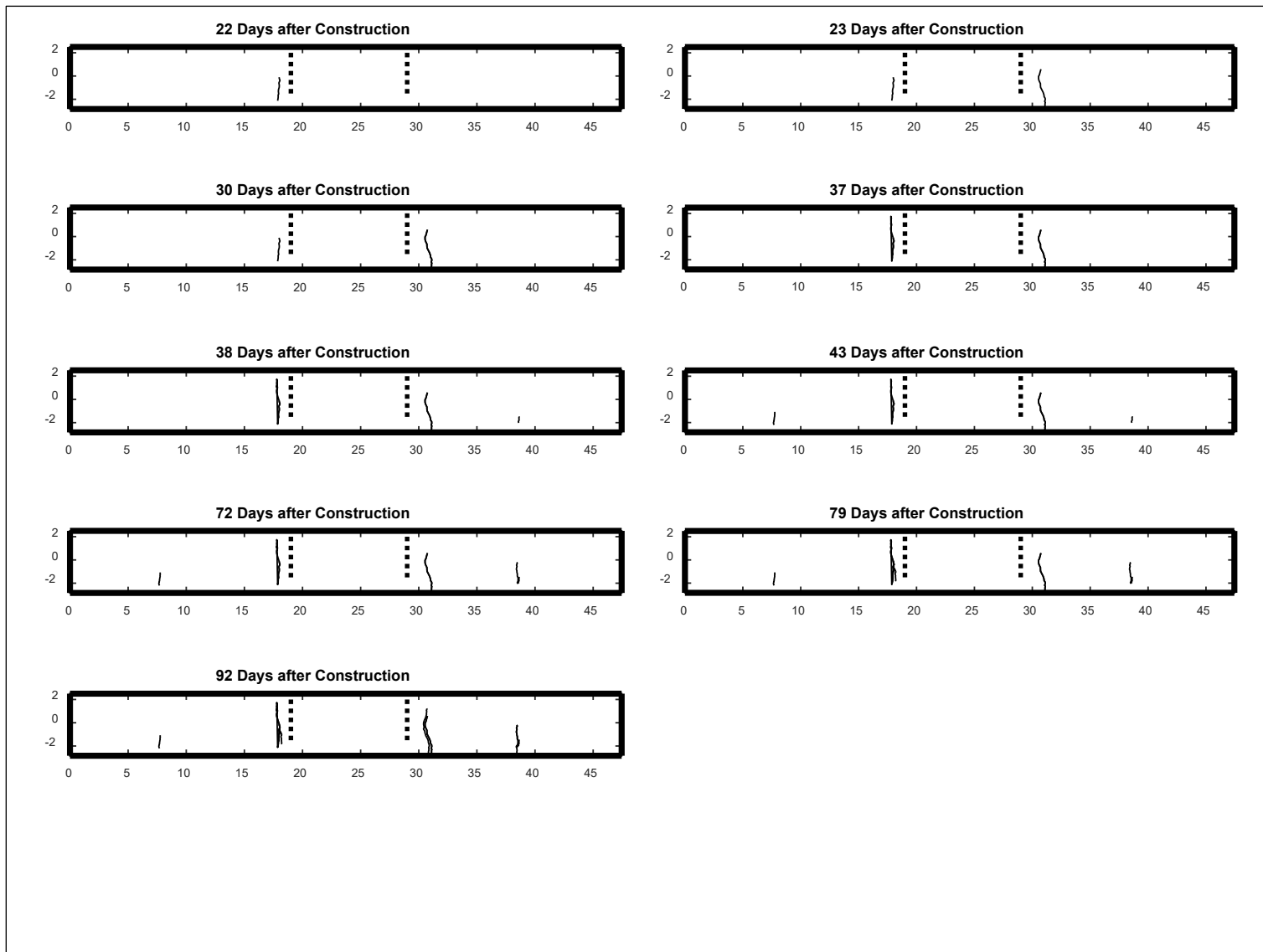
Figure B.100: Cell S12: Crack development.
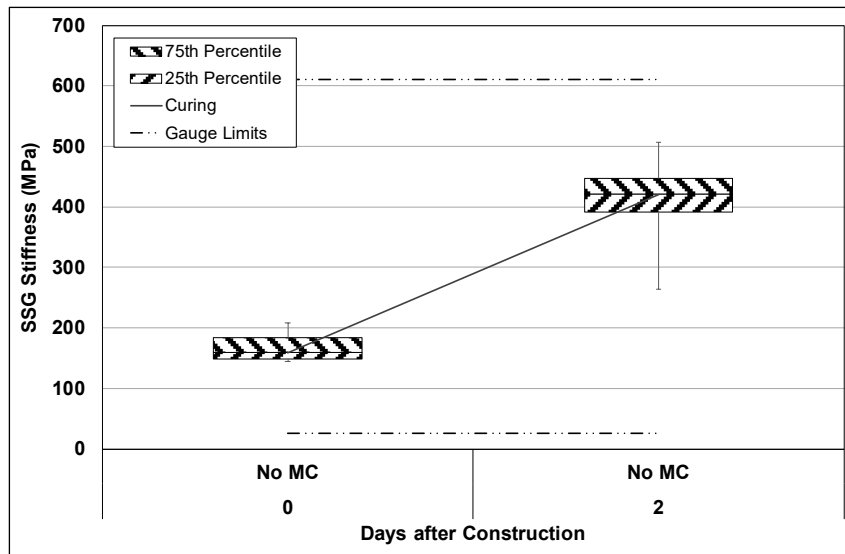
Figure B.101: Cell S13: SSG measured stiffness.
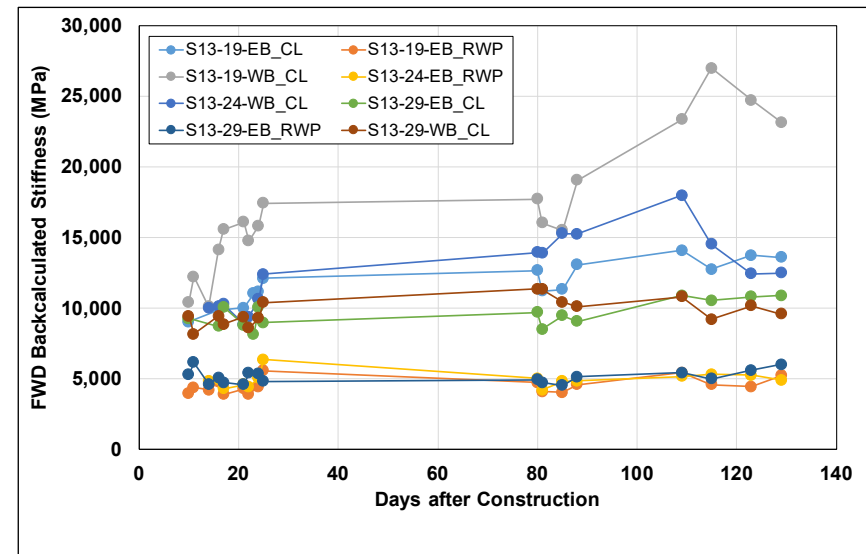
Figure B.102: Cell S13: Change in FWD-backcalculated stiffness.
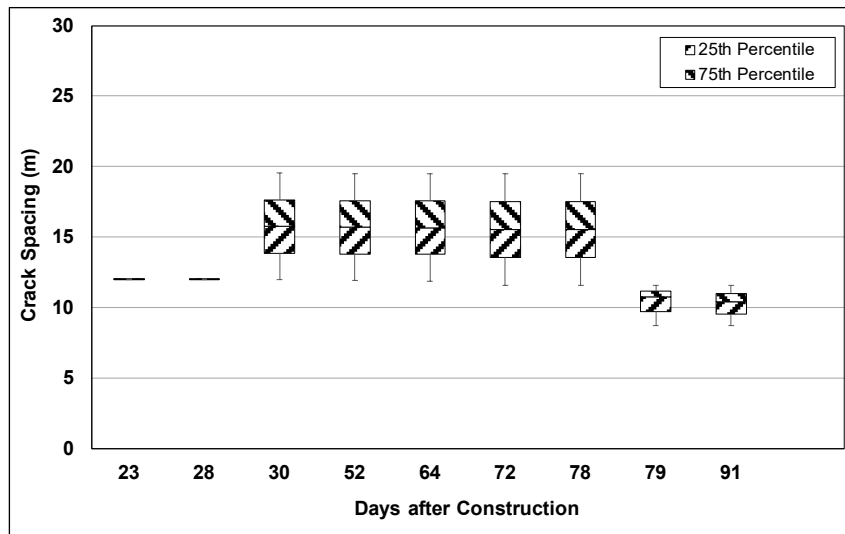
Figure B.103: Cell S13: Change in crack spacing.
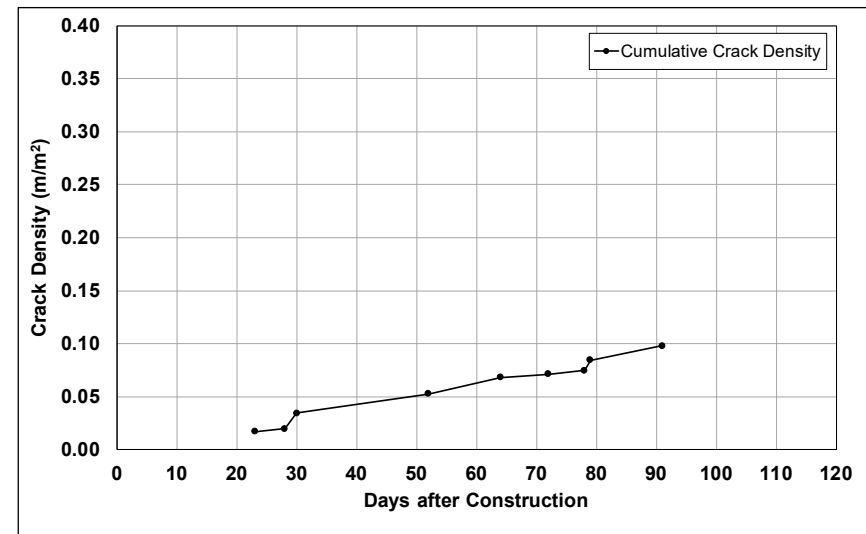
Figure B.104: Cell S13: Change in crack density.
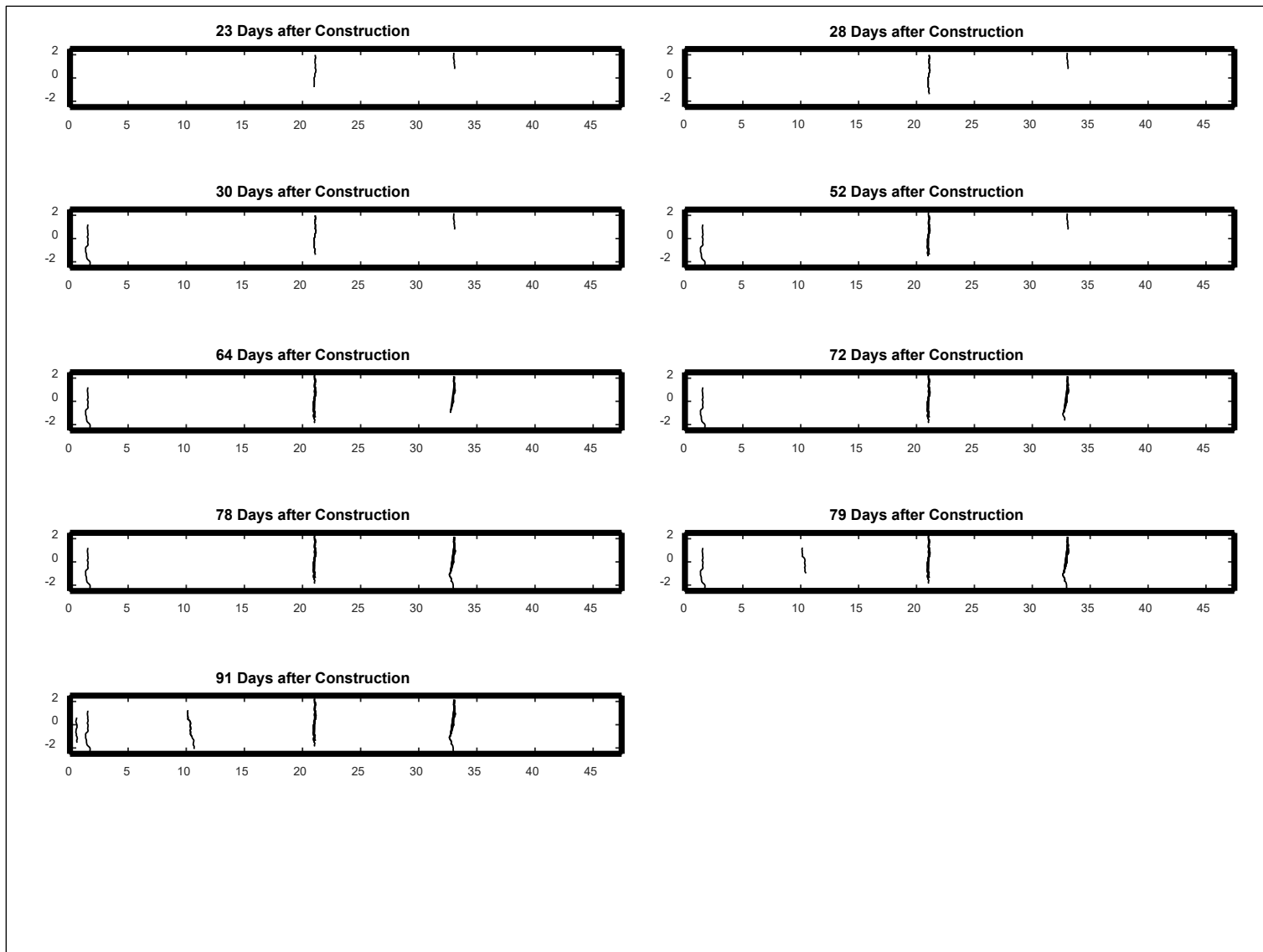
Figure B.105: Cell S13: Crack development.
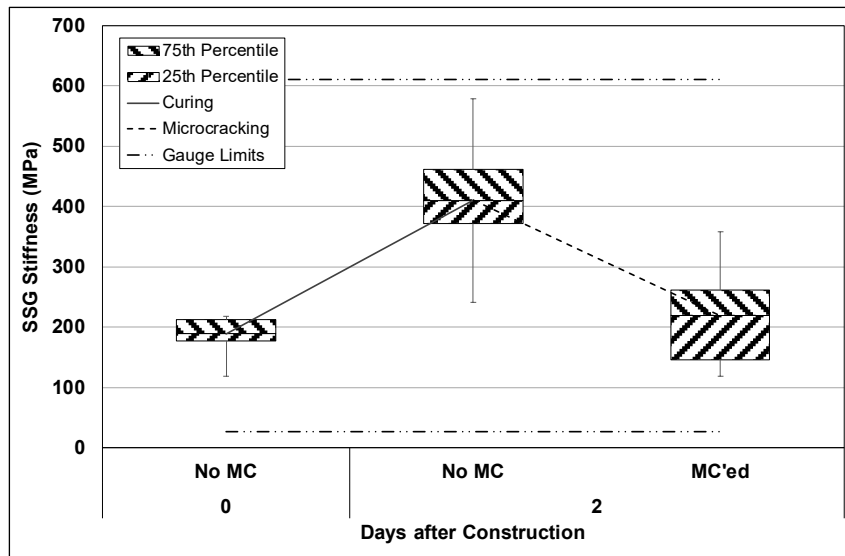
Figure B.106: Cell S14: SSG measured stiffness.
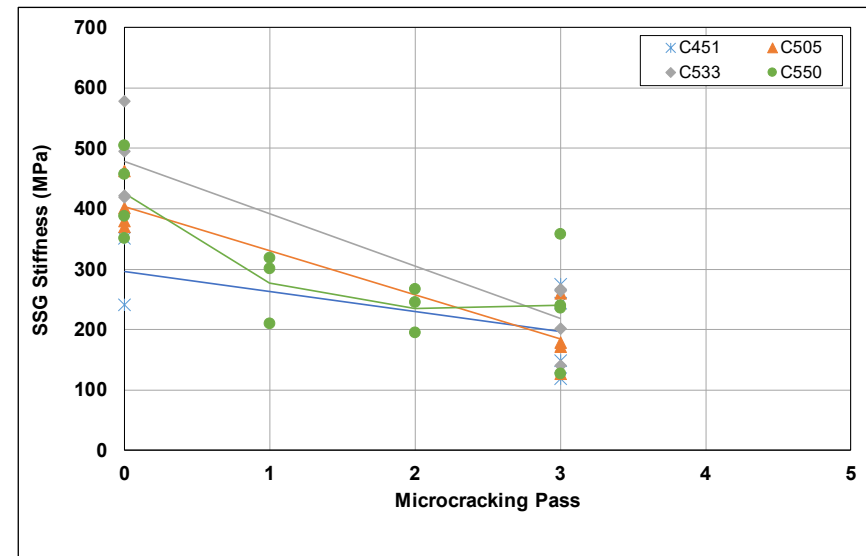
Figure B.107: Cell S14: SSG stiffness results per gauge.
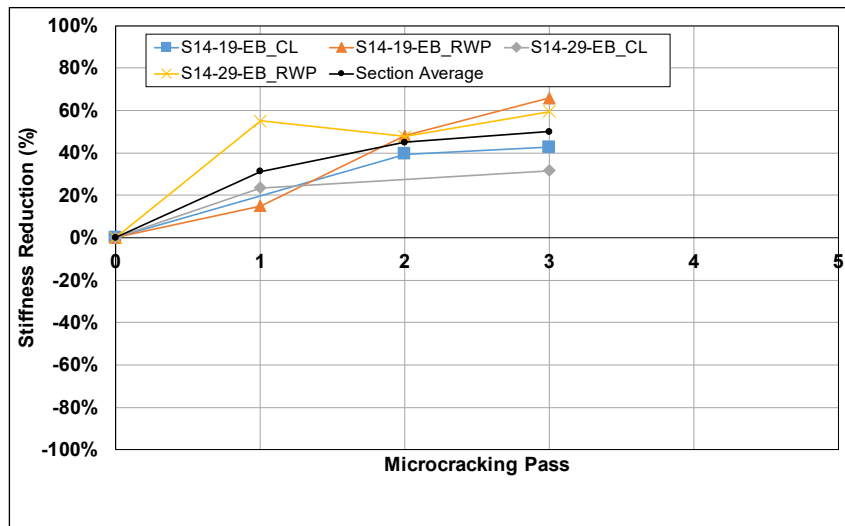
Figure B.108: Cell S14: SSG stiffness reduction per station.
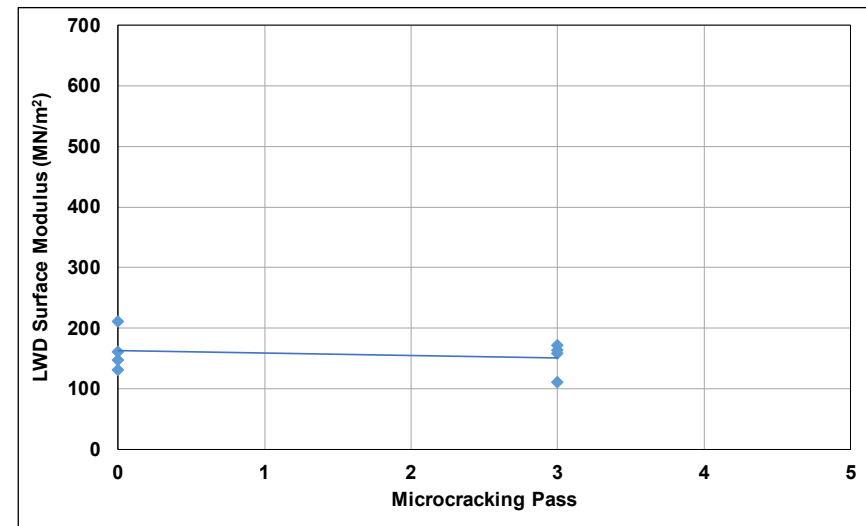
Figure B.109: Cell S14: LWD measured surface modulus.
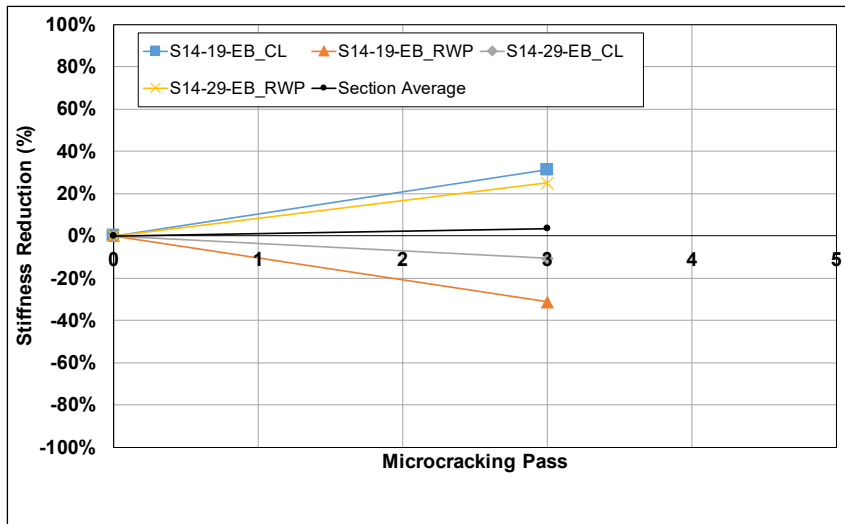
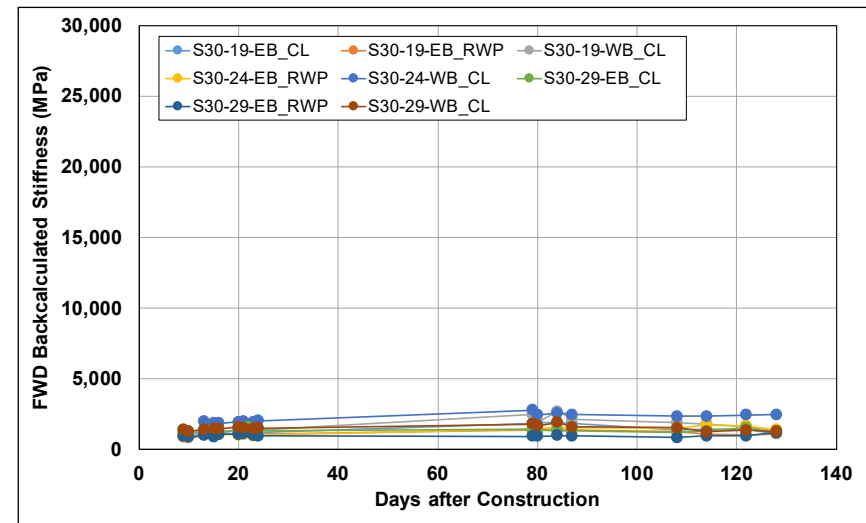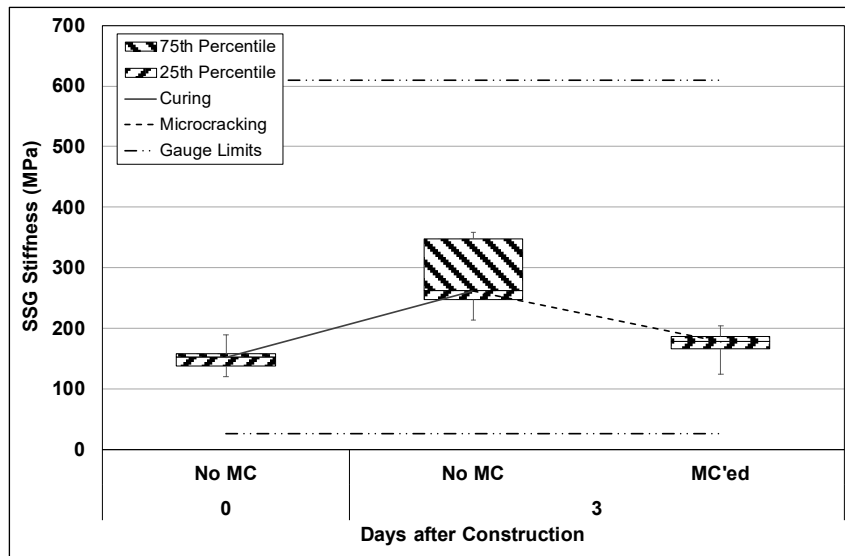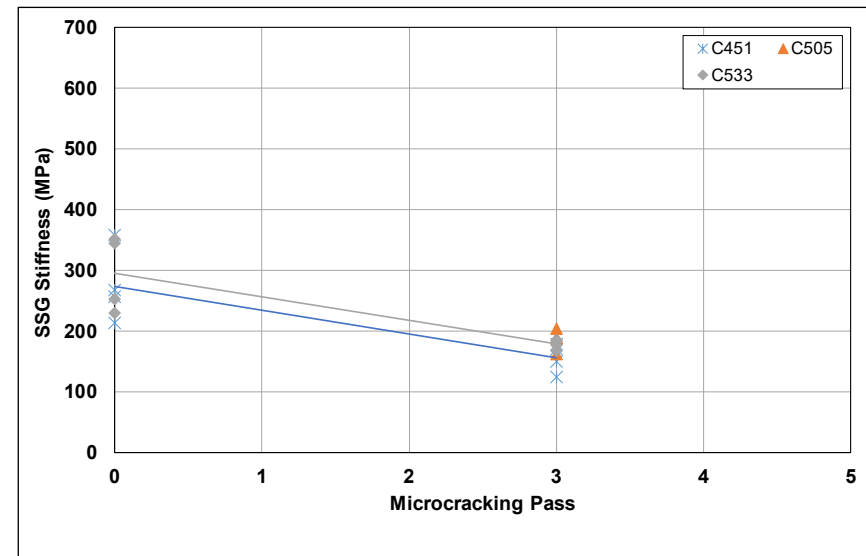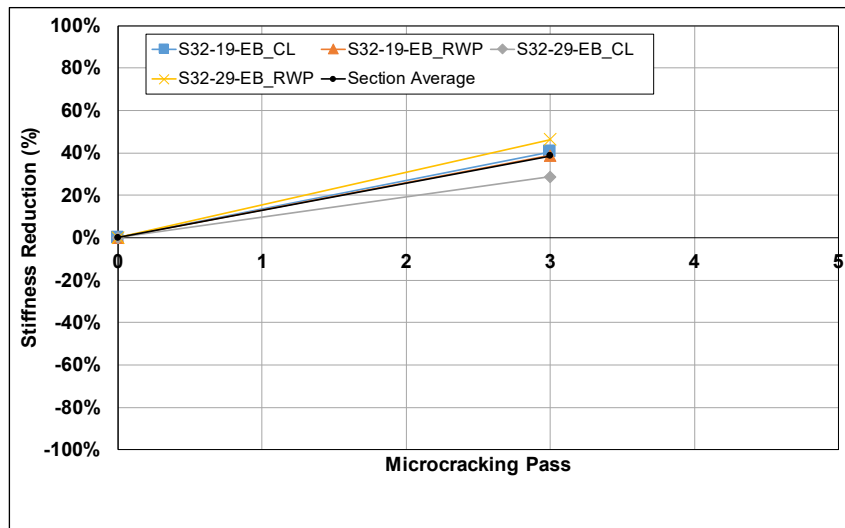**Figure B.110: Cell S14: LWD modulus reduction per station.**
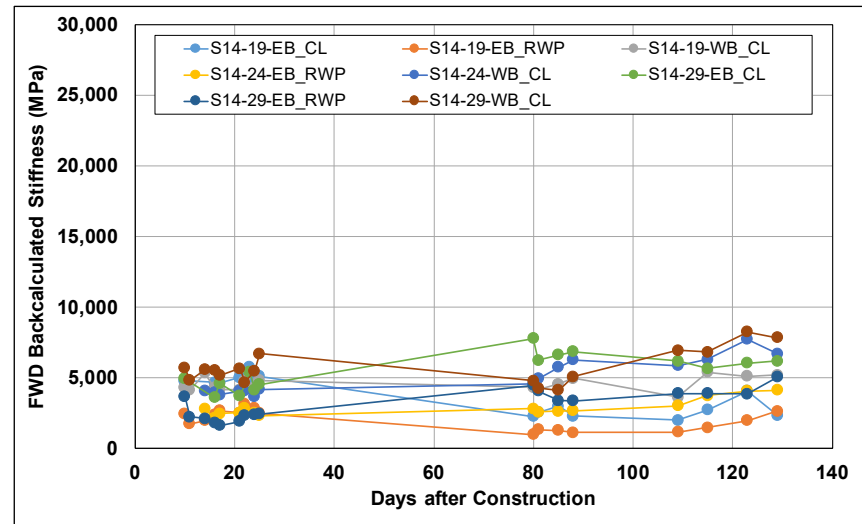
Figure B.111: Cell S14: Change in FWD-backcalculated stiffness.
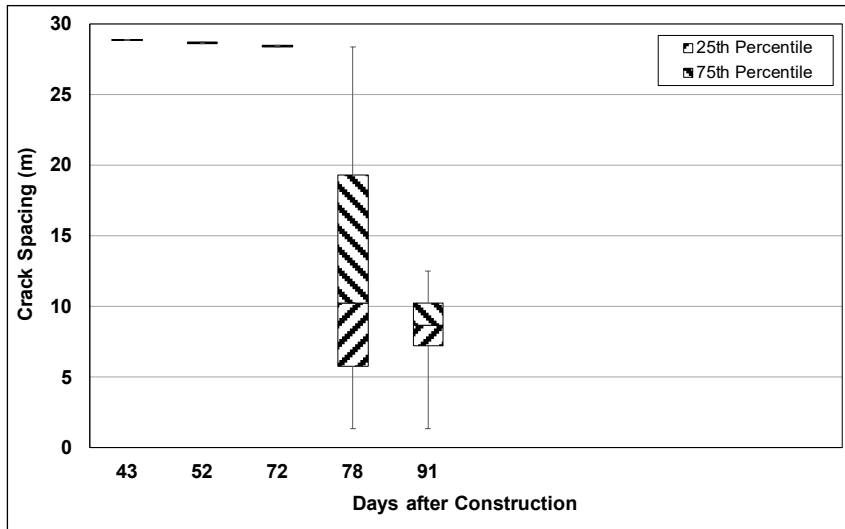
Figure B.112: Cell S14: Change in crack spacing.
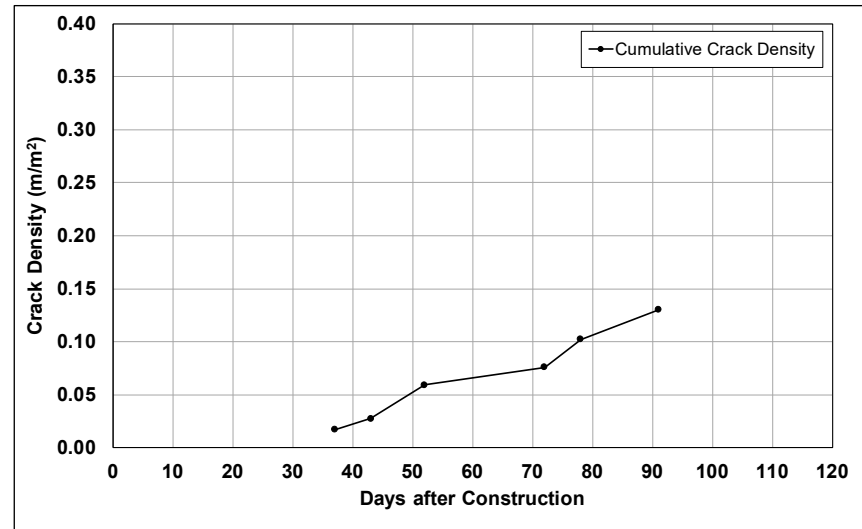
Figure B.113: Cell S14: Change in crack density.
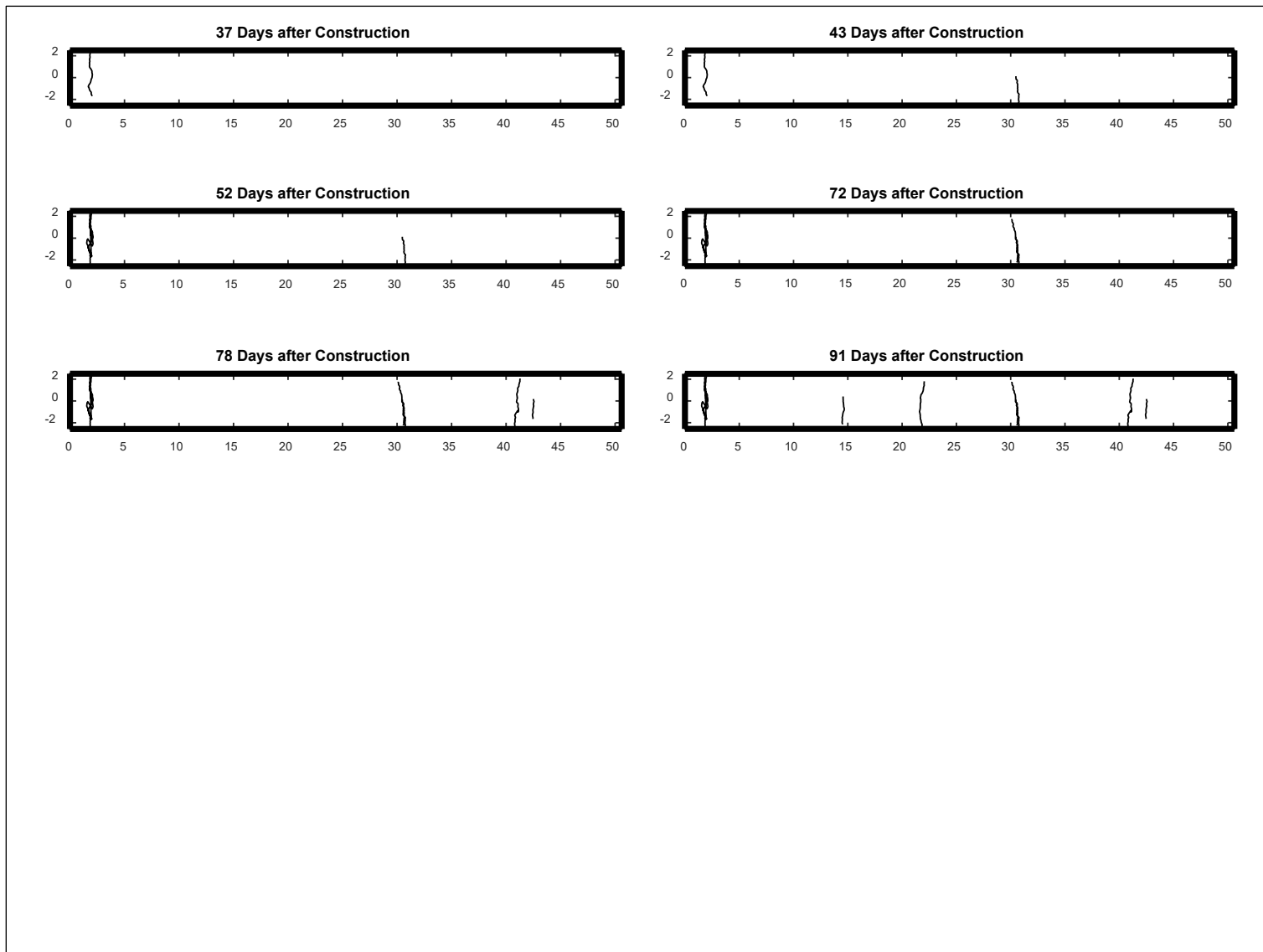
Figure B.114: Cell S14: Crack development.
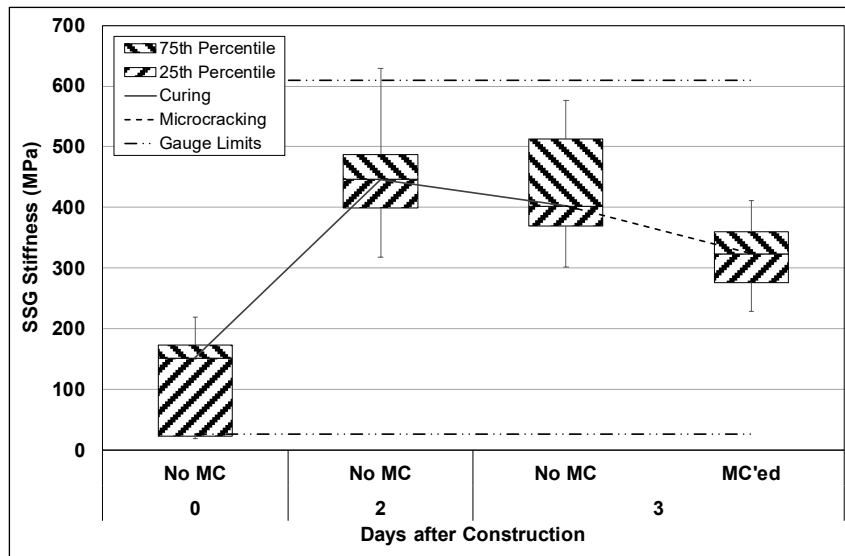
Figure B.115: Cell S15: SSG measured stiffness.
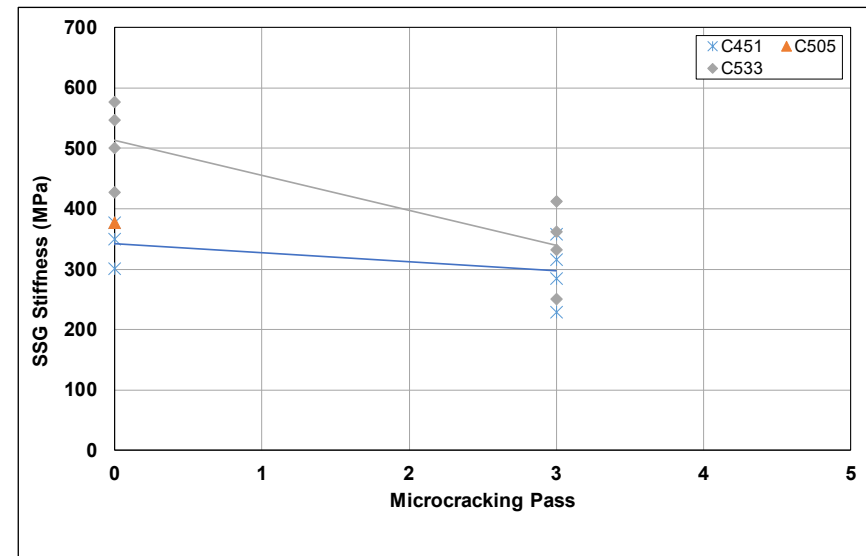
Figure B.116: Cell S15: SSG stiffness results per gauge.
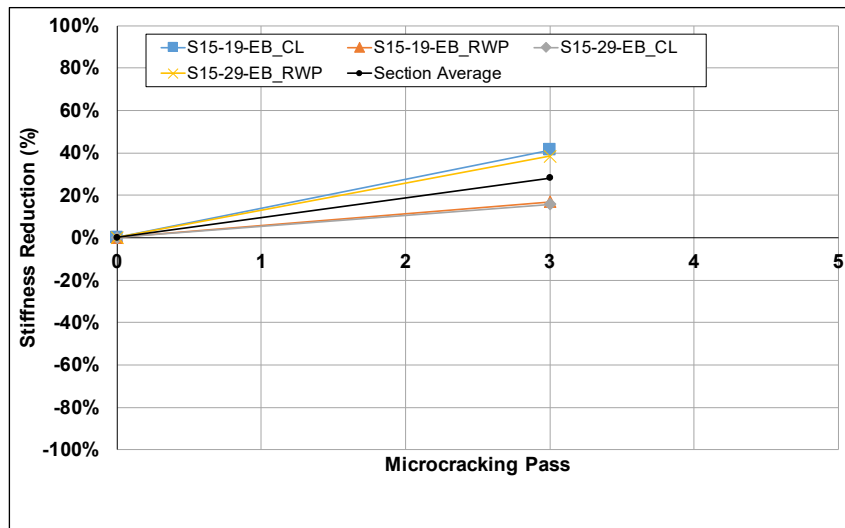
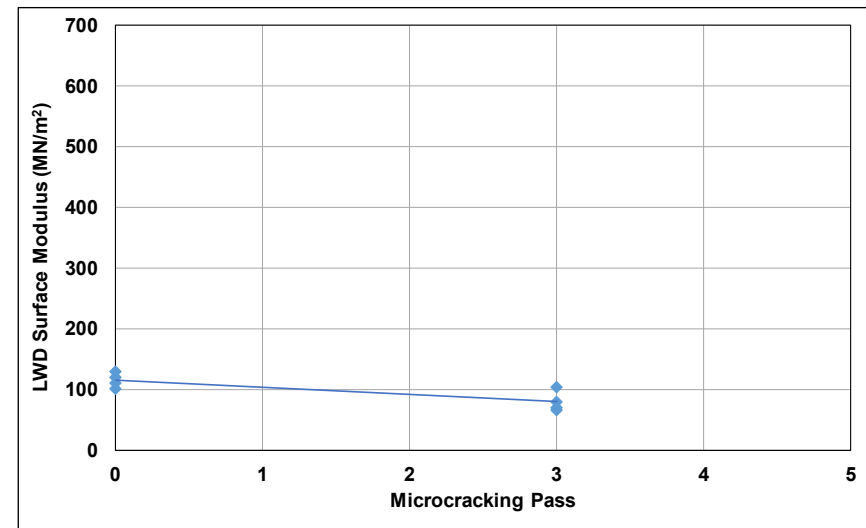**Figure B.117: Cell S15: SSG stiffness reduction per station.**
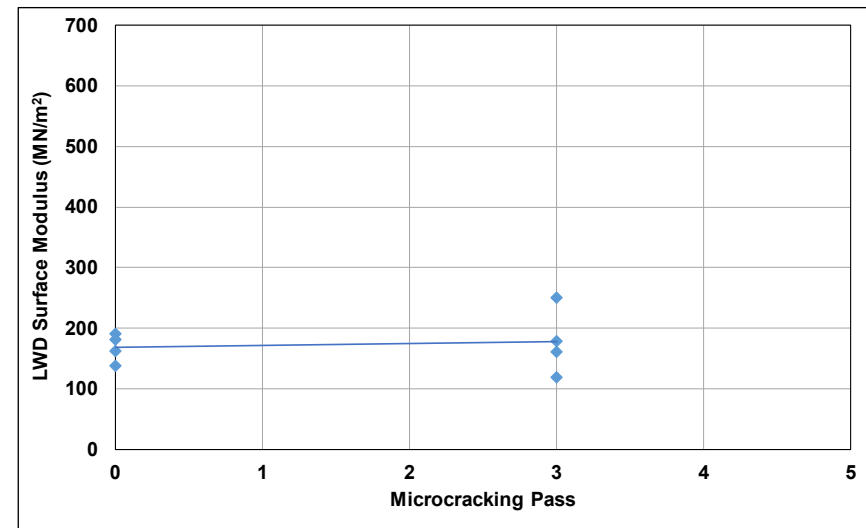
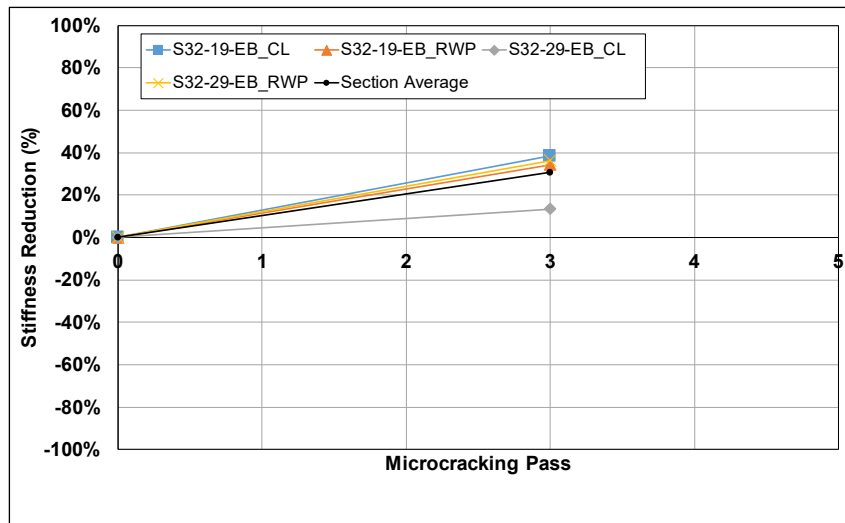
Figure B.118: Cell S15: LWD measured surface modulus.
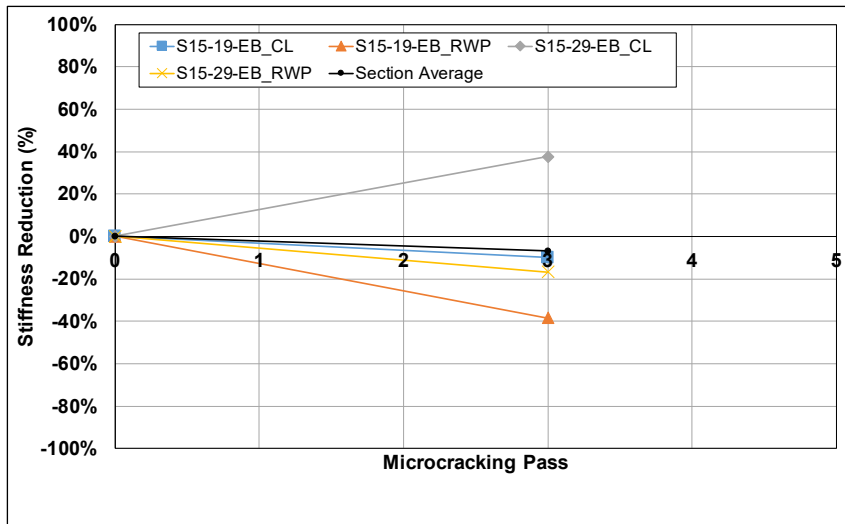
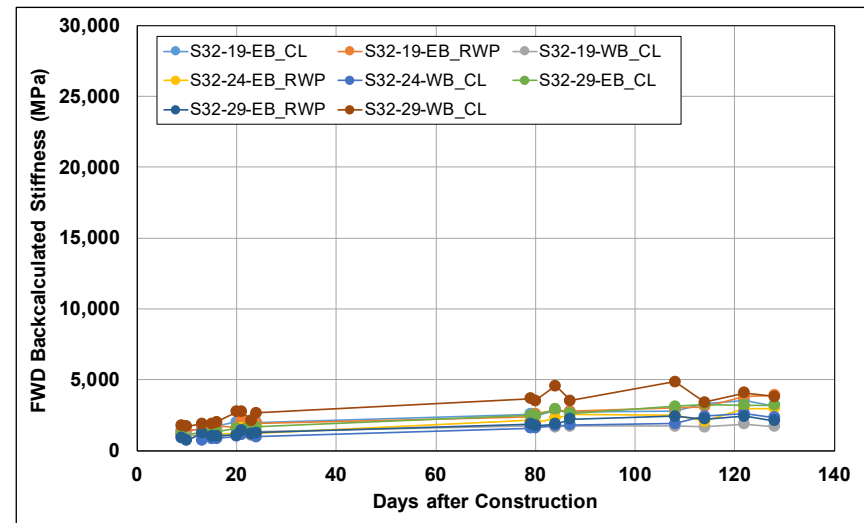Figure B.119: Cell S15: LWD modulus reduction per station.
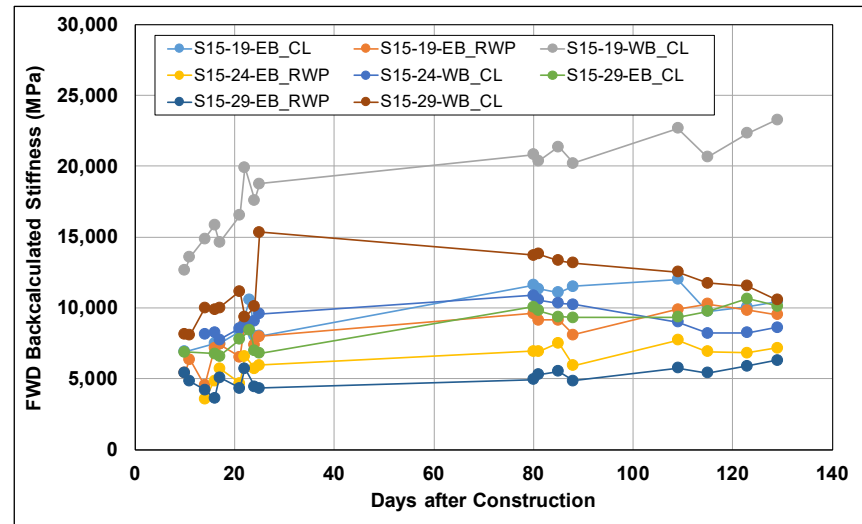
Figure B.120: Cell S15: Change in FWD-backcalculated stiffness.
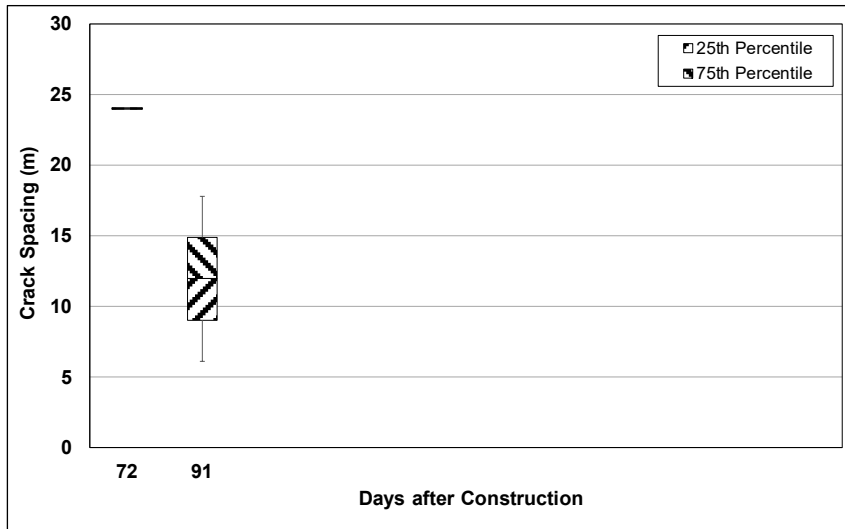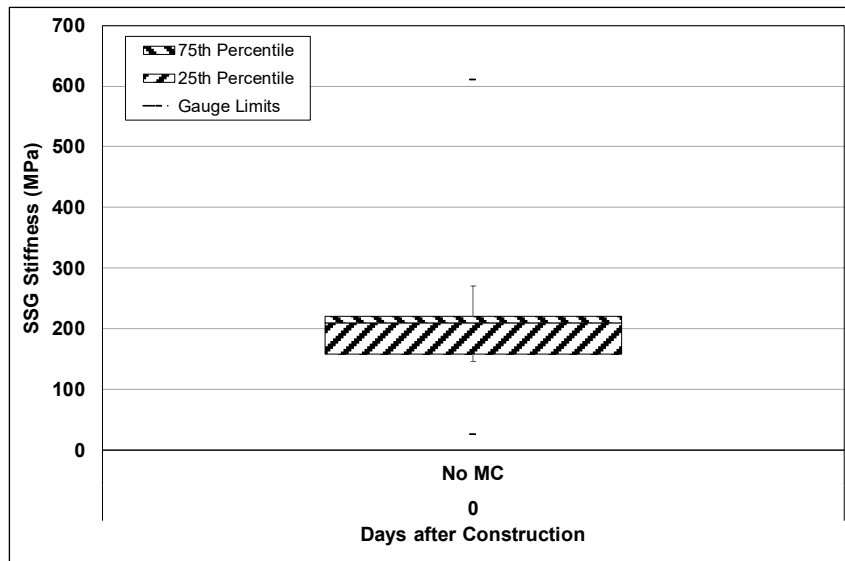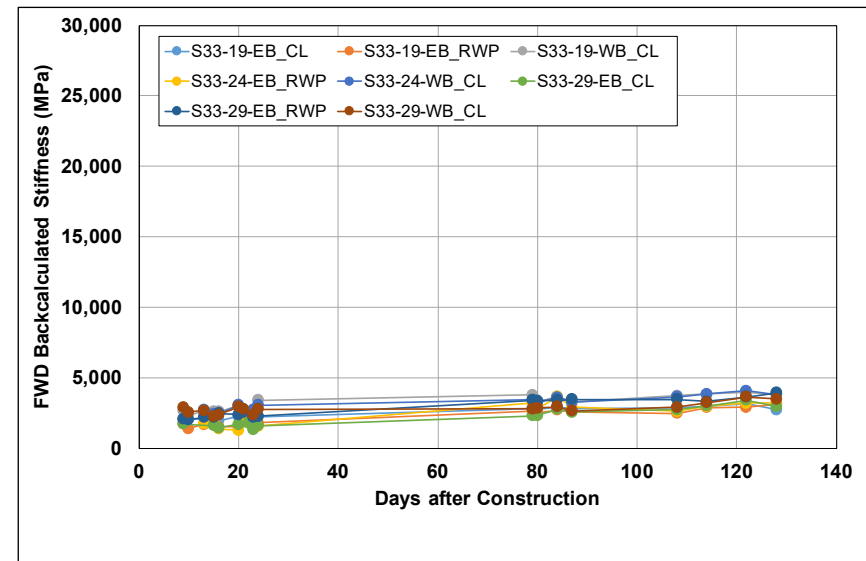

Figure B.121: Cell S15: Change in crack spacing.
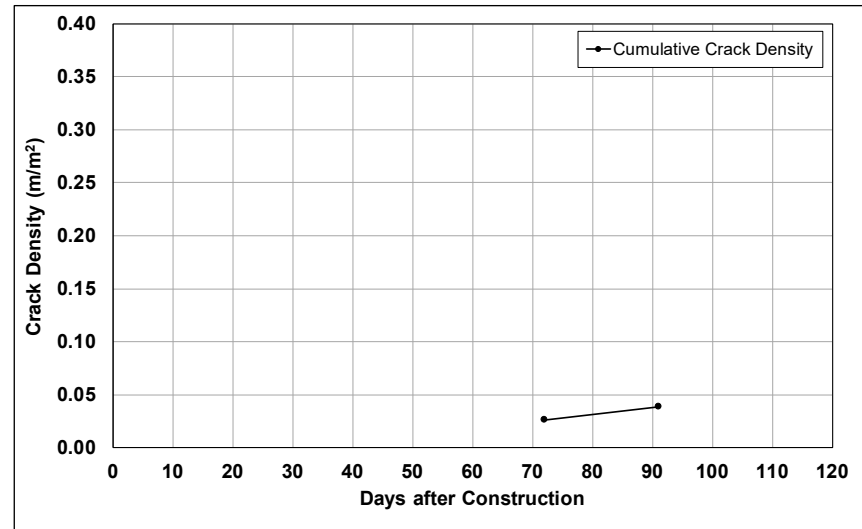
Figure B.122: Cell S15: Change in crack density.

72 Days after Construction

91 Days after Construction
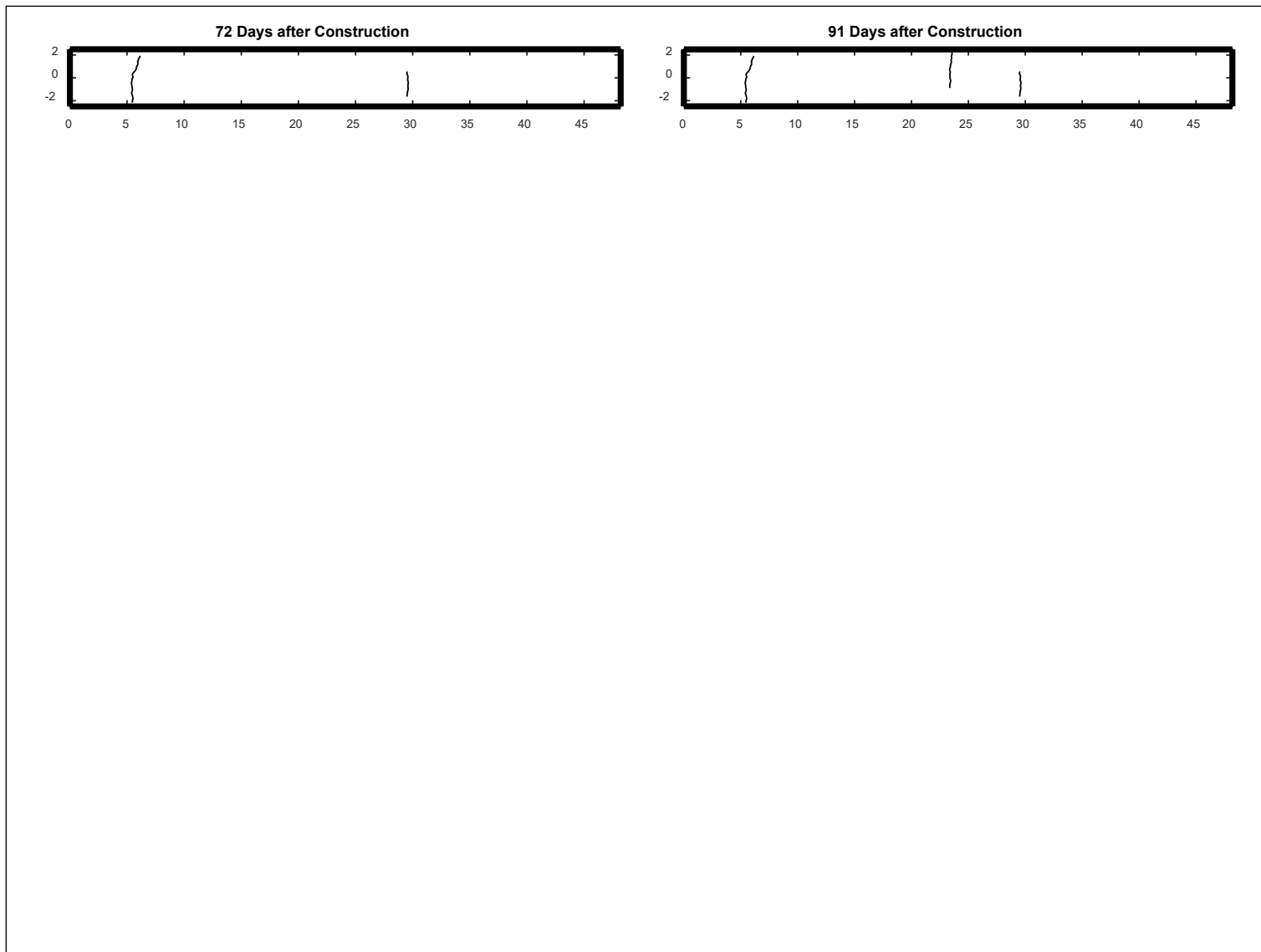
Figure B.123: Cell S15: Crack development.
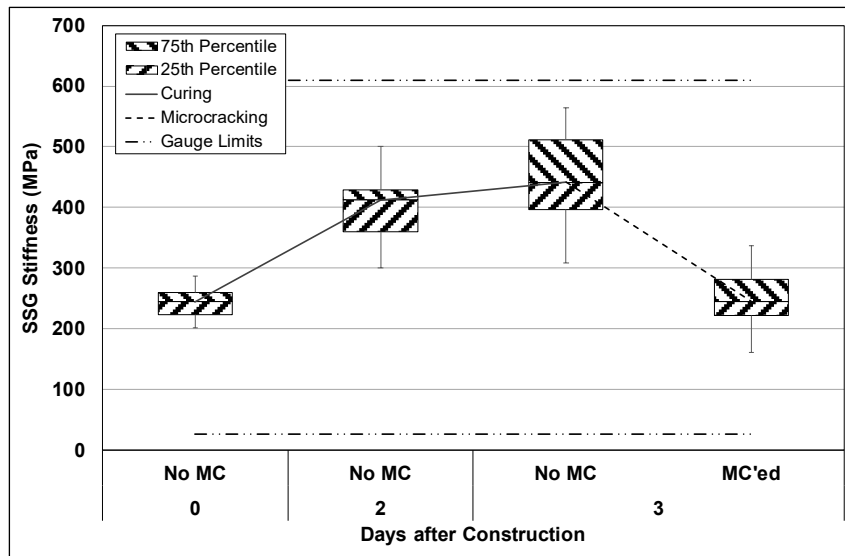
Figure B.124: Cell S16: SSG measured stiffness.
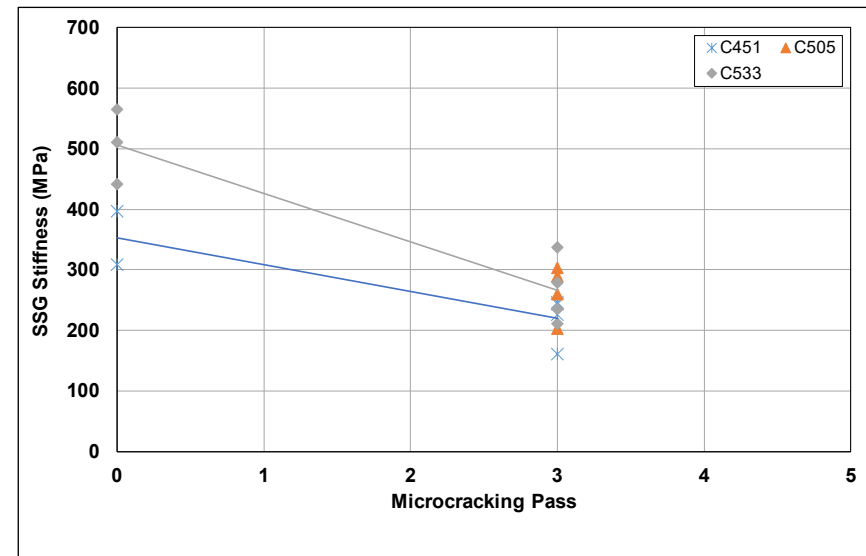
Figure B.125: Cell S16: SSG stiffness results per gauge.
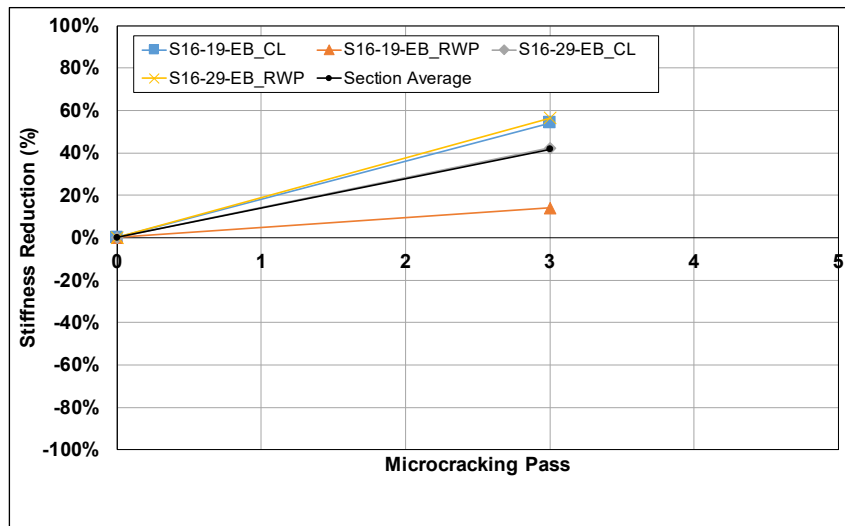
Figure B.126: Cell S16: SSG stiffness reduction per station.
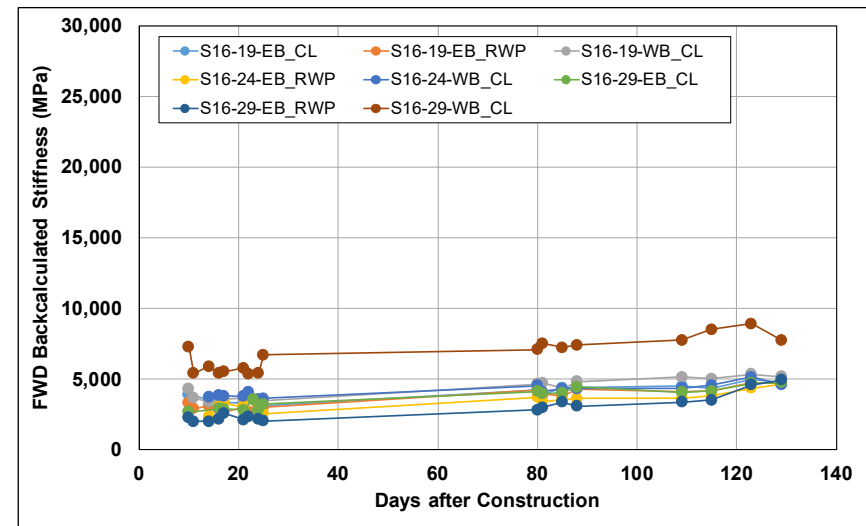
Figure B.127: Cell S16: Change in FWD-backcalculated stiffness.
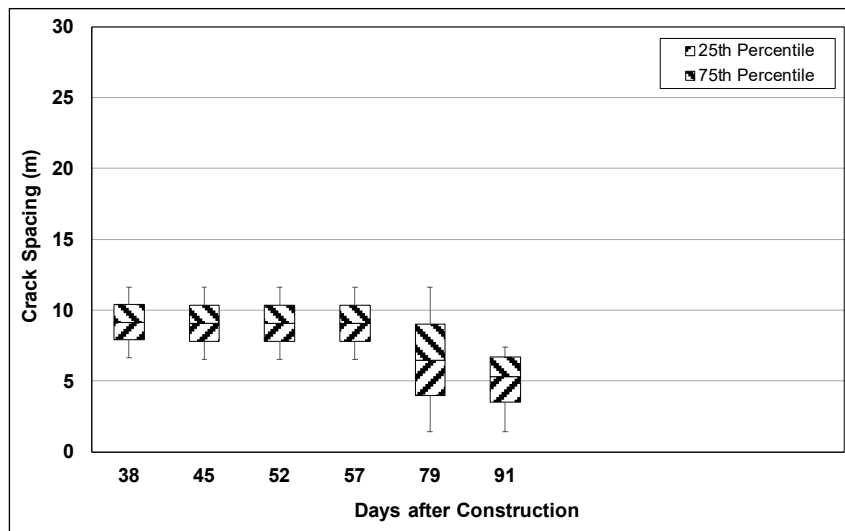
Figure B.128: Cell S16: Change in crack spacing.
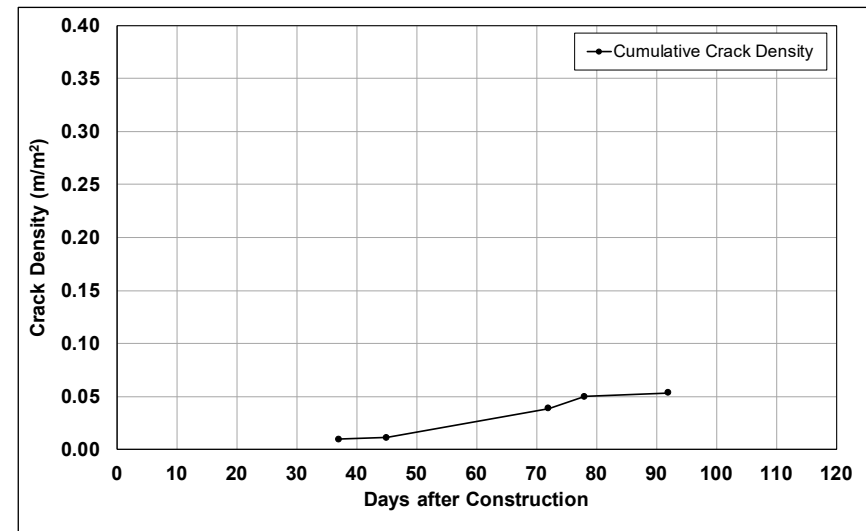
Figure B.129: Cell S16: Change in crack density.
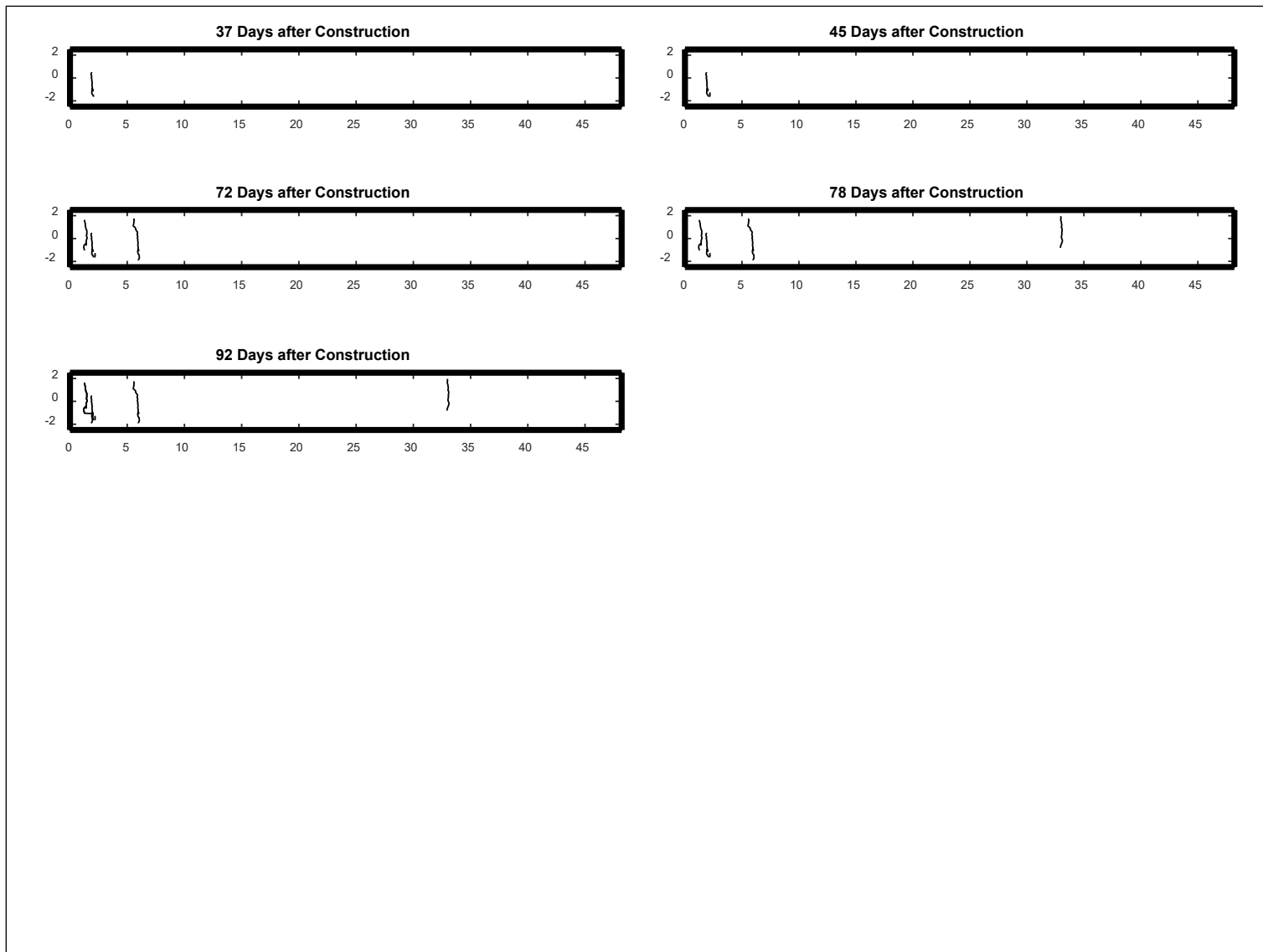
Figure B.130: Cell S16: Crack development.
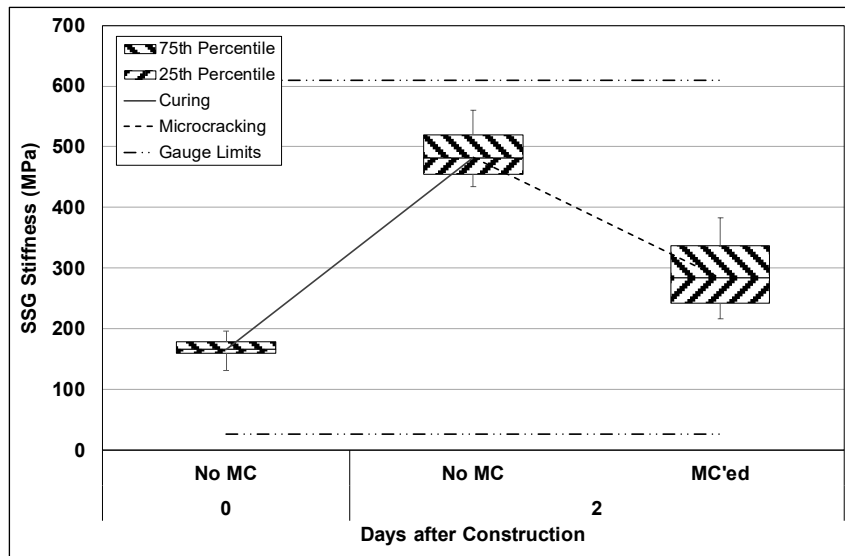
Figure B.131: Cell S17: SSG measured stiffness.
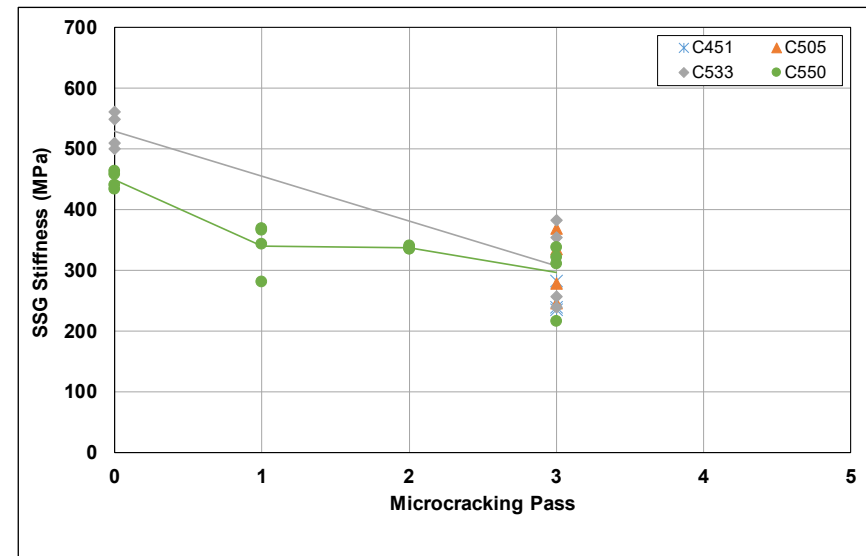
Figure B.132: Cell S17: SSG stiffness results per gauge.
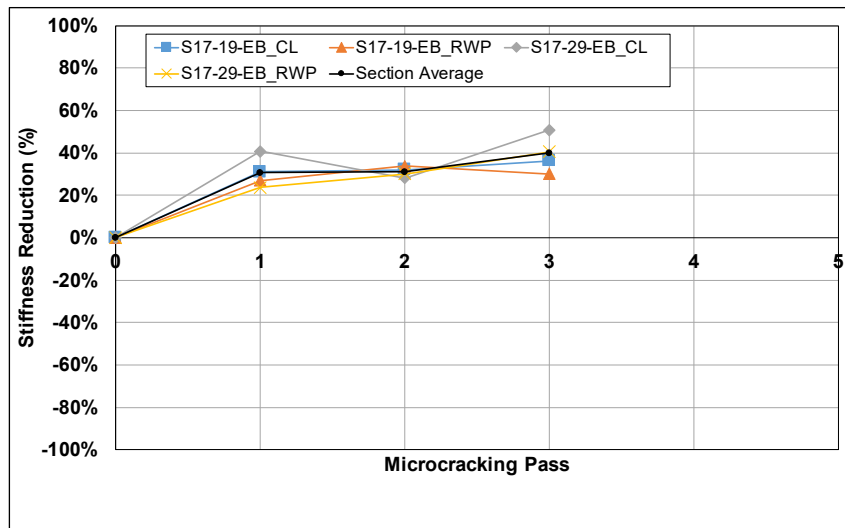
Figure B.133: Cell S17: SSG stiffness reduction per station.
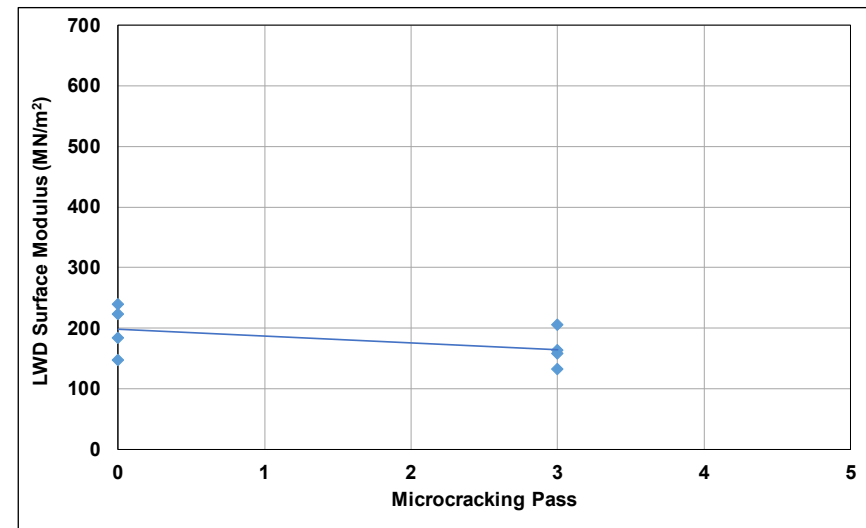
Figure B.134: Cell S17: LWD measured surface modulus.
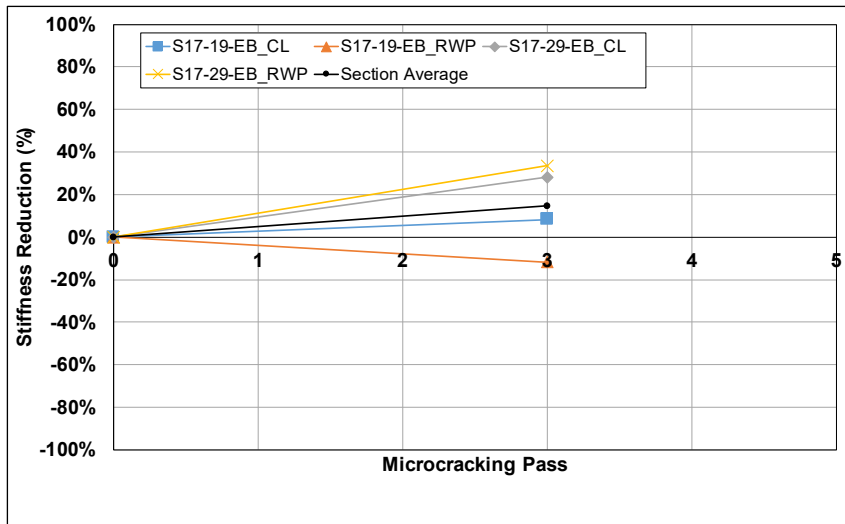
Figure B.135: Cell S17: LWD modulus reduction per station.
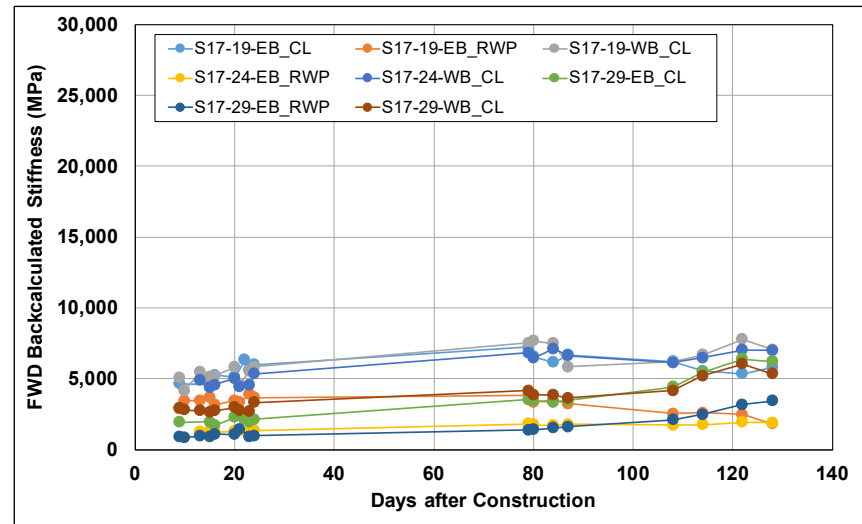
Figure B.136: Cell S17: Change in FWD-backcalculated stiffness.
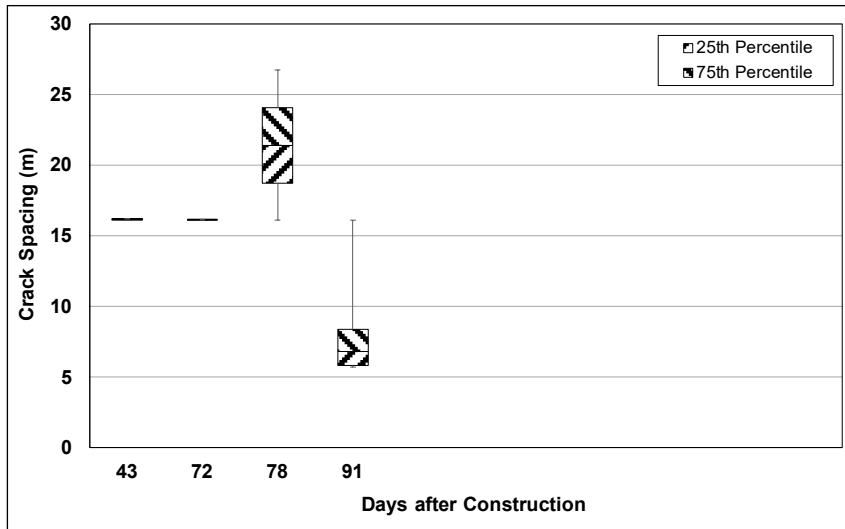
Figure B.137: Cell S17: Change in crack spacing.
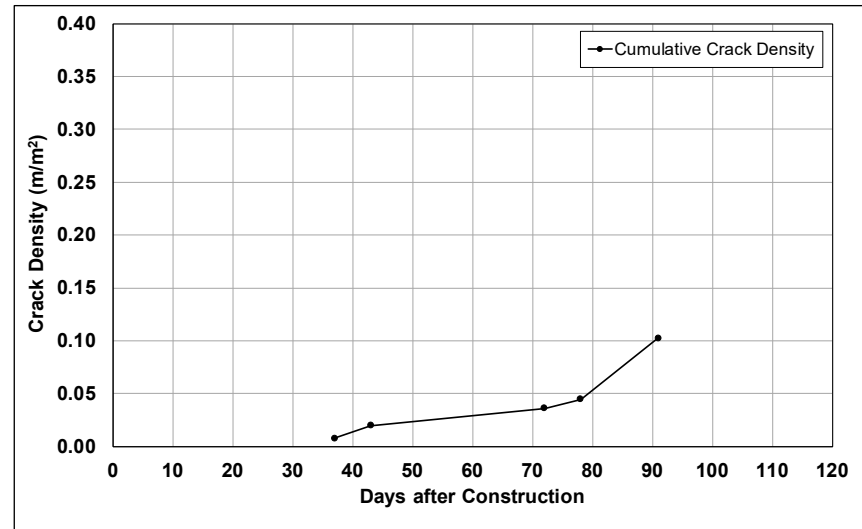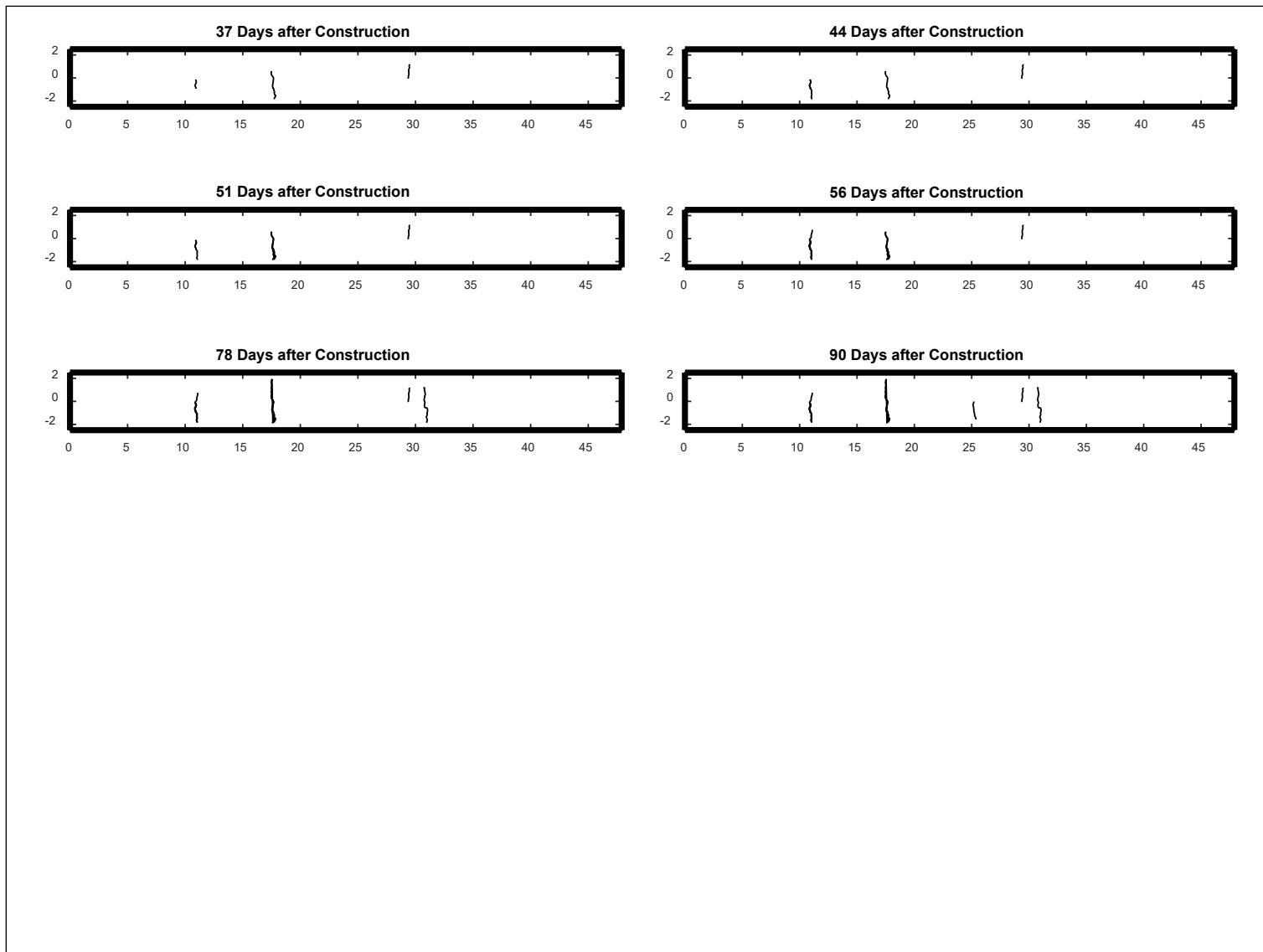

Figure B.138: Cell S17: Change in crack density.
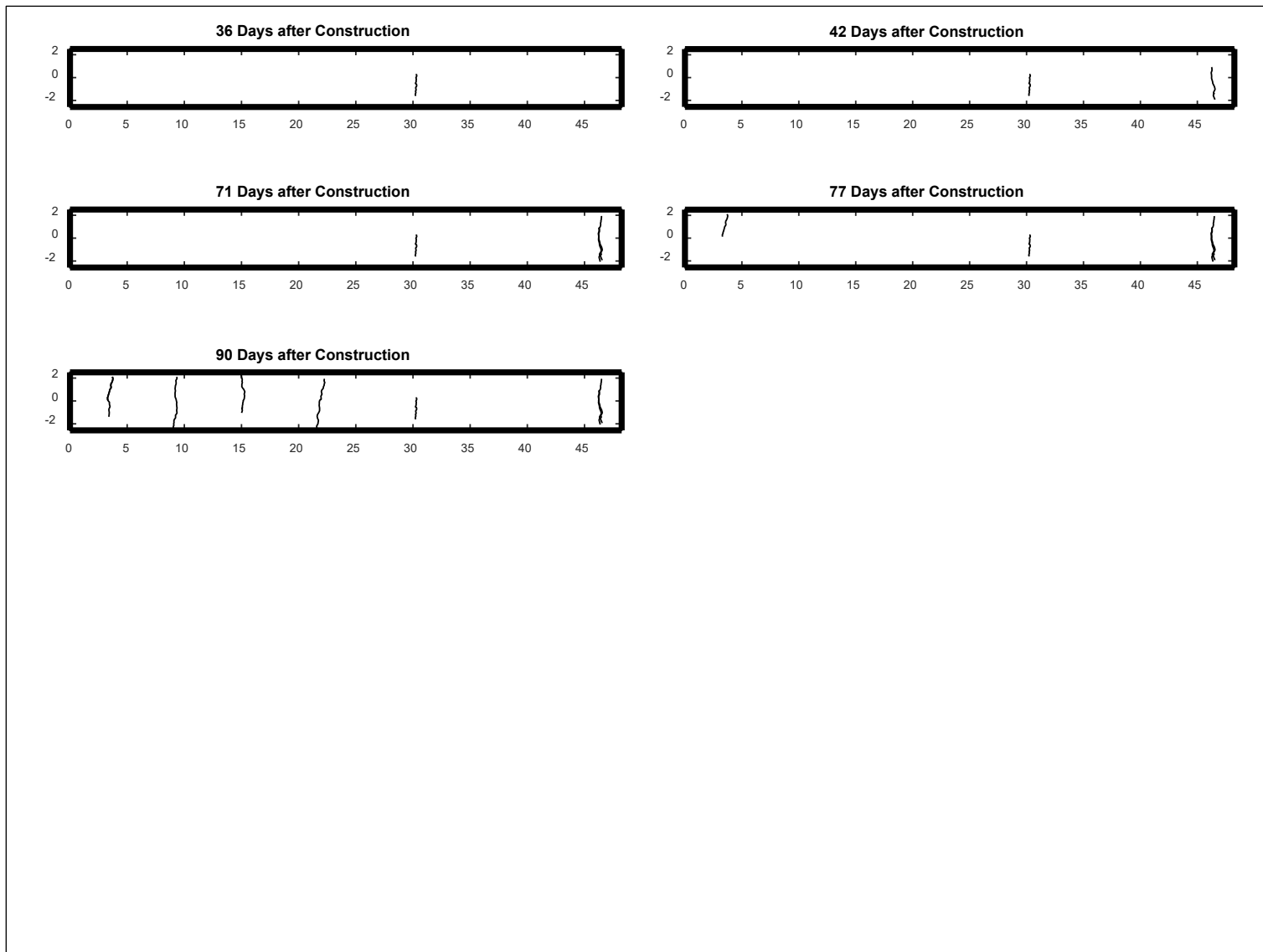
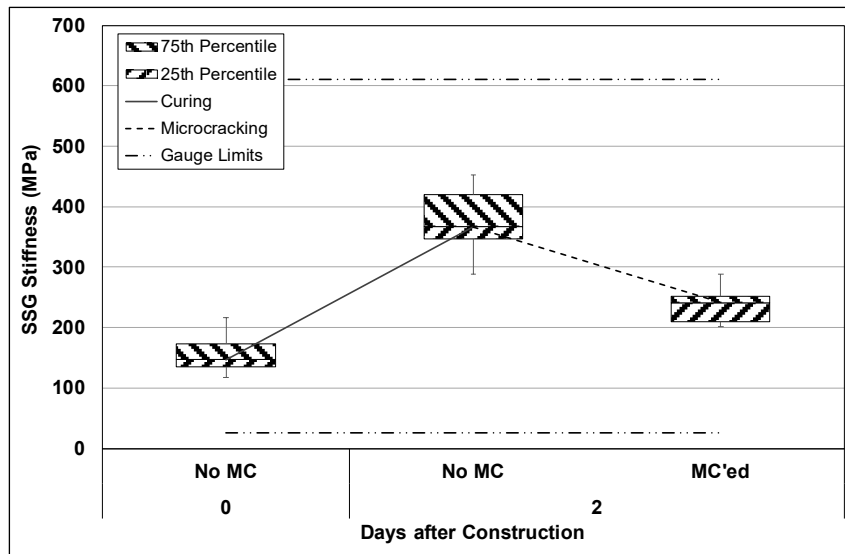**Figure B.139: Cell S17: Crack development.**
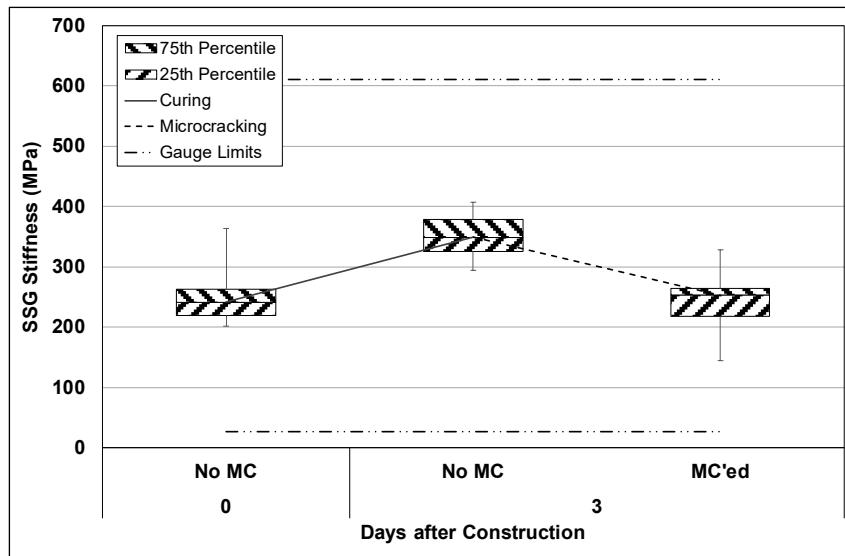
Figure B.140: Cell S18: SSG measured stiffness.
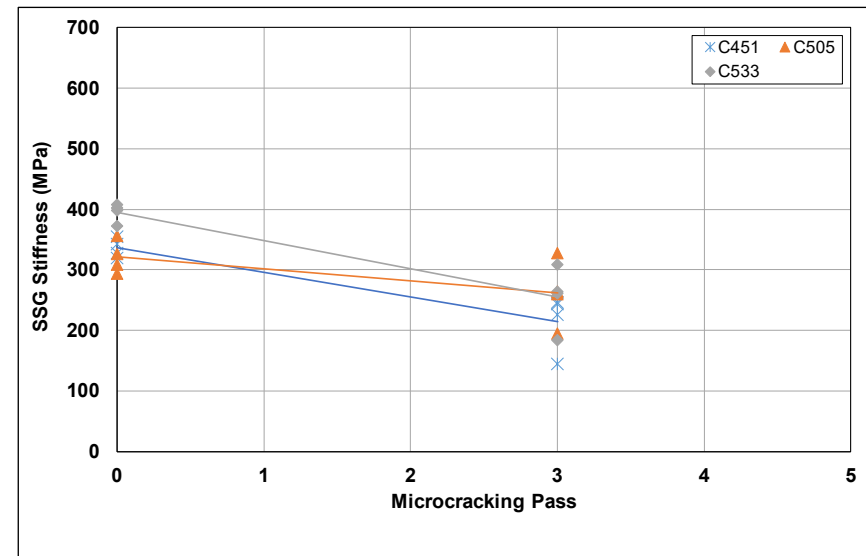
Figure B.141: Cell S18: SSG stiffness results per gauge.
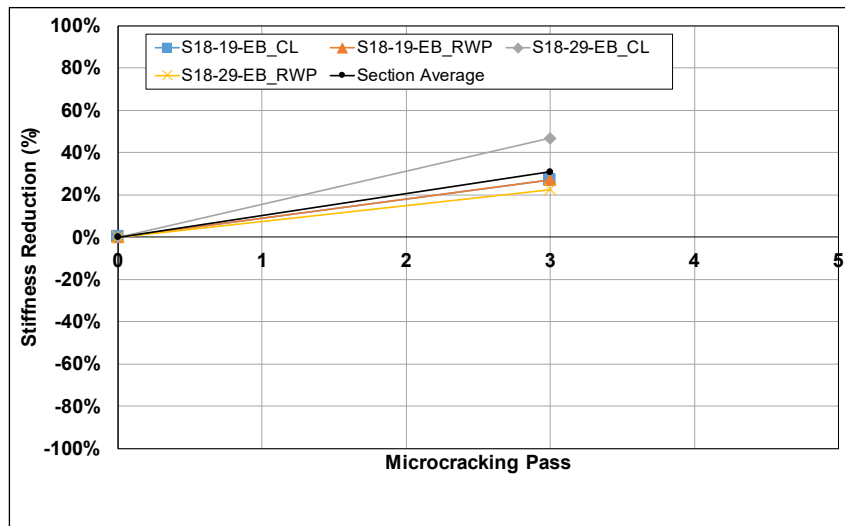
Figure B.142: Cell S18: SSG stiffness reduction per station.
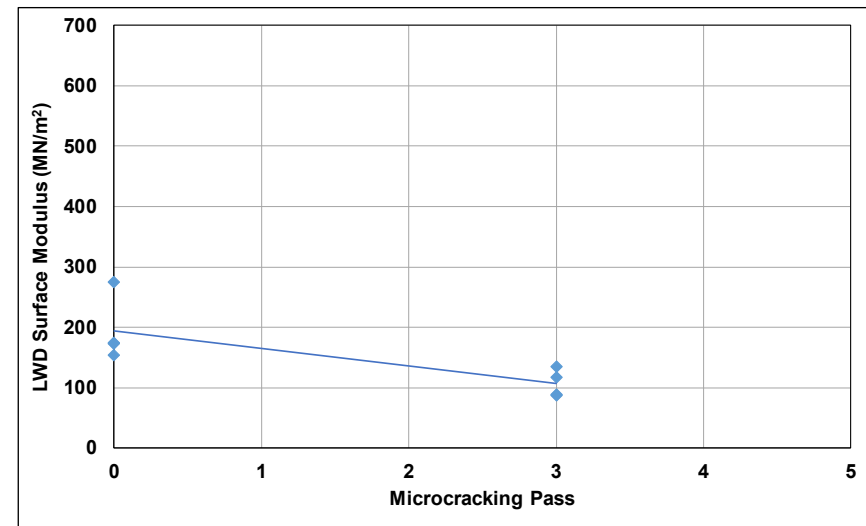
Figure B.143: Cell S18: LWD measured surface modulus.
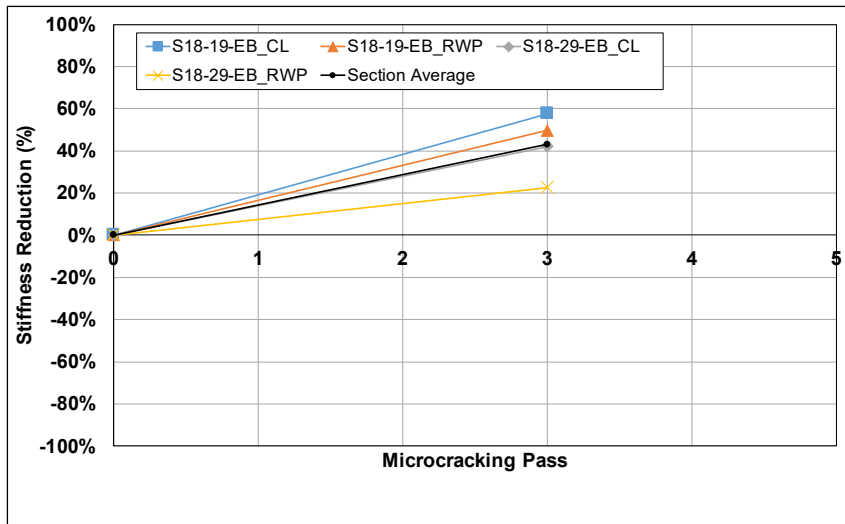
Figure B.144: Cell S18: LWD modulus reduction per station.
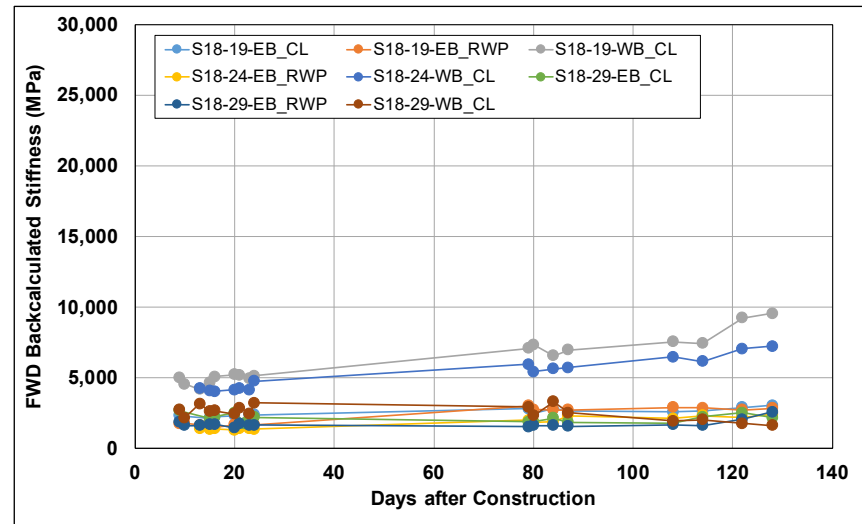
Figure B.145: Cell S18: Change in FWD-backcalculated stiffness.

Figure B.146: Cell S18: Change in crack spacing.
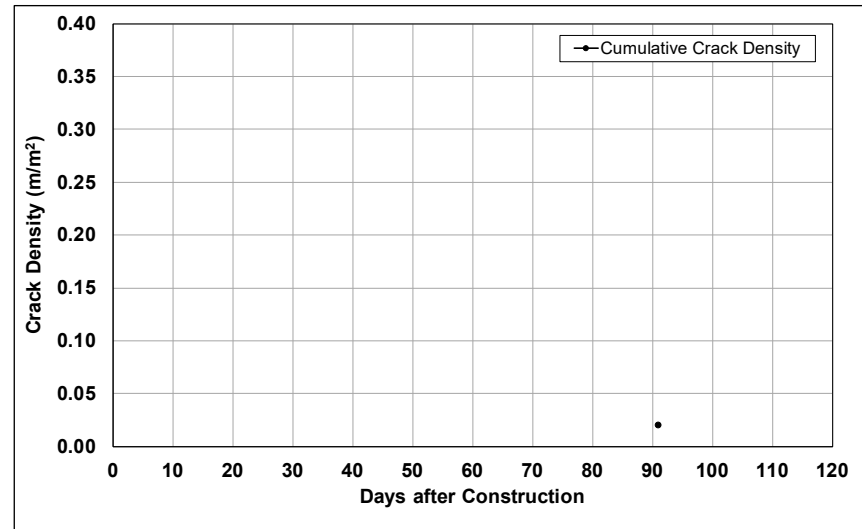
Figure B.147: Cell S18: Change in crack density.
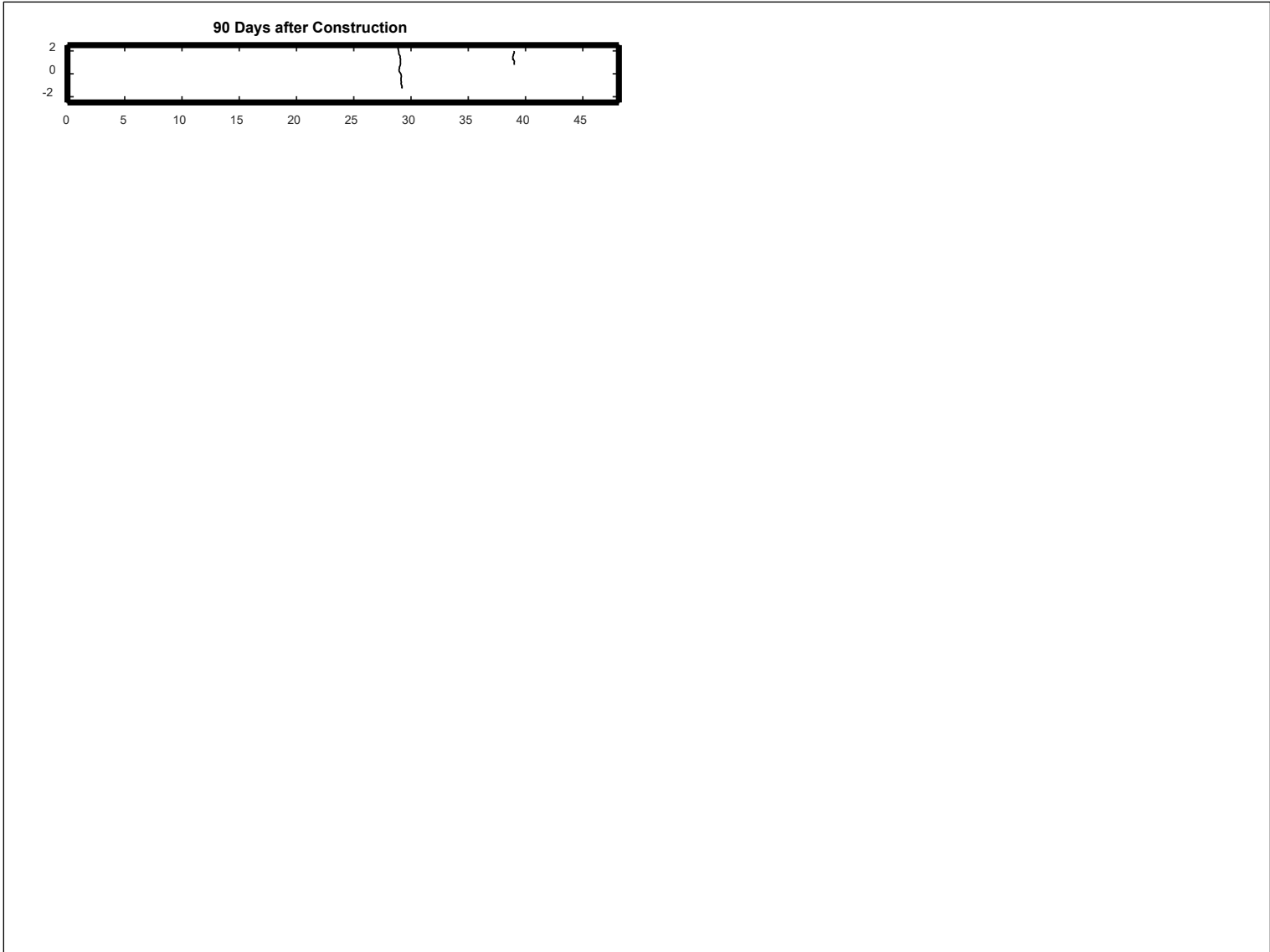
Figure B.148: Cell S18: Crack development.
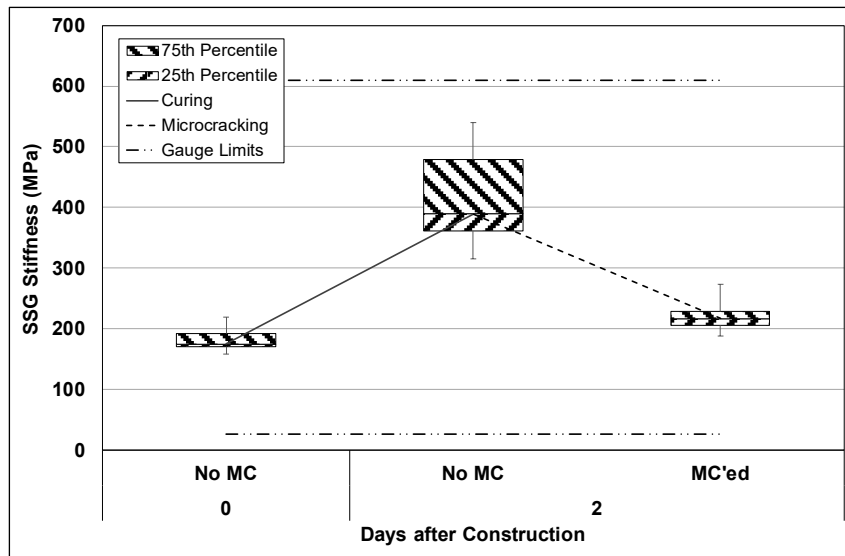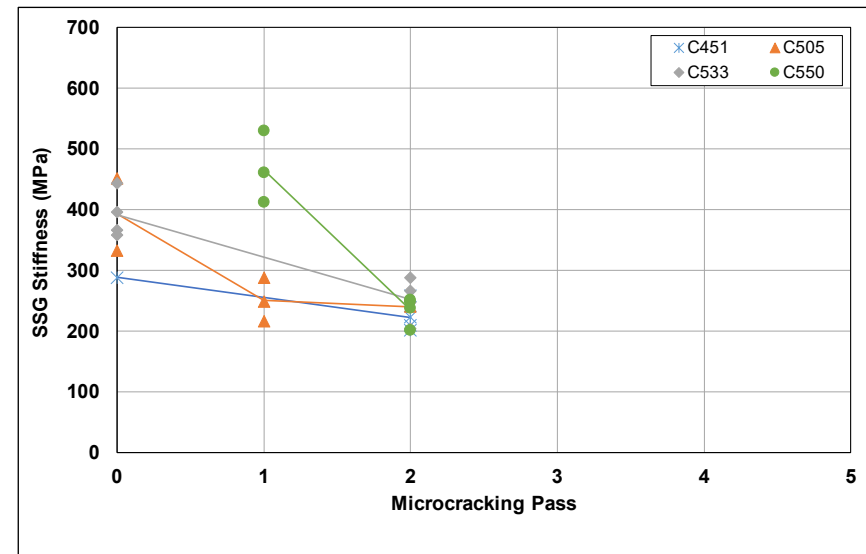
Figure B.149: Cell S19: SSG measured stiffness.
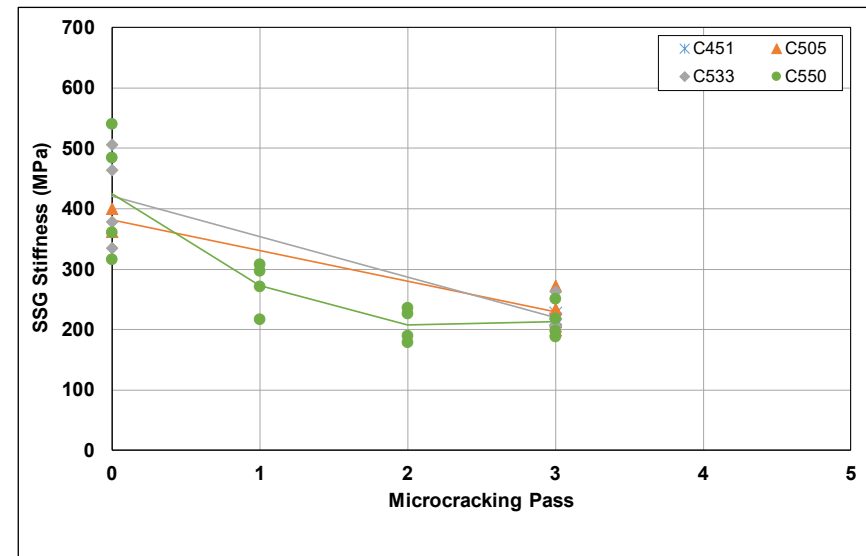
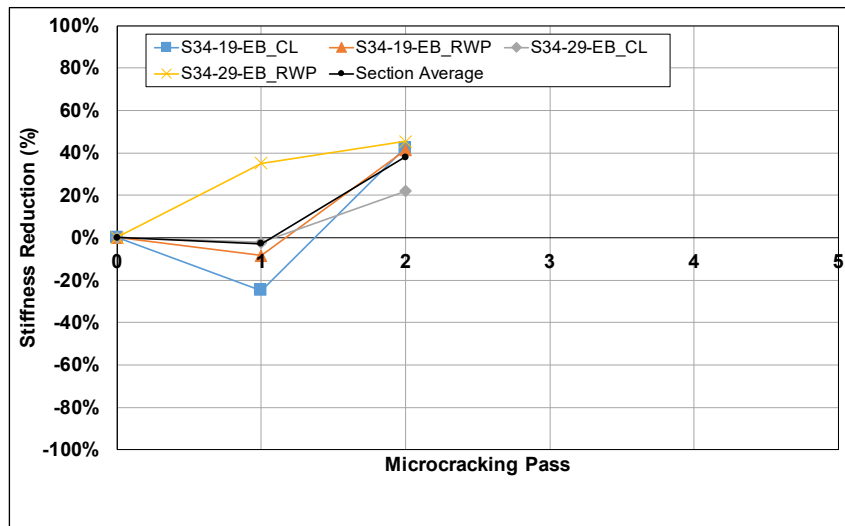Figure B.150: Cell S19: SSG stiffness results per gauge.
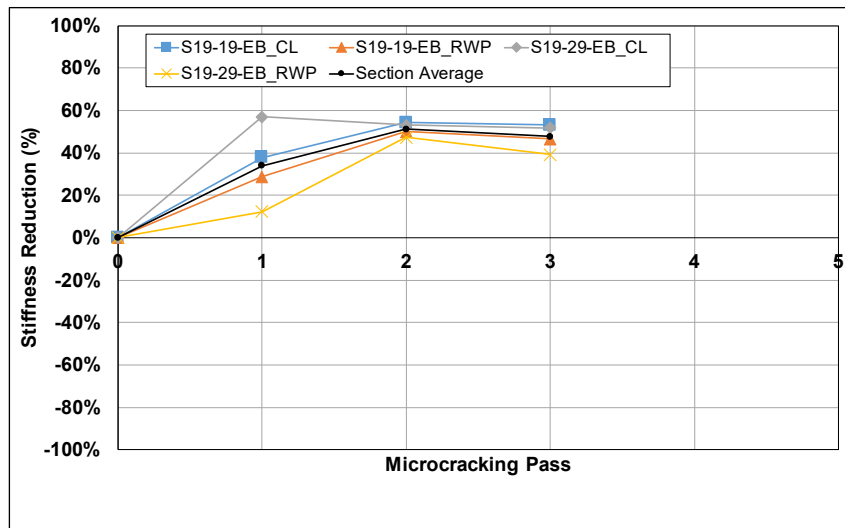
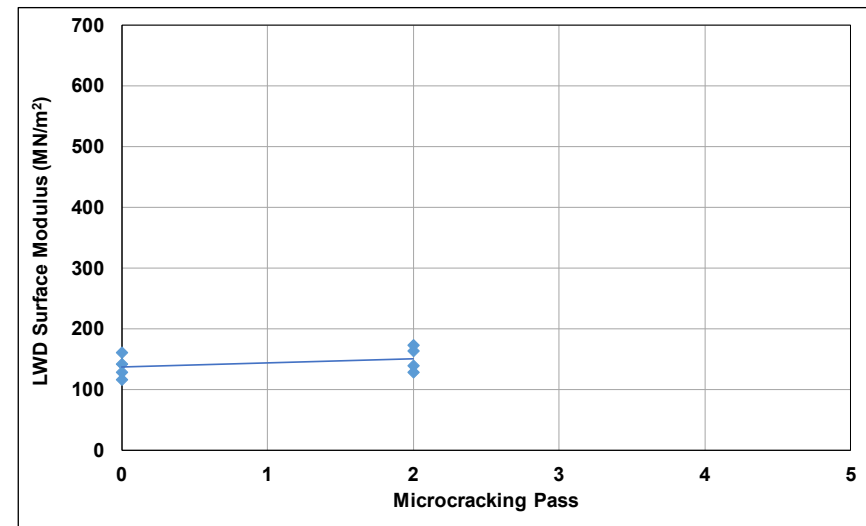Figure B.151: Cell S19: SSG stiffness reduction per station.
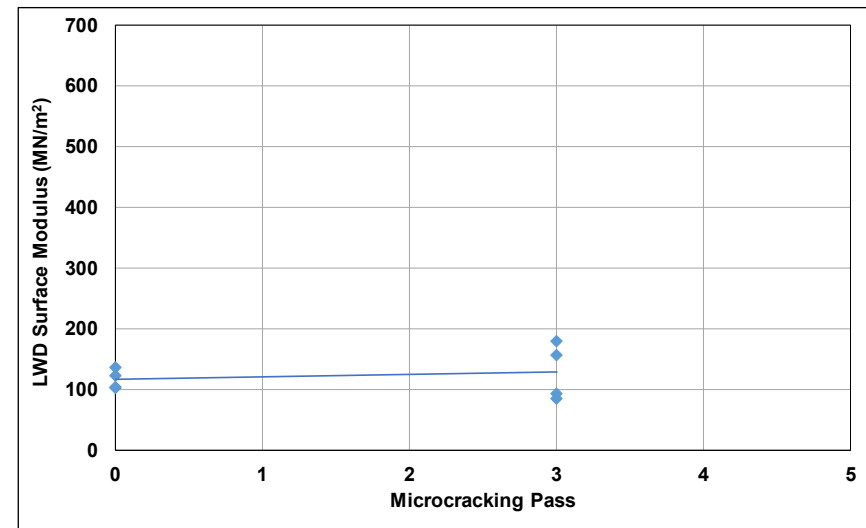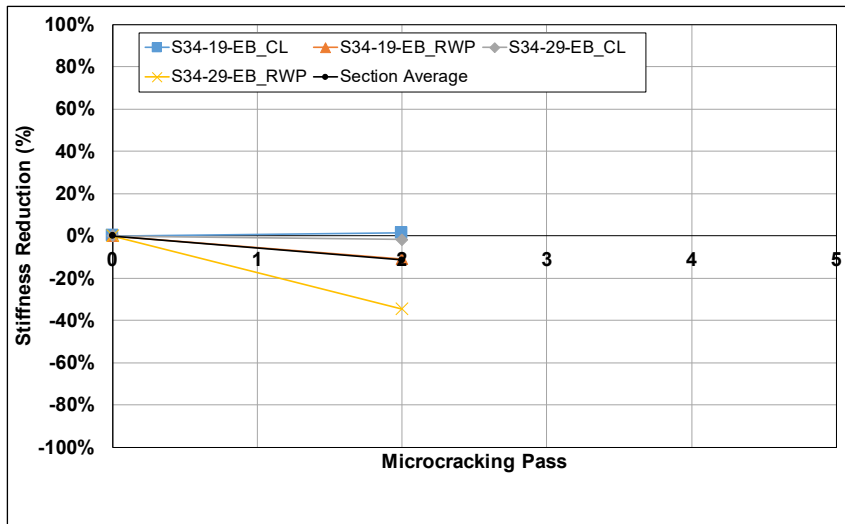

Figure B.152: Cell S19: LWD measured surface modulus.
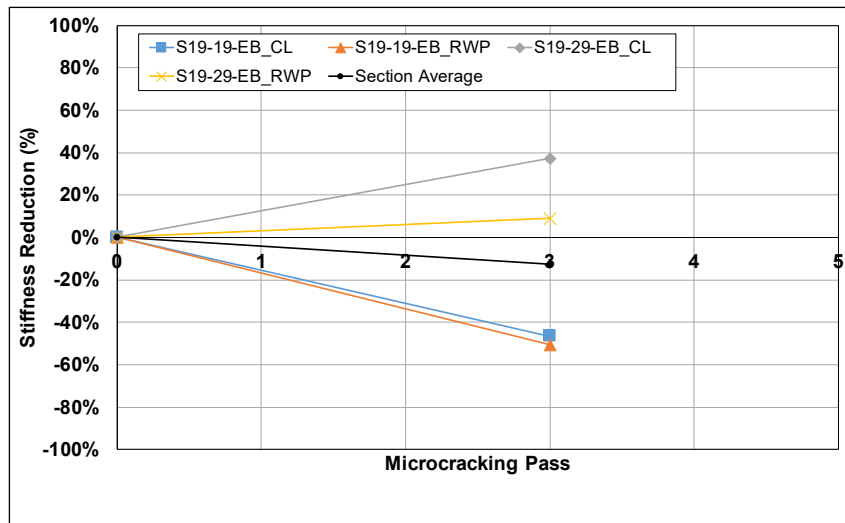
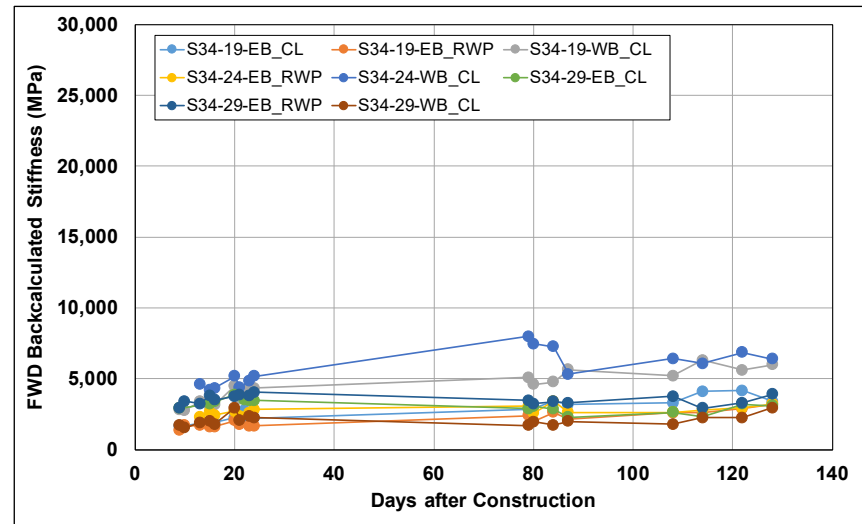**Figure B.153: Cell S19: LWD modulus reduction per station.**
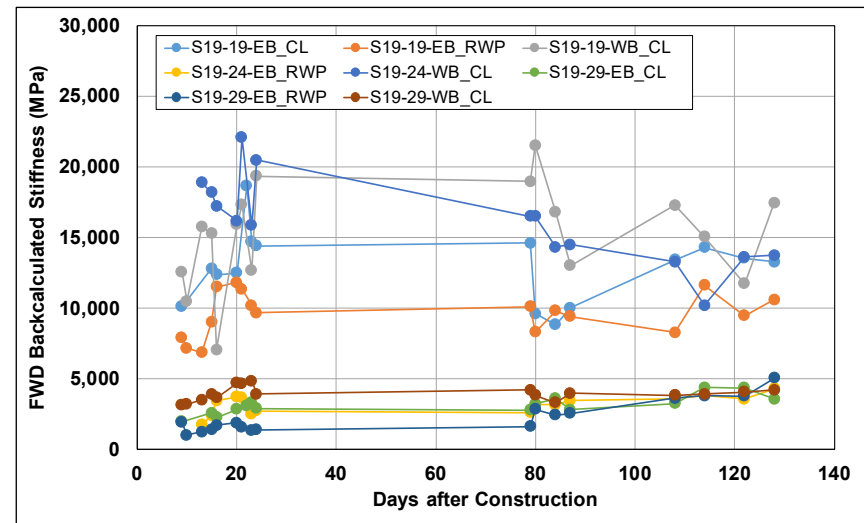
Figure B.154: Cell S19: Change in FWD-backcalculated stiffness.
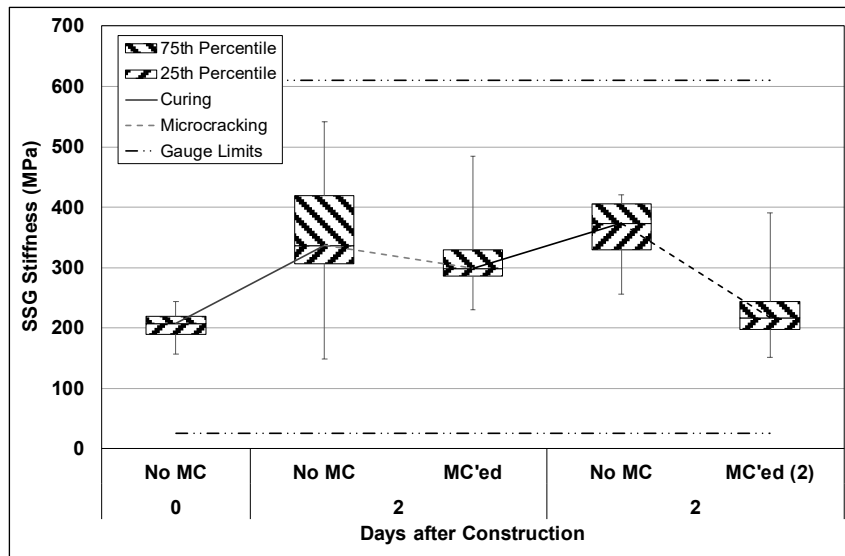
Figure B.155: Cell S20: SSG measured stiffness.
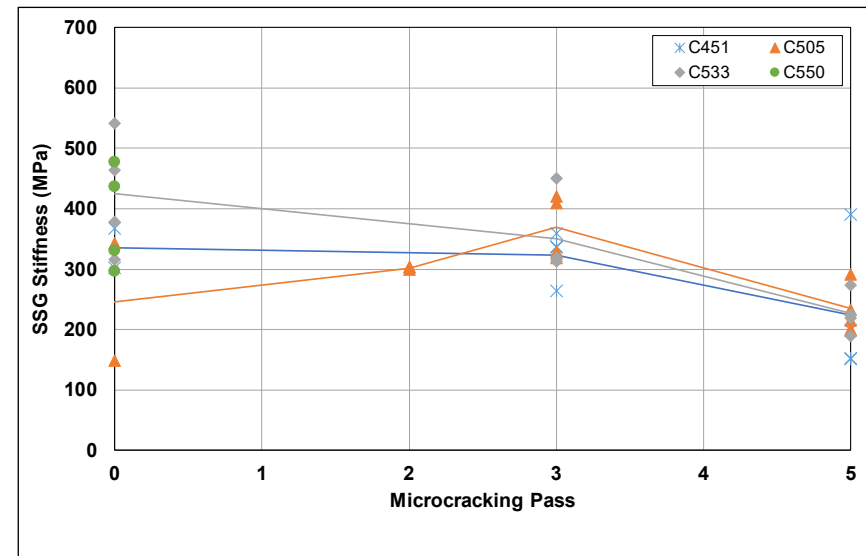
Figure B.156: Cell S20: SSG stiffness results per gauge.
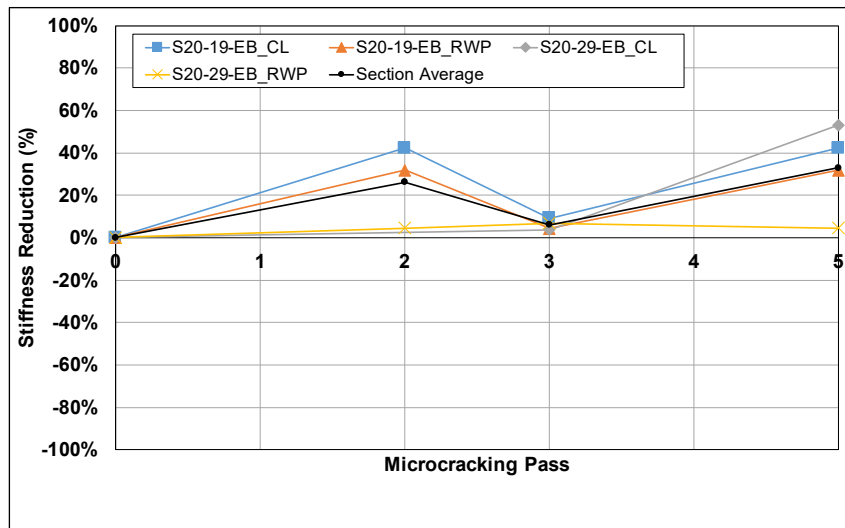
Figure B.157: Cell S20: SSG stiffness reduction per station.
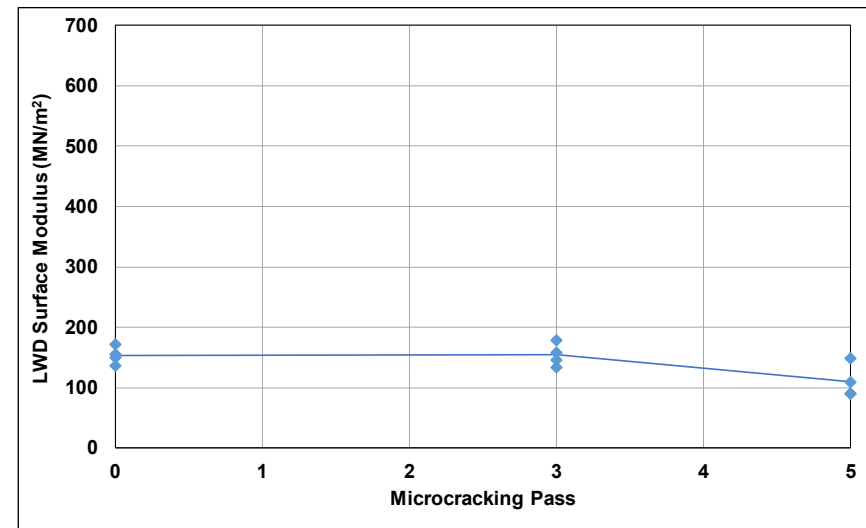
Figure B.158: Cell S20: LWD measured surface modulus.
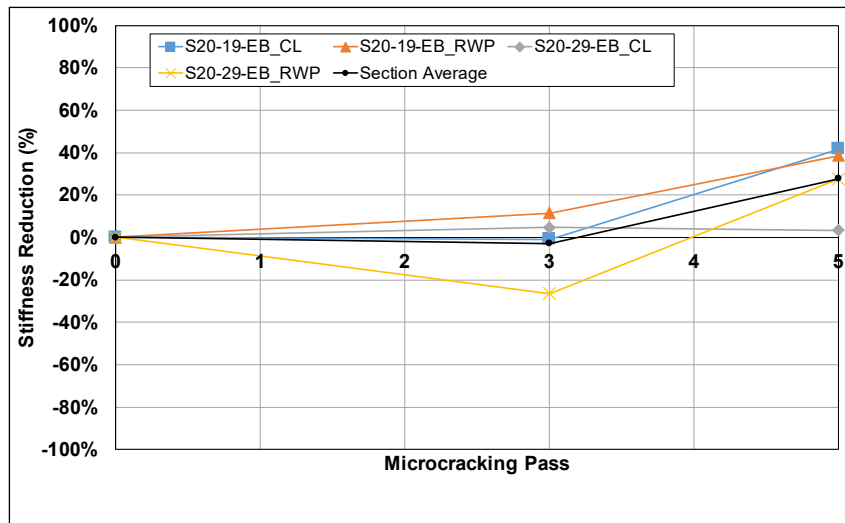
Figure B.159: Cell S20: LWD modulus reduction per station.
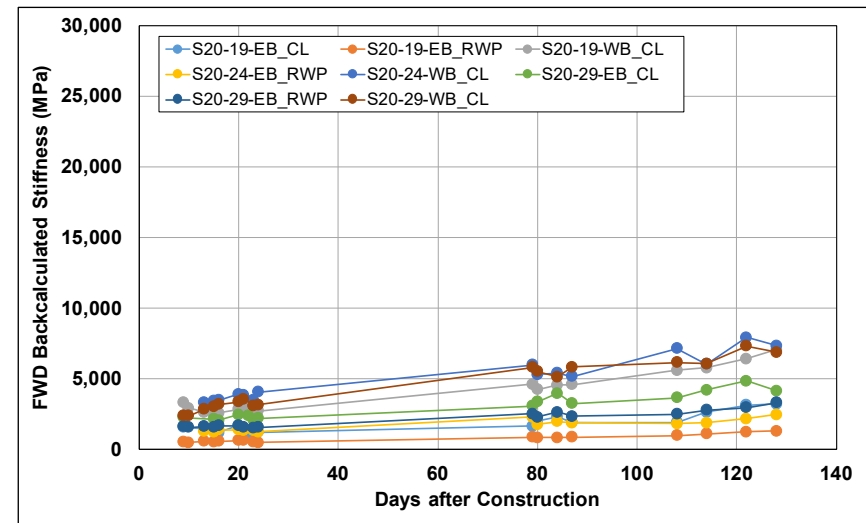
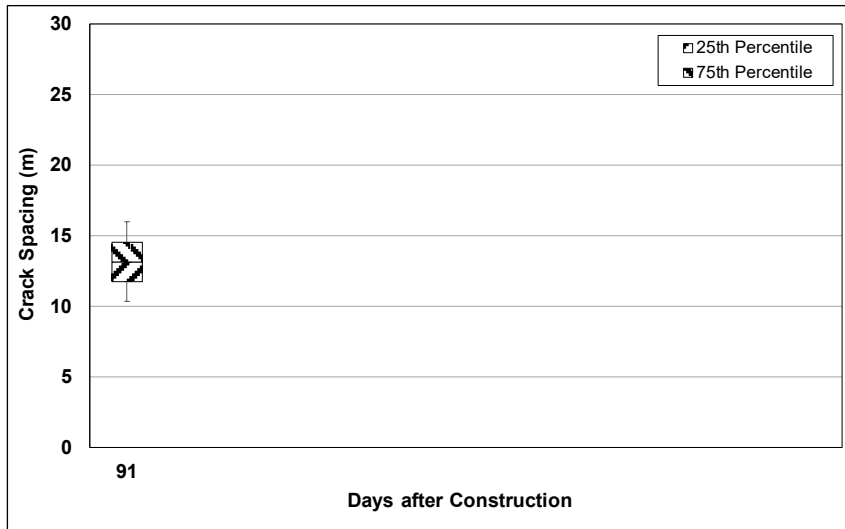**Figure B.160: Cell S20: Change in FWD-backcalculated stiffness.**
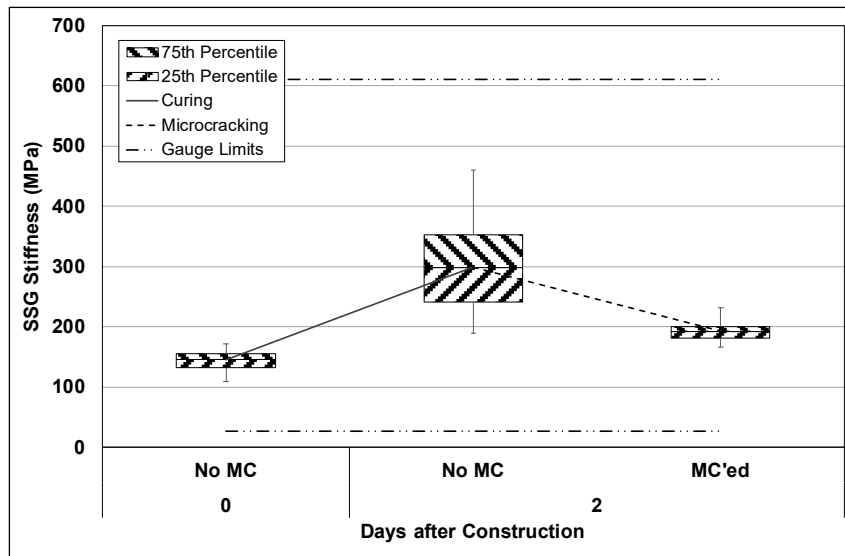
Figure B.161: Cell S21: SSG measured stiffness.
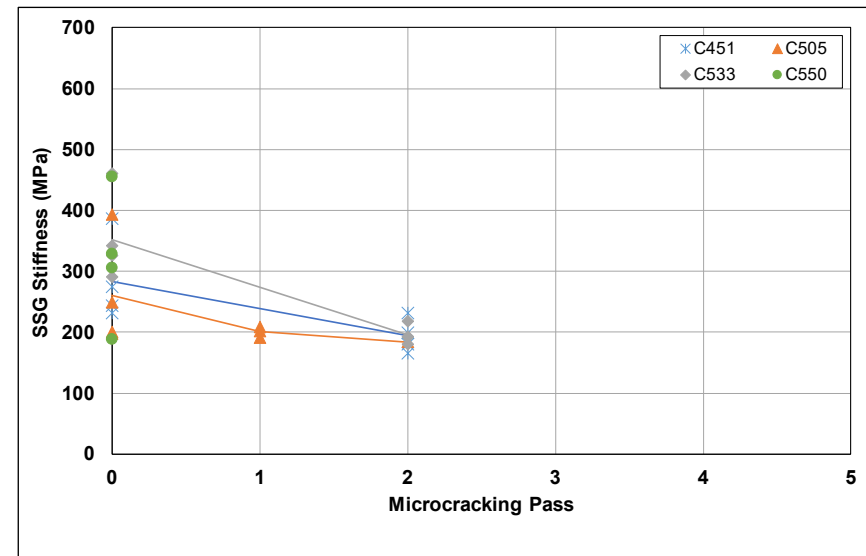
Figure B.162: Cell S21: SSG stiffness results per gauge.
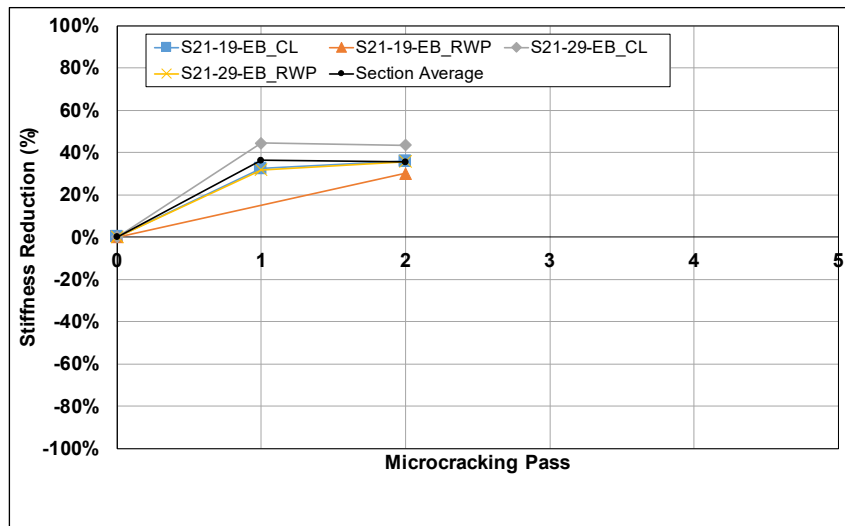
Figure B.163: Cell S21: SSG stiffness reduction per station.
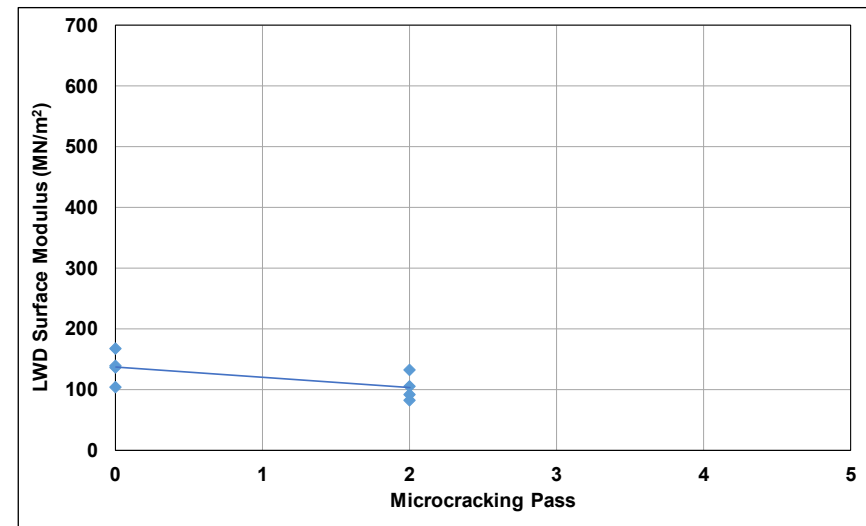
Figure B.164: Cell S21: LWD measured surface modulus.
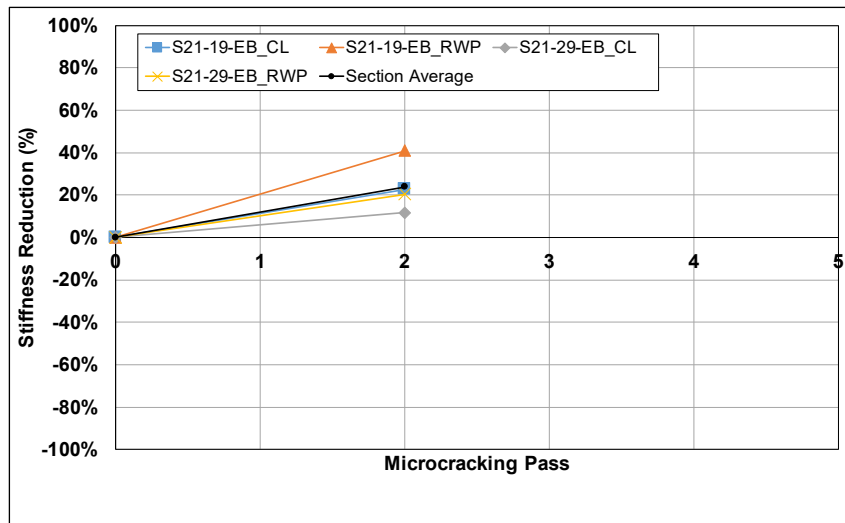
Figure B.165: Cell S21: LWD modulus reduction per station.
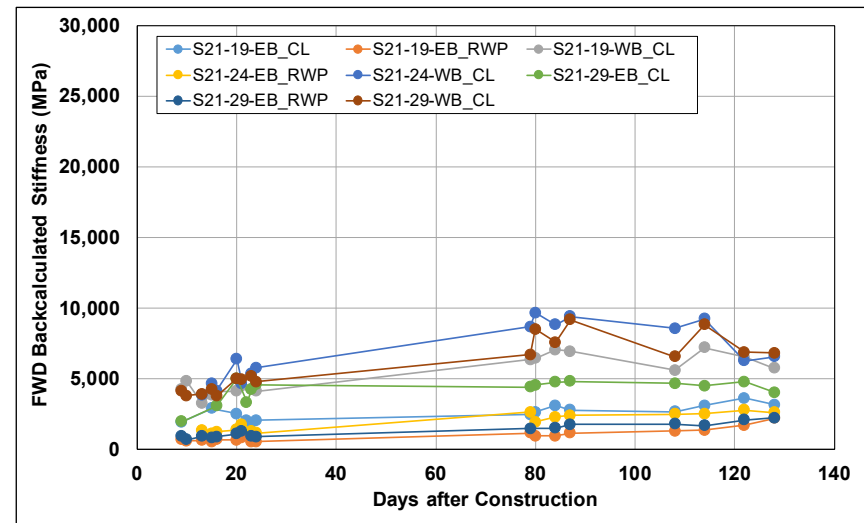
Figure B.166: Cell S21: Change in FWD-backcalculated stiffness.
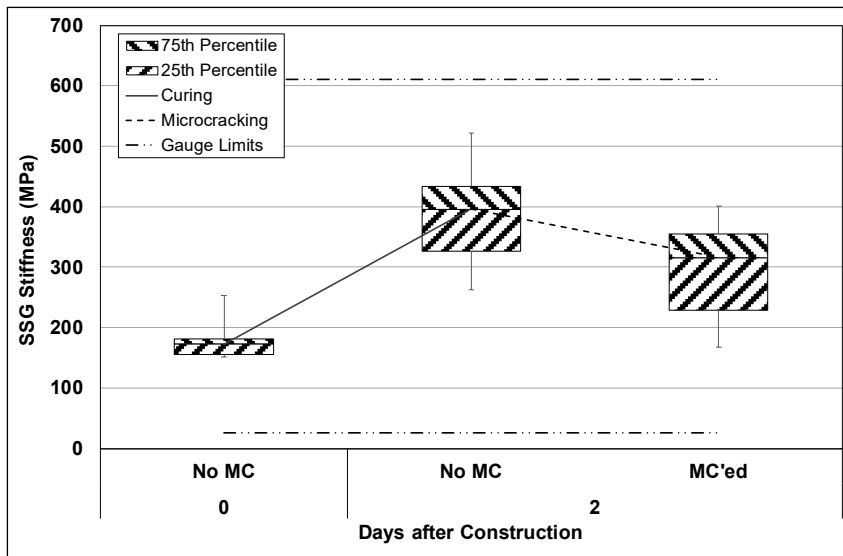
Figure B.167: Cell S22: SSG measured stiffness.
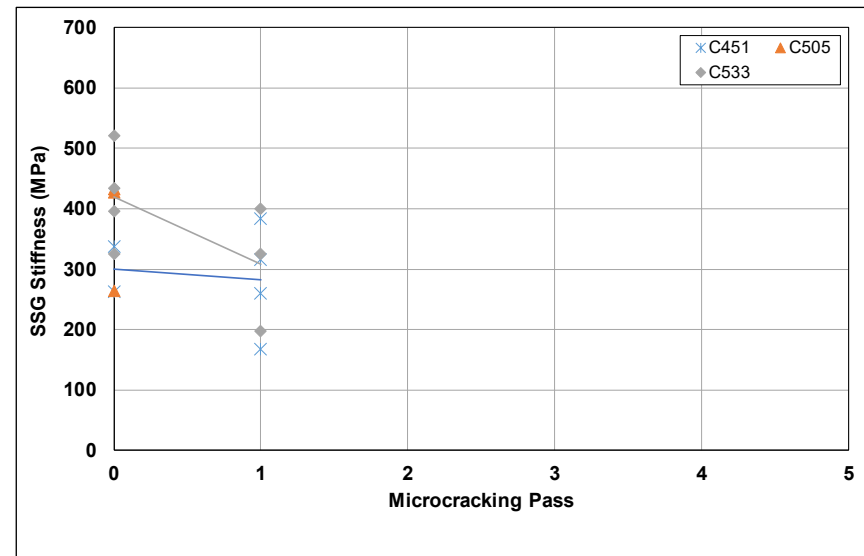
Figure B.168: Cell S22: SSG stiffness results per gauge.
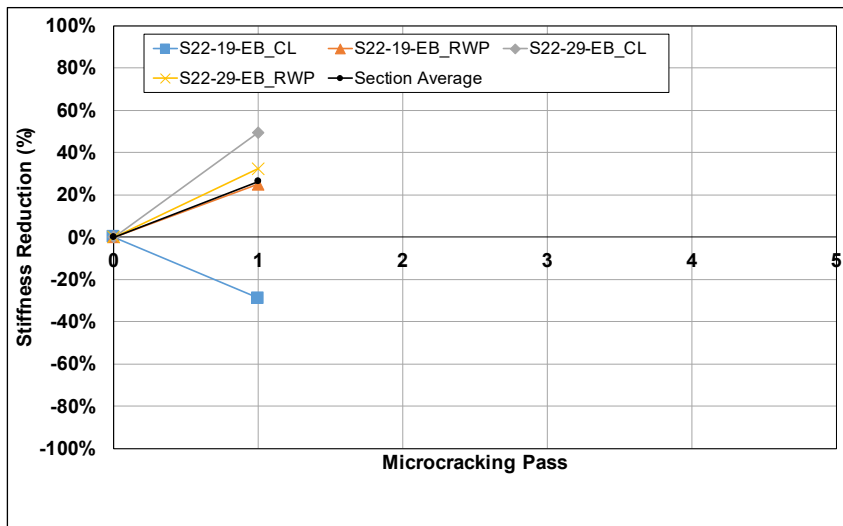
Figure B.169: Cell S22: SSG stiffness reduction per station.
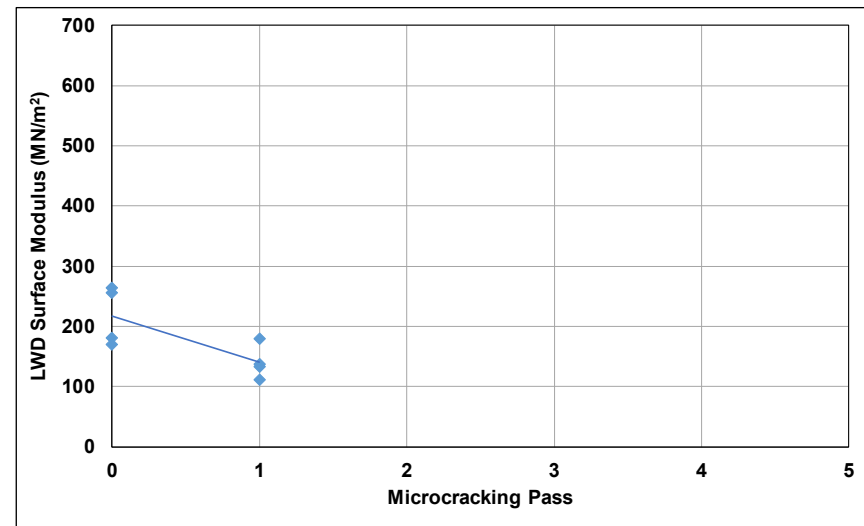
Figure B.170: Cell S22: LWD measured surface modulus.
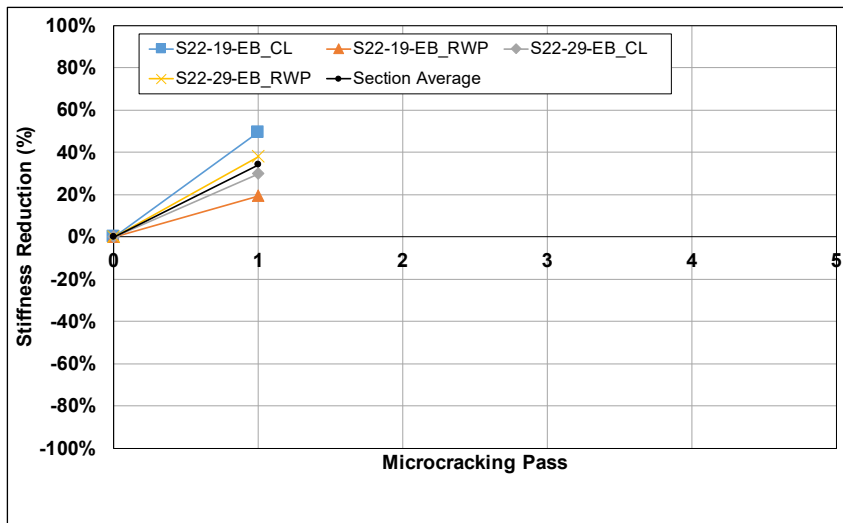
Figure B.171: Cell S22: LWD modulus reduction per station.
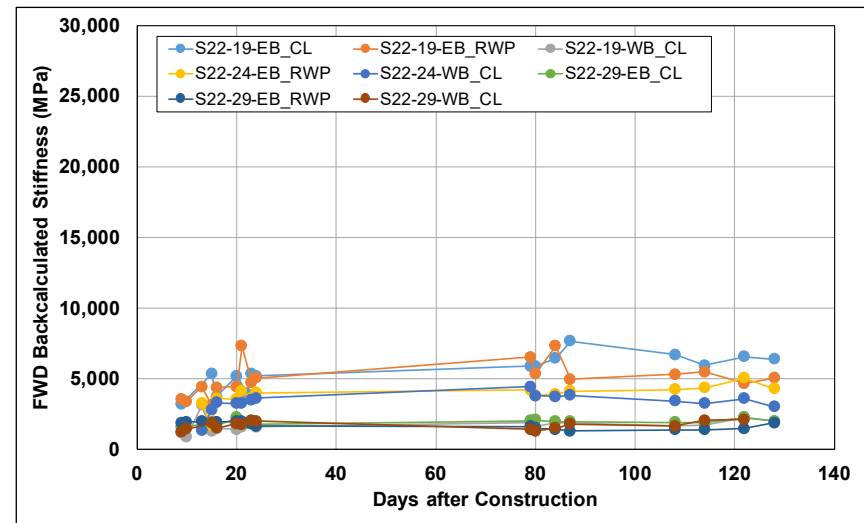
Figure B.172: Cell S22: Change in FWD-backcalculated stiffness.
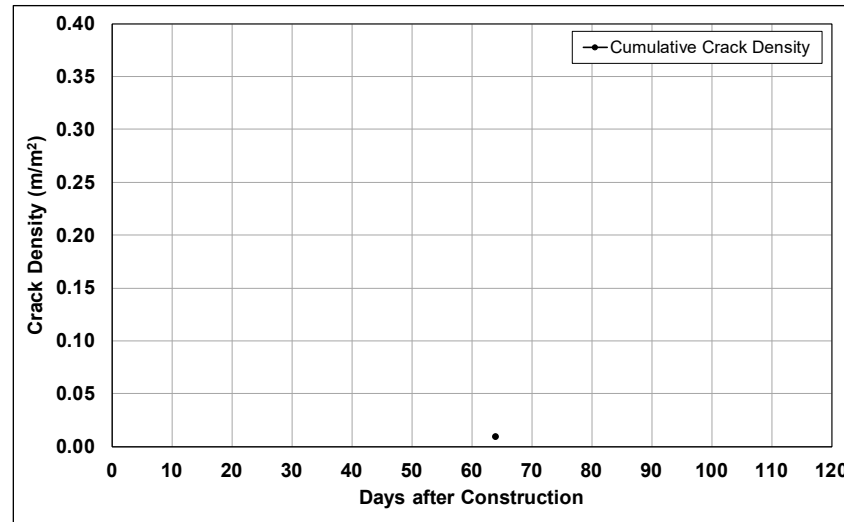
Figure B.173: Cell S22: Change in crack density.
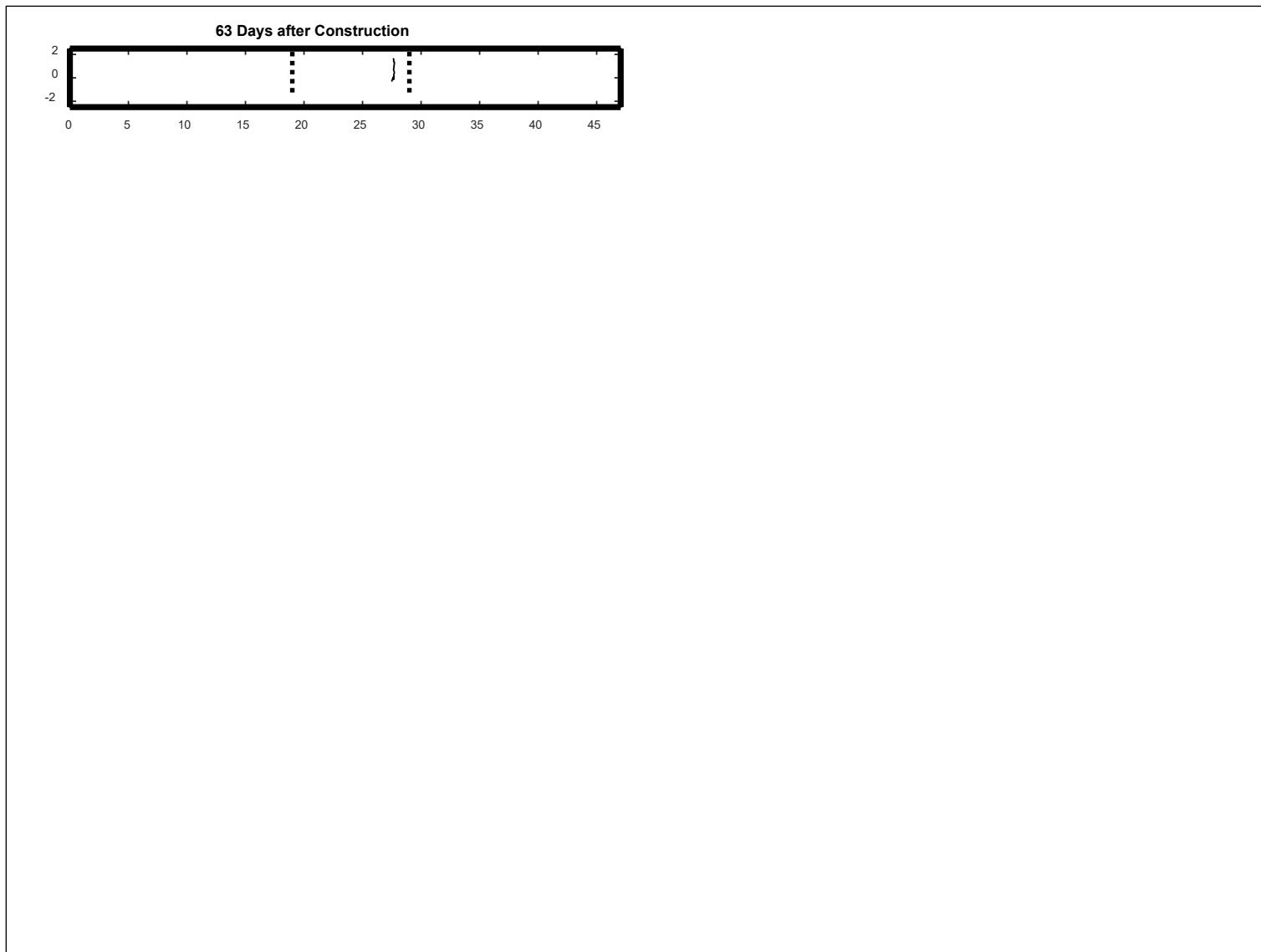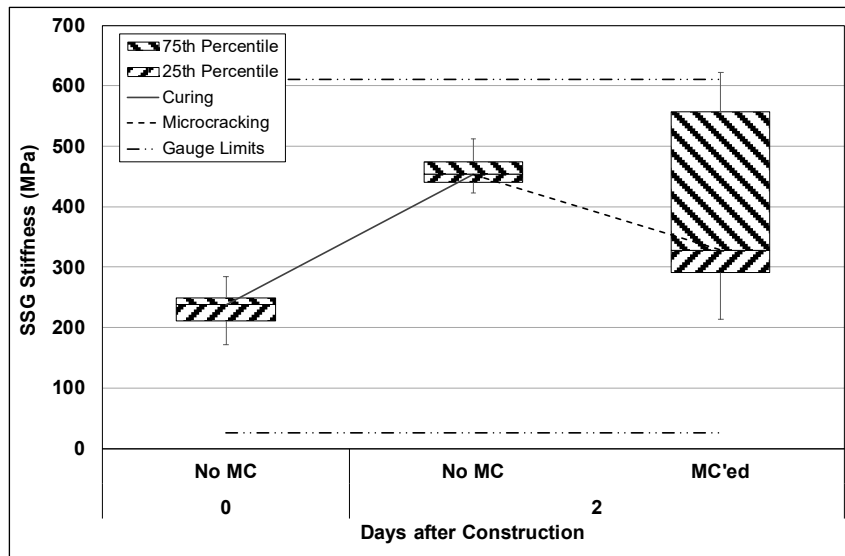
Figure B.174: Cell S22: Crack development.
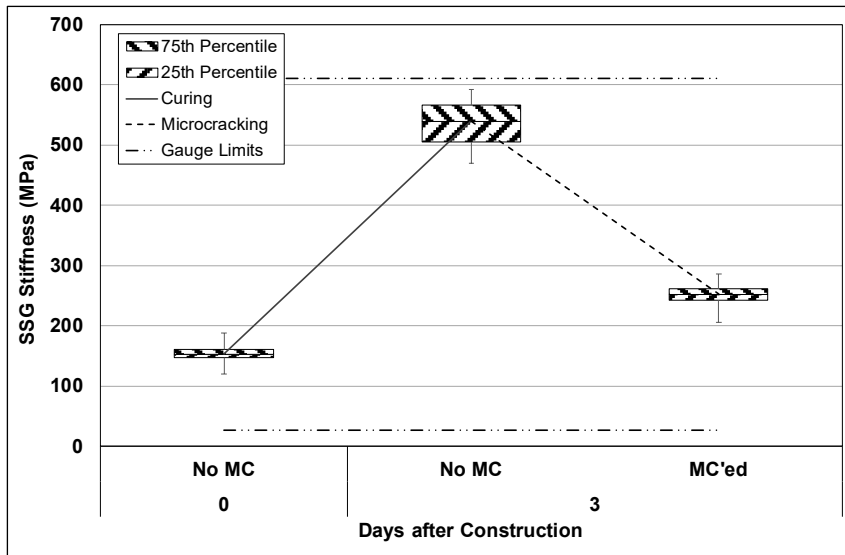
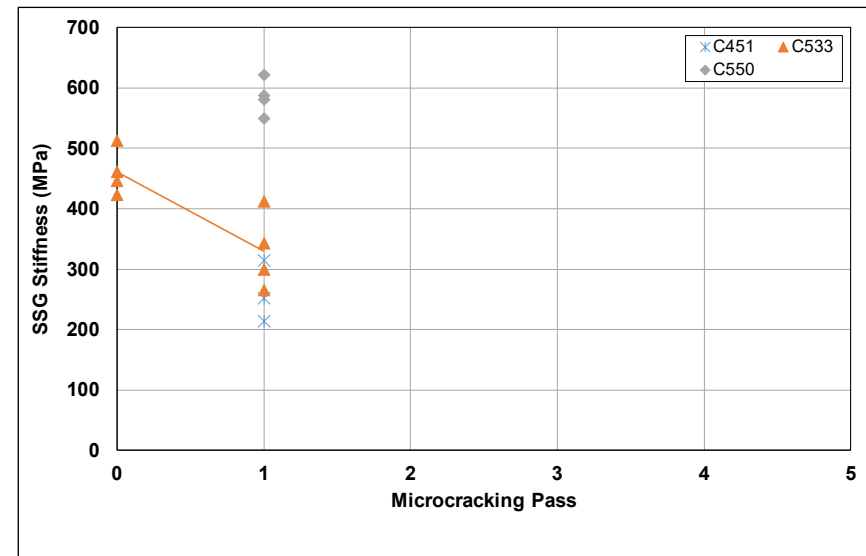**Figure B.175: Cell S23: SSG measured stiffness.**
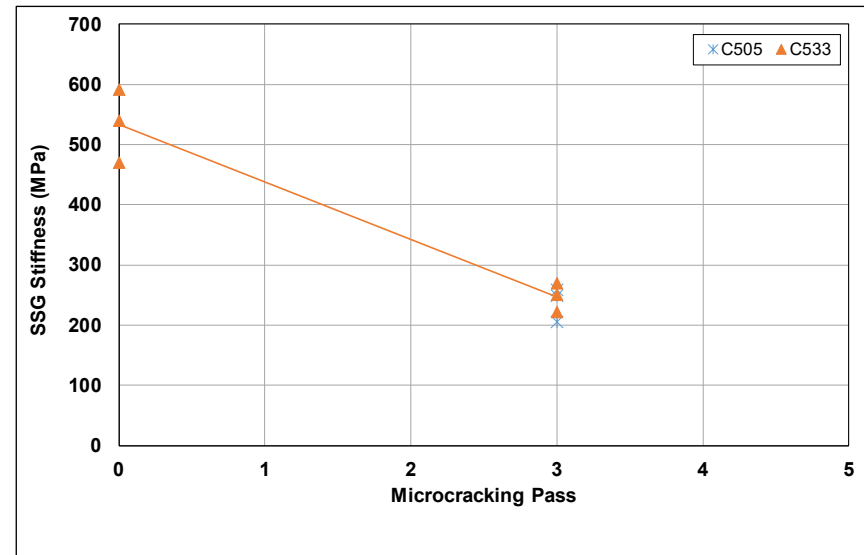
**Figure B.176: Cell S23: SSG stiffness results per gauge.**
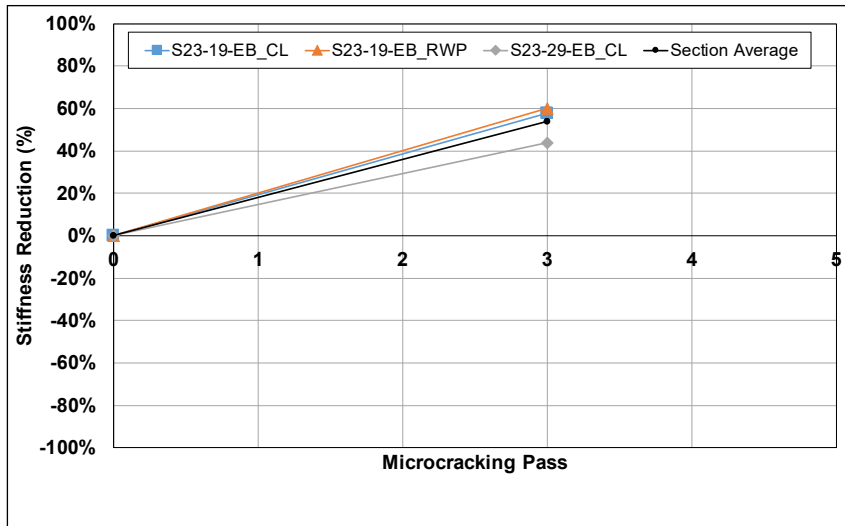
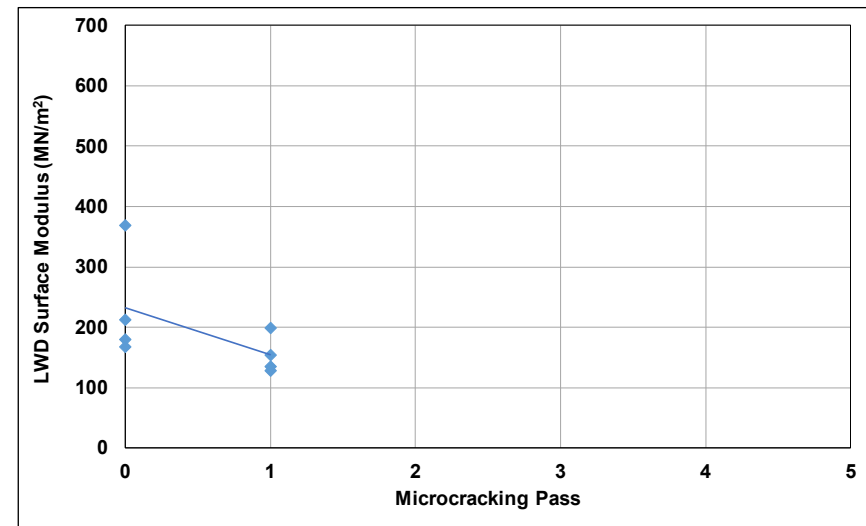**Figure B.177: Cell S23: SSG stiffness reduction per station.**
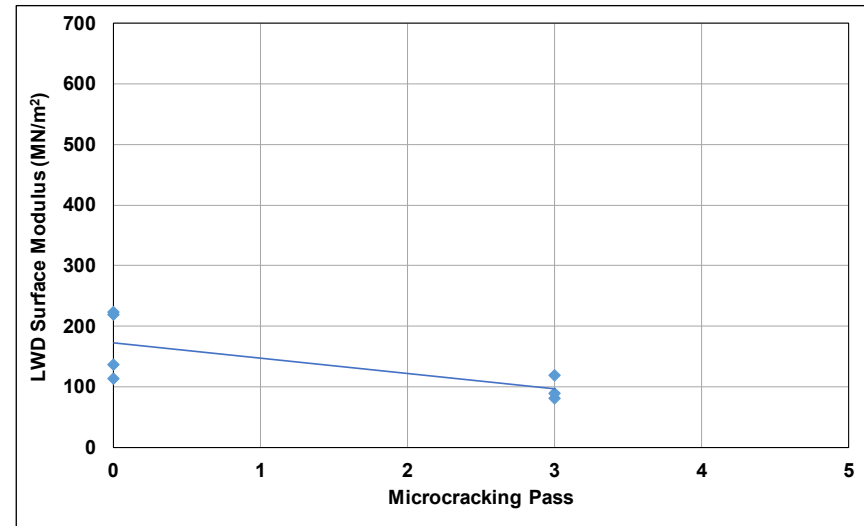
Figure B.178: Cell S23: LWD measured surface modulus.
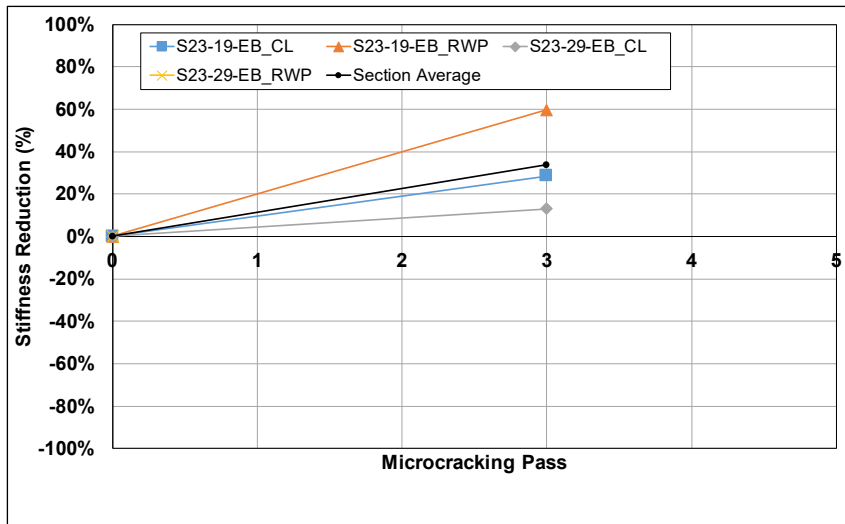
Figure B.179: Cell S23: LWD modulus reduction per station.
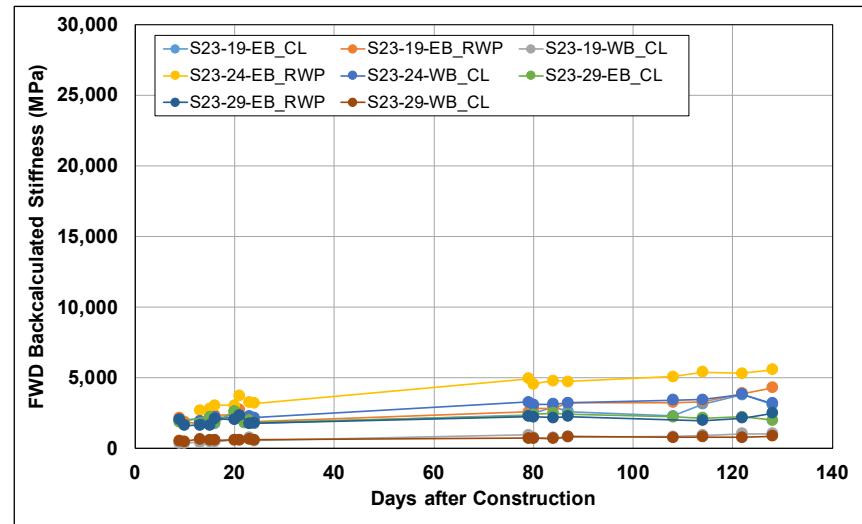
Figure B.180: Cell S23: Change in FWD-backcalculated stiffness.
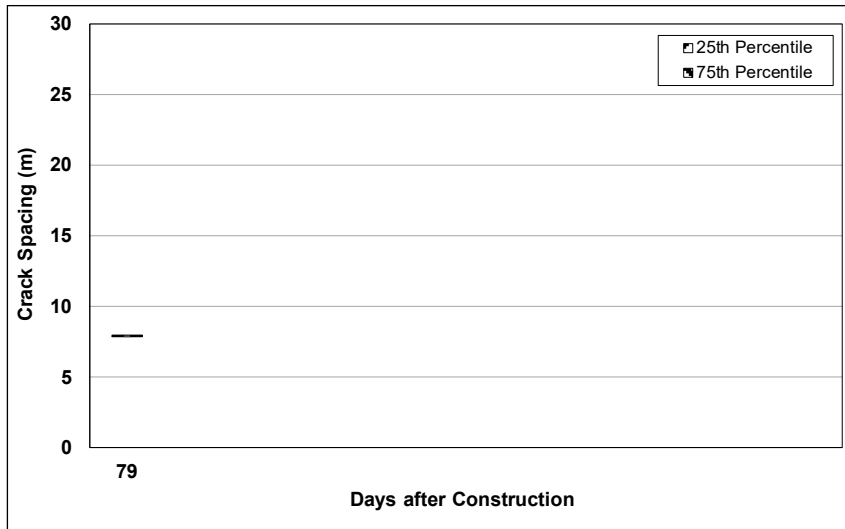
Figure B.181: Cell S23: Change in crack spacing.
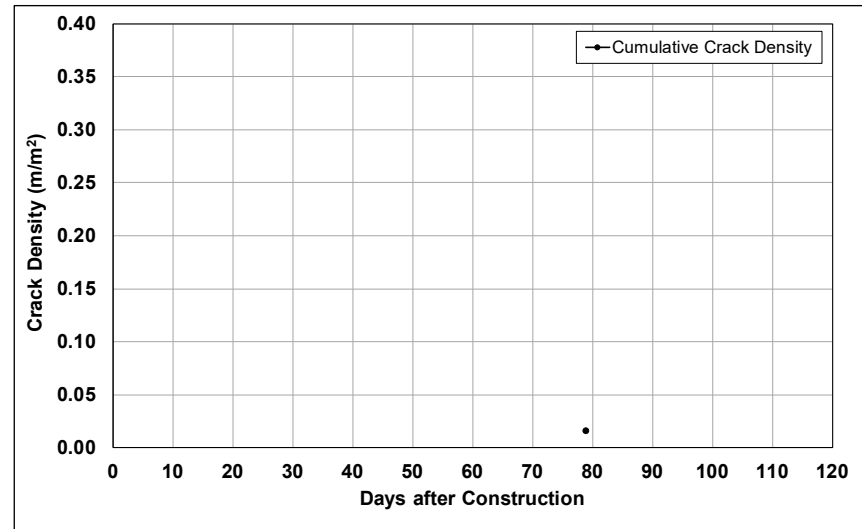
Figure B.182: Cell S23: Change in crack density.
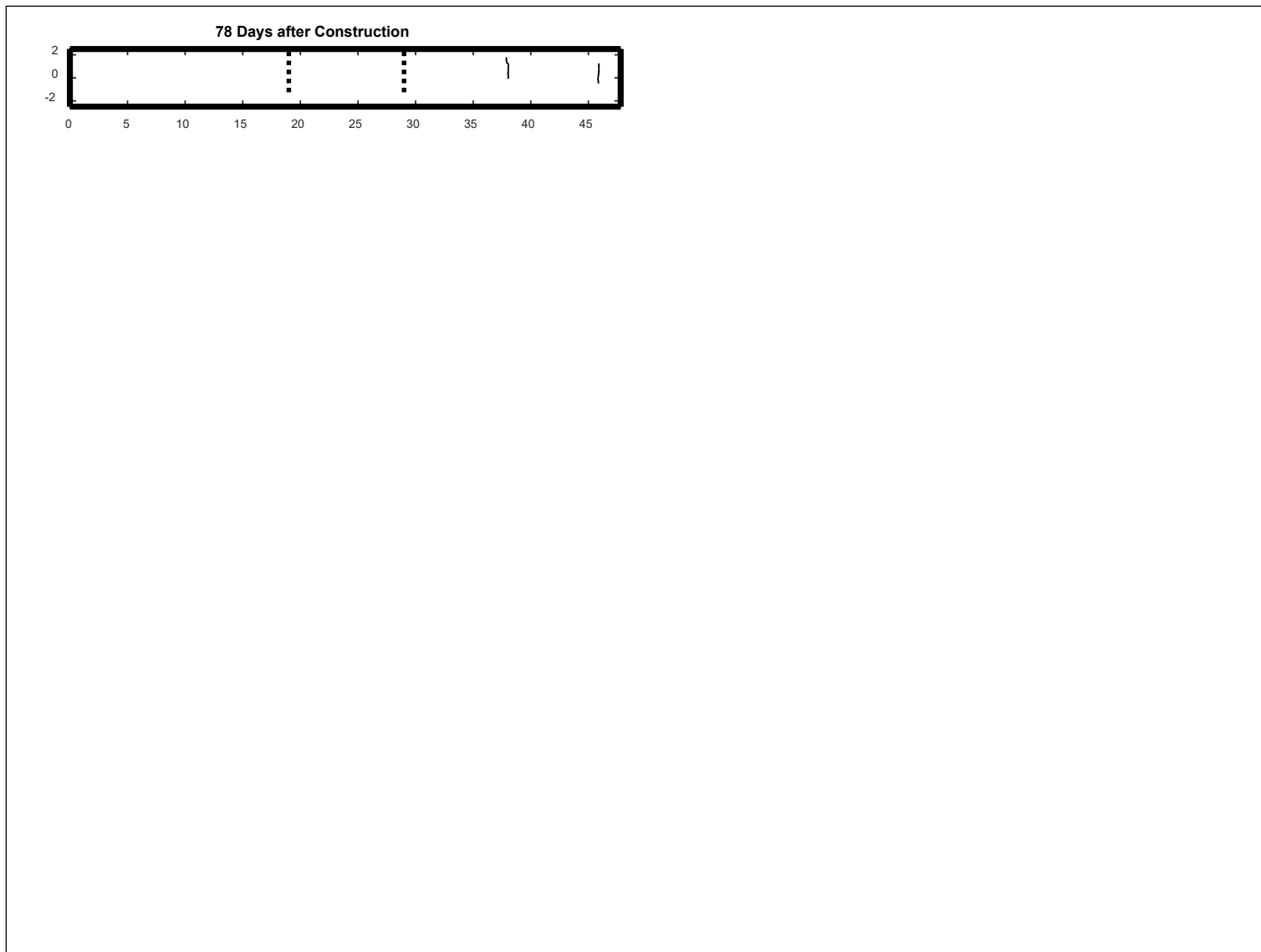
Figure B.183: Cell S23: Crack development.
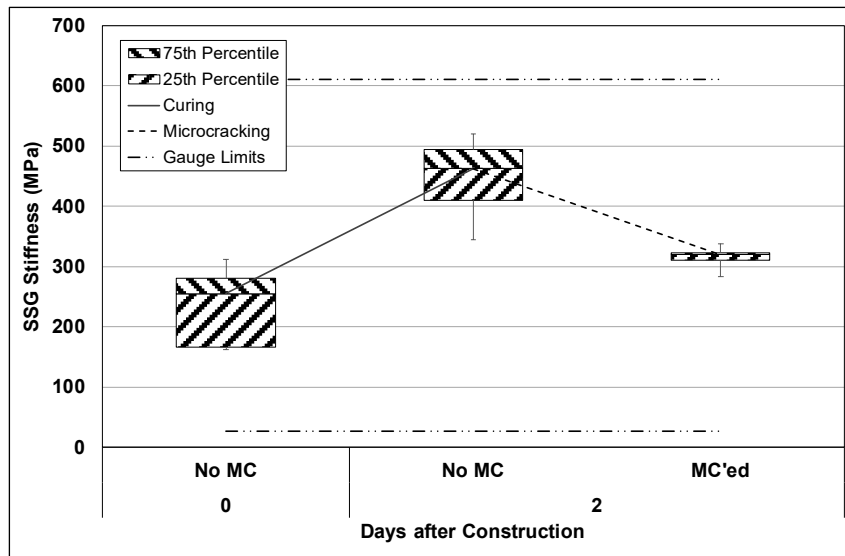
Figure B.184: Cell S24: SSG measured stiffness.
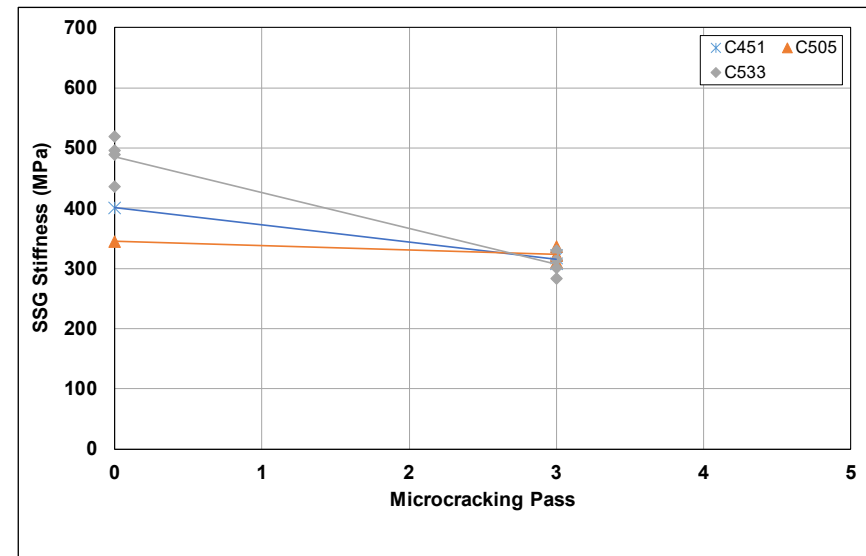
Figure B.185: Cell S24: SSG stiffness results per gauge.
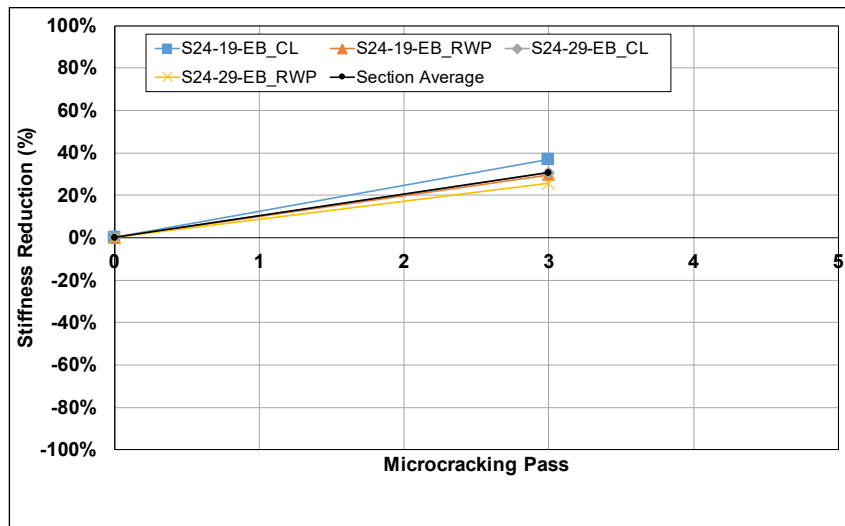
Figure B.186: Cell S24: SSG stiffness reduction per station.
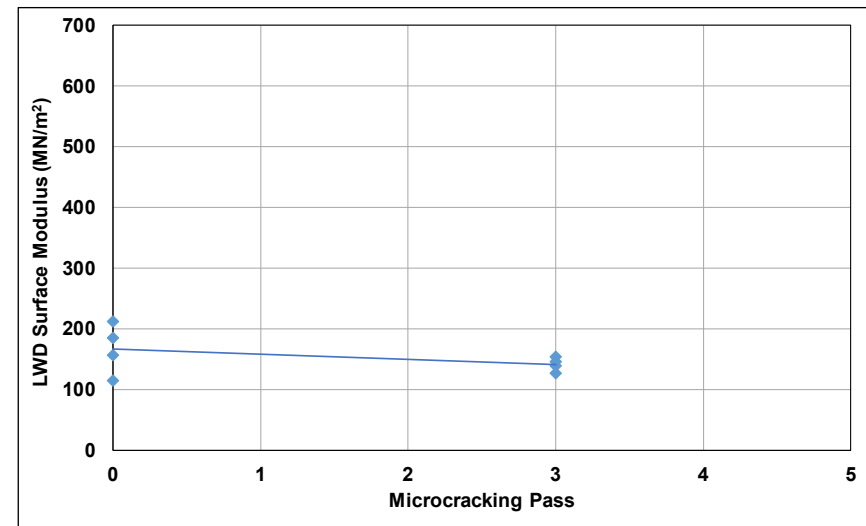

Figure B.187: Cell S24: LWD measured surface modulus.
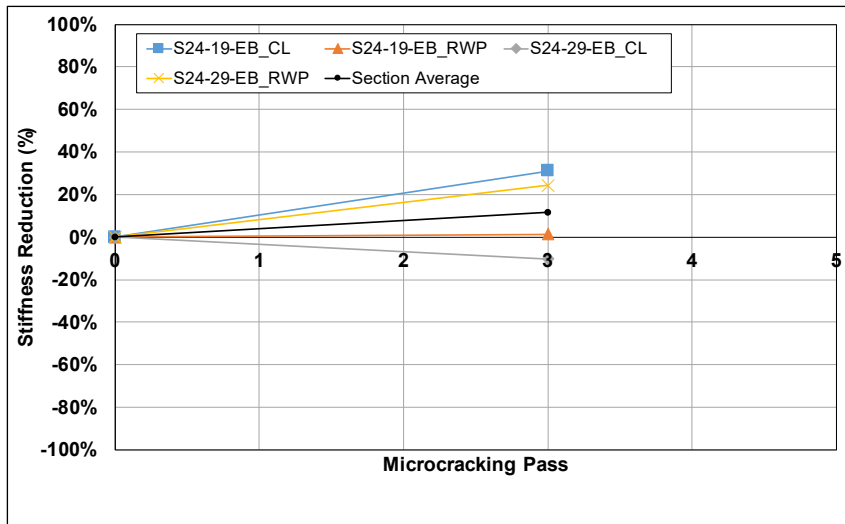
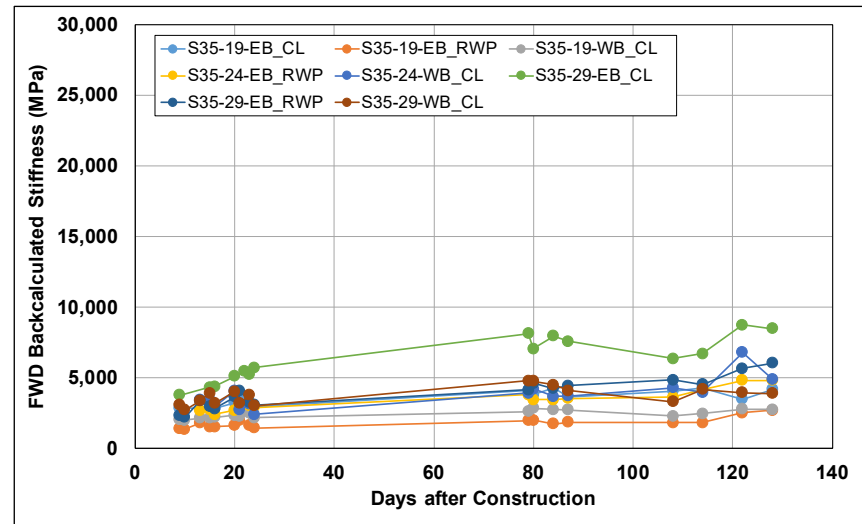**Figure B.188: Cell S24: LWD modulus reduction per station.**
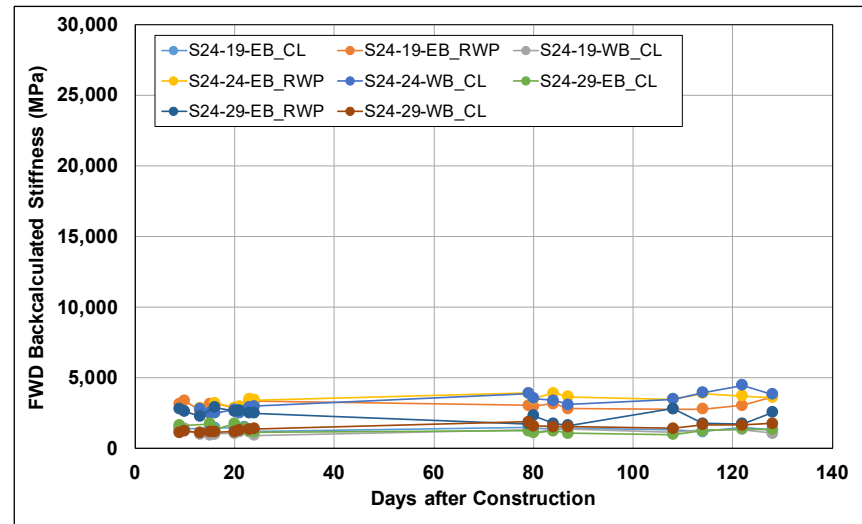
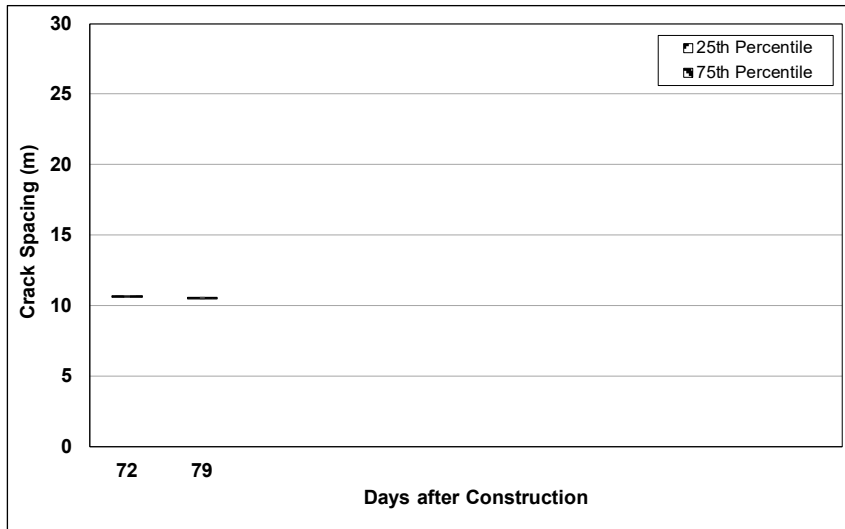**Figure B.189: Cell S24: Change in FWD-backcalculated stiffness.**
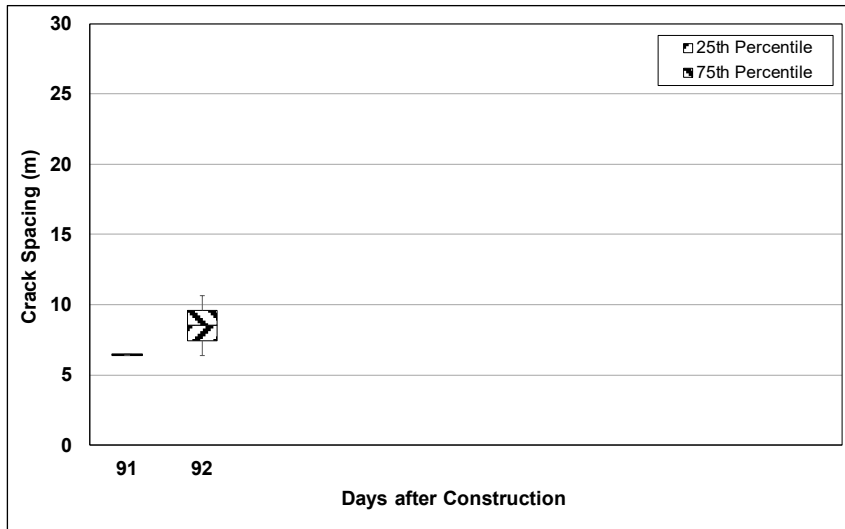
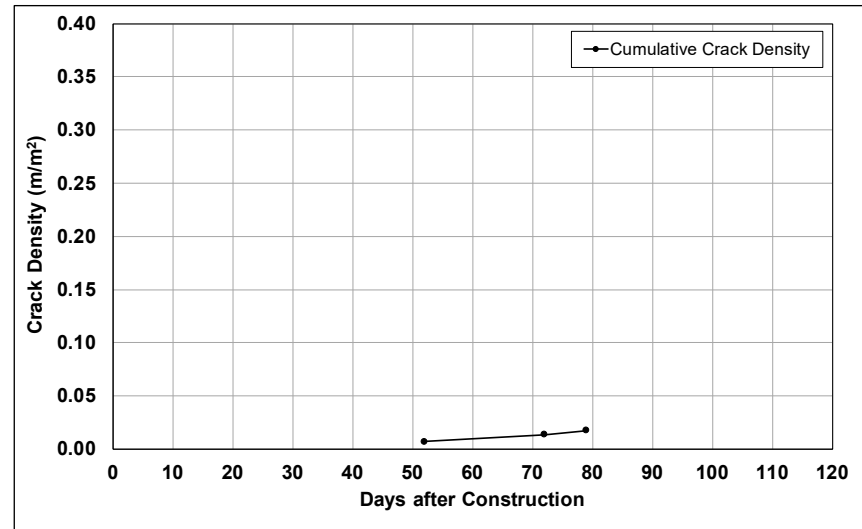**Figure B.190: Cell S24: Change in crack spacing.**
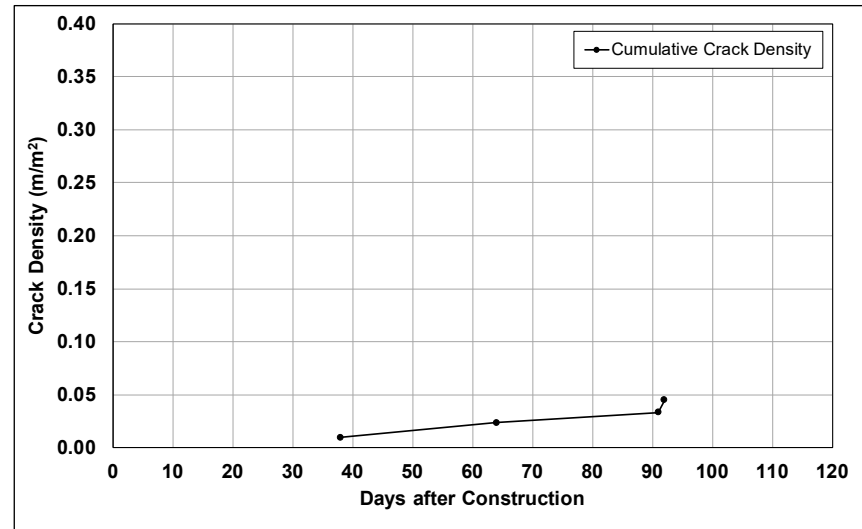
Figure B.191: Cell S24: Change in crack density.
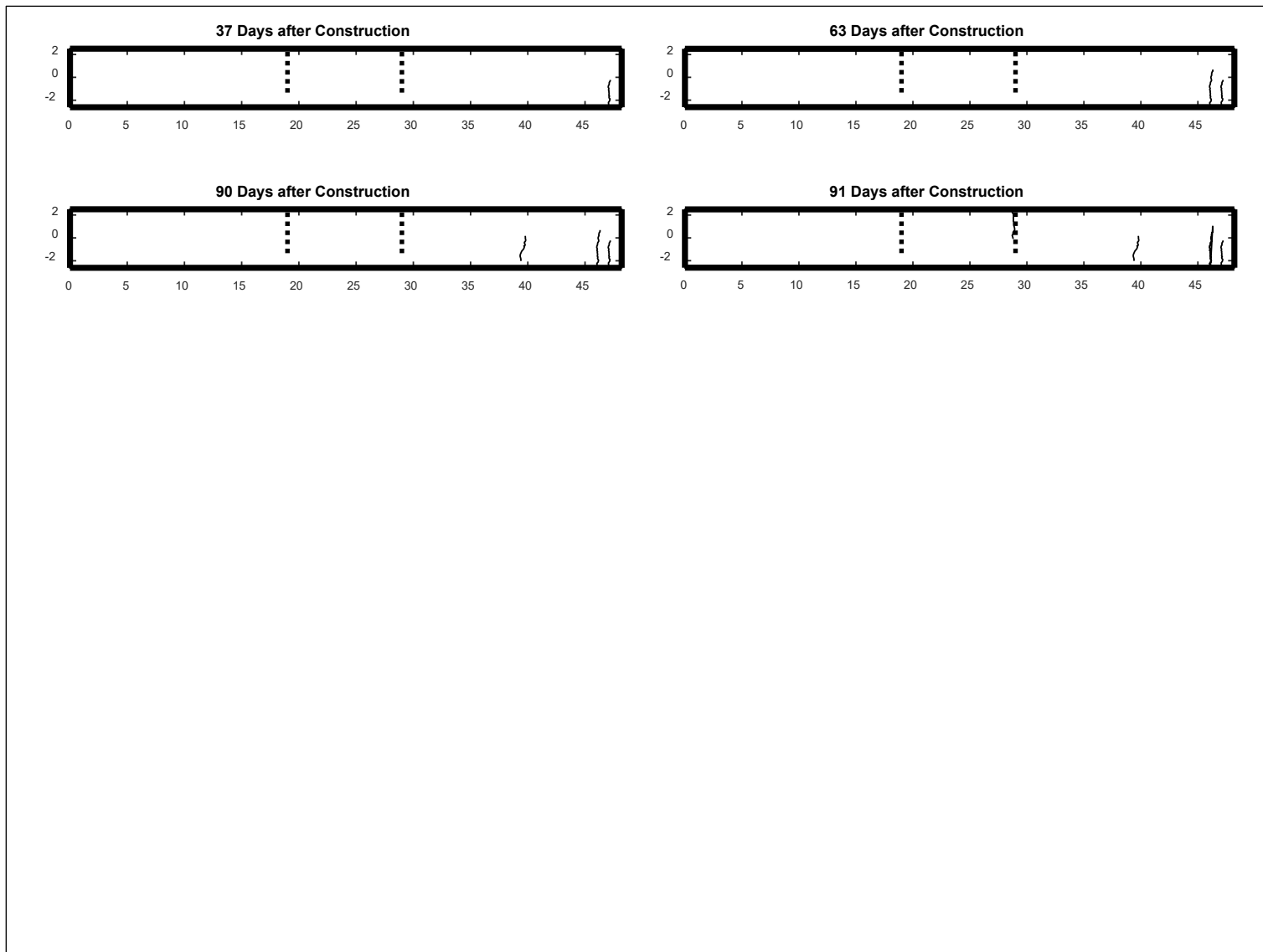
Figure B.192: Cell S24: Crack development.
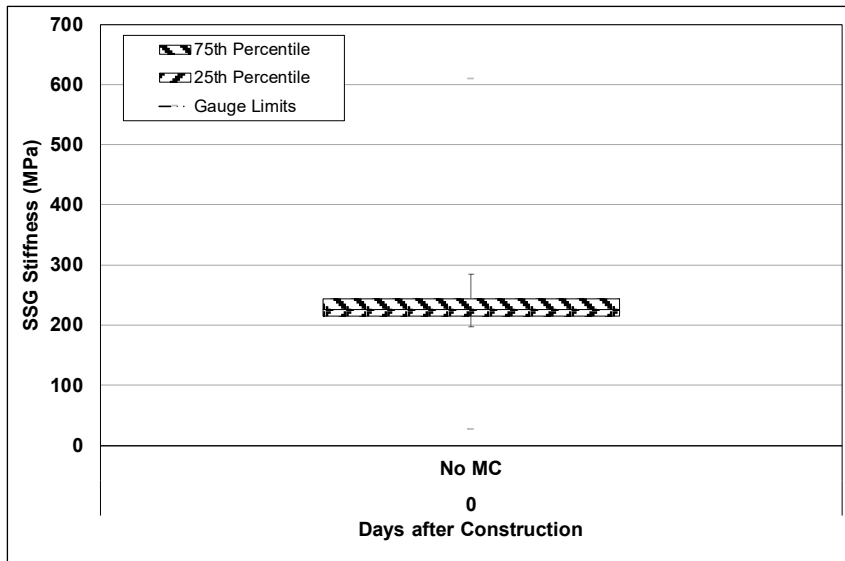
Figure B.193: Cell S25: SSG measured stiffness.
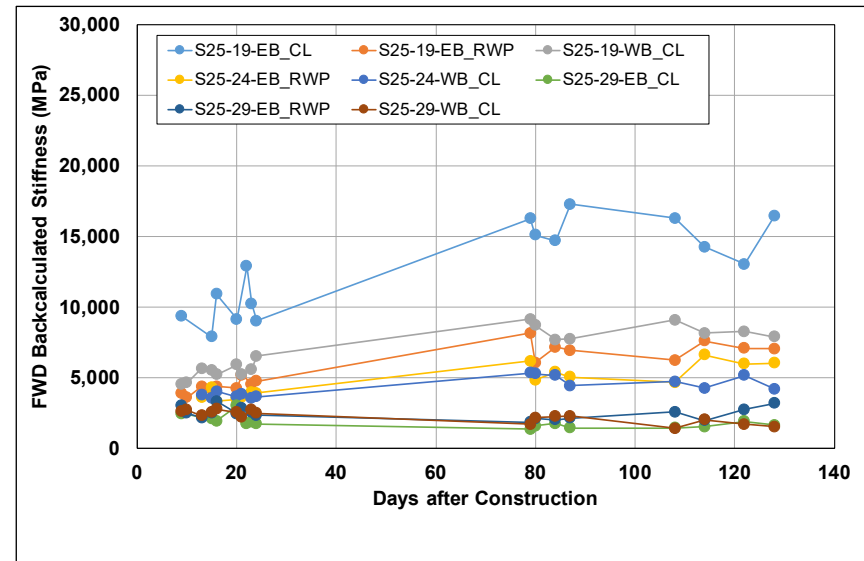
Figure B.194: Cell S25: Change in FWD-backcalculated stiffness.
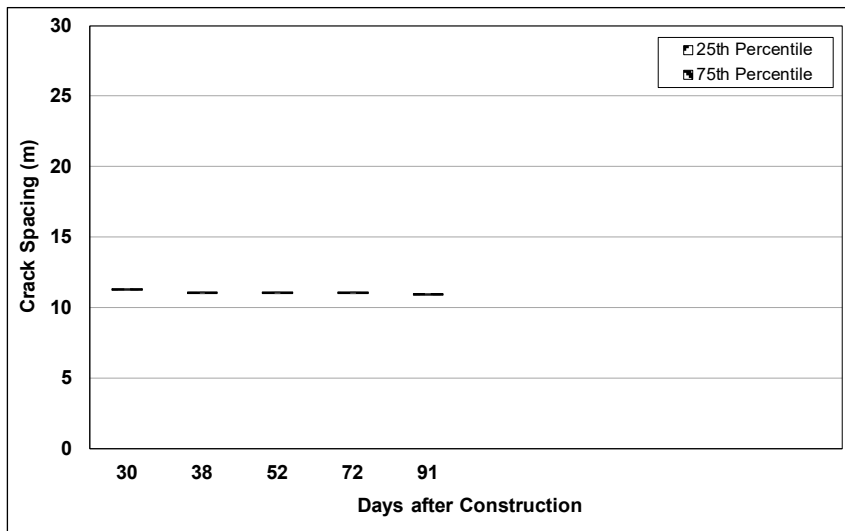
Figure B.195: Cell S25: Change in crack spacing.
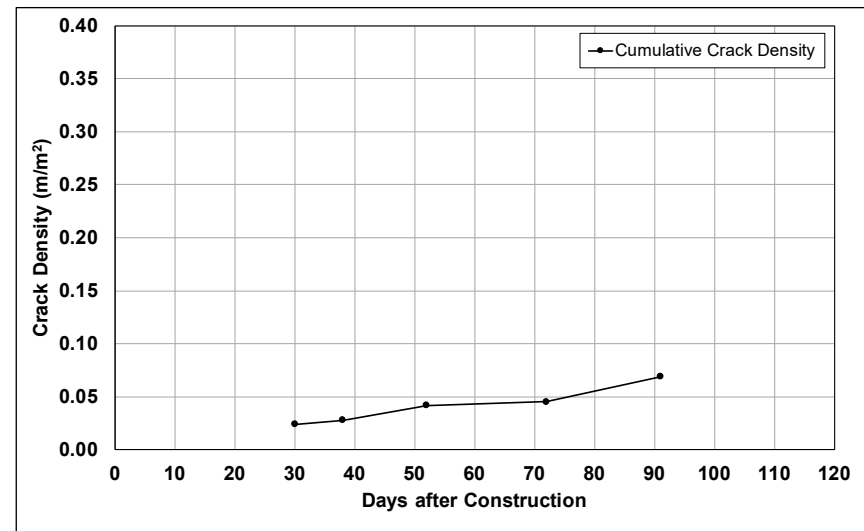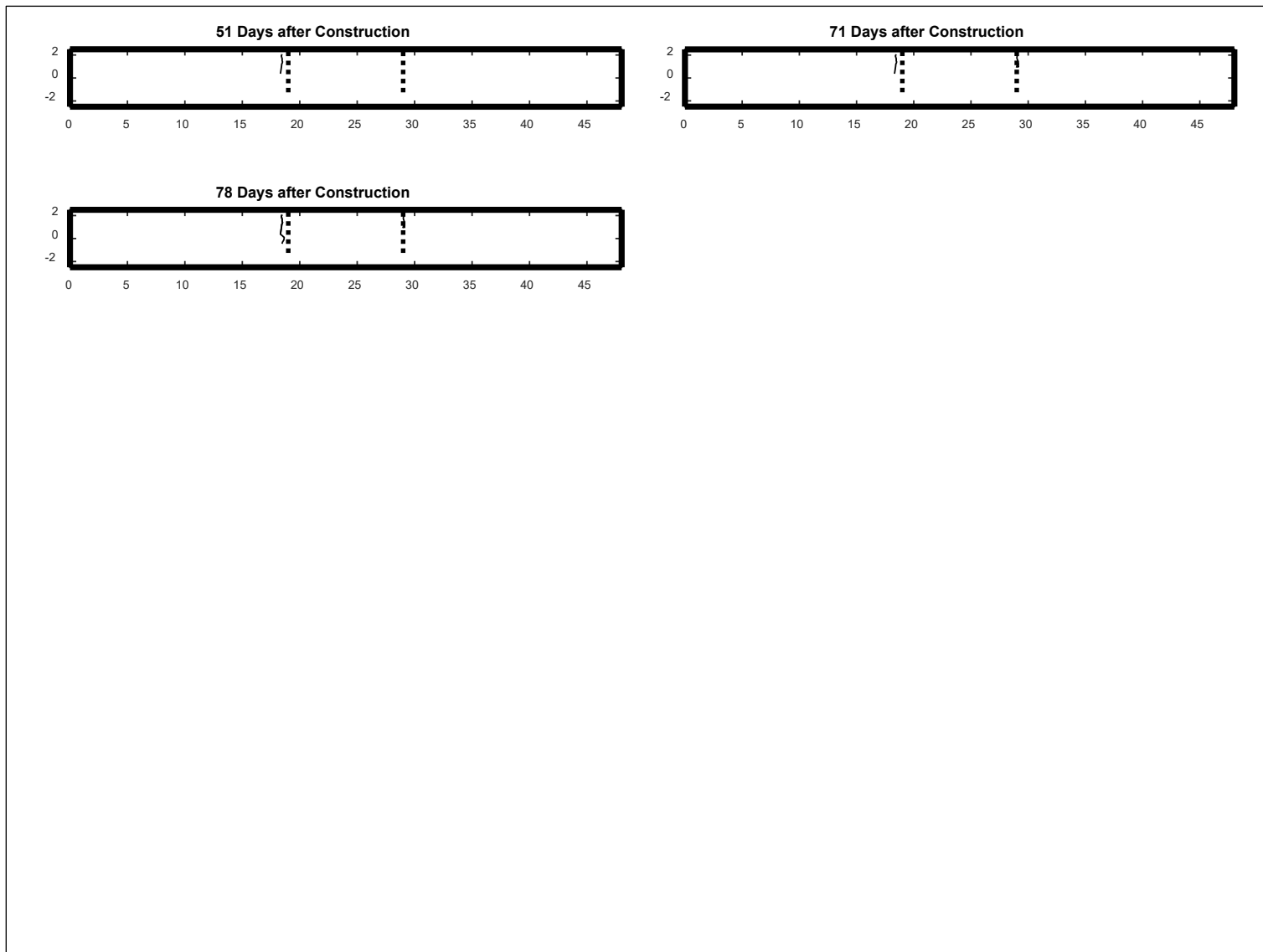

Figure B.196: Cell S25: Change in crack density.
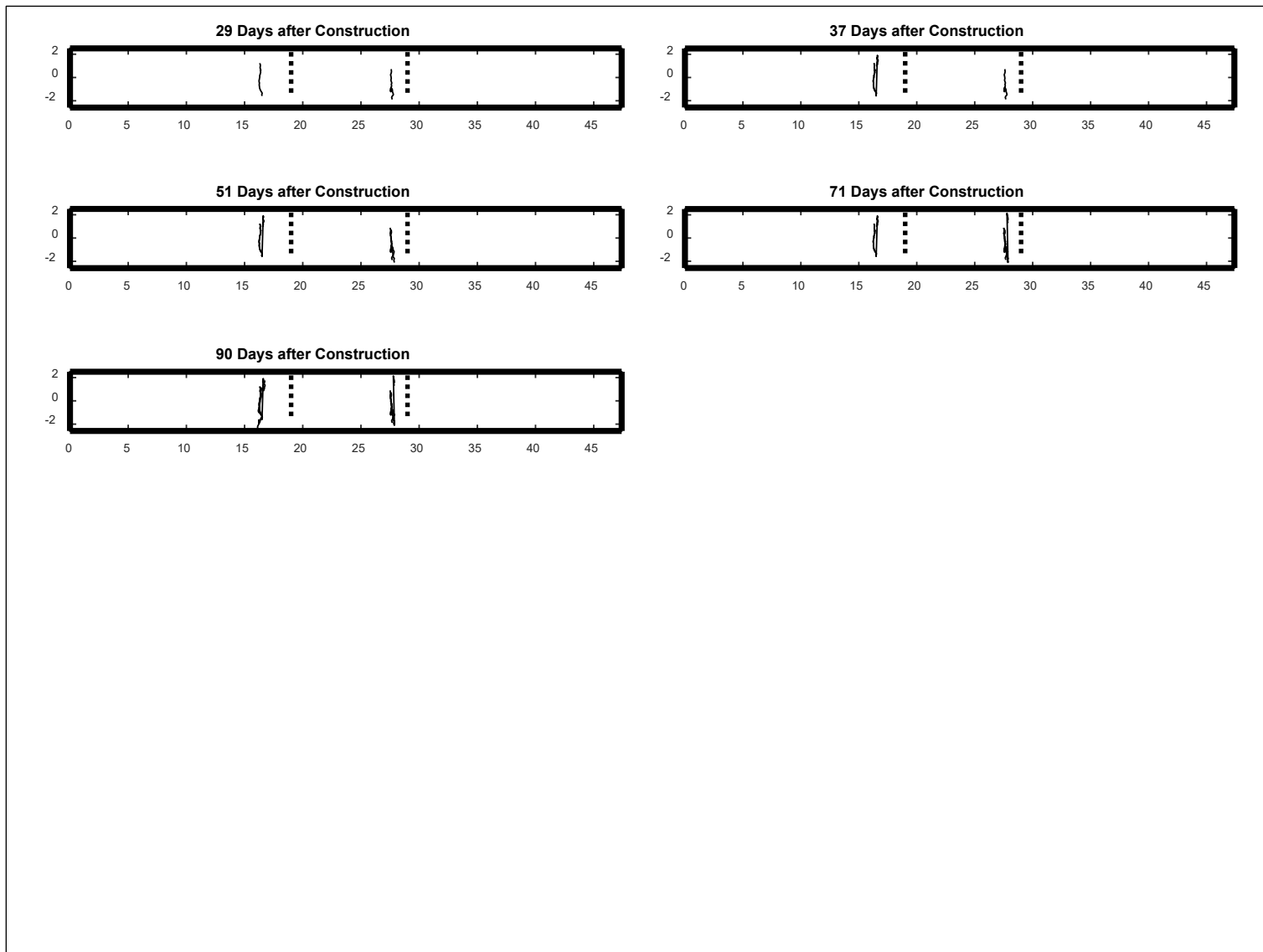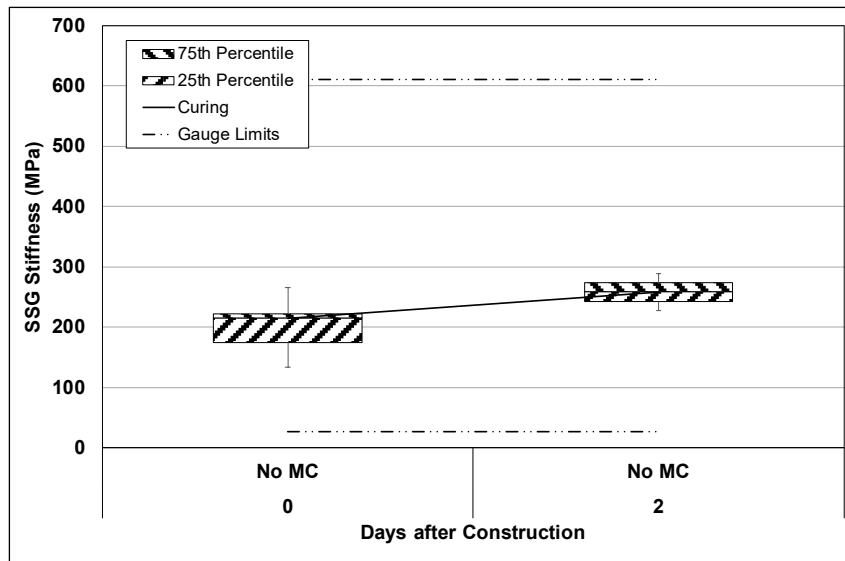
Figure B.197: Cell S25: Crack development.
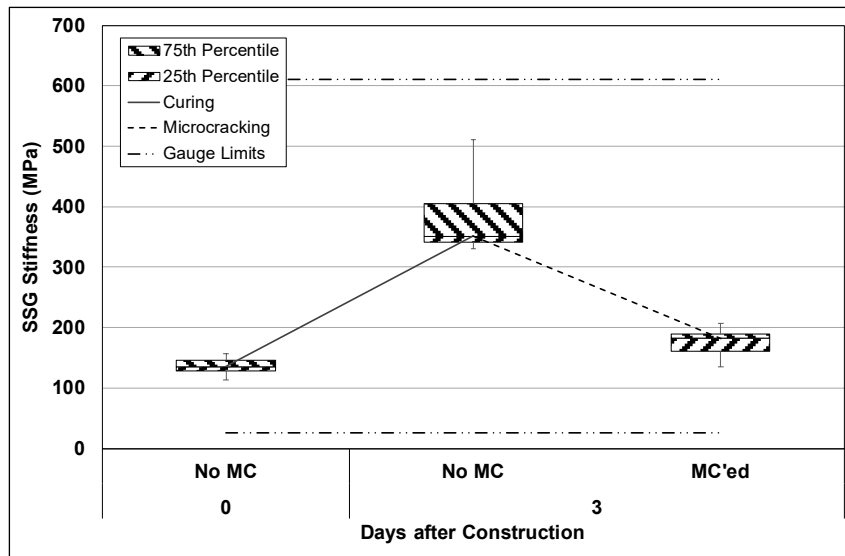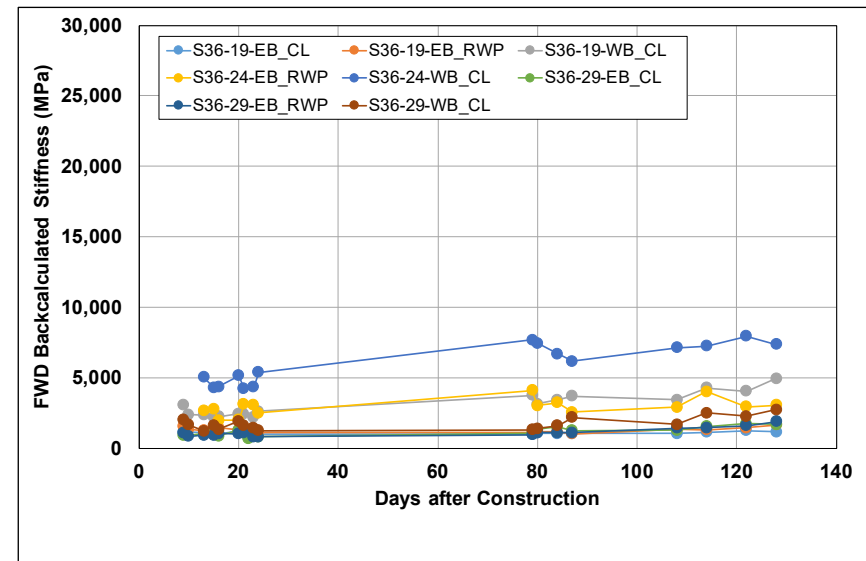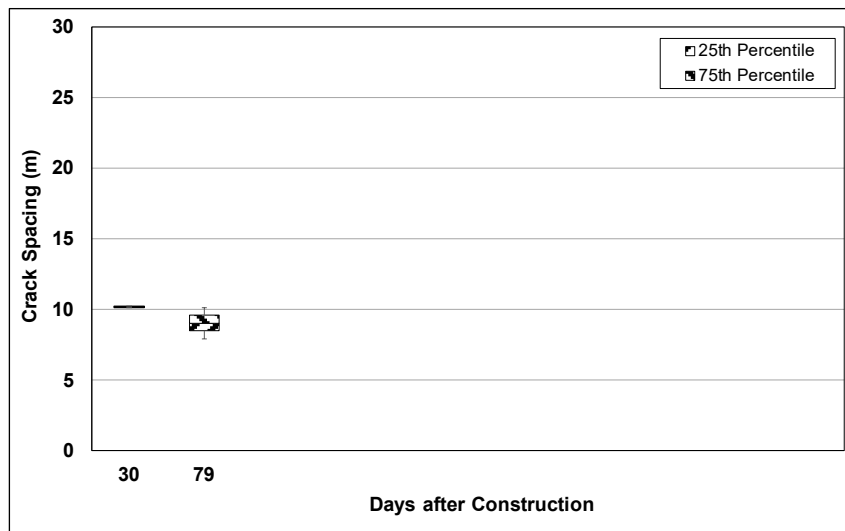
Figure B.198: Cell S26: SSG measured stiffness.

Figure B.199: Cell S26: SSG stiffness results per gauge.

Figure B.200: Cell S26: SSG stiffness reduction per station.

Figure B.201: Cell S26: LWD measured surface modulus.

Figure B.202: Cell S26: LWD modulus reduction per station.

Figure B.203: Cell S26: Change in FWD-backcalculated stiffness.

Figure B.204: Cell S27: SSG measured stiffness.

Figure B.205: Cell S27: SSG stiffness results per gauge.

Figure B.206: Cell S27: SSG stiffness reduction per station.

Figure B.207: Cell S27: LWD measured surface modulus.

Figure B.208: Cell S27: LWD modulus reduction per station.

Figure B.209: Cell S27: Change in FWD-backcalculated stiffness.

Figure B.210: Cell S28: SSG measured stiffness.

Figure B.211: Cell S28: Change in FWD-backcalculated stiffness.


Figure B.212: Cell S28: Change in crack spacing.
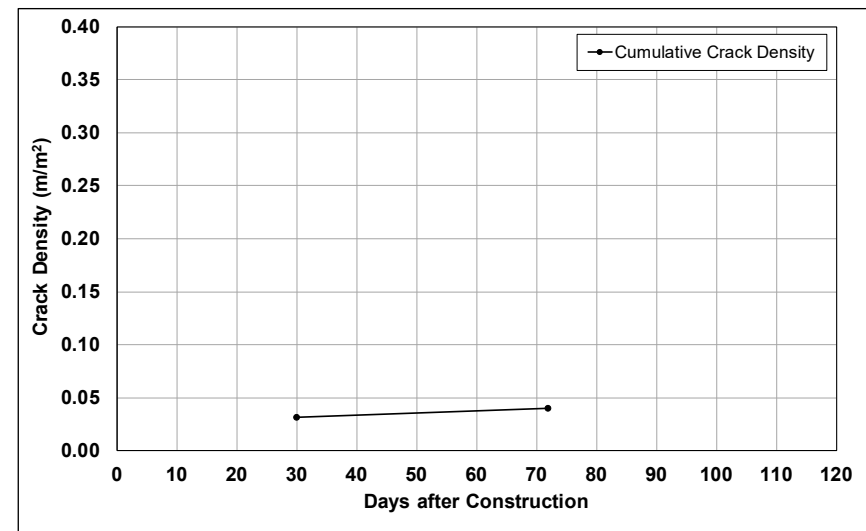

Figure B.213: Cell S28: Change in crack density.
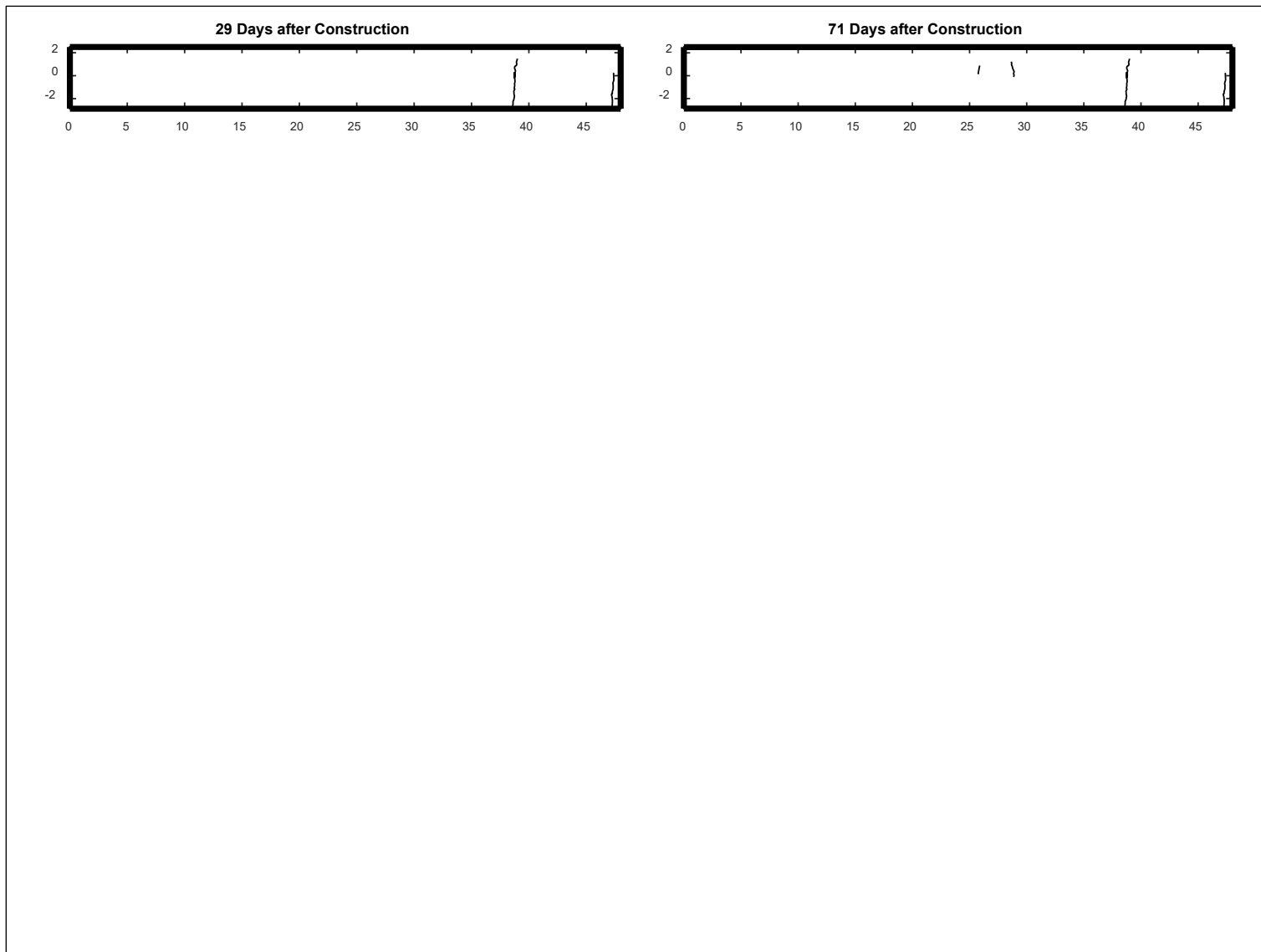
Figure B.214: Cell S28: Crack development.
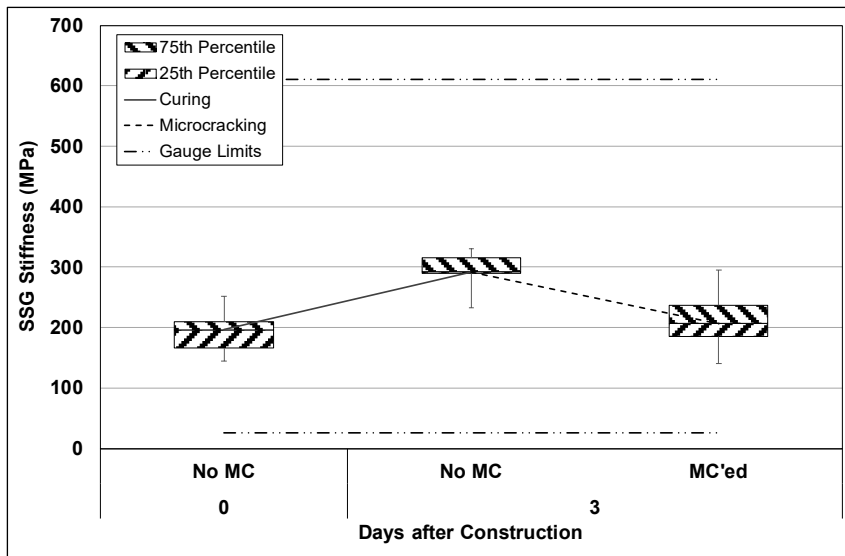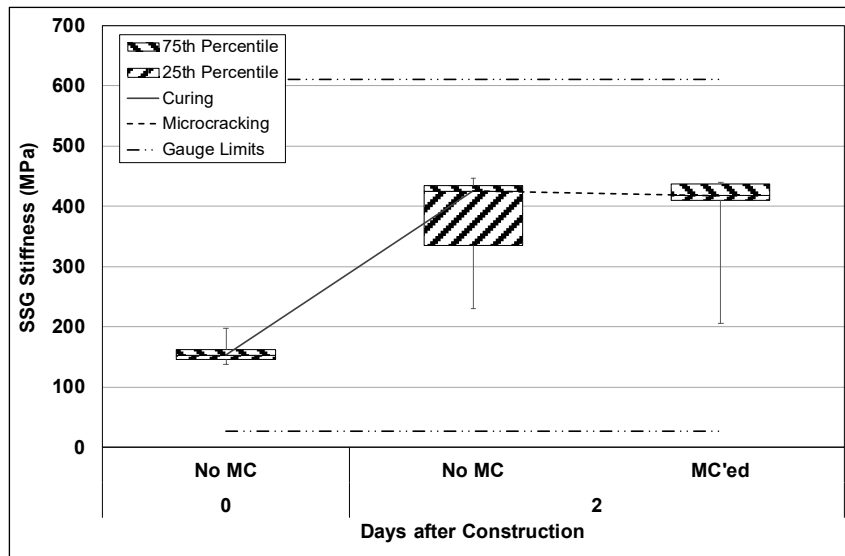
**Figure B.215: Cell S29: SSG measured stiffness.**
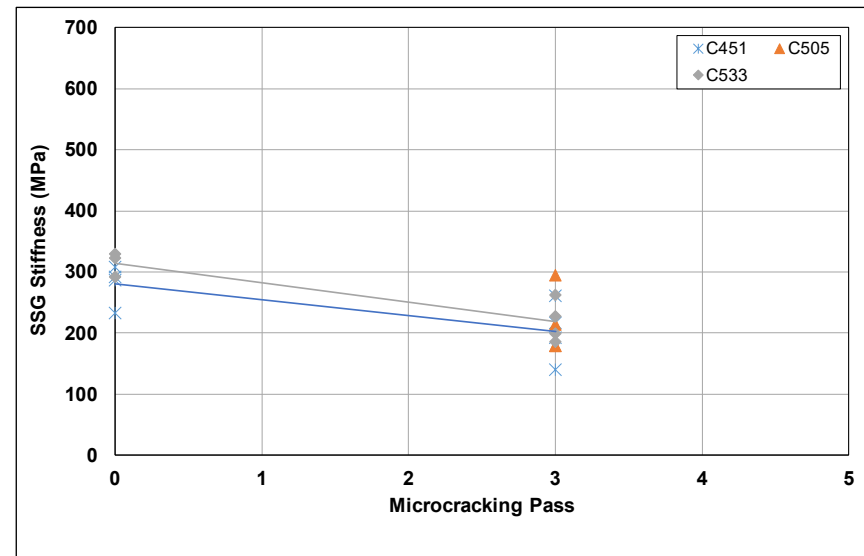
**Figure B.216: Cell S29: SSG stiffness results per gauge.**

Figure B.217: Cell S29: SSG stiffness reduction per station.

Figure B.218: Cell S29: LWD measured surface modulus.

Figure B.219: Cell S29: LWD modulus reduction per station.

Figure B.220: Cell S29: Change in FWD-backcalculated stiffness.
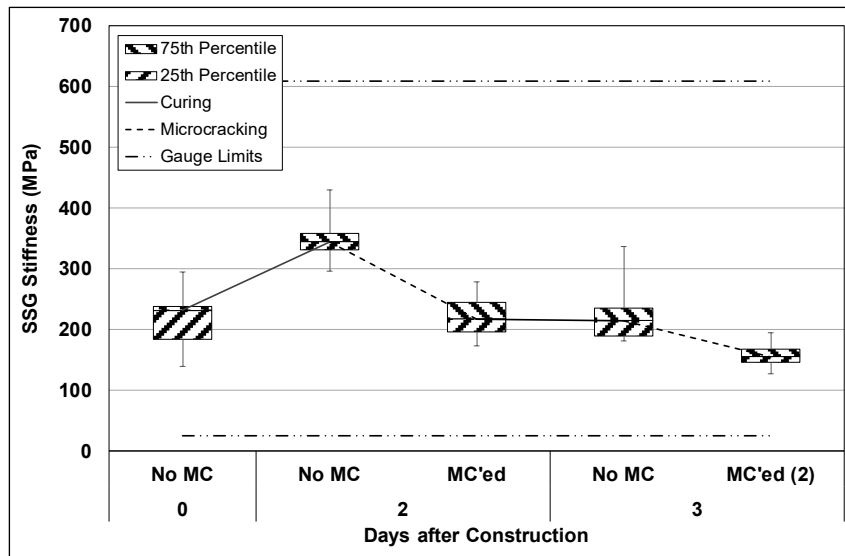
Figure B.221: Cell S30: SSG measured stiffness.
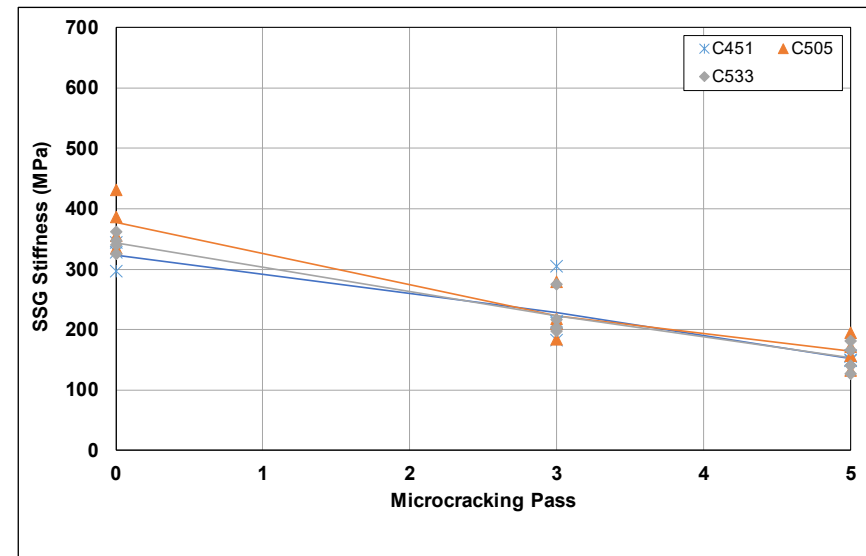
Figure B.222: Cell S30: SSG stiffness results per gauge.

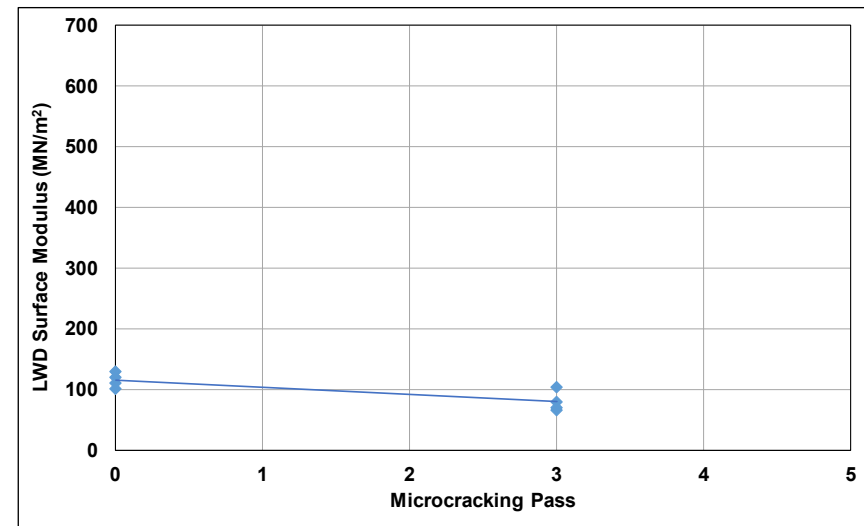**Figure B.223: Cell S30: SSG stiffness reduction per station.**

**Figure B.224: Cell S30: LWD measured surface modulus.**

Figure B.225: Cell S30: LWD modulus reduction per station.

Figure B.226: Cell S30: Change in FWD-backcalculated stiffness.

Figure B.227: Cell S30: Change in crack spacing.
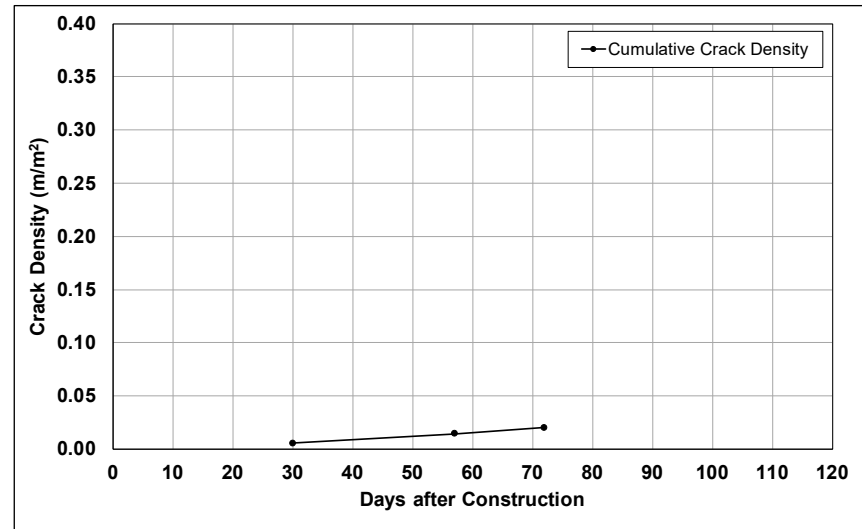
Figure B.228: Cell S30: Change in crack density.
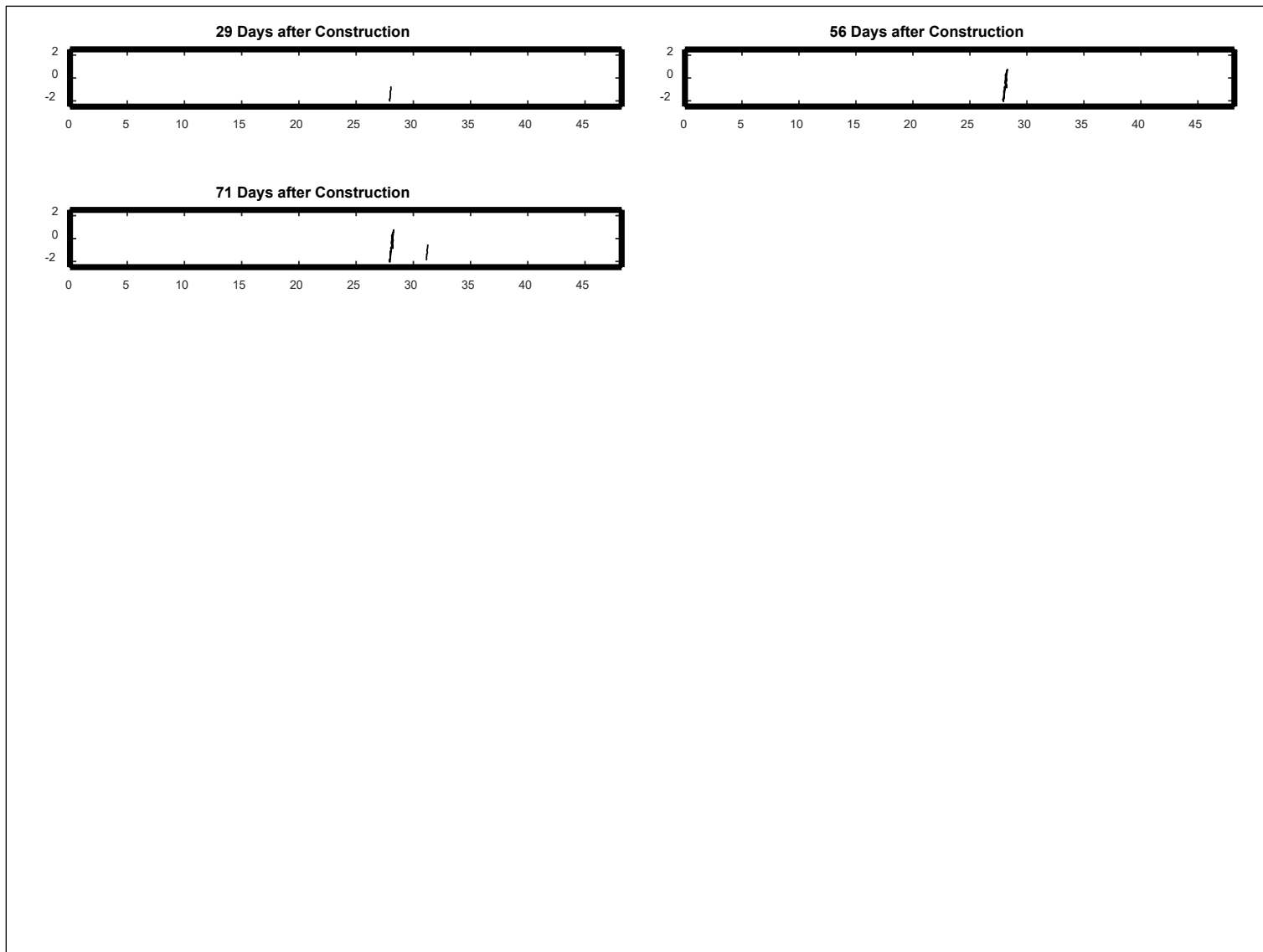
Figure B.229: Cell S30: Crack development.
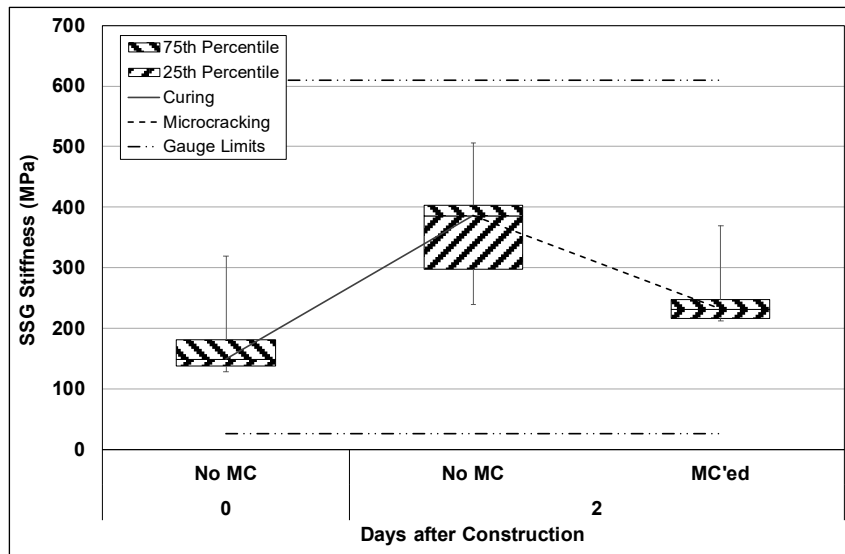
Figure B.230: Cell S31: SSG measured stiffness.

Figure B.231: Cell S31: SSG stiffness results per gauge.

Figure B.232: Cell S31: SSG stiffness reduction per station.

Figure B.233: Cell S31: LWD measured surface modulus.

**Figure B.234: Cell S31: LWD modulus reduction per station.**

Figure B.235: Cell S31: Change in FWD-backcalculated stiffness.

Figure B.236: Cell S32: SSG measured stiffness.

Figure B.237: Cell S32: SSG stiffness results per gauge.

Figure B.238: Cell S32: SSG stiffness reduction per station.

Figure B.239: Cell S32: LWD measured surface modulus.

Figure B.240: Cell S32: LWD modulus reduction per station.

Figure B.241: Cell S32: Change in FWD-backcalculated stiffness.

Figure B.242: Cell S33: SSG measured stiffness.

Figure B.243: Cell S33: Change in FWD-backcalculated stiffness.

Figure B.244: Cell S33: Change in crack spacing.
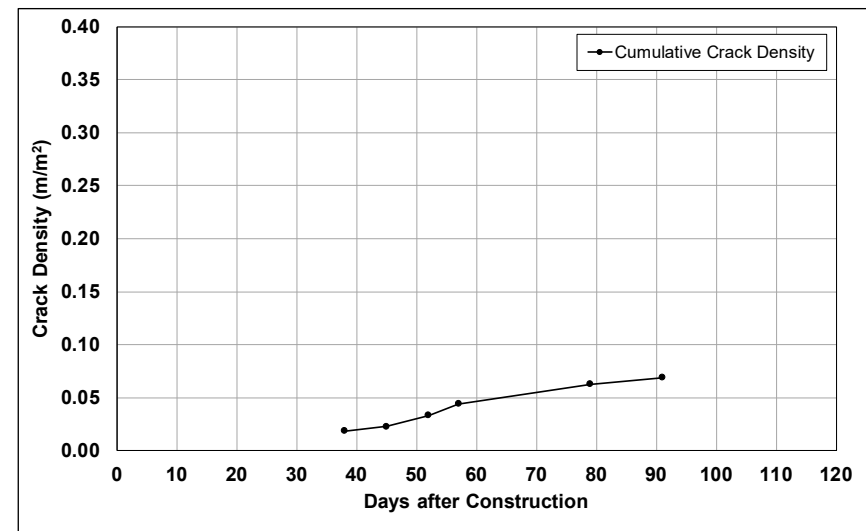
Figure B.245: Cell S33: Change in crack density.

Figure B.246: Cell S33: Crack development.

Figure B.247: Cell S34: SSG measured stiffness.

Figure B.248: Cell S34: SSG stiffness results per gauge.

Figure B.249: Cell S34: SSG stiffness reduction per station.

Figure B.250: Cell S34: LWD measured surface modulus.

Figure B.251: Cell S34: LWD modulus reduction per station.

Figure B.252: Cell S34: Change in FWD-backcalculated stiffness.

Figure B.253: Cell S34: Change in crack spacing.
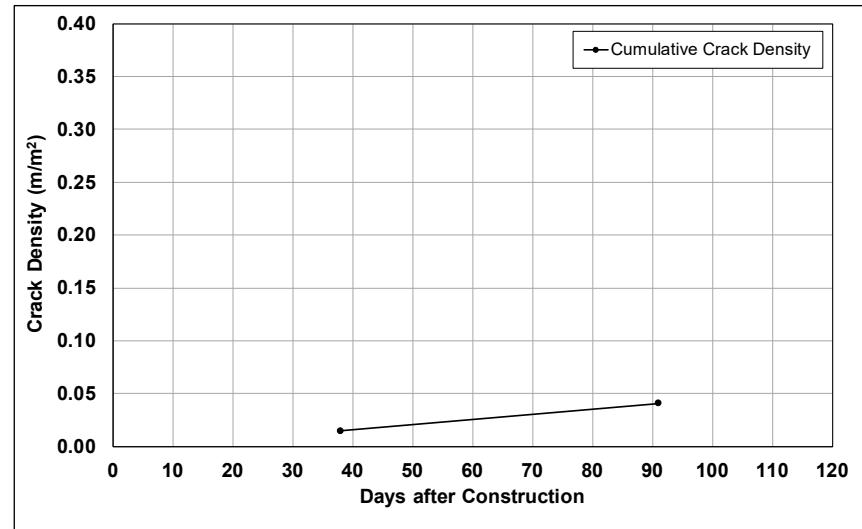
Figure B.254: Cell S34: Change in crack density.
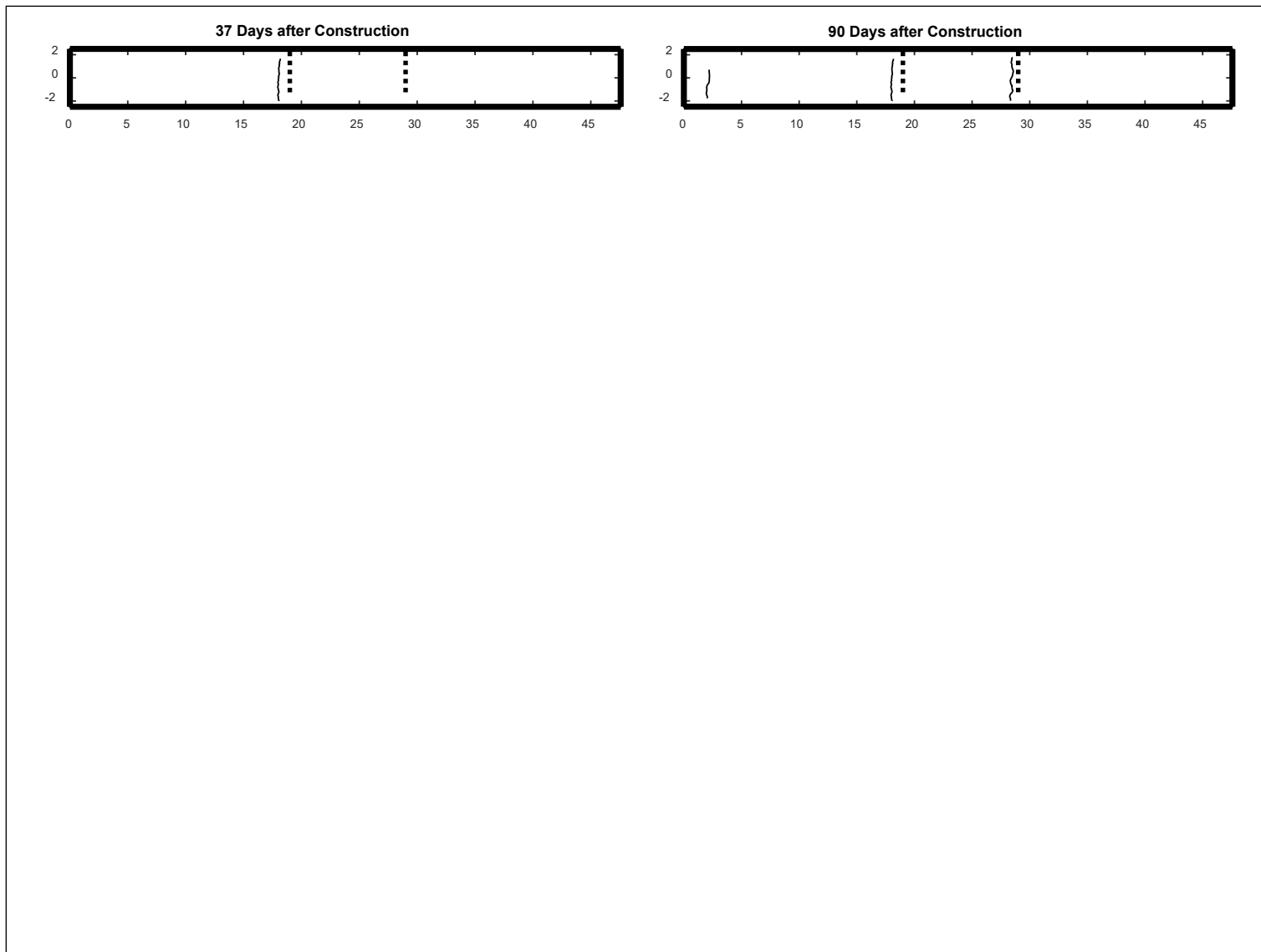
Figure B.255: Cell S34: Crack development.

Figure B.256: Cell S35: SSG measured stiffness.

Figure B.257: Cell S35: SSG stiffness results per gauge.
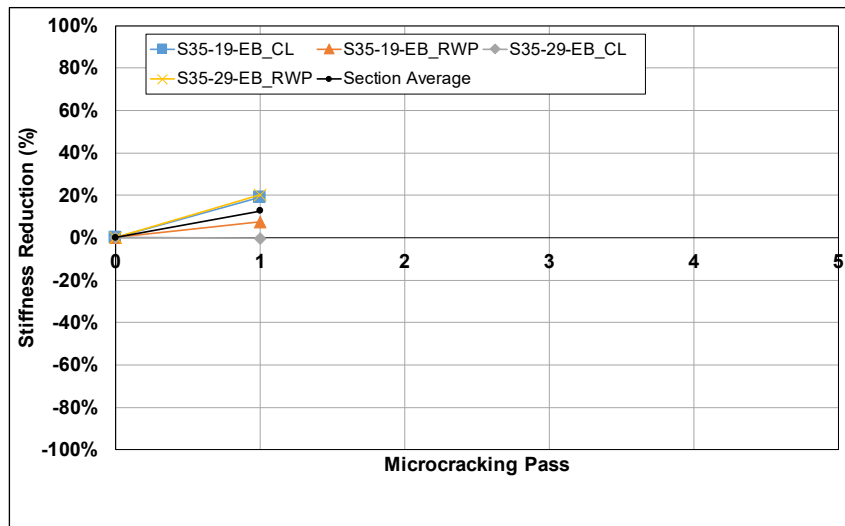
Figure B.258: Cell S35: SSG stiffness reduction per station.

Figure B.259: Cell S35: LWD measured surface modulus.
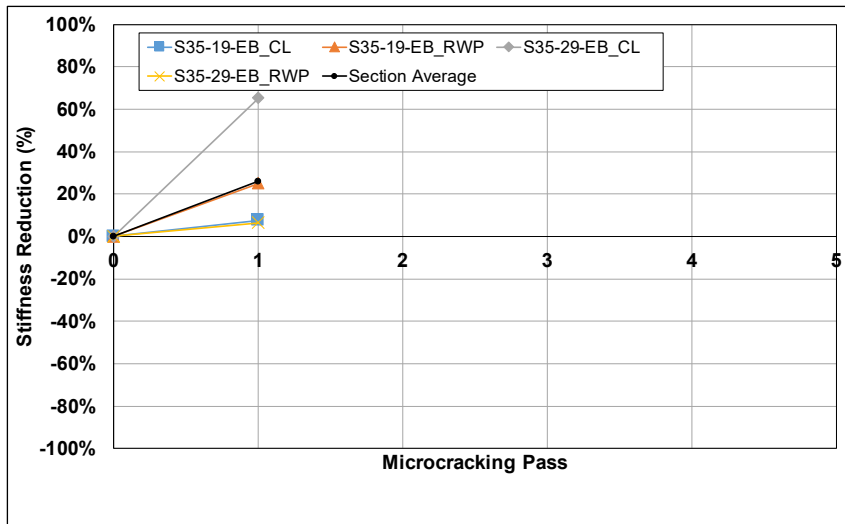
Figure B.260: Cell S35: LWD modulus reduction per station.

Figure B.261: Cell S35: Change in FWD-backcalculated stiffness.

Figure B.262: Cell S35: Change in crack spacing.

Figure B.263: Cell S35: Change in crack density.

Figure B.264: Cell S35: Crack development.

Figure B.265: Cell S36: SSG measured stiffness.

Figure B.266: Cell S36: Change in FWD-backcalculated stiffness.

Figure B.267: Cell S36: Change in crack spacing.
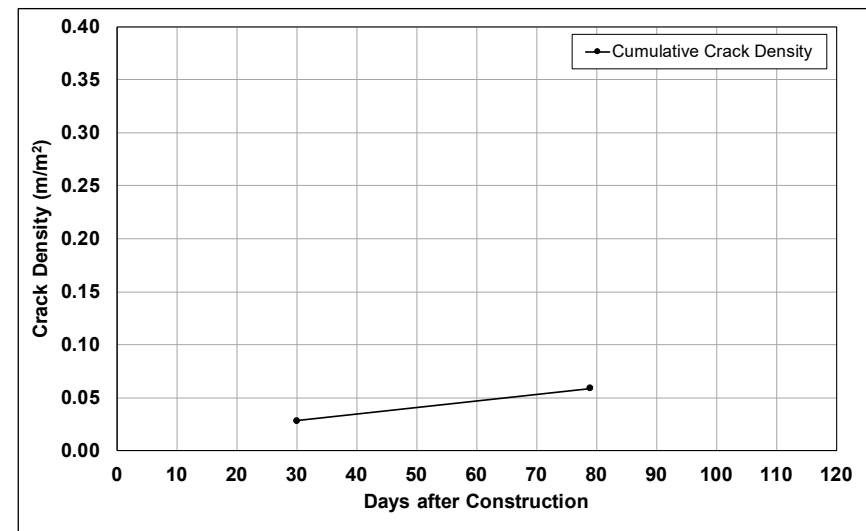
Figure B.268: Cell S36: Change in crack density.
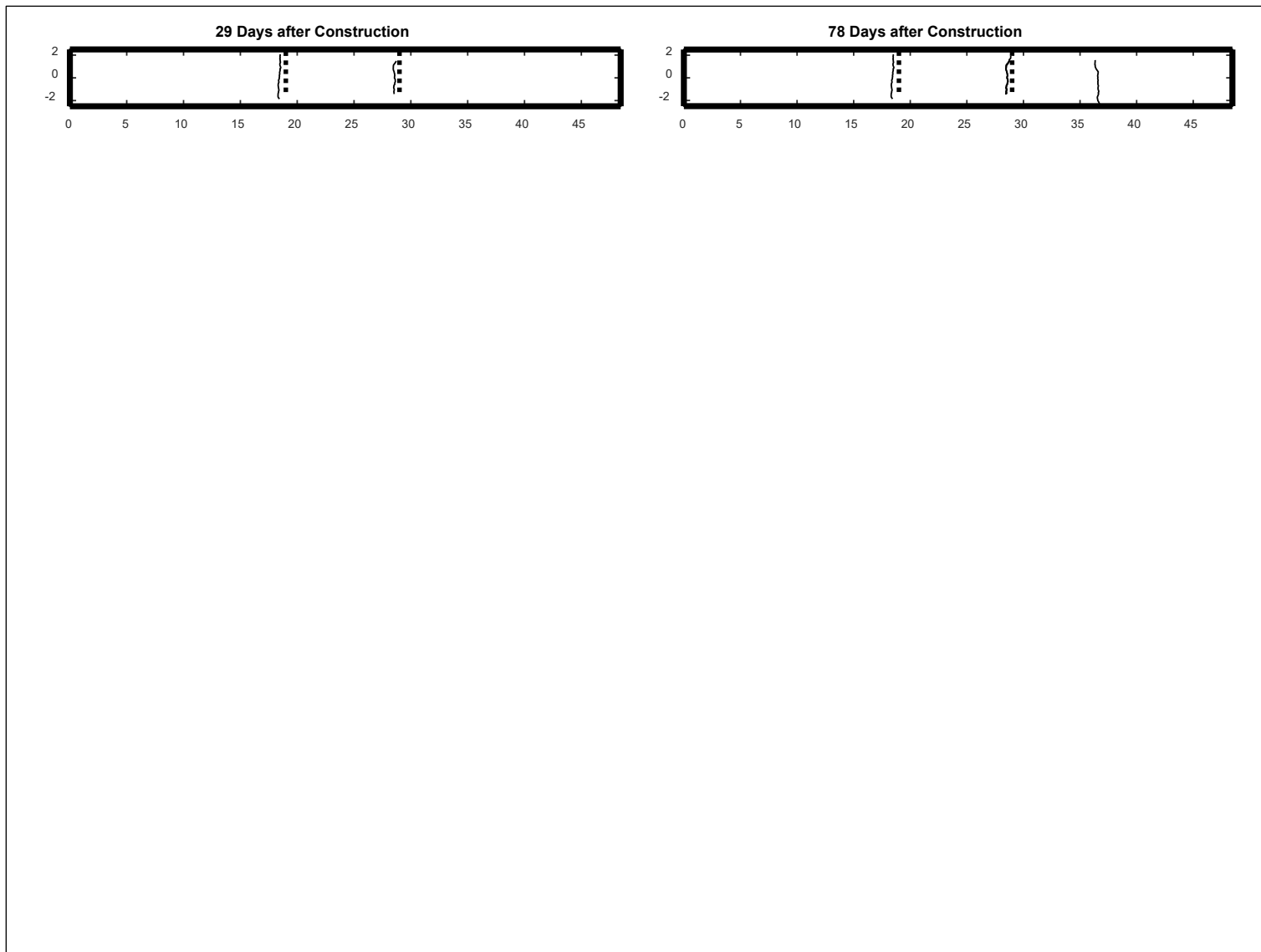
Figure B.269: Cell S36: Crack development.

Figure B.270: Cell S37: SSG measured stiffness.
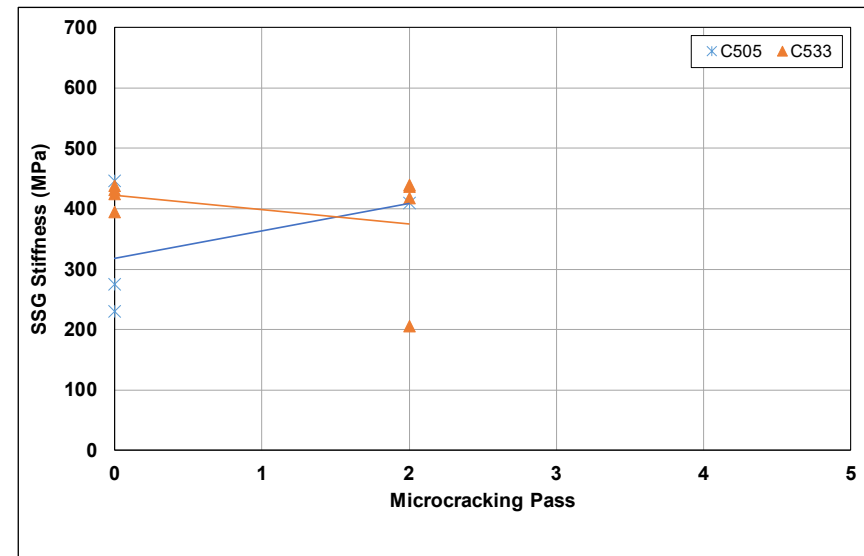
Figure B.271: Cell S37: SSG stiffness results per gauge.
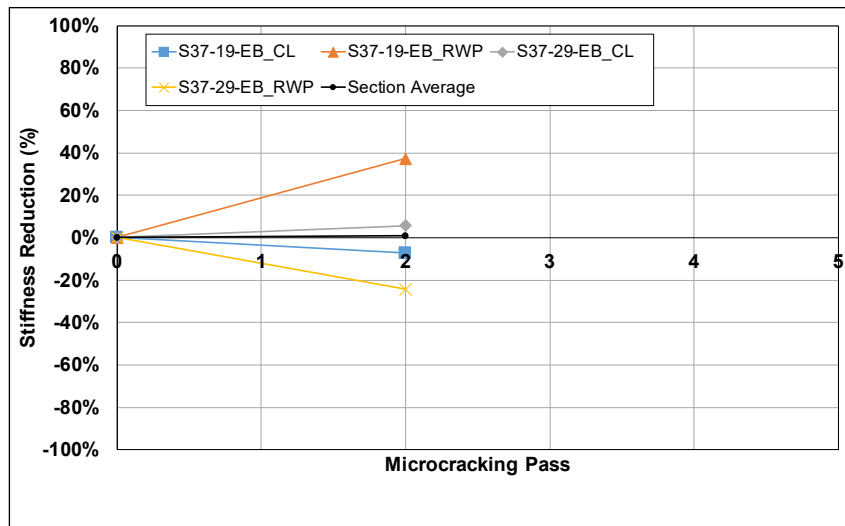
Figure B.272: Cell S37: SSG stiffness reduction per station.

Figure B.273: Cell S37: LWD measured surface modulus.
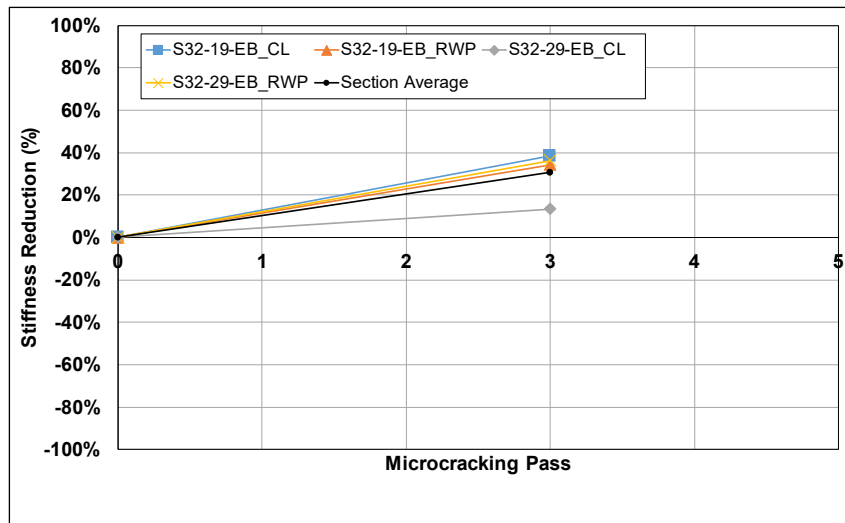
Figure B.274: Cell S37: LWD modulus reduction per station.
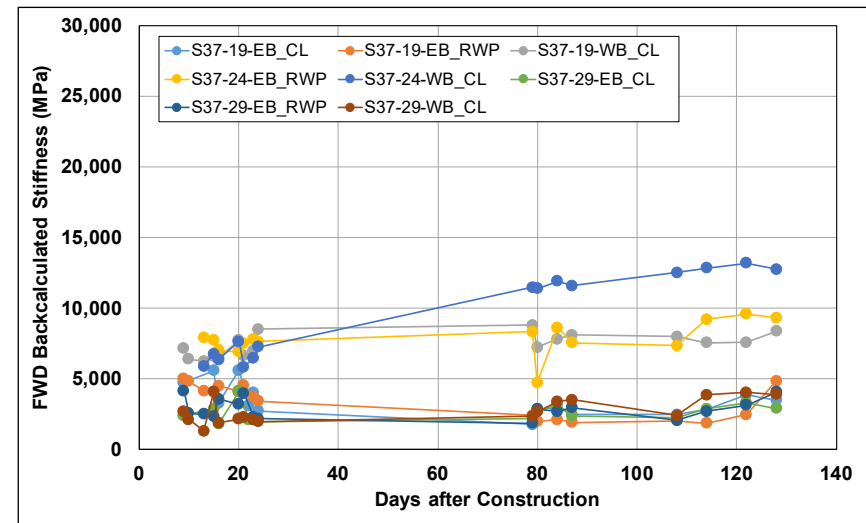
Figure B.275: Cell S37: Change in FWD-backcalculated stiffness.

APPENDIX°C: SOIL STIFFNESS GAUGE RESULTS USED IN ASSESSMENT FACTORS

The average stiffness reduction results in terms of the experiment factorial are plotted in Figure C.1 through Figure C.22 for all stations, measured during microcracking with the soil stiffness gauges. The results include all the data collected on all sections during microcracking, including the results per pass on the relevant sections. Factors assessed include effect of:

- Curing time prior to microcracking (Figure C.1 through Figure C.6)
- Roller weight (Figure C.7 through Figure C.10)
- Vibration amplitude (Figure C.11 through Figure C.14)
- Cement content (Figure C.15 through Figure C.20)
- Microcracking effort (Figure C.21 through Figure C.22)
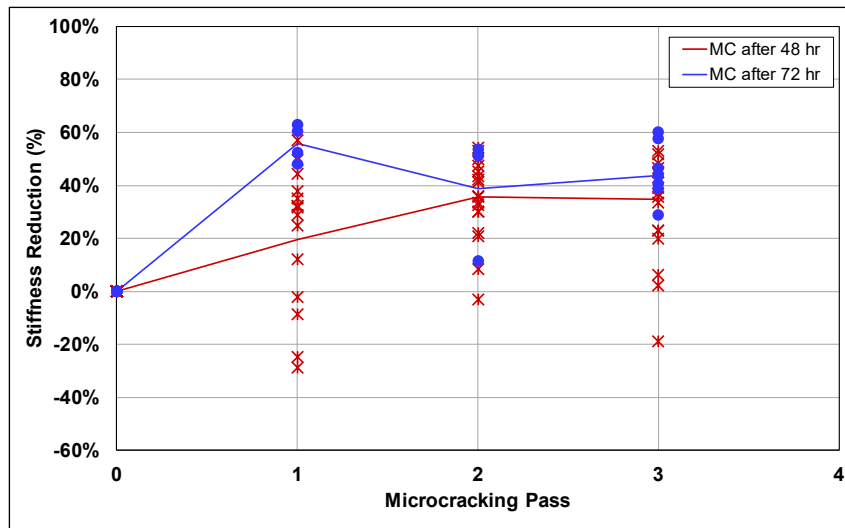
Figure C.1: 2.5% Cement: SSR with high vibration amplitude.
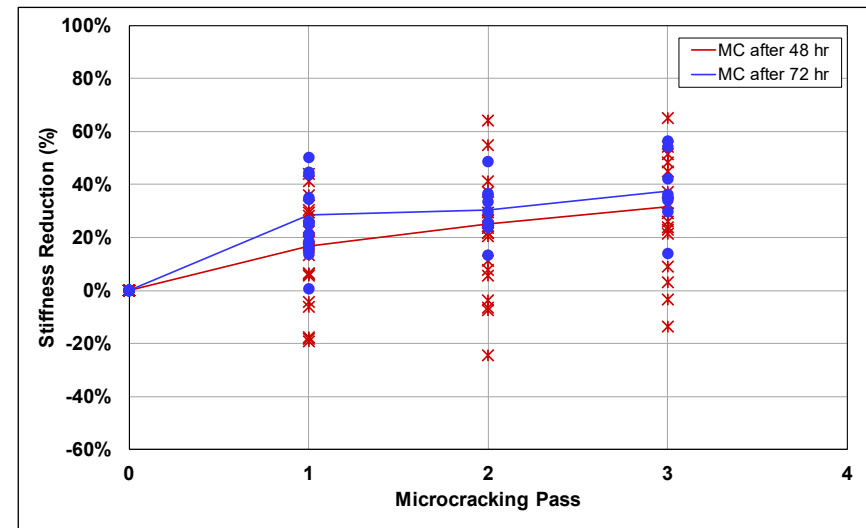
Figure C.2: 4% Cement: SSR with high vibration amplitude.
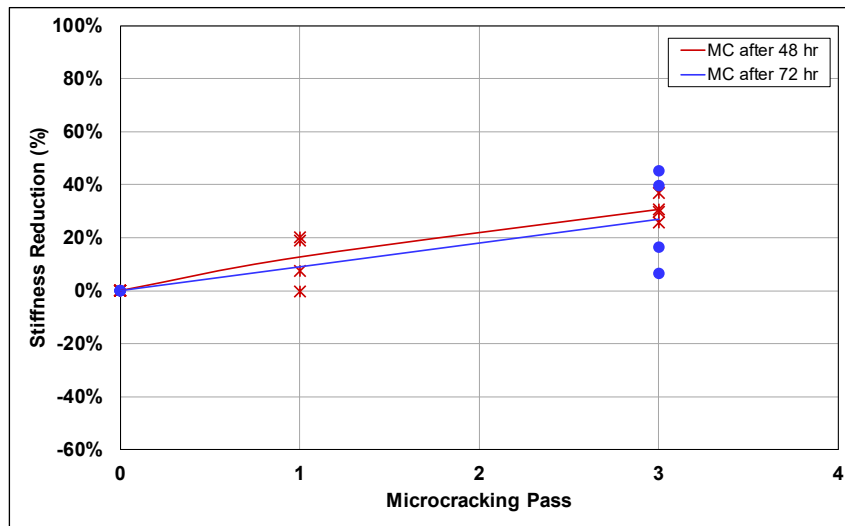
Figure C.3: 2.5% Cement: SSR with low vibration amplitude.
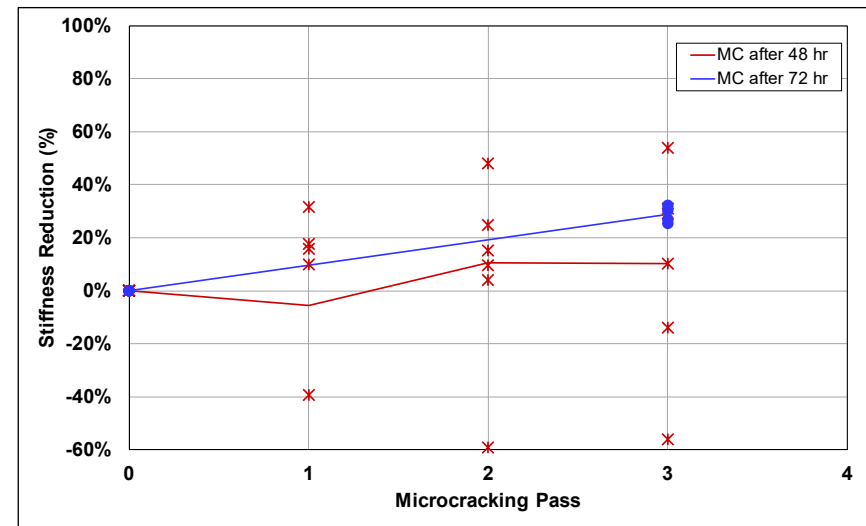
Figure C.4: 4% Cement: SSR with low vibration amplitude.
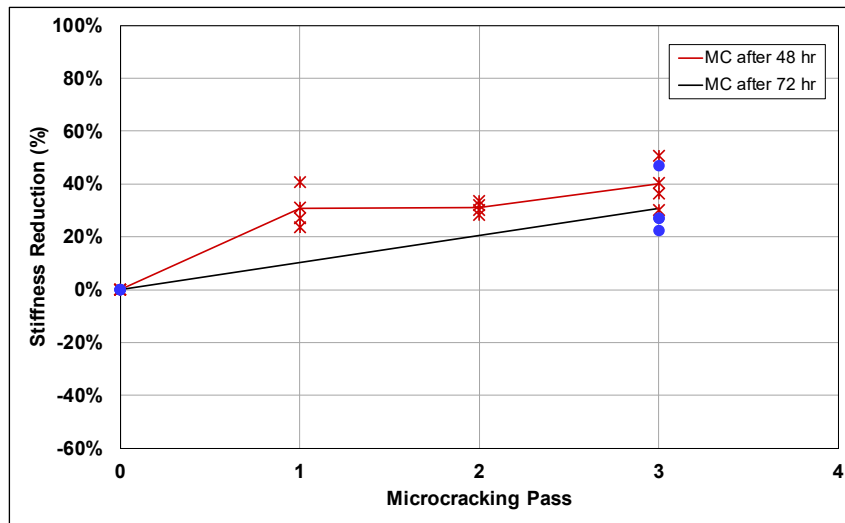
Figure C.5: 2.5% Cement: DSR with high vibration amplitude.
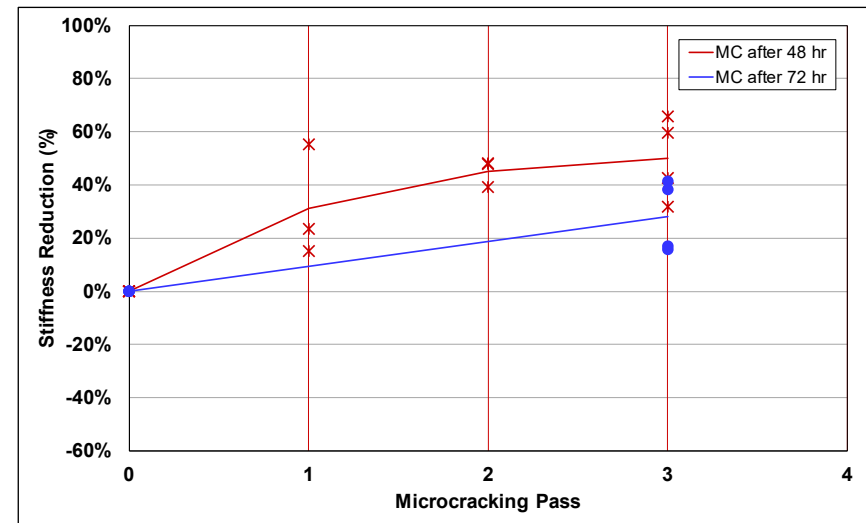
Figure C.6: 4% Cement: DSR with high vibration amplitude.
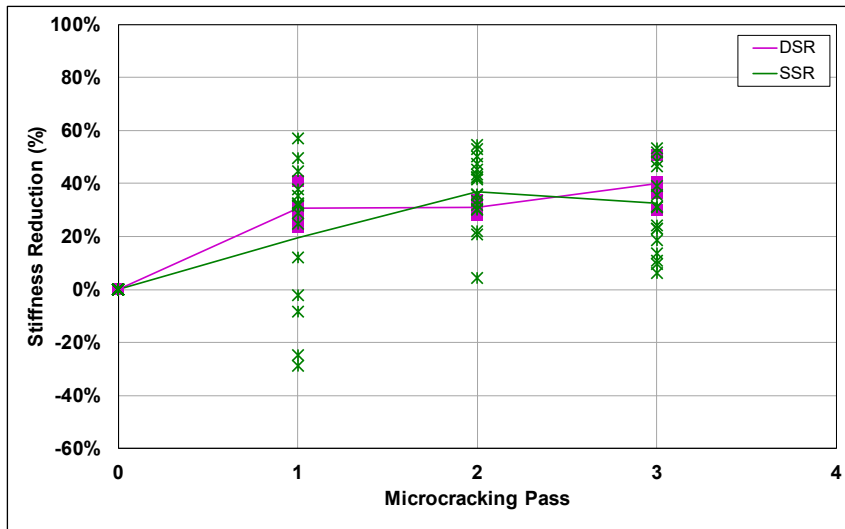
Figure C.7: 2.5% Cement: High vibration amplitude after 48 hours.
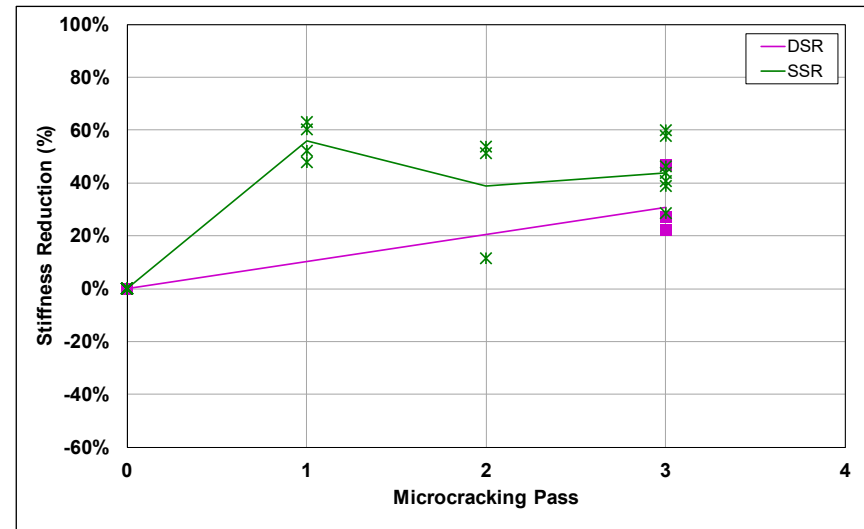
Figure C.8: 2.5% Cement: High vibration amplitude after 72 hours.
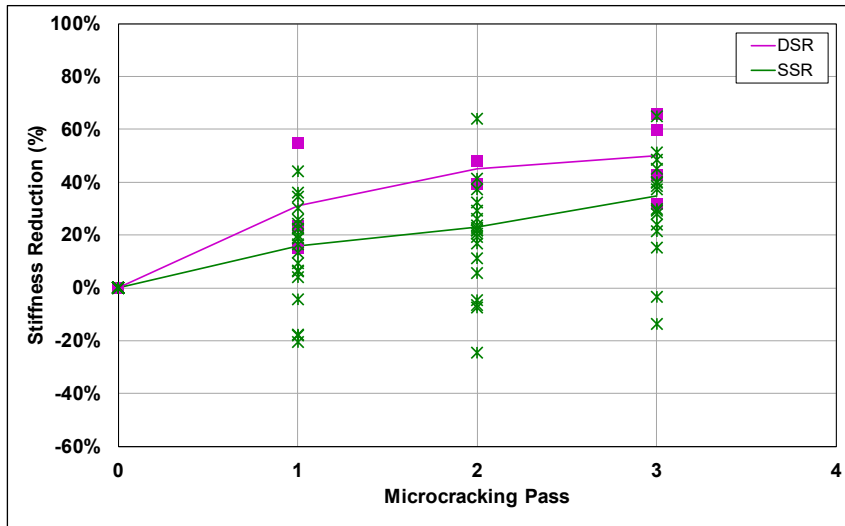
Figure C.9: 4% Cement: High vibration amplitude after 48 hours.
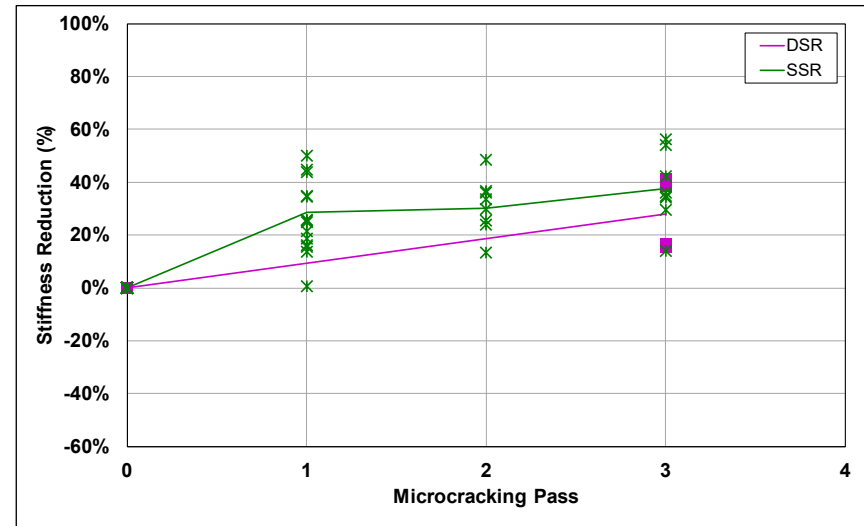
Figure C.10: 4% Cement: High vibration amplitude after 72 hours.
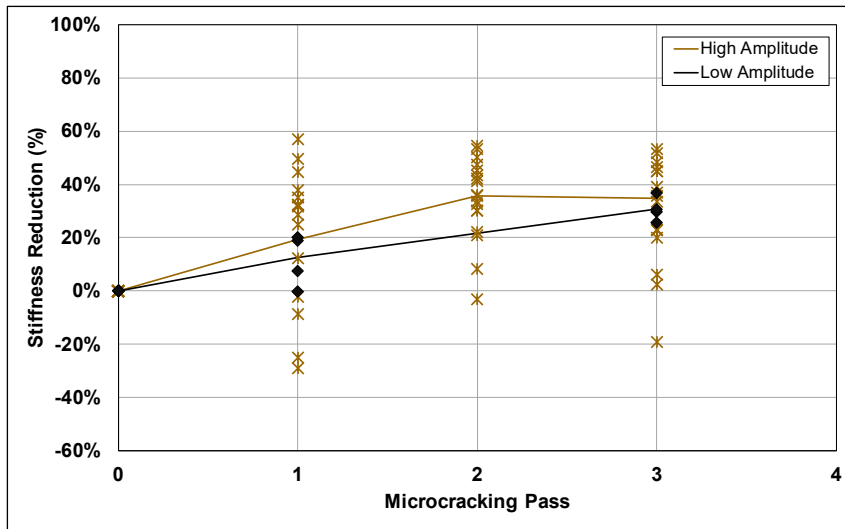
Figure C.11: 2.5% Cement: SSR vibration amplitudes after 48 hours.
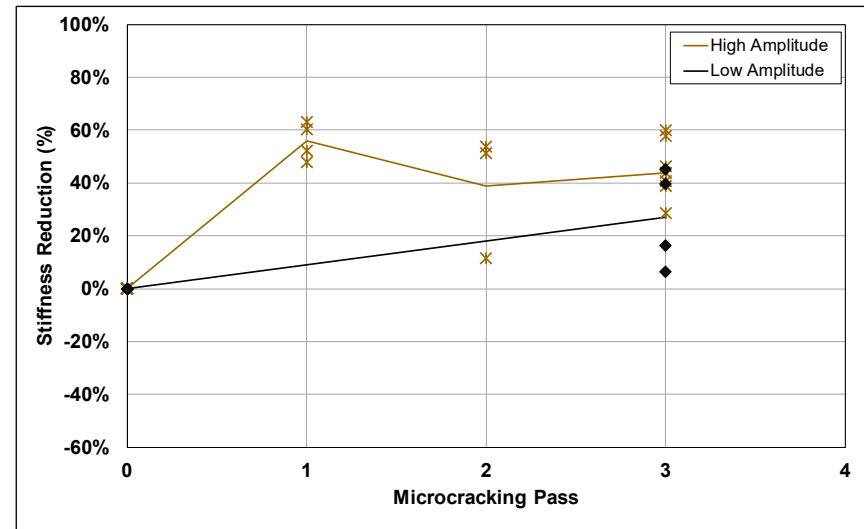
Figure C.12: 2.5% Cement: SSR vibration amplitudes after 72 hours.
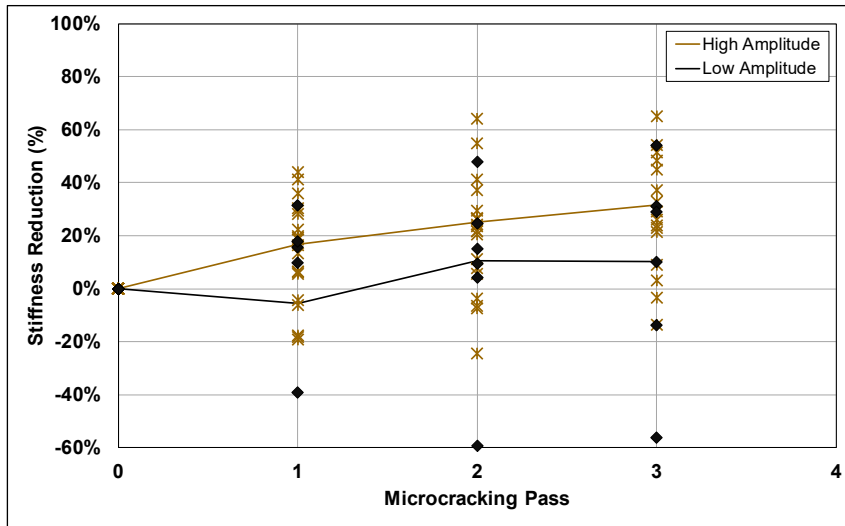
Figure C.13: 4% Cement: SSR vibration amplitudes after 48 hours.
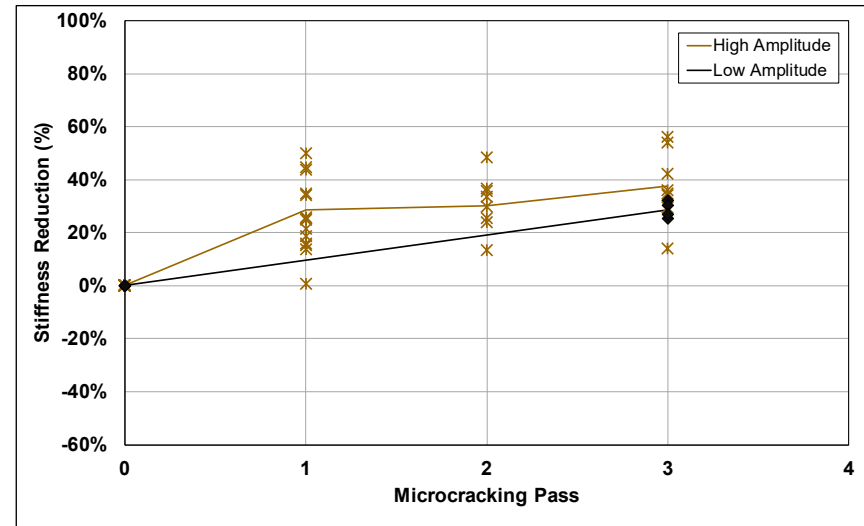
Figure C.14: 4% Cement: SSR vibration amplitudes after 72 hours.
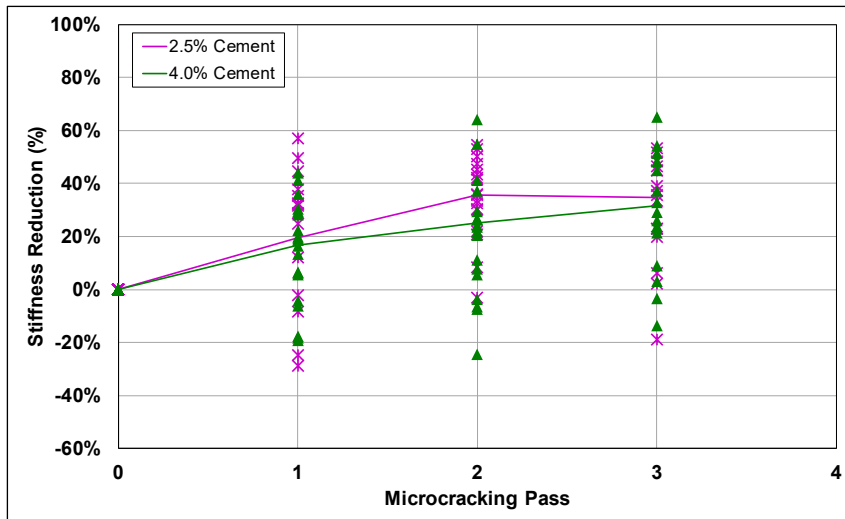
Figure C.15: Stiffness reduction with SSR at high amplitude after 48 hours.
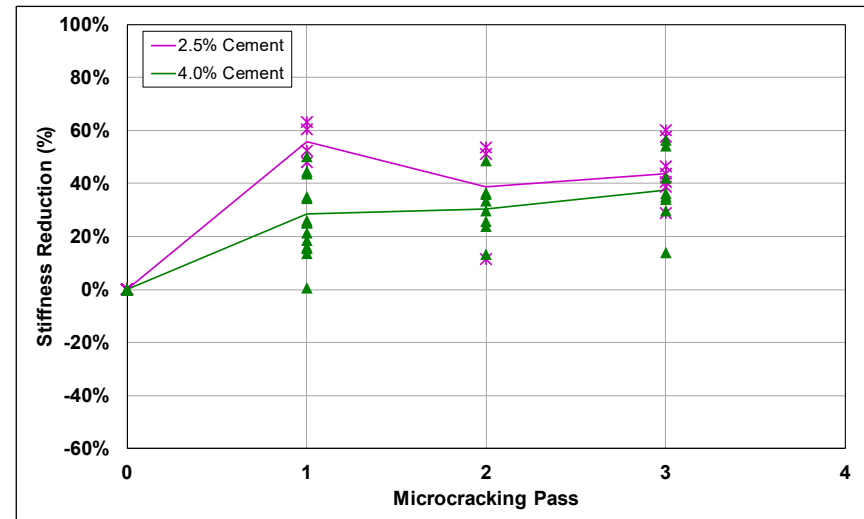
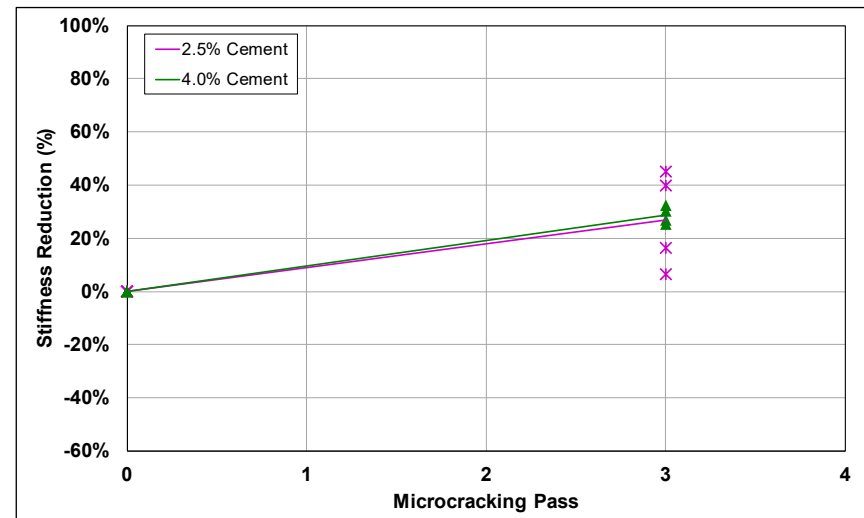**Figure C.16: Stiffness reduction with SSR at high amplitude after 72 hours.**
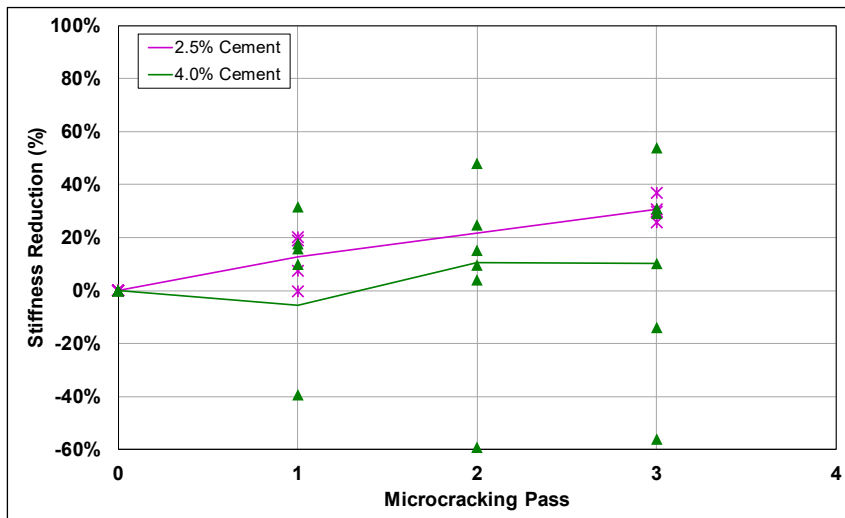
Figure C.17: Stiffness reduction with SSR at low amplitude after 48 hours.

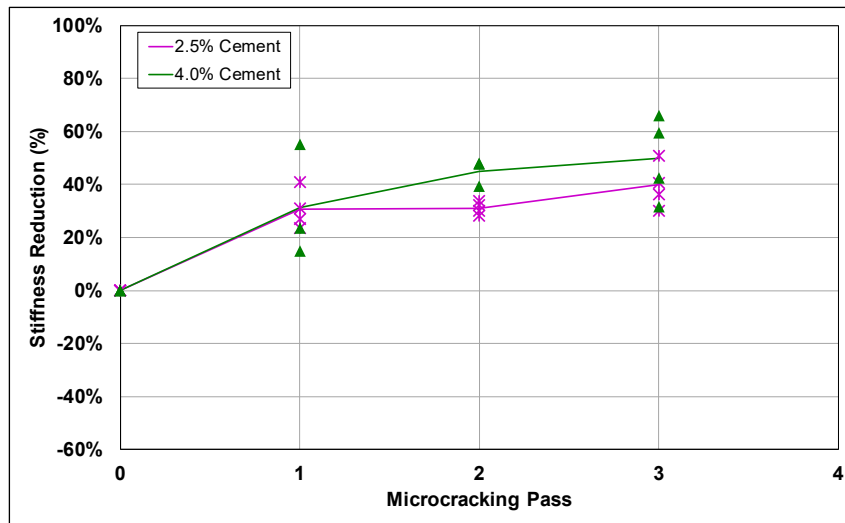**Figure C.18: Stiffness reduction with SSR at low amplitude after 72 hours.**

Figure C.19: Stiffness reduction with DSR at high amplitude after 48 hours.
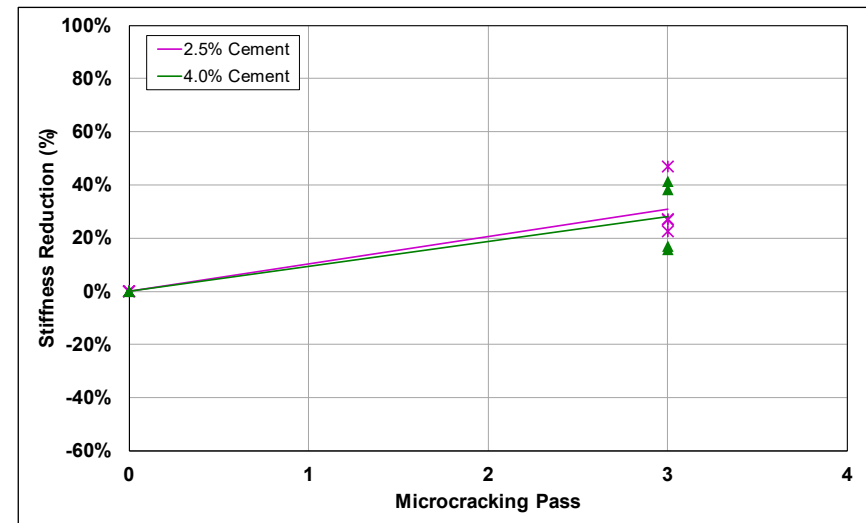

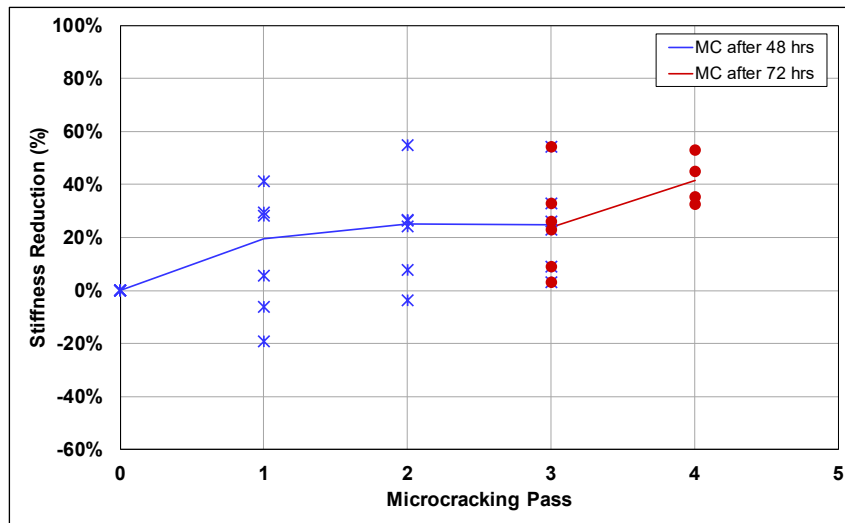**Figure C.20: Stiffness reduction with DSR at high amplitude after 72 hours.**

Figure C.21: 2.5% Cement: Microcracking with SSR at high amplitude after both 48 and 72 hours.
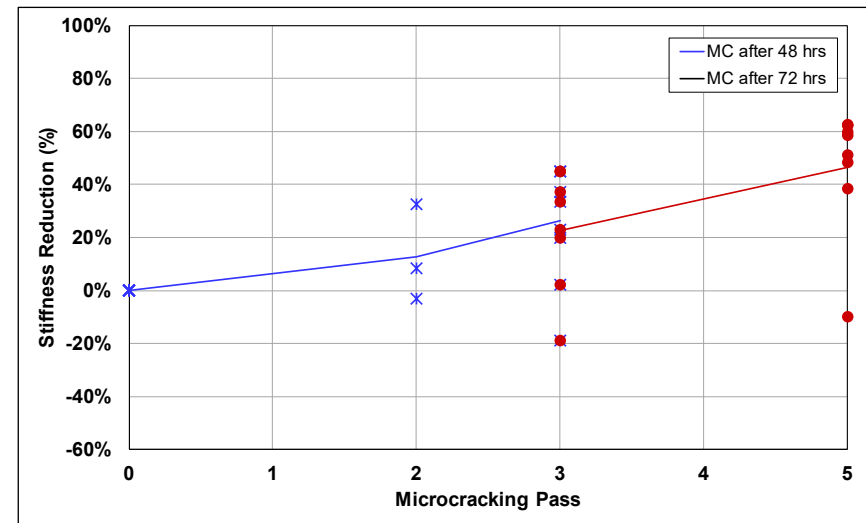

Figure C.22: 4% Cement: Microcracking with SSR at high amplitude after both 48 and 72 hours.